UNIVERSITY OF CALIFORNIA SAN DIEGO

Energy Autonomous Microgrids for Wearable Sensors and Fully Integrated Wearable Systems

A dissertation submitted in partial satisfaction of the requirements for the degree

Doctor of Philosophy

in

NanoEngineering

by

Lu Yin

Committee in charge:

Professor Joseph Wang, Chair
Professor Jinhye Bae
Professor Renkun Chen
Professor Tse Na Ng
Professor Sheng Xu

2022

The dissertation of Lu Yin is approved, and it is acceptable in quality and form for publication on microfilm and electronically.

University of California San Diego

2022

DEDICATION

To my family, who supported me unconditionally.

And to my mentors, who guided me wholeheartedly.

EPIGRAPH

知者不博，博者不知。

Translation – The wise does not know extensively,
The one learns extensively does not know.

- Tao Te Ching, Laozi

TABLE OF CONTENTS

LIST OF FIGURES

LIST OF TABLES

ACKNOWLEDGEMENTS

First and foremost, my deepest gratitude extends to my Ph.D. advisor Prof. Joseph Wang, who supported me with his constant encouragement, guidance, and unparalleled scientific enthusiasm throughout my Ph.D. life, while offering me the trust and freedom for me to explore, learn, and grow as a researcher, an innovator, and a leader. The opportunity to join your world-class research group as an undergraduate student has changed my life, and none of my achievements since then would be possible without you.

My most sincere thanks also go to Prof. Shirley Ying Meng and Prof. Sheng Xu, who are among the most talented and achieved young professors with a drive for excellence. Most of my research would not have been possible without learning from you and your research group. It has been a great pleasure to have multiple opportunities to collaborate with you and many of your students. I would also like to extend my thanks to my other committee members, Prof. Jinhye Bae, Prof. Tina Ng, and Prof. Renkun Chen who have been extremely helpful and supportive.

I would like to give special thanks to my coworkers, Dr. Rajan Kumar, Prof. Amay Bandodkar, Dr. Jian Lv, Dr. Aleksander Karajic, and Dr. Hazhir Teymourian, who shared their wisdom and taught me the way of doing research. I am also grateful to have the chance to give back and mentor undergraduate students who joined the lab just like me years ago, Lingye Xie, Xinyu Liu, Davina Joshuia, Jessica Ma, Viet Le, Jialu Yu, Ruixiao Liu, and Connor Wicker, who are voracious learners and devoted workers that I am proud of. I am also honored to share my journey with many whom I worked with closely, Prof. Itthipon Jeerapan, Dr. Julian Sempionatto, Dr. Kyeong Nam Kim, Dr. Jong-Min Moon, Dr. Wanxin Tang, Dr. Songsong Tang, Fangyu Zhang, Muyang Lin, Mengzhu Cao, Dr. Farshad Tehrani, Dr. Jonathan Scharf, Dr. Cristian Silva, and Dr.

Xiaohong Chen. Thank you for your hard work that has led to many fruitful collaborations with more to come. Thanks to the entire Nanobioelectronics (NBE) team, its alumni, and all my co-authors listed below. The work presented in this dissertation would not be possible without all of your contributions.

Chapter 1, in full, is a reprint of the material as it appears in Energy & Environmental Science, 2022, by Lu Yin, Kyeong Nam Kim, Alexander Trifonov, Tatiana Podhajny, and Joseph Wang. The dissertation author was the primary author of this paper.

Chapter 2, in full, is a reprint of the material as it appears in Joule, 2021, by Lu Yin, Jonathan Scharf, Jessica Ma, Jean-Marie Doux, Christopher Redquest, Viet L. Le, Yijie Yin, Jeff Ortega, Xia Wei, Joseph Wang, and Ying Shirley Meng. The dissertation author and Jonathan Scharf were the primary investigators and co-authors of this paper.

Chapter 3, in part, is a reprint of the material as it appears in Advanced Functional Materials, 2019, by Xiaohong Chen, Lu Yin, Jian Lv, Andrew J Gross, Minh Le, Nathaniel Georg Gutierrez, Yang Li, Itthipon Jeerapan, Fabien Giroud, Anastasiia Berezovska, Rachel K O'Reilly, Sheng Xu, Serge Cosnier, and Joseph Wang. The dissertation author, Xiaohong Chen, and Jian Lv were the primary investigator and co-author of this paper. In part, is the material as it appears in Advanced Functional Materials, 2021, by Jian Lv, Lu Yin, Xiaohong Chen, Itthipon Jeerapan, Cristian A Silva, Yang Li, Minh Le, Zhihua Lin, Luwen Wang, Alexander Trifonov, Sheng Xu, Serge Cosnier, and Joseph Wang. The dissertation author, Jian Lv, Xiaohong Chen, and Itthipon Jeerapan were the primary investigators and co-authors of this paper.

Chapter 4, in full, is a reprint of the material as it appears in Nature Communications, 2021, by Lu Yin, Kyeong Nam Kim, Jian Lv, Farshad Tehrani, Muyang Lin, Zuzeng Lin, Jong-Min

Moon, Jessica Ma, Jialu Yu, Sheng Xu, and Joseph Wang. The dissertation author, Kyeong Nam Kim, and Jian Lv were the primary investigators and co-authors of this paper.

Chapter 5, in full, is a reprint of the material as it appears in Joule, 2021, by Lu Yin, Jong-Min Moon, Juliane R Sempionatto, Muyang Lin, Mengzhu Cao, Alexander Trifonov, Fangyu Zhang, Zhiyuan Lou, Jae-Min Jeong, Sang-Jin Lee, Sheng Xu, and Joseph Wang. The dissertation author, Jong-Min Moon, and Juliane R Sempionatto were the primary investigators and co-authors of this paper.

Chapter 6, in full, is a reprint of the materials as appears in the preprint on Research Square and has been submitted for publication for the material as it may appear in Nature Electronics, 2022, by Lu Yin, Mengzhu Cao, Kyeong Nam Kim, Muyang Lin, Jong-Min Moon, Juliane Sempionatto, Jialu Yu, Ruixiao Liu, Connor Wicker, Alexander Trifonov, Fangyu Zhang, Hongjie Hu, Jaekyung Go, Sheng Xu, Joseph Wang. The dissertation author, Mengzhu Cao, and Kyeong Nam Kim were the primary investigators and co-authors of this paper.

Chapter 7, in full, is a reprint of the material as it appears in Advanced Materials Technologies, 2020, by Lu Yin, Jian lv, and Joseph Wang. The dissertation author and Jian Lv were the co-authors of this paper.

Chapter 8, in full, is a reprint of the material as it appears in National Science Review, 2022, by Lu Yin and Joseph Wang. The dissertation author was the primary author of this paper.

VITA

2017	Bachelor of Science, University of California San Diego
2017	Teaching Assistant, University of California San Diego
2018	Master of Science, University of California San Diego
2018-2022	Research Assistant, University of California San Diego
2022	Doctor of Philosophy, University of California San Diego

SELECTED PUBLICATIONS

1. L. Yin, M. Cao, K.N. Kim, M. Lin, J. Sempionatto, J.M. Moon, J. Yu, R. Liu, C. Wicker, A. Trifonov, F. Zhang, H. Hu, J. Go, S. Xu, J. Wang, Fully integrated, all-stretchable epidermal electronics with digital electrochromic display for rapid electrochemical sensing, Preprint at Research Square, DOI: 10.21203/rs.3.rs-1176014/v1, 2022.

2. L. Yin, J. Wang, Wearable Energy Systems: What are the limits and limitations? National Science Review, DOI: 10.1093/nsr/nwac060, 2022.

3. K. Du, R. Lin, L. Yin, J.S. Ho, J. Wang, C.T. Lim, Electronic textiles for energy, sensing, and communication, iScience 5, 104174, 2022.

4. L. Yin, K.N. Kim, A. Trifonov, T. Podhajny, J. Wang, Designing wearable microgrids: towards autonomous sustainable on-body energy management, Energy & Environmental Science 15, 82-101, 2022.

5. L. Yin, J.M. Moon, J.R. Sempionatto, M. Lin, M. Cao, A. Trifonov, F. Zhang, Z. Lou, J.M. Jeong, S.J. Lee, S. Xu, J. Wang, High energy return on investment: efficient passive perspiration biofuel cell, Joule 5 (7), 1888, 2021.

6. J. Lv, L. Yin, X. Chen, I. Jeerapan, C.A. Silva, Y. Li, M. Le, Z. Lin, L. Wang, A. Trifonov, S. Xu, S. Cosnier, J. Wang, Wearable biosupercapacitor: harvesting and storing energy from sweat. Advanced Functional Materials, 2102915, 2021.

7. W. Tang, L. Yin, J.R. Sempionatto, J.M. Moon, H. Teymourian, J. Wang, Touch-based stress-less cortisol sensing. Advanced Materials 33 (18), 2008465, 2021.

8. L. Yin, K.N. Kim, J. Lv, F. Tehrani, M. Lin, Z. Lin, J.M. Moon, J. Ma, J. Yu, S. Xu, J. Wang, A self-sustainable wearable multi-modular E-textile bioenergy microgrid system. Nature Communications 12, 1542, 2021.

9. J.R. Sempionatto, M. Lin, L. Yin, K. Pei, T. Sonsa-ard, A.N. de Loyola Silva, A.A. Khorshed, F. Zhang, N. Tostado, S. Xu, J. Wang, An epidermal patch for the simultaneous monitoring of haemodynamic and metabolic biomarkers. Nature Biomedical Engineering, Nature Biomedical Engineering, 5, 737-748, 2021.

10. L. Yin, J. Scharf, J. Ma, J.M. Doux, C. Redquest, V.L. Le, Y .Yin, J. Ortega, X. Wei, J. Wang, Y.S. Meng, High performance printed AgO-Zn rechargeable battery for flexible electronics, Joule, 5 (1), 228-248, 2021.

11. C.A. Silva, J. Lv, L. Yin, I. Jeerapan, G. Innocenzi, F. Soto, Y.G. Ha, J. Wang, Liquid metal based island-bridge architectures for all printed stretchable electrochemical devices. Advanced Functional Materials. 30 (30), 2002041, 2020.

12. L. Yin, J. Lv, J. Wang, Structural innovations in printed, flexible, and stretchable electronics. Advanced Materials Technologies, 5 (11), 2000694, 2020.

13. X. Chen, L. Yin, J. Lv, A.J. Gross, M. Le, N.G. Gutierrez, Y. Li, I. Jeerapan, F. Giroud, A. Berezovska, R.K. O'Reilly, S. Xu, S. Cosnier, J. Wang, Stretchable and flexible buckypaper-based lactate biofuel cell for wearable electronics. Advanced Functional Materials, 29 (46), 1905785, 2019.

14. L. Yin, J.K. Seo, J. Kurniawan, R. Kumar, J. Lv, L. Xie, X. Liu, S. Xu, Y.S. Meng, J. Wang, Highly stable battery pack via insulated, reinforced, buckling-enabled interconnect array. Small, 14 (43), 1800938, 2018.

15. L. Yin, R. Kumar, A. Karajic, L. Xie, J. You, D. Joshuia, C.S. Lopez, J. Miller, J. Wang, From all-printed 2d patterns to free-standing 3d structures: controlled buckling and selective bonding. Advanced Materials Technologies, 3 (5), 1800013, 2018.

16. J. Lv, I. Jeerapan, F. Tehrani, L. Yin, C.A. Silva-Lopez, J.H. Jang, D. Joshuia, R. Shah, Y. Liang, L. Xie, F. Soto, C. Chen, K. Karshalev, C. Kong, Z. Yang, J. Wang, Sweat-based wearable energy harvesting-storage hybrid textile devices. Energy & Environmental Science, 11 (12), 3431-3442

FIELDS OF STUDY

Major Field: Material Science, Energy, Analytical chemistry

Studies in Nanoengineering

Professor Joseph Wang

ABSTRACT OF THE DISSERTATION

Energy Autonomous Microgrids for Wearable Sensors and Fully Integrated Wearable Systems

by

Lu Yin

Doctor of Philosophy in NanoEngineering

University of California San Diego, 2022

Professor Joseph Wang, Chair

Wearable devices have seen tremendous growth in the recent decade in the consumer electronics space, which promotes research on their next-generation technologies and form factors for comprehensive physical, physiological and biochemical sensing, as well as high flexibility, conformity, and stretchability form factors toward more intimate human-machine interactions. However, the current development of wearable sensors and electronics has been hindered by the

lack of efficient, autonomous economical, and practical energy systems. In particular, the power of wearable energy harvesters and the energy density of flexible energy storage devices cannot satisfy the demand of common wearable applications, which fundamentally challenges the concept of self-sustainable wearable devices. Aiming to address this challenge, in this dissertation, the concept of designing a microgrid-like wearable system was proposed, describing a new design concept for wearables that features reliable, practical, sustainable, and autonomous operation. The scenario-specific design considerations for eliminating the performance mismatch between components, minimizing individual disadvantaged characteristics, and maximizing the system's energy reliability are discussed. Towards establishing high-performance microgrids on wearable platforms, advances in wearable bioenergy harvesters and batteries, along with implementations of the wearable microgrid concept into electronic textile and electronic skins platforms are presented. Such implementations include systematic integrations of energy harvesting, storage, and regulation modules into self-sustainable biosensing platforms, which operate independently on the human body without requiring external energy input. Separately, structural innovations to enable flexibility and stretchability in wearable electronics are introduced. Lastly, this dissertation summarizes existing challenges, theoretical limitations, and prospects of wearable microgrids for commercializing next-generation wearable electronics.

Chapter 1 Introduction to Wearable Microgrids

1.1 Introduction

Wearable electronics have recently witnessed spectacular growth due to their tremendous potential for a broad range of applications, including human health monitoring, robotics, human-machine interfacing, and informatics.[1–5] The sensing of motions, biomarker fluctuations, hemodynamic activities of humans, and our interaction with electronics through visual, audio, or tactile elements, along with various means of wireless data transmission, are changing our lifestyles dramatically.[6–10] Such tremendous progress has led to the development of corresponding wearable energy devices for addressing the rapidly growing power demands of on-body electronics systems.[11,12] Correspondingly, emerging wearable energy harvesting devices demonstrated the possibility of harvesting energy from the human body (e.g., motion, sweat, body heat) or from its surrounding environment (e.g., sunlight, heat, moisture), freeing wearable devices from drained bulky and rigid batteries and tethered or close-range power transmissions.[11,13–23] We have since seen scattered examples of using wearable energy harvesters for powering physiological and biochemical sensors, displays, wireless data transmissions, microcontroller units (MCU), and system-on-a-chip (SoC).[10,24–31] However, while most related studies have focused on the characterization of individual modules, the discussion of their reliability, practicality, and sustainability as part of an independent powering system is still lacking. Such individual powering modules rely on monolithic and volatile energy sources, operate intermittently in limited, specific scenarios, and demand high-intensity activities for energy input. Such operation leads to low harvesting reliability and poor energy return of investment (EROI), all of which limit the reliability and practicality of self-powered wearable systems.[32,33]

A strategic energy utilization thus represents a critical challenge for advancing self-sustainable wearable technology. Such a challenge requires a systematic assessment of integration strategies of diverse energy harvesting, storage, and management modules. Seeking inspiration from large-scale deployed renewable energy generators and their successful integration into modern power grids, we envision the possibility of establishing in the human body a self-sustainable energy network through the concept of microgrids. Similar to the challenges of deploying renewable energy generators, such as wind turbines and solar cells, to power small isolated communities, wearable electronics are facing reliability and consistency challenges.[34] The concept of microgrid has thus been introduced to combine power generation, storage, distribution, and consumption in one network, which links the supply of ample renewable resources to the demand of local communities through advanced controlling algorithms.[35–37] In the microgrid, hierarchical control systems are employed to ensure the compatibility of modules with diverse characteristics, along with dynamic prediction and budgeting of energy income, storage, and output, thus ensuring reliable and sustainable operation of the system.[34,37–39] Viewing the systematic integration of various wearable devices through the concept of microgrid, we see the growing need for applying similar strategies towards designing reliable self-powered on-body systems: the leverage of multiple generation mechanisms to diverse energy inputs, appropriate storage modules to rectify energy demands, and the rational selection of modules customized for the specific environment and use case.

In this chapter, we discuss the concept of "wearable microgrid" and summarize the system-level design considerations in the modular integration of energy harvesters and storage devices using components with complementary characteristics and commensurate performance. To guide the judicious selection of components essential for maximizing the practicality and reliability of

the system, we propose the complementary pairing of multiple wearable harvesters and storage devices that are use-case specific. We also summarize and compare the power and energy ratings of various wearable energy harvesting and storage technologies, along with the power consumption required for achieving different functionalities in the wearable sensing system, for selecting modules with commensurate performance and optimal energy budgeting. Next, we discuss key engineering considerations in integrating various textile-based and epidermal energy systems, toward the secured connection of modules with compatible form factors. We also summarize the limitations of current wearable energy systems and discuss expanding the wearable "microgrid" design concept into a broader context of miniaturized energy systems for implantable and ingestible electronic systems. Lastly, we share our perspective on future developments of smart wearable microgrids based on accurate dynamic energy budgeting, leveraging data and algorithm-assisted user-behavior analysis, for responding autonomously to changing energy demands. In this chapter, we wish to avoid the lengthy discussions and comparisons of individual components in a wearable system. Instead, we would like to share our vision of a wearable microgrid with its related system-level design considerations. In addition to existing device-oriented review articles and perspectives summarizing the novel materials and structures of wearable platforms (e.g., energy harvesters[14,18–20,40], energy storage devices[15,20,41], sensors[17,42]), this chapter adds in an in-depth discussion of applying the microgrid concept towards the rational design of self-powered, self-sustainable wearable systems with maximized efficiency, reliability, autonomy, and practicality.

1.2 Concept of Wearable Microgrid

The concept of the wearable microgrid originated from the traditional isolated, "island-mode" microgrid – a small network of various power generation units, energy storage units,

hierarchical control systems, and loads that can operate independently from the main power grid.[36,43,44] There is a significant social and economic impact of developing such independent microgrids for powering remote villages, underdeveloped countries, islands, or even in large ships, which have limited access to established main power grids.[45–48] Even for entities such as colleges, hospitals, and large facilities with direct access to the main power grids, the establishment of microgrids can be highly beneficial for endowing a higher level of energy sovereignty against unexpected system power outages or shutdowns during high peak power demands.[48–50] Not only relying on small-scale fuel-based generators, independent microgrids often involve renewable distributed energy generators, such as solar cells, wind turbines, and small hydroelectric systems, whose energy input are mostly stochastic and uncontrollable, and unable to meet the energy demand of the loads in the network at all times.[44,51] For example, solar cells generate most energy during the mid of the day with sufficient sunlight, whereas the peak power demand period for residential use often occurs in the early morning and after sunset. To meet the energy demands and avoid power outages, microgrids powered by solar cells require energy storage solutions that bridge the gap between energy production and consumption.[52] Larger independent microgrid systems, with diverse users and various distributed energy sources, rely on several essential elements for ensuring the system reliability, including advanced algorithms for predicting the energy supplies and demands, hierarchical supervisory control systems that accurately monitor and regulate the energy flow at each level, as well as commensurate energy reserves for energy security (**Figure 1.1 A**).[37,44,50,51]

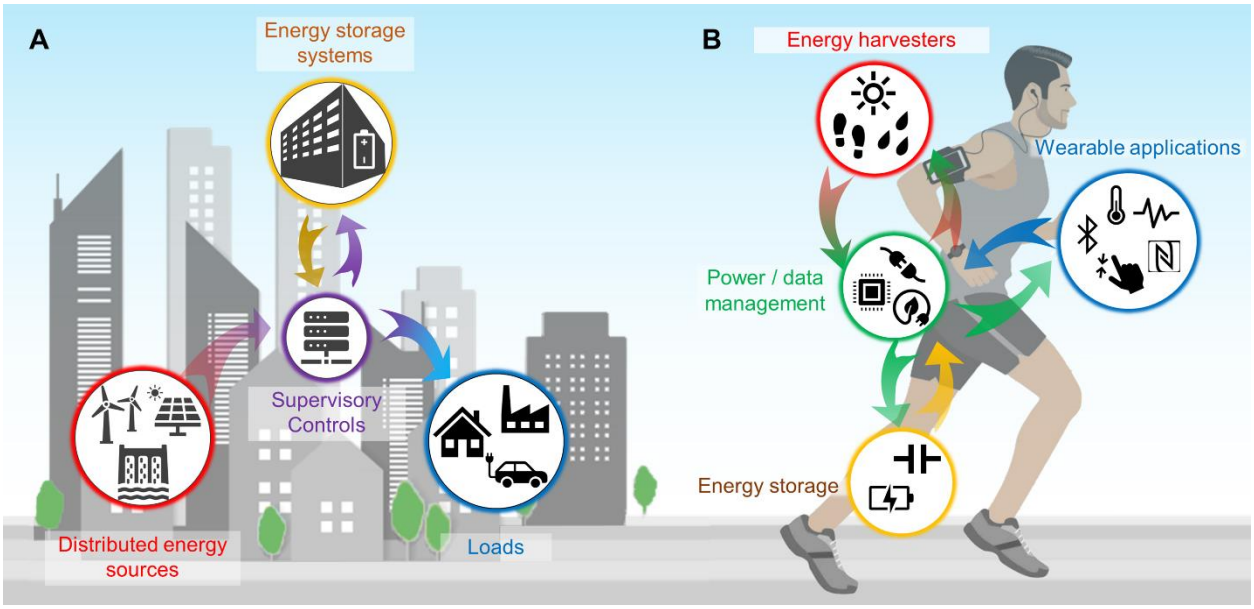

Figure 1.1. Concept of wearable microgrids and similarity to traditional microgrids. **A**. The structure of a traditional microgrid includes distributed energy sources and energy storage facilities that are managed by supervisory controls to sustainably power various loads within the grid. **B**. The structure of a wearable microgrid includes wearable energy harvesters and energy storage devices managed by the control system to power wearable applications for sensing, display, data transmissions, interfacing, and control, and ensure system reliability.

System-level considerations of such distributed networks can easily be translated to wearable devices. Usually, wearable devices do not have all-time access to our household power, as the loads stay on the human body and have changed locations constantly. Current wearable devices, such as headphones, smartwatches, or various on-body activity sensing devices mostly rely on Li-ion battery-based energy storage solutions. Yet, the need for frequent battery recharges requires constant (often daily) maintenance, hence negatively affecting the users' daily workflow.[53,54] With the rapid rise of the new class of wearable sensors, displays, and human-machine interfacing devices, a larger number of discrete wearable modules will be added to enable comprehensive health monitoring and human-machine interactions. Correspondingly, the energy demands of these modules need to be addressed individually, resulting in more complex daily

maintenance routines. Similar to the end-users in a microgrid, such diverse demands of individual devices can benefit from an integrated energy management system that handles the power distribution for the wearable device, thus enhancing the energy reliability while reducing the system complexity.[24]

Energy harvesters represent another important constituent of the wearable analog of microgrids. The main incentive of including wearable energy harvesters in the system is to introduce additional energy inputs to extend the system runtime and eventually replace the need for recharging, leading to partial to full autonomy. To this end, numerous wearable power generators, leveraging various mechanisms, such as photovoltaics, thermoelectric, pyroelectric, osmotic, piezoelectric, and triboelectric effects, have been proposed[11–23,40,55–57] With extensive re-engineering of materials, structures, and form factors, such as wearable energy harvesting devices have been transformed from rigid and bulky forms to their durable, flexible, bendable, or even stretchable and washable counterparts.[16,17,58] However, the availability of diverse energy inputs raises challenges in their systematic integration since the power, voltage, and pattern of the harvested energy differ largely from each other. Each harvester also features various drawbacks, such as dependence on direct sunlight, perspiration, or movements, that often limit their practicality. Such inconsistency is analogous to that of many renewable energy sources, such as solar cells and wind turbines, whose reliability in a microgrid requires systematic control, regulation, and judicious integration with energy storage devices. To fully utilize the discrete and diverse wearable energy harvesters, the systematic integration of such harvesters would not only be helpful towards generating larger amounts of power but will also allow to mitigate the limitation of each harvesting mechanism and hence enhance the practicality of the entire system in different usage scenarios.

These considerations indicate that it will be extremely beneficial to consider all wearable devices and energy harvesters in terms of an integrated system. This integrated approach will not only reduce the energy demand complexity but will also improve the reliability of the energy supply. Using the analogy of a self-powered microgrid, we conceptualized the idea of "wearable microgrids" – an integrated system connecting multiple on-body energy harvesting and storage devices, along with control systems for power regulation and redistribution to various applications. As illustrated in **Figure 1.1 B**, the wearable harvesters, as the energy input, resemble the power generation stations in a microgrid, providing the system with diverse yet irregular energy. Controlled by the energy regulation modules, the energy input with various voltages and currents in different durations can be stored in suitable energy storage devices, which offset differences in the energy supply and demand throughout the operation. The control system further distributes the stored energy to power the wearable applications, considering their individually ranked priority along with a budgeted energy allowance. We envision that the rational design of a wearable microgrid with modularized components distributed around our body can achieve high energy generation and utilization efficiency, along with good reliability and practicality, towards complete system energy autonomy.

Although numerous wearable sensors and energy devices have been developed, wearable electronics (other than smartwatches and wireless earphones) have rarely been commercialized. One of the major challenges for widespread commercialization is the lack of energy-wise systematic considerations, which greatly limits the practicality and reliability of individual devices. Transitioning from designing individual wearable devices to a practical integrated wearable platform is a challenging step that requires interdisciplinary collaborations. To this end, in the following sections, we discuss three important concepts, including:

1. the accurate budgeting of the energy flow;

2. the scenario-based prediction of the system operation and the corresponding selection of system modules; and

3. the specific considerations in module development, depending on various wearable form factors.

We believe that these concepts can guide the conceptualization of a practical wearable system with high energy autonomy and reliability.

1.3 Energy-centered system-level budgeting

The rise of wearable energy harvesters offers an attractive solution to the increasingly demanding energy requirements of wearable applications. The integration of various wearable harvesters, depending on the level of power output, can extend the runtime of devices or eliminate the need for recharges. Although a plethora of wearable harvesters has been developed, the specific requirements for the wearable form factors (such as softness, flexibility, stretchability, and washability) restrict the potential structures and materials and hence may compromise the generated power. Currently, only a limited amount of energy (sub-mW level) can be scavenged from such wearable harvesters; this amount cannot support the continuous power for the majority of wearable applications, which run on electronics demanding tens to hundreds of mW. Realizing absolute energy autonomy requires that the energy input from the harvesters, energy reserved in the batteries and capacitors/supercapacitors, and the energy demand from the electronics, are budgeted and balanced accurately to ensure the system operates with maximum continuity and stability. Thus, when designing a wearable microgrid for a specific application, its operation requirement in terms of time and power must be calculated. Then, energy harvesters must be

selected based on their corresponding power ratings and the appropriate usage scenario (which will be elaborated on in the following section), and their sizes will be determined by the power requirement of the applications. At this point, the possibility of achieving energy autonomy can be analyzed, leveraging basic Fermi estimation – the estimation of order-of-magnitude of the energy and power input vs. output. Lastly, suitable energy storage units with sufficient (but not excessive) capacity must be selected to ensure that the device can operate for the intended duration. On the other hand, if the energy harvesting modules in the microgrid are initially identified with the target of achieving energy autonomy, then the order-of-magnitude estimation is due to determining the functionalities that such systems can support. This is followed by similar accurate selections of energy storage units with capacity ratings that are appropriate for both the harvesters and the applications.

1.3.1 Energy input from wearable harvesters

Figure 1.2 (center) summarizes the range of power inputs from different harvesters and the corresponding power demands of various common wearable applications to guide the order-of-magnitude estimation. As wearable devices are usually designed in planar configurations to conform to skin or textiles, their performance is usually reported in terms of areal power density. Due to the limited area available on the human body, this criterion is important not only to compare the performance of different technologies but is also helpful for estimating the harvester footprint toward balanced energy budgeting.

Among different energy harvesters, photovoltaic solar cells (PVs) can provide the highest power density.[40] Considering the power conversion efficiency of ~5-30% and the fact that the solar radiation on the earth's surface can reach a magnitude of 10^2 mW/cm^2, wearable solar panels can

provide energy in the order of 10^0 - 10^1 mW/cm^2 under direct outdoor sunlight.[5,59–62] It is worth noting that such performance is strongly dependent on many factors, such as time or weather, that determine the transmittance and the angle of incidence.[63] Hence, the harvested energy by wearable PVs is usually an order of magnitude lower in their daily usage. In most cases, the fraction of time people stay in the indoor environment is considerably longer than that of the outdoor. The indoor illumination level is significantly lower due to indirect sunlight with the filtering of windowpanes and glasses. In indoor settings, natural lighting can only provide ~10^1 mW/cm^2 of irradiance, whereas artificial lighting provides a significantly lower irradiance level (10^{-2} mW/cm^2) with a narrower spectrum.[64] Thus, in reality, in indoor settings, wearable PVs present only a power rating of 10^{-1} – 10^{-3} mW/cm^2 level, depending on the light source, equalizing its available energy levels with other types of wearable harvesters. As PVs are used to harvest energy from the light, which usually comes from above, it is recommended to assume only a maximum device area of 10^1-10^2 cm^2 suitable for wearable form factors, which translates to the power of 10^1 - 10^2 mW outdoor and 10^{-1} - 10^1 mW indoor per device, and to a maximum total of 10^2 mWh of energy throughout a day.

Wearable fuel cell energy harvesters represent a class of energy conversion devices that consumes fuel via catalytic reactions to generate energy. Some efforts have been made to convert hydrogen, methanol, or ethanol fuel cell into wearable form factors. However, such devices cannot be classified as wearable harvesters due to their need for external fuel and hence are not discussed here.[65,66] Wearable biochemical energy harvesting relies on enzymatic biofuel cells (BFCs) and microbial fuel cells (MFCs), which leverage bioelectrocatalytic reactions that consume metabolites present in body fluids to generate power.[67–71] Among these, sweat lactate-based BFCs have the highest reported power density (level of a few mW/cm^2) due to the high sweat lactate concentration (2 - 50 mM). Theoretically, the maximum sweat rates of adults can reach the order 10^4 mL per day,

which translates to a total daily harvestable energy of 10^3 mWh from lactate alone.[72,73] In addition, a wide range of other metabolites (e.g., glucose, urea, alcohol) present in various biofluids (e.g., saliva, tears, urine) can also be used as the source of energy, which further enhances the total amount of harvestable energy.[68] However, several other factors limit the power of wearable BFCs, including the collection of sweat, the fuel dilution due to excessive sweating, the limited reaction rates, as well as the stability and biocatalytic activity of enzymes in given operating conditions. Currently, the characterization of the BFC power primarily uses scanning voltammetric methods, which report unrealistic high power, which can be 1-2 orders of magnitude higher than their actual power when operating over an extended time.[24,32] In general, as the lactate concentrations and sweat rates vary per different users, the actual obtainable power by BFCs is only assumed to be 1 - 10^{-2} mW/cm^2. The large area of skin on the body can theoretically permit a device footprint ranging in 10^0-10^2 cm^2, translating to the total power output of the device as high as 10^2 mW, with a total harvestable energy of 10^3 mWh per day. Such level is along with the same order of magnitude as that of its theoretical maximum harvestable energy. Recent progress also demonstrated continuous energy harvesting using passive, thermoregulatory sweat, which is extremely attractive due to its high energy return-on-investment and the possibility for day-long operation without the need for exercise, even while sleeping.[32]

Piezoelectric and triboelectric nanogenerators (PENGs and TENGs) are among the most popular wearable energy harvester research topics.[74] Such energy harvesting relies on a charge exchange induced by various sliding, bending, stretching, and tapping motions in connection to a wide range of materials. As a result of such a high degree of design freedom, various form factors of wearable PENG and TENG harvesters have been developed. These nanogenerators can be located in different body locations to scavenge the kinetic energy from activities such as breathing,

finger moving, running, or stepping. The generation mechanism of PENG relies on the strain-induced charge redistribution within the lattice of intrinsically polarized material, and has been discussed extensively in several reviews.[75–77] In their wearable implementations, PENGs typically deliver unrectified peak open-circuit voltages of 10^0 - 10^1 V, peak short-circuit current density up to 10^{-1} mA/cm^2, and peak power of up to 10^0 mW/cm^2.[18,77–79] It is worth noting that such peak power only occurs transiently upon applying and removing the strain on the PENG; thus, the time-averaged power generation is highly dependent on the load pairing, force applied, and frequency of movements, giving only up to 10^{-2} mW/cm^2 under regular biomechanical inputs from users. Generating power by electrostatic charge exchange between two surfaces with different charge affinities, TENGs deliver superior performance, generating peak open-circuit voltage up to 10^3 V, peak power up to 10^6 mW, and charge density reaching 10^2 nC/cm^2.[79–83] Considering the average human movement frequency within the order of 10^1 Hz, with proper rectification and impedance matching, the averaged power (total energy over time) of such harvesters can reach the level of 10^{-2} - 10^{-1} mW/cm^2 during active usage at certain locations of the body.[82,83] Considering the numerous locations on the body that can implement the TENG and PENG harvesters, we can safely assume the total device footprint to reach up to 10^1 - 10^3 cm^2. A high-frequency and high-intensity movement can only account for a maximum of a few hours throughout a day, followed by mostly low-frequency and low-intensity dynamics that result in a lowering of 1 - 2 orders of magnitude in power generation. Therefore, the total amount of energy harvestable throughout a day via PENG and TENG can be estimated at the 10^1 – 10^2 mWh levels.

Thermoelectric generators (TEG) have been investigated for energy harvesting since the discovery of the Seebeck effect about two centuries ago.[84] Relying primarily on the junctions of n-type and p-type semiconductors, the TEGs are usually built with complicated serial-connection

structures and rigid, bulky materials.[85] Recent progress on polymeric thermoelectric materials, as well as advances in printing fabrication techniques have resulted in TEGs with high flexibility, stretchability, and even self-healing functionalities, making them more suitable for wearable devices.[22,86–88] Wearable TEGs can generate a low voltage from the temperature gradient between the human body and the ambient environment and can thus continuously harvest energy as long as the temperature gradient persists. However, the power output of TEGs is generally low, delivering 10^{-3} mW/cm^2 power in a typical ambient environment ($\Delta T \sim 10^0$ - 10^1 °C).[22] Considering the large possible device footprint of 10^2 - 10^3 cm^2 and the day-long harvesting duration, the total amount of energy obtainable with TECs is only 10^0 mWh.

In addition to these four types of prominent wearable energy harvesters, other types of harvesters have also been developed, including electromagnetic generators (EMGs) and magnetoelastic generators that generate power using the movements of permanent magnets,[89,90] pyroelectric nanogenerators that generate power from temperature fluctuations,[28,91,92] antennas that harvest from either directed long-range power delivery or radio-frequency radiations.[93,94] Due to the scope of this chapter, these harvesters are not discussed in detail, although similar methods of order-of-magnitude calculation can be applied to estimate their energy input to a wearable microgrid.

1.3.2 Energy demands of typical wearable applications

In general, most wearable applications can be classified as control, sensing, displaying, and wireless communications. The operation of such electronics typically runs on integrated circuits (ICs) that: 1. rectify and regulate the energy input; 2. manage the power and voltage of the energy input and output; 3. use analog-to-digital converters (ADC), digital-to-analog converters (DAC),

an amplifier for signal generation and processing; 4. execute, store, and compute codes, programs, and data; 5. transmit data or information wirelessly to other devices; 6. controls the connected displays for visual interactions. Depending on the functionalities of a wearable system, the power consumption can vary drastically over an extremely wide range of pW to W.[11,12,95,96] Knowledge of system-level power consumption is critical for balancing the power input and power output toward establishing a self-sufficient energy network. Conversely, knowing the system-level energy input is crucial also for budgeting the known amount of energy to support various functionalities with the desired amount of runtime. **Figure 1.2** (left) maps the general power consumption of various electronics for realizing different wearable applications.

As the heart of most wearable electronics, system-on-chips (SoCs), and microcontroller units (MCUs) enable a wide range of functionalities to execute from simple instructions to complex programs. In this context, MCUs refer to controllers with limited functionalities, memories, and input/output (I/O). It is commonly used in electronics with simple functionalities with small, embedded control systems, typically featuring low power consumption in the order of 10^{-1} – 10^{3} mW when active for commercial MCUs.[97–99] Customized MCUs with very specific functionality can further reduce the need for unnecessary memories, processing speed, and I/Os, which can enable the power at the level of 10^{-1} mW when active and 10^{-7} mW when in low-power/sleep modes. SoCs is a more encompassing term describing ICs with central computing units (CPUs), graphics processing units (GPU), memory, and/or signal processing functions embedded, which features more computing power, I/O, and programmability. It is commonly seen on electronics with programmable interfaces or even operating systems and is widely used on smartphones, smartwatches, and even some personal computers. Although its power consumption is similar to that of MCUs, SoC is usually coupled with more peripherals, which leads to higher

power consumption as a system. As a rule of thumb, the clock speed of the processors is positively correlated with their input voltage and current; thus, a faster processing speed would require larger power consumption. For sensors requiring a high data sampling rate, resolution, and signal-to-noise ratio (SNR), the integrated ADC and DAC can consume a significant amount of power.

Sensors stand at the forefront of wearable applications as they enable direct interaction of the human body with electronics, monitoring and translating a myriad of signals within and around our body. Sensors for the monitoring of touch, motion, temperature, chemicals, light, physiological signals, and biomarker levels have been developed in the wearable form factors, featuring a wide spectrum of signal transduction methods. In general, the sensors vary in their electrical properties (e.g., resistance, impedance, capacitance, voltage, current), or their optical properties (e.g., color, transmittance) in response to the chemical or physical changes, and these analog signals are eventually converted into digital electrical signals for further processing.[3,5,100,101] Depending on the type of signal transduction methods, the operation of the sensor results in drastically different power consumptions. Some sensors require high SNR and resolution to obtain high sensitivity but not high temporal resolution. For example, many electrochemical sensors measure nA - pA current signals at low time intervals (e.g., every few minutes) and thus require converters with high resolutions.[102,103] Other wearable sensors, based on acoustic or optical transducers, or electrocardiogram (ECG) sensors for physiological signal monitoring, require high temporal resolution and thus, sample thousands to millions of data points per second, which poses high demand on processor clock speed and system memory.[104] As another example, wearable devices with integrated optical sensors or cameras for image processing (e.g., bar-code scanning, feature recognition) can have high power demands associated with the graphical computing function. Many self-powered electrochemical sensors have been proposed to generate an analytical response

with no energy input, which somewhat reduces the system complexity and power consumption.[92,105,106] In some rare cases, the self-powered sensor can harvest sufficient energy to power the electronics, which endows system energy autonomy.[25,107–110]

As a channel for controlling the electronics and interfacing with the obtained data, wireless communication and displays are critical components of wearable electronic systems. The power consumption of the wireless module largely depends on the range and data size of the transmitted signal.[111,112] Bluetooth, which is widely used for data transmission over distances of tens of meters, consumes power in the range of $1 – 10^1$ mW.[113,114] Less common in low-power wearable devices, Wi-Fi and cellular technologies enable a longer transmission range along with higher data speed and 10^1-10^3 mW energy consumption range. Alternatively, near-field wireless technologies, such as near-field communication (NFC) and radio frequency identification (RFID), in addition to untethered power delivery, can also be used for data transmission that extracts power from the external reader and require no internal power supply; however, the readers require $1 – 10^3$ mW of power and such systems in general lack operational independence.[115,116] Displays are another critical element for many wearable devices as they offer direct visual interaction with users. Among them, active displays requiring light-emitting elements (e.g., liquid crystal displays (LCDs) with backlighting, quantum dot displays, electroluminescent displays, or light-emitting diodes (OLED)) consume a significant amount of power, in the range of 10^2-10^3 mW in the case of wearable electronics.[10,117–119] As low-power alternatives, low-resolution LCDs, electronic-ink (e-ink) displays, or electrochromic displays (ECD) consume significantly less power, down to the 10^{-3}-10^{-1} mW level, and thus provide a very attractive and elegant designing solution as self-sustainable wearable electronics.[32,120–122]

1.3.3 Power regulation and energy storage

In a wearable microgrid system, energy management systems (EMS) are crucial for efficient energy regulation. Similar to an electric microgrid, a hierarchical control system is usually required, in which regulators regulate and maximize the power input from various wearable harvesters, battery manage circuits that control and monitor the currents and voltages in and out of energy storage modules, and controllers adjusting the availability, duration, and interval of different services of the wearable applications.

The regulator modules are usually dedicated for each type of energy conversion mechanism to regulate their current and voltage inputs to be compatible for storage in the energy storage modules or direct powering of wearable applications. For common low-voltage direct current (DC) harvesters, such as BFCs and TEGs that deliver sub- 1 V input, a boost converter is commonly employed to elevate the voltages to levels that are compatible with the wearable applications in exchange for lower current. For high voltage DC harvesters, such as PV groups that typically deliver 12 V or 24 V input, buck converters that reduce the voltages in exchange for higher current can be used. Typically the use of these DC-DC converters involves some energy loss due to the non-ideality of the diodes, inductors, capacitors, and switches in the circuits.[123,124] For wearable electronics that typically deliver low current, step-down buck converters typically deliver lower efficiency with higher input voltages, whereas step-up boost converters deliver lower efficiency with lower input voltages; notably, for harvesters that deliver sub-mA level current, commercially available DC-DC converters can suffer from 50% - 90% energy loss.[125,126] The DC energy harvesters typically have optimal loads or operating voltages which allow maximum power output, correspondingly, the regulating circuits can employ maximum power point tracking (MPPT) algorithms that automatically and dynamically adjust the output by perturbing the output or

measuring the harvesters' conductance or parasitic capacitance.[127,128] For alternating current (AC) input harvesters, such as PENGs, TENGs, and EMGs, bridge rectifiers are typically used to convert AC inputs into DC inputs for storage. To further stabilize the rectified but rippling single-directional input, simple resistors and capacitors (RC) circuits can be used to reduce the ripples and stabilize the output voltage. More advanced power management modules were proposed that can further enhance the energy harvesting efficiency from the high-voltage, low-current PENGs and TENGs, including the use of serial and parallel switch mechanisms, inductor and capacitor (LC) circuits, transformers with primary and secondary coils for reducing voltage, and spark switches that reduce current leakages.[83,129–131] Similar to the DC harvesters, such AC harvesters also deliver higher power with proper impedance matching, which can be simulated using their corresponding equivalent circuits.[132,133]The regulated energy can thereafter be stored in capacitors, supercapacitors, and/or batteries, which are then discharged to power electronics.

Among the different energy storage modules in wearable devices, capacitors are the most essential element for circuits that regulate power and filter signals. Capacitors are typically integrated with the circuit, have the capacitance of 10^{-9} - 10^{-2} F, and are rated at tens to hundreds of volts. Capacitors used for storing energy are typically rated at 10^{-4} – 10^{-2} F and can store energy in the range of 10^{-4}-10^{-1} mWh. Such energy level can be used to power electronics only for a brief period (< 1 s) and is typically recharged repeatedly throughout one usage session.[26,27,32] Supercapacitors can hold a significantly larger amount of charge, rated with the capacitance of 1 - 10^{4} F, albeit at a lower voltage (typically < 5 V).[134–136] Wearable supercapacitors are typically limited by their form factors and can only store up to a few F, thus storing only 1 – 10^{1} mWh of energy. Such energy levels are sufficient to power low-power electronics for a moderate amount of time (minutes to hours). In comparison, batteries feature significantly higher energy density,

with their wearable version typically holding $1 – 10^1$ mWh per cm^2.[137–140] Batteries can thus store up to 10^3 mWh of energy with a device footprint of 10^3 cm^2, which is sufficient for many wearable electronics in the market. Controlling circuits are usually necessary to control the voltage and current in and out of the wearable energy storage modules, and hence to avoid overcharge or over-discharge, which are detrimental to the device's performance and may pose safety concerns.[134,141] Depending on the battery chemistry, the maximum, minimum, and nominal voltages are different, and should be closely managed. Typical Li-ion batteries operate between 2 V and 4 V, with the overcharging resulting in the risk of thermal runaway and over-discharging resulting in capacity degradation, current collector corrosion, and internal short-circuiting; rechargeable aqueous batteries typically operate at a lower potential between 2 V to 0.5 V, although having less risk of explosion, still face the risk of electrolyte breakdown and gas evolution if overcharged or over-discharged due to the limited electrochemical window of water (1.21 V). The energy ratings of both energy storage technologies are represented in **Figure 1.2** (right); currently, many micro-SC, SC, and batteries in flexible and stretchable form factors have been developed for powering various wearable applications.[137,142–148]

Accurate energy budgeting and selection of commensurate energy storage modules are crucial for enabling self-sustainable operation. A system should select storage modules with sufficient capacity to hold the harvested energy over the target use time. However, the excess capacity will result in a large device footprint, high self-discharge, long charging time, and is generally inefficient.[24] On the other hand, insufficient energy storage will bottleneck the power demand and operational runtime of the electronics, hence limiting the possible functionalities of the system. As an example, for a wearable system integrated with a 20 mW solar cell to harvest energy for 2 h in a day-long operation, a battery rated at 50 mWh would be sufficient to power an

SoC with 8-bit ADC sampling and Bluetooth connectivity with a low-power e-ink display. Alternatively, for a wearable system integrated with a 5 μW thermoelectric harvester that harvests energy continuously throughout the day, a capacitor of 2 - 5 mF is sufficient for energy storage to briefly power an MCU-controlled thermometer several times every hour. A budget list calculating the power consumption and energy demand of the applications and the energy income from all harvesters within a usage period can not only guide the selection of compatible components but is also necessary for assessing the reliability of the entire system. Envisioning a typical usage scenario that reflects the peak demand and peak supply, along with the required energy storage to offset the gap between the two, towards the system's reliable continuous operation, as will be discussed in the following section.

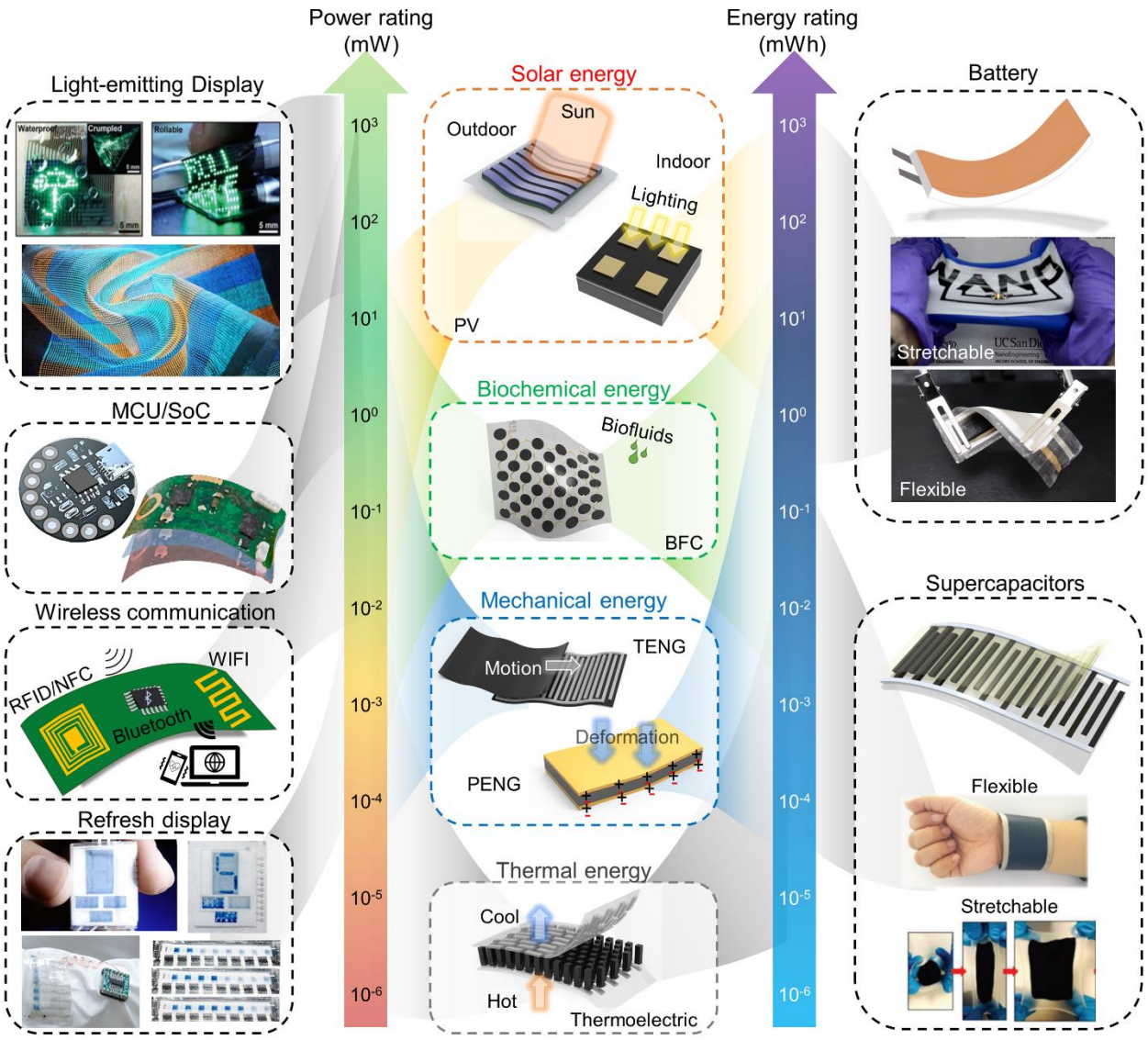

Figure 1.2. Power and energy ratings of wearable devices.
Left: Power requirement of various wearable electronic loads. Middle: Power and daily energy rating of various wearable energy harvesting technologies. Right: Energy rating of battery and supercapacitors. Images of light-emitting displays, copyright, Elesvier, 2018[118] and Springer Nature, 2021.[10] Refresh display images are adapted from ref [24,32]. Copyright, Elsevier, 2021.[32] Stretchable battery images, copyright, Wiley VCH, 2017[142]. Supercapacitors, images, copyright, Elsevier, 2018[147] and American Chemical Society, 2016.[146]

1.4 Scenario-specific design based on complementary characteristic

Towards maximizing energy generation, the deployment of renewable energy was always coupled with a thorough investigation of the corresponding meteorological, hydrographical and geological resource availability and its potential environmental impacts. While energy diversity is generally beneficial to the stability of a microgrid, the installation of various types of energy harvesters should always match realistic scenarios, e.g., the weather, usage pattern, land availability, module affordability, and ease of maintenance.[35,37,52] Such considerations are critical to guide the selection of modules and the design of the microgrid. Similarly, the scenario-specific selection of energy harvesting and storage modules is of tremendous importance in improving the efficiency, reliability, and practicality of any autonomous system. Aside from energy budgeting considerations discussed in the previous section, factors such as the location of the device, available area, user's activity pattern, the surrounding environment, and impact on the user's daily workflow are to be considered when proposing and designing a new integrated wearable system. Furthermore, depending on the characteristics of various components in a system, the coupling of complementary harvesters and/or storage modules can result in additive or synergistic behavior, which can be highly desirable.

Currently, several studies have showcased the activity-specific operation of self-powered systems.[13,24,26,27,30] These systems were coupled with low energy demand applications and only operate for a short amount of time (from tens of minutes to a few hours), thus having relatively low system energy rating requirements. In this context, self-powered sweat-sensing offers great examples for the scenario-specific design of a wearable system (**Figure 1.3 A**). The generation of sweat for subsequent sensing usually requires high-intensity, sweat-inducing exercises. Thus, BFC, which harvests energy from the sweat, and various motion-based harvesters (e.g., PENG, TENG,

EMG), can be integrated into the same system compatible with the activity. Similarly, motion-induced energy can also be used for various physical sensors for gait monitoring, pedometers, or motion tracking, which the energy harvesting is compatible with the usage scenario. Applying a similar strategy, one can also envision a system using PV and TEG to harvest energy from the radiation and thermal energy of the sunlight.[28] With sufficient power harvested, we can envision the use of such power for wearable Peltier cooler patches for personal temperature regulation on a hot, sunny day. Such scenario-specific selection of modules in a wearable system does not only enhance the practicality of the system but also reduces the system complexity and disruptions to the user's workflow.

Most current energy harvesting studies are focusing on energy harvesting from movements, based on various motion-based harvesters (e.g., PENG, TENG, EMG) that generate charge from various sliding, tapping, stretching, and shaking movements.[92,109,149] The deployment of such harvesters at different body locations can fully utilize the limited area and generate a sizable amount of energy. For example, an E-textile shirt for a running session can integrate the TENG modules on the side of the torso and the EMG modules on the wrists to harvest energy both from the sliding between the arm and the waist as well as from the swinging of the arm itself. Both TENG and EMG additively contribute to biomechanical energy harvesting using natural body movements, maximizing the overall efficiency. Moreover, in some scenarios, the coupling of two harvesters scavenging different types of energy, can act synergistically, offering additional benefits to the system (**Figure 1.3 B**). As an example, wearable PVs can be coupled with TEGs that harvest thermal gradients induced by the sunlight, thus delivering additional power using the same device footprint.[30] In a previous report, Yin et al. demonstrated the pairing of TENG and BFCs, which harvest from the motion-induced biomechanical energy and the biochemical energy from the

generated sweat, respectively (See Chapter 4).[24] Besides the additive effect of combining two harvesters, such complementary coupling of BFC and TENG offers advantages of faster system booting (compared to BFC along) and more extended harvesting (compared to TENG along).[24,150] The integration of multiple harvesters ensures the diversity in energy source, which enhances the reliability of a system when part of the energy input becomes unavailable. Furthermore, the coupling of complementary harvesters can address the limitations while amplifying the advantages of individual modules. **Table 1.1** summarizes the advantages and limitations of wearable energy harvesting and storage technologies in different scenarios, which are crucial characteristics in establishing a synergistic, complementary wearable microgrid; accordingly, their maximum power and energy ratings and their applicable scenarios are also summarized.

Table 1.1. Characteristics of various wearable energy harvesters

	PV	BFC	PENG	TENG	TEG
Merits	• Harvest solar energy • Continuous power • High output power • DC output • Large-area compatible	• Harvest biochemical energy • Continuous power • Less dependent on external environment • DC output	• Harvest biomechanical energy • High voltage • Less dependent on external environment • Unsensitive to surface contamination • Large-area compatible	• Harvest biomechanical energy • Less dependent on external environment • Wide material selections, low-cost • High voltage • Large-area compatible	• Continuous power • DC output • Unsensitive to surface contamination • Large-area compatible
Limitations	• Low-performance indoor or without direct sunlight • Highly dependent on external environment • Biocompatibility	• Low voltage • Expensive material • Limited fuel availability • Enzyme stability • Sensitive to surface contamination	• Pulsed AC input • Require constant movement • Limited material selections • Biocompatibility	• Pulsed AC input • Require constant movement • Sensitive to surface contamination/damage	• Low voltage • Low performance • Limited material selections & biocompatibility • Complex structure • Highly dependent on external environment
Max. Power	• 10^{0} mW/cm^{2}	• 10^{0} mW/cm^{2}	• Up to 10^{-2} mW/cm^{2}	• 10^{-1} mW/cm^{2}	• 10^{-3} mW/cm^{2}
Max. Energy/day	• 10^{1} – 10^{2} mWh	• 10^{3} mWh	• 10^{1} mWh	• 10^{2} mWh	• 10^{0} mWh
Use-case	• Outdoor preferred • Stationary (sitting, standing) • Active	• Indoor & outdoor OK • Rigorous full-body exercise • Stationary (sitting/ standing/sleeping)	• Indoor & outdoor OK • Rigorous & moderate exercise • Localized movement	• Indoor & outdoor OK • Rigorous & moderate exercise • Localized movement	• Indoor/outdoor (with temperature difference) • Stationary (sitting/standing/ sleeping) • Active

Future development of an integrated system will focus on a more diverse system, integrating additional energy harvesting and storage modules, thus ensuring its day-long, week-long, and eventually year-long autonomous operation. Such a system will thus incorporate more scenario-specific considerations, as the pattern of a user's daily life will determine its energy supply and demand. **Figure 1.3 C** illustrates the energy flow in a proposed wearable system for an urban office worker throughout the day. We can see that in this use case, the user switches between different scenarios, from active to sedentary and from indoor to outdoor settings; correspondingly, the energy supply from several energy harvesters and the energy demand from a few wearable applications vary significantly throughout the day. Considering such a use case, the system will

benefit significantly from diverse energy sources that ensure constant energy supply to the system, as well as the inclusion of supercapacitors or batteries that regulate the energy flow and offset the differences between the supply and demand. In another more extreme example, illustrated in **Figure 1.3 D**, involving a soldier deployed in a desert for a week-long mission, the energy supply can be drastically different due to the extreme environment. The corresponding microgrid design is optimized for such a scenario, focusing primarily on harvesting solar energy and sweat-based BFC bioenergy during the day and on high-capacity energy storage that ensures continuous operation of the device overnight.

Currently, self-sustainable wearable systems with an extended operation time do not exist due to the low energy/power rating, practicality, durability, and lack of compatibility among the modules. The limited power from the current wearable harvesting technologies thus demands the judicious, scenario-specific selection of modules to maximize the energy supply. Energy harvesters that can operate in all scenarios, independent of the external environment, and generate power regardless of user activity are highly desirable, as they will greatly improve the system's practicality and reliability. Recently, BFCs that harvest energy from passive thermoregulatory sweat from fingertips and operate in most of the scenarios, even during sleep, were developed and were thus considered a major improvement to the practicality of wearable energy harvesters.[32] Future technological advances in developing more complementary harvesters and scenario-specific deployment of such harvesters will aid the realization of more practical wearable microgrids.

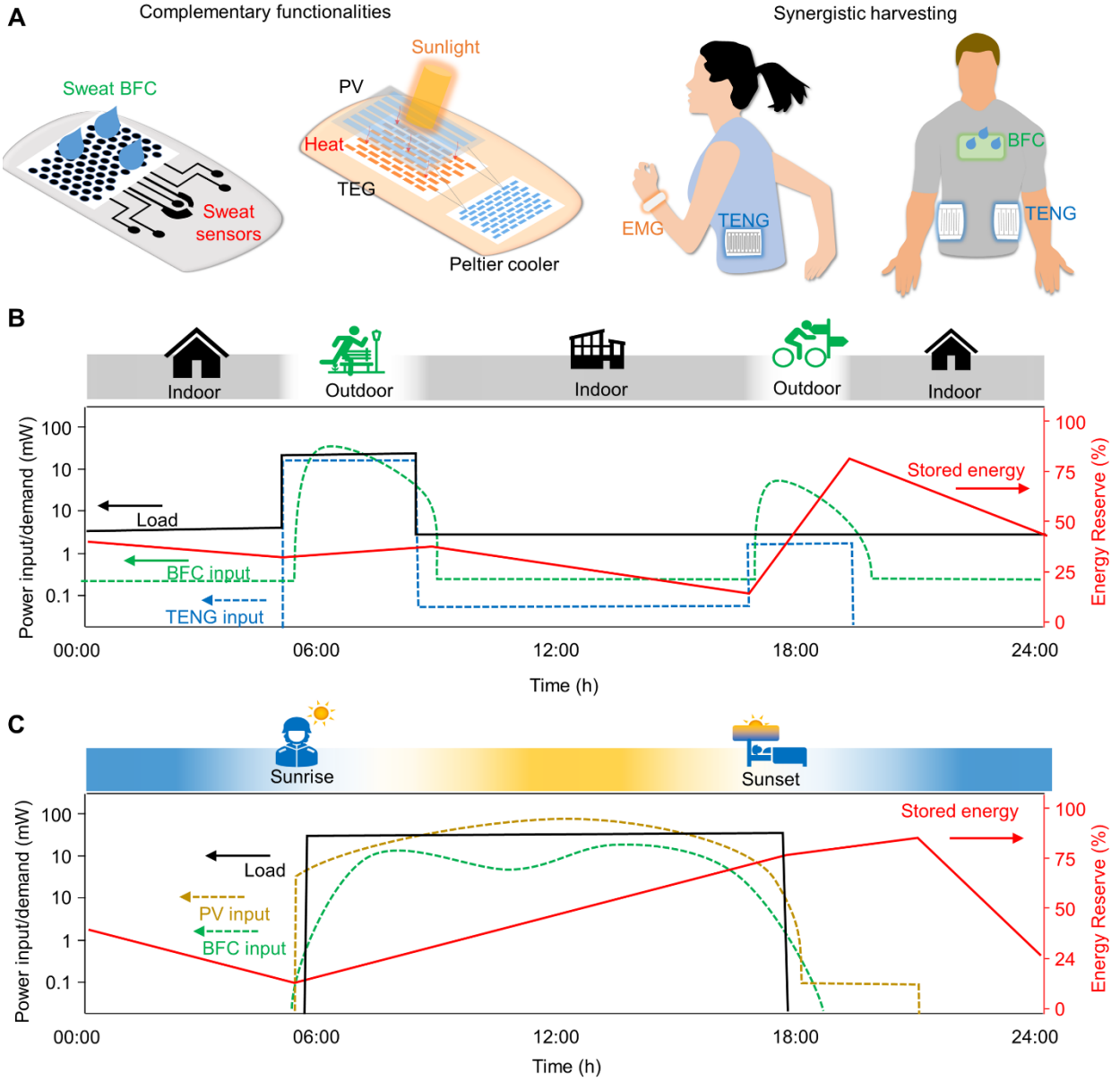

Figure 1.3. Complimentary, scenario-specific selection of modules.
A. Examples of the complementary pairing of wearable harvesters and applications in their proposed scenario, and synergistic pairing of energy harvesters for a proposed use case. **B**. A proposed power supply and demand and energy reserve for an urban office worker. **C**. A proposed power supply and demand and energy reserve for a soldier deployed in a mission.

1.5 Compatible form factors toward practical wearable systems

The form factors of wearable devices are possibly the most well-considered aspect, as the majority of research reports predominantly focus on showcasing the flexibility, stretchability, durability, and washability of the developed wearable devices to effectively attract the public's attention. For designing a wearable microgrid, the form factor considerations are certainly of great importance, as they are deterministic to the wearable system's applicable scenarios, durability, and practicality. As many previous reviews have already discussed in length the advances in novel form factors in various wearable harvesters, storage devices, and applications,[5,11,25,151–155] this chapter aims to discuss only briefly a few key points in logistically determining the necessary form factors in an integrated system.

Wearable electronic systems can be roughly discriminated into three groups: standalone rigid wearables, skin-based wearables, and textile-based wearables. Currently, the standalone rigid wearables are dominating the consumer wearable electronics market, with the greatest number of shipments in smartwatches, fitness trackers, wireless headphones/earbuds, hearing aids, virtual/augmented reality gears, and wearable cameras.[156,157] The rising market of industrial internet-of-things and medical wearables has also shown rapid development, delivering point-of-care products such as continuous glucose monitoring devices, insulin pumps, and drug-delivery patches for patients, or heated clothing, wearable scanners, and exoskeletons for users in special industries.[158–160] In addition, wearable electronics in less-common form factors, such as glasses, contact lenses, mouthguards, neckbands, or shoes, have also been investigated.[93,161–165] Such wearable devices have seen tremendous advances in functionalities and their market growth over the past decade and have fueled the excitement of the public. However, such standalone technologies mostly lack the desirable flexible, stretchable, and conformal features expected for

next-generation wearable electronics. In addition, this current generation of wearable electronics is still relying on rigid electronics, powered by Li-ion or disposable batteries, acting as foreign devices that we mindfully add to our daily workflows. Instead, many academic researchers would envision the next-generation wearable electronics as integrated electronic systems that are soft, unintrusive, intimately and seemingly integrated with the human body, physically unnoticeable, and logistically non-disruptive to the user's daily activities. To this end, many studies have chosen platforms that are already inseparable and integral to people's daily lives – namely, the skin and the textiles.

Epidermal wearable electronics, sometimes also referred to as electronics skins, have grown with exciting development in biochemistry, material science, and structural engineering.[12,58,166] Conformal devices with mechanical properties similar to that of skin featuring novel structures or intrinsically stretchable materials to accommodate for the curved skins undergoing constant deformations have been developed.[167–171] Prominent examples include epidermal sensors worn as tattoos or patches for monitoring sweat and interstitial fluid biomarker fluctuations, physiological activities, physical movements, or surrounding environments (**Figure 1.4 A**).[7,170,172,173] Similarly, skin-worn energy harvesters and energy storage devices activated by sweat have been proposed, providing potential energy solutions for the aforementioned sensing activities.[68,153,174] LED display on skin has also been reported, featuring futuristic visual elements on skin.[175] In general, such epidermal electronics often have a rather strict requirement on the mechanical modulus (10^4 Pa – 10^6 Pa, similar to that of skin) to ensure device conformity.[176,177] In addition, ca.10 - 30% stretchability would be required to ensure the device's uninterrupted operation during movements.[167,178] Safety is another important consideration as epidermal electronics require direct contact with the skin for an extended amount of time; sweat and other

biofluids are typical of high salinity and corrosive; hence, such epidermal devices would require materials with high biocompatibility and chemical stability to avoid leakages or damage to the skin and the electronics.[179] Practically, epidermal electronics are designed to be used for a limited amount of time, which requires special consideration during product development. Due to the lack of battery technologies that meet these requirements in conformity and safety, such devices can only operate with wired connections or near-range power delivery, thus limiting the user's mobility and the device's level of independence. Furthermore, typical epidermal electronic devices are constructed onto a patch-sized geometric area (10^0 -10^1 cm^2) which limits the area and types of modules that can be integrated. Lacking secure connections between individual patches, energy harvesting, storage and sensing distribution around the body also become challenging and require special engineering solutions. Owing to the above limitations, most epidermal systems are dependent on external devices and connections and used for stationary users, with only a few examples demonstrating a well-constructed miniaturized autonomous system, capable of energy harvesting, storage, and sensing.

Alternative to epidermal electronics, smart electronic textiles (e-textile) expand the platform of wearable electronics from our skin to clothing (**Figure 1.4 B**). Textile-based wearable systems feature many advantages compared to their epidermal counterparts, including larger usable area, diverse types of fabrics, well-developed textile engineering technologies, and wider applicable use cases. The fabrication of textile-based wearable devices can be classified as "bottom-up" and "top-down" methods, where the former refers to the fabrication of functional devices into yarns and threads that thereafter weave, sew, or embroider into fabrics, while the latter refers to the direct printing, adhering, or stitching functional devices onto or into the textiles. Using these methods, a myriad of energy harvesters (e.g., PVs, TENGs, PENGs, TEGs, BFCs), batteries,

SCs, physical and biochemical sensors, wireless antennas, and large-area displays have been developed as functional textiles and integrated e-textile systems.[10,18–20,24,138,142,180–185] Endowed by various microstructures and patterns within textiles, textile-based electronics can feature flexibility and stretchability even without developing intrinsically stretchable materials.[58] Well-distributed wearable energy harvesting, storage, and applications around the body can be easily achieved through connections within the textile, thus allowing a wired but untethered system. Numerous textile-based wearable systems have been demonstrated, featuring the sensing, display, and wireless communications powered by the integrated textile-based energy harvesting and storage devices. As textile-based electronic systems are intended to be used in normal clothing, the textile form factor poses strict requirements in terms of the durability of the devices against friction, repeated flexing, stretching, and washing while maintaining the softness and breathability of the textiles.

Overall, to ensure form-factor compatibility, one should first keep in mind the distinctions between epidermal and textile platforms and select the most appropriate platform and device architecture based on the use-case-specific requirements (e.g., reusability, energy consumption, device footprint) of the wearable applications. The second step requires the preliminary energy budgeting of the modules under the proposed applicable scenario to establish a balanced energy supply and demand within the system. The third step should involve the selection of the material, structure, and fabrication process of each module, ensuring that the key requirements for the system (e.g., power, flexibility, durability) are satisfied by each individual module as well as the interconnections between them to remove any "Achilles' heel" in the system. With the preliminary performance of modules characterized, these steps should be reiterated to make adjustments on the use of materials, structures, sizes, etc., which leads to updated performance data for further

adjustments. Only through this iterative process, a wearable microgrid system with compatible form factors, commensurate energy rating, and complimentary device characteristics can be obtained.

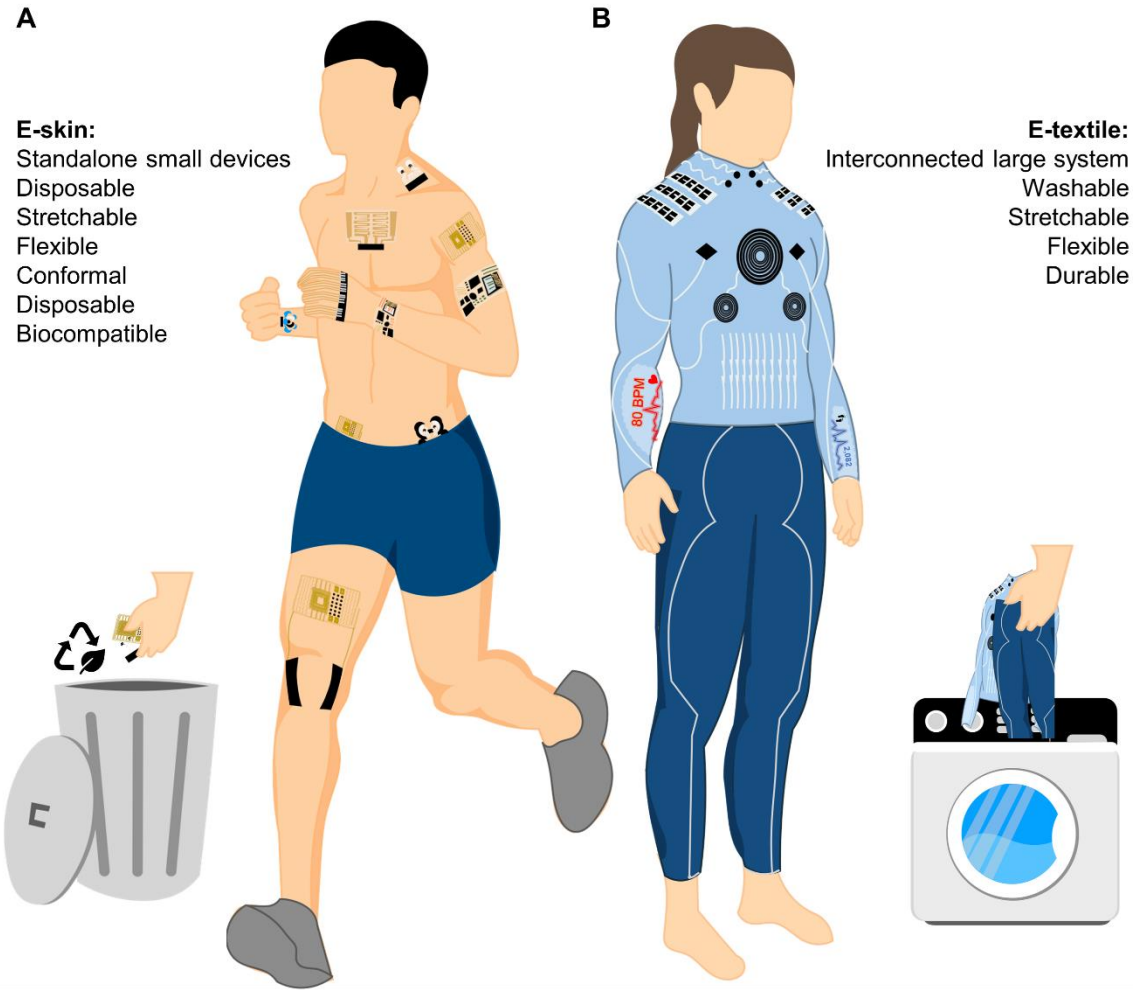

Figure 1.4. Wearable Microgrid Form Factor Considerations.
A. Form factor considerations for E-skin epidermal microgrid systems. **B**. Form factor considerations for E-textile-based microgrid systems.

1.6 Outlook and summary

Through the above discussion of a wearable microgrid, this chapter aims to stimulate system-level discussions in designing an energy-autonomous wearable system. The integration of

three pillars of wearable microgrids - the energy harvesting devices, the energy storage devices, and the applications – is to be implemented using key design considerations - accurate energy budgeting, scenario-specific complementary characteristics, and compatible form factors – towards the practical execution of a seamlessly integrated system. In addition, efficient and reliable cooperation among modules requires systematic management that predict, balance, and regulate the energy supply and demand of individual modules in the system. Such awareness of system-level energy considerations is crucial from the very beginning of building a wearable microgrid system, since the rational selection of modules depends strongly on its use case, specific energy supply, and demands, and form factor requirements. The critical understanding of the energy ratings of the various components in specific scenarios will allow both retrospective planning of energy harvesting and storage modules for meeting the energy demands of wearable electronics, as well as the prospective feasibility assessment of adaptable applications based on the maximum energy supply from the harvesters. Considerations of the use-case and scenario of the system will further aid the accurate energy budgeting accounting for different usage patterns while simultaneously helping to determine the necessary form factors for its reliable on-body operation. The three key considerations are thus intertwined in establishing an efficient wearable microgrid for the rational design of self-sustainable wearable energy systems (**Figure 1.5 A**).

Recent advances in integrated wearable systems have demonstrated the possibilities of establishing such wearable microgrid systems. However, their future advances are hindered by the low performance of wearable energy harvesters that bottlenecked the overall energy demand of a system, resulting in a large mismatch in the power rating of various wearable applications. To bridge this major gap between energy demand and supply, major improvements are needed to further enhance the performance of existing energy harvesting technologies, and expand the type

of harvesters while reducing the power consumption of various wearable sensors, ICs, wireless technologies, and displays. Specifically, the improvements on wearable harvesters will rely on several aspects of technological advances, including the development of new materials featuring higher performance and stability, the discovery of new synthesis and fabrication methods leading to lower cost, better scalability, and biocompatibility, as well as research into new device structures and architectures for improved efficiency and robustness. Beyond incremental performance improvements, exciting new breakthroughs in proposing new use-cases and applicable scenarios of existing energy harvesters and the discovery of new energy conversion mechanisms can open new doors towards bioenergy harvesting with drastically higher practicality, energy return-on-investment, and performance. Similarly, wearable energy storage modules suffer from trade-offs between electrochemical performance, mechanical performance, and safety, which can be addressed with material and structural innovations. Efforts toward developing advanced and sophisticated fabrication processes for wearable batteries and SCs, compatible with such new materials and structures, will improve their scalability, reliability, and cost-effectiveness. In addition, wearable energy storage beyond electrochemical cells has rarely been explored, which may grant new possibilities in advanced energy regulation strategies for wearable microgrids. The addition of new and more powerful wearable harvesters and storage devices will greatly diversify the energy sources within a wearable microgrid system, towards reliable 24/7 uninterrupted operation of various on-body applications compatible with diverse scenarios and lifestyles.

Furthermore, the current energy budgeting concept in wearable microgrids is still presumptive, crude, and can be inaccurate, depending on the specific user and scenario. We envision that the next phase in developing wearable microgrids should resemble the traditional microgrids, which more often feature data-driven prediction of energy supply and demand in the

grid and adjustable control of various loads toward effective energy budgeting and flow that ensure highly reliable and sustainable microgrid operation. Guided by modern artificial intelligence and machine learning techniques and advanced algorithms, smart energy budgeting for wearable systems will thus rely on the dynamic prediction of energy supply from weather, geological location, daily schedule, diet, or health conditions, is possible. This would allow adjusting the power consumption of wearable applications, e.g., by increasing or decreasing the frequency of sensing or the data transmission, in order to maintain continued sustainable system operation (**Figure 1.5 B**). Such design concepts can be also applied to the rising class of implantable and ingestible electronics for biomedical applications, in which autonomous and extended operations are highly desirable. Using the wide range of mechanical and biochemical energies within the body ready to be scavenged, electronics can become independent, battery-less, self-powered designs for various in-vivo neurostimulation, drug delivery, and comprehensive monitoring applications.

The rise of the 5^{th} generation mobile network and the internet-of-things has led to the development of many precursor technologies for the eventual evolution of wearable electronics. Endowed by advanced internet infrastructure, distributed edge computing has equipped our homes, cars, and pockets with physically standalone wirelessly connected devices as our daily workflows become increasingly informative and interactive. Traditional wearable electronic industries have slowly evolved around diverse form factors of wireless earbuds, smartwatches, and epidermal devices that are functionally advanced yet rigid, bulky, battery-dependent, and lack independence. Despite the growing advocacy towards the transition from rigid and bulky platforms to soft and conformal ones, the development of flexible and stretchable wearable devices (in both e-skin and e-textile form factors) is still limited to the scope of initial proof-of-concept. We believe that this lagged development is due to a lack of necessary “infrastructures”: standardized protocols for the

inter-modular connections that ensure compatibility between various modules from different developers; standardized characterization method and performance reporting format for benchmarking each energy harvesting and storage technologies; commercially available mechanically robust soft energy storage devices that deliver performance comparable to that of their rigid counterparts for fast prototyping; low-cost, scalable assembly processes that connect current rigid, high-performance Si-based electronics and the new soft peripheral energy devices and applications; and eventually, new semiconductor technologies and standardized protocol for fabricating and packaging of intrinsically soft, high-performance integrated electronics.

Currently, the wearable market has shown appreciable growth in medical, personal wellness, and industrial applications and features relatively price-insensitive state-of-art soft electronics. We envision the roadmap of future wearable electronics development, where rigid wearable devices along with novel e-textile and e-skin platforms for biomedical applications lead the continued development of this field. This is followed by breakthroughs in low-cost, high-performance flexible or stretchable energy storage devices, that will enable a wider range of flexible electronics, which previously lack high-performance batteries with compatible form-factors, to quickly expand the wearable market and advanced functionalities in sensing, communication, and interaction. Lastly, with the development of low-power electronics and high-power energy harvesters, the gap between the power supply and demand in wearable systems will be narrowed, allowing applications to operate autonomously, independently, and maintenance-free (**Figure 1.5 C**). Towards this goal, the concept of the wearable microgrid will greatly promote the development of integrated wearable technologies featuring smart and efficient energy budgeting and management. We believe that such cross-disciplinary efforts for realizing the wearable microgrid vision will enhance the practicality of wearable electronic systems in different usage

scenarios and will lead to next-generation electronics, characterized by high efficiency, reliability, autonomy, and practicality.

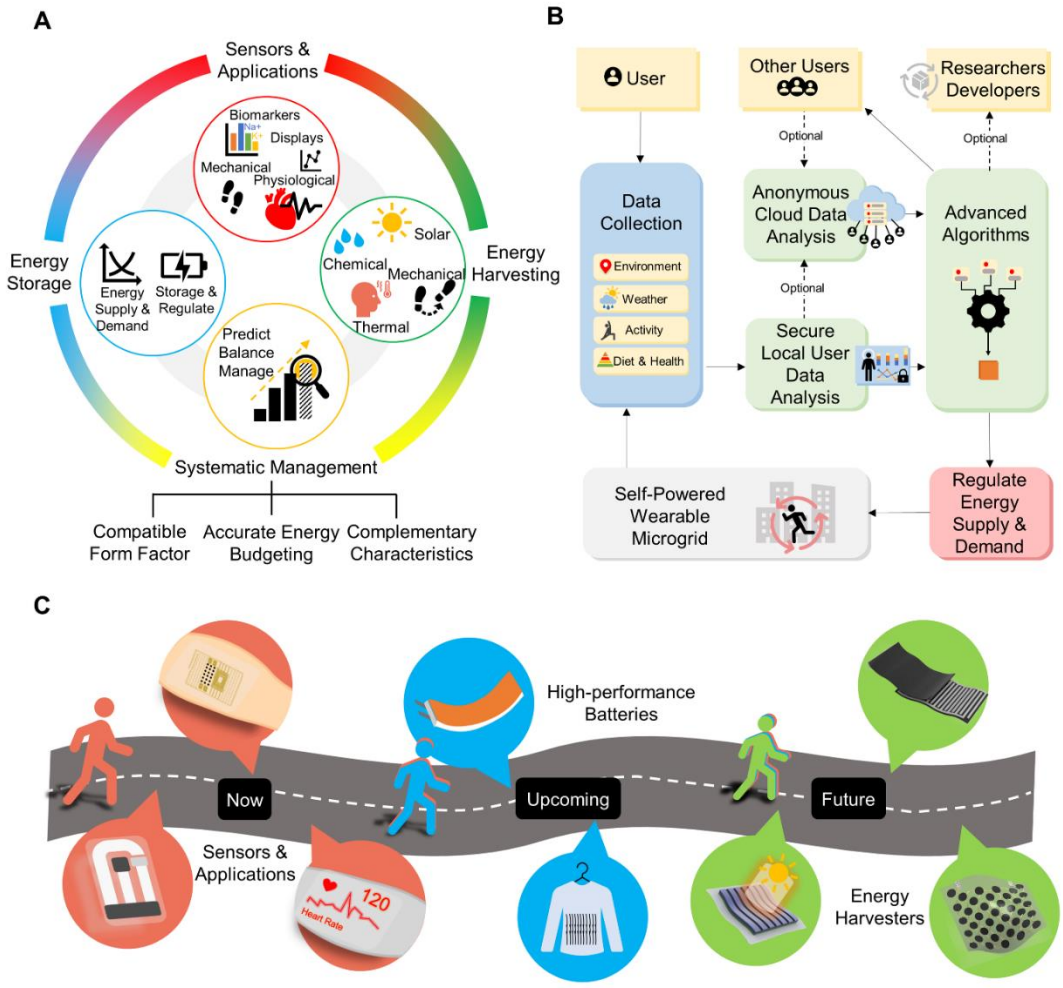

Figure 1.5. Summary and prospects of wearable microgrid systems.
A. Key component and corresponding design considerations in a wearable microgrid system. **B**. Established smart wearable microgrid with advanced algorithm to improve system energy reliability. **C**. Proposed developmental roadmap for energy-independent wearable electronics.

Chapter 1, in full, is a reprint of the material as it appears in Energy & Environmental Science, 2022, by Lu Yin, Kyeong Nam Kim, Alexander Trifonov, Tatiana Podhajny and Joseph Wang. The dissertation author was the primary author of this paper.

1.7 References

1. Kim, J., Campbell, A. S., de Ávila, B. E.-F. & Wang, J. Wearable biosensors for healthcare monitoring. *Nat. Biotechnol.* **37**, 389–406 (2019).

2. Heikenfeld, J. *et al.* Accessing analytes in biofluids for peripheral biochemical monitoring. *Nat. Biotechnol.* **37**, 407–419 (2019).

3. Bandodkar, A. J., Jeang, W. J., Ghaffari, R. & Rogers, J. A. Wearable Sensors for Biochemical Sweat Analysis. *Annual Review of Analytical Chemistry* **12**, 1–22 (2019).

4. Bariya, M., Nyein, H. Y. Y. & Javey, A. Wearable sweat sensors. *Nat. Electron.* **1**, 160–171 (2018).

5. Ray, T. R. *et al.* Bio-Integrated Wearable Systems: A Comprehensive Review. *Chem. Rev.* **119**, 5461–5533 (2019).

6. Gao, W. *et al.* Fully integrated wearable sensor arrays for multiplexed in situ perspiration analysis. *Nature* **529**, 509–514 (2016).

7. Sempionatto, J. R. *et al.* An epidermal patch for the simultaneous monitoring of haemodynamic and metabolic biomarkers. *Nat. Biomed. Eng.* **5**, 737–748 (2021).

8. Sundaram, S. *et al.* Learning the signatures of the human grasp using a scalable tactile glove. *Nature* **569**, 698–702 (2019).

9. Awad, L. N. *et al.* A soft robotic exosuit improves walking in patients after stroke. *Science Translational Medicine* **9**, eaai9084 (2017).

10. Shi, X. *et al.* Large-area display textiles integrated with functional systems. *Nature* **591**, 240–245 (2021).

11. Gao, M. *et al.* Power generation for wearable systems. *Energy Environ. Sci.* **14**, 2114 (2021).

12. Gong, S. & Cheng, W. Toward Soft Skin-Like Wearable and Implantable Energy Devices. *Advanced Energy Materials* **7**, 1700648 (2017).

13. Pu, X. *et al.* Wearable Power-Textiles by Integrating Fabric Triboelectric Nanogenerators and Fiber-Shaped Dye-Sensitized Solar Cells. *Advanced Energy Materials* **6**, 1601048 (2016).

14. Tebyetekerwa, M. *et al.* Critical insight: challenges and requirements of fibre electrodes for wearable electrochemical energy storage. *Energy Environ. Sci.* **12**, 2148–2160 (2019).

15. Li, L., Wu, Z., Yuan, S. & Zhang, X.-B. Advances and challenges for flexible energy storage and conversion devices and systems. *Energy Environ. Sci.* **7**, 2101–2122 (2014).

16. Wu, H., Huang, Y., Xu, F., Duan, Y. & Yin, Z. Energy Harvesters for Wearable and Stretchable Electronics: From Flexibility to Stretchability. *Advanced Materials* **28**, 9881–9919 (2016).

17. Lim, H.-R. *et al.* Advanced Soft Materials, Sensor Integrations, and Applications of Wearable Flexible Hybrid Electronics in Healthcare, Energy, and Environment. *Advanced Materials* **32**, 1901924 (2020).

18. Dong, K., Peng, X. & Wang, Z. L. Fiber/Fabric-Based Piezoelectric and Triboelectric Nanogenerators for Flexible/Stretchable and Wearable Electronics and Artificial Intelligence. *Advanced Materials* **32**, 1902549 (2019).

19. Shi, X.-L., Chen, W.-Y., Zhang, T., Zou, J. & Chen, Z.-G. Fiber-based thermoelectrics for solid, portable, and wearable electronics. *Energy Environ. Sci.* **14**, 729–764 (2021).

20. Huang, L. *et al.* Fiber-Based Energy Conversion Devices for Human-Body Energy Harvesting. *Advanced Materials* **32**, 1902034 (2020).

21. Vallem, V., Sargolzaeiaval, Y., Ozturk, M., Lai, Y.-C. & Dickey, M. D. Energy Harvesting and Storage with Soft and Stretchable Materials. *Advanced Materials* **33**, 2004832.

22. Nozariasbmarz, A. *et al.* Review of wearable thermoelectric energy harvesting: From body temperature to electronic systems. *Applied Energy* **258**, 114069 (2020).

23. Liu, Y. *et al.* Piezoelectric energy harvesting for self-powered wearable upper limb applications. *Nano Select* **2**, 1459–1479 (2021).

24. Yin, L. *et al.* A self-sustainable wearable multi-modular E-textile bioenergy microgrid system. *Nature Communications* **12**, 1542 (2021).

25. Song, Y., Mukasa, D., Zhang, H. & Gao, W. Self-Powered Wearable Biosensors. *Acc. Mater. Res.* **2**, 184–197 (2021).

26. Yu, Y. *et al.* Biofuel-powered soft electronic skin with multiplexed and wireless sensing for human-machine interfaces. *Science Robotics* **5**, eaaz7946 (2020).

27. Song, Y. *et al.* Wireless battery-free wearable sweat sensor powered by human motion. *Science Advances* **6**, eaay9842 (2020).

28. Li, H. *et al.* A wearable solar-thermal-pyroelectric harvester: Achieving high power output using modified rGO-PEI and polarized PVDF. *Nano Energy* **73**, 104723 (2020).

29. Xue, H. *et al.* A wearable pyroelectric nanogenerator and self-powered breathing sensor. *Nano Energy* **38**, 147–154 (2017).

30. Chen, J. *et al.* Micro-cable structured textile for simultaneously harvesting solar and mechanical energy. *Nature Energy* **1**, 16138 (2016).

31. Seo, B., Cha, Y., Kim, S. & Choi, W. Rational Design for Optimizing Hybrid Thermo-triboelectric Generators Targeting Human Activities. *ACS Energy Lett.* **4**, 2069–2074 (2019).

32. Yin, L. *et al.* A passive perspiration biofuel cell: High energy return on investment. *Joule* **5**, 1888–1904 (2021).

33. Raugei, M. Energy Return on Investment: Setting the Record Straight. *Joule* **3**, 1810–1811 (2019).

34. Issa, W. R., Khateb, A. H. E., Abusara, M. A. & Mallick, T. K. Control Strategy for Uninterrupted Microgrid Mode Transfer during Unintentional Islanding Scenarios. *IEEE Transactions on Industrial Electronics* **65**, 4831–4839 (2018).

35. Zia, M. F., Elbouchikhi, E. & Benbouzid, M. Microgrids energy management systems: A critical review on methods, solutions, and prospects. *Applied Energy* **222**, 1033–1055 (2018).

36. Lasseter, B. Microgrids [distributed power generation]. in *2001 IEEE Power Engineering Society Winter Meeting. Conference Proceedings* vol. 1 146–149 (2001).

37. Olivares, D. E. *et al.* Trends in Microgrid Control. *IEEE Transactions on Smart Grid* **5**, 1905–1919 (2014).

38. Ou, T. C. & Hong, C. M. Dynamic operation and control of microgrid hybrid power systems. *Energy* **66**, 314–323 (2014).

39. Li, Y., Yang, Z., Li, G., Zhao, D. & Tian, W. Optimal Scheduling of an Isolated Microgrid With Battery Storage Considering Load and Renewable Generation Uncertainties. *IEEE Transactions on Industrial Electronics* **66**, 1565–1575 (2019).

40. Hashemi, S. A., Ramakrishna, S. & Aberle, A. G. Recent progress in flexible–wearable solar cells for self-powered electronic devices. *Energy Environ. Sci.* **13**, 685–743 (2020).

41. Lv, J., Chen, J. & Lee, P. S. Sustainable wearable energy storage devices self-charged by human-body bioenergy. *SusMat* **1**, 285–302 (2021).

42. Khan, Y., Ostfeld, A. E., Lochner, C. M., Pierre, A. & Arias, A. C. Monitoring of Vital Signs with Flexible and Wearable Medical Devices. *Advanced Materials* **28**, 4373–4395 (2016).

43. Ross, M., Hidalgo, R., Abbey, C. & Joós, G. Energy storage system scheduling for an isolated microgrid. *IET Renewable Power Generation* **5**, 117–123 (2011).

44. Kuang, Y. *et al.* A review of renewable energy utilization in islands. *Renewable and Sustainable Energy Reviews* **59**, 504–513 (2016).

45. Longe, O. M., Rao, N., Omowole, F., Oluwalami, A. S. & Oni, O. T. A Case Study on Off-grid Microgrid for Universal Electricity Access in the Eastern Cape of South Africa. *International Journal of Energy Engineering* **7**, 55–63 (2017).

46. Xie, H., Zheng, S. & Ni, M. Microgrid Development in China: A method for renewable energy and energy storage capacity configuration in a megawatt-level isolated microgrid. *IEEE Electrification Magazine* **5**, 28–35 (2017).

47. Jayasinghe, S. G., Meegahapola, L., Fernando, N., Jin, Z. & Guerrero, J. M. Review of Ship Microgrids: System Architectures, Storage Technologies and Power Quality Aspects. *Inventions* **2**, 4 (2017).

48. Bosisio, A., Moncecchi, M., Cassetti, G. & Merlo, M. Microgrid design and operation for sensible loads: Lacor hospital case study in Uganda. *Sustainable Energy Technologies and Assessments* **36**, 100535 (2019).

49. Washom, B. *et al.* Ivory Tower of Power: Microgrid Implementation at the University of California, San Diego. *IEEE Power and Energy Magazine* **11**, 28–32 (2013).

50. Jin, X. *et al.* Hierarchical microgrid energy management in an office building. *Applied Energy* **208**, 480–494 (2017).

51. Hafez, O. & Bhattacharya, K. Optimal planning and design of a renewable energy based supply system for microgrids. *Renewable Energy* **45**, 7–15 (2012).

52. Murakami, D., Yamagata, Y., Yoshida, T. & Matsui, T. Optimization of local microgrid model for energy sharing considering daily variations in supply and demand. *Energy Procedia* **158**, 4109–4114 (2019).

53. Min, C. *et al.* Exploring current practices for battery use and management of smartwatches. in *Proceedings of the 2015 ACM International Symposium on Wearable Computers - ISWC '15* 11–18 (ACM Press, 2015). doi:10.1145/2802083.2802085.

54. Ferreira, D., Dey, A. K. & Kostakos, V. Understanding Human-Smartphone Concerns: A Study of Battery Life. in *Pervasive Computing* (eds. Lyons, K., Hightower, J. & Huang, E. M.) vol. 6696 19–33 (Springer, 2011).

55. Kim, B. J. *et al.* Highly efficient and bending durable perovskite solar cells: Toward a wearable power source. *Energy and Environmental Science* **8**, 916–921 (2015).

56. Thakre, A., Kumar, A., Song, H.-C., Jeong, D.-Y. & Ryu, J. Pyroelectric Energy Conversion and Its Applications—Flexible Energy Harvesters and Sensors. *Sensors* **19**, 2170 (2019).

57. Logan, B. E. & Elimelech, M. Membrane-based processes for sustainable power generation using water. *Nature* **488**, 313–319 (2012).

58. Yin, L., Lv, J. & Wang, J. Structural Innovations in Printed, Flexible, and Stretchable Electronics. *Advanced Materials Technologies* **5**, 2000694 (2020).

59. Odele Coddington, Judith L. Lean, Doug Lindholm, Peter Pilewskie, & Martin Snow. NOAA CDR Program (2015): NOAA Climate Data Record (CDR) of Solar Spectral Irradiance (SSI), NRLSSI Version 2. *NOAA National Centers for Environmental Information* doi:doi:10.7289/V51J97P6.

60. Yan, C. *et al.* Non-fullerene acceptors for organic solar cells. *Nat Rev Mater* **3**, 1–19 (2018).

61. Jinno, H. *et al.* Stretchable and waterproof elastomer-coated organic photovoltaics for washable electronic textile applications. *Nat Energy* **2**, 780–785 (2017).

62. Huang, W. *et al.* Efficient and Mechanically Robust Ultraflexible Organic Solar Cells Based on Mixed Acceptors. *Joule* **4**, 128–141 (2020).

63. Page, J. Chapter IIA-1 - The Role of Solar-Radiation Climatology in the Design of Photovoltaic Systems. in *Practical Handbook of Photovoltaics* (eds. McEvoy, A., Markvart, T. & Castañer, L.) 573–643 (Academic Press, 2012). doi:10.1016/B978-0-12-385934-1.00017-9.

64. Reynaud, C. A. *et al.* Evaluation of indoor photovoltaic power production under directional and diffuse lighting conditions. *Solar Energy Materials and Solar Cells* **200**, 110010 (2019).

65. Zhai, Q. *et al.* Intrinsically Stretchable Fuel Cell Based on Enokitake-Like Standing Gold Nanowires. *Advanced Energy Materials* **10**, 1903512 (2020).

66. Thampan, T., Shah, D., Cook, C., Novoa, J. & Shah, S. Development and evaluation of portable and wearable fuel cells for soldier use. *Journal of Power Sources* **259**, 276–281 (2014).

67. Jeerapan, I., Sempionatto, J. R. & Wang, J. On-Body Bioelectronics: Wearable Biofuel Cells for Bioenergy Harvesting and Self-Powered Biosensing. *Advanced Functional Materials* **30**, 1906243 (2020).

68. Manjakkal, L., Yin, L., Nathan, A., Wang, J. & Dahiya, R. Energy Autonomous Sweat-Based Wearable Systems. *Advanced Materials* **33**, 2100899 (2021).

69. Bandodkar, A. J. Review—Wearable Biofuel Cells: Past, Present and Future. *Journal of The Electrochemical Society* **164**, H3007–H3014 (2017).

70. Choi, S. Microscale microbial fuel cells: Advances and challenges. *Biosensors and Bioelectronics* **69**, 8–25 (2015).

71. Pang, S., Gao, Y. & Choi, S. Flexible and Stretchable Biobatteries: Monolithic Integration of Membrane-Free Microbial Fuel Cells in a Single Textile Layer. *Advanced Energy Materials* **8**, 1702261 (2017).

72. Taylor, N. A. & Machado-Moreira, C. A. Regional variations in transepidermal water loss, eccrine sweat gland density, sweat secretion rates and electrolyte composition in resting and exercising humans. *Extreme Physiology & Medicine* **2**, 4 (2013).

73. Sawka, M. N., Wenger, C. B. & Pandolf, K. B. Thermoregulatory Responses to Acute Exercise-Heat Stress and Heat Acclimation. in *Comprehensive Physiology* 157–185 (American Cancer Society, 2011). doi:10.1002/cphy.cp040109.

74. Zou, Y., Raveendran, V. & Chen, J. Wearable triboelectric nanogenerators for biomechanical energy harvesting. *Nano Energy* **77**, 105303 (2020).

75. Anton, S. R. & Sodano, H. A. A review of power harvesting using piezoelectric materials (2003–2006). *Smart Mater. Struct.* **16**, R1–R21 (2007).

76. Safaei, M., Sodano, H. A. & Anton, S. R. A review of energy harvesting using piezoelectric materials: state-of-the-art a decade later (2008–2018). *Smart Mater. Struct.* **28**, 113001 (2019).

77. Sezer, N. & Koç, M. A comprehensive review on the state-of-the-art of piezoelectric energy harvesting. *Nano Energy* **80**, 105567 (2021).

78. Alluri, N. R. *et al.* Scavenging Biomechanical Energy Using High-Performance, Flexible BaTiO3 Nanocube/PDMS Composite Films. *ACS Sustainable Chem. Eng.* **5**, 4730–4738 (2017).

79. Gu, L. *et al.* Enhancing the current density of a piezoelectric nanogenerator using a three-dimensional intercalation electrode. *Nat Commun* **11**, 1030 (2020).

80. Zi, Y. *et al.* Standards and figure-of-merits for quantifying the performance of triboelectric nanogenerators. *Nat Commun* **6**, 8376 (2015).

81. Zou, H. *et al.* Quantifying and understanding the triboelectric series of inorganic non-metallic materials. *Nat Commun* **11**, 2093 (2020).

82. Wu, H., Wang, S., Wang, Z. & Zi, Y. Achieving ultrahigh instantaneous power density of 10 MW/m2 by leveraging the opposite-charge-enhanced transistor-like triboelectric nanogenerator (OCT-TENG). *Nat Commun* **12**, 5470 (2021).

83. Wang, Z. *et al.* Ultrahigh Electricity Generation from Low-Frequency Mechanical Energy by Efficient Energy Management. *Joule* **5**, 441–455 (2021).

84. Seebeck, T. J. Ueber die magnetische Polarisation der Metalle und Erze durch Temperaturdifferenz. *Annalen der Physik* **82**, 253–286 (1826).

85. Siddique, A. R. M., Mahmud, S. & Heyst, B. V. A review of the state of the science on wearable thermoelectric power generators (TEGs) and their existing challenges. *Renewable and Sustainable Energy Reviews* **73**, 730–744 (2017).

86. Ren, W. *et al.* High-performance wearable thermoelectric generator with self-healing, recycling, and Lego-like reconfiguring capabilities. *Science Advances* **7**, eabe0586 (2021).

87. Shin, S. *et al.* High-Performance Screen-Printed Thermoelectric Films on Fabrics. *Scientific Reports* **7**, 7317 (2017).

88. Shi, Y., Wang, Y., Mei, D., Feng, B. & Chen, Z. Design and Fabrication of Wearable Thermoelectric Generator Device for Heat Harvesting. *IEEE Robotics and Automation Letters* **3**, 373–378 (2018).

89. Wu, Z., Tang, J., Zhang, X. & Yu, Z. An energy harvesting bracelet. *Appl. Phys. Lett.* **111**, 013903 (2017).

90. Zhou, Y. *et al.* Giant magnetoelastic effect in soft systems for bioelectronics. *Nat. Mater.* 1–7 (2021) doi:10.1038/s41563-021-01093-1.

91. Zhang, T., Yang, T., Zhang, M., Bowen, C. R. & Yang, Y. Recent Progress in Hybridized Nanogenerators for Energy Scavenging. *iScience* **23**, 101689 (2020).

92. Zhao, K., Ouyang, B., Bowen, C. R., Wang, Z. L. & Yang, Y. One-structure-based multi-effects coupled nanogenerators for flexible and self-powered multi-functional coupled sensor systems. *Nano Energy* **71**, 104632 (2020).

93. Takamatsu, T., Chen, Y., Yoshimasu, T., Nishizawa, M. & Miyake, T. Highly Efficient, Flexible Wireless-Powered Circuit Printed on a Moist, Soft Contact Lens. *Advanced Materials Technologies* **4**, 1800671 (2019).

94. Masotti, D., Costanzo, A. & Adami, S. Design and realization of a wearable multi-frequency RF energy harvesting system. in *Proceedings of the 5th European Conference on Antennas and Propagation (EUCAP)* 517–520 (2011).

95. Zhao, B., Mao, J., Zhao, J., Yang, H. & Lian, Y. The Role and Challenges of Body Channel Communication in Wearable Flexible Electronics. *IEEE Transactions on Biomedical Circuits and Systems* **14**, 283–296 (2020).

96. Chong, Y.-W., Ismail, W., Ko, K. & Lee, C.-Y. Energy Harvesting For Wearable Devices: A Review. *IEEE Sensors Journal* **19**, 9047–9062 (2019).

97. Flynn, D., Aitken, R., Gibbons, A. & Shi, K. *Low Power Methodology Manual: For System-on-Chip Design*. (Springer Science & Business Media, 2007).

98. STM32 Ultra Low Power Microcontrollers. https://www.st.com/en/microcontrollers-microprocessors/stm32-ultra-low-power-mcus.html.

99. Low-Power Microcontrollers and Microprocessors. https://www.microchip.com/en-us/solutions/low-power.

100. Homayounfar, S. Z. & Andrew, T. L. Wearable Sensors for Monitoring Human Motion: A Review on Mechanisms, Materials, and Challenges. *SLAS TECHNOLOGY: Translating Life Sciences Innovation* **25**, 9–24 (2020).

101. Dahiya, A. S. *et al.* Review—Energy Autonomous Wearable Sensors for Smart Healthcare: A Review. *J. Electrochem. Soc.* **167**, 037516 (2019).

102. Klonoff, D. C., Ahn, D. & Drincic, A. Continuous glucose monitoring: A review of the technology and clinical use. *Diabetes Research and Clinical Practice* **133**, 178–192 (2017).

103. Joseph Wang. Electrochemical Sensors. in *Analytical Electrochemistry* 201–243 (John Wiley & Sons, Ltd, 2006). doi:10.1002/0471790303.ch6.

104. Mukhopadhyay, S. C. Wearable Sensors for Human Activity Monitoring: A Review. *IEEE Sensors Journal* **15**, 1321–1330 (2015).

105. Grattieri, M. & Minteer, S. D. Self-Powered Biosensors. *ACS Sens.* **3**, 44–53 (2018).

106. Valdés-Ramírez, G. *et al.* Microneedle-based self-powered glucose sensor. *Electrochemistry Communications* **47**, 58–62 (2014).

107. Shi, Y. *et al.* A novel self-powered wireless temperature sensor based on thermoelectric generators. *Energy Conversion and Management* **80**, 110–116 (2014).

108. Zhao, J. *et al.* A Fully Integrated and Self-Powered Smartwatch for Continuous Sweat Glucose Monitoring. *ACS Sens.* **4**, 1925–1933 (2019).

109. Zhu, M. *et al.* Self-Powered and Self-Functional Cotton Sock Using Piezoelectric and Triboelectric Hybrid Mechanism for Healthcare and Sports Monitoring. *ACS Nano* **13**, 1940–1952 (2019).

110. Jeerapan, I., Sempionatto, J. R., Pavinatto, A., You, J.-M. & Wang, J. Stretchable biofuel cells as wearable textile-based self-powered sensors. *Journal of Materials Chemistry A* **4**, 18342–18353 (2016).

111. Seneviratne, S. *et al.* A Survey of Wearable Devices and Challenges. *IEEE Communications Surveys Tutorials* **19**, 2573–2620 (2017).

112. Wang, Q., Hempstead, M. & Yang, W. A Realistic Power Consumption Model for Wireless Sensor Network Devices. in *2006 3rd Annual IEEE Communications Society on Sensor and Ad Hoc Communications and Networks* vol. 1 286–295 (2006).

113. Lee, J.-S., Su, Y.-W. & Shen, C.-C. A Comparative Study of Wireless Protocols: Bluetooth, UWB, ZigBee, and Wi-Fi. in *IECON 2007 - 33rd Annual Conference of the IEEE Industrial Electronics Society* 46–51 (2007). doi:10.1109/IECON.2007.4460126.

114. Dementyev, A., Hodges, S., Taylor, S. & Smith, J. Power consumption analysis of Bluetooth Low Energy, ZigBee and ANT sensor nodes in a cyclic sleep scenario. in *2013 IEEE International Wireless Symposium (IWS)* 1–4 (2013). doi:10.1109/IEEE-IWS.2013.6616827.

115. Kim, H.-J. *et al.* Review of Near-Field Wireless Power and Communication for Biomedical Applications. *IEEE Access* **5**, 21264–21285 (2017).

116. Lathiya, P. & Wang, J. *Near-Field Communications (NFC) for Wireless Power Transfer (WPT): An Overview*. *Wireless Power Transfer – Recent Development, Applications and New Perspectives* (IntechOpen, 2021). doi:10.5772/intechopen.96345.

117. Fernández, M. R., Casanova, E. Z. & Alonso, I. G. Review of Display Technologies Focusing on Power Consumption. *Sustainability* **7**, 10854–10875 (2015).

118. Kim, J. *et al.* Ultrathin Quantum Dot Display Integrated with Wearable Electronics. *Advanced Materials* **29**, 1700217 (2017).

119. Zhou, Y. *et al.* Stretchable High-Permittivity Nanocomposites for Epidermal Alternating-Current Electroluminescent Displays. *ACS Materials Lett.* **1**, 511–518 (2019).

120. Andersson, P., Forchheimer, R., Tehrani, P. & Berggren, M. Printable All-Organic Electrochromic Active-Matrix Displays. *Advanced Functional Materials* **17**, 3074–3082 (2007).

121. Andersson Ersman, P., Kawahara, J. & Berggren, M. Printed passive matrix addressed electrochromic displays. *Organic Electronics* **14**, 3371–3378 (2013).

122. Rogers, J. A. *et al.* Paper-like electronic displays: large-area rubber-stamped plastic sheets of electronics and microencapsulated electrophoretic inks. *Proceedings of the National Academy of Sciences of the United States of America* **98**, 4835–40 (2001).

123. Nikhar, A. R., Apte, S. M. & Somalwar, R. Review of various control techniques for DC-DC interleaved boost converters. in *2016 International Conference on Global Trends in Signal Processing, Information Computing and Communication (ICGTSPICC)* 432–437 (2016). doi:10.1109/ICGTSPICC.2016.7955340.

124. Ghosh, S., Satpathy, S., Das, S., Debbarma, S. & Bhattacharyya, B. K. Different Controlling Method of Closed Loop DC-DC Buck Converter: A review. in *2018 International Conference on Smart Systems and Inventive Technology (ICSSIT)* 29–33 (2018). doi:10.1109/ICSSIT.2018.8748695.

125. TPS628503-Q1 datasheet. https://www.ti.com/document-viewer/TPS628503-Q1/datasheet/GUID-DFA56A7D-14AB-4D63-88FA-4ADBBFA5F128#TITLE-SLUSDM0X188.

126. *TI bq25505 Datasheet*.

127. Hohm, D. P. & Ropp, M. E. Comparative study of maximum power point tracking algorithms. *Progress in Photovoltaics: Research and Applications* **11**, 47–62 (2003).

128. Chaibi, Y., Allouhi, A., Salhi, M. & El-jouni, A. Annual performance analysis of different maximum power point tracking techniques used in photovoltaic systems. *Protection and Control of Modern Power Systems* **4**, 15 (2019).

129. Zi, Y. *et al.* Effective energy storage from a triboelectric nanogenerator. *Nat Commun* **7**, 10987 (2016).

130. Cheng, G., Lin, Z.-H., Lin, L., Du, Z. & Wang, Z. L. Pulsed Nanogenerator with Huge Instantaneous Output Power Density. *ACS Nano* **7**, 7383–7391 (2013).

131. Cheng, X. *et al.* High efficiency power management and charge boosting strategy for a triboelectric nanogenerator. *Nano Energy* **38**, 438–446 (2017).

132. Niu, S. *et al.* Simulation method for optimizing the performance of an integrated triboelectric nanogenerator energy harvesting system. *Nano Energy* **8**, 150–156 (2014).

133. Niu, S. *et al.* Optimization of Triboelectric Nanogenerator Charging Systems for Efficient Energy Harvesting and Storage. *IEEE Transactions on Electron Devices* **62**, 641–647 (2015).

134. González, A., Goikolea, E., Barrena, J. A. & Mysyk, R. Review on supercapacitors: Technologies and materials. *Renewable and Sustainable Energy Reviews* **58**, 1189–1206 (2016).

135. Borenstein, A. *et al.* Carbon-based composite materials for supercapacitor electrodes: a review. *Journal of Materials Chemistry A* **5**, 12653–12672 (2017).

136. Zhang, Y. *et al.* Progress of electrochemical capacitor electrode materials: A review. *International Journal of Hydrogen Energy* **34**, 4889–4899 (2009).

137. Yin, L. *et al.* High Performance Printed AgO-Zn Rechargeable Battery for Flexible Electronics. *Joule* **5**, 228–248 (2021).

138. He, J. *et al.* Scalable production of high-performing woven lithium-ion fibre batteries. *Nature* **597**, 57–63 (2021).

139. Wang, D. *et al.* Energy density issues of flexible energy storage devices. *Energy Storage Materials* **28**, 264–292 (2020).

140. Li, H. *et al.* Advanced rechargeable zinc-based batteries: Recent progress and future perspectives. *Nano Energy* **62**, 550–587 (2019).

141. Wen, J., Yu, Y. & Chen, C. A Review on Lithium-Ion Batteries Safety Issues: Existing Problems and Possible Solutions. *Materials Express* **2**, 197–212 (2012).

142. Kumar, R. *et al.* All-Printed, Stretchable Zn-Ag2O Rechargeable Battery via Hyperelastic Binder for Self-Powering Wearable Electronics. *Advanced Energy Materials* **7**, 1602096 (2017).

143. Chen, X., Huang, H., Pan, L., Liu, T. & Niederberger, M. Fully Integrated Design of a Stretchable Solid-State Lithium-Ion Full Battery. *Advanced Materials* **31**, 1904648 (2019).

144. Yin, L. *et al.* Highly Stable Battery Pack via Insulated, Reinforced, Buckling-Enabled Interconnect Array. *Small* **14**, 1800938 (2018).

145. Tehrani, F. *et al.* Laser-Induced Graphene Composites for Printed, Stretchable, and Wearable Electronics. *Advanced Materials Technologies* **4**, 1900162 (2019).

146. Yu, J. *et al.* Omnidirectionally Stretchable High-Performance Supercapacitor Based on Isotropic Buckled Carbon Nanotube Films. *ACS Nano* **10**, 5204–5211 (2016).

147. Liang, X. *et al.* High performance all-solid-state flexible supercapacitor for wearable storage device application. *Chemical Engineering Journal* **345**, 186–195 (2018).

148. Xu, S. *et al.* Stretchable batteries with self-similar serpentine interconnects and integrated wireless recharging systems. *Nat Commun* **4**, 1543 (2013).

149. Zi, Y. *et al.* Triboelectric–Pyroelectric–Piezoelectric Hybrid Cell for High-Efficiency Energy-Harvesting and Self-Powered Sensing. *Advanced Materials* **27**, 2340–2347 (2015).

150. Li, H. *et al.* A Hybrid Biofuel and Triboelectric Nanogenerator for Bioenergy Harvesting. *Nano-Micro Lett.* **12**, 50 (2020).

151. Heo, J. S., Eom, J., Kim, Y.-H. & Park, S. K. Recent Progress of Textile-Based Wearable Electronics: A Comprehensive Review of Materials, Devices, and Applications. *Small* **14**, 1703034 (2018).

152. Rong, G., Zheng, Y. & Sawan, M. Energy Solutions for Wearable Sensors: A Review. *Sensors* **21**, 3806 (2021).

153. Manjakkal, L., Pullanchiyodan, A., Yogeswaran, N., Hosseini, E. S. & Dahiya, R. A Wearable Supercapacitor Based on Conductive PEDOT:PSS-Coated Cloth and a Sweat Electrolyte. *Advanced Materials* **32**, 1907254 (2020).

154. Mukherjee, R., Ganguly, P. & Dahiya, R. Bioinspired Distributed Energy in Robotics and Enabling Technologies. *Advanced Intelligent Systems* doi:10.1002/aisy.202100036.

155. Parrilla, M. & De Wael, K. Wearable Self-Powered Electrochemical Devices for Continuous Health Management. *Advanced Functional Materials* doi:10.1002/adfm.202107042.

156. IDC - Wearable Devices Market Share. *IDC: The premier global market intelligence company* https://www.idc.com/promo/wearablevendor.

157. Wearable Technology Forecasts 2021-2031. https://www.idtechex.com/en/research-report/wearable-technology-forecasts-2021-2031/839 (2021).

158. Amjadi, M., Sheykhansari, S., Nelson, B. J. & Sitti, M. Recent Advances in Wearable Transdermal Delivery Systems. *Advanced Materials* **30**, 1704530 (2018).

159. Lee, H. *et al.* Device-assisted transdermal drug delivery. *Advanced Drug Delivery Reviews* **127**, 35–45 (2018).

160. Kong, X. T. R., Luo, H., Huang, G. Q. & Yang, X. Industrial wearable system: the human-centric empowering technology in Industry 4.0. *J Intell Manuf* **30**, 2853–2869 (2019).

161. Kim, J. *et al.* Wearable salivary uric acid mouthguard biosensor with integrated wireless electronics. *Biosensors and Bioelectronics* **74**, 1061–1068 (2015).

162. Sempionatto, J. R. *et al.* Eyeglasses based wireless electrolyte and metabolite sensor platform. *Lab Chip* **17**, 1834–1842 (2017).

163. Sempionatto, J. R. *et al.* Eyeglasses-based tear biosensing system: Non-invasive detection of alcohol, vitamins and glucose. *Biosensors and Bioelectronics* **137**, 161–170 (2019).

164. Hou, T.-C. *et al.* Triboelectric nanogenerator built inside shoe insole for harvesting walking energy. *Nano Energy* **2**, 856–862 (2013).

165. Zhu, G., Bai, P., Chen, J. & Lin Wang, Z. Power-generating shoe insole based on triboelectric nanogenerators for self-powered consumer electronics. *Nano Energy* **2**, 688–692 (2013).

166. Benight, S. J., Wang, C., Tok, J. B. H. & Bao, Z. Stretchable and self-healing polymers and devices for electronic skin. *Progress in Polymer Science* **38**, 1961–1977 (2013).

167. Kim, D.-H. *et al.* Epidermal Electronics. *Science* **333**, 838–843 (2011).

168. Lipomi, D. J. *et al.* Skin-like pressure and strain sensors based on transparent elastic films of carbon nanotubes. *Nature Nanotech* **6**, 788–792 (2011).

169. Kaltenbrunner, M. *et al.* An ultra-lightweight design for imperceptible plastic electronics. *Nature* **499**, 458–463 (2013).

170. Miyamoto, A. *et al.* Inflammation-free, gas-permeable, lightweight, stretchable on-skin electronics with nanomeshes. *Nature Nanotech* **12**, 907–913 (2017).

171. Yeo, W.-H. *et al.* Multifunctional Epidermal Electronics Printed Directly Onto the Skin. *Advanced Materials* **25**, 2773–2778 (2013).

172. Chung, H. U. *et al.* Binodal, wireless epidermal electronic systems with in-sensor analytics for neonatal intensive care. *Science* **363**, eaau0780 (2019).

173. Wang, C. *et al.* Monitoring of the central blood pressure waveform via a conformal ultrasonic device. *Nature Biomedical Engineering* **2**, 687–695 (2018).

174. Bandodkar, A. J. *et al.* Sweat-activated biocompatible batteries for epidermal electronic and microfluidic systems. *Nature Electronics* **3**, 554–562 (2020).

175. Yokota, T. *et al.* Ultraflexible organic photonic skin. *Science Advances* **2**, e1501856 (2016).

176. Wang, B. *et al.* High-k Gate Dielectrics for Emerging Flexible and Stretchable Electronics. *Chem. Rev.* **118**, 5690–5754 (2018).

177. Liu, Y., Pharr, M. & Salvatore, G. A. Lab-on-Skin: A Review of Flexible and Stretchable Electronics for Wearable Health Monitoring. *ACS Nano* **11**, 9614–9635 (2017).

178. Wang, C., Wang, C., Huang, Z. & Xu, S. Materials and Structures toward Soft Electronics. *Advanced Materials* **30**, 1801368 (2018).

179. Oh, J. Y. & Bao, Z. Second Skin Enabled by Advanced Electronics. *Advanced Science* **6**, 1900186 (2019).

180. Chen, G., Li, Y., Bick, M. & Chen, J. Smart Textiles for Electricity Generation. *Chem. Rev.* **120**, 3668–3720 (2020).

181. Lv, J. *et al.* Sweat-based wearable energy harvesting-storage hybrid textile devices. *Energy & Environmental Science* **11**, 3431–3442 (2018).

182. Jia, W. *et al.* Wearable textile biofuel cells for powering electronics. *J. Mater. Chem. A* **2**, 18184–18189 (2014).

183. Lin, R. *et al.* Wireless battery-free body sensor networks using near-field-enabled clothing. *Nature Communications* **11**, 444 (2020).

184. Tian, X. *et al.* Wireless body sensor networks based on metamaterial textiles. *Nature Electronics* **2**, 243–251 (2019).

185. Wang, L. *et al.* Weaving Sensing Fibers into Electrochemical Fabric for Real-Time Health Monitoring. *Advanced Functional Materials* **28**, 1804456 (2018).

Chapter 2 High Performance Printed Battery for Wearable Energy Storage

2.1 Introduction

Recent interest in multifunctional flexible electronics for applications in sensing, displays, and wireless communication advocates for the development of complementary flexible energy storage solutions.[1,2] Accordingly, numerous efforts have been made to tackle the challenges of fabricating batteries with robust mechanical resiliency and high electrochemical performance. To do so, several studies focused on adapting novel battery fabrication techniques, such as substrate pre-stretching, textile-embedding, and "island-bridge", wire/cable, kirigami, and origami structuring to endow structural flexibility and stretchability to batteries.[3–9] Other studies focused on tackling the challenge by the means of material innovation, developing polymer-based current collectors, electrodes, separators, and electrolytes for various intrinsically flexible and stretchable batteries.[10–17] However, due to the exponential growth in the wearable flexible electronics market, manufacturers started to realize the urgent need for scalable, low-cost, and high-performance flexible battery technologies to provide practical energy storage solutions for the tens of millions of devices produced every year. Many flexible batteries rely on fabrication processes that are complex, low throughput, and high cost, and thus have limited practicality which hinders their lab-to-market transformation. Addressing the need for flexibility and scalability while maintaining low cost, printed high-performance batteries is crucial for realizing most of the commercially viable battery technology. Using low-cost thick-film fabrication technologies, flexible battery components can be printed sheet-to-sheet or roll-to-roll using traditional, low-maintenance screen printing or doctor blade casting equipment, thus realizing low-cost mass production of flexible batteries.[18]

Among many commercialized printed flexible batteries, aqueous zinc (Zn)-based conversion cells were successful in developing products with high throughput and low production cost.[19] The Zn anode chemistry has been of special interest to the flexible battery market due to its low material cost, high theoretical capacity (820 mAh/g, 5854 Ah/L), good rechargeability, and safe chemistry.[20,21] In addition, as Zn and the aqueous electrolyte can be readily handled in an ambient environment, the equipment and production costs of Zn-based batteries are often considerably lower compared to lithium-ion batteries. However, commercial Zn-based printed flexible batteries are usually non-rechargeable and feature low capacity and high impedance, thus limiting their application in low-power, disposable electronics only. Addressing these limitations, several studies have reported the development of printable, rechargeable, and high-performance Zn-based batteries.[16,22,23] Among them, the silver oxide-zinc (Ag_2O-Zn) battery has attracted particular attention due to its rechargeable chemistry and its tolerance to high-current discharge.[24,25] The redox reaction relies on the dissolution of zinc ions (Zn^{2+}) and silver ions (Ag^{+}) in the alkaline electrolyte and their supersaturation-induced precipitation, which takes place rapidly while maintaining a stable voltage at 1.56 V (**Equation 2.1 – 2.3**). [26,27] All E° potentials are indicated using the standard hydrogen electrode (SHE) as a reference.

Anode:

(Dissolution) $Zn\ (s) + 4OH^-\ (aq) \leftrightarrow Zn(OH)_4^{2-}\ (aq) + 2e^-$ (**Equation 2.1**)

(Relaxation) $Zn(OH)_4^{2-}(aq) \leftrightarrow ZnO\ (s) + H_2O\ +\ 2OH^-\ (aq)$ **(Equation 2.2**)

(Overall) $Zn\ (s) + 2OH^-\ (aq) \leftrightarrow ZnO + H_2O + 2e^-$ $\mathrm{E^o} = -1.22$ V vs. SHE

(**Equation 2.3**)

Cathode:

(Dissolution) $Ag + OH^- \leftrightarrow AgOH(aq) + e^-$ (**Equation 2.4**)

(Relaxation) $2AgOH(aq) + 2OH^- \leftrightarrow Ag_2O(s) + H_2O$ (**Equation 2.5**)

(Overall) $Ag_2O(s) + H_2O \leftrightarrow 2Ag(s) + 2OH^-(aq)$ $E^o = +0.34$ V vs. SHE

(**Equation 2.6**)

Most of these batteries rely solely on the use of the lower oxidation state of silver to obtain a reversible redox reaction, while the higher oxidation state (AgO), with its redox reaction described in **Equation 2.7**, has been rarely utilized.

$2AgO\ (s) + H_2O + 2e^- \leftrightarrow Ag_2O\ (s) + H_2O\ (l)$ $E^o = +0.60$ V vs. SHE

(**Equation 2.7**)

The underutilization of AgO can be attributed to its instability, namely, its lattice phase change when transitioning into Ag_2O, which may result in irreversible shape changes that impede rechargeability, and its high charging potential is responsible for possible electrode gassing due to oxygen evolution reaction.[8,28–31] However, once addressing these issues, it is possible to access a much higher theoretical cathode capacity (from 231 mAh/g for Ag_2O to 432 mAh/g for AgO). So far, printed silver-zinc batteries reported in the literature still have low rechargeability (< 50 cycles), limited capacity (< 12 mAh/cm^2 for primary cell, < 3 mAh/cm^2 for secondary cell), along with high internal resistance (~10^2 Ω) that results in large voltage drop during operation.[10,29,32–34] Such limitations are hindering the adaptation of silver-zinc printed batteries in flexible electronics.

Herein, we present a novel fabrication process of all-printed, flexible, and rechargeable AgO-Zn batteries with ultra-high areal capacity, low impedance, and good rechargeability as a practical energy storage solution for flexible electronics. The fabrication of the cell relies on low-cost, high-throughput, layer-by-layer printing of formulated powder-elastomer composite inks to form the current collectors, Zn anode, AgO cathode, and their corresponding separators. The battery adopts a low-footprint stacked configuration, with potassium hydroxide (KOH) - poly(vinyl alcohol) (PVA) hydrogel as a low impedance electrolyte sandwiched between the two fully printed electrodes. Using the thermoplastic styrene-ethyl-butylene-styrene block copolymer (SEBS) elastomer-based substrate, the assembled battery can be directly heat- and vacuum-sealed to preserve the electrolyte and ensure appropriate cell pressure during operation. This fabrication and assembly process can be applied to different cell sizes with adjustable areal capacity, allowing customizable battery form factors that are tailored for specific applications. Fully utilizing the higher oxidation state of the AgO, the as-printed cells were able to reach a high areal capacity of > 54 mAh/cm^2 while maintaining a low internal resistance (~10 Ω) for primary applications. Furthermore, utilizing an optimized cycling profile, the printed cells were recharged for over 80 cycles, sustaining 0.2 C – 1 C discharges without exhibiting significant capacity loss, while maintaining low impedance throughout each cycle. Moreover, the fabricated cells displayed outstanding robustness against repeated bending and twisting deformations. To demonstrate their performance in powering typical flexible electronics, the fabricated batteries were successfully implemented in a flexible E-ink display system with an integrated microcontroller unit (MCU) and Bluetooth modules that require pulsed high-current discharge. Leveraging a low-cost scalable production process, polymer-based flexible architecture, and customized ink formulations, the all-printed AgO-Zn battery, with its desirable mechanical and electrochemical performance, presents

a practical solution for powering the next-generation flexible electronics, and sets a new benchmark for the further development of printable flexible batteries.

2.2 Experimental Section

2.2.1 Chemicals

Bi_2O_3, $Ca(OH)_2$, KOH (pellets, ≥85%), LiOH, 4-methylpentan-2-one (MIBK), toluene, cellulose (microcrystalline powder, 20 μm), Triton-X 114, Poly(ethylene oxide) (PEO) (MW 600,000), and PVA (MW = 89000 – 98000, 99+% Hydrolyzed) were purchased from Sigma Aldrich (St. Louis, MO, USA). Zn (Grillo-Werke AG, Germany), AgO (Ames Goldsmith, South Glens Falls, NY, USA), and TiO_2 (CR-470, Tronox Holdings plc, New York, NY, USA) were obtained from ZPower LLC (Camarillo, CA, USA). The fluorocopolymer (GBR-6005, poly(vinylfluoride-co-2,3,3,3-tetrafluoropropylene)) was obtained from Daikin US Corporation (New York, NY, USA). SEBS (G1645) was obtained from Kraton (Houston, TX, USA). Graphite powder was purchased from Acros Organics (USA). Super-P carbon black was purchased from MTI Corporation (Richmond, CA, USA). All reagents were used without further purification.

2.2.2 Cell Fabrication

The electrode resin was prepared by adding 5 g of the fluorine rubber to 10 g of MIBK solvent and left on a shake table overnight, until the mixture was homogeneous. The SEBS resin was prepared by adding 40 g of the SEBS into 100 mL of toluene and left on a shake table until the mixture was homogeneous.

The silver current collector ink was formulated by combining Ag flakes, SEBS resin, and toluene in 4: 2: 1 weight ratio and mixing in a planetary mixer (Flaktak Speedmixer^{TM} DAC 150.1

FV) at 1800 rotations per minute (RPM) for 5 min.[35] The carbon current collector ink was formulated by firstly mixing graphite, Super-P, and PTFE powder in 84: 14: 2 weight ratio with a set of pestle and mortar. The mixed powder was mixed with the SEBS resin and toluene in a 10: 12: 3 weight ratio using the mixer at 2250 RPM for 10 min to obtain a printable ink.[10]

The Zn anode ink was formulated by firstly mixing the Zn and Bi_2O_3 powders in a 9:1 weight ratio with a set of pestle and mortar until the Zn particles are evenly coated with the Bi_2O_3 powder. The evenly mixed powder was then mixed with the electrode resin and MIBK in a 20: 4: 1 weight ratio using the mixer at 1800 RPM for 5 min to obtain a printable ink. The AgO cathode ink was formulated by firstly mixing the AgO and Super-P powders in a 95: 5 weight ratio using a set of pestle and mortar until homogeneous. The powder was then mixed with the electrode resin and MIBK in 5: 5: 2 weight ratio using the mixer at 2250 RPM for 5 min to obtain a printable ink.

The TiO_2 separator ink was prepared by firstly mixing TiO_2 and cellulose powder in a 2: 1 weight ratio using a set of pestle and mortar. The mixed powder was then added with the SEBS resin, toluene and Triton-X in 50: 55: 75: 3 weight ratio and mixed with the mixer at 2250 RPM for 10 min to obtain a printable ink. The addition of Triton-X surfactant in the anode separator ensures the proper wetting of the thick Zn anode, hence increasing the effective electrochemical surface area of the anode and avoiding high local current density that would lead to dendrite growth. The cellulose separator ink was prepared by firstly mixing TiO_2 and cellulose powder in a 26: 9 weight ratio using a set of pestle and mortar. The mixed powder was then added with the electrode resin, MIBK in an 8: 7: 4 weight ratio and mixed with the mixer at 2250 RPM for 10 min to obtain a printable ink. All inks above were formulated empirically to obtain a screen-printable consistency, which was adjusted with various amounts of solvent to achieve good printing quality.

SEBS was dissolved in toluene with a weight ratio of 6 to 8.7 and was left on a linear shaker (Scilogex, SK-L180-E) overnight or until the mixture became transparent and homogeneous. Wax paper was used as the temporary casting substrate, and a film caster with a clearance of 1000 um was used to cast the SEBS resin onto the wax paper. The cast resin was firstly dried in the ambient environment for 1 h, followed by curing in a conventional oven at 80 °C for 1 h to remove the excess solvent. The transparent, uniform SEBS film, which can be readily peeled off from the wax paper after curing, was used as the substrate for subsequent battery printing.

Stencils for printing the current collectors, electrodes, and separators were designed using AutoCAD software (Autodesk, San Rafael, CA, USA) and produced by Metal Etch Services (San Marcos, CA), with dimensions of 12 in × 12 in. The stencils used in this work were stainless steel cut-out stencils without meshes. The thickness of the stencils was designed to be 100 µm for the carbon and silver current collectors, 300 µm for the TiO_2 separator and the Zn anode, and 500 µm for the cellulose separator and the AgO cathode. The printing of the following layers was performed using a semi-automatic MPM-SPM printer (Speedline Technologies, Franklin, MA, USA) with an 8-inch metal blade squeegee. The stencil and squeegee pressure were optimized for each stencil, correspondingly. To print the anode, the silver ink was first printed onto the SEBS substrate and cured in a conventional oven at 80 °C for 10 min. The Zn ink was then printed onto the silver current collectors and cured at 80 °C for 30 min. The TiO_2 ink was lastly printed onto the anode and cured at 80 °C for 10 min. To print the cathode, the carbon ink was firstly printed onto the SEBS substrate and cured at 80 °C for 10 min. PET sheets were cut using a computer-controlled cutting machine (Cricut Maker®, Cricut, Inc., South Jordan, UT, USA) into a mask exposing the printed carbon electrodes, and the masked carbon current collector was sputtered with ~ 400 nm of Au and adhesion interlayer of Cr at a DC power of 100W and 200W respectively and an Ar gas flow rate of 16 SCCM using a Denton Discovery 635

Sputter System (Denton Discovery 635 Sputter System, Denton Vacuum, LLC, Moorestown, NJ, USA). The AgO ink was then printed onto the sputtered current collectors and cured at 50 °C for 60 min. Lastly, the cellulose ink was printed onto the cathode and cured at 50 °C for 60 min. To print multiple layers of electrodes or the separators, the stencil was offset by an additional 65 µm for each layer of AgO and 100 µm for each layer of Zn to compensate for the electrode thickness. See **Figure 2.1** for the step-by-step printing and assembly process of the batteries and **Figure 2.2** for the thickness calibration for the printing of anode and cathode.

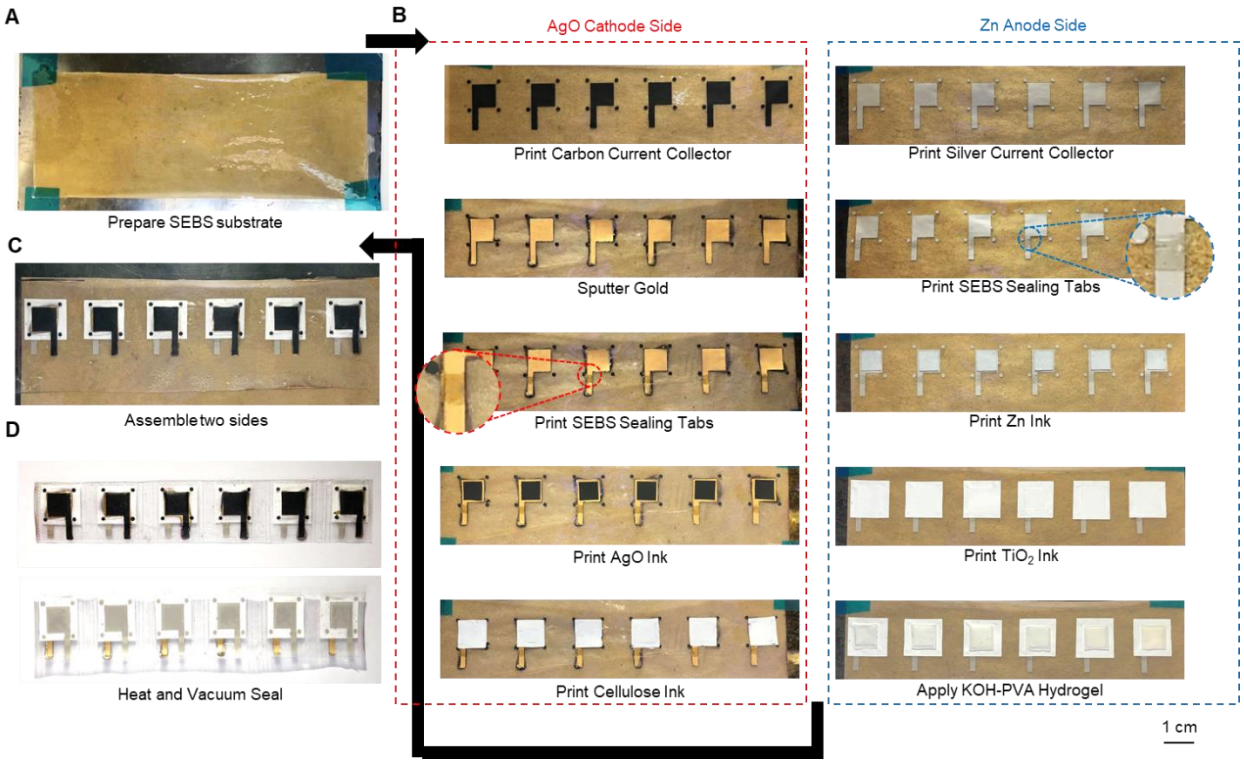

Figure 2.1. The images of the step-by-step batched fabrication of the printed AgO-Zn batteries.
A. Prepared SEBS substrate. **B**. The layer-by-layer printing of the AgO cathode (left) and the Zn anode (right). **C**. Placing the cathode side onto the anode side with the hydrogel electrolyte in between. **D**. Heat and vacuum sealing of the batteries. Each cell was separated by further heat sealing after the entire batch was vacuum sealed.

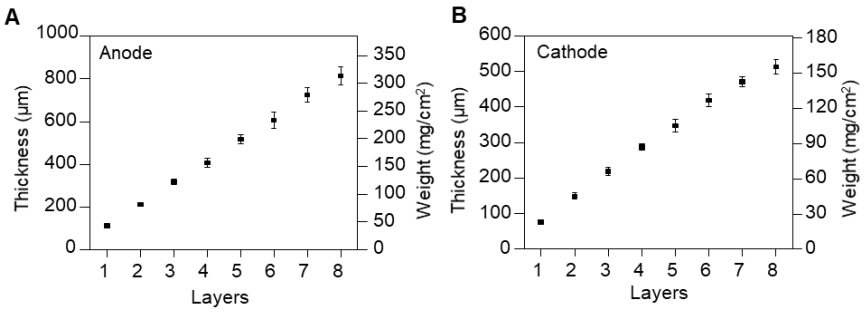

Figure 2.2. Printing thickness calibration.
A. anode and **B**. cathode printed using their corresponding stencils. Five samples were taken to generate the average thicknesses and standard deviations of each data point.

The hydrogel is synthesized by mixing the PVA solution and the hydroxide solution into a gel precursor and dried in a desiccator until the desired weight is reached. For synthesizing the 36.5% hydroxide gel used in this study, the following formulations were used. A hydroxide solution was prepared by dissolving 9.426 g KOH and 0.342 g LiOH into 50 mL deionized (DI) water. 0.5g $Ca(OH)_2$ was then added to the solution and stirred in a closed container under room temperature for 1 h to saturate the solution with $Ca(OH)_2$, and the excess $Ca(OH)_2$ was then removed from the solution. A PVA solution was prepared by dissolving 4.033 g PVA and 0.056 g PEO into 50 mL DI water heated to 90 °C. The precursor solution was prepared by mixing the hydroxide solution and the PVA solution in the weight ratio of 13.677: 10 and poured into a flat petri dish with the weight of 0.2 g/cm^2. The precursor was left to dry in a vacuum desiccator until the weight decreased to 26.12% of precursor weight to obtain a soft, translucent hydrogel with its caustic material taking 36.5% of the sum of caustic material and the water content. Additional weight and conductivity information for different hydroxide concentrations can be found in **Table 2.1**. The hydrogel can be then cut into desired sizes and directly used or stored in a hydroxide solution with the same weight ratio of hydroxide without PVA. The storage solution for the 36.5% KOH-PVA gel was prepared similarly

to the hydroxide solution, where 10.777 g KOH, 0.391 g LiOH, and 0.5g $Ca(OH)_2$ were dissolved into 15 mL DI water and the excess $Ca(OH)_2$ was removed. More images of the fabrication of the hydrogel are shown in **Figure 2.3**.

Table 2.1. KOH-PVA electrolyte information

Caustic Concentration	Removed Precursor Water wt%	σ_0 (mS/cm)	E_a (eV)
26.3%	65.77%	2.037×10^4	0.109
31.8%	70.72%	3.155×10^4	0.115
36.5%	73.88%	6.029×10^4	0.138

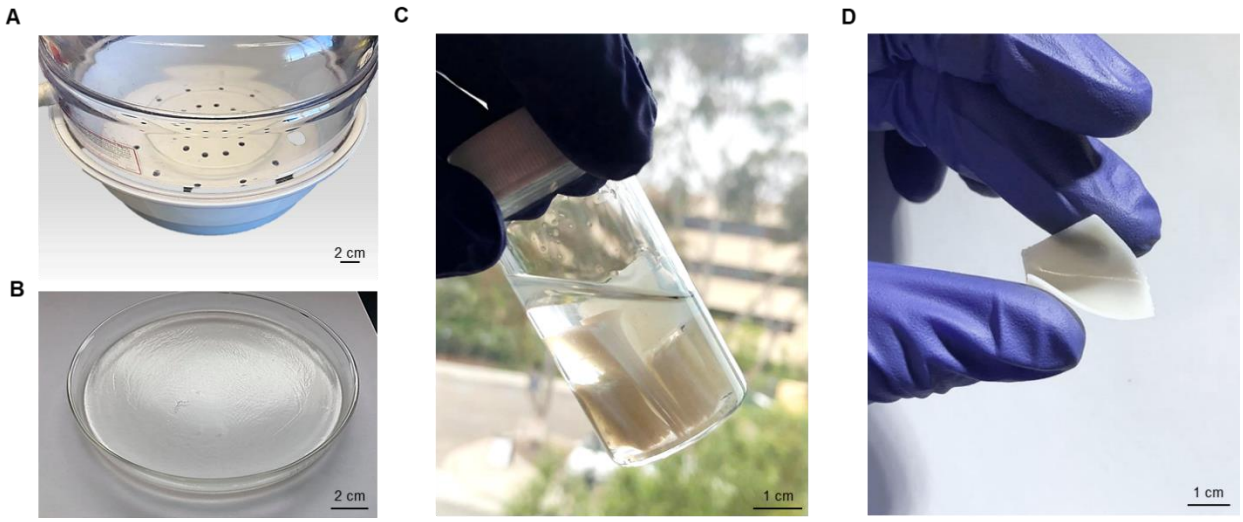

Figure 2.3. Images of the fabrication of the KOH-PVA electrolyte gel.
A. Drying of the precursor solution to desired concentration in a vacuum desiccator. **B**. The crosslinked 36.5 % hydrogel after drying. **C**. Storage of the hydrogel pieces after cutting into desired sizes. **D**. A bent 2 × 2 cm^2 hydrogel.

Morphological analyses of the current collectors, separators, and active material electrodes were performed with SEM and micro-CT. SEM images were taken using an FEI Quanta FEG 250

instrument with an electron beam energy of 15 keV, a spot size of 3, and a dwell time of 10 µs. Micro-CT experiments were conducted using a ZEISS Xradia 510 Versa. For individual film analysis, micro-CT samples were prepared by punching 2 mm radii disks and stacking them in a PTFE cylindrical tube with alternating PTFE films to provide separation between neighboring film disks. For the Micro-CT of full and sealed cell bending, a 1×5 cm^2 AgO-Zn battery was bent or rolled around a polyethylene (PE) cylindrical tube with a diameter of 1cm.

For the micro-CT active material electrodes, the heavier metals, such as Zn and Ag, warranted higher X-Ray energies than the printed polymer separator films. Accordingly, scans at 140 keV and a current of 71.26 µA were performed with high energy filters and a magnification of 4X on the Zn and AgO films with voxel sizes of 2.5 µm and 0.75 µm and exposure times of 2 s and 18 s respectively. For the polymer separators, 80 keV scans with an 87.63 µA current were used with low energy filters at a magnification of 4X with voxel resolutions of 0.75 µm and 1.1 µm and exposure times of 8 s and 1 s for the printed anode and cathode separators respectively. For scans of the full cell bending, a voltage of 140 keV and a current of 71.26 µA with a 4X magnification was applied with the following voxel resolutions and exposure times for the respective cases: 18.35 µm and 2 s for low resolution bending scan, 3.54 µm and 5 s for higher resolution bending scan, and 7.55 µm and 2 s for rolled cell scan. For all micro-CT scans conducted, 1801 projections were taken for a full 360˚ rotation with beam hardening and center shift constants implemented during the data reconstruction. Post-measurement imaging and analysis were performed by Amira-Avizo using the Despeckle, Deblur, Median Filter, Non-local Means Filter, Unsharp Mask, and Delineate modules for data sharpening and filtration provided by the software.

2.2.3 Electrochemical Characterization

The 3-electrode half-cell CV characterization was performed on a cell assembled with the printed electrodes as the working electrode, a platinum foil as the counter electrode, Zn metal foil as the reference electrode, and 2 pieces of KOH-PVA hydrogel as the electrolyte. The 3-electrode full-cell CV characterization was performed between 1.35 V to 2 V on a cell assembled similar to the typical battery architecture but with an extra Zn metal foil as the reference electrode. The structures of both cells are illustrated in **Figure 2.4**. The CV was performed using an Autolab PGSTAT128N potentiostat/galvanostat with an additional pX-1000 module. In the 3-electrode full-cell CV, the AgO cathode was connected to the working electrode probe, the Zn anode was connected to the counter and reference electrode probes, and the pX-1000 module was used to monitor the potential between the cathode and the reference Zn foil. The potential of the anode vs. Zn was obtained by subtracting the cathode vs. Zn potential from the full cell potential. A scan rate of 10 mV/s was used for all CV tests.

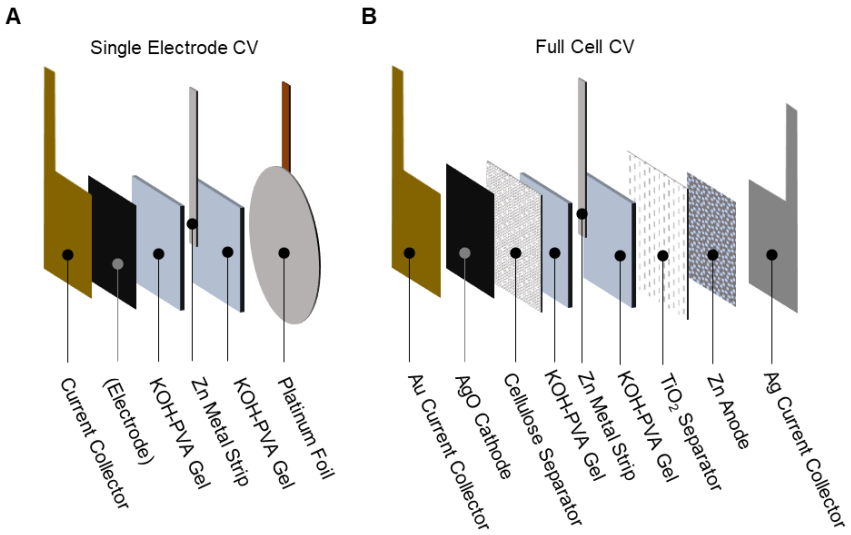

Figure 2.4. The cell structure used for the CV analysis.
A. The cell structure used for single electrode scanning for testing the current collectors. **B**. The cell structure used for full cell scanning with an external Zn metal strip as the reference electrode.

The constant current complete discharge of the battery for primary applications was performed with the following procedure. Firstly, the assembled and vacuum-sealed battery was left idle for 1 hr to allow the electrolyte to fully permeate through the electrodes. Then, the battery was discharged using a battery test system (Landt Instruments CT2001A) at the desired current, until reaching the lower cut-off voltage of 1.35 V.

To enable the secondary application of the battery, cycling protocols were established that rely on the accurate control of the potential and DOD of the battery. To perform charge-discharge cycling on a fabricated battery, 50% of its maximum capacity, which was estimated by the low-current complete discharges, was first determined as the cyclable capacity and the basis to determine the C-rates of the protocol. The battery was firstly discharged at the C-rate of 0.1 C from 100% to 40% DOD. Then, the battery was recharged at the C-rate of 0.2 C until reaching 2V, and then at 2 V until reaching 90% DOD or C-rate of 0.05C. The battery could be then discharged and recharged at the desired C-rates between 1.35 V and 2 V, with the DOD maintained between 40% and 90% of its maximum value. Unless specified otherwise, all cycling data were performed using cells with 1×1 cm^2 form factor with 2 layers of active electrode materials.

The pulsed discharge protocol was designed to simulate the battery's performance in powering a typical MCU-controlled wearable device with integrated BT functionality. The battery was discharged using an Autolab PGSTAT128N potentiostat/galvanostat implementing fast chrono methods.

Electrochemical Impedance Spectroscopy (EIS) measurements were performed with a Biologic SP-150 in a 3-electrode configuration. The AgO-Zn three electrodes cell was fabricated with a Zn reference wire placed between an extra layer of hydrogel electrolyte and the original

electrolyte layer. The Zn reference wire was then connected to an Au sputtered heat-sealable SEBS-based printed carbon tab that was vacuum sealed to ensure complete cell sealing to hinder electrolyte dehydration. The working electrode (WE) and counter electrode (CE) were connected to the AgO cathode and Zn anode, respectively.

The impedances of the two half cells and the full cell were monitored in-situ during charging and discharging to analyze impedance changes most closely related to practical cycling conditions with a galvanostatic-EIS (GEIS) measurement. Accordingly, the DC base current was set to the current of the charging/discharging step, while the AC amplitude was set to 300 μA, approximately one-fifth of the cycling current. The frequency sweep was between 1 MHz and 1 Hz with 10 points per decade and an average of 8 measures per frequency. The cycling script implemented with GEIS is similar to that of the capacity-limited electrochemical cycling protocol, with the exception that the voltage limits applied were 1.95 V and 1.4 V vs. the reference instead of the anode for the charging and discharging respectfully. For each charge and discharge step, 10 GEIS was measured for 15 complete cycles, resulting in a total of 870 separate Nyquist plots (29 steps × 10 measures × 3 cell configurations). For analysis simplicity, only the 5^{th} cycle's discharge and charge were analyzed.

Both half-cell Nyquist plots for the 5^{th} cycle's discharge and charge steps were fitted to equivalent circuits using a slightly modified version of the Zfit function available as open-source code from Mathworks.[41] Zfit utilizes another Mathworks open source code, fminsearchbnd, to minimize the error of simulated impedances with the experimental values by altering the impedance parameters (i.e. resistance values, constant phase element values, etc.) under realistic parameter boundary conditions.[42] The use of this code allowed for streamlining the fitting of many successive Nyquist to provide insights into observable trends in the fitted parameters.

The ionic conductivity of the gel electrolyte was measured by a customized two-electrode (Stainless Steel 316L) conductivity cell with an inner impedance at 0.54 Ω. The cell constant is frequently calibrated by using OAKTON standard conductivity solutions at 0.447, 1.5, 15, and 80 $mS \cdot cm^{-1}$ respectively. A constant thickness spacer was positioned between the two electrodes which ensure no distance changes during multiple-time measurements. The electrolytic conductivity value was obtained with a floating AC signal at a frequency determined by the phase angle minima given by Electrochemical Impedance Spectroscopy (EIS) using the following equation:

$$\Sigma = KR^{-Q} \qquad \textbf{(Equation 2.8)}$$

where R is the tested impedance (Ω), K is the cell constant (cm^{-1}) and Q is the fitting parameter.[43] All of the data acquisition and output were done by LabView Software, which was also used to control an ESPEC BTX-475 programming temperature chamber to maintain the cell at a set temperature in 30 minutes intervals.

2.2.4 Mechanical Deformation Tests

The mechanical testing of the battery was performed on the 1 × 5 cm^2 batteries and was composed of three parts. The first part consists of the bending and twisting of the cell with a controlled bending radius and angles. For the bending tests, the sample was bent around an Eppendorf tube towards the anode (outward) or the cathode (inward) with a radius of 0.5 cm, until folded in half (180°) or looped around (360°), at a speed of 1 bending per second. Due to the large deformation with complex movement involved in this test, the bending of the test was conducted manually with the guiding of the tube. Similarly, the twisting of the cell was performed manually, where the 1 × 5 cm^2 sample was twisted 180° clockwise followed by counterclockwise around its

long axis at a speed of 1 twisting per second. Secondly, to quantitatively assess the influence of the bending to the capacity and cycle life of the battery, 500 repetitions of 360°, 0.5 cm radius bending was applied to the sample prior to cycling the battery. The battery was then charged/discharged for 10 cycles at a rate of 0.2 C, followed by bending the battery 500 times outward 360° with a 0.5 cm radius and cycled for 10 more cycles the same rate. The capacity of the battery was monitored to quantitatively measure the influence of bending on the cell. The third part of the testing was performed using a linear motor, where the 1×5 cm^2 sample was bent freely without angle confinement, from a radius of 3 cm at 40° to a radius of 0.5 cm at 70° repeatedly, while being charged and discharged at 0.2 C.

2.2.5 Assembly of Flexible Display Electronics

To demonstrate the battery's ability to power flexible electronics, a Waveshare 2.9-inch e-Paper flexible display was powered by two AgO-Zn batteries in series. The display module was connected to an Adafruit Feather nRF52 Bluefruit Low Energy (LE) chip and programmed using Arduino and C. MATLAB code was used to convert images to hexadecimal format to be uploaded to the board and the display. The BluefruitConnect IOS app was used to connect the Adafruit chip via Bluetooth to change the display. The pulsed current profile needed to power the Bluetooth chip and display was determined using an oscilloscope by measuring the voltage across a 10 Ω resistor connected in series with the circuitry. A model pulsed profile was then extracted to be applied to flexible batteries for further testing.

2.3 Results and Discussion

2.3.1 All-printed Polymer-based Fabrication

The all-printed fabrication of the flexible AgO-Zn battery was designed based on the careful selection of elastomers for the substrate, sealing, and ink binders based on their mechanical properties, chemical stabilities, and processabilities. SEBS was selected as the substrate material for its good solvent processability, chemical stability under high pH, outstanding elasticity, as well as its appropriate melting point (~200 °C), allowing it to be easily cast into films that are chemically stable, flexible, and heat-sealable to support and seal the battery.[35] Screen-printing, a low-cost high-throughput thick-film technique was used for ink deposition, as it allows the efficient fabrication of the current collectors, electrodes, and separators into their preferred shapes and thicknesses.[18] The screen-printing of the batteries relies on the customized formulation of 6 inks corresponding to the current collectors, electrodes, and the separators for both the anode and cathode. Conductive and flexible silver ink and carbon ink were printed as the anode and cathode current collectors, respectively. Both inks use SEBS as the elastomer binder and toluene as the solvent to allow the ink to firmly bond to the toluene-soluble SEBS substrate. The anode ink is composed of Zn particles with bismuth oxide (Bi_2O_3) as an additive to reduce dendrite formation and suppress H_2 gassing, while the cathode ink is mainly composed of AgO powder with a small amount of lead oxide coating to enhance the electrochemical stability and carbon black added to enhance the electronic conductivity of the electrode.[29] A high-pH stable, elastomeric fluorocopolymer was used as the binder for both electrodes for its solubility in lower ketones which is less prone to oxidation by the highly oxidative AgO. Cellulose powder was used to form the porous cathode separator that mimics the use of cellophane to capture and reduce dissolved silver ions and prevent material crossover.[8,19] A titanium dioxide (TiO_2)-based ink was formulated for

the anode separator, acting as a physical barrier to Zn dendrite growth. The inclusion of TiO_2 also aids the recrystallization of zincate, hence preventing the Zn from traveling towards the cathode. Lastly, a solid-phase polyvinyl alcohol (PVA) hydrogel crosslinked with potassium hydroxide (KOH) was prepared as the electrolyte, which complements the cell flexibility without the risk of leaking. Lithium hydroxide (LiOH) and calcium hydroxide ($Ca(OH)_2$) were used as additives in the electrolyte to maintain electrolyte chemical stability and minimize Zn dissolution, which in turn prevents the uncontrolled recrystallization of Zn during charging which leads to the dendrite growth.[36,37]

The fabrication of the batteries begins with the preparation of the substrates, where a resin of SEBS dissolved in toluene was cast onto wax papers using film casters and dried in the oven to form a transparent elastic film. The layer-by-layer printing process is illustrated in **Figure 2.5 A**. Firstly, the Ag and the carbon inks were printed onto the SEBS substrate as current collectors, with a 400 nm layer of gold sputtered onto the carbon current collectors to enhance their conductivity and chemical stability. Then, the Zn and the TiO_2 inks, and the AgO and the cellulose inks were printed onto their corresponding current collectors. To complete the cells, the KOH-PVA hydrogel electrolyte was cut to size and sandwiched between the two electrodes. Lastly, the sheet of batteries was heat and vacuum sealed and separated into individual cells, finalizing the scalable sheet-by-sheet fabrication of multiple cells in one sitting. The flexible, vacuum-sealed AgO-Zn batteries comprised of 9 layers of composite materials, can thus be easily fabricated using layer-by-layer screen-printing (**Figure 2.5 B**). The major advantage of the stencil printing technique is the customizable dimension of the cells that can be tailored for different applications with specific form factors and capacity requirements. Cells in different sizes were fabricated using the same fabrication process (**Figure 2.5 C**) and could be integrated with different sizes of flexible

electronic devices. Regardless of the shapes and sizes, the assembled cells are highly flexible and durable under repeated mechanical deformations (**Figure 2.5 D**), making them highly suitable for powering wearable and flexible electronics that require high resiliency to various deformations. Furthermore, the superior electrochemical performance of the fabricated AgO-Zn battery greatly expands the application of flexible printed batteries in electronics with high power demands. This capability was demonstrated by powering a flexible display system with microcontroller and Bluetooth modules (**Figure 2.5 E**), as discussed in the later section.

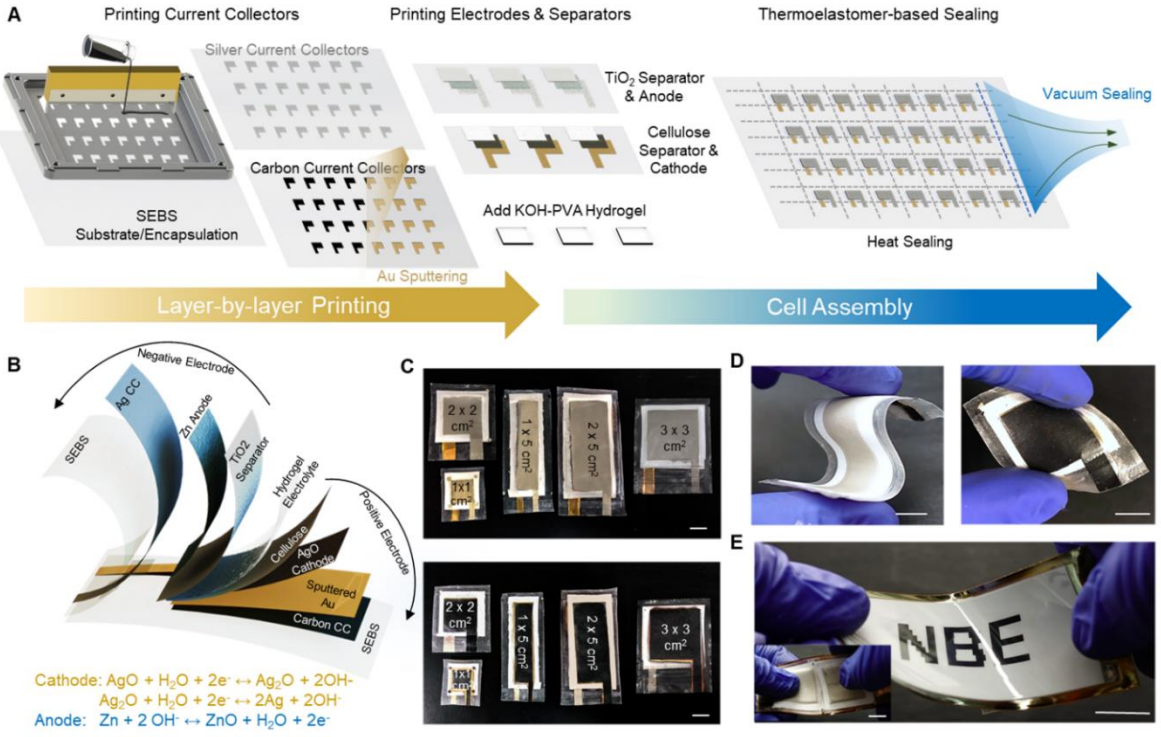

Figure 2.5. All-printed fabrication of the flexible, rechargeable, and high-capacity AgO-Zn battery.
A. Illustration of the layer-by-layer printing and vacuum sealing assembly processes. **B**. Illustration of the AgO-Zn battery cell structure. The cell is composed of a hydrogel electrolyte sandwiched between the 2 electrodes, with each side composed of a heat-sealable SEBS substrate, current collectors, active material electrodes, and corresponding separators. **C**. Photo images of the assembled cells in different customized sizes. **D**. Photo images demonstrating the flexibility of the printed batteries. **E**. Photo images of a flexible E-ink display system powered by the flexible AgO-Zn batteries. Scale bar, 1 cm.

2.3.2 Microstructural and Electrochemical Characterization

The printed electrodes and separators (**Figure 2.6 A**) were characterized by scanning electron microscopy (SEM), as well as non-intrusive, in-situ micrometer-scale X-ray computed tomography (micro-CT). The introduction of micro-CT enables the capability of non-destructive inspection of the battery, which can be highly beneficial to characterize the devices under deformation without the need to disassemble the cells. As shown in **Figure 2.6 B**, the micro-CT images show a morphology in agreement with the SEM images of the pristine anode, cathode, cellulose separator, and TiO_2 separator. Accordingly, the 3-dimensional (3D) imaging of these films shown in **Figure 2.7** offers gives a more comprehensive understanding of the material structures. The loosely packed Zn anode used in this work is made of large particles, with sizes in the range of 50 - 100 μm, which hence reduces the surface passivation induced by the spontaneous reaction with the electrolyte. Energy Dispersive X-Ray Analysis (EDX) further shows the homogeneous coverage of the Bi_2O_3 and the fluoropolymer binders on the surfaces of the Zn particles (**Figure 2.8**). As the dissolved zincate ion preferably redeposits onto the Bi surface during charge, this homogeneous coverage of the Bi_2O_3 particles can reduce the possible formation of Zn dendrite. The TiO_2 separator contains much smaller particles to form a dense and homogenous film, thus can effectively reduce the dendrite growth by providing a field of nucleation sites for dissolved zincate ions to precipitate next to the anode. (**Figure 2.9**). In comparison, the AgO electrode uses 1 - 20 μm particles to produce a porous electrode, which was paired with a separator with similar particle sizes to capture the dissolved Ag species (**Figure 2.10 and Figure 2.11**). Overall, the porous electrodes grant easy permeation of the electrolyte, thus allowing the fabrication of cells with thicker electrodes to increase areal capacity. The conductivity of the PVA-based electrolyte (**Figure 2.6 C**) is in the 10^2 mS/cm order in a wide range of temperatures (-10 °C

to 60 °C), similar to that of other gel electrolytes reported in the literature.[15,42] The solid-phase hydrogel holds the ability to properly wet the electrodes which allow higher current cycling while serving as a leak-free electrolyte barrier blocking dendrite growth. The hydroxide concentration was shown to have little effect on the electrolyte conductivity (**Figure 2.12**), but had a significant impact on the cycle life of the battery (**Figure 2.13**), and was thus optimized to be 36.5% by weight.

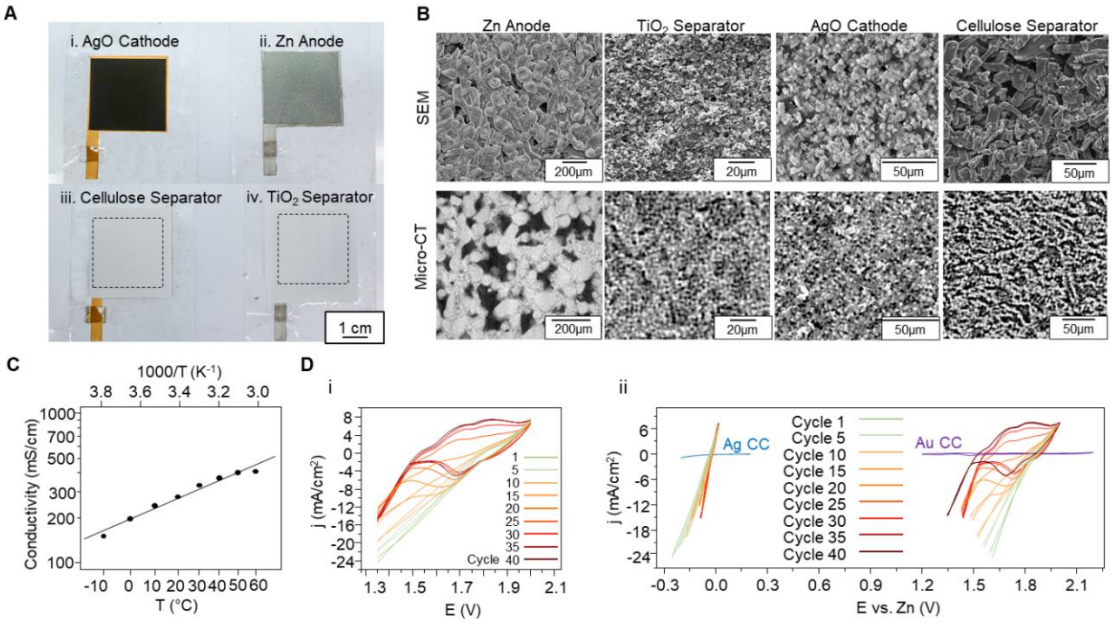

Figure 2.6. Morphological and electrochemical characterization of the printed battery. **A**. Photo images of the printed 3 × 3 cm^2 cell with the (i) AgO electrode, (ii) Zn electrode, (iii) Cellulose separator, and (iv) TiO_2 separator layers. **B**. Microscopic images of corresponding layers of the cell taken via SEM and Micro-CT. **C**. The conductivity of the gel electrolyte as a function of temperature. **D**. 40 cycles of CV between 2 V and 1.35 V of the (i) full cell and (ii) corresponding potential shifts in the anode (left) and the cathode (right) using a 3-electrode cell with a Zn metal pseudo-reference electrode. The CVs of the current collectors within the corresponding voltage windows (anode -0.3 V – 0.3 V, cathode 1.2 V – 2.2 V) under the electrolyte environment are overlaid onto the electrode CVs. Scan rate: 10 mV/s.

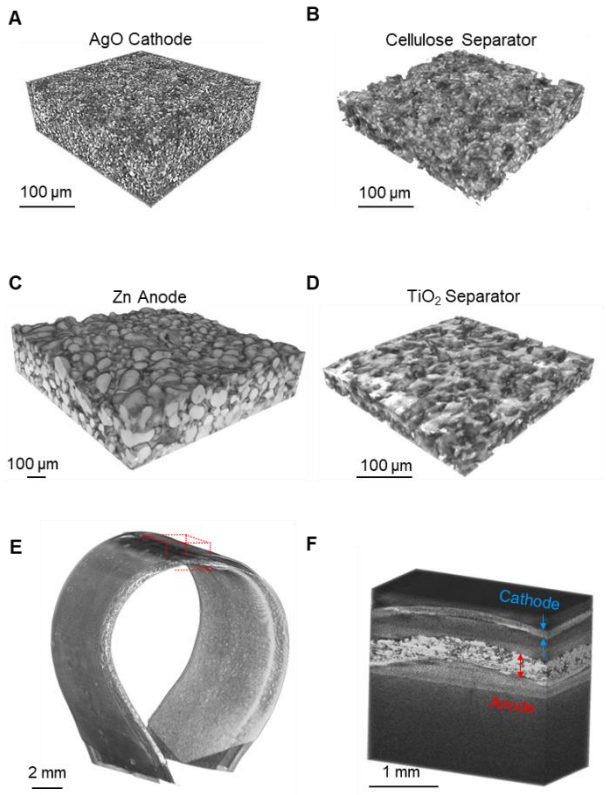

Figure 2.7. Additional microscopic 3D images.
Microscopic 3D images of the A. cathode, B. cellulose separator, C. anode, and D. TiO_2 separator generated using the micro-CT. E. the 3D image of the bent 1 × 5 cm^2 battery in a different angle and F. the zoomed-in view of the top of the cell showing no cracking nor delamination between the layers.

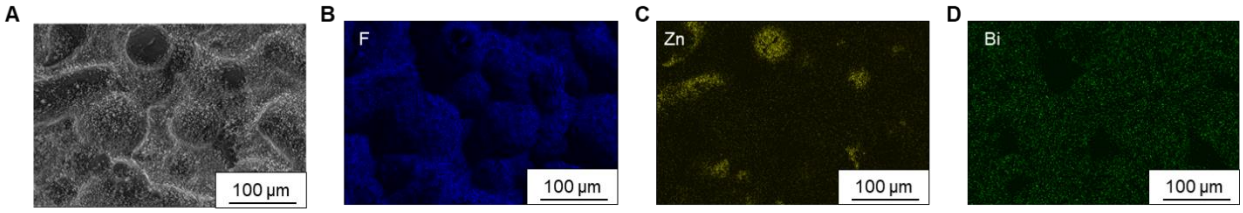

Figure 2.8. Anode SEM-EDX
A. The SEM and corresponding EDX mapping of **B**. fluorine (from the binder), **C**. Zn, and **D**. bismuth of the anode.

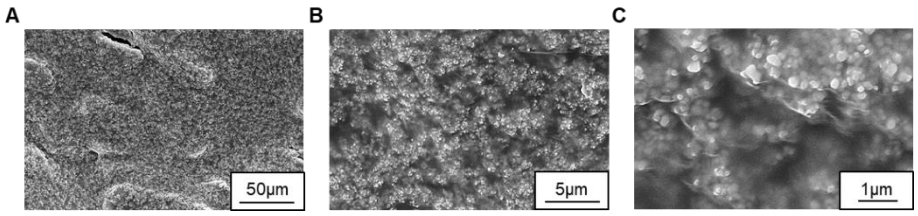

Figure 2.9. Additional SEM images of the printed TiO_2 separator with different magnifications.

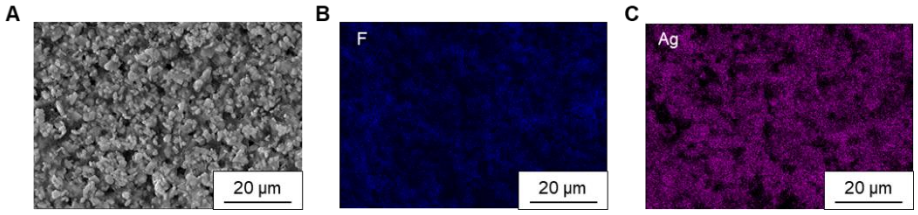

Figure 2.10. Cathode SEM-EDX
A. The SEM and corresponding EDX mapping of **B**. fluorine (from the binder) and **C**. Ag of the cathode.

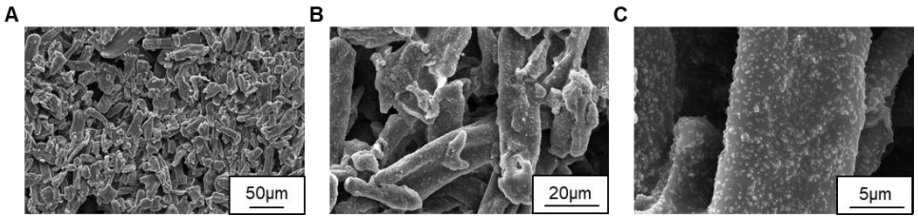

Figure 2.11. Additional SEM images of the printed cellulose separator with different magnifications.

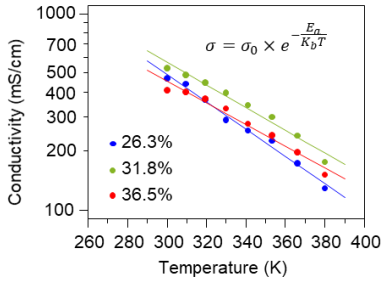

Figure 2.12. The conductivity of the hydrogel with different caustic material concentrations. The linear trendline was fitted using the given equation and listed in **Table 2.1**.

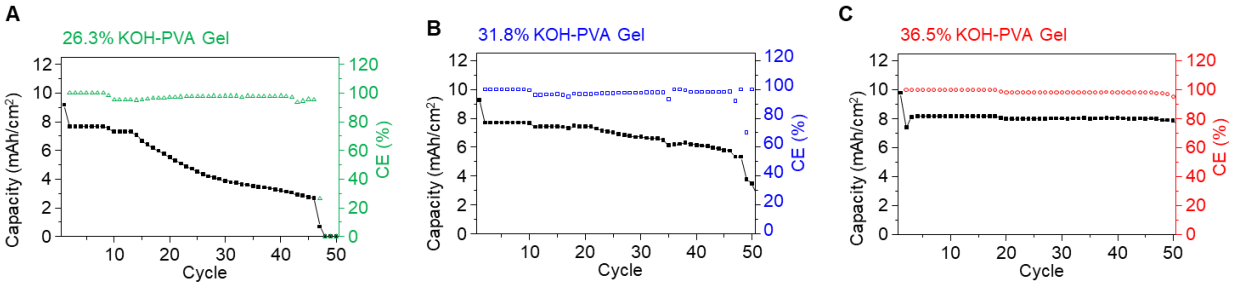

Figure 2.13. The cycling of the battery with different electrolyte concentrations. Electrolyte concentration of **A**. 26.3 %, **B**. 31.8 %, and **C**. 36.5 %. The 50 % capacity range was used and the cells were cycled at the rate of 0.2 C.

Figure 2.4 displays 3-electrode cells, using a Zn foil as a pseudo-reference electrode, that was used for cyclic voltammetry (CV) analysis. The AgO-Zn battery is designed to charge and discharge within the window of 1.35 V to 2 V which is used as the CV scanning range. As shown in the full cell CV in **Figure 2.6 D-i**, within the scanning rate of 10 mV/s, the cell can undergo a high current density of up to 20 mA/cm^2, proving the cell's ability to discharge at a high current. It is worth noting that the CV scan in the initial cycles is discharging the battery, hence leading to a shift in the voltammogram, which eventually stabilizes as the charging and discharging current

reaches equilibrium in each cycle. Using the external Zn reference, the full cell CV can be used to gauge the potential shifts of each electrode separately. As shown in **Figure 2.6 D-ii**, the relative anode potential (left) does not shift significantly during the sweep, whereas the cathode potential (right) contributes to the majority of the potential change in the cell, suggesting that the AgO cathode is being the rate-limiting electrode in the charge-discharge process. The CV of the current collectors in the corresponding voltage window (**Figure 2.14**) is overlaid in **Figure 2.6 D-ii**, demonstrating the electrochemical stability of the current collectors within the expected potential range. It is worth noting that the current density of the Ag current collector increases towards the negative potential direction, which corresponds to the possible hydrogen evolution reaction that taken place on the anode during the charging process. Such undesirable reaction is generally avoided as lower current density is used in the normal charging processes, corresponding to lower anode polarization (**Figure 2.15**).

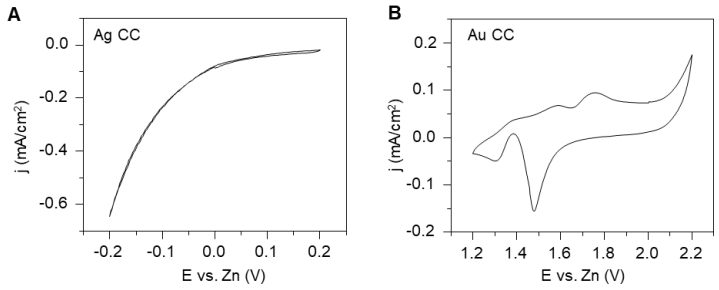

Figure 2.14. The CV of the printed electrodes.
CV of **A**. Ag anode current collector (CC) and **B**. the Au-sputtered carbon cathode CC in their corresponding voltage range used in Figure 2D-ii. Scan rate: 10 mV/s.

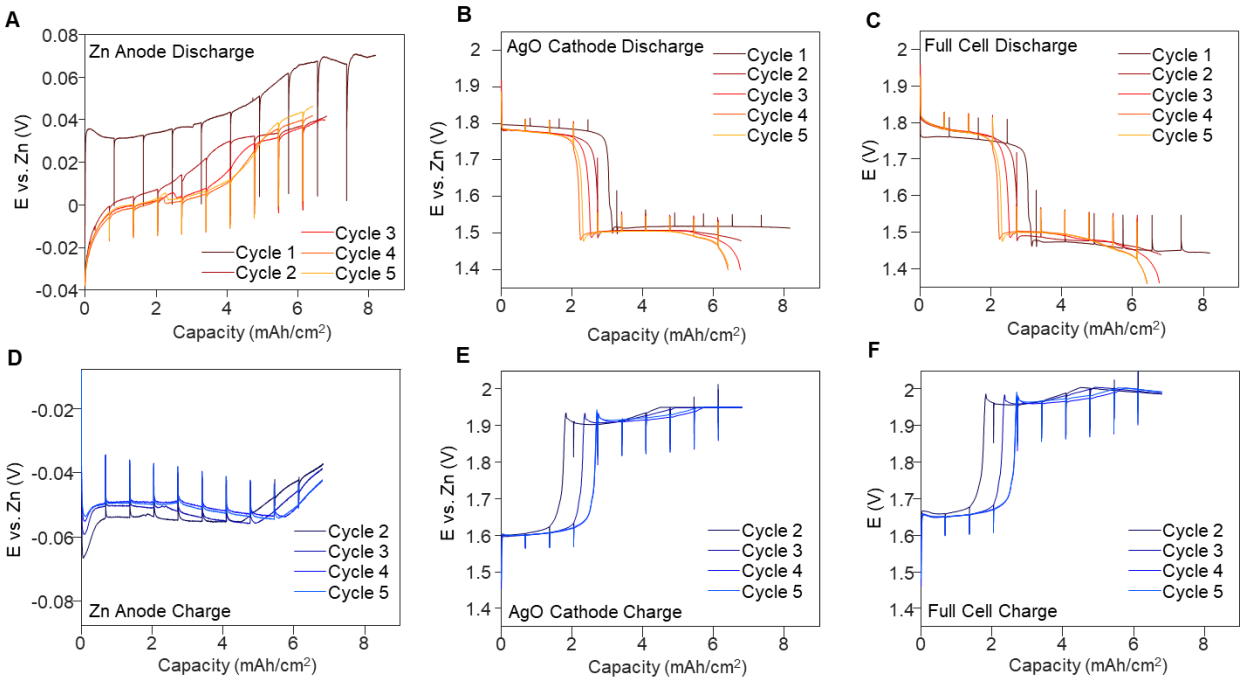

Figure 2.15. Electrode potential profiles during charging and discharging.
The potential profile of the anode (**A**, **D**) and cathode (**B**, **E**) vs. Zn reference and the full cell (**C**, **F**) within the first 5 cycles of (**A-D**) discharging and (**D-F**) corresponding 4 cycles of charging. The vertical lines correspond to the places where an EIS measurements were taken.

2.3.3 AgO-Zn Battery as A High Areal Capacity Primary Cell

The ability of the cell design to adapt to different cell sizes and areal loadings was evaluated. Cells with the same electrode thickness but different form factors, by varying the electrode designs, as well as the cells with the same form factors and different thicknesses by varying the number of layers of active material printed, were fabricated and discharged at a constant 1 mA current. As shown in **Figure 2.16 A**, cells with 1-layer (anode ~ 120 µm, ~ 45 mg/cm^2, cathode ~ 75 µm, ~ 26 mg/cm^2) of electrode thickness with the sizes of 1 × 1 cm^2, 2 × 2 cm^2, 1 × 5 cm^2, 2 × 5 cm^2 and 3 × 3 cm^2 were prepared, and the capacity increases proportionally to the cell area, with an average areal capacity of 8 mAh/cm^2. Two distinct plateaus observed in the discharge voltage curves

correspond to the transition of AgO to Ag_2O (~1.8 V) at the beginning of the discharge and the transition of Ag_2O to Ag (~1.5 V) as the higher-oxidation-state AgO depletes in the cathodes. The impedance of these cells was measured via 2 electrodes EIS, presented in **Figure 2.16 B**. The overall increase in impedance throughout the high frequency and low-frequency domain suggests an increase in cell contact resistance, caused by the increase in resistance of the current collector as the cell size increases. Cells with a size of 2 × 2 cm^2 were also characterized by increasing areal loadings by printing 1, 2, 3, 6, and 8 layers of electrodes. As demonstrated in **Figure 2.16 C**, as the areal loading of active material increases, the areal capacity of the cell increases proportionally, reaching as high as 54 mAh/cm^2 with 8 layers of electrodes (anode ~ 800 µm, ~ 310 mg/cm^2, cathode ~500 µm, ~ 180 mg/cm^2). The EIS on the cells with different thicknesses also showed no significant impedance increase as the thickness increased: only a minor increase in impedance in the low-frequency domain suggests a slight increase in the diffusion resistance due to thicker electrodes (**Figure 2.16 D**). This negligible increase can be attributed to the large pore sizes in both the anode and the cathode relative to the size of the hydroxide ions (OH^-), which applies negligible hindrance to the OH- ion mass transfer when diffusing through the electrodes. Overall, the printed AgO-Zn cell was able to uphold superior performance in a wide range of sizes and areal loading, thus proving its customizability as a primary battery to power various electronics with appropriate sizes and capacity. A comparison between this and other flexible batteries is shown in **Table 2.2** and **Figure 2.17**, showing the obtained areal capacity of 54 mAh/cm^2 being the highest among all printed batteries.

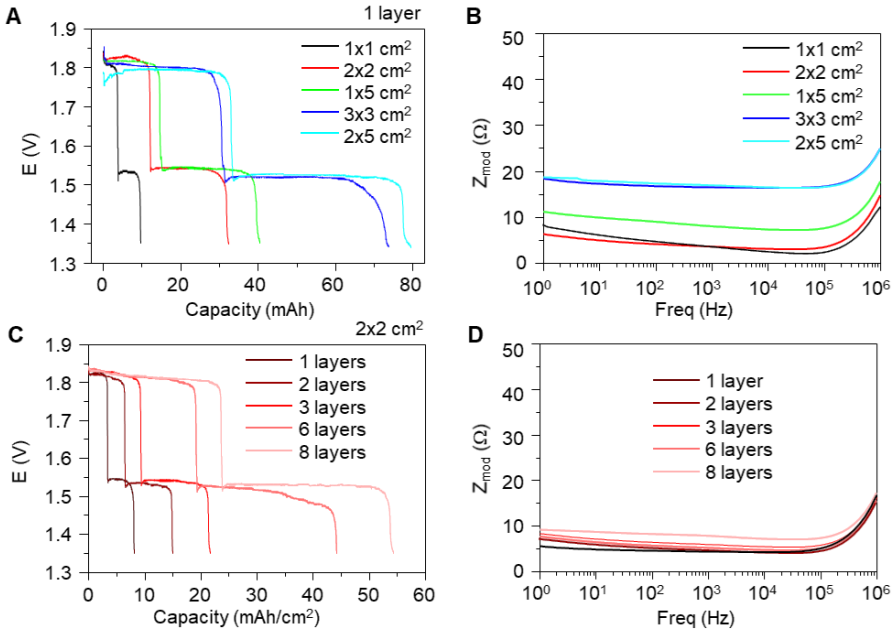

Figure 2.16. Electrochemical performance of the AgO-Zn cells as primary batteries.
A. The obtainable capacity of various sizes of cells that were printed with 1 layer of active materials, discharged at a current of 1 mA. **B**. Bode plot reflecting the corresponding impedance of cells of different sizes. **C**. The obtainable capacity of the 2 × 2 cm^2 cells with active material loading from 1 layer to 8 layers. **D**. Bode plot reflecting the corresponding impedance of the 2 × 2 cm^2 cells with different areal loading.

Table 2.2. Comparison of areal capacities of various published and commercialized thick-film batteries.

Battery Type	Fabrication	Max. Areal Capacity (mAh/cm^2)	Configuration	Cycle Number	Ref
Zn-Ag_2O	Screen Printing	1.6	In-plane	11	[29]
Zn-Ag_2O	Screen Printing	~3	In-plane	30	[10]
Zn-Ag_2O	Extrusion Printing	~2.8	In-plane	Primary	[42]
Zn-Ag_2O	Screen Printing	1.5	In-plane	13	[43]
Zn-MnO_2	Plotting	~2.2	In-plane	30	[44]
Zn-MnO_2	Doctor Blade	<0.077	Stacked	140	[45]
Zn-Ag_2O	Drop-cast/ Electroplating	0.11	In-Plane	33	[24]
Zn-MnO_2	Screen Printing	5.6	Stacked	Primary	[46]
Zn-Ag_2O	Screen Printing	5.4	Stacked	Primary	[33]
Zn-Ag_2O	3D Printing	2.4	Interdigitated Pillars	7	[47]
Zn-MnO_2	Soaking	3.775	In-plane	Primary	[7]
LTO-LFP	3D Printing	1.5	In plane Interdigitated	30	[48]
Zn-Air	Screen Printing	1.4	Stacked	Primary	[49]
Zn-Ag_2O	Screen Printing	11	Stacked	Primary	[32]
Si/CNT-NMC	Doctor Blade	30	Stacked	50	[50]
Zn-MnO_2	NA	~1	In-plane	Primary	[51]
Zn-MnO_2	NA	~3	NA	Primary	[52]
Zn-MnO_2	NA	~1.5	NA	Primary	[53]
Li-MnO_2	NA	~2.5	Stacked	Primary	[54]
Zn-AgO	Screen Printing	54	Stacked	80	This work

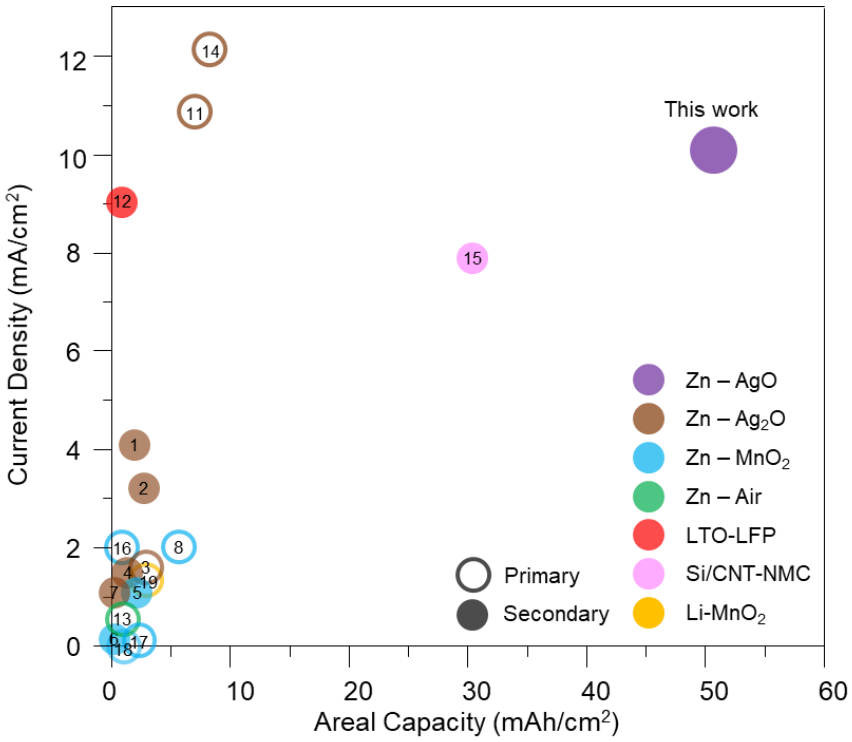

Figure 2.17. Comparison of the maximum current densities and areal capacities of various printed batteries.

2.3.4 AgO-Zn Battery as High-performance Secondary Cell

Beyond the application as a primary battery, the electrochemical performance of the flexible AgO-Zn battery as a secondary cell was also characterized. As a cell operating with conversion-type chemistry, it is crucial to avoid over-oxidation of the anode materials or over-reduction of the cathode material that would lead to irreversible particle shape change. Previous studies report that the loss of capacity in this system is due to the increased thickness of the ZnO layer that passivates the anode surface, as well as the coarsening of the AgO/Ag_2O particles leading to a decrease in cathode surface area.[8,40] Such behavior can be effectively mitigated by accurately controlling the degree of charge and discharge to limit the occurrence of irreversible electrode shape changes. The optimized charge-discharge algorithm was determined to cycle the cell

between 40% and 90% of its maximum capacity, with larger ranges resulting in lower cycle life as shown in **Figure 2.18**. **Figure 2.19 A** demonstrates the cycling of a cell with 2-layer electrodes with a maximum capacity of ~ 16 mAh/cm^2. A formation cycle is firstly performed, discharging 10 mAh/cm^2 (60% of max. areal capacity) at the rate of 0.1C, allowing the electrode to slowly relax into its preferred morphology with increased surface area and reduced impedance. Then, the batteries were charged at 0.2 C rate until reaching 2 V and charged at constant voltage until the C-rate dropped to below 0.04 C or the capacity reached 8 mAh/cm^2 (50% of max. areal capacity). The battery was then discharged at 0.2 C until reaching a columbic efficiency of 100% or a voltage of 1.35V. The entire charge-discharge process is accurately controlled by capacity in the initial cycles, ensuring the cell is cycled between 40% to 90% of its maximum capacity. As shown in **Figure 2.19 C**, after a few cycles at the rate of 0.2 C, the cell slowly relaxed from capacity-controlled discharge to voltage-controlled discharge, with the higher plateau to lower plateau ratio resembling the behavior of the primary cells. Using this charge-discharge algorithm, the cycle life of the unstable AgO oxidation state could be controlled, and a significantly increased cycle life can be obtained compared to previous studies.[10,29,39] Due to the supersaturation-precipitation reaction mechanism of both the anode and the cathode during discharge, the cell can be discharged at a high C-rate of up to 1 C without any loss in capacity and columbic efficiency, as shown in **Figure 2.19 A**-**B**. Recharging at a higher C-rate is also possible, as shown in **Figure 2.20**, although this would require a higher capping voltage, reducing the rechargeability and increasing the risk of oxygen evolution on the cathode, thus was not preferred.

Impedance measurements of the flexible batteries showed relatively low impedances throughout cycling. The impedance of the batteries was either determined during cycling of the full-cell using direct current internal resistance (DCIR) method, or during cycling of the separated

anode and cathode half-cells using a 3-electrode configuration with a Zn foil serving as the reference. The DCIR analysis offers a straightforward and simple way to gauge the change in the internal resistance of the battery. As shown in **Figure 2.19 D**, 2-electrode DCIR analysis with both charging and discharging current was performed before each charge and discharge for a battery cycling at 0.2 C, and the battery was able to maintain low internal resistance throughout the cycles, suggesting no formation of high-impedance passivating layers on the surface of the electrode throughout cycling. To obtain detailed information on the change in the impedance of each electrode during each cycle, multiple 3-electrode EIS analyses were performed on the battery while cycling at 0.2 C, and are plotted against the degree of discharge (DOD) of the battery. As presented in **Figure 2.19 E**, the anode half-cell started at a low impedance of 1 – 4 **Ω**, with 2 depressed semicircles attributed to the high-speed charge transfer at the Zn particle interface and the lower speed hydroxide ions (OH-) diffusion in the porous network.[38] With discharging, the low-frequency semicircle slowly expands due to the formation and growth of the ZnO species that impedes the OH^- transport and increases the double-layer capacitance. During charging, the oxygen species are liberated from the reactions in **Equations 2.1 - 2.3** to form OH^- ions that diffuse readily out of the anode. This results in the fast mass transport of OH^- ions out of the anode and a rapid drop in the impedance at the onset of charging that eventually recovers to the initial level, thus showing the reversibility of the anode. For the cathode half-cell EIS shown in **Figure 2.19 F**, at the start of the discharge (0% DOD), a single semi-circle corresponding to the mass transfer resistance and capacitance of the Ag_2O formation is observed with a low-frequency impedance tail at an angle of approximately 45º suggesting standard Warburg diffusion of OH^-. As the cell is discharged, the overall impedance decreases with a second semicircle emerging near the low-frequency domain which can be attributed to the charge transfer resistance and capacitance of Ag

formation from Ag_2O. During charging, this second low-frequency semicircle disappears as all the Ag oxidizes to form Ag_2O and eventually AgO.

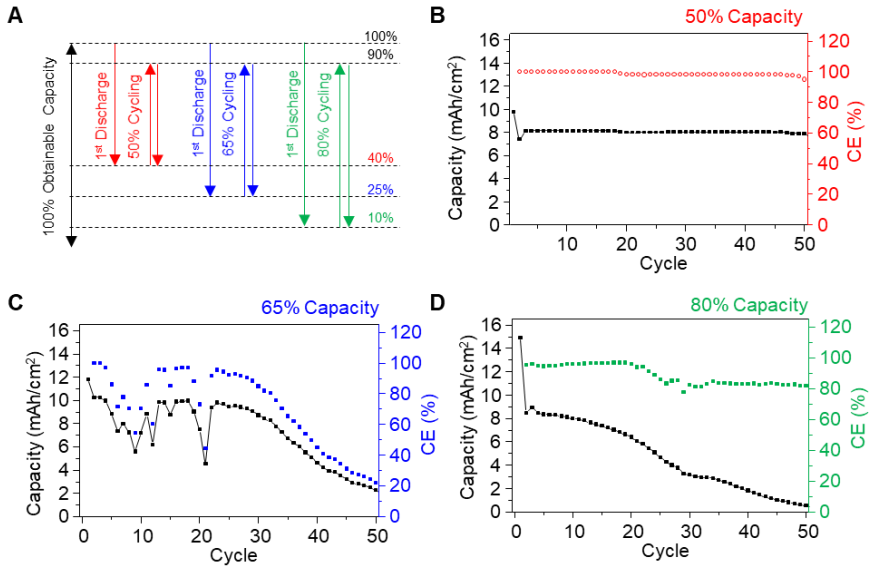

Figure 2.18. The cycling of the battery at the different capacity range.
A. The illustration comparing 3 different charging and discharging capacity regions. **B**. Cycling the battery between 40 % and 90 % state of charge (50 %). **C**. Cycling the battery between 25 % and 90 % state of charge (65 %). **D**. Cycling the battery between 10 % and 90 % state of charge (80 %). Electrolyte with the concentration of 36.5 % was used, and the cells were cycled at the rate of 0.2 C.

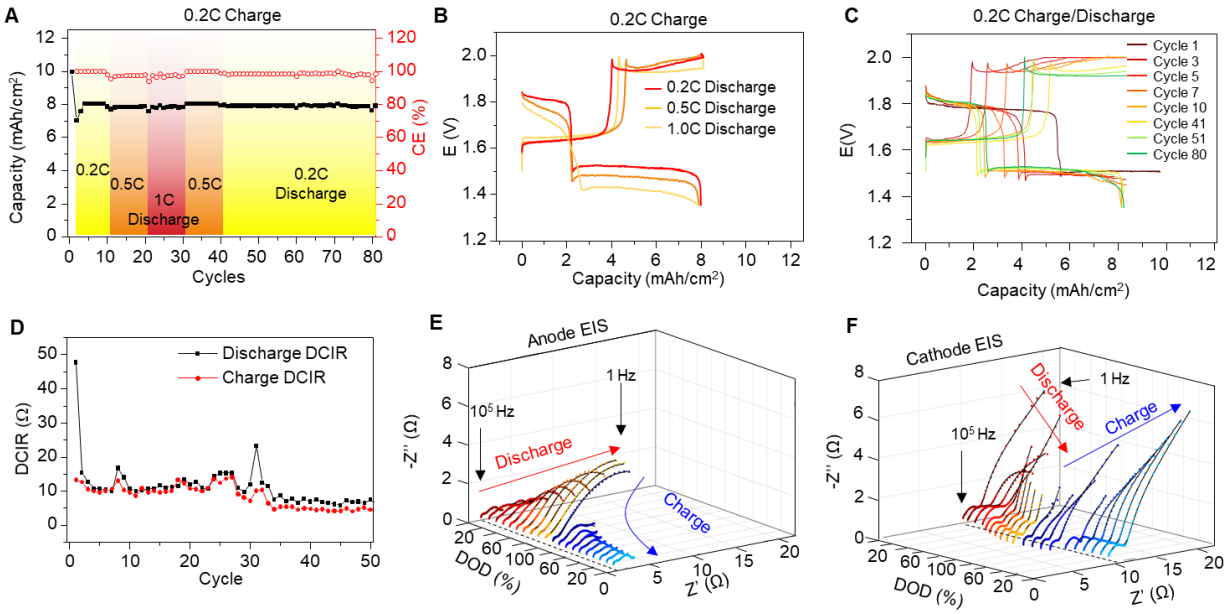

Figure 2.19. Electrochemical performance of the AgO-Zn cells operating as rechargeable batteries.

A. The cycling performance of the printed battery with a charging C-rate of 0.2C and varying discharge rate of 0.2C, 0.5C, and 1C. **B**. The voltage-capacity plot of the battery under different discharging C-rates. **C**. The voltage-capacity plot of the AgO-Zn battery at different number of cycles showing the stabilization of the charge-discharge profile. **D**. The DCIR of the AgO-Zn within 50 cycles cycled at the C-rate of 0.2C. The EIS profile of the **E**. Zn anode and **F**. AgO cathode within 1 complete discharge-charge cycle on a 3-electrode cell with a Zn metal pseudo-reference electrode.

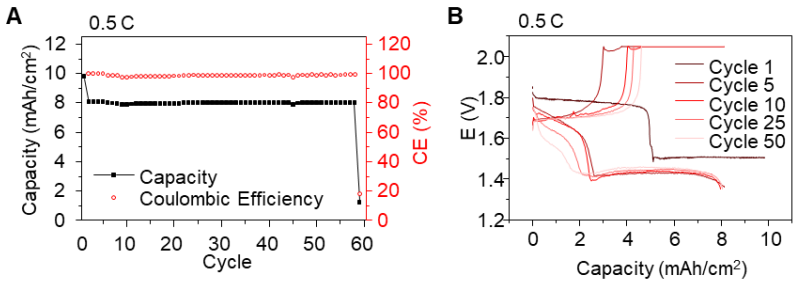

Figure 2.20. The cycling of the battery at the rate of 0.5 C.

The electrolyte with the concentration of 36.5% and the capacity range of 50% was used.

Overall, the 3-electrode impedance results provide a deeper insight into the reaction and possible routes in improving the battery's cycle life and performance. These data indicate that the impedance of the AgO cathode is responsible for the majority of the cell impedance. Therefore, a beneficial next step will be to incorporate additives that can increase the cathode electrical conductivity to improve the performance in high-current applications. For the anode, the monitoring of ZnO formation via EIS can be paired with topological characterization methods to better control the conversion of Zn electrodes towards extended cycle life and is expected to be extremely useful for future analysis. More data and discussion of 3-electrode EIS can be found in **Figure 2.21**, **Figure 2.22**, and **Figure 2.23**.

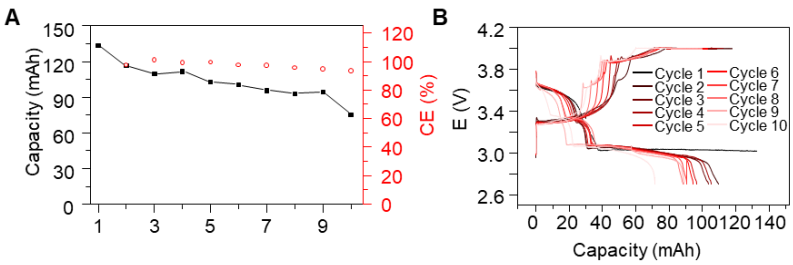

Figure 2.21. The cycling of two 8-layer 2 × 2 cm^2 battery connected in series at the rate of 0.05 C.

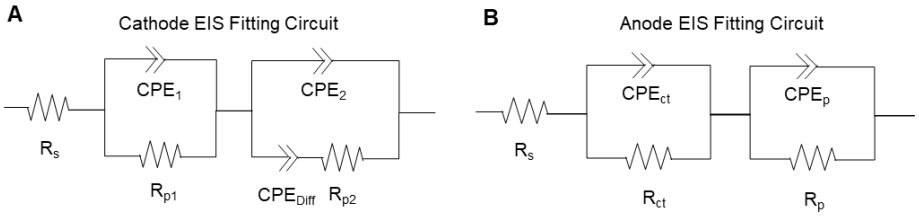

Figure 2.22. The equivalent circuit used for the A. cathode and B. anode EIS fitting.

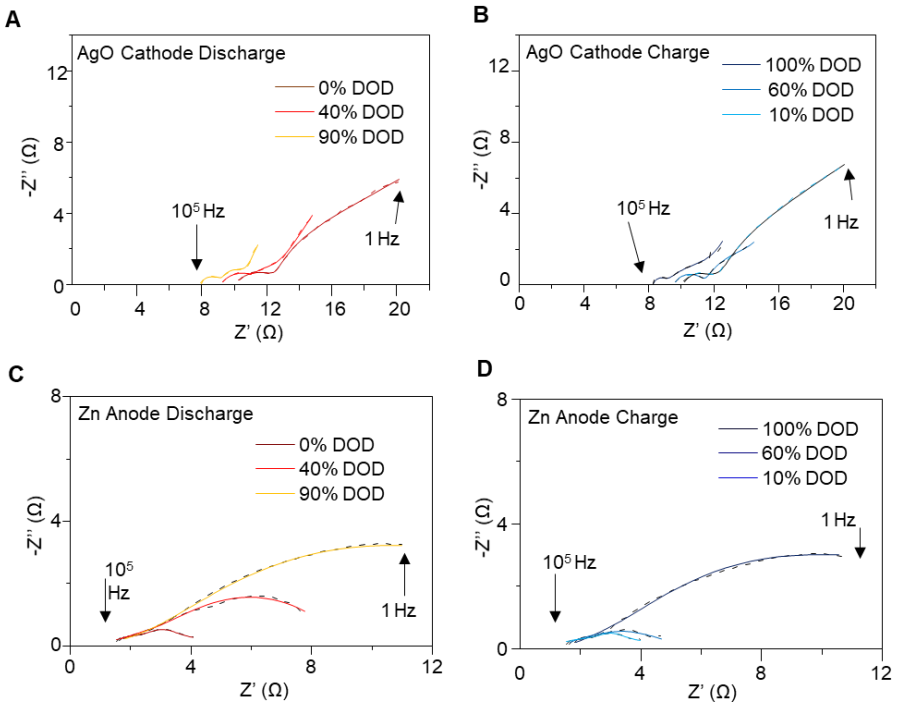

Figure 2.23. The Nyquist plot and the EIS fitting of the cathode during the 5th cycle.
The EIS during **A**. discharging and **B**. charging, and the corresponding anode **C**. charging and **D**. discharging.

2.3.5 Mechanical Stability of The Flexible AgO-Zn Battery

Compared to coin-cell, cylindrical or prismatic cells, the printed flexible batteries have the unique advantage of allowing bending, flexing, and twisting without causing sudden structural failure. To endow such mechanical resiliency, the printed AgO-Zn batteries are composed of flexible and stretchable polymer-particle composite layers containing highly elastic binders that can accommodate the applied strain while maintaining the overall structural integrity. During bending, this flexibility and stretchability allow the layers to elongate on the outer rim of the arc to react to the tensile strain, thus allowing the battery to avoid delamination between layers even when very thick electrodes are used. After vacuum sealing, the atmospheric pressure is exerted on

the cell and ensures intimate contact between the different layers, further avoiding possible delamination. To test the performance of the batteries under small-radius, large-angle deformation, a 2-layer 1 × 5 cm^2 cell was fabricated and discharged at a current of 1 mA while undergoing repeated bending and twisting deformations. As illustrated in **Figure 2.24 A**-**B**, the cell was tested manually with 180° and 360° bending towards the anode (outward) and towards the cathode (inward) around a cylinder with a radius of 0.5 cm, as well as 180° twisted in both directions from head to end. The corresponding voltage change during 100 cycles (1 s per cycle) of deformation was recorded, as shown in **Figure 2.24 C**. In general, the cell exhibited stable performance during bending and twisting in both directions, with negligible fluctuation in voltage during the 180° bending cycles, and roughly 10 mV fluctuation during the 180° bending and twisting cycles. The inward bending in general shows slightly more variations, which is suspected to be caused by the softer Ag current collector on the anode size undergoing more stretching on the outside during bending. More data on the cell under 10% stretching deformation can be found in **Figure 2.25**. The effect of bending on the capacity of the cell was also analyzed via a small-radius, repeated bending experiment. A 1 × 5 cm^2 battery was first bent inward 360º 500 times with a bending radius of 0.5 cm and was then charged and discharged for 10 cycles. Thereafter, the battery was similarly bent outward 360º for 500 times and charged and discharged for 10 more cycles. As shown in **Figure 2.24 D**, no significant drop in capacity nor coulombic efficiency was observed after the bending cycles, hence demonstrating the stable mechanical performance of the battery as a flexible, rechargeable cell. The rechargeability of the cell was also not interrupted by the repeated deformation during cycling, as shown in **Figure 2.24 E-F**, where the battery can be normally charged and discharged while undergoing ~2500 cycles of 180° bending cycles. To ensure the mechanical stability of the cell, micro-CT was used to characterize the cell after the repeated

deformation. As shown in **Figure 2.24 G-H**, the entire cell can be scanned at a high resolution to obtain a 3-dimensional (3D) image reflecting the microscopic structure of the cell under deformation after repeated bending and twisting. The zoom-in view of the cross-section of the battery further shows no cracks or delamination after the repeated bending cycles, reflecting the robust mechanical resiliency of the battery against such deformation. More 3D visualizations of the battery under bending deformation can be found in **Figure 2.26**. Overall, pairing the superior electrochemical and mechanical performance, the printed AgO-Zn battery is proven to be well-suited to reliably and sustainably power various wearable and flexible electronics.

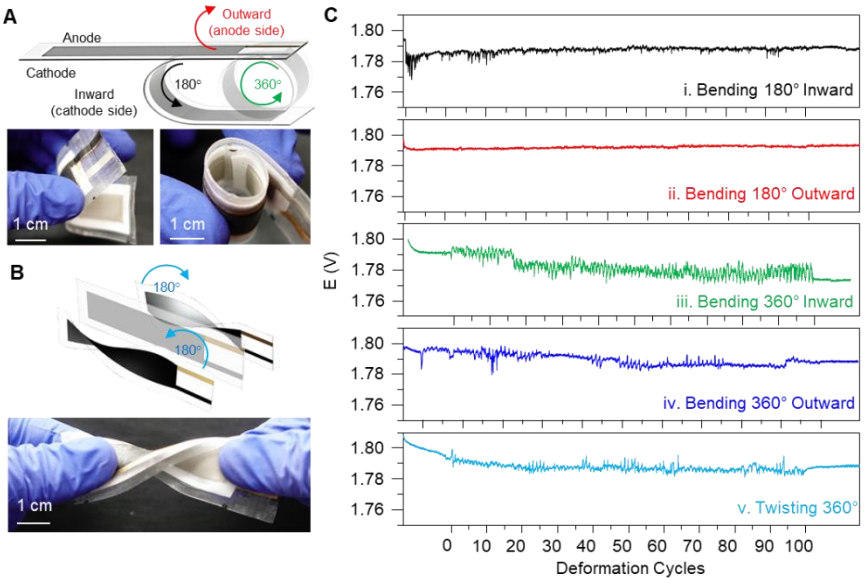

Figure 2.24. Performance of the AgO-Zn cell under various mechanical deformations. **A**. Illustrations and corresponding photo images of a 2-layer loading, 1 × 5 cm^2 battery undergoing . 180° and 360° bending deformations and **B**. 360° twisting deformation. **C**. The corresponding voltage profile of the battery during 1 mA discharge while undergoing 100 cycles of (i) 180° outward bending, (ii) 180° inward bending, (iii) 360° inward bending, (iv) 360° outward bending with a bending diameter of 1 cm, and (v) 360° head-to-end twisting.

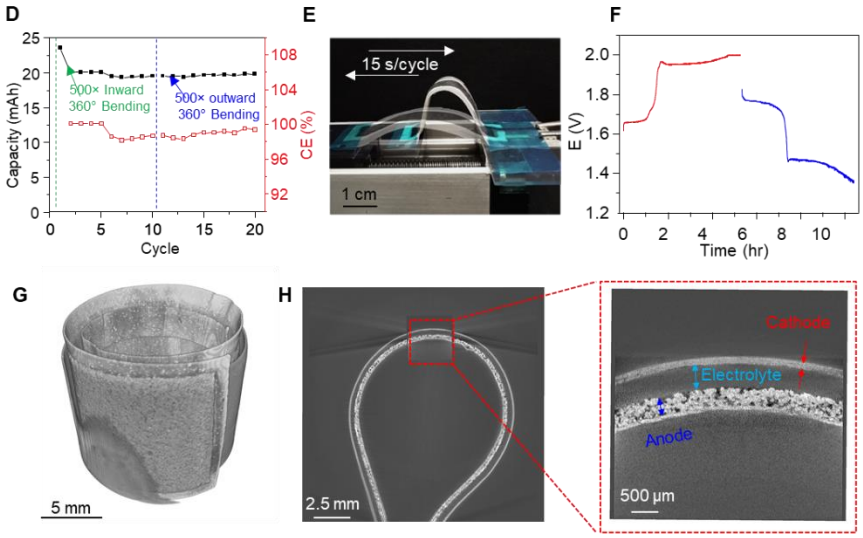

Figure 2.24. Performance of the AgO-Zn cell under various mechanical deformations. (Continued)
D. Assessing the effect of bending to the capacity of the battery. A 2-layer loading, 1 × 5 cm^2 battery undergoing 500 cycles of inward 360º bending and 500 cycles of similar 500 cycles of outward bending demonstrated no drop in battery capacity nor coulombic efficiency. **E**. Photo illustration of a battery under repeated 180° bending cycles controlled by a linear stage at the speed of 15 s/cycle, and **F**. the corresponding voltage-time plot of the charging (red) and discharging (blue) of the battery during ~2500 repetitions of bending. **G**. The micro-CT image of the entire 1 × 5 cm^2 cell after repeated bending and twisting cycles rolled in a diameter of 1 cm, and **H**. the cross-section of it bent in a diameter of 1cm (left) and a zoomed-in view (right) of the electrodes, demonstrating no structural damage or delamination of the cell after repeated mechanical deformations.

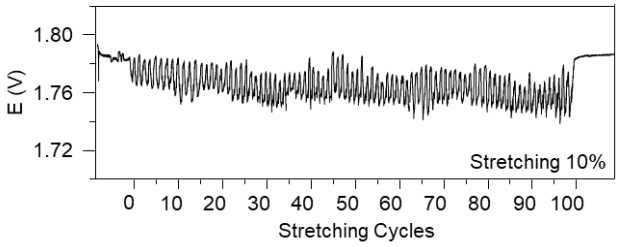

Figure 2.25. The voltage profile of the 1 × 5 cm^2 battery during 1 mA discharge while undergoing 100 cycles of 10 % lengthwise stretching.
Although the battery was not optimized for stretchability, a certain amount of stretchability is required for the battery to endure low-radius bending and accommodate for the outer-layer strain.

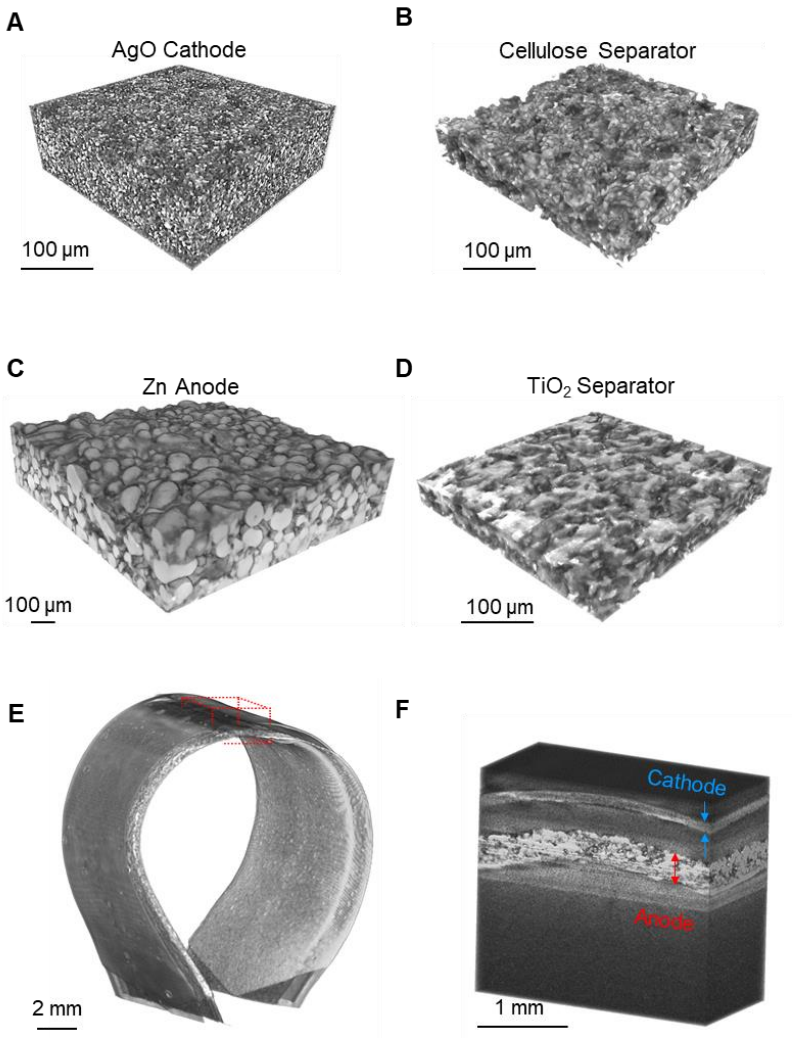

Figure 2.26. Additional microscopic 3D images.
Microscopic 3D images of the **A**. cathode, **B**. cellulose separator, **C**. anode, and **D**. TiO_2 separator generated using the micro-CT. **E**. the 3D image of the bent 1 × 5 cm^2 battery in a different angle and **F**. the zoomed-in view of the top of the cell showing no cracking nor delamination between the layers.

2.3.6 Powering Flexible Electronics

To demonstrate the performance of the battery powering typical flexible electronics, we designed a flexible E-ink display system controlled by an Arduino-type microcontroller unit with added Bluetooth (BT) communication module, which resembles many prototypes of IoT, wearable

and flexible devices (**Figure 2.27 A**, **Figure 2.28**, and **Figure 2.29**). The system is powered by two 2 × 2 cm^2 batteries with 2-layer electrodes connected in series, which can supply enough voltage (>3 V) to boot the system. A mobile device can connect and transmit data and commands to the BT module, which is processed by the microcontroller that refreshes the E-ink display. First, the energy consumption of the system under different operation modes operating at 3.6 V was measured. **Figure 2.27 B** displays the current draw when (1) the system is broadcasting to seek connection, which contains short bursts of current peaks around 20 mA (in black); (2) the system is connected to a mobile device, with an average current of 9 mA (in red); and (3) the system is actively transmitting data between the cellphone and the display, with the current alternating between a higher baseline of 8.5 mA with peaks of 13 mA, and a lower baseline of 4 mA with peaks of 10 mA (in blue). The batteries are thus discharged using a script simulating the power consumption of the flexible E-ink display system working in repeated discrete sessions, with 10 s of BT broadcasting, 10 s of idle after establishing the connection, 10 s of active data transmission, followed by 30 s of resting (powered off) (**Figure 2.27 C** and **Figure 2.30**). As illustrated in **Figure 2.27 D**, The two batteries in series were able to sustain the pulsed, high-current discharge in the 3.6 V – 2.4 V window to deliver power to the system constantly for over 12 hours, and is able to maintain its capacity of ~60 mAh, similar to the capacity obtained from the constant low-current 1 mA discharge. By pairing with the high-areal capacity flexible AgO-Zn battery, the flexible E-ink display was able to operate while undergoing bending deformations. In comparison, commercial lithium coin cells with similar rated capacity were not able to sustain the high current pulsed discharge, resulting in a significant loss in capacity when discharged using the same script (**Figure 2.31**). The low-impedance and high-energy-density battery is therefore proven to have both outstanding electrochemical and mechanical performance for powering a typical prototype of

a flexible electronic system. With performances even surpassing non-flexible commercial coin cells counterpart, this all-printed battery can be considered extremely attractive due to its customizability, and flexibility towards real-life applications. A typical application of using this battery to illuminate an LED bulb while applying various mechanical deformations was also tested, where the light intensity did not change as the battery was bent, folded, twisted, and stretched.

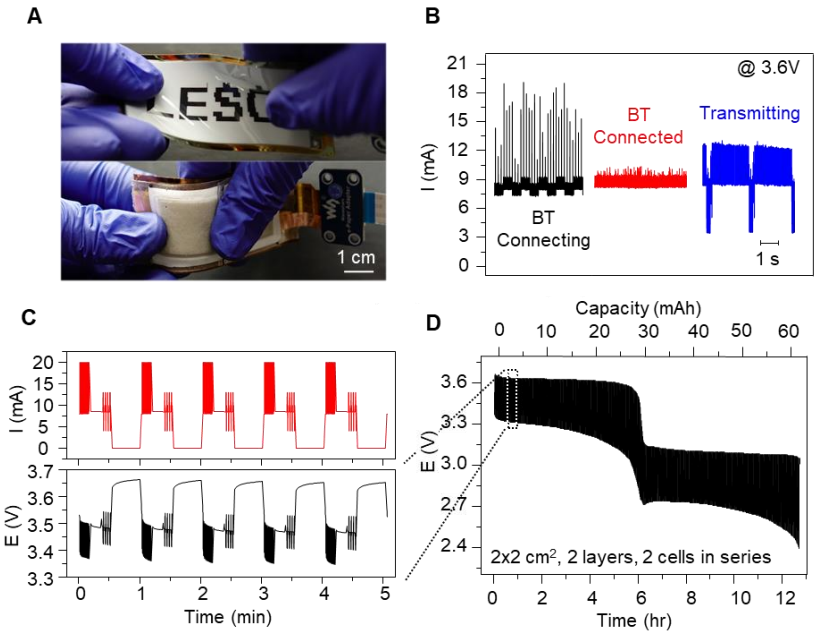

Figure 2.27. The powering of a flexible E-ink display system by the flexible AgO-Zn batteries. **A**. Photo images of the flexible E-ink display and the placement of two 2-layer loading, 2 × 2 cm^2 batteries connected in series on the back of the display. **B**. The power consumption of the E-ink display system with integrated BT and MCU modules during BT connection (black), after establishing the connection (red), and during active data transmission (blue). **C**. Simulated discharge current profile with varying pulses and baselines (red) and the corresponding voltage response of the battery (black). **D**. The complete discharge profile of the two cells connected in series implementing the simulation discharge profile.

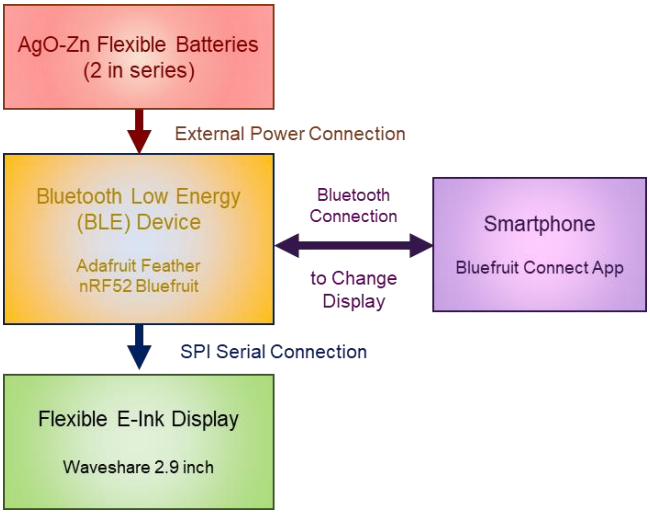

Figure 2.28.The system diagram of the assembled flexible E-ink display system.

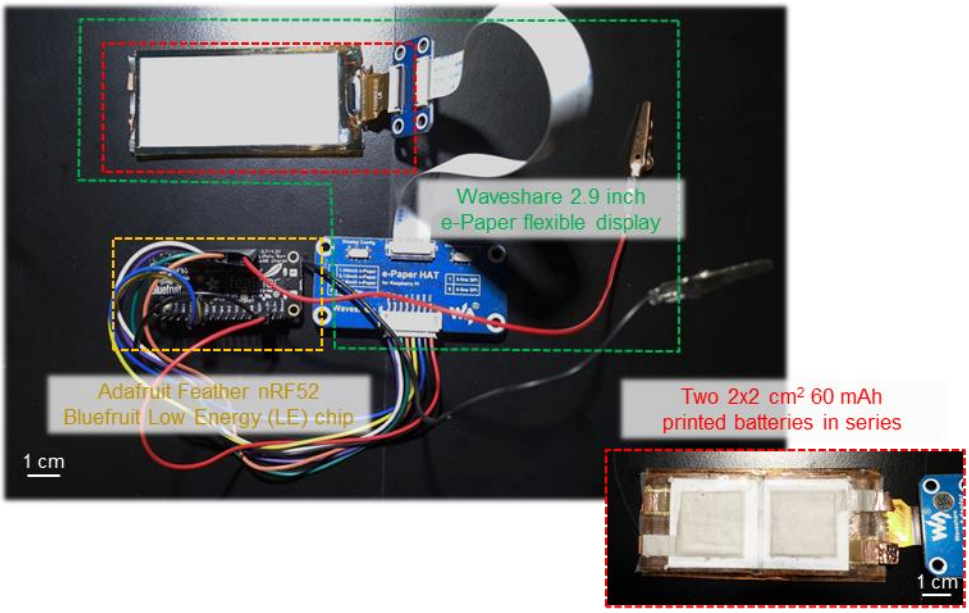

Figure 2.29. The photo of the assembled flexible E-ink display system with 2 batteries attached to the backside of the display panel.

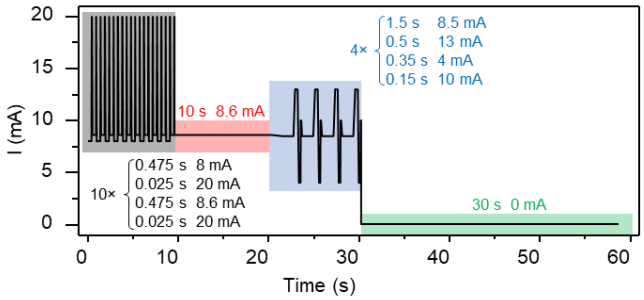

Figure 2.30. The detailed breakdown of the pulsed discharge profile.

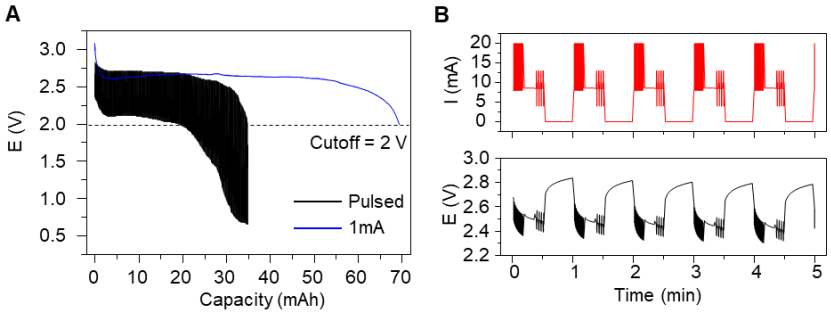

Figure 2.31. Battery discharge comparison with commercial coin cell.
A. The discharge curve of a CR1620 Lithium coin cell battery rated at 68 mAh nominal capacity under continuous 1 mA discharge and pulsed discharge.[20] Significant capacity fade is observed for the battery with pulsed discharge. **B**. Zoomed in view of the current and voltage change of the CR1620 battery.

2.4 Conclusion

In this chapter, we have demonstrated a flexible and high-performance AgO-Zn battery based on the rechargeable conversion chemistry. Using specially formulated ink with stretchable elastomeric binders and thermoplastic elastomeric substrates, the batteries can be printed layer-by-layer using low-cost, high-throughput screen-printing techniques and assembled with heat and vacuum sealing processes. To obtain a low device footprint while maintaining easy processability, printable and flexible separators and a solid-phase KOH-PVA hydrogel were developed to allow a stacked sandwich configuration. The printable battery is compatible with various cell sizes and areal loading, leading to a high areal capacity of 54 mAh/cm^2 in connection to repeated multilayer

printing for primary applications. The battery is also rechargeable upon implementing the capacity-controlled cycling algorithm, with high cycle life beyond 70 cycles with varying discharge C-rates without loss in capacity and coulombic efficiency. The battery exhibited low impedance within each discharge-charge cycle, while maintaining low internal resistance throughout multiple cycles, suggesting stable and reversible electrode morphological change during electrode redox reactions. As a flexible energy storage unit for powering various flexible, wearable electronics, the performance of the battery was evaluated under rigorous mechanical testing, demonstrating that the battery offers remarkable resiliency against repeated large deformation bending and twisting cycles. The fabricated batteries were used in the powering of a customized flexible E-ink display system with BT connectivity and delivered an outstanding performance that surpassed commercial coin cells under the high-current pulsed discharge regime required by the electronics. Future work leveraging advanced electrochemical and topological characterization on this promising battery chemistry will be conducted to further improve its performance and cycle life. This will involve further optimization of the fabrication process, the ink composition, and the layer thicknesses and porosities should lead to a practical, commercially viable product with higher cycle life, lower impedance, smaller device footprint, and lower production cost. Overall, this work demonstrates the scalable fabrication of flexible AgO-Zn batteries with highly desirable electrochemical and mechanical performance and tremendous implications towards the development of novel energy storage devices for the powering of next-generation electronics.

Chapter 2, in full, is a reprint of the material as it appears in Joule, 2021, by Lu Yin, Jonathan Scharf, Jessica Ma, Jean-Marie Doux, Christopher Redquest, Viet L. Le, Yijie Yin, Jeff Ortega, Xia Wei, Joseph Wang, and Ying Shirley Meng. The dissertation author and Jonathan Scharf were the primary investigators and co-authors of this paper.

2.5 References

1. Gong, S. & Cheng, W. Toward Soft Skin-Like Wearable and Implantable Energy Devices. *Advanced Energy Materials* **7**, 1700648 (2017).

2. Ray, T. R. *et al.* Bio-Integrated Wearable Systems: A Comprehensive Review. *Chem. Rev.* **119**, 5461–5533 (2019).

3. Yin, L. *et al.* Highly Stable Battery Pack via Insulated, Reinforced, Buckling-Enabled Interconnect Array. *Small* **14**, 1800938 (2018).

4. Xu, S. *et al.* Stretchable batteries with self-similar serpentine interconnects and integrated wireless recharging systems. *Nat Commun* **4**, 1543 (2013).

5. Weng, W. *et al.* A Gum-Like Lithium-Ion Battery Based on a Novel Arched Structure. *Advanced Materials* **27**, 1363–1369 (2015).

6. Huang, Y. *et al.* Weavable, Conductive Yarn-Based NiCo//Zn Textile Battery with High Energy Density and Rate Capability. *ACS Nano* **11**, 8953–8961 (2017).

7. Gaikwad, A. M. *et al.* Highly Stretchable Alkaline Batteries Based on an Embedded Conductive Fabric. *Advanced Materials* **24**, 5071–5076 (2012).

8. Zamarayeva, A. M. *et al.* Fabrication of a High-Performance Flexible Silver–Zinc Wire Battery. *Advanced Electronic Materials* **2**, 1500296 (2016).

9. Li, H. *et al.* Waterproof and Tailorable Elastic Rechargeable Yarn Zinc Ion Batteries by a Cross-Linked Polyacrylamide Electrolyte. *ACS Nano* **12**, 3140–3148 (2018).

10. Kumar, R. *et al.* All-Printed, Stretchable Zn-Ag2O Rechargeable Battery via Hyperelastic Binder for Self-Powering Wearable Electronics. *Advanced Energy Materials* **7**, 1602096 (2017).

11. Liu, W. *et al.* 3D Porous Sponge-Inspired Electrode for Stretchable Lithium-Ion Batteries. *Advanced Materials* **28**, 3578–3583 (2016).

12. Mackanic, D. G. *et al.* Decoupling of mechanical properties and ionic conductivity in supramolecular lithium ion conductors. *Nature Communications* **10**, 5384 (2019).

13. G. Mackanic, D., Chang, T.-H., Huang, Z., Cui, Y. & Bao, Z. Stretchable electrochemical energy storage devices. *Chemical Society Reviews* **49**, 4466–4495 (2020).

14. Kaltenbrunner, M., Kettlgruber, G., Siket, C., Schwödiauer, R. & Bauer, S. Arrays of Ultracompliant Electrochemical Dry Gel Cells for Stretchable Electronics. *Advanced Materials* **22**, 2065–2067 (2010).

15. Li, H. *et al.* An extremely safe and wearable solid-state zinc ion battery based on a hierarchical structured polymer electrolyte. *Energy & Environmental Science* **11**, 941–951 (2018).

16. Song, W.-J., Lee, S., Song, G. & Park, S. Stretchable Aqueous Batteries: Progress and Prospects. *ACS Energy Letters* **4**, 177–186 (2019).

17. Ma, L. *et al.* Super-Stretchable Zinc–Air Batteries Based on an Alkaline-Tolerant Dual-Network Hydrogel Electrolyte. *Advanced Energy Materials* **9**, 1803046 (2019).

18. Kim, J., Kumar, R., Bandodkar, A. J. & Wang, J. Advanced Materials for Printed Wearable Electrochemical Devices: A Review. *Advanced Electronic Materials* **3**, 1600260 (2017).

19. Lanceros-Méndez, S. & Costa, C. M. *Printed Batteries: Materials, Technologies and Applications*. (John Wiley & Sons, 2018).

20. Pan, H. *et al.* Reversible aqueous zinc/manganese oxide energy storage from conversion reactions. *Nature Energy* **1**, 16039 (2016).

21. Lee, J.-S. *et al.* Metal-Air Batteries with High Energy Density: Li-Air versus Zn-Air. *Advanced Energy Materials* **1**, 34–50 (2011).

22. Zeng, Y. *et al.* Achieving Ultrahigh Energy Density and Long Durability in a Flexible Rechargeable Quasi-Solid-State Zn–MnO2 Battery. *Advanced Materials* **29**, 1700274 (2017).

23. Li, Y. *et al.* Recent Advances in Flexible Zinc-Based Rechargeable Batteries. *Advanced Energy Materials* **9**, 1802605 (2019).

24. Yan, C. *et al.* Stretchable Silver-Zinc Batteries Based on Embedded Nanowire Elastic Conductors. *Advanced Energy Materials* **4**, 1301396 (2014).

25. Venkatraman, M. & Van Zee, J. W. A model for the silver–zinc battery during high rates of discharge. *Journal of Power Sources* **166**, 537–548 (2007).

26. Bonk, J. F. & Garrett, A. B. A Study of the Silver (I) Oxide-Silver (II) Oxide Electrode. *J. Electrochem. Soc.* **106**, 612–615 (1959).

27. Takeda, K. & Hattori, T. Optimal Process for Fabricating AgO Cathode for AgO/Zn Cells Improved in High Drain Pulse Performance at Low Temperatures. *J. Electrochem. Soc.* **146**, 3190 (1999).

28. Parkhurst, W. A. Thermogravimetry-Evolved Gas Analysis of Silver Oxide Cathode Material. *Journal of The Electrochemical Society* **131**, 1739–1742 (1984).

29. Wang, S. J. *et al.* Deposition of ZnO on bismuth species towards a rechargeable Zn-based aqueous battery. *Phys. Chem. Chem. Phys* **18**, 26376–26382 (2016).

30. Xu, W. *et al.* Hierarchically structured AgO films with nano-porosity for photocatalyst and all solid-state thin film battery. *Journal of Alloys and Compounds* **802**, 210–216 (2019).

31. McMillan, J. A. Higher Oxidation States of Silver. *Chem. Rev.* **62**, 65–80 (1962).

32. Kumar, R., Johnson, K. M., Williams, N. X. & Subramanian, V. Scaling Printable Zn–Ag2O Batteries for Integrated Electronics. *Advanced Energy Materials* **9**, 1803645 (2019).

33. Braam, K. & Subramanian, V. A Stencil Printed, High Energy Density Silver Oxide Battery Using a Novel Photopolymerizable Poly(acrylic acid) Separator. *Advanced Materials* **27**, 689–694 (2015).

34. Choi, K. H., Ahn, D. B. & Lee, S. Y. Current Status and Challenges in Printed Batteries: Toward Form Factor-Free, Monolithic Integrated Power Sources. *ACS Energy Letters* **3**, 220–236 (2018).

35. Entezam, M., Poormadadkar, H., Khonakdar, H. A. & Jafari, S. H. Melt rheology and interfacial properties of binary and ternary blends of PS, EOC, and SEBS. *Journal of Applied Polymer Science* **137**, 48791 (2020).

36. Turney, D. E. *et al.* Rechargeable Zinc Alkaline Anodes for Long-Cycle Energy Storage. *Chemistry of Materials* **29**, 4819–4832 (2017).

37. Mainar, A. R. *et al.* Alkaline aqueous electrolytes for secondary zinc–air batteries: an overview. *International Journal of Energy Research* **40**, 1032–1049 (2016).

38. Braam, K. T., Volkman, S. K. & Subramanian, V. Characterization and optimization of a printed, primary silver–zinc battery. *Journal of Power Sources* **199**, 367–372 (2012).

39. Bandodkar, A. J. *et al.* Tattoo-based potentiometric ion-selective sensors for epidermal pH monitoring. *Analyst* **138**, 123–128 (2013).

40. Yin, L. *et al.* From All-Printed 2D Patterns to Free-Standing 3D Structures: Controlled Buckling and Selective Bonding. *Advanced Materials Technologies* **3**, 1800013 (2018).

41. Dellis, J.-L. Zfit. https://www.mathworks.com/matlabcentral/fileexchange/19460-zfit.

42. D'Errico, J. fminsearchbnd, fminsearchcon. https://www.mathworks.com/matlabcentral/fileexchange/8277-fminsearchbnd-fminsearchcon.

43. Rustomji, C. S. *et al.* Thin-film electrochemical sensor electrode for rapid evaluation of electrolytic conductivity, cyclic voltammetry, and temperature measurements. *J Appl Electrochem* **46**, 59–67 (2016).

Chapter 3 Wearable Biofuel Cells for Bioenergy Harvesting

3.1 Wearable Biofuel Cell

3.1.1 Introduction

There is a continuously growing interest for wearable electronic devices, particularly, devices for fitness and health monitoring applications such as motion monitoring, physicochemical signal sensing,[1,2] and wound healing.[3] The surging development of wearable devices demands the development of efficient reliable and conformal power sources that can be easily integrated on the human body. Despite the tremendous recent progress of wearable devices, most of these devices are still powered by rigid and bulky batteries which pose environmental concerns. Enzymatic biofuel cells, which rely on oxidoreductases to bioelectrocatalytically convert biofuel present in human body fluids, have been considered as promising candidates for powering next generation wearable electronic devices.[4,5] Specifically, epidermal skin-worn biofuel cells using lactate as the substrate has been widely studied given the easy access of lactate in human sweat and the facile integration with wearable electronics.[6–8] The power output of biofuel cells and their flexibility are two major challenges in this field considering the limited concentration of lactate in sweat and the external strain imposed from body movements. To overcome these issues, it is essential to develop electrode materials that can enhance enzyme electron transfer efficiency and provide flexibility and conformity when mounted on skin.

Carbon nanotubes (CNTs) have been widely used to construct bioelectrodes given their exceptional electronic properties, electrochemical inertness and high surface area.[9] To construct electrodes for practical biofuel cell applications, CNTs are often shaped into inks,[10] pellets,[7,11] papers,[12,13] and fibers.[14] Screen-printed CNT electrodes have been popular for wearable biofuel

cells; however, this type of electrode requires mixing with elastomeric binder, which inevitably blocks the active surface of CNTs and compromises power performance. CNT pellets, used in the first generation of implantable biofuel cells, are several millimeters thick and therefore bulky, have slow mass transfer efficiency, and are fragile.

In this part of the chapter, we demonstrate the use of buckypaper (BP) as the electrode material. BP is a self-supported conductive paper-like material formed by entangled CNT network.[15] Previously, a buckypaper-based lactate/O_2 BFC was explored in synthetic tears.[16] A buckypaper-based lactate bioanode coupled with a photocathode was very recently reported.[18] However, the power density of both devices was rather low and no stretchability was demonstrated. In both systems, commercial MWCNT BP was utilized as the electrode material, while in the work in this chapter, lab-made BP was exploited instead given its superior catalytic performance, for example, for bilirubin oxidase (BOx) catalyzed oxygen reduction.[18] A new class of flexible BPs has been developed in the Cosnier group based on the crosslinking of CNTs with polynorbornene linear polymers with pyrene groups, and showing that polynorbornene-BP is an excellent matrix for mediator and enzymes immobilization.[13,19,20] However, the lack of intrinsic stretchability has impeded the application of BP in epidermal BFCs.

In this part of the chapter, we describe a high power, stretchable, flexible wearable BFC through a unique combination of highly conductive and catalytic BP electrodes with a structurally stretchable substrate to harvest energy from perspiration. To meet the requirement of wearable devices to endure rigorous movements and deformation during human exercise, a "2-degree" stretchability was realized by combining a stretchable ink formula with an "island-bridge" architecture. The electrodes of the device were separated into "islands", which are firmly bonded to the substrate, along with serpentine-shaped interconnecting "bridges", which are soft and

stretchable and can unwind under stress.[10] When external strain is applied, the stress will be distributed to the flexible "bridges" around the hard non-stretchable "islands", therefore maintaining electrical resistance stability. Here, a free-standing, buckling-enabled interconnect design, adopted from our previous work, is chosen to further enhance its flexibility and conductivity.[21]

3.1.2 Experimental Section

3.1.2.1 Chemicals and Reagents

1,4-naphthoquinone (1,4-NQ), protoporphyrin IX (PPIX, ≥95%), bovine serum albumin (BSA), glutaraldehyde, chitosan, toluene, L(+)-lactic acid, potassium phosphate dibasic (K_2HPO_4), potassium phosphate monobasic (KH_2PO_4), polyvinyl alcohol (PVA, MW 146 000–186 000 and MW 89 000-98 000), potassium hydroxide (KOH), ethanol, acetone, acetic acid, N,N-dimethylformamide (DMF, 99.9%) and Ag flakes (10 μm) were purchased from Sigma-Aldrich. Tetrahydrofuran (THF) was purchased from EMD Millipore. Hydroxyl-functionalized multi-walled carbon nanotubes (MWCNT-OHs, Ø = 10–20 nm, 10–30 μm length, >95% purity) were purchased from Cheap Tubes Inc. Commercial grade multi-walled carbon nanotubes (MWCNTs, Ø = 9.5 nm, 1.5 μm length, ≥90% purity) for buckypaper fabrication were purchased from Nanocyl. L-Lactate oxidase (LOx) from *Microorganism* was purchased from Toyobo. Bilirubin oxidase (BOx) from *Myrothecium sp.* was a gift from Amano Enzyme. Polyurethane (PU, Tecoflex SG-80A) was purchased from Lubrizol LifeSciences. Polystyrene (PS) was obtained from polystyrene foam packaging material. Styrene Ethylene Butylene Styrene copolymer (SEBS) was purchased from Kraton. Ecoflex® 00-30 (Smooth-On, Inc. PA.) was prepared by mixing equal volumes of pre-polymers A and B, provided by the supplier. Perme-roll® Lite (L34R10) was

purchased from Nitto Denko. Carbon paste (C2030519P4) was purchased from Gwent Group. 0.5 M pH 7.4 Potassium phosphate buffer solution (PBS) was prepared from potassium phosphate dibasic and potassium phosphate monobasic. Ultra-pure deionized water (DI, 18.2 MΩ) was used for all of the aqueous solutions.

3.1.2.2 Device Fabrication

A thin layer of Ecoflex was printed on the adhesive side of a Perme-Roll® Lite film and cured at 65 ℃ for 10 min to form the low elastic modulus substrate. The layers were printed onto screen printing of several layers using an MPM-SPM semi-automatic screen printer (Speedline Technologies, Franklin, MA, USA). A 100 μm-thick stainless-steel printing stencils were designed in AutoCAD (Autodesk, USA) and laser-cut (Metal Etch Services, San Marcos, CA, USA). The printing steps are as follows: first, to enhance the adhesion, a PU interlayer was printed on top of the substrate and cured at 60 ℃ for 15 min. Thereafter, a rigid "island-like" structure layer was printed using the PS-SEBS ink onto of the modified stretchable film and cured at 65 ℃ for 15 min. Then, the sacrificial layer was printed using PVA and cured at 80 ℃ for 10 min. A stretchable insulating serpentine "bridge-like" structure layer was then printed using the SEBS ink and cured at 65 ℃ for 15 min. A stretchable conductive serpentine "bridge-like" structure layer was subsequently printed using the Ag-SEBS ink and cured at 65 ℃ for 15 min. Then another insulating layer was printed on top of the silver pattern using the SEBS ink and cured at 65 ℃ for 15 min. Then a rigid conductive "island-like" layer was printed on top of the PS-SEBS using commercial carbon paste and left to dry at room temperature and then cured at 60 ℃ for 15 min. Then, a backbone serpentine layer was printed using the PS-SEBS ink and cured at 65 ℃ for 15 min. Finally, the sacrificial layer was removed by dissolving in DI. Conductive stainless steel thin

conductive threads (Adafruit, New York, USA) were attached to the contact points of the device using Ag-SEBS inks. The contact points were then insulated using PS-SEBS ink.

The polynorbornene homopolymer with pyrene group ((Py_{50}), M_n, SEC = 10.2 kg mol^{-1}, $Đ_{SEC}$ = 1.22) was synthesized as previously reported via ring opening metathesis polymerization.[22] 66 mg MWCNT was dispersed in 66 mL DMF, followed by sonication for 30 min. 6.6 mg of the polymer was added to the suspension. The suspension was then sonicated for a further 30 min. The as-prepared suspension was filtrated using a diaphragm pump (MZ 2C NT model, Vaccubrand) on a Millipore PTFE filter (JHWP, 0.45 mm pore size). The resulting BP was rinsed with water, left under vacuum for 1 h, then left to dry in air overnight.

For anode preparation, the BP was first cut into square electrode (3 × 3 mm). 5 μL of 5 mg mL^{-1} MWCNT-OHs dispersed in 0.2M NQ in 9:1 vol/vol ethanol/acetone solution was dropcast onto the cut BP electrode surface. For the cathode, the BP was cut into rectangular electrodes (3 × 6 mm). 10 μL of 40 mM PPIX in 9:1 vol/vol ethanol/acetone solution was dropcast onto the cut BP electrode surface. The modified BP was then left to dry in air. Carbon paste was subsequently used to glue individual BPs onto screen-printed carbon "islands" and left to dry in an oven at 50 °C for 30 min. Thereafter, the cathodic BP was functionalized by dropcasting 10 μL of 40 mg mL^{-1} BOx in PBS. The anodic BP was first rinsed with PBS to remove loosely bound 1,4-NQ, and then followed by dropcasting 5 μL of a mixture with 40 mg mL^{-1} LOx and 10 mg mL^{-1} BSA. 3 μL of 1% glutaraldehyde solution was then dropcast onto the surface followed by dropcasting 3 μL of 1 wt% chitosan in 0.1 M acetic acid. The BFC device was then left to dry overnight at 4 °C.

3.1.2.3 Fabrication of the DC voltage booster circuit

A layer of poly(methyl methacrylate) (PMMA) (495K, A6) was coated onto a glass slide at a speed of 1500 rpm for 20 s, then cured by baking for 150 °C on a hotplate for 1 min. Afterwards, an Ecoflex (Smooth-On, 1:1) layer of 100-μm thickness was coated on top of the PMMA and cured at room temperature for two hours. On a separate glass slide, a layer of polydimethylsiloxane (PDMS, Sylgard 184 silicone elastomer, 20:1) was coated at 3000 rpm for 30 s, followed by curing in an oven at 150 °C for 30 min. A Cu sheet (20-μm-thick, Oak-Mitsui Inc.) was coated with PI (from poly(pyromellitic dianhydride-co-4,40-oxydianiline) amic acid solution, PI2545 precursor; HD MicroSystems) at 4000 rpm for 60 s, soft baked on a hotplate at 110 °C for 3 min, 150 °C for 1 min and finally cured in a nitrogen oven at 300 °C for 1 h. This Cu sheet was transferred on top of the PDMS/glass substrate. The interconnect layout, designed in AutoCAD, is patterned onto the Cu sheet via laser ablation. A laser (wavelength 1064 nm, pulse energy 0.42 mJ, pulse width 1 μs, frequency 35 kHz and mark speed 500 mm s^{-1}) ablated the Cu sheet into the designed pattern, and residual Cu material was removed. The Cu pattern was picked off of the substrate with water soluble tape (3M Inc.) and transferred onto the prepared PMMA/Ecoflex/glass substrate. The water-soluble tape was removed by room-temperature tap water. The Cu interconnections were cleaned by flux (WOR331928, Worthington Inc.) for removal of surface oxides. Sn42Bi57.6Ag0.4 alloy paste (Chip Quick Inc., SMDLTLFP-ND, low melting point 138 °C) was used to solder the chip components (including the BQ25504 Ultra Low-Power Boost Converter for Energy Harvesting, Texas Instruments) onto the Cu interconnects, followed by baking on a hotplate at ~150 °C for 4 min, and then cooling to room temperature. Finally, the entire surface of the circuit was encapsulated by Ecoflex with 1-mm thickness and cured at room temperature for 4 hours. The

combined Ecoflex/Cu interconnect/circuit device was then removed from the glass/PMMA substrate using a razor blade.

3.1.2.4 Device Characterization

The morphology of the BP was characterized using scanning electron microscope (Phillips XL30 ESEM) with an accelerating voltage of 20 kV.

The electrochemical performances of the half cells and BFC were conducted using a μAutolab Type II commanded by Nova software (Version 2.1). In-vitro table-top electrochemical characterization was performed in 0.5 M pH 7.4 PBS. The enzyme-catalyzed lactate oxidation and oxygen reduction reactions at the bioanode and biocathodes were characterized by linear sweep voltammetry (LSV) in a three-electrode system with a scan rate of 5 mV s^{-1}. The three-electrode system consisted of a BP electrode as the working electrode, a Platinum (Pt) wire as the counter electrode and an Ag/AgCl (3M KCl) as the reference electrode. The assembled BFC device was characterized in a two-electrode system with the bioanode as the counter and reference electrode and the biocathode as the working electrode. LSV Polarization curves of the BFC in different lactate concentrations were obtained by scanning from OCV to 0.01V at 5 mV s^{-1}. The calculation of the power density of a single BFC was based on the geometrical area of the cathode (0.18 cm^2). CV and galvanostatic charge/discharge (GCD) techniques were used to characterize the capacitive behavior of the BFC. CVs were performed from 0 V to 0.8 V with a scan rate of 50 mV s^{-1}, while the GCD tests were carried out at current densities of 0.1, 0.2, 0.5 and 1 mA cm^{-2}. The capability of the BFC to serve as the pulse generator was characterized by chronopotentiometry. The minimum voltage at the end of each 10 ms pulse discharge was used to calculate the power density.

The mechanical resiliency studies were conducted on a motorized linear stage connected to a controller (A-LST0250A-E01 Stepper Motor and Controller, Zaber Technologies, Vancouver, Canada). Four linear motors with the same speed were used to conduct 20% biaxial stretching. The stability of the BFC during the mechanical deformations was studied by measuring the resistance of the screen-printed current collector and the current output of the BFC with a 33 kΩ loading during 20% biaxial stretching.

3.1.2.5 On-body Experiments

The flexible buckypaper BFC was mounted on the arm of one volunteer with the assistance of an adhesive film (Perme-Roll). The stainless conductive steel yarn was used to connect the BFC and a 510 Ω resistor to reach the maximal power density, with stretchable Ag ink as the joint bonding resin. The current of the circuit was record every 5 s by a potentiostat during which the volunteer was doing stationary cycling. The capability of the BFC to power one LED was demonstrated by using the flexible DC-DC converter to boost the voltage and a switch to control the "on" and "off" status. The voltage of the LED was tested in both pulse and continuous working mode. All on-body experiments were approved by the Human Research Protections Program at University of California, San Diego, and followed the guidelines of institutional Review Boards (IRB).

3.1.3 Results and Discussion

As illustrated in **Figure 3.1**, the stretchable and flexible wearable BFC is fabricated by integrating buckypaper-based BFC and stretching current collector. The stretchable substrate is fabricated via high-throughput and low-cost screen-printing methods. The carbon-based electrode "islands" are interconnected by high-conductivity silver composite "bridges" in a serpentine shape.

A “skeleton” layer composed of polystyrene (PS) and styrene ethylene butylene styrene (SEBS) is added below the carbon islands to enhance their mechanical stability, and a water-soluble sacrificial layer is added below the serpentine interconnects to allow their separation from the substrate. A flexible polymer is printed on both sides of the silver interconnects to avoid the direct contact of Ag and the electrolyte. The printed sacrificial layer is dissolved in water to enable buckling of the serpentine structures during deformation. To complete the assembly of the skin patch illustrated in **Figure 3.1** A, pre-cut anodic and cathodic BP electrodes were thereafter attached to the carbon islands. A thin sheet of phosphate buffer solution-polyvinyl alcohol (PBS-PVA) hydrogel was added as electrolyte and a sweat reservoir was applied onto the electrodes. The fabrication process is illustrated in detail in **Figure 3.2**.

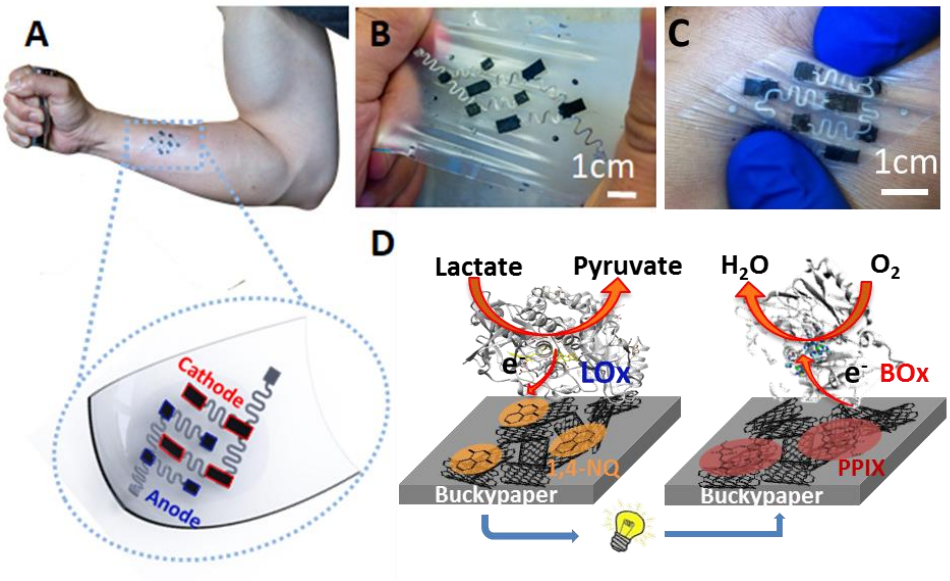

Figure 3.1. Illustration of the stretchable BFC patch.
A. Photograph of the stretchable BFC device on a human arm, (zoom) schematic illustration of the skin-mountable wearable BFC device. (**B**, **C**) Photographs of the BFC under stretching and bending, respectively. **D**. Schematics of the redox energy generation from sweat lactate oxidation at the anode and O_2 reduction at the cathode by BFC.

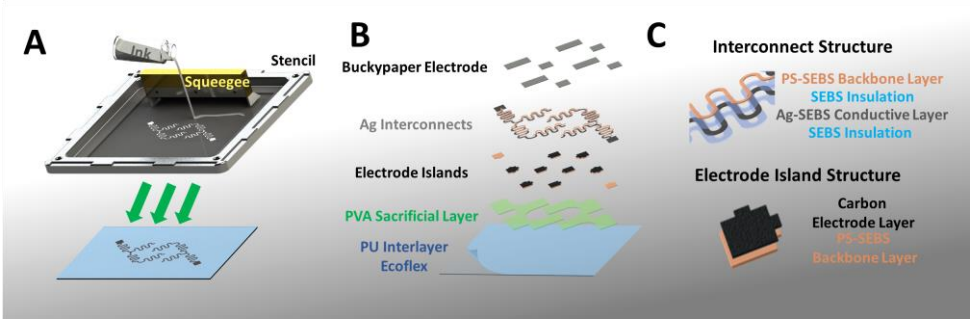

Figure 3.2. Schematic illustration of the printing process

The printed patch can be attached to the human epidermis in a wide range of locations while maintaining high conformity (**Figure 3.1**). The system has been designed to endure mechanical strains caused by bodily movements. Endowed by the advantageous island-bridge structure, the BFC patch is highly flexible and stretchable (**Figure 3.1 B**) and endures severe bending (**Figure 3.1 C**). The serpentine structures can thus accommodate most of the stress. The patch can be activated once perspiration takes place a few minutes after exercise, where the lactate in the sweat is absorbed into the hydrogel electrolyte and permeates to the electrodes. The reaction mechanism is illustrated in **Figure 3.1 D**. The anode consists of pyrene-polynorbornene functionalized BP immobilized with lactate oxidase (LOx) from *Microorganism* to catalyze the oxidation of lactate into pyruvate with 1,4-naphthoquinone (NQ) as the electron transfer mediator. The cathode consists of BP immobilized with bilirubin oxidase (BOx) from *Myrothecium sp.* to catalyze the oxygen reduction reaction (ORR). For the cathode, BP is modified with protoporphyrin IX (PPIX) molecules which can orientate the enzyme preferentially with the T1 center of BOx to facilitate direct electron transfer with carbon nanotubes.[13,23] The current and voltage generated from the anodic and cathodic reactions can thereafter be exploited to power various electronics in a biofuel cell configuration.

The morphology of BP functionalized with the pyrene-polynorbornene homopolymer was characterized using SEM and revealed a homogenous mesoporous structure of entangled CNT bundles (**Figure 3.3 A**). The electrochemical performance of the biocathode and bioanode was evaluated individually using a three-electrode set-up with a platinum counter electrode and Ag/AgCl (3M KCl) reference electrode. **Figure 3.3 B** shows overlaid linear sweep voltammograms (LSVs) for the bioanode in the presence of 0 and 15 mM lactate in 0.5 M phosphate buffered solution (PBS, pH 7.4), respectively. Upon addition of lactate, the mediated bioelectrocatalytic current of lactate oxidation starts to flow and results in a current density of 1.3 mA cm^{-2} at 0.2 V. **Figure 3.3 C** shows LSVs for the biocathode. The oxygen reduction current starts to increase dramatically at a potential close to 0.5 V, reaching a maximum current density of -1.5 mA cm^{-2} at 0 V. The presence of lactate did not affect the performance of the BOx bioelectrode as the onset potential for ORR and the limiting current were unchanged. The high onset potential and steep oxygen reduction reaction slope indicate a more efficient direct electron transfer between the T1 center of BOx and CNTs. The excellent performance is in accordance with other reported protoporphyrin-modified biocathodes.[13,23]

The power performance of the BFC was investigated using a unit cell device comprising a single biocathode and a single bioanode, as depicted in **Figure 3.1 D**. The area of the biocathode was designed to be two times larger than the bioanode to ensure that BFC performance is not limited by the cathode. LSVs were recorded from open circuit voltage (OCV) to 0 V in different lactate concentrations. The power-voltage curves are shown in **Figure 3.3 D**. Both the OCV and peak power density increased with increasing lactate concentrations, reaching saturation at 10 mM lactate. A maximum power density of 0.5 mW cm^{-2} was recorded at 0.55 V in 10 mM lactate. However, for subsequent characterization experiments, 15 mM lactate was chosen to match the

average lactate concentration in sweat.[24] Although the power density in this work is lower than the maximum value of ca.1.2 mW cm cm^{-2} reported previously,[7] in this work, an oxygen reducing enzymatic biocathode was used instead of a battery type silver oxide cathode. The power performance stability of the BFC was investigated periodically by performing LSV in 15 mM lactate over an extended period of 48 hours (**Figure 3.3 E**). As shown in **Figure 3.3 F**, the power density at 0.55 V decreases only by 16 % after 48 hours. Control power-voltage curves of BFCs fabricated by immobilizing enzymes on screen-printed current collectors and CNT ink[8] electrodes are included in **Figure 3.4** and **Figure 3.5**, respectively. In these two alternative systems, the power performance in 15 mM lactate is negligible compared to the BP-based BFC, highlighting that the excellent performance of BFC originates from the BPs used in the present work.

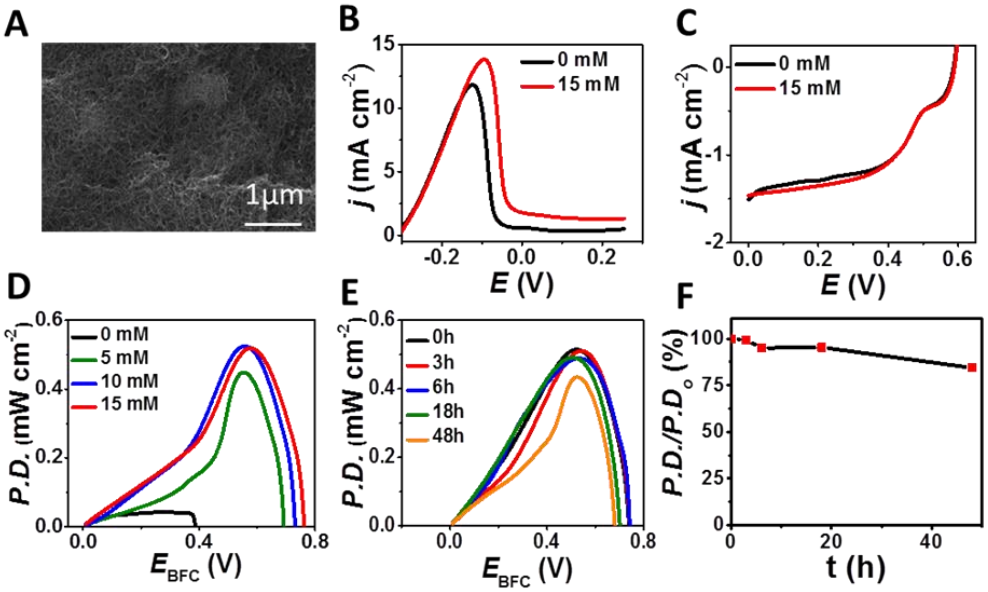

Figure 3.3. BFC performance characterization.
A. SEM image of buckypaper functionalized with pyrene-polynorbornene. **B**. LSV of the BP bioanode in the presence of (black) 0 mM and (red) 15 mM lactate in 0.5 M PBS (pH 7.4) at 5 mV s^{-1}. **C**. LSV of the BP biocathode in air-equilibrated buffer with (black) 0 mM and (red) 15 mM lactate at 5 mV s^{-1}. **D**. The power density versus voltage plots for the stretchable lactate BFC under different lactate concentrations (0, 5, 10 and 15 mM) in 0.5 M PBS (pH 7.4). **E**. Plots showing the stability of the stretchable BFC in the presence of 15 mM lactate at different times up to 48 hours. **F**. The calculated relative change of power density at 0.55 V over 48 hours, based on the data in E.

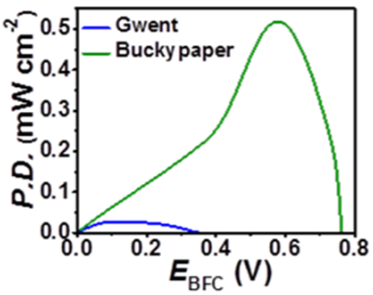

Figure 3.4. Plots of power density versus voltage of screen-printed current collector modified with enzymes and stretchable buckypaper BFC.

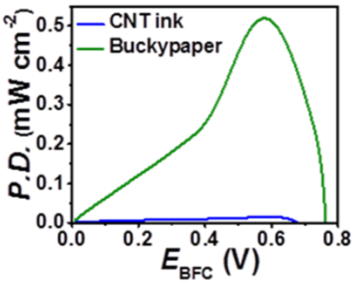

Figure 3.5. Plots of power density versus voltage of screen-printed BFC using CNT ink and stretchable buckypaper BFC.

The ability of the BFC to function also as a self-powered supercapacitor was investigated. **Figure 3.6 A** shows cyclic voltammograms (CVs) recorded of the BFC in the presence of 0 mM and 15 mM lactate in PBS. A quasi-symmetric rectangular shape of the CV curves indicates high capacitive behavior, which is expected for high surface area nanostructured carbon electrodes.[11,25] Upon addition of 15 mM lactate, the capacitive current increased, which can be explained by the additional electronic loading on CNT matrix by enzymatic oxidation of lactate. The capacitance of the device was further investigated by performing galvanostatic charge-discharge (GCD) at different current densities. GCD curves and the calculated areal capacitance at different current

densities are shown in **Figure 3.7**. A high capacitance of 40 mF cm^{-2} was observed at 0.1 mA cm^{-2}, which is comparable to other reported self-charging supercapacitors.[26,27] We note that no extra modification of the bioelectrodes such as manganese oxide was needed to obtain this capacitive performance. Current pulse chronopotentiometry was performed to evaluate the BFC power performance in pulse operation mode. **Figure 3.6 B** shows the overlay of potential profiles of the BFC discharged at 2 to 25 mA cm^{-2} over 10 ms. The potential profile at all discharge current densities showed the same feature, with an initial IR drop followed by capacitive discharge and then self-recharge back to its original voltage after the pulse duration. The calculated pulse power delivered by the BFC is shown in **Figure 3.6 C**, reaching a maximum power of 6.5 mW cm^{-2} at 20 mA cm^{-2}. This value is around 13 times higher than the power delivered in normal BFC mode. The BFC show also high stability at high frequency discharge. As shown in **Figure 3.6 D**, the BFC is discharged at 5 mA cm^{-2} at 33 Hz frequency (10 ms discharge and 20 ms rest) and the OCV only decreases slightly.

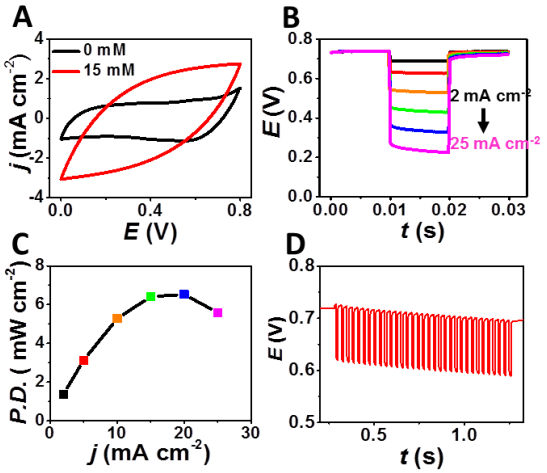

Figure 3.6. BFC super-capacitive behavior characterization.
A. CV of BFC in the presence of (black) 0 mM and (red) 15 mM lactate in 0.5 M PBS (pH 7.4) at 50 mV s^{-1}. **B**. Overlay of potential profiles obtained from BFC discharge at 2, 5, 10, 15, 20 and 25 mA cm^{-2} over 10 ms. **C**. Plot of the calculated pulse power density as a function of the discharge current density. **D**. Potential profile of the BFC during a discharge at 5 mA cm^{-2} at 33 Hz frequency.

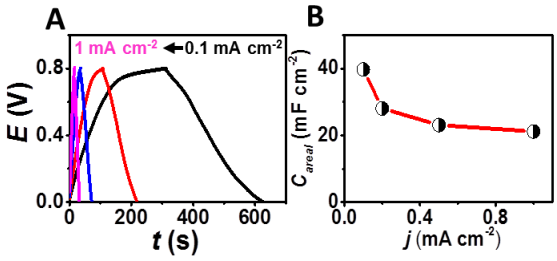

Figure 3.7. BFC capacitance study.
A. GCD curves of the BFC at different charge-discharge current density (0.1, 0.2, 0.5, 1.0 mA cm^{-2}). **B**. The calculated corresponding areal capacitance.

To highlight the resiliency of the BP-based "island-bridge" BFC, we examined its performance under severe mechanical distortions (**Figure 3.8**). The mechanical stability of the buckypaper BFC was evaluated using a stepping-motor controlled biaxial stretching stage. The printed BFC is stretched repeatedly to 120% of its original size in both directions (**Figure 3.8 B**). The resistance of the circuit between the silver contact on the end of the patch and the central printed carbon electrode is measured during a 100-cycle stretching test, as shown on **Figure 3.8 C**. The resistance of the circuit varies less than 1 Ω in each stretching cycle (**Figure 3.8 C** inset), with no trend of increasing resistance after all of the stretching cycles. The mechanical stability was further validated by monitoring the discharge current of the BFC under a constant load. One pair of electrodes is covered in PBS-PVA gel electrolyte with 15 mM lactate and connected to a 33 kΩ resistor, as shown in **Figure 3.8 A**. The discharge current exhibits no significant change during 20 cycles of stretching, which further validates the mechanical stability of the patch as a practical wearable energy-harvesting device. The durability of generated power performance was examined in connection to numerous stretching cycles. A LSV scan was performed every 20 cycles of 20% biaxial stretching. The power density remained highly stable after 100 cycles of stretching (**Figure 3.8 E - F**).

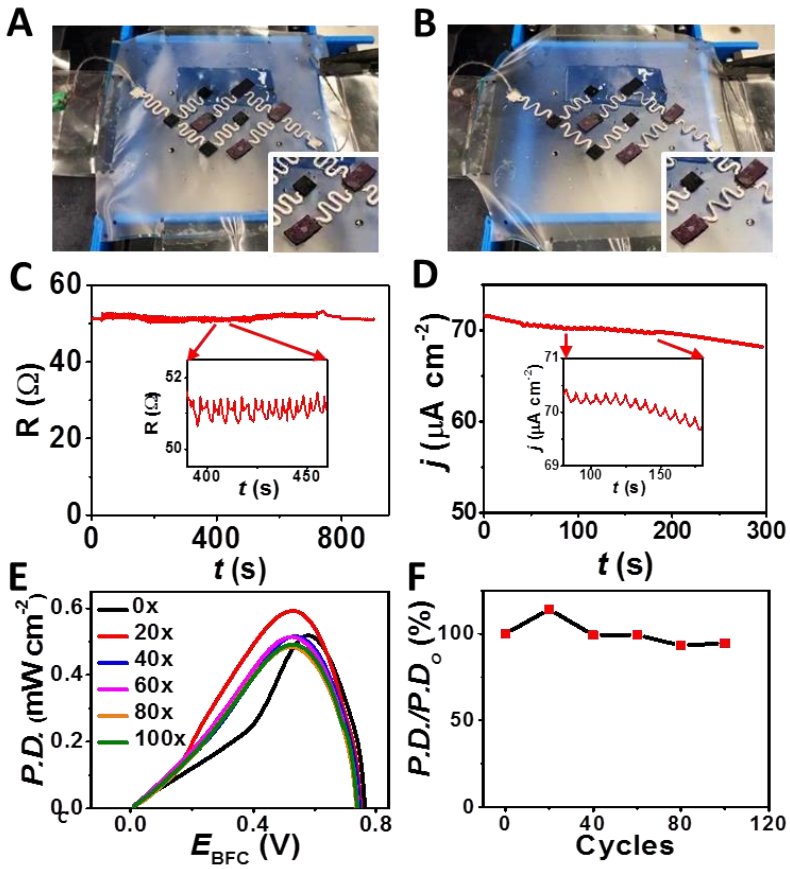

Figure 3.8. Mechanical resilience studies.
Image of the wearable BFC **A**. before and **B**. after 20 % stretching. **C**. Resistance profile obtained during 20% stretching, (inset) zoom of resistance fluctuations. **D**. Current density output profile of the BFC under a 33 kΩ load in PVA gel immersed in 15 mM lactate, (inset) zoom of current density fluctuations. **E**. Plots of BFC power density versus voltage under 20% stretching for 0, 20, 40, 60, 80 and 100 cycles in 15 mM lactate. **F**. The calculated relative change of power density at 0.55 V over 100 stretching cycles.

The real-time power outputs of the wearable buckypaper BFC was tested by monitoring the current of the circuit (with 510 Ω load) when the volunteer was doing constant stationary cycling exercise. The power change of the BFC during the whole process is shown in **Figure 3.9 A**. The power is very low before the volunteer started to sweat due to the absence of the fuel. After 10 minutes exercise, the obvious perspiration is formed and the power density of BFC experiences a rapid increase when more lactate molecules from the sweat transfer to the interface of the LOx bioanode.

The highest power density obtained is around 450 μW after 30 minutes of perspiration, which is an output that is sufficient to power various wearable devices considering their low power requirements.[28] When the volunteer stopped cycling, a constant drop of power is observed, probably caused by the insufficient supply of lactate and oxygen dissolved in the sweat.[29] The capability of the flexible buckypaper BFC to serve as the power source for wearable electronic devices was demonstrated by powering a LED during stationary cycling exercise. The voltage of the EFC was boosted using a flexible DC-DC converter, as shown in **Figure 3.9 C** and **Figure 3.10**. **Figure 3.9 B** illustrates the circuit connection of the patch, the voltage booster, LED and a switch which was used to control the "on" and "off" function of the LED. When connected with the sweat-based BFC, the LED is lit up (**Figure 3.9 E**) and its voltage can reach over 1.4 V both in pulse mode and continuous discharging modes (**Figure 3.11**), illustrating the feasibility of voltage boosted buckypaper BFCs to supply energy for wearable electronics.

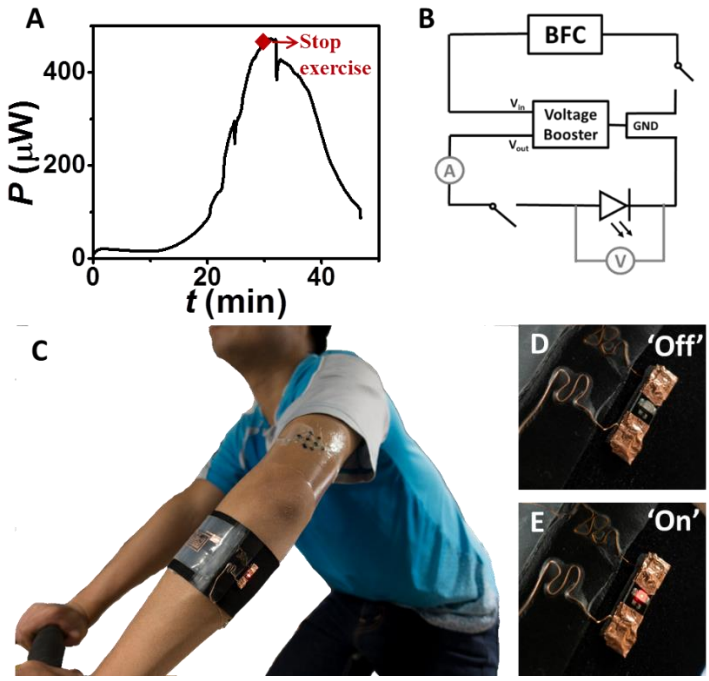

Figure 3.9. On-body performance of the BFC patch.
A. Power output profile under 510 Ω load during an on-body experiment. **B**. The circuit schematics for using the flexible and stretchable epidermal BFC patch to power an LED via a flexible DC-DC convertor. **C**. Image of on-body experiment set up with a BFC mounted on the arm of the volunteer. **D**. and **E**. Images of the LED switched on and off, respectively.

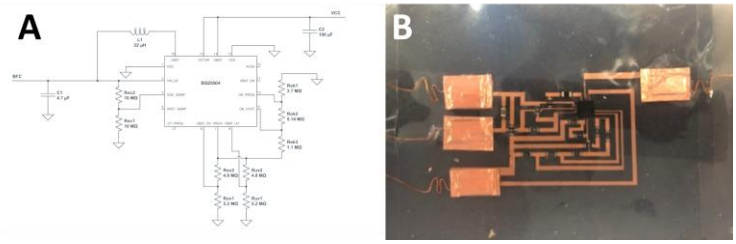

Figure 3.10. Voltage Booster for BFC patch.
A. The circuit diagram and B. the photo of the prepared flexible voltage boosting circuit.

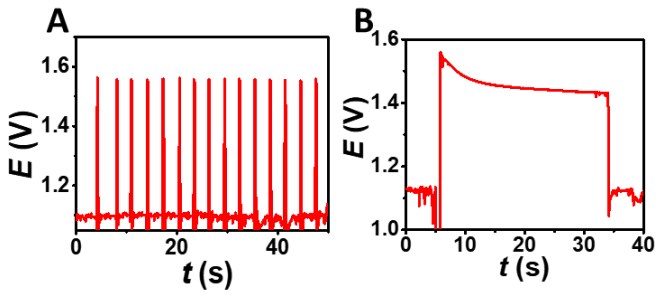

Figure 3.11. BFC discharge for the powering of LED.
A. and **B**. Voltage output profile under 0.2s pulsed discharge and continuous discharge during exercise, respectively.

3.1.4 Conclusion

In summary, a stretchable and wearable enzymatic BFC that harvests energy from sweat has been created through the combination of a screen-printed current collector substrate and flexible enzyme-modified polynorbornene-based BPs. During in vitro experiments, the assembled BFC had a high OCV of 0.74 V and a maximum power density of 520 µW cm^{-2}. The stretchability of the device was realized through the coupling of an "island-bridge" architecture and strain-enduring inks. The device was able to remain its performance stability under multiple stretching cycles. After coupling with a voltage booster, the BP-based BFC was able to power a commercial LED both in pulse mode and in continuous mode. We have demonstrated the promising potential of using BP as a high-performance carbon electrode material for epidermal BFC with a stretchable supporting substrate. Such stretchable skin-worn devices are expected to contribute to the development of epidermal energy harvesting systems and wearable electronics, in general. A more powerful lactate BFC can be envisioned by replacing the cathode with an air-breathing electrode. Future studies will aim at improving the biocompatibility, the catalytic anode performance, further electronics integration along with extensive on-body operations.

3.2 Wearable Biosupercapacitors

3.2.1 Introduction

In recent years, the field of wearable electronics has been experiencing a transition from rigid, bulky, and non-conformal devices to miniaturized, flexible, and stretchable devices that conform and adapt to the human body with high intimacy.[30,31] Built upon the work of numerous researchers, the state-of-the-art flexible and stretchable electronics, ranging from mechanical and electrochemical sensors[32–34] to complex systems such as multi-sensor arrays, transistor arrays, or electronic displays,[35–38] have been assembled into a comprehensive ecosystem of various class of devices with distinct functionalities. However, one of the main challenges that impede such wide adoption of flexible and stretchable wearable electronics is the lack of an equally flexible, stretchable, and miniaturized energy source that can supply sufficient power over extended periods. Depending on the functionalities of the device,[39] most wearable electronics consume power ranging from as low as nano-watts to more common milli-watts, with expected usage ranging from a few hours to multiple days. Tremendous efforts have been dedicated to the fabrication of wearable systems to harvest and store energy from various sources, such as human movement, perspiration, sunlight, or the air.[40–44] Among these, wearable biofuel cells (BFCs) that convert chemical energy from human perspiration to electrical energy via enzymatic electrochemical reactions are considered a promising potential solution.[45–49] Nevertheless, one of the key shortcomings of such sweat-based energy harvesters is the need for the constant supply of fuel from human perspiration and the presence of the oxidizer. To address this issue, hybrid devices that combine energy harvesting and storage modules have been reported.[50,51] For example, we demonstrated previously a stretchable textile-based wearable hybrid BFC-supercapacitor (SC) device, where energy is generated from human sweat by the BFC and stored in the SC for later

use.[50] However, these integrated hybrid devices still rely on the external connection of the two separate harvesting and storage modules. Some recent efforts demonstrated the possibility of endowing multiple functionalities onto one single device via material innovations, storing energy in multiple modes, or simultaneously harvesting and storing mechanical and chemical energy; however, such multi-functional materials and designs have not been demonstrated for wearable energy systems.[52–54] We envision the integration of harvesting and energy storage functionalities at the material level would be more beneficial for the miniaturization of a sustainable high-power energy supply unit for wearable electronics.

Self-charging biosupercapacitors (BSCs) that can store energy and be self-charged via chemical or solar energy conversion have recently attracted considerable attention.[55–57] BSCs are biomaterial-based two-electrode systems that combine both BFC and SC functionalities in a single device.[58] Compared with traditional BFCs, the BSCs can generate higher power pulses due to their high-capacitance electrodes that allow rapid discharges. Supercapacitance can be realized by using nanostructured electrode materials to increase electrochemical double-layer capacitance[54] or by the addition of redox molecules[59] and conductive polymers[60] to endow pseudocapacitive behavior. Compared with traditional SCs, which require external power input, self-charging BSCs rely on biocatalysts, such as microbes, organelles, or enzymes, immobilized onto highly capacitive material that allows energy conversion from body fluids or sunlight and its subsequent storage.[58] The dual-functionality feature of BSCs can greatly simplify the design of wearable systems as no external connection is needed, hence improving the energy efficiency and facilitating the miniaturization of the electronic device. For chemical-energy-based BSCs, glucose- and other fuel-based BSCs have been studied.[27] However, to the best of our knowledge, there are no reports on sweat-operated BSCs for on-body wearable applications. For a wearable BSC, the flexibility,

stretchability, and skin conformity of the device are of considerable importance. Different materials have been used previously to fabricate electrodes for BSCs, including carbon paper, carbon nanotube (CNT) pellets, or graphite foil.[46,54,59,60] However, these materials are either bulky, rigid, or fragile, and therefore cannot serve as suitable candidates for stretchable conformal wearable electronic devices.

In this part of the chapter, we demonstrate the first example of an all-printed dual-functional stretchable and wearable BSC, fabricated on top of low-elastic modulus and adhesive elastic films, to harvest and store energy from sweat while maintaining intimate contact with the human skin. This wearable hybrid device, functioning as both a BFC and an SC, is demonstrated to deliver high-power pulses and be rapidly self-charged using enzymatic oxidation of lactate biofuel from human perspiration. Compared to an early multi-module BFC and SC system,[50] this work enabled material-level integration of both functionalities on the same set of electrodes, thus reducing the system complexity and minimizing the device footprint. A scalable and low-cost screen-printing process, using stress-enduring inks, is used to fabricate the BSC (combining the BFC and SC functions on the same printed anode and cathode) and meeting the softness, stretchability, and scalability requirements for this skin-worn wearable device. The stable, conformal, and stretchable energy harvesting-storage dual-function device has been realized through the highly efficient planar electrode design with an island-bridge structure and the use of such strain-enduring inks.[31,61] The island-bridge structure is fabricated on a soft silicone rubber substrate; a non-elastic backbone layer is printed at the bottom of the active electrode "islands" for mechanical support, while silver interconnections are printed in serpentine patterns as "bridges".[62] The stress in the electrode area is thereby distributed to the surrounding flexible region when the device is under deformation, hence ensuring attractive mechanical resiliency. Compared to the

common lactate/O_2 BFC, the greatly enhanced capacitance of the BSC is achieved by the synergistic effect of the CNT-based ink and the electrodeposited polypyrrole conductive polymer on the anode and of the high-surface-area cauliflower-like structured porous Pt on the cathode. The resulting wearable dual-functional BSC can support high-power pulsed output while maintaining stable charge-discharge performance in human sweat-level lactate. The self-rechargeable hybrid device has been mounted on the user's arm and demonstrated harvesting high power up to 1.7 mW cm^{-2}, suggesting its considerable potential as a power source for the next generation of wearable devices.

3.2.2 Experimental Section

3.2.2.1 Chemicals and Reagents

Polystyrene-block-polystyrene (SIS), toluene, 1,4-naphthoquinone (NQ), glutaraldehyde bovine serum albumin (BSA), chitosan, Nafion (20%), L(+)-lactic acid, tetrahydrofuran (THF), terpineol, potassium phosphate dibasic (K_2HPO_4), and Ag flakes (10 μm) were purchased from Sigma-Aldrich. Hydroxyl-functionalized multi-walled carbon nanotubes (OH–MWCNTs) (purity >95%, diameter 10–20 nm, length 10–30 μm) were purchased from Cheap Tubes Inc., USA. LOx was purchased from Toyobo, Japan. Styrene ethylene butylene styrene copolymer (SEBS) was obtained from Kraton, TX, USA. Polyurethane (PU) (Tecoflex SG-80A) was obtained from Lubrizol Life Sciences, OH, USA. Ecoflex 00-30 was purchased from Smooth-On, Inc. PA, USA., and the Perme-roll Lite (L34R10) was obtained from Nitto Denko, Japan. Water-based polyurethane resin Dispercoll U-42 and Bayhydur 302 crosslinker were purchased from Covestro. Ultra-pure deionized water (18.2 M Ω) was used for preparing all aqueous solutions.

3.2.2.2 Device Fabrication

The preparation of the stretchable Ag and CNT ink is similar to that reported in our previous work[50]. The synthesis of Ag ink comprises the preparation of a polymeric resin consisting of 0.4 g mL^{-1} of SIS in toluene, then 0.7 g of the resin was mixed with 1.4 g of silver flakes in a dual asymmetric centrifugal mixer (Flacktek Speedmixer, DAC 150.1 KV-K, FlackTek, SC, USA) under a speed of 1800 rpm for 5 min. To enhance the mixing of the ink, Zirconia (YSZ) beads (3 mm, Inframat Advanced Materials, CT, USA) were also added. The CNT ink is synthesized by dispersing 100 mg OH-MWCNT in a solution containing 5 mL of THF and 0.5 mL of terpineol by probe sonication (FS-600 N, Ultrasonic processor, SX Ultrasonics, China) for 5 min. Thereafter, 100 mg of Tecoflex PU beads were added to the mixture and shaken for 12 h. The formulation of the PU interlayer was followed as previously reported[50], where 4 g of water-based Polyurethane resin was mixed with 250 mg of crosslinker before its deposition. The formulation of the PU interlayer ink is formulated by mixing 4 g of water-based polyurethane with 250 mg of crosslinker before its deposition.

A thin layer of Ecoflex was printed on the adhesive side of a Perme-Roll® Lite film and cured at 65 ℃ for 10 min to form the low elastic modulus substrate. The layers were printed onto screen printing of several layers using an MPM-SPM semi-automatic screen printer (Speedline Technologies, Franklin, MA, USA). A 100 μm-thick stainless-steel printing stencils were designed in AutoCAD (Autodesk, USA) and produced by laser-cut (Metal Etch Services, San Marcos, CA, USA). The printing steps process for the BSC are as follows: A rigid “island-like” structure layer was printed using the dielectric ink firstly onto the modified stretchable film and cured at 80 ℃ for 15 min. Thereafter, to enhance the adhesion, the PU interlayer ink was printed on top of the dielectric layer and was cured at 80 ˚C for 15 min. Then, the CNT ink was printed on top of the

PU layer and cured at room temperature for 8 h followed by 30 min at 80 ℃. Finally, a stretchable conductive serpentine “bridge-like” structure layer was printed using the Ag-SIS ink and cured at 60 ℃ for 15 min.

The electrodeposition of the PPy and porous Pt were performed in the three-electrode system, with Pt wire as the counter electrode and Ag/AgCl (in saturated KCl solution) as the reference electrode. The PPy deposition protocol followed previous work with minor changes.[63] Shortly, a constant potential of 0.8 V vs. Ag/AgCl was applied to the electrodes immersed into a solution containing 0.15 M pyrrole, 0.2 M K_2HPO_4, and 5 mM $KClO_4$ for 20 s. A similar technique using commercial Pt electroplating solution was used to deposit the Pt cathode. A high potential of E = -0.95 V vs. Ag/AgCl was set for 15 min to deposit the Pt with high porosity. After the electrodeposition, both electrodes were washed using deionized water 4 times and dried at room temperature.

The fabrication of the bioanode was performed by consecutively drop-casting solutions onto the CNT-based electrode surface. The sequence and the formulations of the drop-casting solutions for each electrode (0.16 cm^2) were as follows: First, a 5 µL 5 mg mL^{-1} of OH-MWCNTs dispersed in 0.2 M NQ in 9:1 vol/vol ethanol/acetone solution was cast. Subsequently, a 5 µL aliquot of 40 mg mL^{-1} LOx in 10 mg mL^{-1} BSA and 5 µL of 1% glutaraldehyde solution were dropped cast and then covered with 5 µL of 1 wt% chitosan in 0.1 M acetic acid. Each of the above-mentioned steps was followed by a room temperature drying before adding the next layer. The chitosan layer was allowed to dry overnight.

A layer of Ecoflex® was used to define the active area and insulate the exposed silver. A PVA-PBS electrolyte gel was prepared by dissolving 1 g of PVA in 5 g of deionized water and

crosslinked with an equal weight of 3.3 M KOH solution in a desiccator until 80% weight is lost. After crosslinking, the hydrogel was repeatedly washed with 0.5 M PBS (pH of 7.4) to remove the excess KOH until reaching a neutral pH. The gel can be stored in PBS before use. The hydrogel is of high flexibility and conformity and was used in on-body experiments for sweat collection, establishing a secure interface between the skin and the electrodes (**Figure 3.12**). Conductive stainless steel thin conductive threads (Adafruit, New York, USA) were used to connect the BSC to the output source using a silver conductive epoxy adhesive (8331, MG chemicals, Canada).

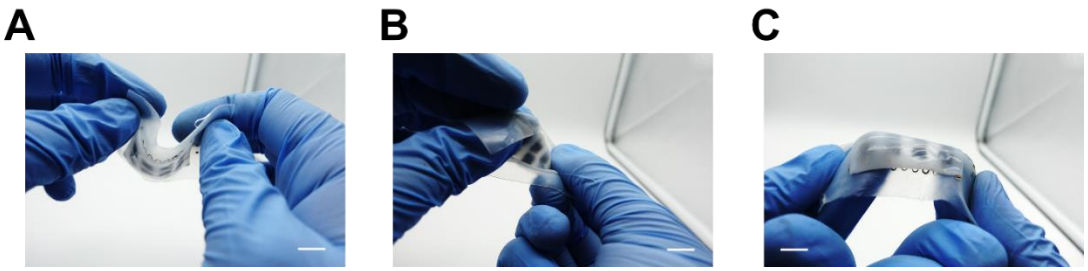

Figure 3.12. Photos demonstrating the conformity of the hydrogel on the BSC.
A fully hydrated PVA hydrogel on the BSC during **A**. bending upside down, **B**. twisting, and **C**. stretching. Scale bar: 1 cm.

3.2.2.3 Device Characterization

Electrochemical studies of the BSC were carried out using μAutolab Type II. Oxygen reduction performance of the cathode was characterized using linear sweep voltammetry (LSV) at 5 mV s^{-1} in 0.5 M phosphate buffer solution (PBS) (pH 7.4). OCV of the BSCs was measured while quantified lactate solution was added to the 0.5 M PBS (pH 7.4). Polarization curves were obtained using LSV by scanning from OCV to 0 V at 5 mV s^{-1}. The geometrical area of each

compartment, 0.64 cm^2, was used to calculate the areal power density. The stability of the BSC was analyzed by obtaining the polarization curve of the BSC every 2 h for up to 8 h in the presence of 10 mM lactate at room temperature. The ability of the BSC to deliver power in continuous mode was evaluated under galvanostatic discharge. The BSC was first immersed in 10 mM lactate for 3 min to reach stable OCV and then discharged from OCV to 0 V at 1 mA cm^{-2}. The capacitance of the BSC was characterized using cyclic voltammetry (CV) and galvanostatic charge/discharge (GCD) techniques. For single electrode characterization, CV was performed in a three-electrode set-up. For the assembled cell characterization, CV was performed in a two-electrode set-up with the cathode as the working electrode and bioanode as the joint counter/ reference electrode. Chronopotentiometry (CP) was used to evaluate the performance of the BSC in the current pulse mode. For practical evaluation of the device performance, the minimum voltage value (V_{min}) at the end of the pulse period was chosen. Power value was obtained by multiplying the current pulse and V_{min}.

Scanning electron microscopy (FEI Quanta FEG 250) was used to obtain morphological information of the printed electrodes. The element composition of the electrodes was characterized by Energy dispersive X-ray (EDX) mapping analysis.

Mechanical tests of the BSC were performed using a motorized linear actuator coupled to a programmable controller (A-LST0250A-E01 Stepper Motor and Controller, Zaber Technologies, BC, Canada). The BSC was stretched repeatedly by 20% at a speed of 0.1 cm s^{-1} from 0% to 20% reversibly. The resistance change was recorded using a Digital multimeter (34411A, Agilent Technologies, CA, USA). The on-body test was performed by attaching the BSC device facing down to the skin of the arm. A thin film of Perme-Roll® Lite was used to hold and insulate the device onto the skin. Stainless steel thin conductive threads were used to connect the device into

output, and silver conductive epoxy was used in the interconnections. All the on-body tests were carried out with consent from the subject volunteers, approved by the Human Research Protections Program at the University of California, San Diego, and in strict compliance with the guidelines of Institutional Review Boards (IRB). The LED pulsed illumination test was conducted by connecting 2 BSC patches in parallel and adding the PBS solution with respective lactate concentrations onto the patch. The patch is connected to a BQ25504 Power Management chip (Texas Instrument, TX, USA) with a complementary circuit, with the output connected to a yellow LED (Sparkfun, CO, USA). The connection is controlled manually. A digital multimeter and a potentiostat are used to simultaneously monitor the current and voltage through/across the LED.

3.2.3 Results and Discussion

The new soft, dual functional, and skin-worn BSC, integrated on a conformal elastomeric substrate, was designed in a planar structure to harvest and store energy from human sweat (**Figure 3.13 A - B**). The surface and structure of the device have been tailored to merge the BFC and SC functions into one single wearable device (**Figure 3.13 C**). The surface of both electrodes was thus modified to combine the energy harvesting capability with the energy storage functionality. Polypyrrole (PPy) is an attractive electrode material for SC operation owing to its favorable conductivity and pseudocapacitance.[64,65] Therefore, the anode was assembled based on the PPy-electrodeposited multiwalled carbon nanotubes (CNTs) and decorated by lactate oxidase (LOx) enzyme, mediated by 1,4-naphthoquinone (NQ) relay units. In the anode, the LOx catalyzed lactate oxidation is facilitated by the NQ that regenerates the flavine mononucleotide (FMN) cofactor, allowing continuous fuel oxidation. The cathode is composed of the same CNTs-based electrode, functionalized by an electrodeposited high-surface-area porous Pt catalytic layer, offering high electrochemical double-layer capacitance. The Pt-catalyzed oxygen reduction reaction provides a

driving force for the continuous electron flow from the anode to the cathode, producing and storing electric energy on the same device.

A phosphate buffer solution–polyvinyl alcohol (PBS–PVA) hydrogel was implemented as the electrolyte that allowed free diffusion of sweat to the electrode surface.[51] By such design, the wearable BSC can be continuously charged in open circuit mode, then generating stable high-power pulses on the order of seconds when discharged at a high current (**Figure 3.13 D-F**).

Screen printing, a low-cost and large-scale fabrication method, was used to manufacture the stretchable and conformal BSC device (**Figure 3.14**). The design of the device included an "island-bridge" configuration and was fabricated with customized strain-enduring inks. The "island-bridge" structure is designed to maximize the mechanical robustness of the device, where the functional electrodes are separated into several individual compartments as "islands" and are interconnected by highly stretchable conductive silver interconnections which act as the "bridges". Besides, a flexible, non-stretchable "skeleton" layer with high elastic modulus and mechanical strength is added below the "islands" as reinforcement to further minimize any strain applied to the electrodes.[62] As a result, the strain induced by external deformation can be effectively dispersed around the electrode "islands", and any adverse effects yielded from the deformation can be minimized. Adopted from our previous work, the CNTs and silver inks used in the printing of the stretchable electrodes were customized to obtain outstanding flexibility and stretchability.[66] The stretchability of the CNT ink is inherited from its elastic polyurethane (PU) binder, while the highly conductive and flexible silver ink is made of silver flakes and an elastomeric copolymer binder (polystyrene-block-polyisoprene-block-polystyrene; SIS)[50,66]. Working in conjunction, the elaborate "island-bridge" structure design and ink formulation endow the printed electrodes with electrical conductivity and stability during mechanical deformation.

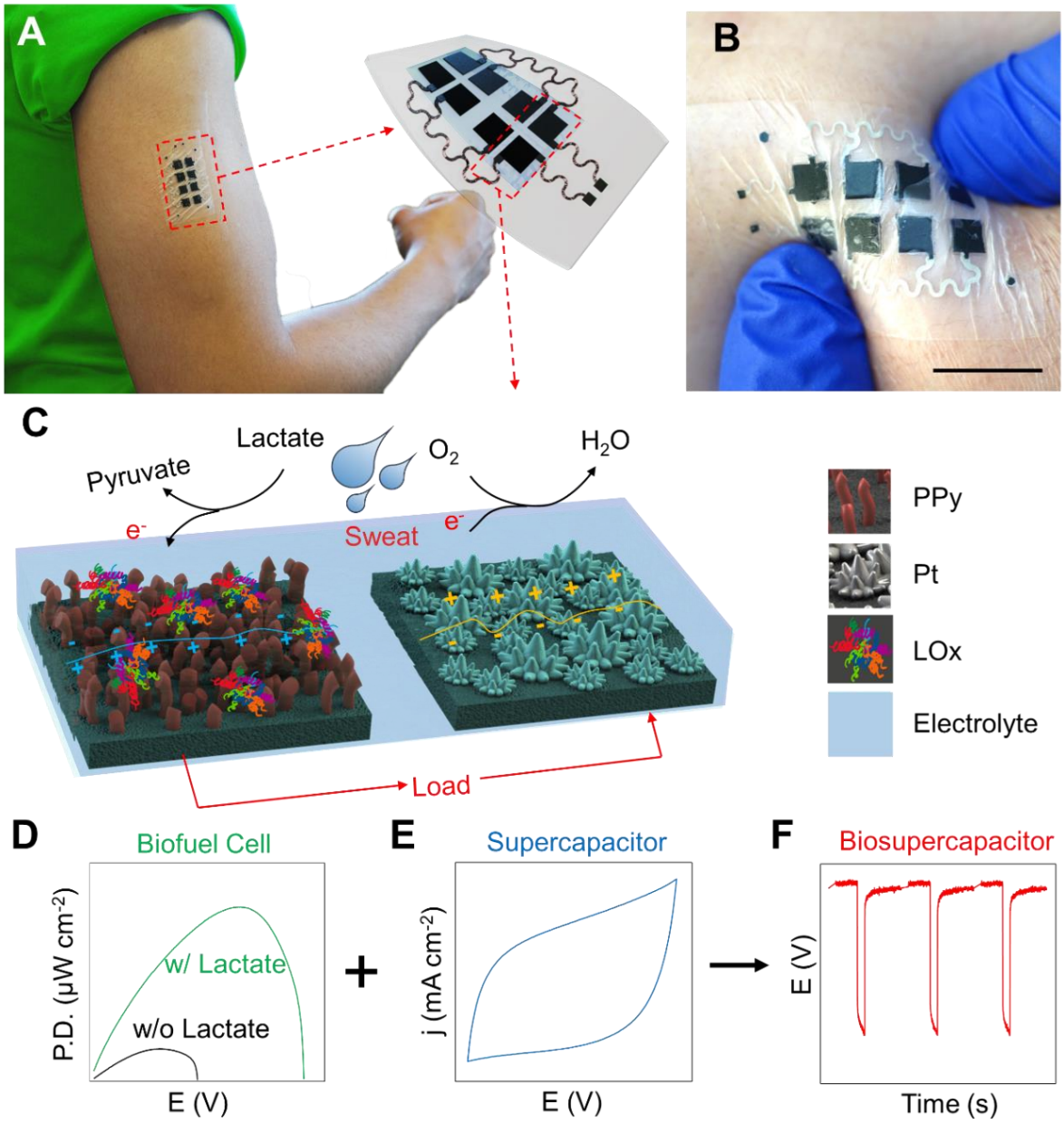

Figure 3.13. Schematic illustration of the epidermal BSC patch.
A. Schematic illustration of the skin-mountable wearable dual-functional (energy harvesting and energy storage) BSC device. **B**. Photograph of the stretchable dual-functional BSC device on human skin, scale bar: 2 cm. **C**. Schematics of the redox energy generation and capacitive energy storage from sweat lactate by the single dual-functional device. **D**.-**F**. The behavior of the BSC combining a BFC (left) and SC (center) to form a dual-functional self-charging BSC that supports high-power pulse discharge (right).

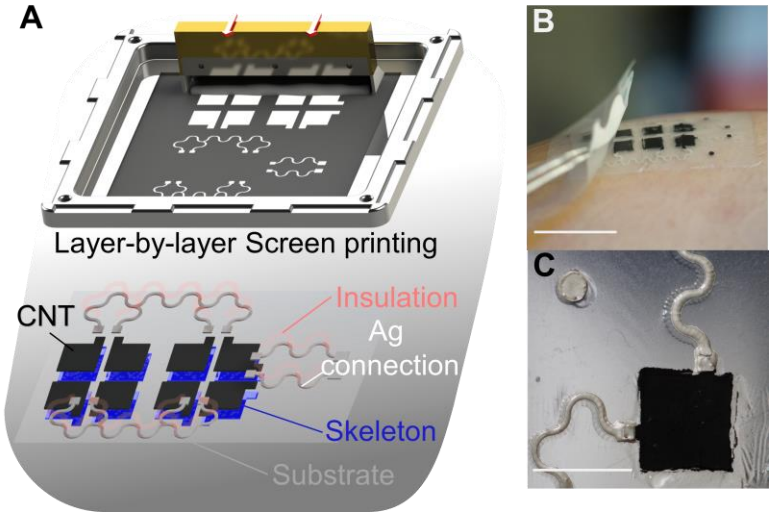

Figure 3.14. Fabrication of the island-bridge patch.
A. Schematic illustration of the printing process for stretchable biosupercapacitor device. **B**. The image about transferring the printed biosupercapacitor device on human skin. Scale bar: 2 cm. **C**. The image of one printed "island" electrode. Scale bar: 5 mm.

The morphology of the electrode surfaces was investigated by scanning electron microscopy (SEM). Compared with the unmodified CNT electrode (**Figure 3.15 A**), the modification of the anode and the cathode has visibly improved the porosity and tortuosity of electrodes (**Figure 3.15 B - C,** respectively). The apparent improvement in surface roughness is expected to contribute to enhancing the capacitive behavior of the modified BFC-based BSC. The deposited Pt and PPy were verified by the SEM imaging with energy-dispersive X-ray spectroscopy (EDS) in **Figure 3.16**. The cathode and anode were characterized by linear and cyclic voltammetry, demonstrated in **Figure 3.17** and **Figure 3.18**, supporting the essential role of porous Pt and LOx as catalysts for oxygen reduction and lactate oxidation, with a catalytic onset potential of E ≈ 0.33 V and -0.15 V vs. Ag/AgCl and improved the electrode's capacitance, respectively. The choice of the PPy, as a capacitive polymer, imparts a porous electrode morphology with

increased surface area and pseudocapacitance along with an overall stable positive charge in the range of 4-8 pH, which is within the range of the pH of human perspiration.[67] The protonation/deprotonation of nitrogen atoms of the polymer is a primary reason for pseudocapacitive behavior and the ability to store the charge. Evidently, on the bioanode, a deposited porous PPy film has allowed stable LOx immobilization on the carbonaceous electrode matrix and significantly improved the electrode's capacitance (by ~2 folds) (**Figure 3.19**).

The energy harvesting performance of the BFC, consisting of the LOx/NQ/PPy-based bioanode and the porous Pt-based cathode, was characterized. **Figure 3.15 D** shows the power density of BFC when discharged against variable resistances in the presence of different lactate levels. The data plots indicate a typical power curve behavior, showing an increase in open-circuit voltage (OCV) from E = 0.28 V to E = 0.55 V upon elevating the lactate concentration from 0 to 15 mM. The power values were also enhanced upon increasing the lactate level until reaching saturation at 10 mM lactate, with a maximal power density of 80 μW cm^{-2} at E = 0.38 V. Over the range of 0–5 mM lactate, the power increases linearly with the fuel concentration, demonstrating an increase of ~ 9 μW cm^{-2} mM^{-1}. A maximum OCV of E = 0.55 V and the closed-circuit current density of 460 μA cm−2 were reached at 10 mM lactate (Figure 2E). Furthermore, a long-term stability test of the BFC, shown in **Figure 3.15 F**, demonstrates a stable output with a small standard deviation of 6.4% during the 8 h study period, and effective output of around 100 μW cm−2 at 0.38 V. It should be noted that the OCV established by the cell exceeds the theoretical value of 0.48 V calculated based on electrochemical characterization of the LOx anode and Pt cathode (**Figure 3.17** and **Figure 3.18**). This effect is attributed to the presence of the redox-active PPy with a charge-storing pseudocapacitance.[68] As the charging of the BSC device increases

significantly at higher voltages, the OCV of 0.55 V, established within 2 h, was considered as a practical OCV value.

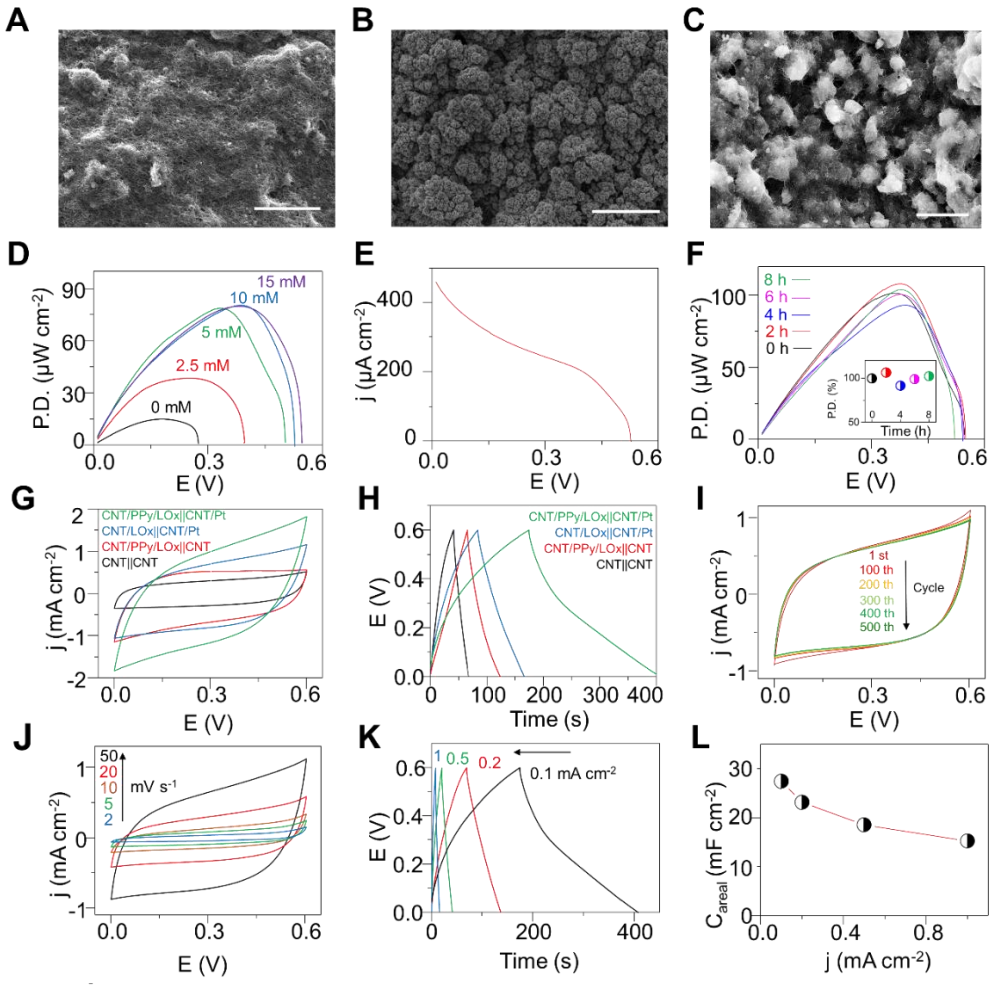

Figure 3.15. BSC Bioelectrocatalytic and capacitive behavior characterizations.
SEM images of A. printed pristine CNT electrode, B. CNT electrode with electrodeposited Pt as the cathode, and C. CNT electrode with electrodeposited PPy for the anode. Scale bar: A. and B. 10 μm; C. 5 μm. D. The power density versus voltage plots of the stretchable BSC using different lactate concentrations (0, 2.5, 5, 10, and 15 mM) in 0.5 M PBS (pH 7.4). E. Polarization curves of the BSC in the presence of 10 mM lactate. F. Long-term stability of the BSC in the presence of 10 mM lactate over 8 h. Inset: power density at 0.38 V over this period. (G-L) BSC capacitive behavior study. G. CV (scan rate: 100 mV s^{-1}) and H. galvanostatic charge-discharge curves (current density: 0.1 mA cm^{-1}) of the BSC in 2-electrode system with different levels of functionalization. (I) The stability of the BSC is tested with 500 CV cycles at the scan rate of 50 mV s^{-1} (J) CV curves of the fully functionalized BSC at different scan rates. (K) GCD curves of the BSC at different charge-discharge current densities (0.1, 0,2, 0.5, 1.0 mA cm^{-2}) and (L) the corresponding areal capacitance.

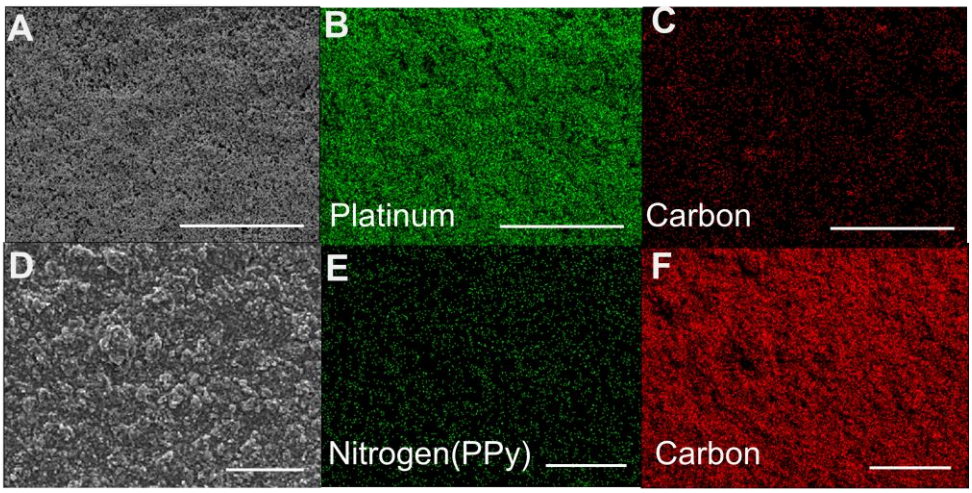

Figure 3.16. Electrode SEM-EDX characterization.
The EDX characterization of the cathode and anode electrode. (A, D) the SEM images of the cathode and anode, respectively. EDX of B. Pt and C. carbon distribution on the cathode, and E. nitrogen and F. carbon elements on the anode. Scale bar: 50 µm.

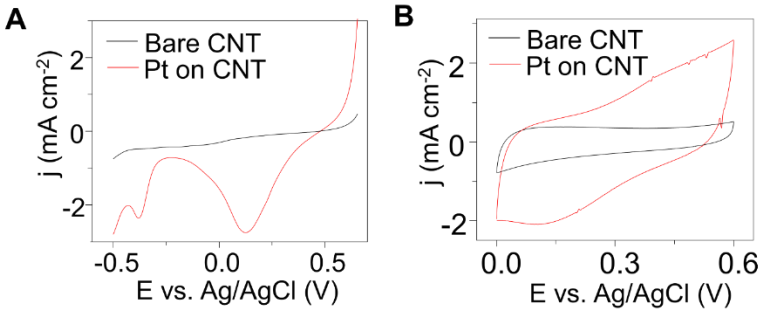

Figure 3.17. Cathode electrochemical characterization.
A. Linear sweep and **B**. Cyclic voltammograms of the bare CNT (black curves) and deposited Pt electrodes (red curves) in the 0.5 M PBS (pH = 7.4) buffer solution, associated with catalytic oxygen reduction (ORR). Scan rate: 10 mV s^{-1}.

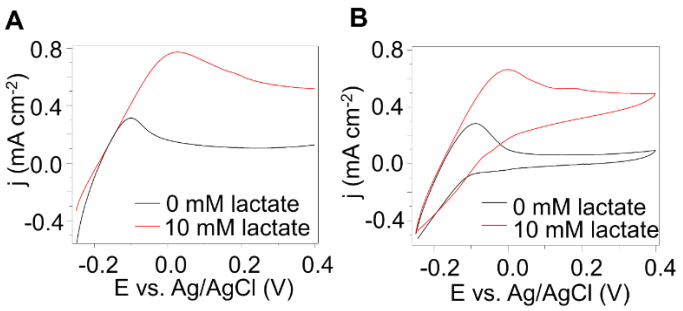

Figure 3.18. Anode electrochemical characterization.
A. Linear sweep and **B**. Cyclic voltammograms of the PPy-LOx-modified anode, associated with catalytic oxidation of lactate in the 0.5 M PBS (pH = 7.4) buffer solution. Scan rate: 10 mV s^{-1}.

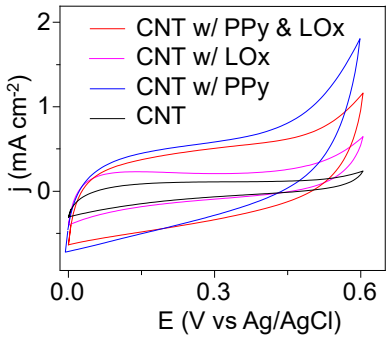

Figure 3.19. CV the anode after each layer of functionalization.
CV curves of bare CNT electrode, CNT electrode deposited with PPy, CNT electrode modified with LOx, and CNT electrode decorated with PPy and LOx enzyme. Scan rate: 10 mV s^{-1}.

The capacitance of the BSC can be maximized through several strategies. A CNT-based composite ink was chosen for its attractive active surface area, which greatly enhances the double-layer capacitance of the electrodes, based on our early studies.[50,69] PPy is electropolymerized onto the anode from a pyrrole-containing $KClO_4$ solution to endow higher capacitance to the bioanode. Pt is electroplated onto the cathode at E = -0.95 V vs. Ag/AgCl to facilitate oxygen-reduction reaction (ORR). Such deposition results in a cauliflower-like structured, high-surface-area Pt,

which further enhances the double-layer capacitance of the BSC. Cyclic voltammetry (CV), used for characterization, demonstrates the significant improvement in BSC capacitance after the PPy and Pt functionalization of the anodes and cathodes, respectively (**Figure 3.15 G**). LOx is thereafter drop-cast onto the anode and immobilized with chitosan. The effect of the capacitive behavior of the BSC was further validated via the galvanostatic charge-discharge (GCD) technique with different current densities. In **Figure 3.15 H**, GCD was conducted between 0 to 0.6 V, and the samples with and without PPy and Pt functionalization were tested at a discharge rate of 0.1 mA cm^{-2} to confirm the increase in capacitance of such treatments. Differences of a 2-fold, 3-fold, and a nearly 5-fold increase in capacitance were observed after the functionalization of Pt alone, PPy alone, and of both Pt and PPy, respectively. The immobilization of LOx leads to a slight decrease in capacitance, demonstrated via EIS and GCD method (**Figure 3.20** and **Figure 3.21**, respectively) due to partial insulation caused by the enzymatic protein shell and the use of chitosan, which reduces the active surface area and increases the interfacial charge transfer resistance of the electrode. Aiming to test the cyclability of the BSC, 500 CV cycles were performed at a scan rate of 50 mV s^{-1}. The results, displayed in **Figure 3.15 I**, indicate only a minor capacitance loss of 4% over time. **Figure 3.15 J** displays cyclic voltammograms of the BSC at scan rates of 5-50 mV s^{-1}. A rectangular-shaped response, with slight polarization, is observed, indicating the highly capacitive behavior associated with the high surface area and PPy functionalization. In addition, symmetrical charge-discharge behavior was observed across all the current densities used in GCD, **Figure 3.15 K**. The capacitance of the BSC decreases upon increasing the current density from 0.1 to 1.0 mA cm^{-2}, as shown in **Figure 3.15 L**. The obtained highest areal capacitance and areal power density of the BSC were calculated to be 27.2 mF cm^{-2} and 0.22 mW cm^{-2}, respectively (~2.4 F g^{-1} and ~20 mW g^{-1} for the sum of active electrode material weighed ~11 mg cm^{-2}), which

are considered very advantageous compared to reported BSC literature as shown in **Table 3.1**. To determine the self-discharge rate of the BSC, its electrical potential was continuously monitored in the absence of lactate, demonstrating the ability to maintain a voltage above 0.4 V for over 100 min after charging to 0.55 V (**Figure 3.22**).

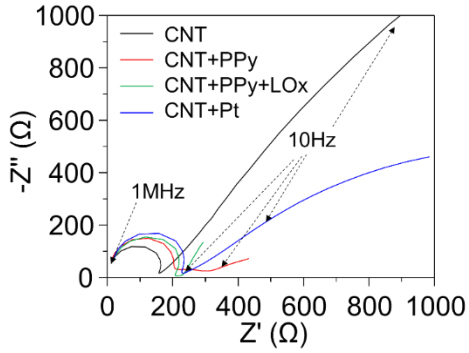

Figure 3.20. Anode EIS characterization.
EIS of the bare CNT electrodes, the CNT electrode functionalized with PPy, the CNT electrode functionalized with PPy and LOx, and the CNT electrode functionalized with Pt. Range: 1 MHz – 1 Hz; 10 pt per decade; amplitude: 10 μA.

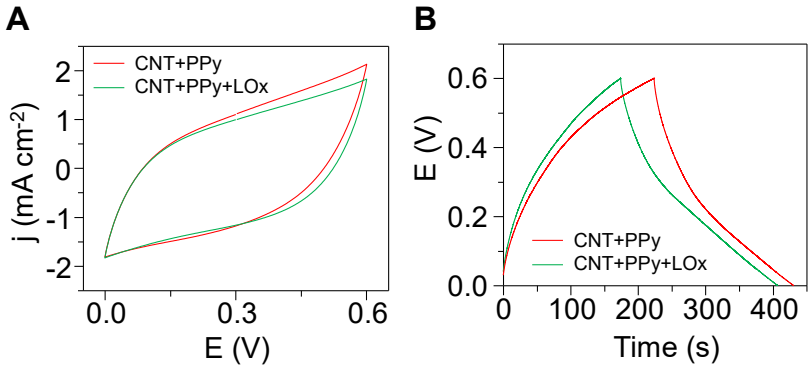

Figure 3.21. Capacitive performance of the BSC.
The **A**. CV and **B**. GCD curves of the biosupercapacitors in 0.5 M PBS before and after the LOx enzyme decoration. Scan rate: 100 mV s^{-1}.

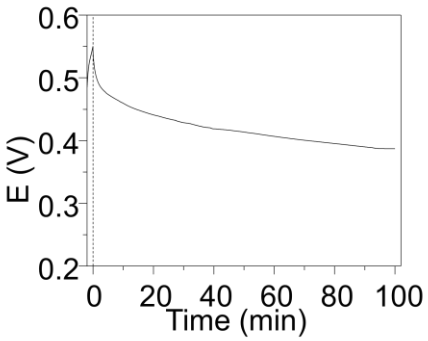

Figure 3.22. The self-discharge of the BSC in 0.5 M PBS without lactate after being charged to 0.55 V.

Table 3.1. Comparisons of different biosupercapacitors.

Platform	Anode	Cathode	Fuel	Conc. (mM)	Cap. density	Power Density	OCV (V)	Ref.
Printed Composite	LOx-PPy	Pt	Lactate	10	27.2 mF cm^{-2} 2.4 F g^{-1}	0.22 mW cm^{-2} 10 mW g^{-1}	0.55	This work
Graphite Foil	CtCDH	MvBOx	Glucose	50	10.6 - 13.1 mF cm^{-2}	7 µW cm^{-2}	0.56	[70]
Pressed CNT Pellet	GOx	Laccase	Glucose	200		3.80 mW g^{-1}	1	[71]
Pressed CNT Pellet	FDh-PPy	Lacc	Fructose	100	65 F g^{-1}	0.64 mW cm^{-2}	0.6	[72]
Film	GDh-Os	BOx-Os	$Os^{2+/3+}$	NA	147 mF cm^{-2}	3.9 mW g^{-1}	0.45	[73]
Transparent Flexible Sheet	CDH/GDH	Box	Glucose	0.05	3.5 mF cm^{-2}	30 µW cm^{-2}	0.6	[56]
Ag-Au Film	NPG/PEDOT/ $Os(bpy)_2PVI$/FAD-GDH	NPG/PEDOT /$Os(bpy)_2PVI$ /BOx	Glucose	20	1.148 mF cm^{-2}	608.8 uW cm^{-2}	0.45	[74]

The ability of the dual-functional BSC to deliver high-power pulses was evaluated using current-pulse chronopotentiometry (CP). The BSC was discharged at 1 mA cm^{-2} for 10 ms and left to recharge for 1 min in the absence and presence of 10 mM lactate. The results shown in **Figure 3.23 A** indicate that in the absence of fuel, the OCV of the BSC is only 0.16 V, and a small power density of 0.13 mW cm^{-2} is delivered. In contrast, in the presence of 10 mM lactate, the OCV and pulse power increase to 0.55 V and 0.5 mW cm^{-2}, respectively, indicating the indispensable role of lactate for self-charging BSC.

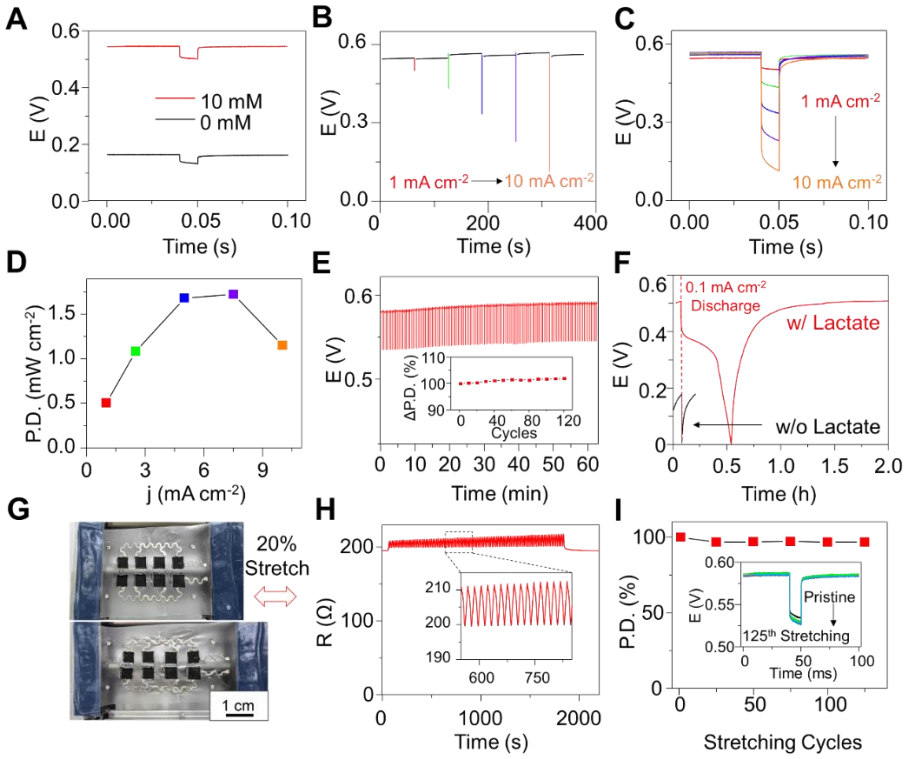

Figure 3.23. BSC self-charge and pulsed discharge behavior characterizations.
A. Potential profile of BSC discharge at 1 mA cm^{-2} current pulse in 0 mM and 10 mM lactate. B. Potential profile of BSC discharge at 1, 2.5, 5, 7.5, and 10 mA cm^{-2} over 10 ms C. Overlay of the BSC potential peak profile and D. the calculated power density at different discharge current densities. E. The stability of potential profile of BSC discharge at 1 mA cm^{-2} during 1 h with a 30 s resting time. F. The discharge-self-charge curve of BSC without and without the presence of 10 mM lactate. G. Image of the wearable BSC under 20% stretching. scale bar: 1 cm. H. Resistance profile during stretching, (inset) zoom of resistance fluctuations. (I) The stability of the power density profile of BSC discharge at 1 mA cm^{-2} for 125 stretching cycles and (inset) discharge self-charging curves.

The performance of the hybrid device was evaluated by applying different current density 10 ms-pulses, ranging from 1 to 10 mA cm^{-2}. As shown in **Figure 3.23 B**, after applying the short current pulses, the BSC can deliver power using the charges stored in the device and then quickly recover to its initial potential value due to the continuous biocatalytic conversion of lactate and O_2 in the biofuel system. The overlay of the potential drop peak is displayed in **Figure 3.23 C**, where a fast ohmic drop and a subsequent slower voltage drop due to capacitance discharge can be observed. These results demonstrate the ability of BSC to withstand a high current density discharge, reaching up to 10 mA cm^{-2}. The plot of the calculated power density versus discharge current density, shown in **Figure 3.23 D**, indicates a maximum power density of 1.7 mW cm^{-2} at 7.5 mA $cm^{-}2$. The detailed method of power density calculation is presented in **Figure 3.24**. These values are 20 times higher than the power delivered by BFC in continuous discharge mode. Such a high power density indicates the great potential of the BSC to power medical devices, such as insulin pumps or wearable electronic devices, e.g., wireless transmitters.[75]

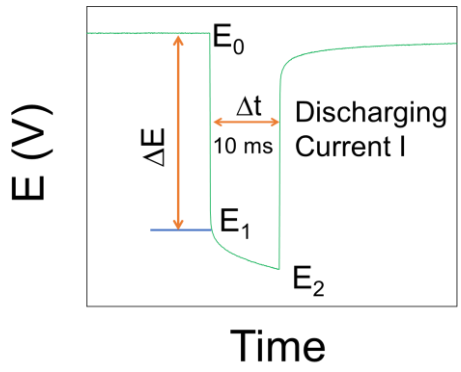

Figure 3.24. Illustration for the power calculation.
The instantaneous power during the on-body test was calculated using the potential E_2 at the end of the 10 ms pulse multiplied by the discharge current of the pulse. In this illustration, E_0 represents the open-circuit potential of the cell, and E_1 represents the potential after the ohmic drop ΔE.

To evaluate the long-time operational stability of the device, a 10 ms 1 mA cm^{-2} current pulse was applied every 30 s for 1 h; the potential evolution is presented in **Figure 3.23 E**. The BSC can maintain a stable voltage drop and quickly recovers to its initial voltage after each current pulse over the long-time operation. The calculated relative pulse power density is shown in the inset of **Figure 3.23 E**, where no significant performance decrease is observed over 120 cycles. Extended pulsed discharge over 12 h is demonstrated in **Figure 3.25**, which shows only minor fluctuations in power and capacitance among thousands of cycles. The performance of the BSC was also evaluated by applying a constant discharge current (0.1 mA cm^{-2}), as shown in **Figure 3.23 F**. Without lactate, the device cannot sustain the discharge and was not able to recharge to OCV above 0.3 V, whereas in the presence of lactate, the BSC can sustain constant discharge for ca. 30 min and can be self-charged to the original voltage, dictated by the fuel concentration. It is worth noting that in contrast to the results demonstrated in **Figure 3.15 K**, the addition of the 10 mM lactate was able to significantly extend the discharge time due to the bioelectrocatalytic reactions that simultaneously charge the BSC.

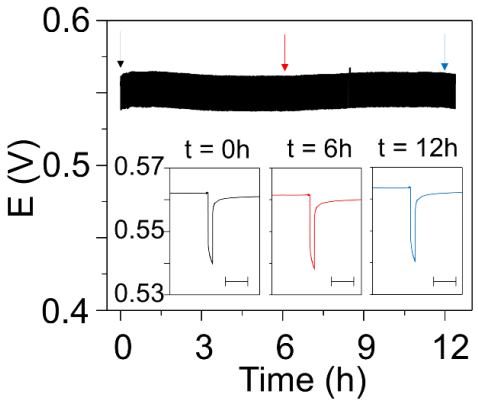

Figure 3.25. Extended in-vitro pulsed discharge of the BSC with 10 mM lactate in PVA hydrogel over 12 h.
Pulse: 1 mA cm^{-2}, 10 ms, 1 pulse every 30 s, 1440 discharge pulses in total. Inset: The pulse waveform at 0 h, 6 h, and 12 h. Inset scale bar: 100 ms.

To highlight the flexibility and stretchability of this wearable self-charging BSC, its mechanical resiliency towards external strain was tested by implementing resistance and CP tests on the SCs before and after stretching. The resistance measurement during continuous stretching is demonstrated in **Figure 3.23 G**. The resistance profile during measuring is shown in **Figure 3.23 H**, where the resistance is fluctuating around 205 Ω with a 5% deviation that corresponds to the continuous deformation of the electrode during measurement to adjust to the external strain. The exceptional mechanical stability allows the resistance to recover to its original value after numerous mechanical deformations. The electrochemical behavior of the anodes and cathodes was measured before and after 100 cycles of 180° bending (3 mm diameter, inward and outward) and 20% stretching (along lengthwise) via CV (**Figure 3.26**), while monitoring their morphological changes via SEM (**Figure 3.27**). The results indicate minimal mechanical damage and changes in performance. **Figure 3.23 I** shows the stability of the potential profile of BSC discharged at 1 mA cm^{-2} for 125 stretching cycles. A 10 ms current pulse was applied after every 25 cycles. The power was maintained at over 96% of the maximal value after 125 cycles of 20% stretching. The results demonstrate the robustness of the hybrid device, confirming its potential as a power source for on-body applications.

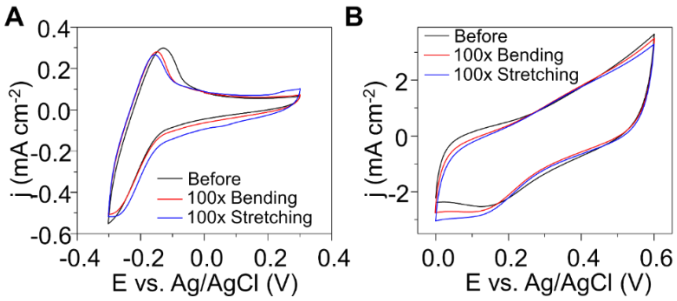

Figure 3.26. CV of the electrodes after mechanical deformations.
The CV of the **A**. anode and **B**. cathode in 0.5 M PBS before and after 100 cycles of inward and outward bending (3 mm diameter) and 100 cycles of 20% stretching lengthwise.

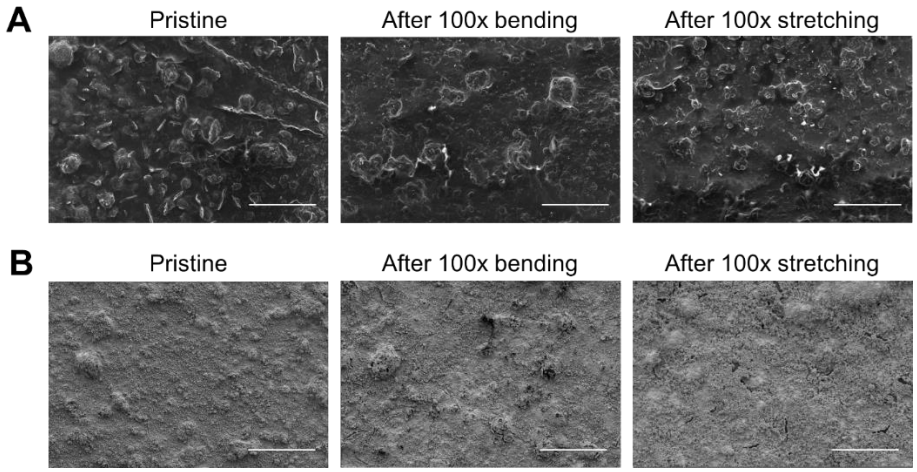

Figure 3.27. SEM of electrodes after mechanical deformations.
SEM images of the **A**. anode and **B**. cathode before and after 100 cycles of inward and outward bending (3 mm diameter) and 100 cycles of 20% stretching lengthwise. Scale bar: 100 μm.

To demonstrate the wearable BSC in real-life scenarios, the printed device was mounted on the arm of a volunteer during the stationary cycling exercise (**Figure 3.29 A**). The whole process consists of three periods: mounting the BSC and start cycling A., stop cycling B., and removing the wearable BSC from the arm of the volunteer C. Three pulses with the 1 mA cm^{-2} current were performed every 5 min, and the voltage of the device was recorded (**Figure 3.29 B**). The OCV of the BSC was around 0.17 V before the sweating and reached 0.48 V after 60 min of cycling. The OCV dropped to around 0.46 V when the volunteer stopped cycling. After 25 min of resting, the printed BSC was removed from the volunteer's arm. The OCV was observed to rapidly regenerate to 0.48 V due to exposure of the device to additional oxygen, enhancing the reduction reaction on the Pt cathode. Even after removing the BSC from the volunteer's arm for 230 min, the OCV of the BSC was still retained at 0.38 V. The pulse output operated at 1 mA cm^{-2} current for 10 ms during these different periods is shown in **Figure 3.29 C**. The power density of the wearable BSC increased from 151 μW cm^{-2} (Point 1) to 343 μW cm^{-2} (Point 2), then decreased to

208 μW cm^{-2} when the volunteer stopped exercising (Point 3) and decreased gradually upon removing the BSC from the skin (Point 4). The power density of the pulses in the whole testing process is shown in **Figure 3.28**, demonstrating that the power of the device peaks with the exercise and drops steadily to ~150 μW cm^{-2} after the exercise stopped. Such performance persisted even after the patch was removed from the body, as the residual stored energy continued to be discharged for another 4 h.

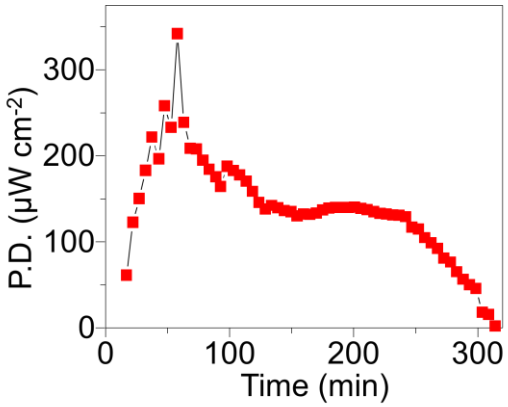

Figure 3.28. The power density of the pulse during an on-body test.

The capability of the BSC to empower commercial electronics is demonstrated in **Figure 3.29 D-i** using a simple assembled circuit. Two BSC patches are thus connected in parallel, and the output voltage is boosted via a DC-DC voltage booster. The photo image of a flexible DC-DC voltage booster with laser-cut copper wiring is shown in **Figure 3.30**. The output signal from the booster was connected to an LED and was controlled by a switch. To visualize the operation of BSCs and simulation an operation duty cycle of 10%, they were connected to the LED, activating the illumination during a 1 s discharge pulse, followed by a 9 s self-recharge (**Figure 3.29 D-ii**).

The discharge and self-charge current and voltage profiles are illustrated in **Figure 3.29 D-iii**; a small current drop is observed during the 1s discharge. Near the turn-on voltage of ca. 1.6 V for the LED, the presence of the lactate allows high current discharge, illuminating the LED in bursts, whereas the absence of lactate cannot provide enough current to surpass the turn-on voltage of the LED. A larger current drop is observed in the 5-min extended discharge, as shown in **Figure 3.31**. The advantage that the pulsed discharge of the BSC exhibits in such use case involves a high-power pulsed discharge that can sustain the short-term power draw and quickly recovers, whereas the current drops exponentially after the extended discharge, which takes a longer period to recover afterward.

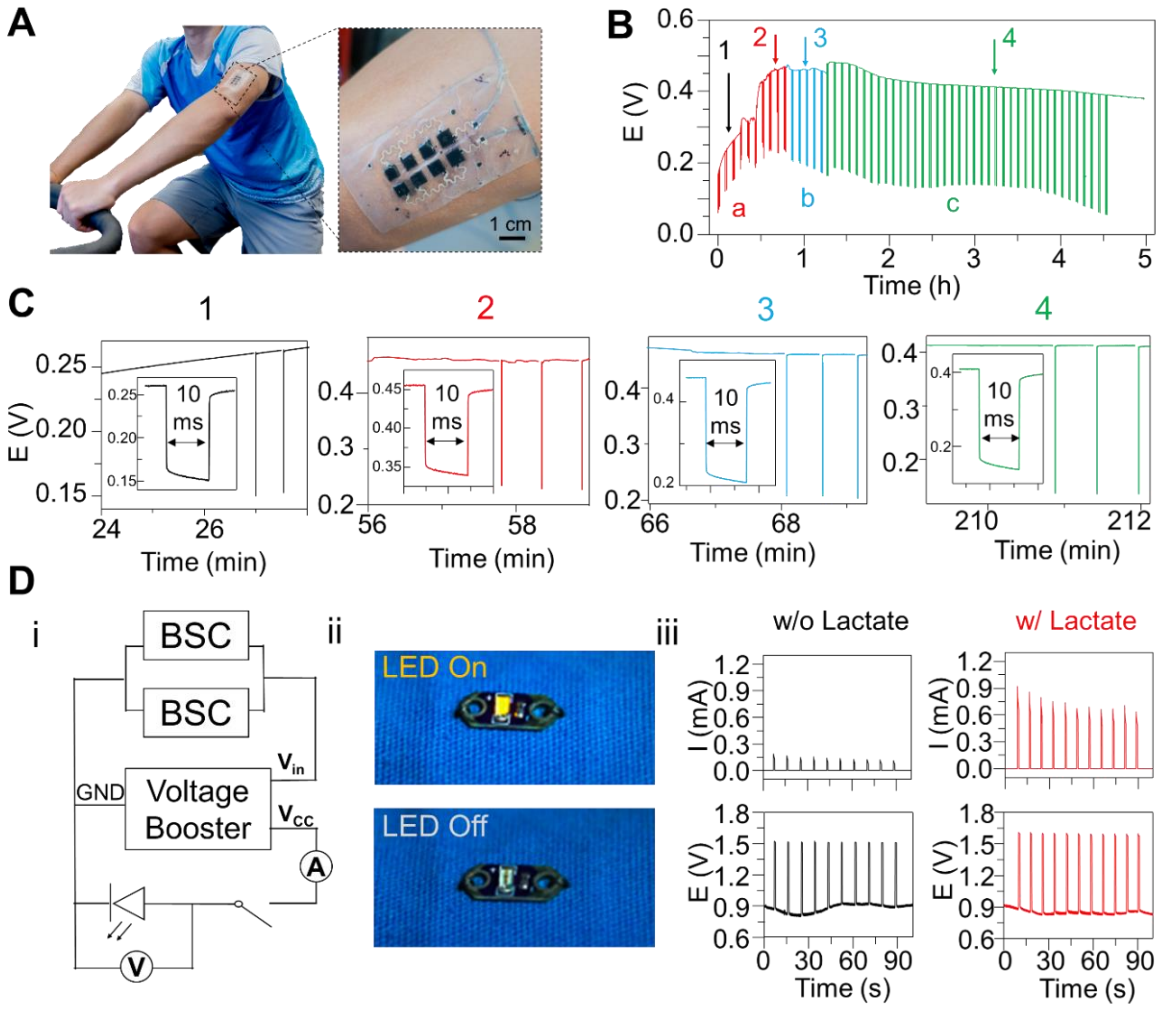

Figure 3.29. BSC On-body behavior.
A. The printed wearable BSC was mounted on the arm of a subject. **B**. The voltage monitoring of the wearable BSC: a. during the on-body constant cycling exercise, b. after cycling exercise, and c. unloading the BSC from the skin. **C**. The pulse outputs of the wearable BSC (1) during cycling exercise, (2) when the voltage output reaches a stable state, (3) after removing from the body, and (4) after removing the wearable BSC from the skin for 2 h. **D**. (i) Circuit schematics demonstrate using two BSC patches to power an LED via a voltage booster. (ii) Photograph of the illuminated LED during and after the pulsed discharge. (iii) The pulsed discharge profile of the BSCs in the absence and presence of 10 mM lactate.

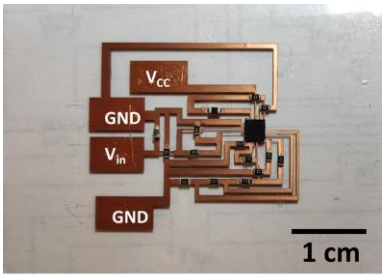

Figure 3.30. The photo image of the flexible voltage booster circuit.

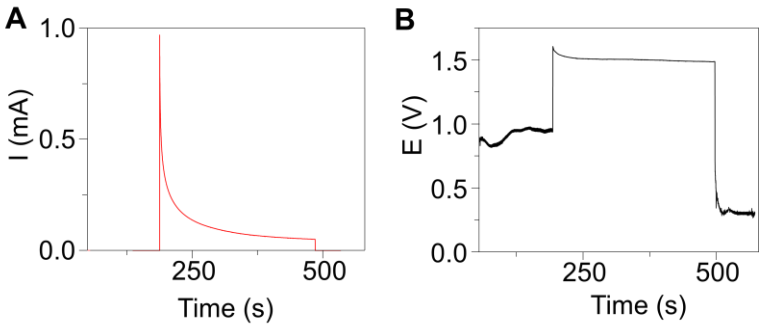

Figure 3.31. Extended discharge of the BSC.
A. current and **B**. voltage output from the voltage booster during 5 minutes of extended discharge with 15mM lactate.

3.2.4 Conclusion

In this chapter, we demonstrated the first example of an all-printed, stretchable dual-functional BSC for harvesting and storing energy from metabolic sweat lactate. This hybrid device can rapidly self-charge from autonomous lactate/O_2 redox reactions and deliver high-power pulses due to its simultaneous function as both a BFC and an SC. A scalable and low-cost screen-printing technique has been used to fabricate the wearable device, merging these BFC and SC functions on a single footprint. The device was fabricated on top of low-elastic modulus adhesive elastic films for maintaining intimate contact with human skin during rigorous exercises. The design of the "island-bridge" structure relies on a rigid backbone layer that restrains electrode deformation and

stretchable, serpentine-shaped silver interconnection for a controlled strain distribution across the device. Compared to the common lactate BFC, the enhanced capacitance of the BSC is endowed to the synergistic effect of the CNT ink with the electrodeposited PPy conductive polymer on the anode and the high-surface-area porous Pt on the cathode. The resulting wearable bifunctional BSC supports high-power pulsed output while maintaining stable cycling performance in human sweat-level lactate. High power of 0.3 mW cm^{-2} was achieved when the self-chargeable hybrid device is mounted on the arm of a human subject. When paired with voltage regulation components, commercial electronics - such as LEDs - can be successfully illuminated in pulsed mode by designed BSC, suggesting its considerable potential as a power source for wearable electronics. As a wearable device with enzymatic electrodes, its stability may be affected by environmental factors, such as temperature, pH, salt ions, or surfactants, which will be assessed in the future. Future efforts will further optimize the operational conditions, cell performance, and electronics integration for advancing the capabilities and applications of this novel dual-functional self-charging device.

Chapter 3, in part, is a reprint of the material as it appears in Advanced Functional Materials, 2019, by Xiaohong Chen, Lu Yin, Jian Lv, Andrew J Gross, Minh Le, Nathaniel Georg Gutierrez, Yang Li, Itthipon Jeerapan, Fabien Giroud, Anastasiia Berezovska, Rachel K O'Reilly, Sheng Xu, Serge Cosnier, and Joseph Wang. The dissertation author, Xiaohong Chen, and Jian Lv were the primary investigators and co-authors of this paper. In part, is the material as it appears in Advanced Functional Materials, 2021, by Jian Lv, Lu Yin, Xiaohong Chen, Itthipon Jeerapan, Cristian A Silva, Yang Li, Minh Le, Zhihua Lin, Luwen Wang, Alexander Trifonov, Sheng Xu, Serge Cosnier, and Joseph Wang. The dissertation author, Jian Lv, Xiaohong Chen, and Itthipon Jeerapan were the primary investigators and co-authors of this paper.

3.3 References

1. Bandodkar, A. J., Jeerapan, I. & Wang, J. Wearable Chemical Sensors: Present Challenges and Future Prospects. *ACS Sensors* **1**, 464–482 (2016).

2. Kim, J. *et al.* Wearable Bioelectronics: Enzyme-Based Body-Worn Electronic Devices. *Acc. Chem. Res.* **51**, 2820–2828 (2018).

3. Banerjee, J. *et al.* Improvement of Human Keratinocyte Migration by a Redox Active Bioelectric Dressing. *PLoS ONE* **9**, e89239 (2014).

4. Bandodkar, A. J. & Wang, J. Wearable Biofuel Cells: A Review. *Electroanalysis* **28**, 1188–1200 (2016).

5. Rasmussen, M., Abdellaoui, S. & Minteer, S. D. Enzymatic biofuel cells: 30 years of critical advancements. *Biosensors and Bioelectronics* **76**, 91–102 (2016).

6. Koushanpour, A., Gamella, M. & Katz, E. A Biofuel Cell Based on Biocatalytic Reactions of Lactate on Both Anode and Cathode Electrodes – Extracting Electrical Power from Human Sweat. *Electroanalysis* **29**, 1602–1611 (2017).

7. Bandodkar, A. J. *et al.* Soft, stretchable, high power density electronic skin-based biofuel cells for scavenging energy from human sweat. *Energy & Environmental Science* **10**, 1581–1589 (2017).

8. Lv, J. *et al.* Sweat-based wearable energy harvesting-storage hybrid textile devices. *Energy Environ. Sci.* **11**, 3431–3442 (2018).

9. Gooding, J. J. Nanostructuring electrodes with carbon nanotubes: A review on electrochemistry and applications for sensing. *Electrochimica Acta* **50**, 3049–3060 (2005).

10. Bandodkar, A. J., Jeerapan, I., You, J.-M., Nuñez-Flores, R. & Wang, J. Highly Stretchable Fully-Printed CNT-Based Electrochemical Sensors and Biofuel Cells: Combining Intrinsic and Design-Induced Stretchability. *Nano Letters* **16**, 721–727 (2016).

11. Agnès, C. *et al.* Supercapacitor/biofuel cell hybrids based on wired enzymes on carbon nanotube matrices: autonomous reloading after high power pulses in neutral buffered glucose solutions. *Energy & Environmental Science* **7**, 1884 (2014).

12. Hussein, L., Urban, G. & Krüger, M. Fabrication and characterization of buckypaper-based nanostructured electrodes as a novel material for biofuel cell applications. *Physical Chemistry Chemical Physics* **13**, 5831 (2011).

13. Gross, Andrew. J. *et al.* A High Power Buckypaper Biofuel Cell: Exploiting 1,10-Phenanthroline-5,6-dione with FAD-Dependent Dehydrogenase for Catalytically-Powerful Glucose Oxidation. *ACS Catal.* 4408–4416 (2017) doi:10.1021/acscatal.7b00738.

14. Kwon, C. H. *et al.* High-power biofuel cell textiles from woven biscrolled carbon nanotube yarns. *Nature Communications* **5**, (2014).

15. Gross, A. J., Holzinger, M. & Cosnier, S. Buckypaper bioelectrodes: Emerging materials for implantable and wearable biofuel cells. *Energy Environ. Sci.* (2018) doi:10.1039/C8EE00330K.

16. Reid, R. C., Minteer, S. D. & Gale, B. K. Contact lens biofuel cell tested in a synthetic tear solution. *Biosensors and Bioelectronics* **68**, 142–148 (2015).

17. Yu, Y., Zhai, J., Xia, Y. & Dong, S. Single wearable sensing energy device based on photoelectric biofuel cells for simultaneous analysis of perspiration and illuminance. *Nanoscale* **9**, 11846–11850 (2017).

18. Chen, X., Gross, A. J., Giroud, F., Holzinger, M. & Cosnier, S. Comparison of Commercial and Lab-made MWCNT Buckypaper: Physicochemical Properties and Bioelectrocatalytic O2 Reduction. *Electroanalysis* **30**, 1511–1520 (2018).

19. Gross, A. J. *et al.* Robust bifunctional buckypapers from carbon nanotubes and polynorbornene copolymers for flexible engineering of enzymatic bioelectrodes. *Carbon* **107**, 542–547 (2016).

20. Fritea, L. *et al.* A bifunctional triblock polynorbornene/carbon nanotube buckypaper bioelectrode for low-potential/high-current thionine-mediated glucose oxidation by FAD-GDH. *J. Mater. Chem. A* (2019) doi:10.1039/C8TA10644D.

21. Yin, L. *et al.* Highly Stable Battery Pack via Insulated, Reinforced, Buckling-Enabled Interconnect Array. *Small* **14**, 1800938 (2018).

22. Cosnier, S., Haddad, R., Moatsou, D. & O'Reilly, R. K. Biofunctionalizable flexible bucky paper by combination of multi-walled carbon nanotubes and polynorbornene-pyrene – Application to the bioelectrocatalytic reduction of oxygen. *Carbon* **93**, 713–718 (2015).

23. Lalaoui, N., Le Goff, A., Holzinger, M. & Cosnier, S. Fully Oriented Bilirubin Oxidase on Porphyrin-Functionalized Carbon Nanotube Electrodes for Electrocatalytic Oxygen Reduction. *Chemistry - A European Journal* **21**, 16868–16873 (2015).

24. Harvey, C. J., LeBouf, R. F. & Stefaniak, A. B. Formulation and stability of a novel artificial human sweat under conditions of storage and use. *Toxicology in Vitro* **24**, 1790–1796 (2010).

25. Pankratov, D., Falkman, P., Blum, Z. & Shleev, S. A hybrid electric power device for simultaneous generation and storage of electric energy. *Energy Environ. Sci.* **7**, 989–993 (2014).

26. Pankratov, D., Blum, Z., Suyatin, D. B., Popov, V. O. & Shleev, S. Self-Charging Electrochemical Biocapacitor. *ChemElectroChem* **1**, 343–346 (2014).

27. Pankratov, D. *et al.* A Nernstian Biosupercapacitor. *Angewandte Chemie International Edition* **55**, 15434–15438 (2016).

28. Gong, S. & Cheng, W. Toward Soft Skin-Like Wearable and Implantable Energy Devices. *Advanced Energy Materials* **7**, 1700648 (2017).

29. Jia, W., Valdés-Ramírez, G., Bandodkar, A. J., Windmiller, J. R. & Wang, J. Epidermal Biofuel Cells: Energy Harvesting from Human Perspiration. *Angewandte Chemie International Edition* **52**, 7233–7236 (2013).

30. Wang, J., Lin, M.-F., Park, S. & Lee, P. S. Deformable conductors for human–machine interface. *Materials Today* **21**, 508–526 (2018).

31. Yin, L., Lv, J. & Wang, J. Structural Innovations in Printed, Flexible, and Stretchable Electronics. *Advanced Materials Technologies* **5**, 2000694 (2020).

32. Kim, J. *et al.* Wearable Bioelectronics: Enzyme-Based Body-Worn Electronic Devices. *Accounts of Chemical Research* **51**, 2820–2828 (2018).

33. Wang, C. *et al.* Monitoring of the central blood pressure waveform via a conformal ultrasonic device. *Nature Biomedical Engineering* **2**, 687–695 (2018).

34. Yan, C. *et al.* Highly Stretchable Piezoresistive Graphene–Nanocellulose Nanopaper for Strain Sensors. *Advanced Materials* **26**, 2022–2027 (2014).

35. Sempionatto, J. R. *et al.* An epidermal patch for the simultaneous monitoring of haemodynamic and metabolic biomarkers. *Nature Biomedical Engineering* 1–12 (2021) doi:10.1038/s41551-021-00685-1.

36. Kim, D.-H. *et al.* Epidermal Electronics. *Science* **333**, 838–843 (2011).

37. Sekitani, T. *et al.* Stretchable active-matrix organic light-emitting diode display using printable elastic conductors. *Nature Materials* **8**, 494–499 (2009).

38. Gao, W. *et al.* Fully integrated wearable sensor arrays for multiplexed in situ perspiration analysis. *Nature* **529**, 509–514 (2016).

39. Gong, S. & Cheng, W. Toward Soft Skin-Like Wearable and Implantable Energy Devices. *Advanced Energy Materials* **7**, 1700648 (2017).

40. Pu, X., Hu, W. & Wang, Z. L. Toward Wearable Self-Charging Power Systems: The Integration of Energy-Harvesting and Storage Devices. *Small* **14**, 1702817 (2018).

41. Gong, X., Yang, Q., Zhi, C. & Lee, P. S. Stretchable Energy Storage Devices: From Materials and Structural Design to Device Assembly. *Advanced Energy Materials* **11**, 2003308 (2021).

42. Yin, L. *et al.* High Performance Printed AgO-Zn Rechargeable Battery for Flexible Electronics. *Joule* **5**, 228–248 (2021).

43. Bandodkar, A. J. & Wang, J. Wearable Biofuel Cells: A Review. *Electroanalysis* **28**, 1188–1200 (2016).

44. Ma, L. *et al.* A Usage Scenario Independent "Air Chargeable" Flexible Zinc Ion Energy Storage Device. *Advanced Energy Materials* **9**, 1900509 (2019).

45. Bandodkar, A. J. *et al.* Soft, stretchable, high power density electronic skin-based biofuel cells for scavenging energy from human sweat. *Energy & Environmental Science* **10**, 1581–1589 (2017).

46. Jeerapan, I., Sempionatto, J. R., Pavinatto, A., You, J.-M. & Wang, J. Stretchable biofuel cells as wearable textile-based self-powered sensors. *Journal of Materials Chemistry A* **4**, 18342–18353 (2016).

47. Bandodkar, A. J. Review—Wearable Biofuel Cells: Past, Present and Future. *J. Electrochem. Soc.* **164**, H3007 (2016).

48. Yin, S., Liu, X., Kaji, T., Nishina, Y. & Miyake, T. Fiber-crafted biofuel cell bracelet for wearable electronics. *Biosensors and Bioelectronics* **179**, 113107 (2021).

49. Chen, X. *et al.* Stretchable and Flexible Buckypaper-Based Lactate Biofuel Cell for Wearable Electronics. *Advanced Functional Materials* **29**, 1905785 (2019).

50. Lv, J. *et al.* Sweat-based wearable energy harvesting-storage hybrid textile devices. *Energy & Environmental Science* **11**, 3431–3442 (2018).

51. Yin, L. *et al.* A self-sustainable wearable multi-modular E-textile bioenergy microgrid system. *Nature Communications* **12**, 1542 (2021).

52. Zuo, W. *et al.* Battery-Supercapacitor Hybrid Devices: Recent Progress and Future Prospects. *Advanced Science* **4**, 1600539 (2017).

53. Chen, H. C. *et al.* Synthesis of amorphous nickel–cobalt–manganese hydroxides for supercapacitor-battery hybrid energy storage system. *Energy Storage Materials* **17**, 194–203 (2019).

54. Pankratov, D., Falkman, P., Blum, Z. & Shleev, S. A hybrid electric power device for simultaneous generation and storage of electric energy. *Energy & Environmental Science* **7**, 989 (2014).

55. Bollella, P. *et al.* Highly sensitive and stable fructose self-powered biosensor based on a self-charging biosupercapacitor. *Biosensors and Bioelectronics* **176**, 112909 (2021).

56. Bobrowski, T. *et al.* Rechargeable, flexible and mediator-free biosupercapacitor based on transparent ITO nanoparticle modified electrodes acting in µM glucose containing buffers. *Biosensors and Bioelectronics* **101**, 84–89 (2018).

57. Jang, Y. *et al.* Implantable biosupercapacitor inspired by the cellular redox system. *Angewandte Chemie International Edition* **60**, 10563–10567 (2021).

58. Shleev, S., González-Arribas, E. & Falk, M. Biosupercapacitors. *Current Opinion in Electrochemistry* **5**, 226–233 (2017).

59. Knoche, K. L., Hickey, D. P., Milton, R. D., Curchoe, C. L. & Minteer, S. D. Hybrid Glucose/O $_2$ Biobattery and Supercapacitor Utilizing a Pseudocapacitive Dimethylferrocene Redox Polymer at the Bioanode. *ACS Energy Letters* **1**, 380–385 (2016).

60. Pankratov, D., Blum, Z., Suyatin, D. B., Popov, V. O. & Shleev, S. Self-Charging Electrochemical Biocapacitor. *ChemElectroChem* **1**, 343–346 (2014).

61. Zhu, M. *et al.* A Highly Durable, Transferable, and Substrate-Versatile High-Performance All-Polymer Micro-Supercapacitor with Plug-and-Play Function. *Advanced Materials* **29**, 1605137 (2017).

62. Yin, L. *et al.* Highly Stable Battery Pack via Insulated, Reinforced, Buckling-Enabled Interconnect Array. *Small* **14**, 1800938 (2018).

63. Fakhry, A., Cachet, H. & Debiemme-Chouvy, C. Mechanism of formation of templateless electrogenerated polypyrrole nanostructures. *Electrochimica Acta* **179**, 297–303 (2015).

64. Wannapob, R., Vagin, M. Yu., Jeerapan, I. & Mak, W. C. Pure Nanoscale Morphology Effect Enhancing the Energy Storage Characteristics of Processable Hierarchical Polypyrrole. *Langmuir* **31**, 11904–11913 (2015).

65. Vagin, M. Yu. *et al.* Water-processable polypyrrole microparticle modules for direct fabrication of hierarchical structured electrochemical interfaces. *Electrochimica Acta* **190**, 495–503 (2016).

66. Yin, L. *et al.* From All-Printed 2D Patterns to Free-Standing 3D Structures: Controlled Buckling and Selective Bonding. *Advanced Materials Technologies* **3**, 1800013 (2018).

67. Zhang, X. & Bai. Surface Electric Properties of Polypyrrole in Aqueous Solutions. *Langmuir* **19**, 10703–10709 (2003).

68. Conzuelo, F., Marković, N., Ruff, A. & Schuhmann, W. The Open Circuit Voltage in Biofuel Cells: Nernstian Shift in Pseudocapacitive Electrodes. *Angewandte Chemie International Edition* **57**, 13681–13685 (2018).

69. Bandodkar, A. J., Jeerapan, I., You, J.-M., Nuñez-Flores, R. & Wang, J. Highly Stretchable Fully-Printed CNT-Based Electrochemical Sensors and Biofuel Cells: Combining Intrinsic and Design-Induced Stretchability. *Nano Lett.* **16**, 721–727 (2016).

70. Pankratov, D., Blum, Z., Suyatin, D. B., Popov, V. O. & Shleev, S. Self-Charging Electrochemical Biocapacitor. *ChemElectroChem* **1**, 343–346 (2014).

71. Agnès, C. *et al.* Supercapacitor/biofuel cell hybrids based on wired enzymes on carbon nanotube matrices: autonomous reloading after high power pulses in neutral buffered glucose solutions. *Energy Environ. Sci.* **7**, 1884–1888 (2014).

72. Kizling, M. *et al.* Biosupercapacitors for powering oxygen sensing devices. *Bioelectrochemistry* **106**, 34–40 (2015).

73. Pankratov, D. *et al.* A Nernstian Biosupercapacitor. *Angewandte Chemie International Edition* **55**, 15434–15438 (2016).

74. Xiao, X., Conghaile, P. Ó., Leech, D., Ludwig, R. & Magner, E. A symmetric supercapacitor/biofuel cell hybrid device based on enzyme-modified nanoporous gold: An autonomous pulse generator. *Biosensors and Bioelectronics* **90**, 96–102 (2017).

75. Mercier, P. & Wang, J. Powered by sweat: Throw out the batteries: Biofuels will change the future of wearable devices. *IEEE Spectrum* **57**, 28–33 (2020).

Chapter 4 Wearable Multi-modular Bioenergy Microgrid on Electronic Textile

4.1 Introduction

The rapid rise of flexible electronics brings forth a myriad of sensors, circuits and energy storage devices in various wearable form factors.[1–9] In order to meet the growing power demands of wearable electronics and eliminate the need for frequent, interrupting recharges and cumbersome wired power transmission, wearable systems have integrated energy harvesters such as solar cells, triboelectric generators (TEGs), and enzymatic or microbial biofuel cells (BFCs) to enable their self-sustainable operation.[10–16] Different wearable devices have recently adapted this strategy to collect energy from humans or the environment followed by regulating and storing the scavenged energy in storage modules such as batteries or supercapacitors (SCs).[17–23] However, the operation of these systems has relied on either a monolithic input source that shares the same limitation in energy availability (e.g. the lack of motion, biofuel, sunlight), or upon multiple harvesters that operate in parallel but are not synergistic in realistic scenarios, and introduce additional limitations instead of compensating existing ones.[24–29] Moreover, the early multi-input hybrid harvesting systems, such as the integration of solar cells with supercapacitors and batteries, relied partially on energy inputs from the external environment (e.g., thermoelectric, pyroelectric, photovoltaic) which are often uncontrollable.[24-27] To scavenge energy efficiently and reliably solely from human activities, system-level considerations are urgently needed to guide the judicious selection of components with complementary characteristics and commensurate performance.

In this regard, wearable energy systems can seek inspiration in the design and deployment of microgrids operating in “island mode”.[31-33] Microgrid, namely, a micro-scale power grid with

components including energy generation, energy storage, various utilities, and management functionality for regulating the flow of energy, can be made self-sustainable and independent from the main power grid by the inclusion of various renewable energy harvesters and appropriate energy storage units. Such self-sustainable microgrids can operate independently from the main grid by harvesting energy from localized sources and regulating and storing the scavenged energy in various energy storage modules. The reliability of renewable sources is fortified by coupling with other generation sources (e.g., fuel-based generators) to ensure a timely energy supply.[33–37] Furthermore, these localized sources are paired with storage modules with optimal capacities based on the load energy demands.[38] Beyond the simple addition of harvesting and storage modules, design of the microgrid relies on the careful selection of components with compatible performance and complementary characteristics.

Inspired by this notion, we herein propose and demonstrate the concept of a wearable e-textile microgrid system: a multi-module, textile-base system with applications powered by complementary and synergistic energy harvesters and commensurate energy storage modules. To demonstrate this concept, we describe in the following section an integrated e-textile microgrid system that unite BFCs and TEGs, two harvesters with distinct and complementary energy conversion mechanisms based on human activities, along with SC modules for regulating the powering of wearable applications with both low and high power demand (**Figure 4.1 A**). Among many proposed integrated harvesters, the pairing of the biomechanical and biochemical harvesters is desirable as they rely solely on human activities. Previous studies demonstrated only such combination working in proof-of-concept in-vitro settings, hence is challenging to be employed for real-life scenarios.[39–41] Adapting the microgrid design concept, this work seamlessly integrates biomechanical and biochemical harvesters along with energy storage devices, with carefully

budgeted energy rating, into one e-textile platform. When this microgrid harvests energy during human movements, the TEG storage modules are firstly activated from the instant motion-induced charge generation to harvest biomechanical energy to rapidly boot the system, while the subsequently activated BFCs harvest biochemical energy from electroenzymatic reactions of sweat metabolites for prolonged power delivery (**Figure 4.1 B**). The complementary relationship between the two bioenergy harvesters thus compensates for the limitations of the BFCs due to delayed perspiration and of the TEGs due to the lack of motion. The SC modules regulate low-current, high voltage inputs from the TEG modules and high-current, low-voltage inputs from the BFC modules, with the optimal capacity to deliver sufficient power for designated applications while maintaining fast booting. The optimized system can thus boot quickly within 3 min to continuously power a microwatt-rated wristwatch with a liquid crystal display (LCD), or a milliwatt-rated sensor-electrochromic display (ECD) system operating in pulsed sessions, and extend their operation to over 30 min in connection to a 10-min movement session (**Figure 4.1 C**). Compared to the early integrated wearable energy systems, the present system relies solely on energy inputs from human activities and hence is not dependent on the external environment. [24,28,29] The performance of the individual modules was characterized, and the energy was carefully budgeted to ensure that the limited amount of harvested energy was efficiently utilized. For compatibility with the wearable form factor, all modules are printed, textile-based, durable and flexible, and can be readily integrated onto a shirt to harvest energy from the sliding motion between the forearms and the torso by TEGs and the sweat generated above the chest by the BFCs (**Figure 4.1 D**). These modules are connected with flexible printed silver interconnections that are secured and insulated by a hydrophobic, water-proof polystyrene-polyethylene-polybutylene-polystyrene (SEBS) block copolymer. The placement of the modules ensures the optimal

collection of biomechanical energy via the TEG module from the arm movements, along with an intimate contact of BFCs to the skin for sweat collection. The placement of BFCs and SCs on the chest also minimizes the possible bending and wrinkling deformation which may affect their energy harvesting and collection efficiency. Implementing the "complementary, commensurate, compatible" design principles, the microgrid e-textile system serves as an attractive example for future integrated on-body systems that are autonomous, reliable, synergistic, sustainable and energy-efficient. While the microgrid concept is introduced here to the field of wearable electronics using complementary BFC and TEG bioenergy harvesters paired with SC storage modules, it can be applied to guiding the development of future miniaturized energy systems based on a judicious selection and integration of different modules towards a variety of self-powered electronics applications.

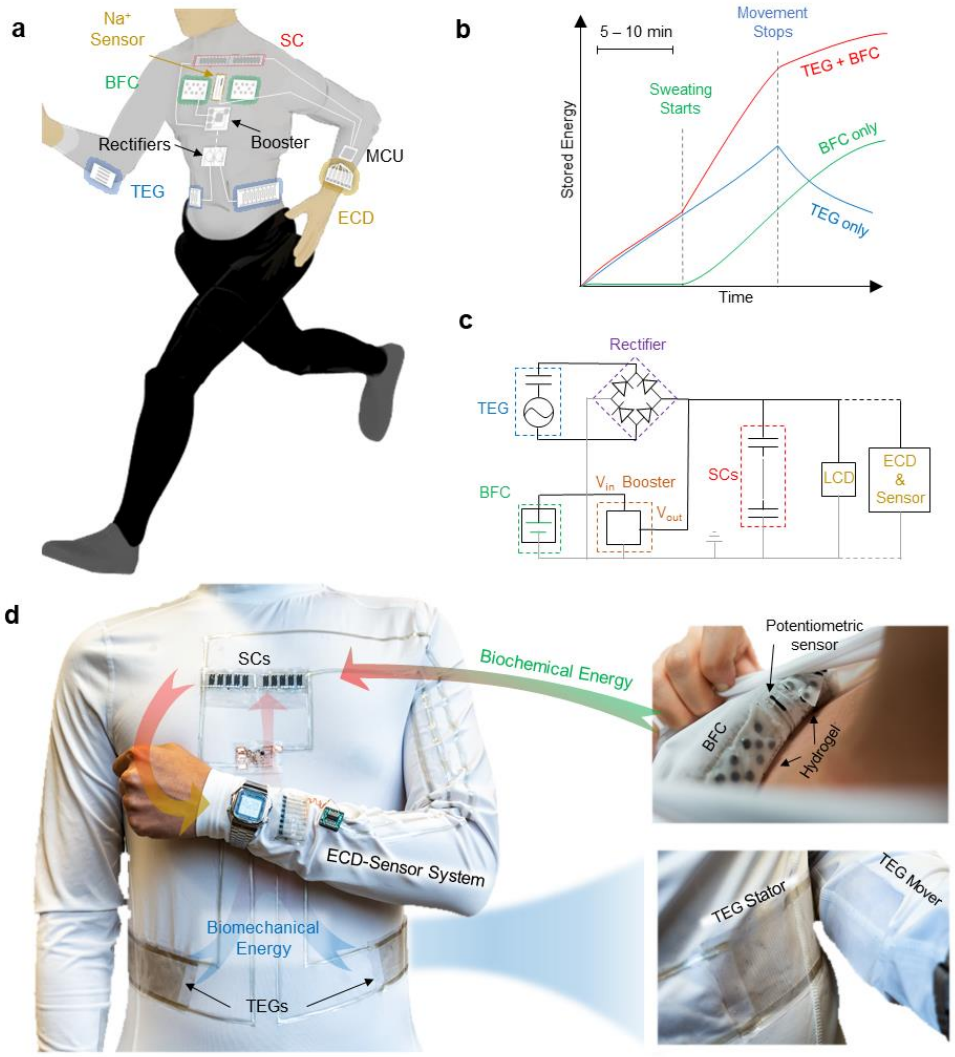

Figure 4.1. Design and concept of the multi-modular energy microgrid system.
A. System diagram of the energy microgrid system, consisting of the TEG, BFC, SC modules and wearable applications. **B**. Graphic illustration of the synergistic effect of integrating the complementary BFC and TEG energy harvesters. **C**. System diagram of the integrated E-textile microgrid powering an LCD or an ECD-sensor system. **D.** Photo images illustrating the arrangement of the individual modules of the wearable microgrid system on a shirt worn on-body, including the TEG modules on the side of the torso, the SC modules on the chest, the BFC modules and potentiometric sensor inside the shirt for direct sweat contact, and wearable electronics that are powered by the microgrid. All components were connected by printed stretchable silver traces insulated with SEBS.

4.2 Experimental Section

4.2.1 Chemicals and reagents

1,4-NQ, bovine serum albumin (BSA), PPIX (≥95%), glutaraldehyde, L(+)-lactic acid, acetic acid, sulfuric acid, chitosan (from shrimp shells, >200 cP, 1 wt. % in 1% acetic acid), silver flakes, PTFE powder (powder, free-flowing, 1 μm particle size) , toluene, methanol, ethanol, PVA (MW = 89,000 – 98,000, 99+ % Hydrolyzed), polyvinyl butyral (PVB) (powder, >100 cps), polyvinyl chloride (PVC), 4-methyl-2-pentanone (MIBK), 1,1,1,2,3,4,4,5,5,5-decafluoropentane (DFP), Poly(sodium 4-styrene sulfonate) (MW ~ 70,000) , sodium tetrakis[3,5-bis(trifluoromethyl)phenyl]borate (Na-TFPB), D-sorbitol, dioctyl sebacate (DOS) and glycerol were purchased from Sigma-Aldrich (St. Louis, MO, USA). L-lactate oxidase (LOx) (80 U mg^{-1}) was purchased from Toyobo (Japan). BOx (> 1.2 U mg^{-1}) was obtained from Amano Enzyme. Carboxyl-functionalized multi-walled carbon nanotubes (MWCNT-COOH, Ø = 10-20 nm, 10-30 μm length, >95% purity) were purchased from Cheap Tubes Inc. Water-based polyurethane resin Dispercoll U-42 was purchased from Covestro (Germany). Tetrahydrofuran (THF) was purchased from EMD Millipore. Ethylcellulose (EC) (Standard 4), polyurethane (PU) (Tecoflex SG-80A) were obtained from Lubrizol Life Sciences. SEBS (G1654) was obtained from Kraton (TX, USA). Fluorinated binder (T-70, a terpolymer of vinylidene fluoride, tetrafluoroethylene and hexafluoropropylene) was obtained from Frechem (Jiangsu, China). Super-P carbon black was purchased from MTI Corporation (Richmond, CA, USA). Graphite powder was purchased from Acros Organics (USA). Stretchable textile Lycra Shiny Milliskin Nylon Spandex Fabric was purchased from Spandex World. Inc (USA). The Capstone^{TM} fluorosurfactant FS-65 is purchased from DuPont (USA). The graphite carbon paste was purchased from Ercon Inc. (Wareham, MA,

USA). The screen printable PEDOT:PSS ink (C2100629D1) was purchased from Sun Chemical Ltd. (Bath, UK).

All metal stencils were designed via Autodesk AutoCAD (CA, USA) and are ordered from Metal Etch Services (San Marcos, CA, USA). The voltage booster (Texas Instruments bq25505) and the microcontroller (Atmel AtTiny441) were purchased from Digi-Key Electronics (MN, USA). The wristwatch (Casio, A178WA-1A) was purchased from Amazon.com (WA, USA).

An MSO-X-3014A oscilloscope (Agilent Technologies) and the designed OP-Amp circuit operated by a power supply (-10 V ~ 10 V) were used to measure the output voltage and currents of the TEG modules under various frequency from 0.88 ~ 3 Hz. Commercial electrolytic capacitors (1 μF ~ 1 mF) were used to characterize the average power, current of TEG. An Autolab PGSTAT204 potentiostat/galvanostat and an Interface 1010E potentiostat (Gamry Instruments, PA, USA) were used to analyze the electrochemical performance of the BFC, SC, sodium sensor and the ECD modules.

4.2.2 Device Fabrication and Optimization

The SEBS resin was prepared by dissolving 4 g of SEBS polymer in 10 mL toluene. The silver ink was made through a method similar to our previous protocol.[48,55] Briefly, flexible silver composite ink was formulated by mixing silver flakes with the SEBS resin (weight ratio = 2: 1) by a dual asymmetric centrifugal mixer (Flacktek Speedmixer, DAC 150.1 KV-K) for 5 min with a speed of 1800 rotations per minute (RPM). The flexible carbon composite ink is formulated by mixing super-P powder, graphite powder, SEBS resin, and toluene (weight ratio = 1: 6: 8.4: 2.1) in the mixer for 5 min at 2150 RPM. The PTFE ink was formulated by mixing the PTFE powder, T-70, DFP and MIBK (weight ratio = 9: 6: 2: 5) in the mixer for 10 min at 1800 RPM. The EC-PU ink was formulated by mixing EC powder, PU and THF (weight ratio = 1: 1: 14) in the mixer for 5

min at 2000 RPM. The CNT-PEDOT:PSS ink for the SC modules was formulated by mixing the MWCNT-COOH, PEDOT:PSS paste and fluorosurfactant (weight ratio = 5: 95: 0.5) in the mixer for 5 min at 2500 RPM. The PVA-acid electrolyte gel was formulated following our previous work by dissolving 1 g of PVA into 10 mL of water, adding 10 g of 1.8 M sulfuric acid and heating with rigorous stirring with a magnetic stir bar on a hot plate at 100 °C until 50 % of the water has evaporated.

4.2.2.1 Design, Fabrication, and optimization of TEGs

The fabrication of the TEG modules is based on screen-printing of formulated polymer composite inks. The TEG module is comprised of two parts: the stator, which includes the positively charged ethylcellulose-polyurethane (EC-PU) composite and the interdigitated flexible silver current collectors; and the mover, which includes the negatively charged PTFE and fluorocopolymer binder. A layer of SEBS resin and EC-PU ink were printed onto the stator and the mover, respectively, as the lining to smoothen the surface. The flexible silver ink was then printed onto the SEBS lining in two sets of interdigitated electrodes. The PTFE powder was mixed with the T-70 fluorocopolymer which was comprised of vinylidene fluoride, tetrafluoroethylene, and hexafluoropropylene were printed onto the mover as the negatively charged electrode. A sheet of EC-PU was cast onto the current collectors as the positively charged stator. The fabrication process is illustrated in **Figure 4.2**.

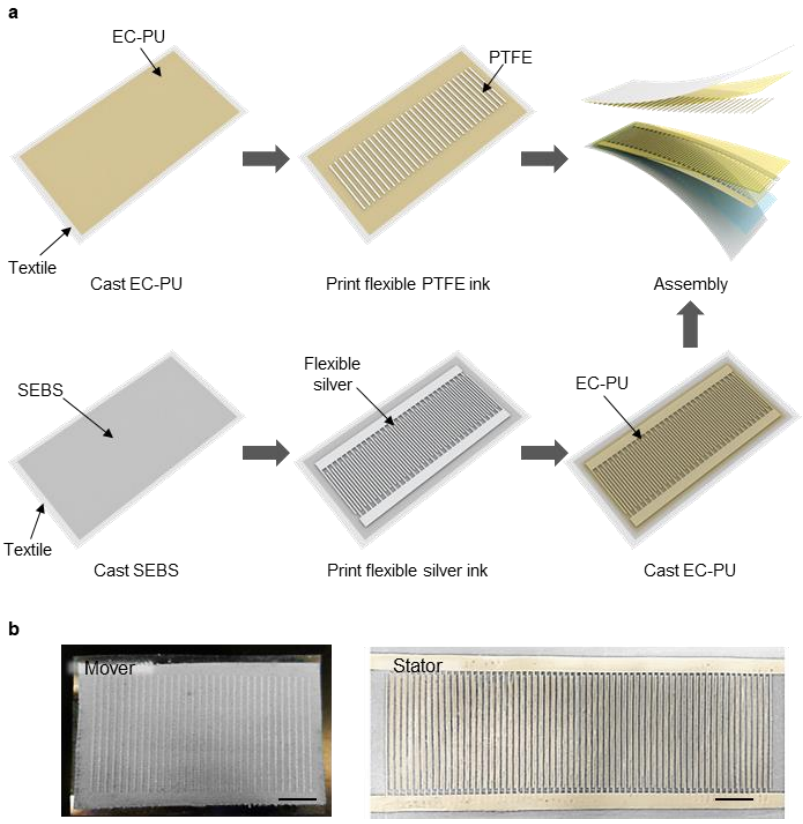

Figure 4.2. Screen-printing fabrication of the TEG module.
A. The layer-by-layer printing process of the mover (top) and the stator (bottom) of the TEG module. **B**. Photo images of the printed mover and stator. Scale bar: 1 cm.

The whole layers of flexible TEG modules were mainly made into a 100 μm-thick metal stencil for printing. The stator of the TEG module is fabricated by firstly casting a layer of SEBS lining with the SEBS resin onto the textile substrate using an adjustable doctor blade with a thickness of 200 μm and cured in an oven at 65 °C for 10 min. Then, the interdigitated silver current collector layer was printed using the flexible silver composite ink and the designed metal stencil and cured at 60 °C for 20 min. After that, a positively charged layer based on EC-PU ink was printed using the doctor blade with a thickness of 50 μm and cured at 60 °C for 10 min. For mover of the TEG, the EC-PU layer was first printed on the surface of the textile using a doctor

blade with 100 μm thick and cured at 60 °C for 10 min as lining. And then, interdigitated, negatively charged layer was printed using the PTFE ink with the metal stencil and cured at 70 °C for 20 min.

The textile-based TEG module can generate electricity from the combination of the electrification of two contacting layers during the sliding motions and the electrostatic induction to the back electrodes. The electrification takes place when the PTFE mover slides across the EC-PU film of the stator, where electrons are transferred at the interface from the PTFE composite to the EC-PU composites due to their difference in the electron affinity, allowing the PTFE electrodes to be negatively charged and the EC-PU to be positively charged temporarily. This effect is combined with the electrostatic induction between the EC-PU and the silver current collector on the stator. When the PTFE mover slides across the stator surface, the parallel PTFE patterns momentarily align with one of the two sets of the interdigitated silver current collectors below the EC-PU layer alternatively. As a result, the current flows from one set of the current collectors and back, alternating the polarity between the two sets of electrodes between positive and negative, and thus forming an alternating current.

To measure the performance of the TEG during the sliding, the two electrodes on the stator were directly connected to an oscilloscope, and their open-circuit voltage (V_{OC}) and short-circuit current (I_{SC}) were recorded. To optimize the design of the TEG module, patterns with different grating density were fabricated and their maximum peak voltage when sliding at 3 Hz was recorded, as shown in **Figure 4.3**. Although the output voltage dropped slightly as the number of segments increases, the peak current increased dramatically with the segments, indicating an increased amount of charge transfer as the grating density. The output reached a maximum of 130 μA with a corresponding peak voltage of 150 V with the 64-segment design. The drop in voltage can be

attributed to the decreased pitch between individual lines, which in turn facilitated the increase in the oscillation frequency and led to a higher peak current. The raw voltage and current output of the TEG module within one stride are illustrated in **Figure 4.4**. Overall, the total transferred charge of the TEG module increased with the grating frequency, thus resulting in an increased current level. The higher grading density within the resolution of screen-printing (~100 μm) was considered favorable to deliver higher power.

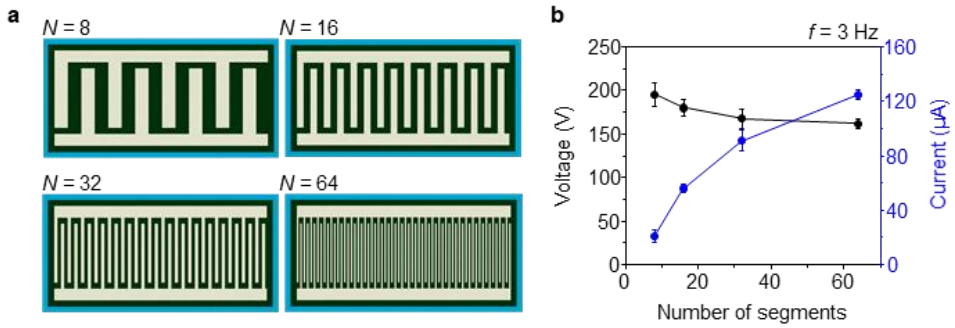

Figure 4.3. Structural optimization of the TEG module with different interdigitated grating units.
A. The schematic images of TEG stators with different number N of interdigitated lines within the length of 10 cm (*N* = 8, 16, 32, 64). **B**. The measured peak V_{OC} and I_{SC} of TEG module with different line density. The operational frequency is fixed at 3 Hz.

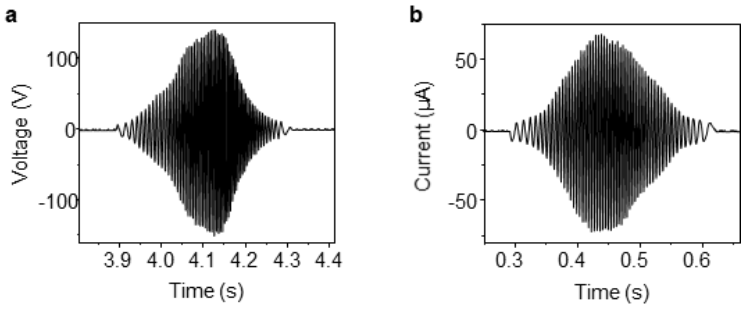

Figure 4.4. Raw voltage and current output of the optimized TEG module.
Raw signal of **A**. V_{OC} and **B**. I_{SC} generated from the TEG module with 64 interdigitated grating units.

The PTFE composite ink was optimized by varying the ratio of PTFE powder and the fluoropolymer in the formulation. In general, PTFE and other perfluorinated alkanes are considered among the most attractive negative electrode material due to its superior electron affinity. To endow printability, durability, and flexibility to the wearable module, a fluoroelastomer terpolymer that is comprised of vinylidene fluoride, tetrafluoroethylene and hexafluoropropylene was selected. Various ratios of the PTFE and the binder were tested under the same condition, as shown in **Figure 4.5**. It can be observed that the output peak voltage and peak current increase linearly with the weight ratio of PTFE, and maximized at 65 wt% with the peak voltage of 160 V and the peak current of 130 µA. The performance then decreased as more PTFE was added. This was caused by the deteriorated durability of the composite due to the lack of binder, where the printed composite peels off from the surface easily after undergoing repeated sliding. The formulation was hence optimized at 65 wt% of PTFE.

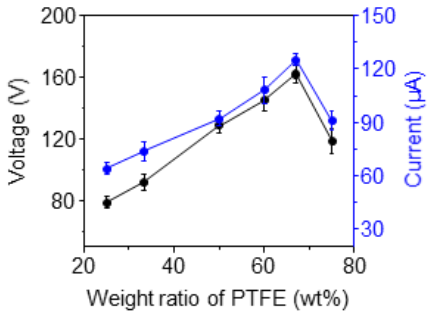

Figure 4.5. The output peak V_{OC} and I_{SC} of the TEG module with different ratios of PTFE with the binder.

The EC-PU ink formulation was optimized by varying the ratio between the positively charged ethylcellulose (EC) powder and the positively charged polyurethane (PU) elastomeric binder, as shown in **Figure 4.6**. Similarly, as the weight ratio of the EC increased and PU decreased,

the performance of the TEG module improved, reaching the maximum peak voltage of 185 V and peak current of 150 μA with 25 wt% of PU. This behavior is within expectation as the EC has shown higher positive charge affinity compared to PU in the triboelectric series[5]. In addition, the decrease in PU binder creates lower friction between the mover and the stator and smoothens the sliding motion between two surfaces, therefore considered more favorable. Yet, not reflected in the data, the flexibility of the module deteriorates significantly with less binder, rendering the high-loading formulations unsuitable for wearable applications. To balance the mechanical durability and the energy-harvesting performance of the TEG module, the formulation of PU at 50 wt% was selected.

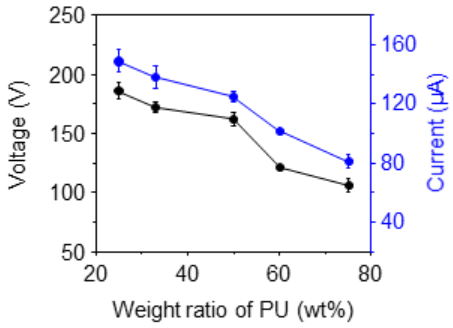

Figure 4.6. The output characteristic of the TEG module with different concentrations of PU for optimization of the positively charged layer.

4.2.2.2 Fabrication and Optimization of the Biofuel Cells

The CNT pellets for the electrode were prepared by formulating a paste that was molded with a thick PTFE stencil. The formulation is modified based on an early publication[11]. The anode paste was formulated by blending 7 mg MWCNT-COOH, 2 mg NQ, 11 μL GA (1% in ethanol) and 56 mg chitosan solution (3 wt% in 0.1 M acetic acid) with mortar and pestle. The cathode past

was formulated by blending 8 mg MWCNT-COOH, 11 μL glutaraldehyde (1 % in water) and 56 mg chitosan solution (3 wt% in 0.1 M acetic acid) with mortar and pestle. The paste was then molded using a PTFE stencil and dried in the oven at 80 °C for 20 min to form pellets. The pellets were chosen for their 3-dimensional, high specific surface area property, which allowed a higher rate of reaction compared to a printed, planar design. Two types of CNT pastes were made as described in the main manuscript. As shown in **Figure 4.7**, a 1.67 mm thick PTFE sheet (McMaster Carr, Elmhurst, IL) with multiple punctured circular 5 mm-diameter holes was used as the stencil. PTFE was chosen as the stencil material due to its hydrophobicity, allowing the deposited paste not to stick to the wall of the stencil. The prepared pastes were printed through the PTFE stencil onto another sheet of PTFE substrate and were dried in the oven at 80 °C for 20 minutes. After drying, the pellets hardened and delaminated from the PTFE substrate. The anode pellets thus shrink to the diameter of 4 mm and thickness of 1.4 mm, while cathode pellets shrink to the diameter of 3.5 mm to a thickness of 1.0 mm. The average weight of anode and cathode pellets was measured to be 8 mg and 6 mg, respectively.

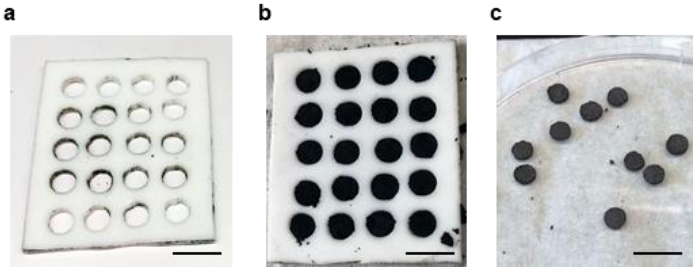

Figure 4.7. The fabrication of the CNT pellets for the BFC modules.
A. PTFE mold for CNT pellets. **B**. PTFE mold filled by the CNT paste. **C**. CNT pellets after drying. Scale bar, 1 cm.

The design of the BFC current collector array was made into a 100 μm-thick metal stencil for printing. To fabricate the current collector, a layer of SEBS resin was firstly cast onto the textile substrate using an adjustable doctor blade with a thickness of 200 μm and cured in an oven at 80 °C for 10 min. The interconnects are then printed using the flexible silver composite ink and cured at 80 °C for 10 min. The flexible carbon composite ink was then printed as the cathode and anode current collectors and cured at 80 °C for 10 min. The anode and cathode pellets were bonded on the carbon current collectors by printing a layer of commercial carbon paste use the metal stencil, mounting the anode and cathode pellets accordingly, and curing the paste at 60 °C for 20 min. To solidify the adhesion between the pellets and current collectors, the water-based PU was coated on the conjunctions and dried at 60 °C for 20 min.

The anode was functionalized by drop-casting 5 μL of LOx (20 mg mL^{-1} in 10 mg mL^{-1} BSA), 5 μL of GA solution (1 % in ethanol) and 5 μL of chitosan (1 wt% in 0.1 M acetic acid) on each pellet. The functionalization of the cathode is similar to that of the anode by drop-casting 5 μL of PPIX (40 mM in 9:1 vol/vol ethanol/acetone), 5 μL BOx (40 mg mL^{-1} in 10 mg mL^{-1} BSA) and 2.5 μL Nafion (1 wt% in ethanol) on each pellet. Each step of drop-casting was separated by 5 min to allow the solvents to evaporate, with chitosan and Nafion used for confining the LOx and BOx, respectively. Lastly, the modified BFC module was left in the refrigerator at 4 °C overnight before use. The formulation of the inks and the sequence of printing is illustrated in **Figure 4.8**. The as-fabricated BFC module was shown in **Figure 4.9**.

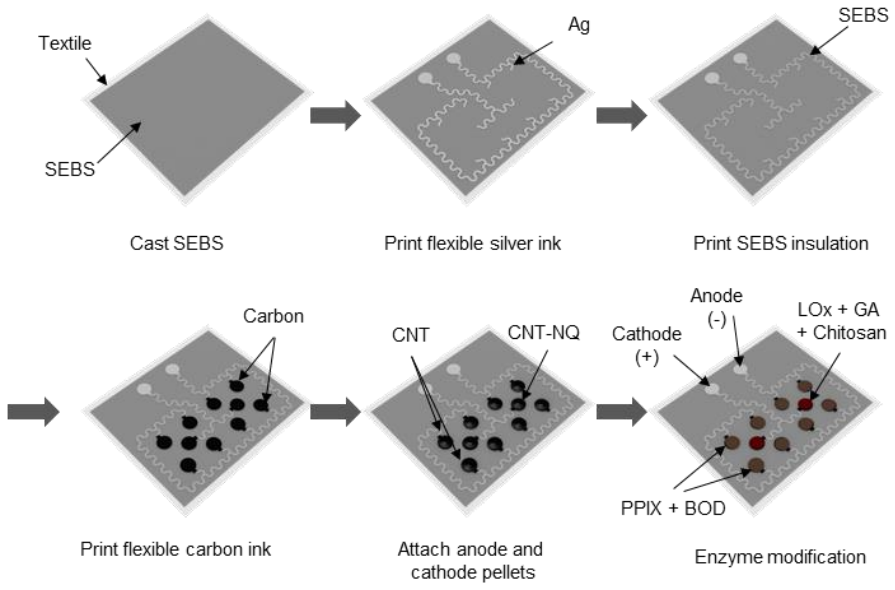

Figure 4.8. Illustration of the step-by-step assembly process of the BFC module.
The current collector was printed layer-by-layer, followed by fixating the prepared CNT pellets and drop-casting of enzyme and other bonding solution.

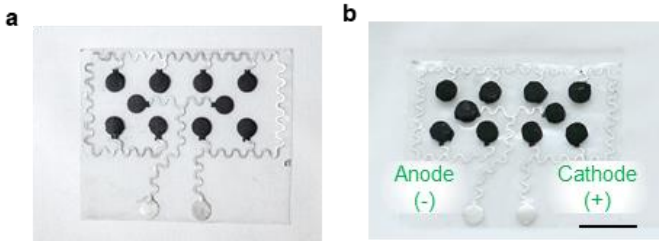

Figure 4.9. Photos of the BFC module.
Top-down view of a fabricated BFC module A. before and B. after attaching the CNT pellets. Scale bar: 1 cm.

The fabrication of the PVA hydrogel for the BFC on-body tests were adapted from a previous work.[49] Shortly, a 20 wt% PVA solution was prepared by dissolving the PVA in water in an 80 ºC water bath, and a 10 wt% KOH aqueous solution was prepared and added to the PVA

solution at 1:1 ratio by weight to form a hydrogel precursor. The precursor was left in desiccator under vacuum for 1 day until crosslinked, and then taken out to then be washed in DI water to remove excess KOH. The washed hydrogel was soaked in 0.5 M (pH 7.4) PBS for later use. The formed hydrogel was measured to be ~0.5 mm thick and was cut into 2 cm by 4 cm pieces to be used for each BFC module.

4.2.2.3 Fabrication of the Supercapacitors

The electrode formulation contains multiwalled carbon nanotubes (CNT), which were chosen for its high surface area and good conductivity as an electrode material. The carboxylate-functionalized variation of the CNT was chosen for its better dispersity in aqueous solvents. A screen-printable poly(3,4-ethylene dioxythiophene) polystyrene sulfonate (PEDOT:PSS) gel is chosen as the binder which offers flexibility, pseudocapacitive behavior and high conductivity. A fluorosurfactant (Capstone FS-65) was chosen as it promotes the dispersion of CNT in the PEDOT:PSS gel as well as the phase separation between PEDOT and PSS which results in superior stretchability and conductivity. The design of the SC modules was made into a 150 μm-thick metal stencil for printing. Firstly, a layer of SEBS resin was cast onto the textile substrate using an adjustable doctor blade with a thickness of 200 μm and cured in an oven at 80 °C for 10 min. The CNT-PEDOT:PSS ink was printed on the stretchable textile as the electrodes and is dried at 60 °C for 10 min and 80 °C for 10 min. The flexible silver composite ink was then printed onto the electrodes as current collectors to connect electrodes in series and cured at 80 °C for 10 min. The PVA-acid gel was printed onto the electrodes as the electrolyte and left to dry in a well-ventilated place under room temperature overnight. As the electrolyte dries in air, the capacity of the SC gradually increases and stabilize as it solidifies, which takes 8~12 hours under ambient environment. Oven-drying at elevated temperature is not recommended as it may cause the PVA

gel to degrade and change color. After drying, the electrolyte became flexible and stretchable. After the electrolyte solidifies, another layer of SEBS was cast onto the printed SC module to enhance its flexibility by enhancing the bonding between electrodes, electrolyte and the substrate, and to protect the SC module by prevent any sweat-induced degradation or dissolution when used on-body. The fabricated module is composed of 5 SC units connected in series, and each module can be connected in parallel or in series to adjust its capacity. The fabrication process and possible configurations of the SC modules are shown in **Figure 4.10**, and corresponding photo images in **Figure 4.11**. The fabricated SC samples are thereafter ready for characterization.

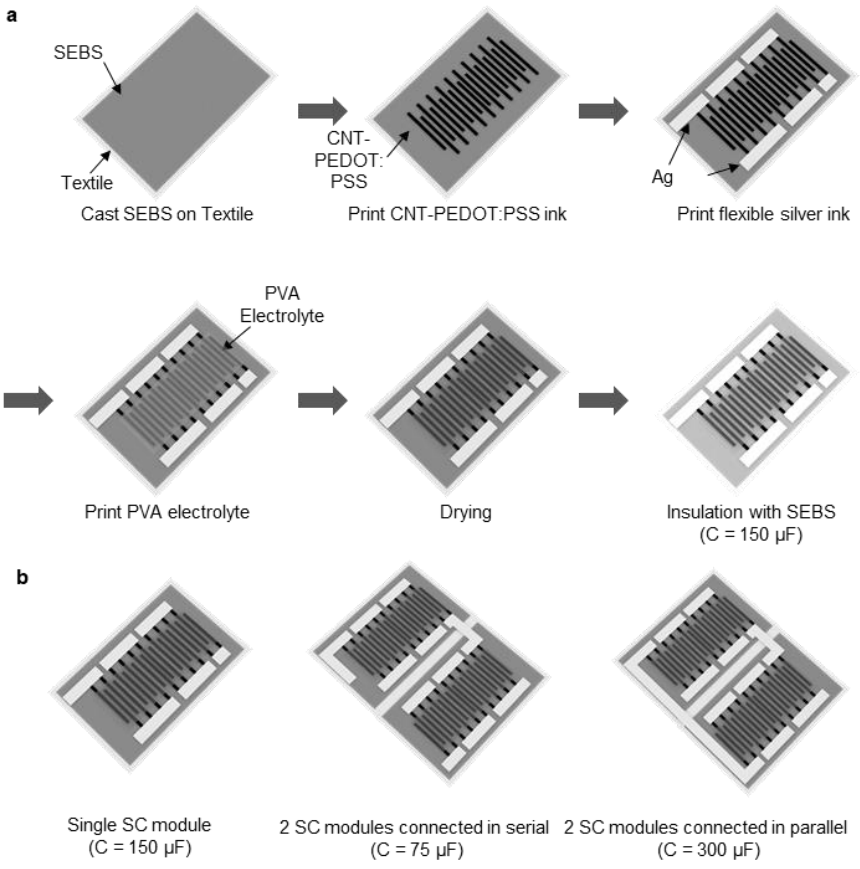

Figure 4.10. Illustration of the fabrication steps of the SC module.
A. Illustration of the layer-by-layer printing process of the SC modules. **B**. Serial and parallel configurations of SC modules which result in a different amount of overall capacitance.

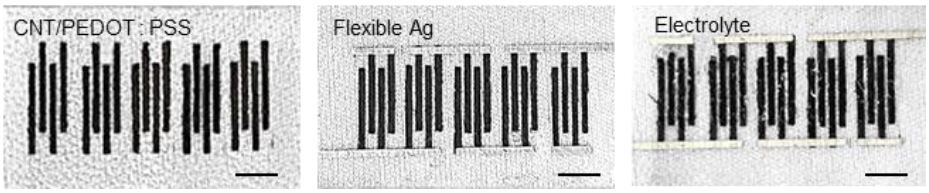

Figure 4.11. Top-down photo images of the printed SC module, where the electrodes, current collectors, and the electrolyte are printed layer by layer. Scale bar: 5 mm.

4.2.2.4 Design, Fabrication, and Characterization of the sodium ion (Na^+) sensor

The fabrication of the sodium ion sensor is illustrated in **Figure 4.12**, which was adapted from previous works[20,21]. The design of the Na^+ sensor was made into a 150 μm-thick metal stencil for screen-printing. Firstly, a layer of the SEBS resin was cast onto the textile substrate using an adjustable doctor blade with a thickness of 200 μm and cured in an oven at 80 °C for 10 min. Then, the collector and reference electrode were printed using the flexible silver ink cured at 60 °C for 20 min. The flexible carbon composite ink was printed as the working electrode and was cured at 80 °C for 20 min. Another layer of the SEBS resin was printed onto the sensor to insulate the interconnections and the junction between the carbon and the silver layer and cured at 80 °C for 10 min.

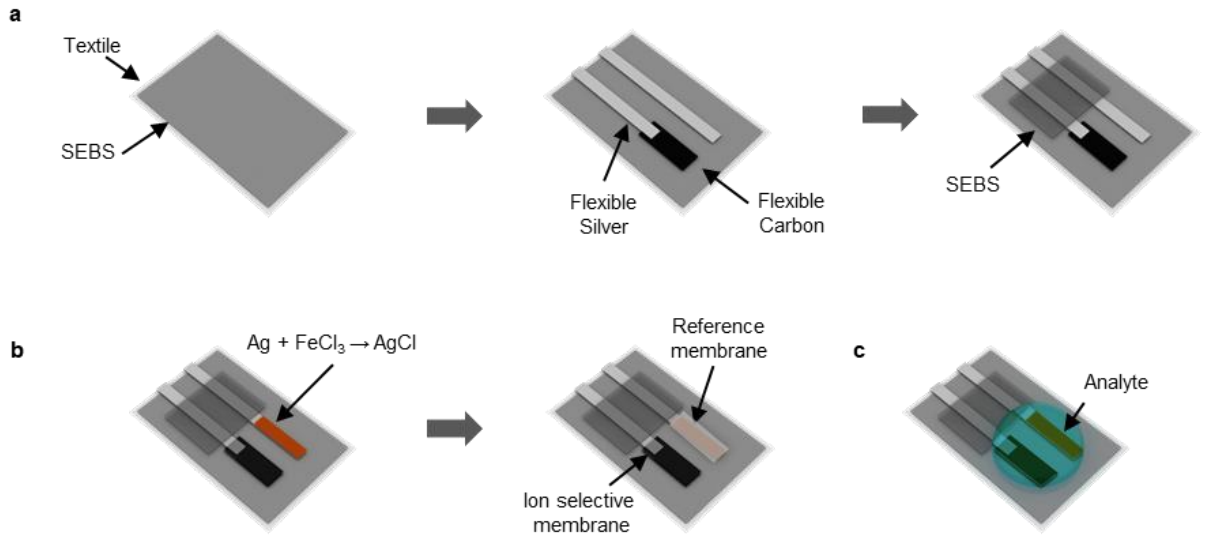

Figure 4.12. Illustration of the fabrication steps of the Na^+ sensor.
A. Layer-by-layer screen-printing of the electrode of the Na^+ sensor. **B**. The functionalization of the Ag/AgCl reference electrode and the Na^+ ion-selective working electrode. **C**. Fabricated Na^+ sensor in operation with the analyte.

To functionalize the reference electrodes, the exposed region of the flexible silver electrode is partially reacted with iron (III) chloride ($FeCl_3$) to form a silver/silver chloride electrode. 5 μL mm^{-2} of 0.1 M $FeCl_3$ solution was drop cast onto the electrode and let react for 1 min before rinsing off with DI water. A cocktail solution was prepared which was consisted of 78.1 mg polyvinyl butyral (PVB) and 50 mg sodium chloride (NaCl) dissolved in 1 mL of methanol. The NaCl was added in excess to ensure saturation. 1.5 μL mm^{-2} of the cocktail was then drop-cast onto the Ag/AgCl surface. 0.5 μL mm^{-2} of the water-based polyurethane was then drop-cast onto the electrode after the cocktail is dried. Another cocktail for the ion-selective working electrode was prepared by dissolving 1 mg sodium ionophore X, 0.55 mg sodium tetrakis[3,5-bis(trifluoromethyl)phenyl]borate (Na-TFPB), 33 mg polyvinyl chloride (PVC) and 65.45 mg dioctyl sebacate (DOS) dissolved in 660 mL of nitrogen-purged tetrahydrofuran (THF). 2.5 μL

mm^{-2} of such cocktail was drop cast onto the carbon working electrode. The decorated completely evaporate the solvents (e.g., THF and distilled water) at room temperature before use.

The response of the Na^+ sensor was tested by measuring the open-circuit potential (OCP) between the working and reference electrodes after being exposed to solutions with various Na^+ concentrations as shown in **Figure 4.13**. The membrane on the working electrode can selectively exchange Na^+ with the external aqueous solution by the use of ion-selective sodium ionophore and the Na-TFPB ion-exchanger dissolved in PVB-DOS in the organic phase. The potential of the sensor is hence dependent on the concentration gradient between the aqueous phase and the organic phase, described by the Nernst equation:

$$\Delta E = \frac{RT}{zF} ln \frac{[Na^+_{(aq)}]}{[Na^+_{(org)}]} \qquad \textbf{(Equation 4.1)}$$

Where ΔE is the change in potential in V, R is the gas constant = 8.3145 J mol^{-1} K^{-1}, T is the temperature in K, z is the charge of the ion, F is the Faraday constant = 96485 mol^{-1}, $Na^+_{(aq)}$ is the sodium concentration in the tested solution, and $Na^+_{(org)}$ is the sodium concentration in the ion-selective membrane, which should be constant[22]. The potential of the sensor hence changes logarithmically with the Na^+ concentration, with a Nernstian response of 0.05913 V per decade at 298 K in the ideal situation.

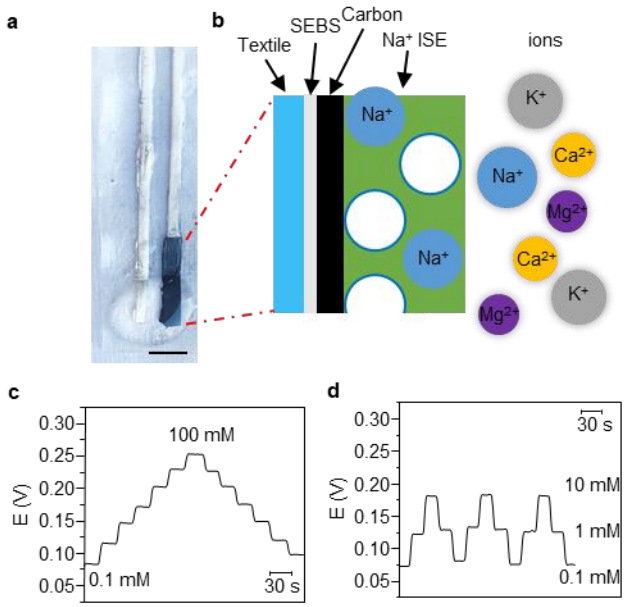

Figure 4.13. Sensing mechanism and characterization of the Na+ sensor.
A. Photo image of the printed and decorated Na^+ sensor. Scale bar, 2 mm. **B**. Illustration of the sensing mechanism of the Na^+ ion-selective electrode (ISE). **C**. The response of the Na^+ sensor to various Na^+ concentrations, ranging from 0.1 mM to 100 mM with the increment and decrement of one decade. **D**. The reversible response of the ISE with 0.1 mM, 1 mM, and 10 mM of Na^+.

Solutions of NaCl with the concentrations of 0.1 mM, 1 mM, 10 mM and 100 mM were prepared by dissolving NaCl in DI water. The sensor is firstly conditioned with 100 mM NaCl solutions for 30 minutes to saturate the Na^+ in the ion-selective membrane and rinsed with DI water. The sensor was then tested in different concentrations with increasing and then decreasing NaCl concentration, as illustrated in **Figure 4.13 C**. The response of the sensor is recorded, which is shown to have a linear response of 0.05719 mV per decade of concentration change by using the least-squares fitting with an R^2 of 0.99716. The reversibility of the sensor was also tested by having the sensor repeatedly exposing the sensor to 0.1 mM, 1 mM, and 10 mM NaCl solutions. As shown in **Figure 4.13 D**, this resulted in a negligible hysteresis to such changes in concentrations.

4.2.2.5 Design, Fabrication, and Characterization of the Electrochromic Display

As a simple demonstration of a complete wearable, self-powered application, a flexible sensor-display system was developed that reports the signal of the sensor directly via a low-energy consumption display. A transparent thermoplastic polyurethane sheet was selected as the substrate. The ECD electrode ink was formulated by mixing 0.5 wt% of Capstone fluorosurfactant into screen-printable PEDOT:PSS in the mixer for 5 min at 2500 rotations per minute (RPM), and sieved through a syringe filter with 1 μm pore size. The ECD electrolyte ink was formulated by mixing poly(sodium 4-styrene sulfonate), water, D-sorbitol, glycerol, and titanium dioxide (TiO_2) in 3: 2: 1: 1: 0.35 ratio by weight with the mixer for 5 min at 2500 RPM. A white opaque insulator ink was formulated by mixing 5 wt% of TiO_2 into the SEBS resin.

The inks were printed layer-by-layer onto the PU substrate using a designed 100 μm-thick metal stencil, as illustrated in **Figure 4.14**. The ECD is composed of the front electrode panel and the back panel with 8 individual electrodes to assemble into 8 electrochromic pixels. To fabricate the back panel, 8 PEDOT:PSS electrodes were printed with the ECD electrode ink and cured in the oven at 80 °C for 60 min. Flexible silver ink as connections and the opaque insulation ink was then printed consecutively and cured at 80 °C for 10 min each. The top panel was printed with the ECD electrode ink and the flexible silver ink with the same curing condition as above. A layer of the ECD electrolyte ink was printed onto the back-panel pixels and two panels were carefully aligned and attached. A heat sealer was used to seal the ECD on all 4 sides, allowing the ECD to be flexible without dislocation between two electrodes.

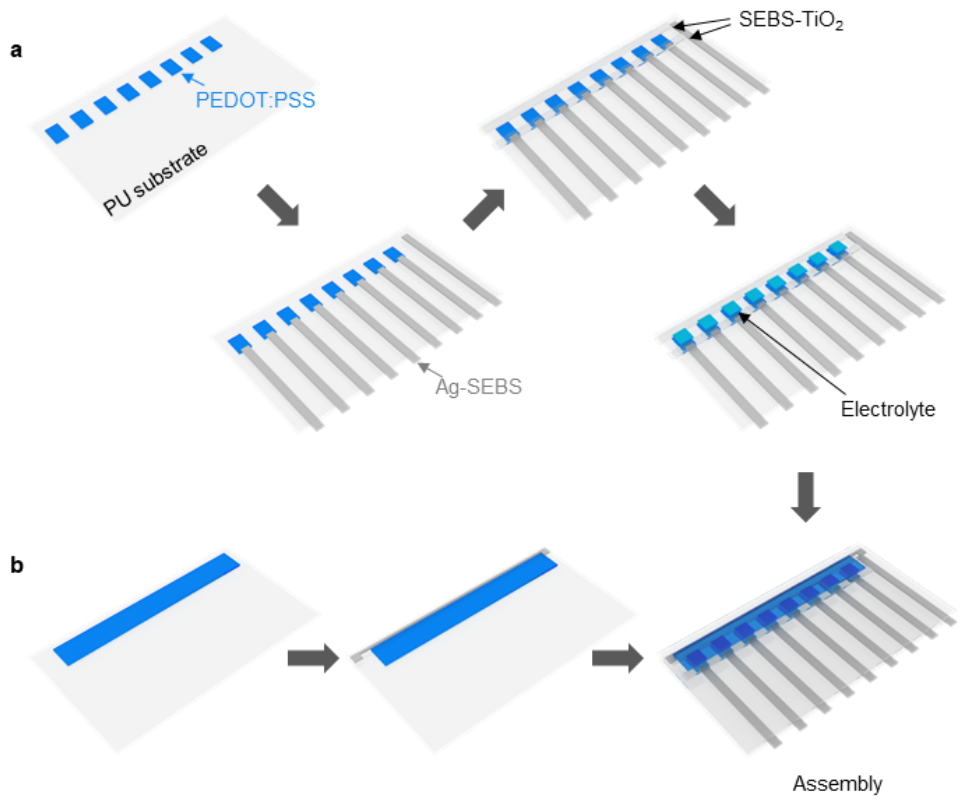

Figure 4.14. Fabrication steps of the ECD device.
The layer-by-layer fabrication process of the ECD which is composed of the printing of **A**. the back panel, **B**. the front panel, and the assembly of the two.

The operation of the ECD pixels follows the simple reversible redox reaction of the PEDOT:PSS, where the oxidation reaction takes place when the positive signal is applied to the positive electrodes on the back panel, and the reduction reaction takes place at the corresponding location of the electrode on the front panel and turns its color from light blue to dark blue. The electrochemical performance of the ECD pixels was tested via CV and CA, as shown in **Figure 4.15**. A 2-electrode CV scan between 0 and 2V is performed to the system, showing the oxidation of the electrode with a broad, non-specific oxidation peak near 1 V, and a sharper reduction peak at 1.2 V. The turn-on and turn-off response was monitored by high-speed CA with a different applied voltage of 1 V, 1.5 V, and 2 V to “turn-on” the pixel and 0 V to “turn-off” the pixel. As

shown, when the potential is applied, the reaction set off rapidly with the majority of the reaction took place within the first 0.1 s and the color of the pixel changes to dark blue instantly. After 0 V is applied, the dark blue color changes back to the original translucent blue color quickly, with the majority of the reaction completed within the first 0.2 s. As demonstrated in **Figure 4.15 C**, the amount of charge transfer increases with the applied potential, indicating a higher amount of power consumption and longer turn-off time when applying a higher potential. As the majority of the reaction takes place within the first 0.1 s, a transient application of on/off signal is sufficient to refresh the status of the ECD, allowing the system to be powered in a quick, pulsed discharge of a capacitor.

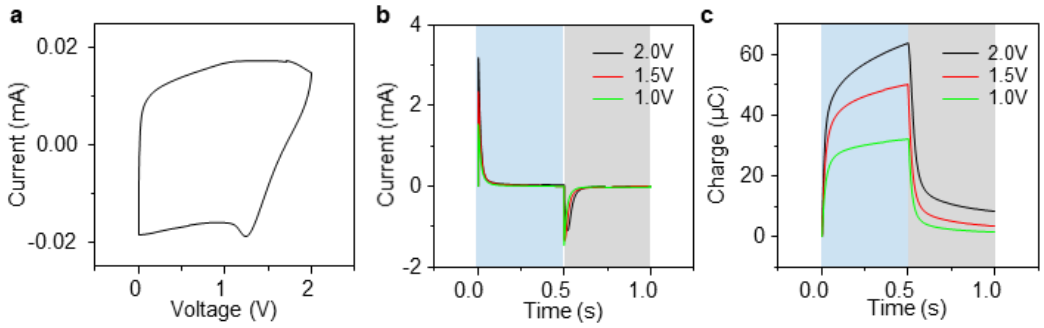

Figure 4.15. Electrochemical characterization of the ECD pixel.
A. CV of an individual ECD pixel with a scan rate of 0.1 V s^{-1}. The turn-on and the turn-off response of the ECD pixels with different turn-on voltages, in terms of **B**. current and **C**. charge. Blue region: set turn-on potential applied. Gray region: 0 V turn-off potential applied.

4.2.3 Wearable Electronic System and On-body Test Setup

The ultra-low-power boost charger circuit was developed based on the bq25505 chip (Texas Instruments). The circuit was configurated to discharge the connected BFC at 0.5 V and charge the connected SC modules up to 5.1 V. The sensing-display circuit was developed based

on the energy-efficient AtTiny441 microcontroller (Microchip Technology). The on-chip 10-bit A/D converter provides the capability of potential reading. Ten digital I/Os was configured for the electrochromic display control. The performance of integrated modules was characterized both in-vitro and on-body in order to find the optimum pairing of the modules and to demonstrate the complementary, commensurate and synergistic behavior of the system. Similar to previous sections, the TEG module was regulated by a bridge rectifier, and the rectified output was directly connected to the SC module for charging. As most of the commercial electronics requires a higher voltage (1.5 - 5 V) than the potential of any BFC can provide, the BFC module requires a voltage boosting circuitry to match the desired high voltage for charging the SC. Based on previous studies, a low-power boost charger chip with battery management function, bq25505 from Texas Instruments, was chosen for regulating the output of the BFC module. The circuit diagram of the booster is illustrated in **Figure 4.16**. The circuit diagram of the sensor-ECD system using the ATTINY441 MCU is illustrated in **Figure 4.17**. The It is worth noting that the efficiency of the booster circuit varies with the input voltage, input current, as well as potential of the storage module. Generally, for a BFC module with 0.5 V input voltage and 30 μA input current, the efficiency varies between 50% - 80% based on the potential of the SC module. By using the battery management function included in the chip, a maximum potential of 5.1 V was set to avoid overcharging the SC module. A reference voltage of 0.5 V was set for the power input, hence regulating the circuit to discharge the BFC module at a constant voltage to ensure maximum input power from the BFC, as discussed in previous sections. The connection of the modules is illustrated in **Figure 4.18**, where the anode of the BFC, SCs, and the negative ends of the rectifier were connected to the ground of the circuit, and the positive output from the booster and the rectifier were connected to the cathode of the SC.

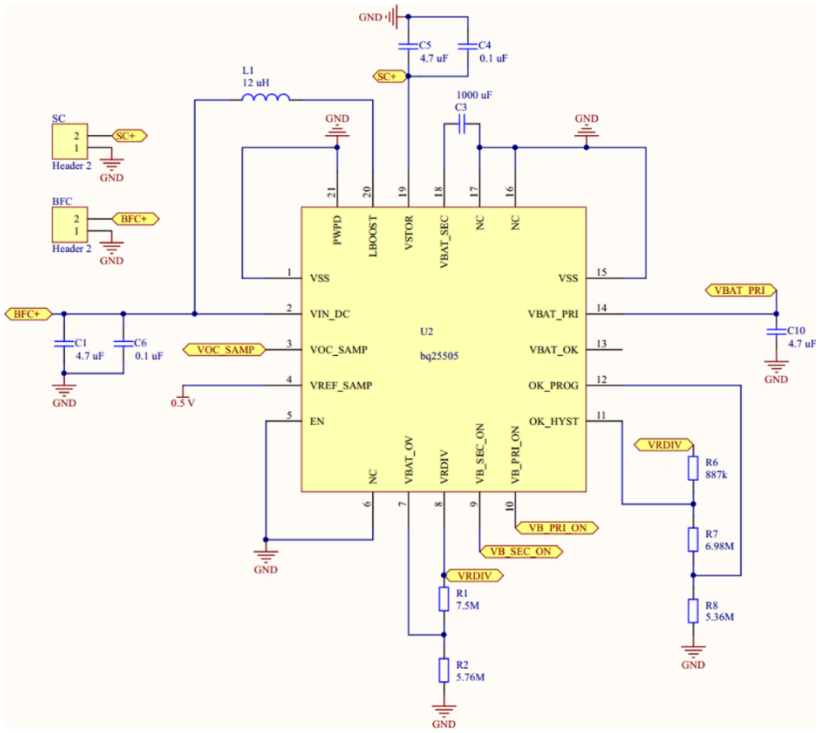

Figure 4.16. Schematics for the booster circuit system.
The booster could extract power from BFC as low as 330 mV, with the desired potential adjustable via a reference voltage. Once the output voltage to the SC reaches 1.8 V, the booster could continuously harvest energy with high efficiency.

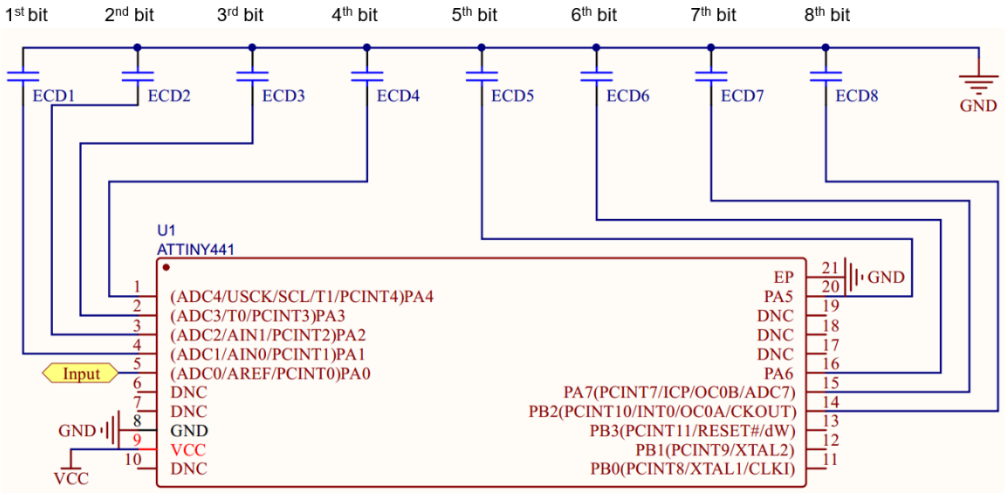

Figure 4.17. Schematics of the sensor-ECD system.
The microcontroller (ATTINY441) is used to control the electrochromic displays. The input pin senses the potential level up to 0.32 V. The sensed voltage is visualized by an 8-bit electrochromic display, and each bit represents 0.04V.

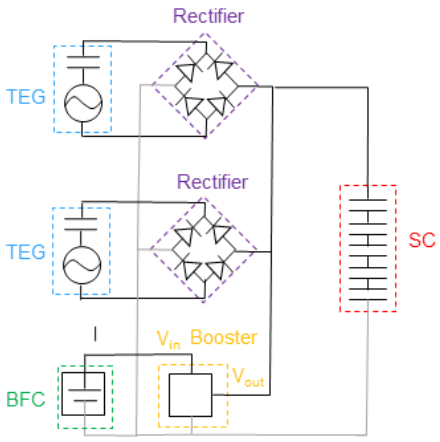

Figure 4.18. Circuit diagram for the integrated BFC and TEG energy harvesting modules, their corresponding regulating circuitry, and the SC energy storage modules.

The in-vitro testing of the system was performed on the desktop, where the frequency-controlled sliding motion was applied to the mover of the TEG on top of the stator to simulate arm movements, and PBS solution spiked by lactate was used to simulate human perspiration BFC module. Two TEG modules and one BFC module were connected to the microgrid as energy inputs, and one SC module was connected as the energy storage module. The potential of SC was monitored during the in-vitro simulation session to study the behavior of the system during different scenarios. The sliding frequency of 1.5 Hz was applied onto the TEG module to simulate the speed of arm swinging during a running exercise. A lactate concentration of 15 mM was selected to simulate the lactate concentration in human sweat. For each BFC module, 1 mL of 0.5 M PBS was applied to cover the electrode surface, and the corresponding amount of 100 mM lactate solution was spiked to the PBS to reach the target lactate concentration. It is worth noting that when the SC voltage is below 1.8 V, the booster requires a cold-start phase, where the energy from the BFC is used to jump-start the system. This process depends on the left-over charge in the system capacitor, input- from the BFC module, and other factors, which cannot be precisely

controlled. For the clarity of the data, the in-vitro tests were performed by pre-charging the capacitor to 1.8 V to avoid the cold-start phase.

A 10 wt% PVA (MW 89,000 – 98,000) was prepared by dissolving in hot water and was mixed with an equal amount of 20 wt% potassium hydroxide (KOH) solution by weight to form the hydrogel precursor. The precursor was dried in a desiccator under vacuum to cross-link into the gel, and the gel was soaked in deionized (DI) water several times to remove excess KOH, and then soaked in 0.5 M PBS for later use. The hydrogel can serve as a stable electrolyte to maintain the ionic connection between the anode and the cathode pellets, and also as a reservoir to absorb and temporarily store the sweat from the human body.

The printed BFC, TEG, and SC modules were attached to a stretchy, nylon-based shirt by adhesives, with their corresponding position shown in **Figure 4.1 C**. Printed, stretchable silver traces and enameled copper wire (36 AWG) was used to connect individual components in the same configuration as the in-vitro settings, and the printed traces and the contact points of the enameled wires were further insulated with SEBS to avoid short-circuiting from sweat. The TEGs were aligned so the natural arm-swinging motion is mostly perpendicular to the interdigitated patterns on the TEG stator so that the patterns on the TEG movers are parallel to the patterns on the stators when in contact. A cycling exercise machine is used to quickly induce sweat in a movement session, and the test subject is asked to ride the cycling machine while swinging their arm along with a metronome set at 180 beats per minute (one stride per beat) for a designed length of time.

Two leads were extended from the SC electrodes and connected to a potentiostat for pre-charging/discharging the SC module (if needed) and monitoring its voltage during the charging

period. Data was generated by pre-charging the module to 2 V before the movement starts. This was done for demonstrating better the synergistic and complementary effect of the system by avoiding the cold-start phase of the booster circuit, similar to the in-vitro tests described above. In the normal use-case, the SC modules were to be charged from 0 V instead of 2 V in a realistic situation, which was tested, and the results are presented and discussed in the following section.

The on-body test was performed by printing/gluing the individual modules onto a long-sleeve polyester shirt (Starter Dri-Star) and connected by printed, stretchable silver traces and enameled copper wire (36 AWG). The printed traces and the contact points of the enameled wires were further insulated with SEBS to avoid short-circuiting from sweat. The applications were connected to the microgrid as illustrated in **Figure 4.19**. The human subject volunteers were informed of the on-body experiment details and asked to sign the consent. The whole process has strictly followed the guidelines of Institutional Review Boards (IRB) and approved by Human Research Protections Program at University of California, San Diego.

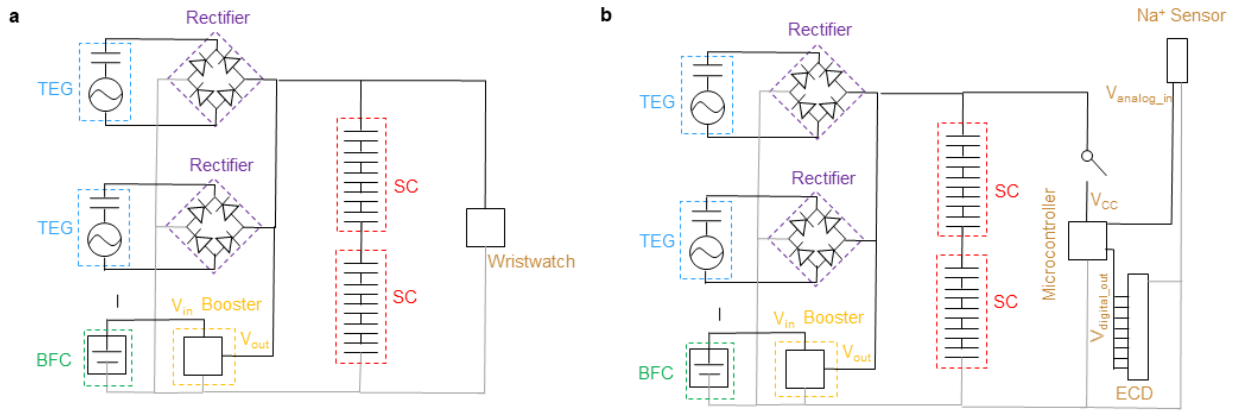

Figure 4.19. System diagram of the wristwatch and the MCU-ECD system.
Circuit diagram for the multi-modular wearable microgrid system with applications including **A**. a wristwatch operating continuously, and **B**. a sensor-ECD system controlled by a microcontroller operating in pulsed sessions. Gray lines: ground.

To power the wristwatch via the bioenergy microgrid, 7 min of cycling activity was carried out while the potential of the SC modules was monitored. The SC was charged from 0 V instead of 2 V to reflect the realistic booting scenario of the microgrid. The benefit of the complementary and synergistic effect between the TEG modules and the BFC module was evident when comparing to the single-harvester operation mode: in the beginning, the TEGs allowed the booster to quickly exit the cold-start phase and raise the potential to above 2.5 V where the LCD of the watch is operational; after movement stopped, the BFC was able to extend the operation time of the watch for at least 20 more minutes. With optimized capacitance paired with the system, the microgrid was able to boot quickly within 3 min, compared to the expected 5-10 min if configurations with larger capacitance were used.

Similarly, to power the sensor-ECD application, a 10 min cycling activity was carried out while the potential of the SC modules was monitored. The integrated harvesters allow the system to quickly boot in ~3 min to 4 V to supply for the first sensing-display refresh session. It was able to maintain ~10 refresh sessions within the 10 minutes of exercise, and > 10 sessions in the later 20 min with a slower refresh rate even after movement stopped. In comparison, the BFC harvester alone was not able to boot until 7 min later towards the end of the activity session, and the TEG harvester was able to boot quickly within 2.5 min but was not able to sustain more discharge sessions once after the movement stopped.

4.3 Results and Discussion

4.3.1 Characterization of The Microgrid Modules

TEGs have been selected as the biomechanical energy harvesters in this wearable microgrid system due to their instant response to motions to generate energy. Since their inception in 2012, TEGs have become the most studied wearable mechanical energy harvesters due to its simple generation mechanism and the abundant selection of materials. [10,42] The present TEG module is composed of a polytetrafluoroethylene (PTFE)-based negative mover and an ethylcellulose-polyurethane (EC-PU)-based positive stator in interdigitated patterns (**Figure 4.20 A** and **Figure 4.2**), and is designed to harvest energy from sliding motions as illustrated in **Figure 4.20**.[43–45] To ensure the compatibility of the fabrication of the TEG elements to the e-textile platform with abundant flexibility and durability, each individual layer in the TEG was formulated into a screen-printable ink with elastomeric binder that is water-proof and resistant to abrasion. The TEG modules were characterized at low sliding frequencies ranging from 0.833 Hz to 3 Hz, simulating the realistic swinging speed of human arms from during walking (below 1 Hz) to running (1.5-3 Hz). As shown in **Figure 4.20 C-D** and **Figure 4.21**, the maximum peak voltage, independent from the frequency, was measured to be ca. 160 V. In contrast, the peak current grows nearly linearly with the frequency, from 45 μA at 0.833 Hz to 130 μA at 3 Hz, reflecting the linearly shortened time of transferring the same amount of charge between the mover and the stator.[46] To ensure that the TEG module is paired with commensurate storage rating, commercial electrolytic capacitors, with known capacitance ranging from 1 μF to 1 mF were used initially for the characterization, which were charged by a rectified TEG module in 60 s, 1.5 Hz sliding sessions while recording the capacitor voltage (**Figure 4.20 E**). To extrapolate the applicable performance

data from the charging curves, the total harvested energy within the period and the harvested energy were calculated with the equation:

$$E = \frac{1}{2}CV^2 \qquad \textbf{(Equation 4.2)}$$

where *E* is the stored energy in the capacitor in J, *C* is a capacitance of the capacitor in F, and *V* is the voltage of the charged capacitor in V; and the average current was calculated with the equation:

$$I = C\frac{dV}{dt} \qquad \textbf{(Equation 4.3)}$$

where *I* is the average current from the TEG module in A, *C* is a capacitance of the capacitor in F, and $\frac{dV}{dt}$ is the rate of voltage change in V s^{-1}. Using the above equations, the total amount of stored energy and the average current was calculated and summarized in **Figure 4.20 F**. The average current remained mostly unchanged at 5.8 μA against different capacitors, while the energy stored maximized at 0.49 mJ near the load of 100 μF. The charging characteristics of the TEG modules at different frequencies were also tested and plotted in **Figure 4.20 G-H**. These data show a near-linear growth in stored energy and average current with the sliding frequency, which corroborated with the behavior observed in **Figure 4.20 D**. The mechanical durability of the TEG modules was also evaluated through repeated folding, crumpling and extended abrasion (**Figure 4.20 I**). The TEG modules were repeatedly folded with the radius below 1 mm for 100 cycles, and their open-circuit voltage (V_{OC}) during 1.5 Hz sliding motion was monitored, which has shown no discernible change (**Figure 4.20 J**). The TEG modules were also crumpled randomly and flattened repeatedly for 100 times, with their V_{OC} when sliding monitored. The crumpling deformation had also shown no change in performance (**Figure 4.20 K**). The durability of the module against constant friction and washing was also tested, where the TEG module underwent constant sliding motion for over

2000 cycles, where no visible drop in V_{OC} was observed (**Figure 4.20 L**). The TEG modules could thus be considered a flexible and durable biomechanical energy harvest and were ready for integration.

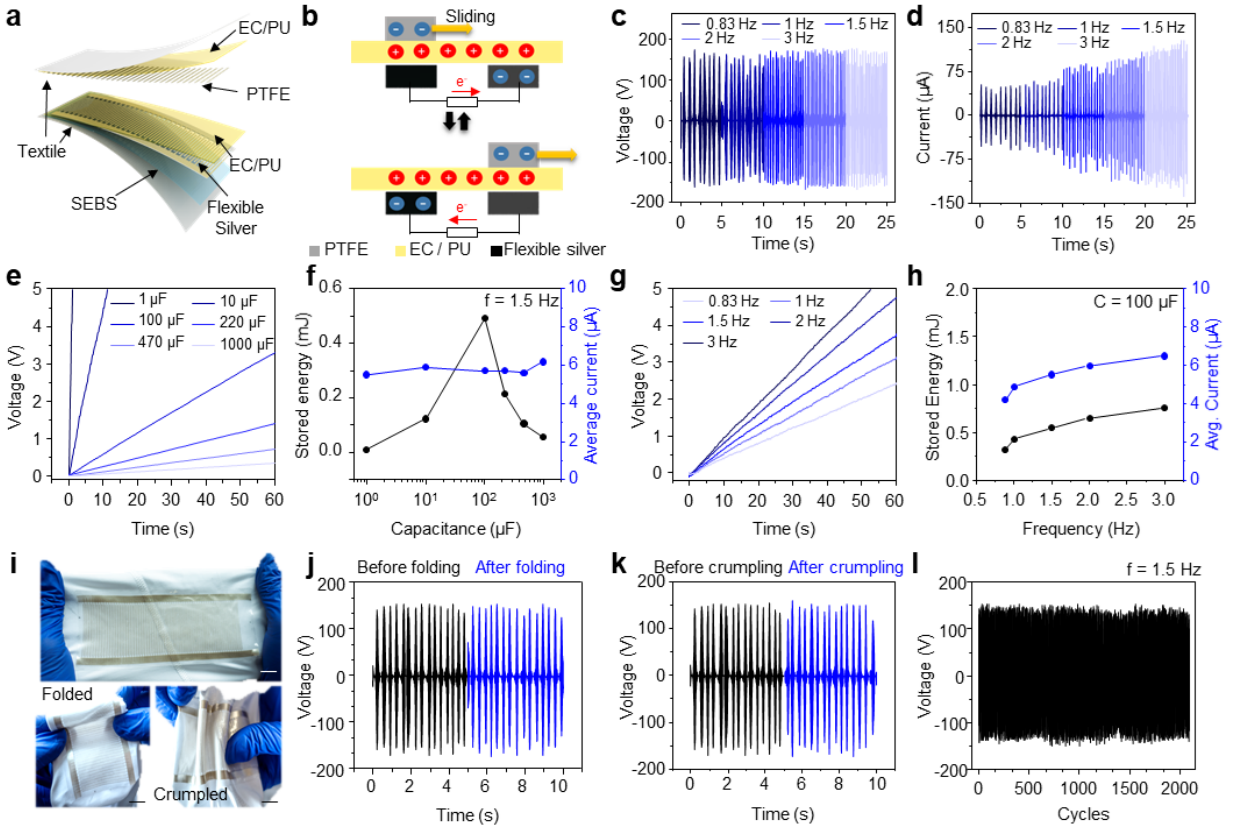

Figure 4.20. Characterization of the performance of the TEG module.
A. Schematic image of the layer-by-layer composition of the textile-based TEG module composed of a PTFE-based mover (top) and an EC-PU-based stator (bottom). **B** The charge generation mechanism of the TEG module under in-plane friction between the mover and the stator. **C-D,** The unrectified output peak voltages (**C)** and peak currents (**D)**. of the TEG at different sliding frequencies. **E-F**. The charging of commercial capacitors with difference capacitance at 1.5 Hz in a 60-second period (**E**). and the corresponding stored energies and equivalent average DC currents (**F**). **G-H**. The charging of 100 μF capacitor at different frequencies in a 60-second period (**G**). and the corresponding stored energies and equivalent average DC currents (**H**). **i** Images of folded and crumpled TEG stator. Scale bar, 1 cm. **J-K** The unrectified output peak voltages before and after 100 cycles of folding (**J**) and crumpling (**K**). **L**. The long-term electrical signal from the TEG module under continuous sliding motions with the frequency of 1.5 Hz.

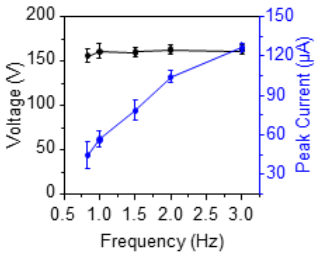

Figure 4.21. The peak voltage and peak current output of the TEG module with different frequencies ranging from 5/6 to 3 Hz of the TEG module.

In the wearable microgrid system, BFCs offer the feature of harvesting biochemical energy continuously from metabolites present in biofluids via electroenzymatic reactions. Due to the high lactate concentrations in human sweat, a variety of sweat-based BFCs has been developed as wearable energy harvesters[47–51]. The wearable BFC modules were also screen-printed using various ink composites onto textile substrates. Carbon nanotubes (CNT)-based pellets were attached to interdigitated "island-bridge" interconnections (**Figure 4.8** and **Figure 4.22 A-B**) composed of flexible carbon composite as currents collectors and flexible silver composite as conductive interconnections. As illustrated in **Figure 4.22 C**, such bioenergy harvesting relies on the oxidation of lactate catalyzed by the lactate oxidase (LOx) immobilized on the bioanode, and on the oxygen reduction reaction facilitated by bilirubin oxidase (BOx) on the cathode. For efficient sweat bioenergy harvesting, the anode CNT pellets were preloaded with the 1,4-naphthoquinone (NQ) mediator while confining LOx with the glutaraldehyde (GA) cross-linker and chitosan; the CNT-based cathode pellets were decorated with protoporphyrin IX (PPIX) as the electron transfer promoter[52], while immobilizing the BOx with Nafion. All in-vitro tests for characterization of the BFC were carried out in 0.5 M phosphate buffer solution (PBS) with pH of 7.4. The single electrode performance of the BFC is shown in **Figure 4.23**. Traditionally, wearable

BFC devices are characterized with LSV, with scan rate near 5 mV s^{-1}.[11,16,49,52] However, for high-surface-area electrodes like the CNT pellets such high-speed LSV will result in an unrealistically high power due to the capacitive currents (**Figure 4.24**). Therefore, the fabricated BFC modules were characterized using chronoamperometry (CA) at different potentials in the presence of 15 mM lactate to reflect the realistic power output of the BFC in extended discharge sessions. The testing of the BFC modules resulted in a maximum power of 21.5 μW per module when discharging the BFC at 0.5 V (**Figure 4.22 D-E**). The response of the BFC to different lactate concentrations has been evaluated using CA, as shown in **Figure 4.22 F**, **Figure 4.25**, and **Figure 4.26**, where the power per module increases from 9.7 μW at 5 mM lactate to 25.3 μW at 25 mM lactate. The mechanical durability and the stability of the BFC were also tested using CA. The module was bent 1000 times to 180° inward then outward with the radius of 1.3 cm (**Figure 4.22G**), with the current at 0.5 V before and after bending in 10 mM lactate environment measured. As shown in **Figure 4.22 H**, the power of the BFC did not show any noticeable change before and after the bending. Such resiliency is attributed primarily to the "island-bridge" structure where the non-flexible, functional electrode pellets as the islands are connected by flexible, conductive silver interconnections. The stability of the BFC was tested also throughout the week (as shown in **Figure 4.27**). The BFC under test was stored in refrigerator under 4 °C and was taken out for testing every 24 hours in a 10 mM lactate environment. The results of the individual CA measurements are summarized in **Figure 4.22 I**. The BFC module's stability in simulated sweat conditions can be found in **Figure 4.28**.

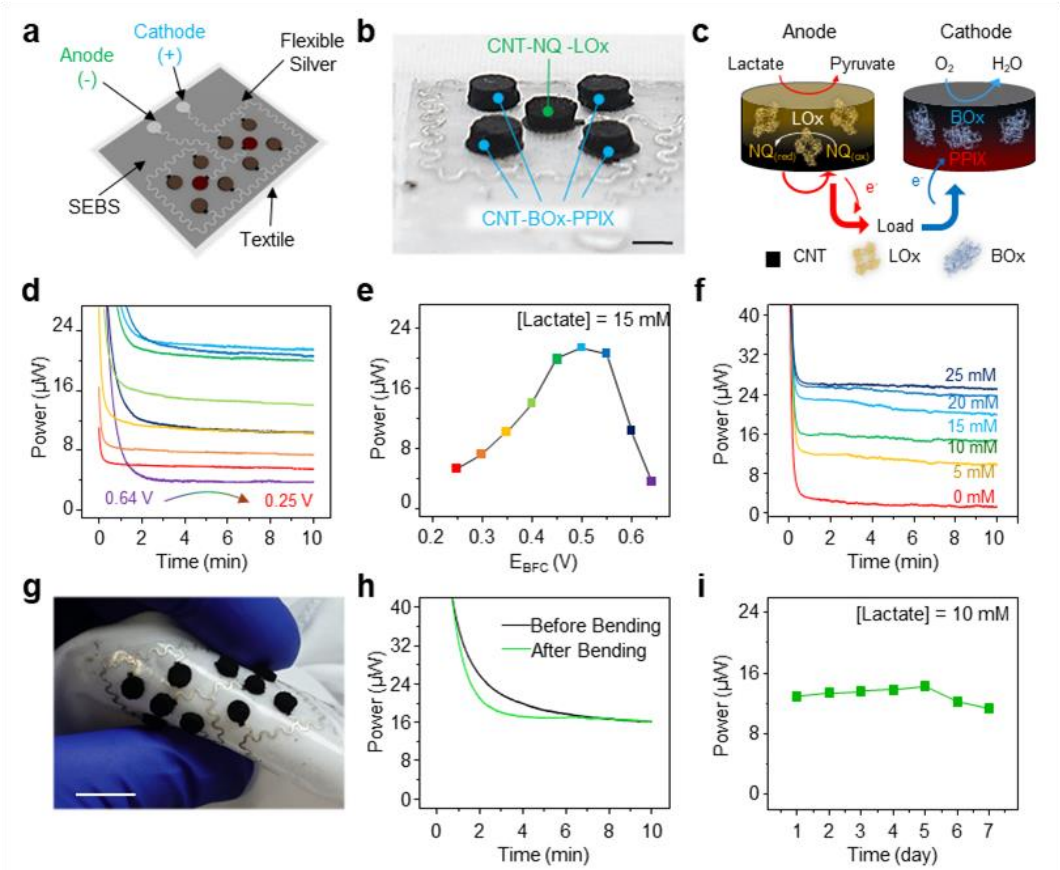

Figure 4.22. Characterization of the performance of the BFC module.
A. Schematic image of the textile-based BFC module composed of eight BOx-based cathodes and two LOx-based anodes connected by printed flexible interconnections. **B.** A zoomed-in photo image of the fabricated BFC module. Scale bar, 5 mm. **C.** The charge generation mechanism of the BFC from lactate and oxygen in sweats. **D.** The output power of the BFC module at different discharge potentials with 15 mM lactate concentration. **E.** The equivalent polarization curve derived from (**D**). **F.** The output power of the BFC module discharged at 0.5 V under various lactate concentrations. **G** Image of the BFC module under 180° outward bending. Scale bar, 1 cm. **H**. The power of the BFC module before and after the 1000 bending cycles. **I.** The output power of the BFC module with 10 mM lactate concentration everyday within a week.

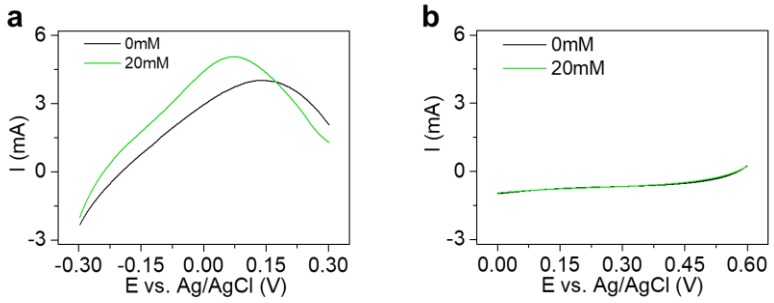

Figure 4.23. BFC single electrode performance with 0 mM and 20 mM lactate.
A. LSV on single anode electrode pellet. **B**. LSV on single cathode electrode pellet. Scan rate: 5 mV s^{-1}.

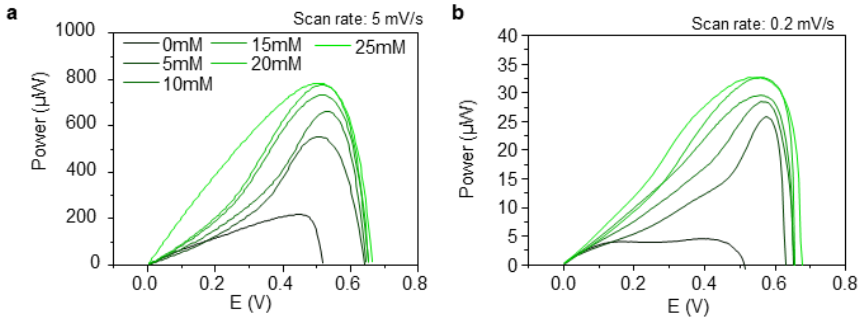

Figure 4.24. LSV characterization of the BFC module at different scan rates.
The LSV polarization curve of one BFC module at different concentrations, characterized with a scan rate of **A**. 5 mV s^{-1} and **B**. 0.2 mV s^{-1}.

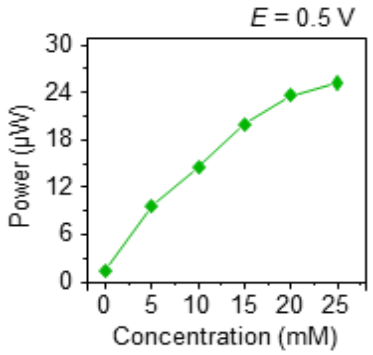

Figure 4.25. The power output of the BFC module discharged at 0.5 V with different lactate concentrations.

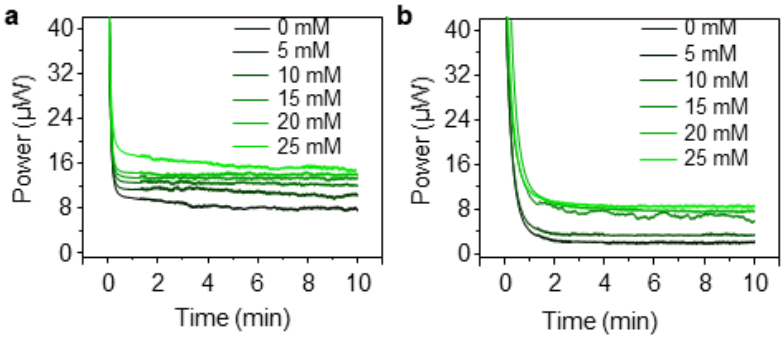

Figure 4.26. CA of the BFC module at different voltages.
The power vs. time plot of a BFC module converted from the CA in the environment of 0, 5, 10, 15, 20, and 25 mM lactate at **A**. 0.4 V and **B**. 0.6 V.

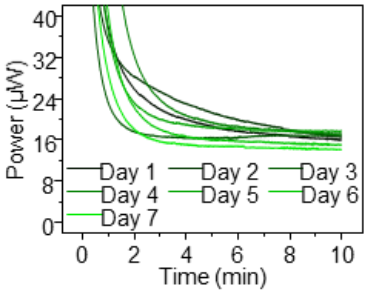

Figure 4.27. The CA of one BFC module scanned everyday within a week.

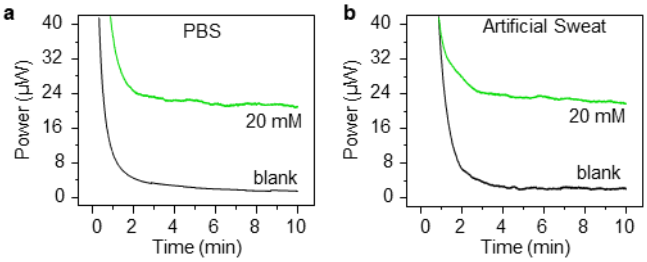

Figure 4.28. Performance characterization of the BFC in PBS and artificial sweat.
The performance of the BFC module in **A**. 0.5 M PBS and **B**. artificial sweat composed of 85 mM of NaCl, 13 mM of KCl, and 16 mM of urea in 0.1 M PBS, with the lactate concentration of 0 mM and 20 mM.

Flexible, printed SCs are selected for its ability to charge and discharge repeatedly and rapidly to deliver a flexible range of powers – a feature highly desirable for fast booting and pulsed high-power applications. A CNT and poly(3,4-ethylene dioxythiophene) polystyrene sulfonate (PEDOT:PSS) hybrid capacitor, offering screen-printability and high flexibility, has been adopted as symmetrical interdigitated electrodes that are connected by flexible silver current collectors (**Figure 4.29 A**).[54] Each SC module consists of 5 SC units connected in series to reach the desired 5 V voltage range for directly powering electronics, with each SC unit featuring four interdigitated CNT-PEDOT:PSS electrode segments covered by a solidified, transparent, flexible, sulfuric acid-

crosslinked polyvinyl alcohol (PVA) electrolyte (**Figure 4.29 B**). The hybrid capacitor stores electric energy via both double-layer capacitance endowed by the high specific surface area CNTs and pseudocapacitance from the PEDOT:PSS, as illustrated in **Figure 4.29 C**. The areal capacitance of the printed SC material was characterized via both cyclic voltammetry (CV) at different scan rates and galvanostatic charge-discharge (GCD) with different current. The GCD was conducted at charge/discharge between 0 V and 1 V with currents at 25, 50, 100, 250 and 500 μA (**Figure 4.29 D**). The capacitance at discharge is used to gauge the capacitance of the SC unit, which is calculated using the equation:

$$C = \frac{I\Delta t}{A(E_f - E_i)} \qquad \textbf{(Equation 4.4)}$$

where C is the areal capacitance in F cm^{-2}, I is the current in A, Δt is the time taken for the discharge, A is the geometric area of electrodes, E_f is the charged potential in V, and E_i is the discharged potential in V. CV was carried out with the scan rates of 5, 10, 25, 50, 100 mV s^{-1} between the window of 0 V and 1 V (**Figure 4.29 E**). The areal capacitance is calculated using the formula:

$$C = \frac{1}{2\nu A(E_f - E_i)} \int_{E_i}^{E_f} I \, dV \qquad \textbf{(Equation 4.5)}$$

where C is the areal capacitance in F cm^{-2}, ν is the scan rate in V s^{-1}, A is the geometric area of electrodes in cm^2, E_f is the higher vertex potential in V, E_i is the lower vertex potential in V, and the I is the current in A. As agreed by both characterization methods, the capacitance of the printed SC was determined to be ca. 10 mF cm^{-2} (**Figure 4.30**). Several SC modules can be connected in series or in parallel to adjust the overall capacitance to fit for harvesters and applications to obtain optimal charging speed and deliver sufficient energy (**Figure 4.29 F**). The stability of the module is analyzed by performing GCD cycles on the SC module. The mechanical stability of the module

was evaluated by applying 1000 cycles of repeated inward-outward bending cycles at 180° with a bending radius of 0.5 cm (**Figure 4.29 G**). As shown in **Figure 4.29 H**, the charge-discharge behavior of the SC does not show any noticeable change before and after the 1000 cycles of bending deformation, suggesting the robust flexibility of the SC module for wearable applications. To prevent the leaching of the acidic electrolyte, the device is sealed by an additional layer of printed SEBS. The device can thus withstand extended wetting and washing without electrolyte leaching or observable degradation in its performance. The electrochemical stability of the SC module was studied by 1000 cycles of GCD between 0 V and 5 V with a current of 50 μA. As demonstrated in **Figure 4.29 I**, the areal capacitance of the SC shows a slight drop of areal capacitance after 1000 cycles to ca. 9 mF cm^{-2}, while the coulombic efficiency gradually increases to 95%. The electrochemical performance of the SC is thus acceptable within the use-case of the microgrid, where roughly a few hundreds of charge-discharge cycles are expected. The charging efficiency and the self-discharge of the SC module is shown in **Figure 4.31** and **Figure 4.32**. Overall, each SC module was rated with the capacitance of ca. 150 μF.

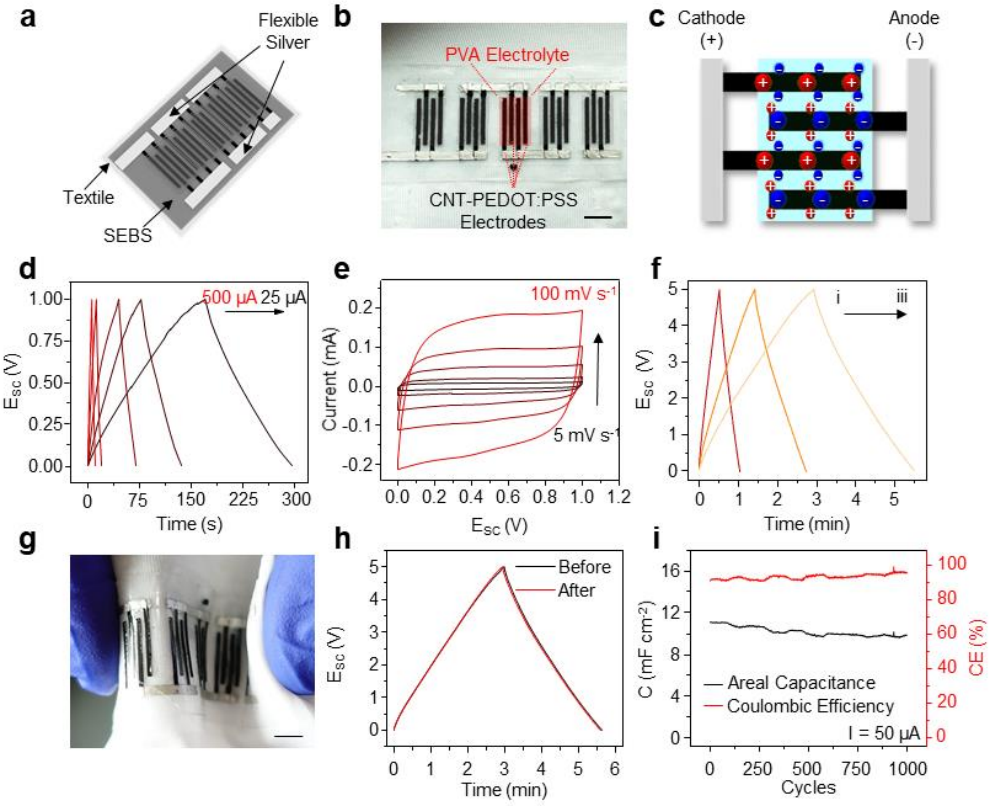

Figure 4.29. Characterization of the performance of the SC modules.
A. Schematic image of the textile-based SC energy storage module consisting of current collectors, CNT-PEDOT:PSS-based electrodes and PVA-based solid gel electrolyte. Each module is composed of five SC units connected in series. **B** The photo image of the printed SC module. Scale bar, 5 mm. **C.** The charge storage mechanism of the hybrid SC unit based on both the double-layer capacitance and pseudocapacitance. **D** GCD with currents of 25, 50, 100, 250 and 500 μA of a SC unit from 0 V to 1 V. **E.** CV with scan rates of 5, 10, 25, 50, 100 mV s^{-1} from 0 V and 1 V of a SC unit. **F.** GCD of the energy storage modules with different configurations, with (i) two storage modules in series; (ii) one storage module; and (iii) two storage modules in parallel. **G** Images of the inward and outward bending of the SC module. Scale bar, 1 cm. **H**. 5 μA GCD of the SC module before and after 1000 cycles of 180º bending deformation. **I**. The areal capacitance and coulombic efficiency of a SC unit in 1000 charge-discharge cycles.

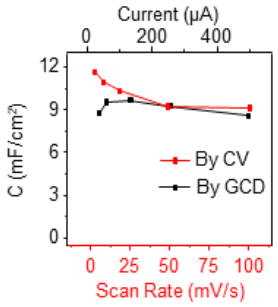

Figure 4.30. Summarized areal capacity of the printed SC characterized using different current in GCD and different scan rates in CV.

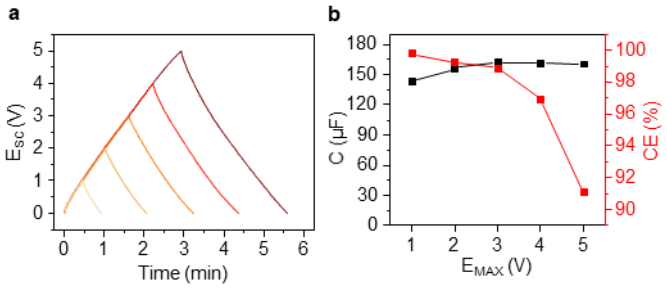

Figure 4.31. Charging efficiency characterization of the SC module.
A. GCD at 5 μA of one SC module between 0 V and the maximum voltage of 1, 2, 3, 4, and 5 V.
B. The summarized capacity and CE at different maximum voltage.

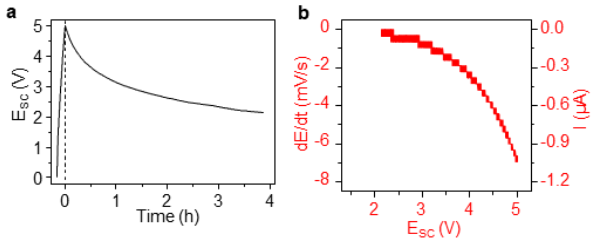

Figure 4.32. Self-discharge of the SC module.
A. Self-discharge of the 150 μF SC module charged to 5V in 4 hours. **B**. The rate of discharging and corresponding self-discharge current at different states of charge of the SC module.

Overall, the washability of the TEG, BFC, and the SC module was tested, which all components has shown stable performance after throughout water washing without detergents (**Figure 4.33**).

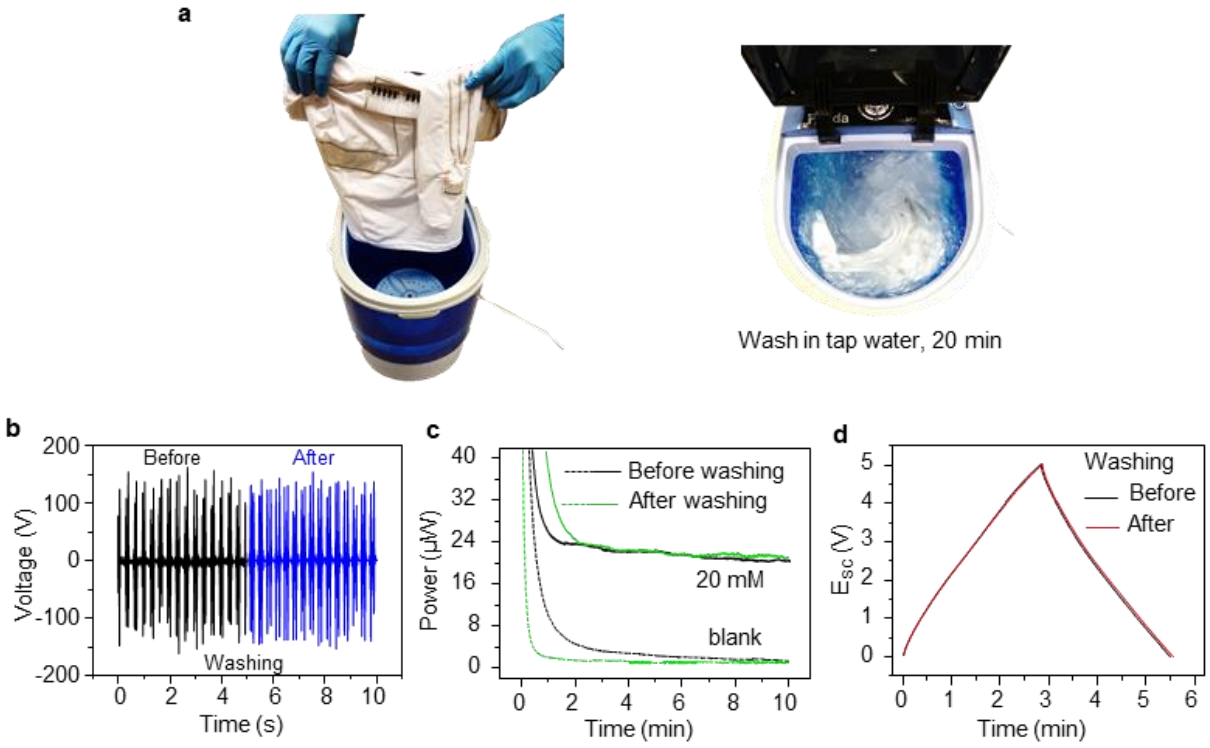

Figure 4.33. Component reliability test under washing tests.
A. Photo demonstrating the washing process of the integrated E-textile system. Room-temperature tap water without detergent was used to wash the shirt using a commercial washing machine for 20 min and dried under ambient environment. **B**. The voltage output of the TEG module before and after the washing test. **C**. The power output of the BFC module before and after the washing test in 0 mM and 20 mM lactate in PBS. **D**. The GCD of the SC module before and after the washing test.

4.3.2 Synergistic Bioenergy harvesting

To demonstrate the synergistic effect of between TEG modules and BFC modules, a typical activity session has been simulated by applying constant 1 Hz - 1.5 Hz sliding motions and spiking of 10 - 15 mM lactate fuel. Using this setting, three scenarios have been simulated: (i)

movement starts followed by the start of perspiration; (ii) movements and perspiration taking place simultaneously; and (iii) movements stop but the perspiration continues. In the 4-min simulations, two TEG modules rectified by a bridge rectifier and one BFC module modulated by a DC voltage booster were used to charge one SC module. Each scenario was tested with only the TEG (blue curve), only the BFC (green curve), and both modules operating together (red curve). As shown in **Figure 4.34 A**, during the starting phase, the TEG module was able to charge the SC module immediately after starting the movement, whereas the BFC module was not able to provide power due to the lack of lactate. When lactate was spiked, the BFC started to respond to the fuel addition to provide power to the SC. The additive effect of integrating two complementary energy harvesters can be observed throughout the rest of the simulation, where their charging speed surpasses the individually operating harvesters. Such additive effect continued throughout the scenario (ii) and the first half of the scenario (iii). As soon as the sliding motion stopped, the TEG module stopped its operation instantaneously. In contrast, the BFC module continued to operate due to the presence of the lactate fuel to charge the SC module without interruption. Beyond the additive effects of two energy harvesters, the advantage of integrating the complementary TEG and BFC modules was demonstrated: at the start of the movement, the fast-booting TEG module can compensate for the slow-booting of the BFC; in return, the transiently harvesting TEG module was compensated by the extended-operating BFC module after the movement stops, as illustrated in **Figure 4.1 B**. This synergistic behavior, not offered by any previous studies, is highly desirable for the reliable and sustainable operation of a self-powered wearable system. As expected, the charging speed of the 1 Hz sliding, 10 mM lactate simulation condition (**Figure 4.34 A i-iii**) was the slowest amongst all three, followed by the 1.5 Hz sliding, 10 mM lactate condition (**Figure 4.34 A iv-vi**), with the 1.5 Hz sliding, 15 mM lactate condition charging the capacitor fastest

(**Figure 4.34 A vii-ix**). In all three situations, the synergistic additive effect was observed in all 3 phases of the condition, and the complementary fast-boosting and extended-harvesting effects were observed for the starting and ending phases of all 3 conditions, correspondingly.

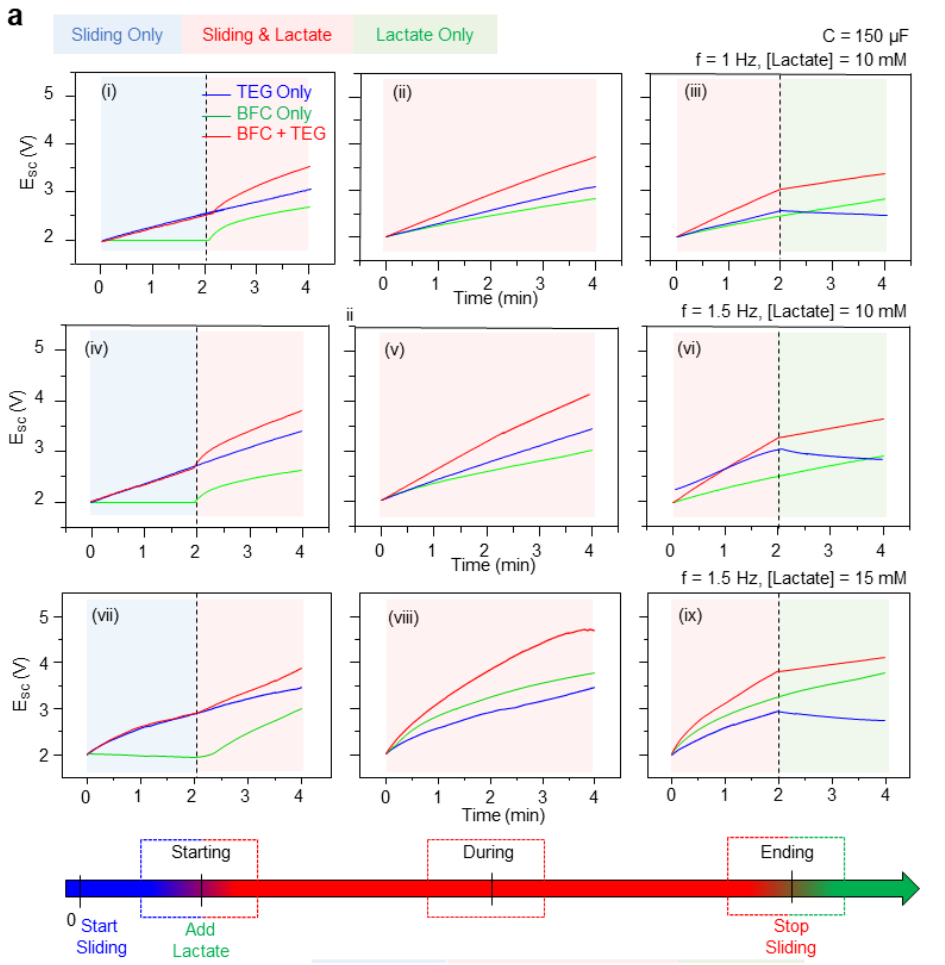

Figure 4.34. In-vitro and on-body charging performance of the wearable bioenergy microgrid system.
A. *In-vitro* charging curves of the individual and integrated harvester with (i)-(iii) 1 Hz frequency and 10 mM lactate; (iv)-(vi) 1.5 Hz frequency and 10 mM lactate; and (vii)-(ix) 1.5 Hz and 15 mM lactate for the TEG modules and the BFC modules, which simulate three representative phases: starting ((i), (iv), and (vii)), exercising((ii), (v), and (viii)) and ending((iii), (vi), and (ix)) of an activity session.

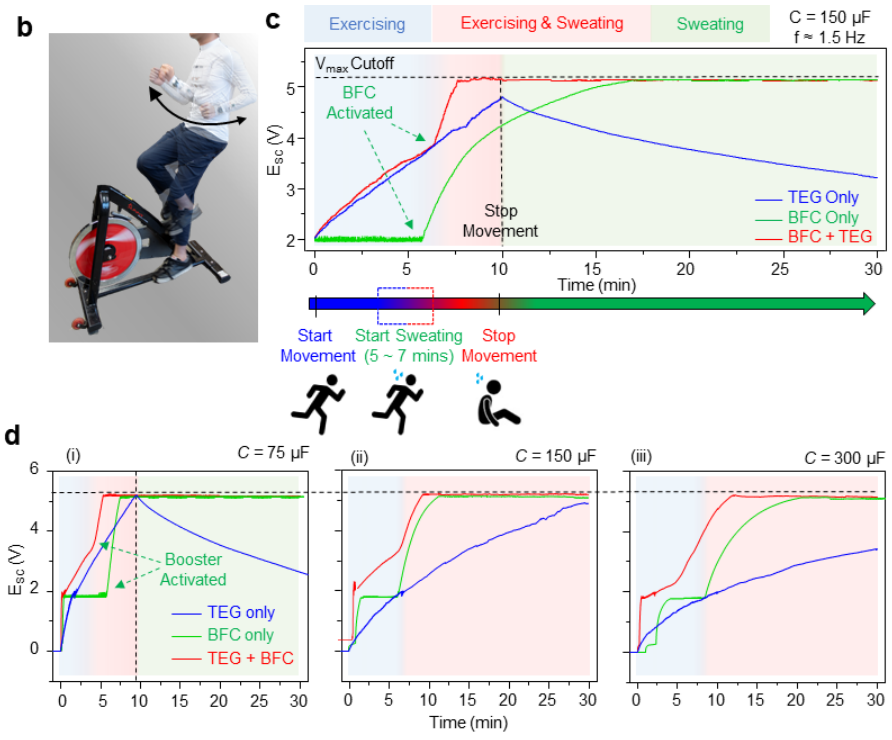

Figure 4.34. In-vitro and on-body charging performance of the wearable bioenergy microgrid system. (Continued)
B. Photo illustration of the on-body testing arrangement. **C**. On-body charging of a 150 μF SC using the individual BFC or TEG module alone, and with both modules combined, in a 10-min exercise session followed by a 20-min resting. **D**. On-body charging of capacitors from SCs with (i) 75 μF, (ii) 150 μF, and (iii) 300 μF from 0 V in a 30-min exercise session to represent the charging of the system including the cold-starting phase of the voltage-booster. During the 30-min period, movement stops once the SC if fully charged to 5.1 V.

The synergistic effect of the integrated energy harvesting was further characterized with on-body tests to gauge the optimal capacitance that can mostly reflect such complementary fast-booting and extended-harvesting effects. Two TEG, two BFC and the corresponding SC modules were printed on the left and right sides of the waist, below the collar and in front of a shirt, respectively, as shown in **Figure 4.1 C**, and were connected via printed silver traces and enameled wires with proper insulations. A PVA-based PBS hydrogel was applied onto the BFC module for sweat capturing. A 10-min exercise session was carried out on a cycling machine, as illustrated in

Figure 4.34 B, where the arm-swinging frequency was kept near 1.5 Hz, followed by 20 min of resting. Similar to the in-vitro simulation, the integrated on-body system was tested with only TEG, only BFC and with all harvesters operating together. **Figure 4.34 C** demonstrates the on-body energy harvesting performance of the integrated system. For the system operating solely on TEG modules, the energy harvesting started immediately after the arm-swinging started and charged the SC module continuously throughout the 10-min exercise session. As soon as the movement stopped, the TEG stopped supplying power, and the SC module slowly self-discharged. For the system operated solely on the BFC module, the system suffered from slow booting with a 6-min delay. However, the BFC was able to supply power to the SC module quickly after sweating started, and fully charged the SC within 17 min. Upon stopping the exercise, the BFC module was able to continuously supply power to the SC module over a 30-min period, reflecting the continuous presence of sweat. Lastly, the integrated system was able to compensate for both the slow booting and the transient harvesting, quickly fully charging the SC module in 7 min, maintaining maximum voltage over a 30-min period. In addition to the data presented in **Figure 4.34 C**, the on-body operation of the system was also tested with SC modules configurated with the capacitance of 75 μF, 150 μF, and 300 μF (**Figure 4.34 D**). The charging is started at 0 V instead of 2 V to demonstrate the booting of the voltage booster in the start of the operation. The SC modules were fully discharged to 0 V and their potential monitored during charging, and the exercise sessions were only stopped when the SC is fully charged to 5.1 V or the limit of 30 min was reached. As shown in the figure, the time taken to fully charge the SC module increased as the capacitance increased for both the individual harvesters and the integrated microgrid harvesters. The synergistic and complementary behavior can still be observed in the booting phase of the charging, where the integrated harvesting system can fully charge the SC module faster than the individual

harvesters, starting from the 4 min for 75 μF capacitor, to the 8 min for 150 μF capacitor and 12 min for the 300 μF capacitor. These results have thus validated the in-vitro simulation, fully illustrating the complementary and synergistic behaviors of the wearable microgrid system which offers fast-booting and extended-harvesting for energy harvesting in an activity session.

Two wearable applications were selected as examples of two operating modes for demonstrating the potential and advantages of the wearable microgrid system (**Figure 4.35 A**). The SC is an attractive energy storage module owing to its flexible discharge rates that allow powering of either low-power application continuously or of high-power application in a brief, pulsed fashion without damaging the module. For efficiently use the limited energy stored in the SC modules, the power consumption of the applications was characterized, and the SC modules were configured with minimum but sufficient capacitance for rapid booting while ensuring successful operation.

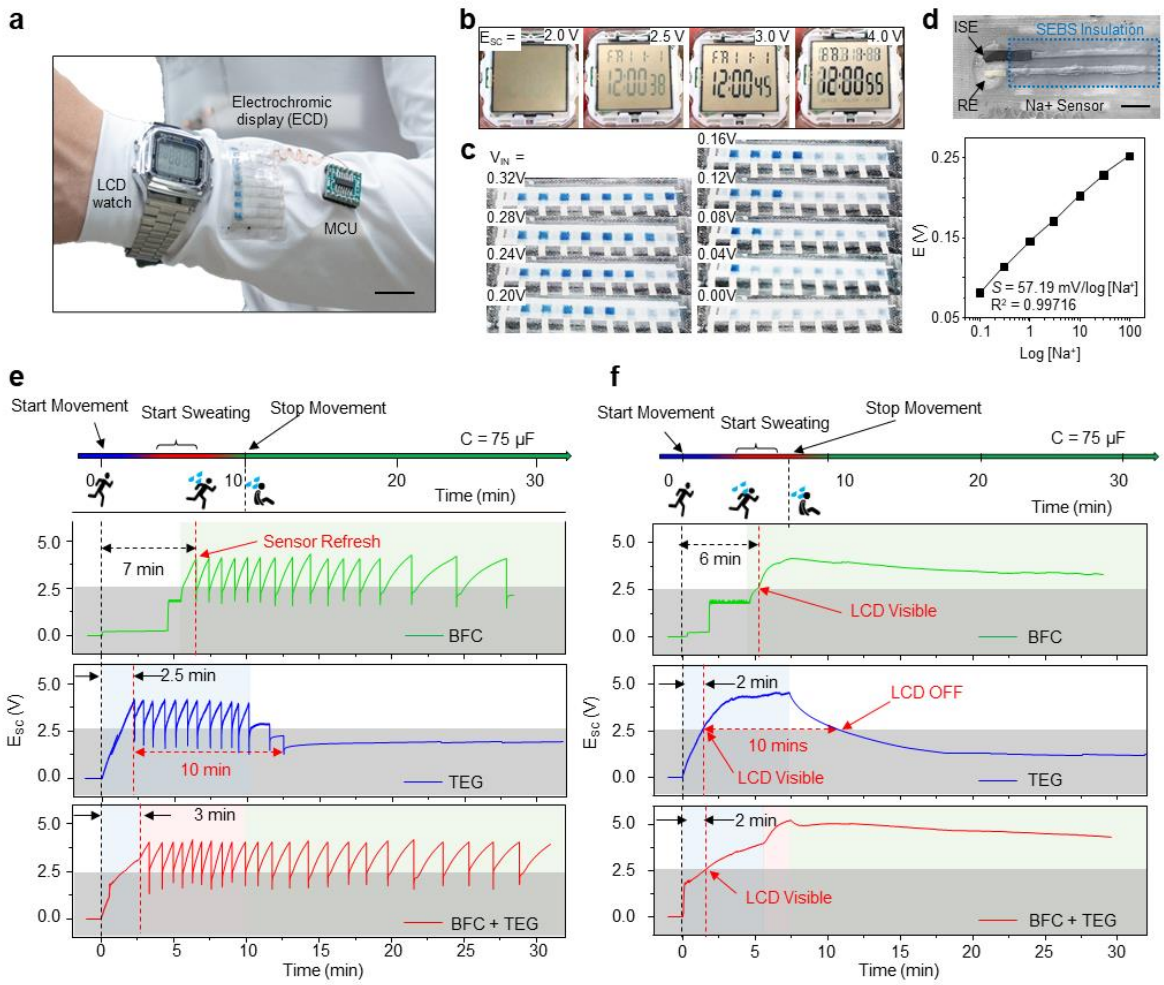

Figure 4.35. Wearable bioenergy microgrid system with different applications.
A. Image of the LCD wristwatch and the ECD for the Na^+ potentiometric sensor. Scale bar, 1 cm. **B**. Images of the LCD screen with different input voltages. **C**. The display of the ECD with different sensor voltage input. **D**. The photo image of the all-printed flexible potentiometric sensor (top) and the calibration curve of the Na^+ sensor (bottom). Scale bar, 2 mm. **E-F**. Voltage vs. time curves of the wearable microgrid system powering the Na^+ sensor-ECD system in pulsed mode during a 10-min running session followed by 20 min of rest, with only the BFC module operating, only the TEG module operating, and both harvesters operating together (**E**); and the LCD wristwatch continuously during a 7-min running session followed by 23 min of rest (**F**).

A textile-based sodium ion (Na^+) sensor integrated with a wearable, flexible ECD pixeled display was developed as an example for applications with higher power demand operating in pulsed mode. The developed potentiometric Na^+ sensor exhibited a near-Nernstian response to the

concentration of the Na^+ target, with a potential change of 57.19 mV per decade of concentration change (**Figure 4.35 D**). The sensor output can be instantly read by the pre-programmed integrated circuit and reported by changing the color of individually controlled ECD pixels, as illustrated in **Figure 4.35 C**. The operation of the ECD pixels follows the simple reversible redox reaction of the PEDOT:PSS,

$$PEDOT^+PSS^- + Na^+ + e^- \leftrightarrow PEDOT^0 + Na^+PSS^- \qquad \textbf{(Equation 4.6)}$$

that takes place when a voltage above +1 V is applied to the back-panel electrodes, and the reduction reaction take place on the front panel and turn its color from light blue to dark blue. A low-power microcontroller unit (MCU) was selected for reading the input from the Na^+ sensor and controlling the on/off of the individual ECD pixels. The ECD is able to refresh rapidly and maintain the display without a continuous supply of power.

The controller was pre-programmed to display potential up to 0.32 V, with each ECD pixel corresponding to one 0.04 V increment of the sensor output. The power consumption of the microcontroller connected to the sensor-ECD system was measured similarly using the potentiostat set at different voltage, as demonstrated in **Figure 4.36**. As shown, the power consumption of the microcontroller exceeded the wristwatch by 3 orders of magnitude, ranging from 4 mW at 2 V to 30 mW at 5 V. Yet, the microcontroller was able to boot quickly within the first 50 ms, take readings and apply signals to the ECD pixels within the first 200 ms, which allow this system to be powered transiently from the discharge of one charged capacitor. The energy consumed by one discharge session can be estimated by the equation:

$$\boldsymbol{E = P \times t} \qquad \textbf{(Equation 4.7)}$$

where *E* is the energy in J, *P* is the power in W, and *t* is the time in s. To supply 200 ms of operation assuming the lowest power of ca. 4-5 mW, the energy required was thus estimated to be ca. 0.8 – 1 mJ. Capacitors ranging from 100 μF to 470 μF were able to supply sufficient energy to the microcontroller in one continuous discharge session with the larger capacitors had shown no substantial extended operation time (**Figure 4.36 B**). The capacitors were discharged with 200 ms pulsed discharge, where more differences were more pronounced. The higher capacitance capacitors were able to sustain multiple refresh sessions, and the number of sessions decreases with the capacitance, as to 1 successful discharge session from the 100 μF with a slightly excess amount of energy, and 1 discharge from the 47 μF capacitor which did not last throughout the entire 200 ms session (**Figure 4.36 C**). It is thus determined that the 75 μF SC modules should retain enough energy to sustain one complete refresh session. The required state of charge of the SC was then characterized by charging the 75 μF SC module to different potentials, and use the SC to power one refresh session, while the color on the ECD recorded to determine the minimum state of charge required for the 75 μF SC module to induce color change with sufficient contrast (**Figure 4.37**). It can be observed that the contrast of the on and off pixels gradually decreased with the initial state of charge of the SC modules, with the difference barely recognizable below 3.5 V. The minimum potential of 4 V before initiating a refresh session was thus decided. To confirm with the calculation above on the energy required for one operation session, the energy stored in the capacitor was calculated using equation:

$$E_{SC} = \frac{1}{2}C(V_i^2 - V_f^2) \qquad \textbf{(Equation 4.8)}$$

where E_{SC} is the energy discharged from the SC in J, *C* is the capacitance of the SC in F, V_i^2 is the potential of the SC before the discharge in V, and V_f^2 is the potential of the SC after the discharge

in V. For a 75 µF SC to discharge from 4 V to 1.25 V, the energy released from the discharge is thus calculated to be 0.88 mJ, which agreed with the previous calculation based on **Equation 4.7**. The 75 µF SC modules with a threshold voltage of 4 V was thus selected to allow fast booting while providing sufficient energy for a successful sense-refresh session.

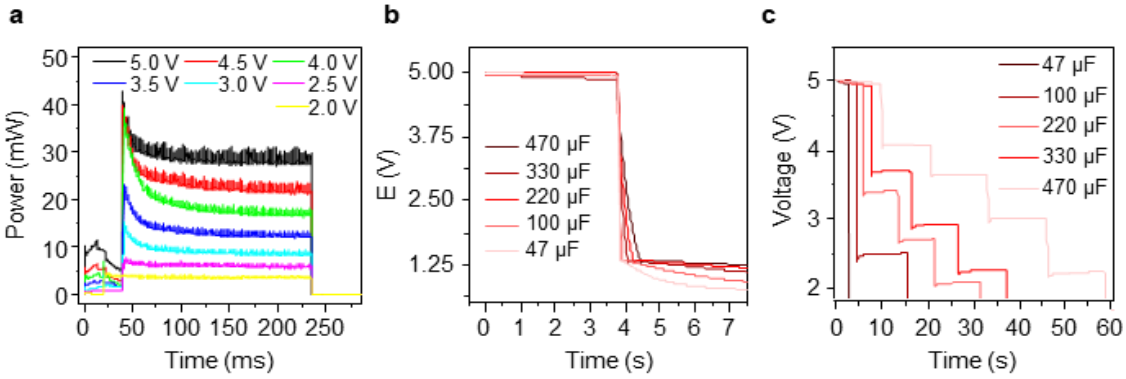

Figure 4.36. Characterizing the power consumption of the MCU.
A. The power consumption with different input voltages within a 200 ms operation session. **B**. The continuous discharge profile of different capacitors charged to 5 V to power the microcontroller. **C**. The repeated pulsed discharge profile of different capacitors charged to 5 V to power the microcontroller.

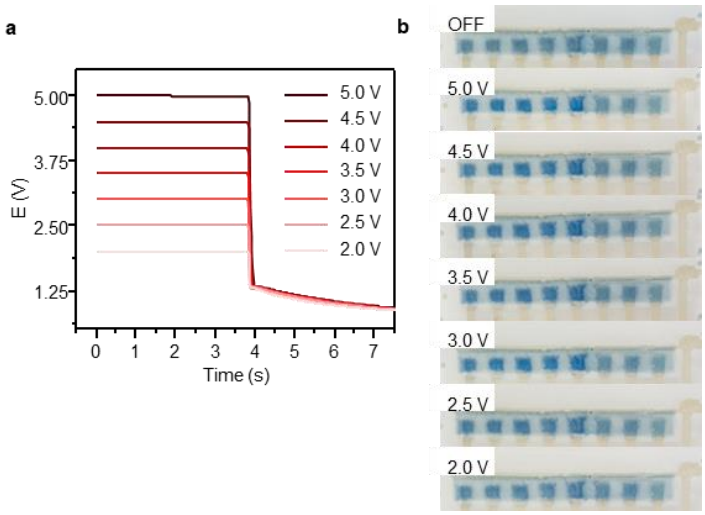

Figure 4.37. Analyzing the minimum energy needed to power the MCU-ECD sensing system. **A**. Continuous discharge by the sensor-ECD system of the 75 μF SC module that was charged to a different state of charge and **B**. the corresponding color change on the ECD.

The integrated wearable sensor-ECD application was integrated into the microgrid and tested on the body in a 10-min exercise session. As shown in **Figure 4.35 E**, the SC module was charged up to 4 V and discharged to refresh the sensor-ECD system. The fully integrated microgrid system was able to boot quickly within 3 min and intermittently refresh the results during the 30-min operation. In comparison, the BFC module suffered from slow booting due to delayed perspiration while the TEG modules were not able to sustain the operation after stopping the movement. It is worth noting that the faster boosting speed for the TEG-only scenario is due to the lack of need to supply a small amount of energy to boost the voltage booster. In both applications with different modes of operation, the wearable microgrid system - with its complementary and synergistic BFC-TEG harvesting and commensurate SC pairing - was able to deliver both fast-booting and extended-harvesting to ensure the autonomous and sustainable operation of the wearable platforms.

A low-power wristwatch with a liquid crystal display (LCD) was chosen as a representative application that is continuously powered by the wearable microgrid system. The voltage of 2.5 V is determined as the turn-on threshold voltage, corresponding to the minimum voltage for the LCD to display with sufficient contrast (**Figure 4.35 B**). The power consumption of the watch was rated below 10 μW which has low requirement in storage unit (**Figure 4.38**). Two SC modules connected in-series with the capacity of 75 μF were selected to offer fast booting while maintaining extended operation when the microgrid harvests from human activities. Short, 8-min exercise sessions were carried out, with the potential of the SC recorded continuously. As illustrated in **Figure 4.35 F**, the simultaneous BFC-TEG energy harvesting was able to quickly boot the wristwatch within 2 min and maintain its continuous operation for over 30 min. In contrast, the BFC-only system suffered from slow booting while the TEG-only system can only maintain the operation for a short time period before the SC module voltage dropped to below 2.5 V.

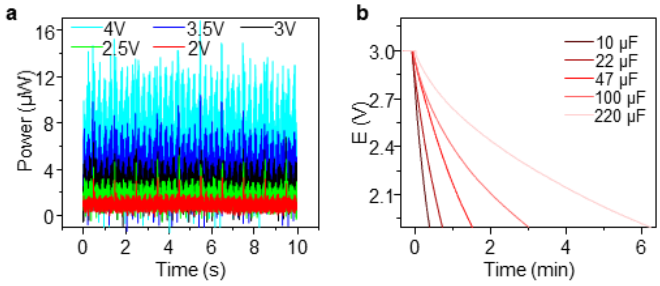

Figure 4.38. Characterizing the power consumption of the wristwatch.
A. the power consumption of the wristwatch when supplying a different level of voltage. **B**. the discharge of capacitors charged to 3 V when connected to the wristwatch.

4.4 Conclusion

In summary, we have demonstrated the concept of wearable bioenergy microgrid via a textile-based multi-module system for sequentially harvesting biomechanical and biochemical energy via the TEG and BFC modules. The microgrid can store and regulate the harvested energy via efficiently paired SC modules to efficiently power wearable applications such as an LCD wristwatch and a sensor-ECD system. Implementing the "compatible, complementary, and commensurate" design principles, all modules were carefully characterized and efficiently integrated to deliver power using the limited amount of harvested energy rapidly, autonomously and sustainably. All printed modules, printed with polymer-based composite inks, are flexible, durable, and ready for seamless integration on textile platforms. Compared to previous integration of wearable energy harvesting and storage devices, this work focuses on the complementary relationship between two bioenergy harvesters that perform synergistically to scavenge energy from human motion, and their pairing with storage modules with commensurate capacity for maximized efficiency and performance. With the optimized pairing of components, such wearable microgrid can quickly boot selected applications while sustaining their operation substantially longer than the exercise sessions, hence ensuring the reliability and practicality of the wearable system. To further improve such E-textile microgrid system, more modular design concepts, such as fabricating patch-like detachable and swappable harvesters, storage devices, and sensors, can be adapted to extend the usage and applicable scenario of the E-textile system. While serving here as an example, such microgrid strategy inspires future miniaturized integrated systems that harvest thermal, chemical or mechanical energies to select complementary, synergistic, commensurate and compatible components for their designated use case. The configuration of the harvesters' connection can also be further explored: instead of parallelly operating harvesters, serial

connections between harvesters of the same type or different types can be considered to increase the output voltage and minimize or eliminate the need for voltage regulation. Future work in developing energy harvesting devices that rely on the harvesting from passive activities will broaden the applicable scenarios and enhance the practicality of the microgrid system. Expanding the microgrid concept from on-body to in-body applications and utilizing the abundant amount of biofuel and biomechanical movements within the body can also allow integrated harvesting system for self-powered implantable or ingestible sensing that are no longer limited by external environment or the need for exercise. Upon improving the power density of various harvesters, high-capacity energy storage options with commensurate rating can also be considered for powering of a wider range of electronics for advanced functionalities. The concept of wearable microgrids and their design principles are thus expected to promote system-level considerations for integrating various new-form-factor modules towards truly self-powered, autonomous, and sustainable systems.

Chapter 4, in full, is a reprint of the material as it appears in Nature Communications, 2021, by Lu Yin, Kyeong Nam Kim, Jian Lv, Farshad Tehrani, Muyang Lin, Zuzeng Lin, Jong-Min Moon, Jessica Ma, Jialu Yu, Sheng Xu, and Joseph Wang. The dissertation author, Kyeong Nam Kim, and Jian Lv were the primary investigators and co-authors of this paper.

4.5 References

1. Kim, J., Campbell, A. S., de Ávila, B. E. F. & Wang, J. Wearable biosensors for healthcare monitoring. *Nat. Biotechnol.* **37**, 389–406 (2019).

2. Gao, W. *et al.* Fully integrated wearable sensor arrays for multiplexed in situ perspiration analysis. *Nature* **529**, 509–514 (2016).

3. Gong, S. & Cheng, W. Toward Soft Skin-Like Wearable and Implantable Energy Devices. *Adv. Energy Mater.* **7**, 1700648 (2017).

4. Gong, S. *et al.* A wearable and highly sensitive pressure sensor with ultrathin gold nanowires. *Nat. Commun.* **5**, 3132 (2014).

5. Wang, C. *et al.* Monitoring of the central blood pressure waveform via a conformal ultrasonic device. *Nat. Biomed. Eng.* **2**, 687–695 (2018).

6. Lee, H. *et al.* A graphene-based electrochemical device with thermoresponsive microneedles for diabetes monitoring and therapy. *Nat. Nanotechnol.* **11**, 566–572 (2016).

7. Wang, L. *et al.* Weaving Sensing Fibers into Electrochemical Fabric for Real-Time Health Monitoring. *Adv. Funct. Mater.* **28**, 1804456 (2018).

8. Xu, S. *et al.* Stretchable batteries with self-similar serpentine interconnects and integrated wireless recharging systems. *Nat. Commun.* **4**, 1543 (2013).

9. Kumar, R. *et al.* All-Printed, Stretchable Zn-Ag_2O Rechargeable Battery via Hyperelastic Binder for Self-Powering Wearable Electronics. *Adv. Energy Mater.* **7**, 1602096 (2017).

10. Fan, F. R., Tian, Z. Q. & Lin Wang, Z. Flexible triboelectric generator. *Nano Energy* **1**, 328–334 (2012).

11. Bandodkar, A. J. *et al.* Soft, stretchable, high power density electronic skin-based biofuel cells for scavenging energy from human sweat. *Energy Environ. Sci.* **10**, 1581–1589 (2017).

12. Hashemi, S. A., Ramakrishna, S. & Aberle, A. Recent Progress in Flexible-Wearable Solar Cells for Self-Powered Electronic Devices. *Energy Environ. Sci.* **13**, 685-743 (2020).

13. Dong, K., Peng, X. & Wang, Z. L. Fiber/Fabric-Based Piezoelectric and Triboelectric Nanogenerators for Flexible/Stretchable and Wearable Electronics and Artificial Intelligence. *Adv. Mater.* **32**, 1902549.

14. Kim, B. J. *et al.* Highly efficient and bending durable perovskite solar cells: Toward a wearable power source. *Energy Environ. Sci.* **8**, 916–921 (2015).

15. Xiong, J. *et al.* Skin-touch-actuated textile-based triboelectric nanogenerator with black phosphorus for durable biomechanical energy harvesting. *Nat. Commun.* **9**, 1–9 (2018).

16. Yu, Y. *et al.* Biofuel-powered soft electronic skin with multiplexed and wireless sensing for human-machine interfaces. *Sci. Robot.* **5**, 7946 (2020).

17. Lv, J. *et al.* Sweat-based wearable energy harvesting-storage hybrid textile devices. *Energy Environ. Sci.* **11**, 3431–3442 (2018).

18. Xu, C., Pan, C., Liu, Y. & Wang, Z. L. Hybrid cells for simultaneously harvesting multi-type energies for self-powered micro/nanosystems. *Nano Energy* **1**, 259–272 (2012).

19. Vosgueritchian, M., Lipomi, D. J. & Bao, Z. Highly Conductive and Transparent PEDOT:PSS Films with a Fluorosurfactant for Stretchable and Flexible Transparent Electrodes. *Adv. Funct. Mater.* **22**, 421–428 (2012).

20. Lee, Y.-H. *et al.* Wearable Textile Battery Rechargeable by Solar Energy. *Nano Lett.* **13**, 5753–5761 (2013).

21. Shi, B. *et al.* Body-Integrated Self-Powered System for Wearable and Implantable Applications. *ACS Nano* **13**, 6017–6024 (2019).

22. Jung, S. *et al.* Wearable Fall Detector using Integrated Sensors and Energy Devices. *Sci. Rep.* **5**, 1–9 (2015).

23. Li, C. *et al.* Flexible perovskite solar cell-driven photo-rechargeable lithium-ion capacitor for self-powered wearable strain sensors. *Nano Energy* **60**, 247–256 (2019).

24. Chen, J. *et al.* Micro-cable structured textile for simultaneously harvesting solar and mechanical energy. *Nat. Energy* **1**, 16138 (2016).

25. Wen, Z. *et al.* Self-powered textile for wearable electronics by hybridizing fiber-shaped nanogenerators, solar cells, and supercapacitors. *Sci. Adv.* **2**, e1600097 (2016).

25. Chen, T. *et al.* An Integrated "Energy Wire" for both Photoelectric Conversion and Energy Storage. *Angew. Chem. Int. Ed.* **51**, 11977–11980 (2012).

26. Zhang, Z. *et al.* Integrated Polymer Solar Cell and Electrochemical Supercapacitor in a Flexible and Stable Fiber Format. *Adv. Mater.* **26**, 466–470 (2014).

28. Yang, Y. & Wang, Z. L. Hybrid energy cells for simultaneously harvesting multi-types of energies. *Nano Energy* **14**, 245–256 (2014).

29. Pu, X. *et al.* Wearable Power-Textiles by Integrating Fabric Triboelectric Nanogenerators and Fiber-Shaped Dye-Sensitized Solar Cells. *Adv. Energy Mater.* **6**, 1601048 (2016).

30. Zhang, Q. *et al.* Green hybrid power system based on triboelectric nanogenerator for wearable/portable electronics. *Nano Energy* **55**, 151–163 (2019).

31. Issa, W. R., Khateb, A. H. E., Abusara, M. A. & Mallick, T. K. Control Strategy for Uninterrupted Microgrid Mode Transfer during Unintentional Islanding Scenarios. *IEEE*

Trans. Ind. Electron. **65**, 4831–4839 (2018).

32. Khan, F. Resilience in numbers. *Nature Energy* **3**, 1020 (2018).

33. Tanrioven, M. Reliability and cost-benefits of adding alternate power sources to an independent micro-grid community. *J. Power Sources* **150**, 136–149 (2005).

34. He, G., Chen, Q., Moutis, P., Kar, S. & Whitacre, J. F. An intertemporal decision framework for electrochemical energy storage management. *Nat. Energy* **3**, 404–412 (2018).

35. Cader, C., Bertheau, P., Blechinger, P., Huyskens, H. & Breyer, C. Global cost advantages of autonomous solar-battery-diesel systems compared to diesel-only systems. *Energy Sustain. Dev.* **31**, 14–23 (2016).

36. Szabó, S., Bódis, K., Huld, T. & Moner-Girona, M. Energy solutions in rural Africa: Mapping electrification costs of distributed solar and diesel generation versus grid extension. *Environ. Res. Lett.* **6**, 034002 (2011).

37. Ou, T. C. & Hong, C. M. Dynamic operation and control of microgrid hybrid power systems. *Energy* **66**, 314–323 (2014).

38. Alsaidan, I., Khodaei, A. & Gao, W. A Comprehensive Battery Energy Storage Optimal Sizing Model for Microgrid Applications. *IEEE Trans. Power Syst.* **33**, 3968–3980 (2018).

39. Pan, C., Li, Z., Guo, W., Zhu, J. & Wang, Z. L. Fiber-Based Hybrid Nanogenerators for/as Self-Powered Systems in Biological Liquid. *Angew. Chem. Int. Ed.* **50**, 11192–11196 (2011).

40. Hansen, B. J., Liu, Y., Yang, R. & Wang, Z. L. Hybrid nanogenerator for concurrently harvesting biomechanical and biochemical energy. *ACS Nano* **4**, 3647–3652 (2010).

41. Li, H. *et al.* A Hybrid Biofuel and Triboelectric Nanogenerator for Bioenergy Harvesting. *Nano-Micro Lett.* **12**, 1–12 (2020).

42. Zou, H. *et al.* Quantifying the triboelectric series. *Nat. Commun.* **10**, 1–9 (2019).

43. Xie, Y. *et al.* Grating-Structured Freestanding Triboelectric-Layer Nanogenerator for Harvesting Mechanical Energy at 85% Total Conversion Efficiency. *Adv. Mater.* **26**, 6599–6607 (2014).

44. Lin, L. *et al.* Segmentally structured disk triboelectric nanogenerator for harvesting rotational mechanical energy. *Nano Lett.* **13**, 2916–2923 (2013).

45. Guo, H. *et al.* A Water-Proof Triboelectric-Electromagnetic Hybrid Generator for Energy Harvesting in Harsh Environments. *Adv. Energy Mater.* **6**, 1501593 (2016).

46. Zhu, G. *et al.* Linear-grating triboelectric generator based on sliding electrification. *Nano*

Lett. **13**, 2282–2289 (2013).

47. Sakharov, D. A. *et al.* Relationship between lactate concentrations in active muscle sweat and whole blood. *Bull. Exp. Biol. Med.* **150**, 83–85 (2010).

48. Yin, L. *et al.* Highly Stable Battery Pack via Insulated, Reinforced, Buckling-Enabled Interconnect Array. *Small* **14**, 1800938 (2018).

49. Chen, X. *et al.* Stretchable and Flexible Buckypaper-Based Lactate Biofuel Cell for Wearable Electronics. *Adv. Funct. Mater.* **29**, 1905785 (2019).

50. Jeerapan, I., Sempionatto, J. R., Pavinatto, A., You, J.-M. & Wang, J. Stretchable biofuel cells as wearable textile-based self-powered sensors. *J. Mater. Chem. A* **4**, 18342–18353 (2016).

51. Harvey, C. J., LeBouf, R. F. & Stefaniak, A. B. Formulation and stability of a novel artificial human sweat under conditions of storage and use. *Toxicol. Vitr.* **24**, 1790–1796 (2010).

52. Lalaoui, N., Le Goff, A., Holzinger, M. & Cosnier, S. Fully Oriented Bilirubin Oxidase on Porphyrin-Functionalized Carbon Nanotube Electrodes for Electrocatalytic Oxygen Reduction. *Chem. - A Eur. J.* **21**, 16868–16873 (2015).

53. Bandodkar, A. J., Jeerapan, I., You, J. M., Nuñez-Flores, R. & Wang, J. Highly Stretchable Fully-Printed CNT-Based Electrochemical Sensors and Biofuel Cells: Combining Intrinsic and Design-Induced Stretchability. *Nano Lett.* **16**, 721–727 (2016).

54. Tehrani, F. *et al.* Laser-Induced Graphene Composites for Printed, Stretchable, and Wearable Electronics. *Adv. Mater. Technol.* **4**, 1900162 (2019).

55. Yin, L. *et al.* From All-Printed 2D Patterns to Free-Standing 3D Structures: Controlled Buckling and Selective Bonding. *Adv. Mater. Technol.* **3**, 1800013 (2018).

Chapter 5 High Energy Return-on-investment Autonomous Sensing System

5.1 Introduction

Wearable electronics have witnessed tremendous growth over the past decade.[1] Current wearable electronics are predominately powered by miniaturized electrochemical energy storage devices (e.g., batteries, supercapacitors), with limited energy and power density that cannot power the electronics over extended operational time.[2] To address this challenge, researchers have focused on reducing energy consumption while introducing energy harvesters to offer extended system runtime.[3–5] Self-powered sensors that autonomously generate signals can reduce the system power consumption but cannot provide sufficient energy to the electronics for the actual measurement or data transmission.[6,7] Recent progress in energy harvesters has enabled self-sustainable systems that continuously harvest energy from sunlight, movements, temperature gradients, or biofuels to power the sensors and electronics intermittently or continuously.[3,5,8–11] Unfortunately, harvesters based on an inconsistent external environment cannot supply energy on command, while mechanical and biochemical energy harvesters require vigorous movement and with high mechanical energy investment, thus are highly inefficient, inconvenient, and lack practicality. An energy harvester relying on a passive constant input from the human body, not relying on irregular external environment nor movements and exercises, is therefore considered a holy grail of energy harvesting devices.

Among all aforementioned energy harvesters, lactate-based biofuel cells (BFCs) have shown considerable promise as self-powered sensors and bioenergy harvesters for powering electronics.[3,12] Relying on the high lactate concentration in human sweat, epidermal BFCs can readily generate energy using a lactate oxidase (LOx) bioanode complemented by the oxygen

reduction reaction (ORR) on the cathode.[13] However, despite their great potential for powering wearable electronic devices, the ability to exploit the rich sweat bioenergy has been hindered by the inherent inaccessibility of natural sweat. While sweat is autonomously generated from the human body in most of the epidermal spaces, its flow rate is extremely low for realizing efficient bioenergy harvesting. Thus, wearable BFCs commonly require vigorous and extended exercise before a sizable amount of sweat can accumulate onto the bioelectrodes for power generation.[10] While epidermal BFCs with high power density have been reported[3,12], the operation of such BFC-powered systems requires massive energy input towards continuous sweat generation, resulting in extremely low conversion efficiency (<1 %) when accounting for the mechanical energy input (**Table 5.1**).[10,14] Alternative approaches for accessing sweat biofuels without intensive exercise are thus urgently needed for routine and practical applications of BFCs in wearable systems.

Table 5.1. Comparison of the energy return of investment (ROI) of various wearable bioenergy harvesters.

Type of harvester	Average Power input*	Power harvested*	Max. Energy ROI*,**	Max. active time in a day(%)*	Ref
Biofuel cell (exercise)	Running/Cycling $10^2 – 10^3$ W	$10^{-5} – 10^{-3}$ W cm^{-2}	0.001%	5%	20–23
Piezoelectric/ triboelectric generator	Finger moving $10^{-3} – 10^{-4}$ W	$10^{-10} – 10^{-7}$ W cm^{-2}	1%	10%	
	Hand moving 0.1 – 1 W	$10^{-6} – 10^{-4}$ W cm^{-2}	0.1%	5%	
	Arm moving 1 – 10 W	$10^{-6} – 10^{-4}$ W cm^{-2}	0.01%	10%	
	Walking 50 -100 W Running 100 - 1000 W	$10^{-6} – 10^{-2}$ W cm^{-2}	0.01%	10%	
Biofuel cell (natural sweat)	Finger contact/pressing $0 – 10^{-5}$ W	10^{-5}W cm^{-2}	1000% - ∞	100%	This work

*Numbers are only accurate to the order of magnitude.
**Assume device area of 10^1 cm^2.

Herein, we present the development of a high energy return-on-investment (EROI) harvesting device powered by natural, passive fingertip sweat and does not require mechanical input to instantly generate power. Differ from energy conversion efficiency, EROI describes the ratio between the harvested energy and the actively invested energy for activating the harvesters that would not be required otherwise. An extremely high EROI is critical for the long-term practicality and viability of energy harvesting processes and should be critically considered in the development of wearable power sources towards a sustainable operation of wearable electronics. Optimized for collecting the natural perspiration from a finger, we developed here a flexible, porous, water-wicking 3-dimensional (3D) carbon nanotube (CNT) foam as the BFC electrodes and decorated the foam with LOx and nanoporous Pt on the anodic and cathodic sites for lactate oxidation and oxygen reduction, respectively, for bioelectrocatalytic power generation (**Figure 5.1 A**, **Figure 5.2**, **Figure 5.3**, and **Figure 5.4**). Unlike other body locations, the sweat rate on the fingertip is considerably high (80 - 160 g h^{-1}).[15] Recent reports demonstrated the advantages of such fingertip natural perspiration for sweat analysis compared to common sweat simulation methods (such as exercise, iontophoresis, or heats).[16,17] Such efficient fingertip sweat generation is extremely attractive for powering BFCs without the need for any sweat-inducing exercise. Porous polyvinyl alcohol (PVA) hydrogel was further employed to eliminate the Laplace pressure of sweat droplets for facilitating continuous sweat transfer from the fingertip to the BFC electrodes, while retaining the fuel toward continuous harvesting (**Figure 5.1 B**, **Figure 5.5**).[18,19] The finger contact-based BFC can harvest continuously 300 mJ of energy per cm^2 over 10 h of sleep without any mechanical input or over 30 mJ energy per hour from a single press of a finger that consumes merely 0.5 mJ mechanical energy, resulting in a 6000% high EROI; repeated touching results in refueling and enhanced convection, and can further boost the power to harvest more energy over

a shorter time period (**Figure 5.1 C**). Implementing the microgrid design concept for self-powered electronic systems,[10] this contact-based BFC has been combined with a lead zirconate titanate (PZT) piezoelectric generator to further increase the harvesting efficiency from the press of a finger, thus achieving synergistic energy scavenging (**Figure 5.1 D**). As a practical application, such efficient hybrid harvesters were used to power an electronic sensing system that contains vitamin C or sodium ion sensors with dedicated low-power electrochromic display (ECD), to operate independently from external devices (**Figure 5.1 E**). Overall, the described touch based BFC harvester demonstrates the most favorable energy EROI ever reported among all bioenergy harvesters (**Table 5.1**) and sets higher standards in the bioenergy collection efficiency of wearable harvesters. The paradigm shift from "work for power" to "live to power" greatly enhances the practicality of existing on-body bioenergy harvesting technologies and offers possibilities of establishing reliable and independent next-generation self-sustainable electronics systems.

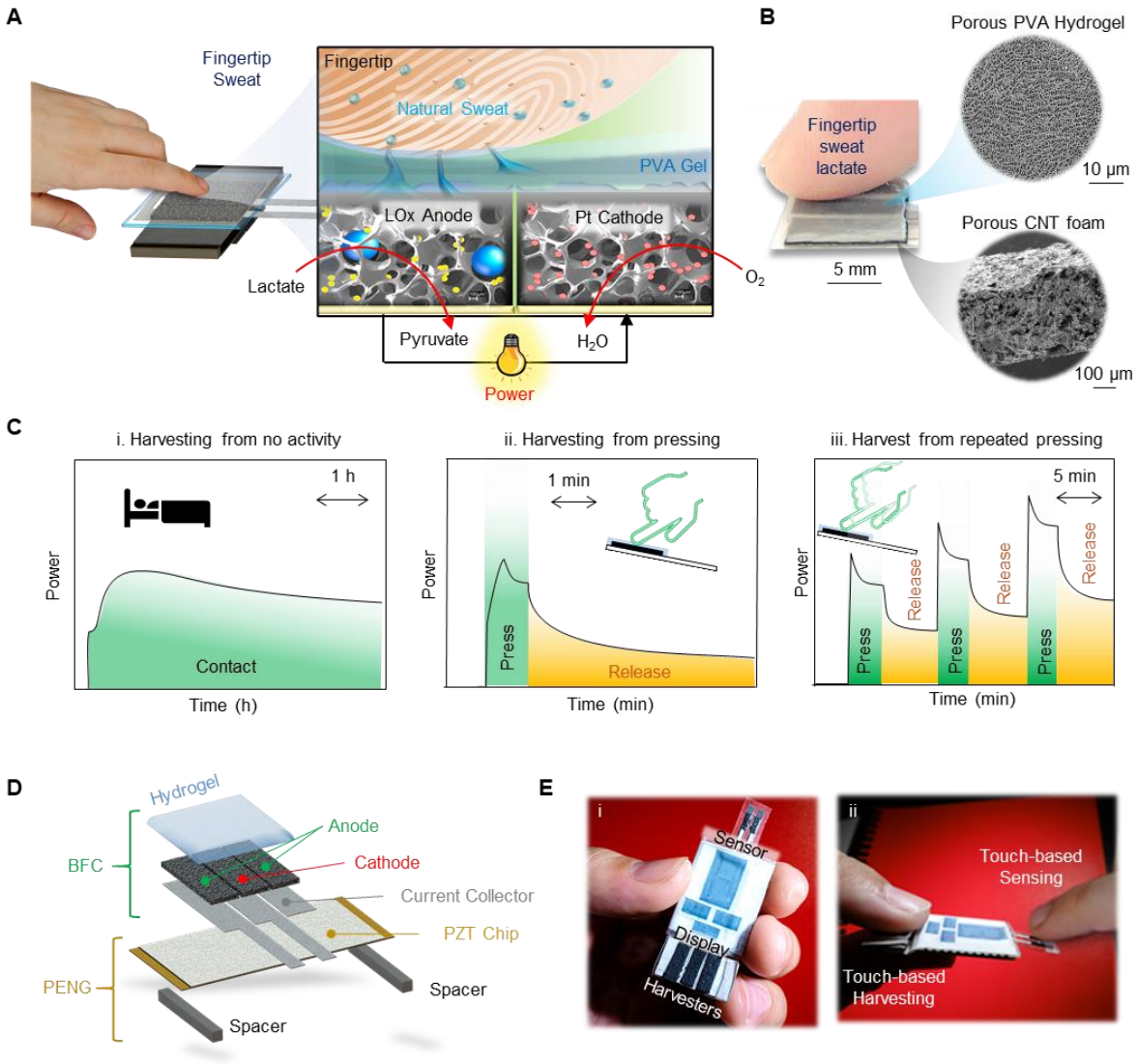

Figure 5.1. Schematics illustrating the operation of the touch-based BFC and bioenergy harvesting system.

A. Schematic illustration and reaction mechanism of the BFC harvesting lactate biofuel from the natural finger sweat using LOx anode and Pt cathode. **B**. Optical and SEM images of the templated porous PVA hydrogel and CNT foam. **C**. Illustration of three operating conditions of the BFC, harvesting energy from (i) passive continuous contact, (ii) active pressing, and (iii) repeated active pressing. **D**. Exploded view of an integrated BFC-PZT harvester to harvest chemical and mechanical energy from the press of fingers. **E**. Photo images of (i) self-powered sensing system with integrated harvesters, sensor, and ECD, and (ii) device sensing sweat composition from the natural finger sweat.

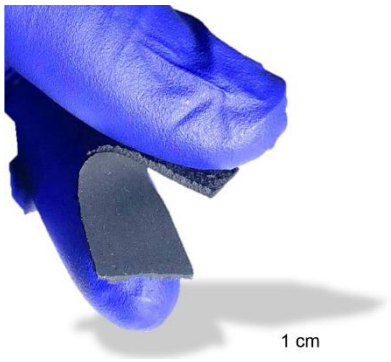

Figure 5.2. Photographic image of bending a strip of 1 cm × 3 cm CNT foam.

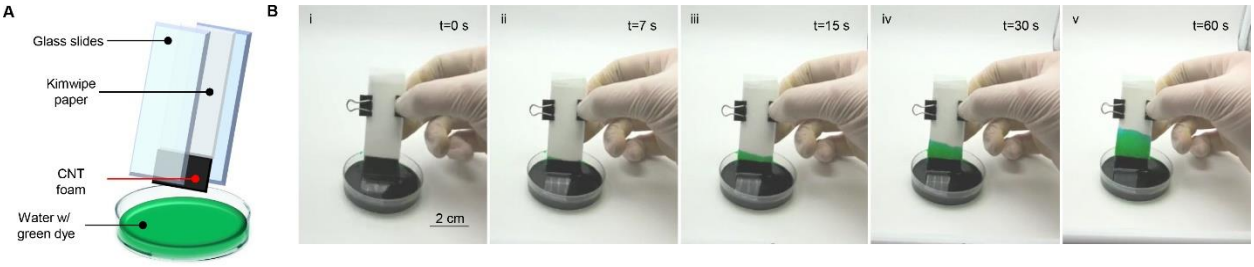

Figure 5.3. Water wicking performance of the CNT foam.
A. Schematics of the water-wicking test of the carbon foam. A piece of 1.5 cm × 2.5 cm CNT foam was sandwiched between two glass slides with Kimwipe paper (same thickness as carbon foam) on top of the foam. A plate with water was prepared with a green dye for visibility. **B.** The time-lapse photographic images at (i) 0s, (ii) 7 s, (iii) 15s, (iv) 30 s, and (v) 60 s after dipping the CNT foam into the water. The water successfully penetrated through the CNT foam within 7 s.

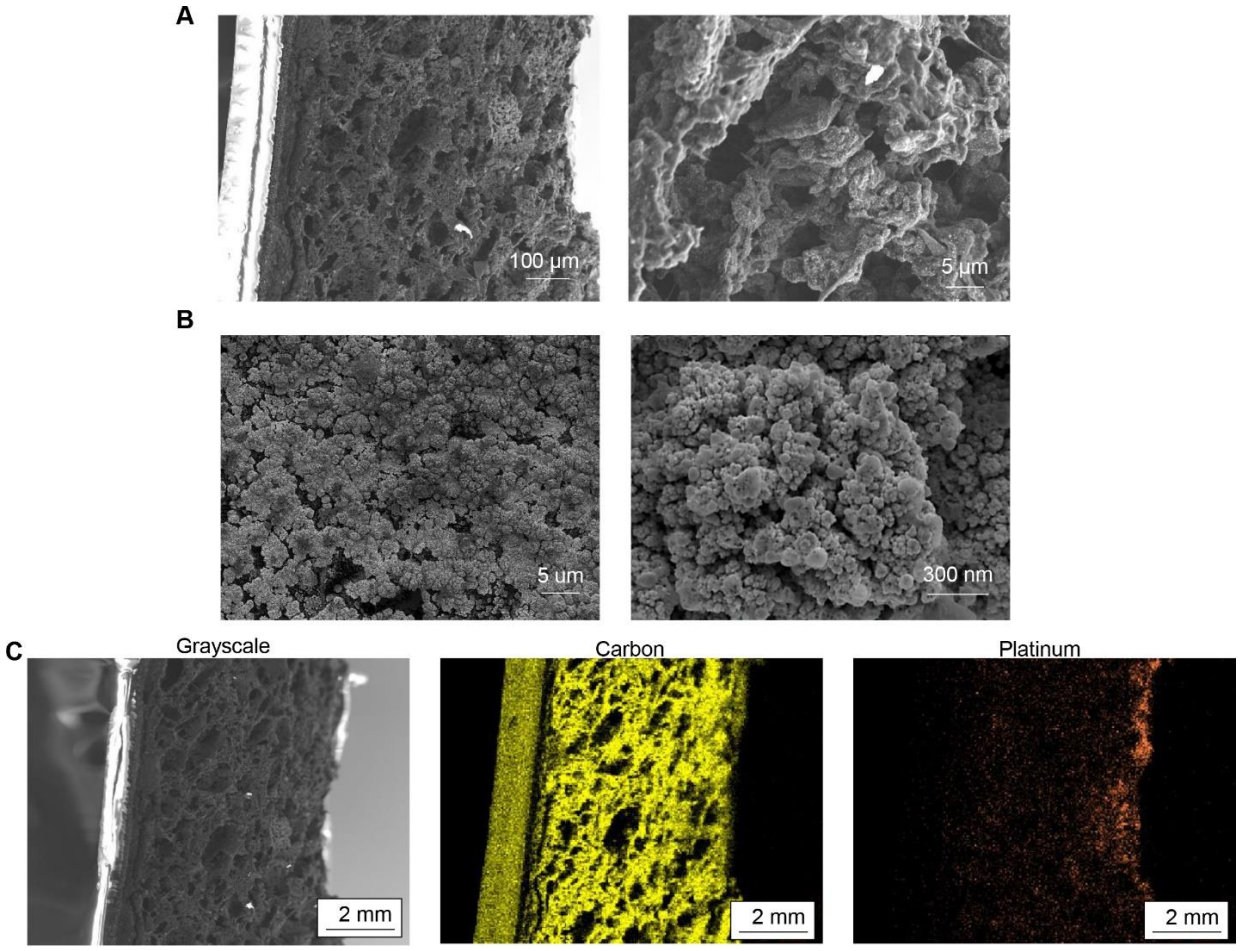

Figure 5.4. SEM images and corresponding EDS mapping of the CNT foam cathode.
A. Cross-sectional view of the p-Pt CF cathode. **B**. Front view of the p-Pt CF cathode. **C**. EDS mapping of carbon and Pt on the cross-section of the p-Pt CF cathode.

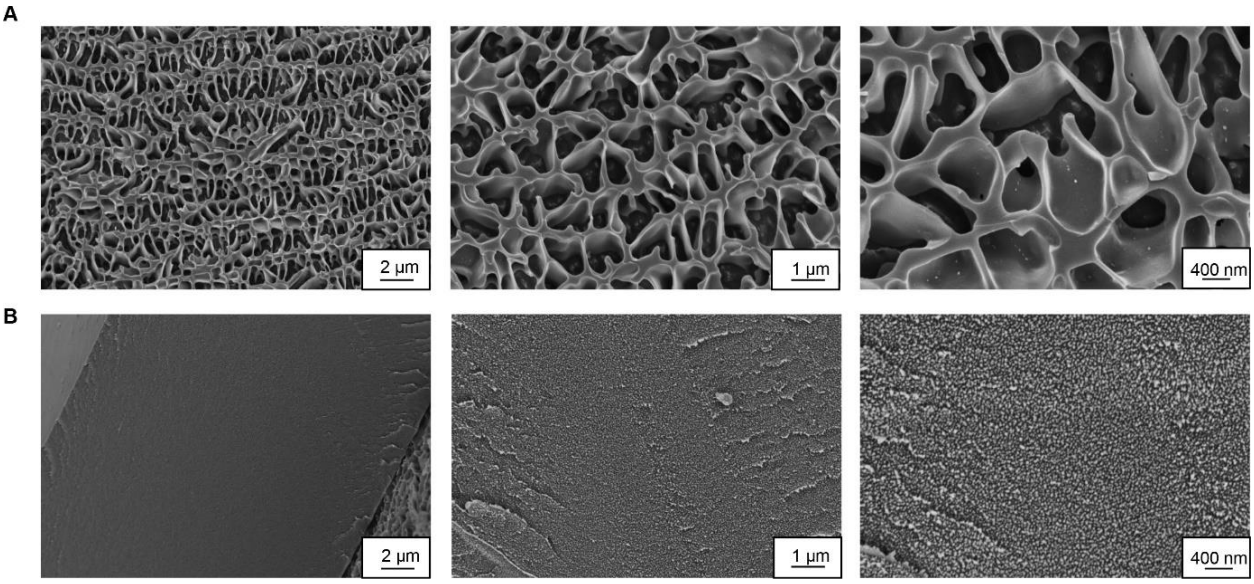

Figure 5.5. Cryo-SEM images of the cross-sections of the porous and non-porous PVA hydrogels.
A. The SEM images of the PVA hydrogel using sucrose as the template. The structure of the gel is highly porous and allows fast penetration of sweat. **B**. The PVA hydrogel without sucrose template.

5.2 Experimental Section

5.2.1 Chemicals

Graphite, toluene, sodium bicarbonate ($NaHCO_3$), acetone, ethanol, hydrochloric acid (HCl), copper sulfate pentahydrate ($CuSO_4$), 1-ethyl-3-(3-dimethylaminopropyl)carbodiimide (EDC), N-hydroxy succinimide (NHS), 1,4-naphthoquinone (NQ), chitosan, glutaraldehyde, acetic acid, Nafion, lactic acid, Ag flake, Ag_2O powder, PVA, potassium hydroxide (KOH), titanium dioxide (TiO_2), sodium ionophore X, sodium tetrakis[3,5-bis(trifluoromethyl)phenyl]borate (Na-TFPB), bis(2-ethylhexyl) sebacate (DOS), tetrahydrofuran (THF), polyvinyl butyral (PVB), sucrose, sodium chloride (NaCl), methanol, iron(III) chloride ($FeCl_3$), sodium polystyrene sulfonate, glycerol, D-sorbitol, acrylamide, N,N'-

methylenebisacrylamide, sodium peroxydisulfate, dodecyl benzene sodium sulfonate were all purchased from Sigma Aldrich. The polyurethane (PU) (Tecoflex EG-80A) was obtained from Lubrizol. Styrene-ethylene-butylene-styrene (SEBS G1645) triblock copolymer was obtained from Kraton. MWCNT-COOH was purchased from Cheap Tubes inc. The printable PEDOT:PSS screen-printable paste was purchased from Sun Chemical. The lactate oxidase (LOx) was purchased from Toyobo. The platinum electrodeposition solution was purchased from Technic Inc. The CapstoneTM fluorosurfactant FS-65 was purchased from DuPont. The PZT disc benders were purchased from APC International Ltd and trimmed into 2 × 1 cm^2 chips. All electronics components were purchased from Digikey. All electrochemical measurements were performed on Autolab PGSTAT204 potentiostat/galvanostat from Metrohm.

5.2.2 Device Fabrication

The fabrication procedure of the flexible CNT foam is described in **Figure 5.6**. In detail, MWCNT-COOH (0.25 g), graphite (0.05 g), and $NaHCO_3$ (6.0 g) were mixed well with a motor and pestle to obtain gray-colored powders, followed by adding 3.0 g of SEBS (dissolved in toluene with 4 (SEBS):10 (toluene) wt%) and stirred at 1800 rpm for 5 min. Subsequently, 2.5 ml of toluene was added and mixed again at 1800 rpm for 5 min to attain a homogeneous paste. The resulting paste was then cast in 1 mm high rectangular-shaped structure, carefully controlled by placing two glass slides (1 mm thick) with controlled spacing in between. Immediately, the cast portion was transferred to ethanol for 20 min to make a solvent exchange that prevents collapse of the structure during evaporation of the solvent (toluene) and then dried in ambient conditions. After that, the dried CNT foam was soaked in 0.5 M HCl for 3 hours to completely remove the $NaHCO_3$ template; this process resulted in the highly porous CNT foam structure. The resulting

porous CNT foam was washed with distilled water for several times and dried at 80 ℃ to obtain flexible CNT foam.

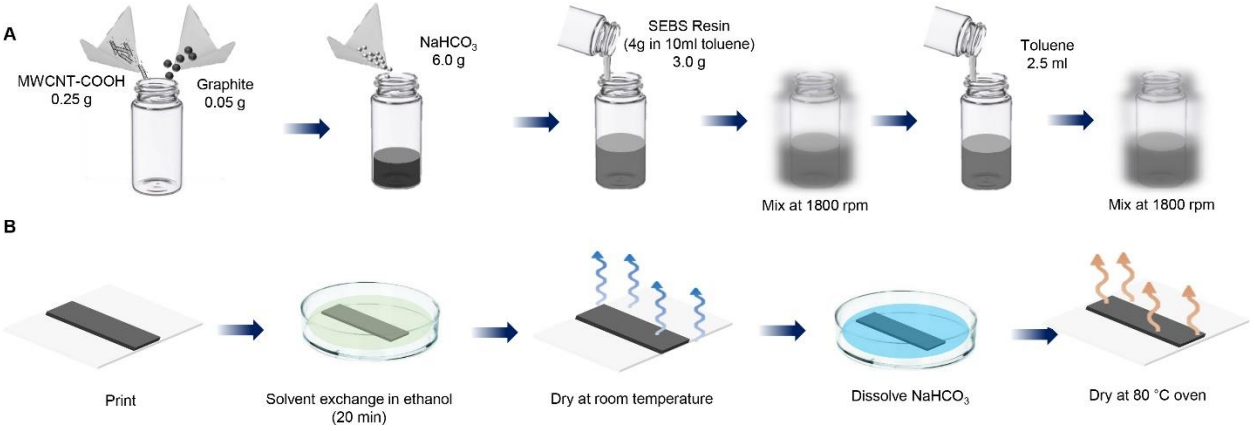

Figure 5.6. Synthesis of the CNT foam.
A. CNT composite paste preparation. **B**. The fabrication steps of the CNT foam using the paste.

Each CNT foam was cut into 0.3 cm^2 (1 cm × 0.3 cm) and two of them (for anodes) were immersed in 10 mM EDC/NHS solution for 6 h to activate the carboxylic acid groups of the MWCNT. After washing the CNT foams with DI water several times, they were attached to the silver current collector with carbon ink placing the cathode between the two anodes. Each bioanode was fabricated by drop-casting 10 µl 0.2 M NQ (dissolved in 1:9 ratio of acetone: ethanol), followed by the addition of LOx (40 mg ml^{-1} in 10 mg ml^{-1} of BSA, 10 µL) for 3 h. For immobilizing the enzyme, 5 µl each of 1 % chitosan in 0.1 M acetic acid and 1 % glutaraldehyde were drop-cast on the anode then kept at 4 °C overnight. Otherwise, the cathode was fabricated by a fixed-potential co-electrodeposition of Pt and Cu at -0.75 V for 600 s followed by de-alloying the Cu with cyclic voltammetry over the potential range of 0 V to 1.5 V for 40 cycles (scan rate

50 mV s^{-1}). After rinsing with DI water several times, 1 % of Nafion was drop cast on the cathode and kept at room temperature until use.

The fabrication of the porous PVA hydrogel was adapted from previous studies.[24] Firstly, solutions of the PVA dissolved in water in a 1:10 weight ratio and KOH dissolved in water in a 1:5 weight ratio were prepared. Then, 14 g of the KOH solution was added dropwise to 10 g of PVA solution with stirring, followed by dissolving 2.6 g of sucrose into the mixture to form the hydrogel precursor. 15g of the precursor was then poured into a Petri dish (diameter ~9 cm) and left in a vacuum desiccator to remove excess water and allow crosslinking until only 1/3 of the weight of the precursor was left. The crosslinked gel was then soaked in 0.1 M PBS buffer to remove the sucrose template and the excess KOH, until the gel is in neutral pH. The gel can then be cut into desired sizes and shapes and stored in PBS or AS for subsequent use.

The ECD was designed using AutoCAD and screen-printed layer-by-layer onto SEBS sheets. The design of the ECD was separated into a front panel and a back panel, which were separated by a layer of a white, opaque insulator and PSS electrolyte, and assembled via heat sealing. The ECD is fabricated using layer-by-layer screen-printing with customized inks. The ink formulation is adapted from a previous work.[6]The printing of the ECD relies on four inks: the electrochromic poly(3,4-ethylenedioxythiophene) polystyrene sulfonate (PEDOT:PSS) ink, the silver ink for interconnection, the opaque insulator ink composed of SEBS and TiO_2, and the sodium polystyrene sulfonate-based electrolyte ink. The PEDOT:PSS ink is composed of PEDOT:PSS paste, toluene, deionized (DI) water, sodium dodecylbenzene sulfonate (DBSS), and Capstone™ fluorosurfactant FS-65 in 10:1.7:1.5:0.1:0.14 weight ratio. The silver ink is composed of silver flake, SEBS, and toluene in a 1:0.16:0.5 weight ratio. The opaque insulator ink is composed of TiO_2, SEBS, and toluene in a 1:6:10 weight ratio. The sodium polystyrene sulfonate

(PSSNa) electrolyte ink is formulated by mixing PSSNa, D-sorbitol, glycerol, TiO_2, and polyacrylamide (PAM) precursor solution in a 4:1:1:0.8:2 weight ratio. The PAM precursor is formulated by mixing acrylamide, DI water, potassium peroxydisulfate, and N,N'-methylenebisacrylamide in a 1:10:0.05:0.01 ratio. All inks are mixed in the planetary mixer at 2500 rpm for 10 min or until homogenous.

The ECD panel is composed of the color-changing front panel and the back panel to control the regional color change. The layer-by-layer printing steps are illustrated in **Figure 5.7**. Shortly, the PEDOT:PSS ink is firstly printed onto the SEBS substrate and cured in the oven at 100 °C for 2 h. The silver interconnection and the opaque insulator layers are printed, with each layer cured at 80 °C for 10 min. Before assembly, the electrolyte is printed onto the back panel and briefly heated in the oven for 15 s at 80 °C to cross-link the PAM in the electrolyte. The front panel is then aligned and covered onto the bottom panel. Lastly, the device is heat-sealed on all four sides to finish the device assembly.

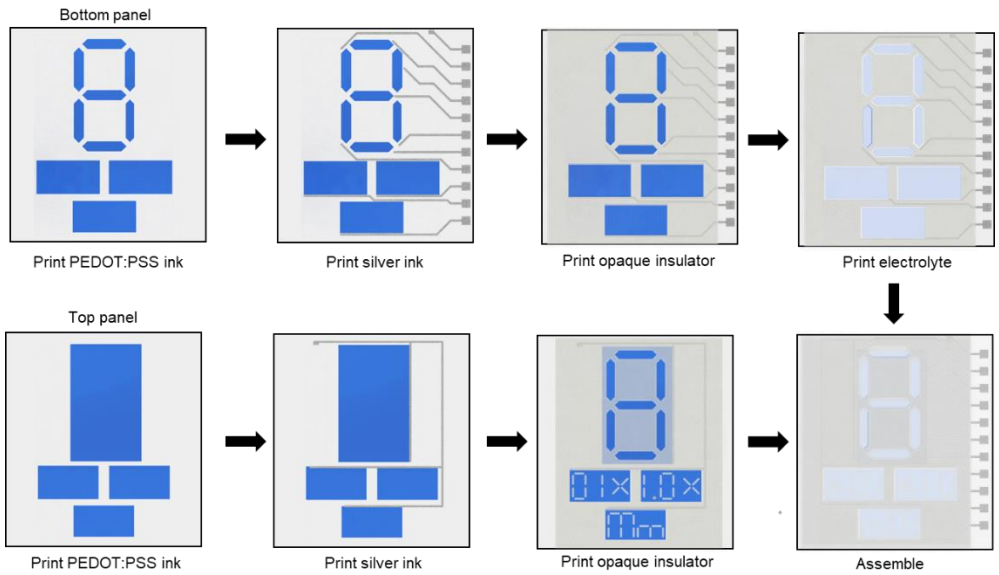

Figure 5.7. Illustration of the layer-by-layer printing and assembly of the ECD panel.

The Na^+ sensors and vitamin C sensors were based on screen-printed electrodes modified via drop-casting. A silver ink, a carbon ink, the SEBS resin, and an Ag_2O ink were used for printing the electrodes. The carbon ink contains graphite, super-P carbon black, SEBS, and toluene were added in a 6:1:3.4:6 weight ratio. The Ag_2O ink contains super-P carbon black, Ag_2O, SEBS, and toluene were mixed in a 0.05:0.95:0.18:0.82 weight ratio. Both inks are mixed in a planetary mixer at 2500 rpm for 10 min or until homogenous prior to printing. After printing each layer, the inks are cured in the oven at 80 °C for 10 min. The printing and modification of both sensors are illustrated in **Figure 5.8**.

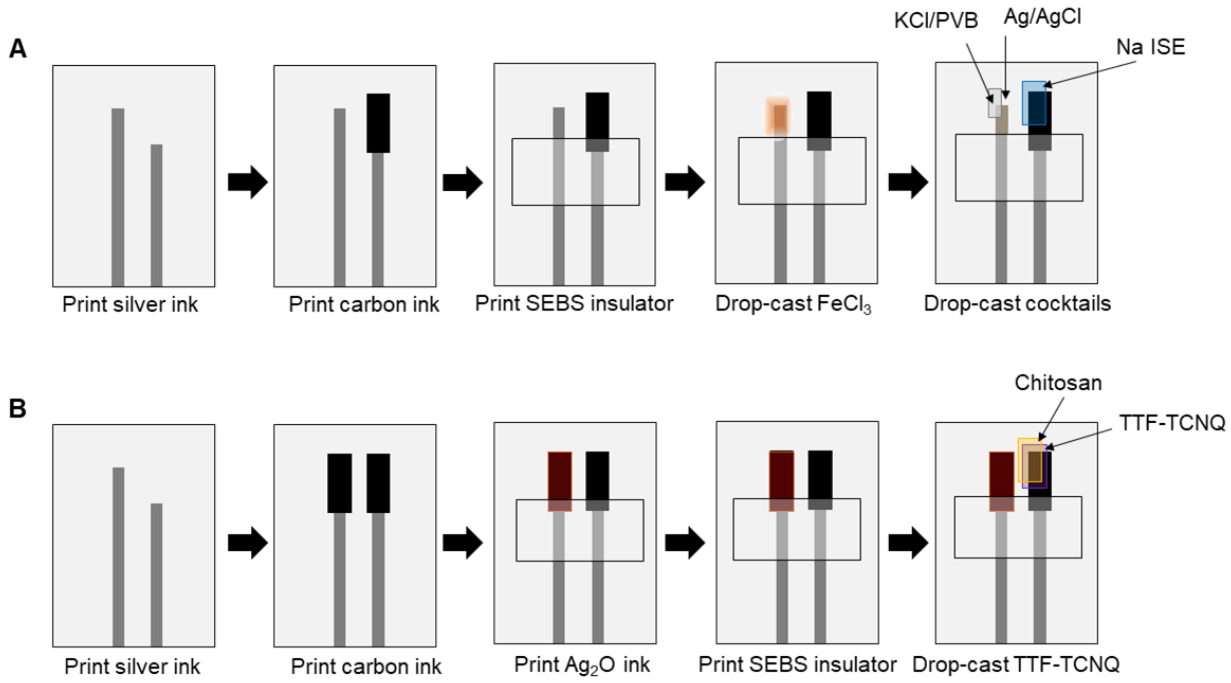

Figure 5.8. Layer-by-layer printing and drop-casting of the sensors.
A. Printing and drop-casting of the Na+ sensor. **B**. Printing and drop-casting of the vitamin C sensor.

The sodium sensor was fabricated using flexible silver and carbon inks based on the previous studies[10]. The silver ink and the carbon ink were printed onto SEBS substrate layer-by-layer and were covered using SEBS resin to define the electrode area, exposing 2 mm^2 of carbon electrode as the working electrode and 1 mm^2 of the silver electrode as the reference electrode. A 0.1 M $FeCl_3$ solution was firstly drop-cast onto the silver electrode to chlorinate the surface and form AgCl.

A cocktail composed of PVB (78.1 mg ml^{-1}) and an excess amount of potassium chloride (50 mg ml^{-1}) dissolved in methanol was drop-cast onto the chlorinated surface (1.5 µl mm^{-2}). A PU resin (1 g in 10 g THF) was then drop-cast onto the dried cocktail layer (2 µl mm^{-2}) to prevent salt leaching. A cocktail for the sodium ion-selective electrode was formulated by dissolving 1 mg of sodium ionophore X, 0.77 mg Na-TFPB ion exchanger, 33 mg PVC, and 66 mg DOS in 660 mL nitrogen-purged THF and drop-cast onto the carbon electrode (2 µl mm^{-2}).

The vitamin C sensor was fabricated using flexible silver, carbon, and silver oxide inks[25]. The inks were printed layer-by-layer onto a SEBS substrate and covered using SEBS resin to define the electrode area, exposing 2 mm^2 of carbon electrode and 4 mm^2 silver oxide electrode. A 10 MΩ resistor was solvent-welded between the two electrodes as the discharging load. A 5 mM solution of TTF-TCNQ, dissolved in ethanol: acetone (1:1) mixture, was drop-casted onto the carbon electrode (1 µl mm^{-2}), followed by drop-casting a 1 µl mm^{-2} chitosan layer (1 wt% in 0.1M acetic acid) and a 0.125 µL mm^{-2} glutaraldehyde layer (0.5% in water) for immobilization.

5.2.3 Electrical circuit design

The circuit was composed of four main components: the MCU (AtTiny 441, Microchip Technology, USA), the analog switch (MAX4715EXK+T, Maxim Integrated, USA), the booster (bq25505, Texas Instruments, USA), and the bridge rectifier (DF02S, ON Semiconductor, USA). The PCB was designed using Altium designer and was manufactured by JLCPCB. The PCB design is illustrated in **Figure 5.9**. Individual components were then soldered onto the PCB via a standard reflow process. The integrated circuit could perform energy harvesting, storage, and power management. The MCU with a built-in ADC could read from the sensor and display the corresponding result via the ECD.

The integrated circuit was designed to regulate and store the harvested energy from the BFC and the PZT chips and use the stored energy to power a microcontroller that record signal from the sensor and display the sensing result on the electrochromic display (ECD). The design of the circuit is modified based on previous work. To regulate the power of the BFC, a voltage booster (Texas Instrument, bq25505) was used, which increase the low voltage of the BFC (0 - 0.6 V) to 2 – 5.5 V. The integrated energy management function in the booster allows programable maximum voltage ($V_{BAT\_OK\_HYST}$) and minimum voltage (V_{BAT_OK}) allowed for the connected energy storage device. A digital output from the booster turns on when the voltage of the connected capacitor increases above $V_{BAT\_OK\_HYST}$ and turns off when the voltage drops below V_{BAT_OK}, which was used to control an analog switch (Maxim Integrated, MAX4715EXK+T) that controls the connection of the capacitor to the microcontroller (Atmel, ATtiny441). A bridge rectifier (ON Semiconductor, DF02S) was used to rectify the alternating input from the PZT generator, and the regulated output was connected to the capacitor to store the harvested energy.

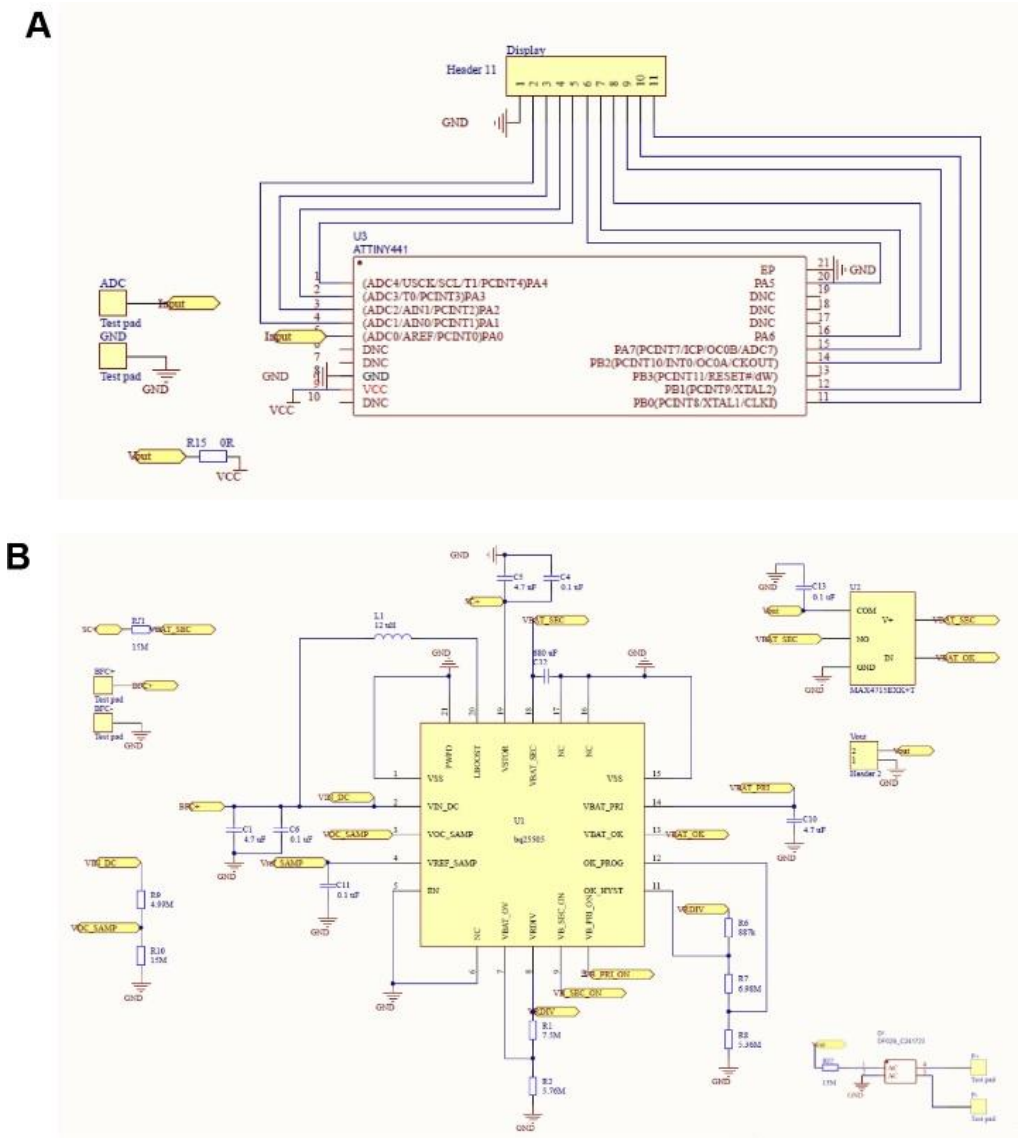

Figure 5.9. Schematics of the integrated circuit board.
A. Circuit layout for the AtTiny441 MCU. **B**. Circuit layout for the bq25505 booster, analog switch, and the bridge rectifier.

5.2.4 Assembly of the self-powered sensing system

An adaptor that connects two sets of BFCs and PZT chips were designed using AutoCAD and screen-printed onto a SEBS sheet (**Figure 5.10**). The front and the back PZT chips were

separately connected to the adaptor and the two PZT chips were placed back-to-back, separated by two spacers (1 mm thick) place on two ends of the chips. The foam BFC electrodes were thereafter fixed onto their corresponding locations using conductive carbon ink and modified using the procedure above. The connector was then connected to the PCB via the "solvent welding process" following previous studies.[26] Similarly, the display and the sensor was connected to the PCB using the same process to complete the assembly of the self-powered sensing system

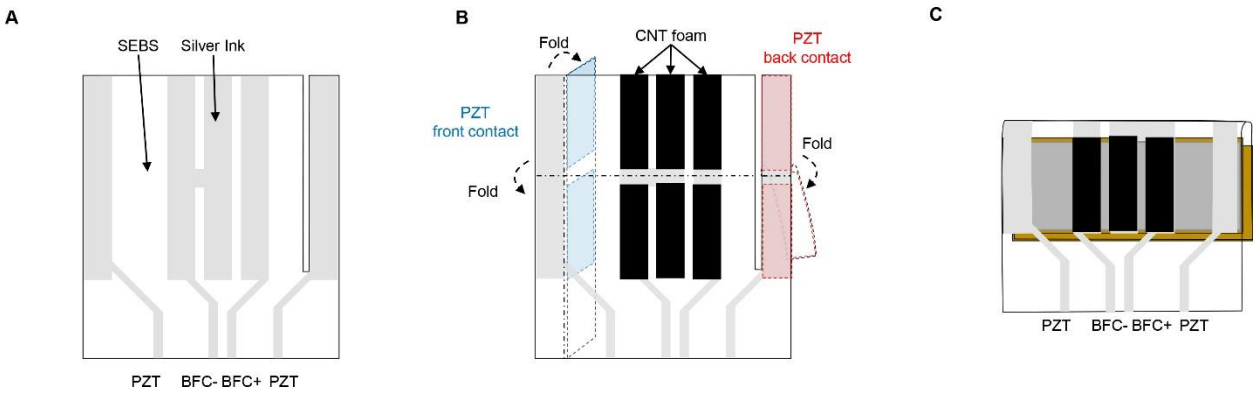

Figure 5.10. Assembly of the CNT foam for BFC and PZT chips.
A. Current collectors were firstly printed onto a SEBS sheet and trimmed to the shape. **B**. The CNT foam pieces (1 cm × 0.3 cm) are attached to the silver current collector using carbon composite ink. **C**. Attaching two PZT chips to their corresponding contact points and folded back-to-back.

5.3 Results and Discussion

5.3.1 Characterization and Optimization

The fabrication of a touch-based BFC that effectively utilizes the natural fingertip sweat pumping, under repeated pressing, relies on soft, durable, porous, sweat-wicking CNT foam

electrodes. These flexible CNT foam electrodes were prepared by using a water-soluble particle template and solvent exchange in a formulated CNT-elastomer composite.

To functionalize the CNT foam as BFC electrodes, the foam was firstly cut into 1 cm × 0.3 cm pieces and glued onto a prepared silver current collector, as shown in **Figure 5.10**. The porous platinum (Pt) electrode (p-Pt CF) was fabricated using co-electrodeposition of copper (Cu) and Pt onto carbon-foam electrode at -0.75 V, followed by electrochemical etching (dealloying) of the Cu using cyclic voltammetry between 0 V to 1.5 V at 50 mV s^{-1} for 40 cycles. The resulting p-Pt nanoparticles not only enhanced electrochemical active surface area but also compressive strained Pt surface layer, which modifies the d-band structure of Pt atom. The structure modified Pt weakens the adsorption energy of the reactive intermediate compared to mere Pt, resulting in increased catalytic activity and improvement in ORR reaction[1–3]. The resultant p-Pt CF is highly porous and deposited throughout the 3D CNT foam, as shown in the scanning electron spectroscopy (SEM) images with electron dispersive X-ray spectroscopy (EDS) on **Figure 5.4**. The resulting electrodes clearly demonstrate the advantages of the 3D p-Pt CF structure over Pt-SPC and Pt CF in terms of onset reduction potential and current density originated from the O_2 electrocatalytic reduction on Pt, as evidenced by the linear sweep voltammetry (LSV) of **Figure 5.11**. Whereas carbon foam-based Pt cathodes showed decent cathodic current stemming from an onset potential of 0.3 V, the p-Pt cathode displayed a higher oxygen reduction reaction (ORR) onset potential originating from 0.4 V (vs. Ag/AgCl) and a higher current density over the operating potential range of the cathode. The anode was fabricated by decorating the carbon foam with 1,4-naphthoquinone (NQ), LOx, and chitosan, to ensure efficient electron mediation and a uniform LOx surface coverage. The anode was also characterized using LSV and displayed an

increase of anodic current, with the onset potential of -0.2 V (vs. Ag/AgCl), upon increasing the lactate concentration from 0 to 15 mM (**Figure 5.12**).

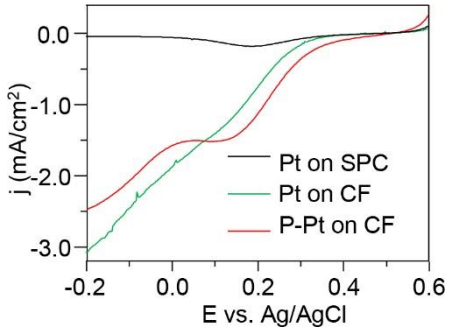

Figure 5.11. LSV characterization of the cathode with different electrode materials.
Pt deposited on planar screen-printed carbon electrode and CNT foam, as well as the p-Pt on the CNT foam, were compared. Scan rate: 1 mV s^{-1}.

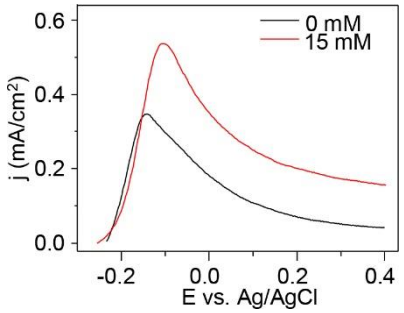

Figure 5.12. LSV characterization of the anode without and with 15 mM of lactate.
Scan rate: 1 mV s^{-1}.

As shown in single-electrode characterization, the current from the cathode is significantly higher compared to the anode. In order to ensure the maximized utilization of both the anode and cathode in a limited area, the area ratio between the anode and cathode was optimized. As shown in **Figure 5.13**, the system, discharged under 0.4 V using chronoamperometry (CA), is mostly

limited by the anode. Presented based on the power per the cathode area, **Figure 5.13** illustrates that the 2:1 anode-to cathode-ratio can almost fully utilize the cathode while occupying less area than the 4:1 ratio. Thus, the anode and cathode of 0.6 cm^2: 0.3 cm^2 selected to maximize the power in a limited area.

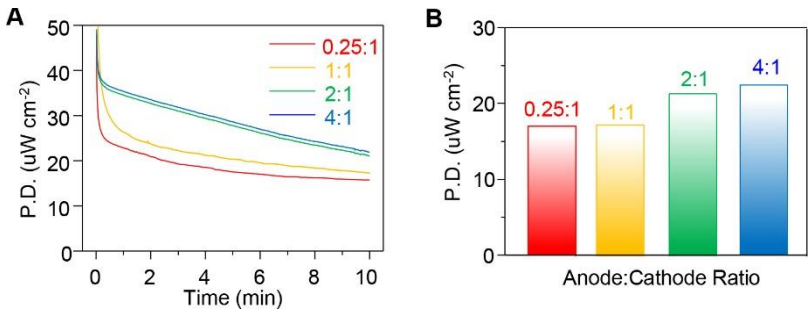

Figure 5.13. BFC anode to cathode area ratio optimization.
A. CA of the BFCs at 0.4 V with the different anode to cathode area ratio in the presence of 20 mM lactate. **B**. bar graph summarizing the obtained power using different anode to cathode ratios after 10 min of CA.

The assembled BFC with the 2:1 ratio was tested using linear scan voltammetry (LSV) under different scan rates, which also showed a large discrepancy of power that varied between ca. 500 µW cm^{-2} at 5 mV s^{-1} and ca. 100 µW cm^{-2} at 0.2 mV s^{-1}, due to the large double-layer charging current on the highly porous electrodes (**Figure 5.14 A**). Thus, to accurately measure the power of the BFC, CA is preferred over LSV to remove the effect of the high charging current. As shown in **Figure 5.14 B**, the change in potential of both the anode and cathode during the 2-electrode LSV scan was monitored via introducing an external Ag/AgCl electrode. It can be observed that the current would likely be limited to the anode, which was more polarized, compared to the less polarized cathode. The individual electrode potential shift during the 2-electrode LSV was also

observed using an external reference electrode, which shows that the power-limiting anode potential shifted from -0.2V to +0.23V vs., as opposed to the cathode that shifted from +0.4 V to +0.23 V only.

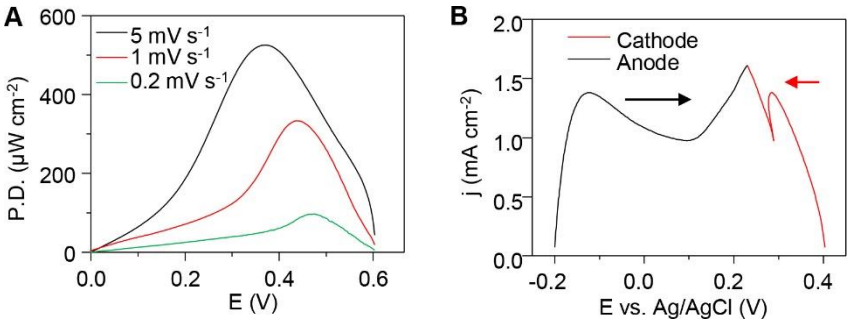

Figure 5.14. LSV response of the BFC after area ratio optimization.
A. LSV power response of the BFC (1 cm^2) with cathode and anode ratio of 1:2 in 0.5 M PBS with 20 mM of lactate at scan rates of 0.2, 1, and 5 mV s^{-1}. **B**. Potential vs. current density polarization curve during the 5 mV s^{-1} LSV measurement. The cathode potential started to decrease from 0.4 V to 0.23 V, while the anode's potential increased from -0.2 V to 0.23 V.

Through optimization, the CNT-foam-based fingertip BFC was designed with the total size of 1 × 1 cm^2, with one cathode electrode paired with two anodes (**Figure 5.1 B**). The operational conditions of the BFC were optimized first using in-vitro tests. The BFCs were traditionally characterized using linear scan voltammetry (LSV) with the scan rates around 5 mV s^{-1}, which was used to gauge the power of the BFC against different fuel concentrations and the peak power potential (**Figure 5.15 A**). However, such method cannot accurately depict the long-term harvesting performance in equilibrium since capacitive charging current makes up a significant part of the measured power output (**Figure 5.14 A)**. Thus, extended chronoamperometry (CA) of 10 min was employed, with potential steps from 0.55 V to 0.2V to accurately evaluate the power

and optimal operating conditions of the BFC. The open-circuit voltage of the cell demonstrated a value of *ca.* 0.55 V, in agreement with the onset potential of LOx/NQ-driven oxidative and Pt-catalyzed reductive reactions, set at -0.2 V and 0.35 V *vs.* Ag/AgCl, respectively. The Pt-based ORR was chosen as a cathodic half-cell over enzymatic biocathodes to minimize the risks involved in the enzyme immobilization and to eliminate energy harvesting fluctuations due to environmental changes. A potential of 0.40 V offered the most favorable performance with the power density of 43 μW cm^{-2} (based on the anode area) in the presence of 15 mM lactate concentration (**Figure 5.15 B**). Expectedly, the response of the BFC to increasing lactate concentrations, ranging from 1 mM to 25 mM, in both the liquid PBS and the PVA hydrogel media (under 50 kPa applied pressure), has been tested at the optimized (0.4 V) potential (**Figure 5.15 C i** and **ii**) and led to higher bioelectrocatalytic currents. **Figure 5.15 C ii** demonstrates that the PVA gel results in similar power output as PBS buffer (**Figure 5.16**). This behavior, characterized by electrochemical impedance spectroscopy (EIS), is attributed to the low impedance of the porous PVA gel as well as to the reduced electrode resistance of the electrodes upon applying pressure (**Figure 5.17**). The diffusion of sweat through the hydrogel was simulated by dropping 1 μL of lactate solution and observing the power profile of the BFC. As illustrated in **Figure 5.18**, this experiment shows that the diffusion time varies based on the concentration of the lactate fuel, increasing from 14 s for 20 mM droplets to 45 s for 100 mM droplets. The BFC stability was examined, showing a stable output throughout a week (**Figure 5.19**).

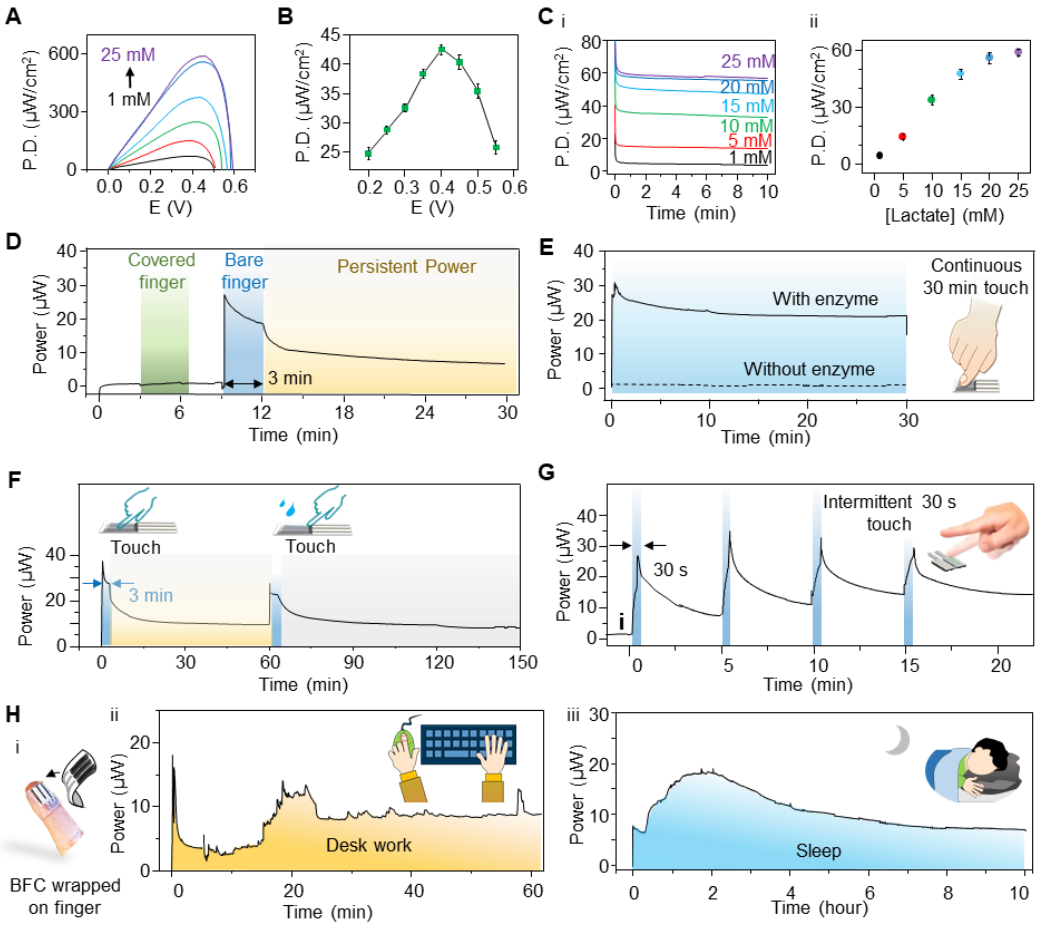

Figure 5.15. In-vitro and in-vivo characterization of the touch-based BFC.
A. Areal power density of the BFC at different lactate concentrations (1, 5, 10, 15, 20, 25 mM), characterized using LSV at 5 mV/s. **B**. The areal power density of the BFC at different potentials, characterized via 10-min CA. (Error bars represent the standard deviation, n = 3) **C**. (i) Power density of the BFC (i) at 0.4 V in PBS with different lactate concentrations and (ii) the power calibration plot of the BFC with different lactate concentrations with the PVA gel. (Error bars represent the standard deviation, n = 3) **D**. Comparison of the power of the BFC touched by a covered finger for 3 min and by a bare finger for 3 min. **E**. Power profile of the BFC during 30-min continuous pressing, using anode decorated with and without LOx enzyme. **F**. Power profile of refueling by pressing the BFC for 3 min after 1 h of resting. **G**. Power profile of the BFC during repeated 30 s pressing every 5 min. Figure 2d-g, pressing pressure, 50 kPa; CA voltage, 0.4 V. **H**. (i) Illustration of the BFC attached to the finger for long-term continuous energy harvesting. (ii) Power profile during a 1-h normal desk work involving intermittent BFC pressing. (iii) Power profile of the BFC passively harvesting bioenergy overnight (10 h sleep) from a finger.

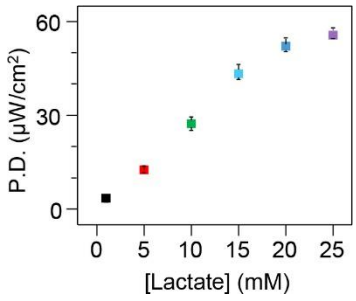

Figure 5.16. The power calibration plot of the BFC with different lactate concentrations in 0.1M PBS.

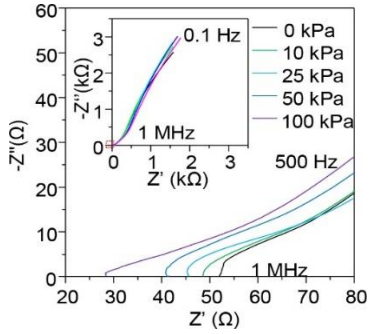

Figure 5.17. EIS Nyquist plot of the 2-electrode BFC covered by the porous PVA hydrogel with different applied pressure.
The hydrogel was soaked in 0.1 M PBS prior to testing. Scan range: 1 MHz – 0.1 Hz; amplitude: 10 mV.

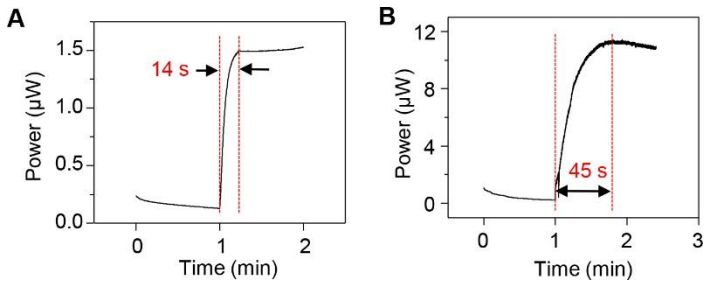

Figure 5.18. Sweat Permeation Test.
The CA response of the BFC discharged at 0.4 V when 1 μL of **A**. 20 mM lactate and **B**. 100 mM lactate is dropped to the top of the PVA hydrogel. The BFC is tested with 0.4V CA.

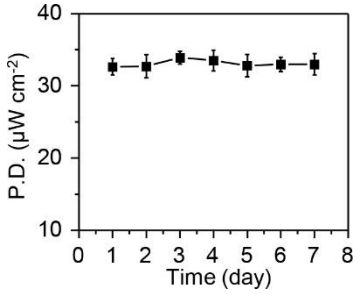

Figure 5.19. The stability of the BFC.
The BFC is tested with 0.4V CA using 20 mM lactate in PBS every day throughout a week.

Figure 5.15 D illustrates the proof-of-concept power response of the touch-based BFC. This power-time temporal profile displays a rapidly increasing power, to around 30 μW, upon pressing the BFC with a bare finger (green section). In comparison, no power generation is observed for similar touching of the BFC using a covered finger (black section), reflecting the absence of fuel transfer. Such comparison clearly demonstrates that the power generation in a BFC is sheerly fueled by the fingertip's natural sweat. Such energy harvesting performance was also shown to be reproducible with the same test subject, with the collected energy varying *ca.* 10% among different BFC samples (**Figure 5.20**).

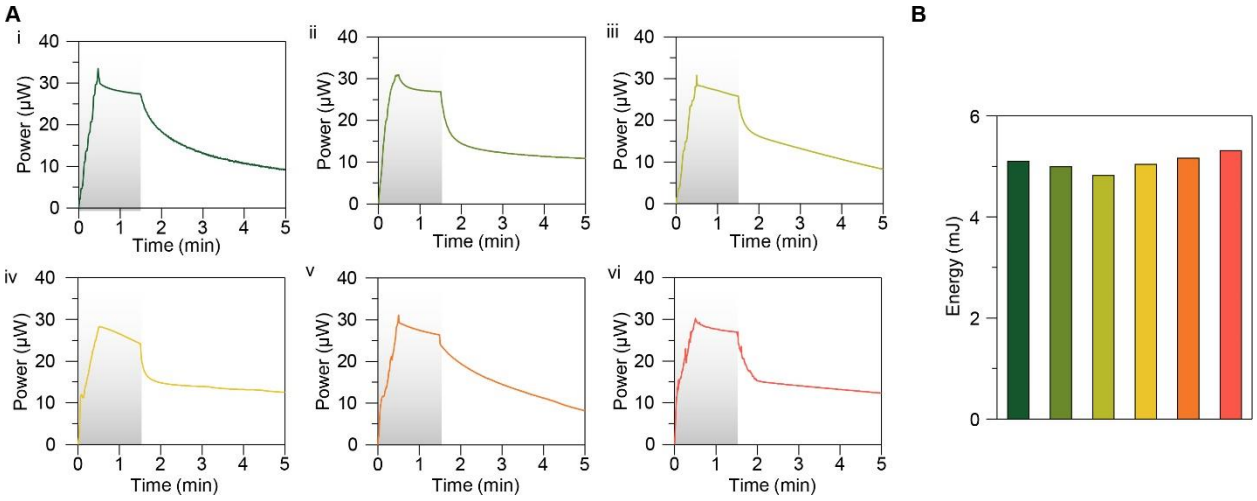

Figure 5.20. BFC on-body reproducibility.
A. The power generation profiles, and **B**. energy harvested within 5 min of 6 BFCs touched for 90 s by a bare finger using a pressing weight of 50 kPa.

Due to the difference in sweat rate and lactate concentration in different individuals, the harvestable power can vary from person to person, giving an advantage of BFC-produced power to individuals with higher fingertip sweat rate. To analyze the performance of the touch-based BFC on different subjects with different passive sweat rates on the finger, the sweat rate of individuals was qualitatively compared. To qualitatively estimate the sweat rate, impressions of the sweat glands were obtained using bromophenol green as the sweat indicator. Bromophenol green is initially colorless, and at pH > 5.4, a blue coloration can be observed. As the sweat pH lies between 5 – 7, bromophenol is used to visualize the number of sweat glands and the amount of sweat. A 5 wt% solution of bromocresol green was prepared by dissolving in silicon oil and sonicated for 20 minutes.[4] The oil was applied to the index finger of three subjects after thoroughly washing and drying the hands, and microscopic optical images were taken up to 10 minutes, as shown in **Figure 5.21**. The 3 subjects exhibited different sweat rates in the first 10 min, with subject 1 exhibiting

the highest number of glands and area of coloration, followed by subject 3 and subject 2 with the lowest sweat rate.

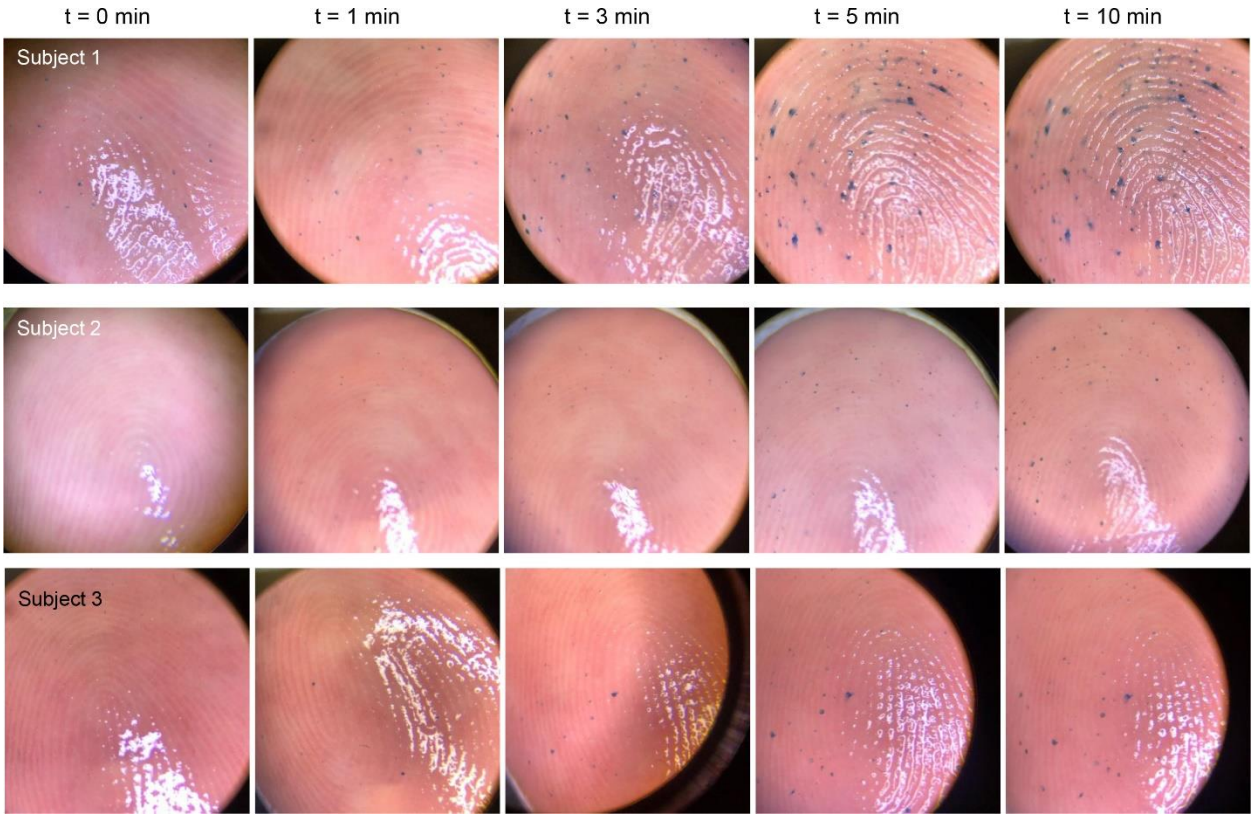

Figure 5.21. Optical microscopic images of the finger with applied bromophenol dye. Bromophenol green as a sweat indicator which is initially colorless and turns blue at above pH 5.4 was used for sweat rate analysis. All subjects washed hands before the experiment and used their index finger to monitor the sweat rate, and the microscope picture was taken until 10 min. The density of blue dots indicates the sweat rate difference on each subject.

As the amount of fuel and its lactate concentration determines the power of the touch-based BFC, the power of the device was tested with all 3 subjects with different sweat rates by pressing their finger on the BFC for 30 s, followed by 30 min of resting. The power and the amount of

energy collected within 30 min are shown in **Figure 5.22**, which shows that the sweat rate is positively correlated with the power and energy harvested from the BFC, with subject 1 giving the most energy of 12 mJ, followed by subject 3 for 7 mJ and subject 2 for 5.5 mJ.

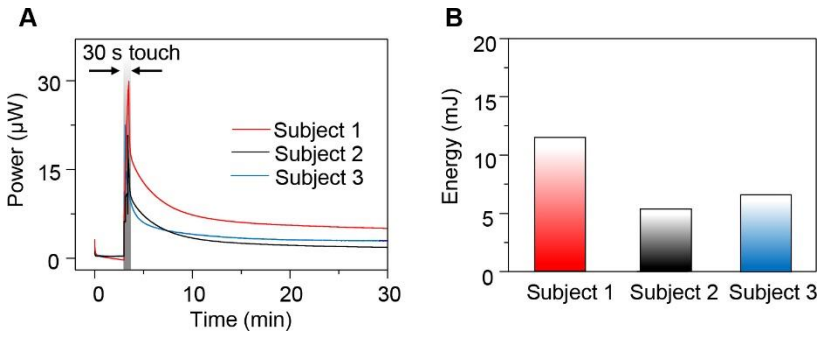

Figure 5.22. BFC performance with subjects with different natural fingertip sweat rates. **A**. Power obtained from different subjects with different sweat rates using CA at 0.4 V. **B**. bar plot representing total harvested energy for 30 min from different subjects.

The harvesting behavior of BFC during continuous pressing was further validated over a 30 min period, which generated over 20 μW of power per finger and harvested over 39.5 mJ energy over 30 min (**Figure 5.15 E**). In comparison, the BFC without LOx enzyme was not able to generate any sizable energy. The ability of the touch-based BFC to continuously harvest energy from the sweat transferred from a brief (3 min) touch is demonstrated in **Figure 5.15 F**, where the BFC was able to harvest energy over an hour and can be refueled upon touching the porous PVA hydrogel. It is worth noting that without enclosure, the collected sweat fails to maintain the PVA gel hydrated due to faster evaporation kinetics, and the gel was rehydrated every hour (**Figure 5.23**). As shown in **Figure 5.15 G**, repeated and frequent pressing on the BFC is beneficial for increasing its harvesting power, with its power increasing after each press. Such behavior can be

utilized to increase rapidly the power harvested without exerting constant force upon the device and can be further exploited with more BFCs for multiple fingers to reach higher power (**Figure 5.24**). The simplicity and practicality of this touch-based BFC harvester were demonstrated in different scenarios, such as during regular desk work that involves typing and mouse-clicking (**Figure 5.15 H** and **Figure 5.25**), or during overnight sleep when no mechanical input was exerted (**Figure 5.15 I** and **Figure 5.26)**. Due to the extended experiment duration, a plastic wrap was applied around the BFC to avoid hydrogel dehydration, as illustrated on **Figure 5.15 H-i** and **Figure 5.27**. These data demonstrate that the BFC can harvest energy continuously in both scenarios, scavenging over 28.4 mJ during 1 h of desk work, or up to 389 mJ energy over 10 h of sleep, without the need for any environmental or mechanical energy input.

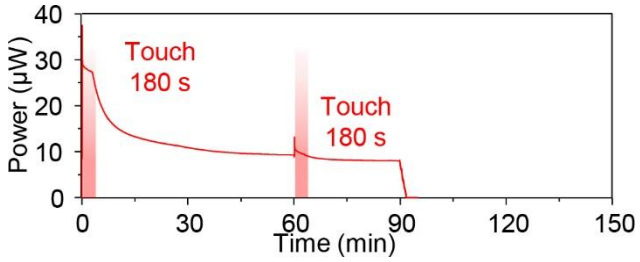

Figure 5.23. Hydrogel stability in extended harvesting tests.
The BFC was covered by the PVA hydrogel and pressed for 3 min and rested for 1 hour. Without rehydrating the hydrogel after 1 hour, the BFC was pressed again for 3 min. The hydrogel was not able to retain the water without encapsulation, and the electrodes lost connection after 90 min.

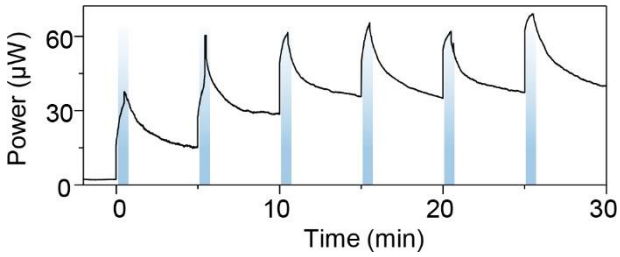

Figure 5.24. Repeated pressing of the BFC.
One BFC device was pressed repeatedly by one finger for 30 s every 5 min. The power generated by the BFC after touching increased from ~15 μW to ~40 μW via repeated refueling of the device. Total energy harvested in 30 min was 67.7 mJ.

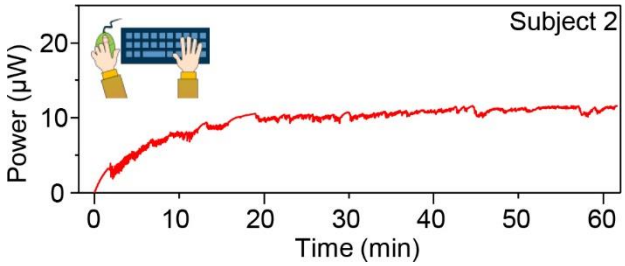

Figure 5.25. Energy harvesting from low-intensity desk work.
The BFC was wrapped around the right index finger of a subject for an hour. The subject was asked to perform normal work such as typing, clicking the mouse, or writing. The graph records the power of BFC during 1 hour of such activity while discharged at 0.4 V. In total, 35.3 mJ of energy was harvested within 1 hour.

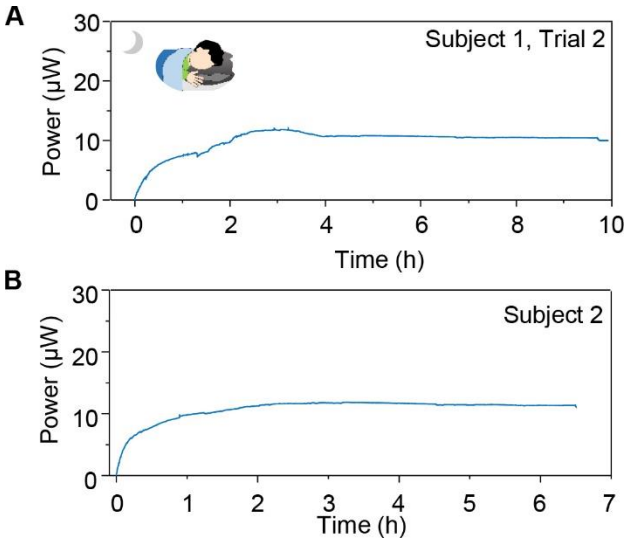

Figure 5.26. Energy harvesting from no activity during overnight sleeping.
A. The power harvested by wrapping one BFC around the index finger of a subject was measured over 10 h of sleep. The total amount of energy harvested was 364.4 mJ. **B**. The power harvested by wrapping one BFC around the index finger of a subject with a lower sweat rate was measured over 6.5 h of sleep; different subjects as in **A**. The total amount of energy harvested was 253.0 mJ.

Figure 5.27. Photo of the experimental setup of long-term on-body test.
The BFC was wrapped with plastic film to avoid dehydration of the hydrogel.

To further investigate and optimize the utilization of the touch-based bioenergy harvesting process, several variables that affect the power generation, including the sweat accumulation time (after cleaning and prior to the touching), the touching pressure, the duration of touching, the number of fingers employed, and the touching frequency, have been systematically studied. Towards the practical goal of quickly powering a device within a short period after touching, the power and the total energy generated during a 5 min touching were monitored and compared. First, the effect of the sweat accumulation time before touching the BFC was examined using a 1 to 10 min time range, and the corresponding power generation was monitored during a 30 s touching time. While longer waiting times were expected to increase the power due to the accumulation of lactate on the fingertip, no significant difference in the power was observed for the different waiting times (**Figure 5.28 A**). Such behavior can be attributed to the constant production and reabsorption rate of sweat at resting state,[27] which leads to a constant sweat volume and composition. On the other hand, the power difference is more pronounced through a longer operation time of 30 min, when the stabilized power and total energy collected from BFC increased slightly upon increasing the waiting time (**Figure 5.29**), reflecting the increased amount of fuel transfer upon touching. Subsequently, we studied the effect of the applied finger pressure on the BFC performance by touching the 1 cm^2 device with increasing pressures of 10, 25, 50, and 100 kPa. **Figure 5.28 B** illustrates that a stronger press force leads to a higher power, which translates to a larger harvested energy within a fixed time. The pressure weight of 50 kPa was determined as the most appropriate since applying a larger pressure required extra effort with only negligible gain in the energy payback. It is worth noting that due to the use of the flexible and durable porous carbon-foam-based BFC and a porous PVA gel, no mechanical damage was observed throughout the process. As illustrated in **Figure 5.28 B**, the power harvested from fingers is directly

proportional to the number of fingers with device deployed with different pressing duration (30 s and 3 min), where the 3-min pressing with 3 fingers harvested as high as 17 mJ over 5 min, translating to an average power of 56.7 μW and EROI of over 1000%, considering the small amount of energy (~0.5 mJ/finger/press) used in pressing the fingers. As was shown earlier in **Figure 5.15**, pressing can increase the instantaneous power of the BFC, with the press time affecting the total amount of energy harvested within a short time period. As expected, the BFC pressing time profoundly affects the energy generation (**Figure 5.28 D**). Such behavior shows good reproducibility in maximum power and collected energy among different BFC samples from the same test subject (**Figure 5.30**). These data display the power-time profiles recorded upon increasing the BFC touching time from 5 to 180 s. Such profiles illustrate that longer touching times lead to higher power generation and the collection of additional energy, indicating that the sweat is able to continuously diffuse through the gel during the touching period. To further examine the benefit of repeated fueling to the power harvesting within a short amount of time (towards quickly powering electronics), the 180 s touching time and the remaining 120 s idling time were divided into 5, 15, 30, and 50 segments, which correspond to touching frequencies of 1, 3, 5, and 12 beats per minutes (BPM), respectively. Such characterization to find the optimal pressing frequency is crucial also for further integration with PENG harvesters that requires repeated pressing for energy harvesting. As shown in **Figure 5.28 E** and **Figure 5.31**, the total energy harvested within 5 min increases to a total of 8 mJ per finger at a touching frequency of 3 BPM and starts to decrease upon raising the BPM to 12, reflecting the rapidly decreasing period when the finger was taken off from the gel.

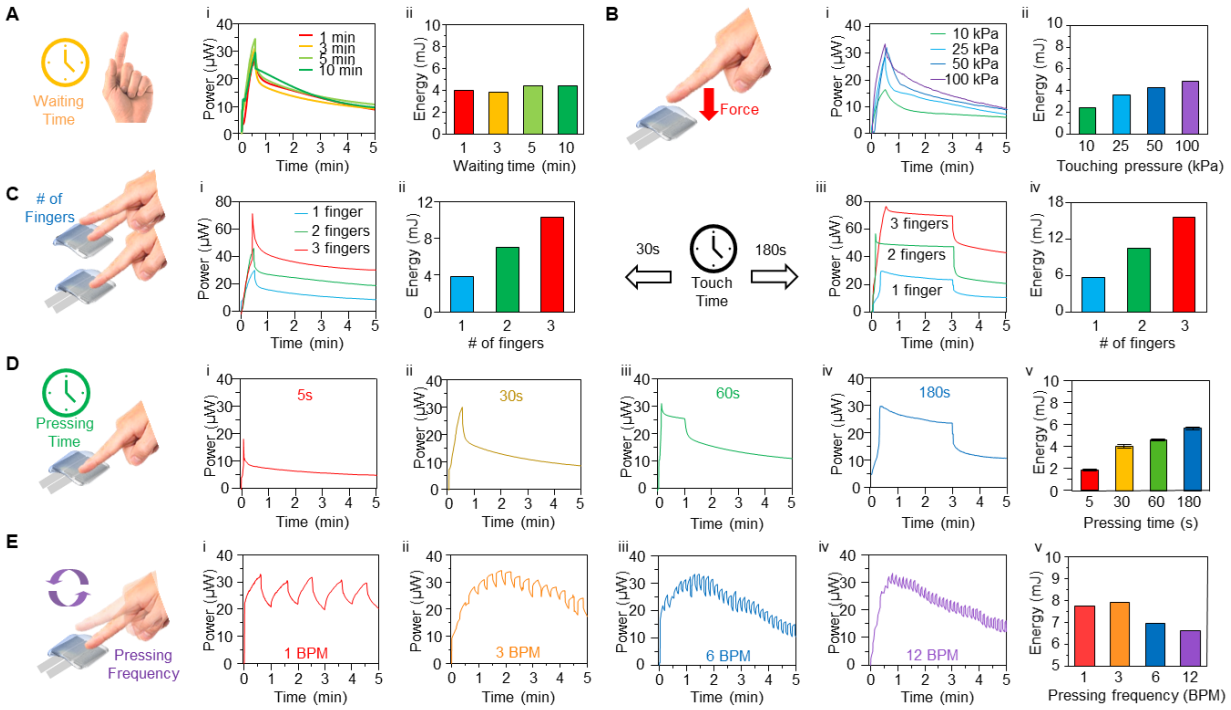

Figure 5.28. Optimization of the BFC usage patterns.
A. The power generation profile and energy harvested within 5 min of the BFC touched with the pressing pressure of 50 kPa by a bare finger that has been cleaned and waited for various time periods before touching once for 30 s. **B**. The power generation profile and energy harvested within 5 min of the BFC touched by a bare finger once for 30 s with different pressing weights. **C**. The power generation profile and energy harvested during 5 min of the BFC touched with the pressing weight of 50 kPa by 1 - 3 fingers paired with a corresponding number of BFCs for (i) 30 s and (ii) 3 min. **D**. The power generation profile and energy harvested within 5 min of the BFC touched with the pressing weight of 50 kPa by a bare finger once for different time periods (5-180 s; i – iv). (Error bars represent standard deviation, n = 4) **E**. The power generation profile and energy harvested for 5 min using different pressing frequencies with a pressing pressure of 50 kPa by one finger.

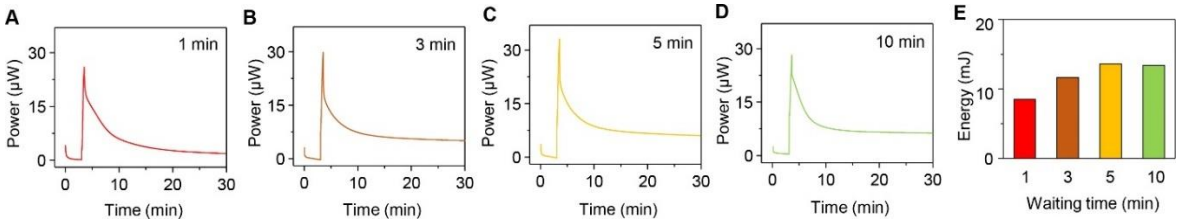

Figure 5.29. Power harvested from the BFC that was pressed by finger with different sweat generation times.
The subject's finger was washed and dried thoroughly and waited for **A**,1 min, **B**, 3 min, **C**, 5 min and **D**, 10 min before pressing the BFC device for 30 s. **E**, Total energy harvested within the 30 min of energy harvesting. Although the energy harvested in the first 5 min was similar, the amount of energy harvested in 30 min showed a larger difference, possibly due to the increased amount of fuel transfer that is limited by their dissolution and diffusion on the surface of the hydrogel. Pressure applied, 50 kPa; discharge voltage, 0.4 V.

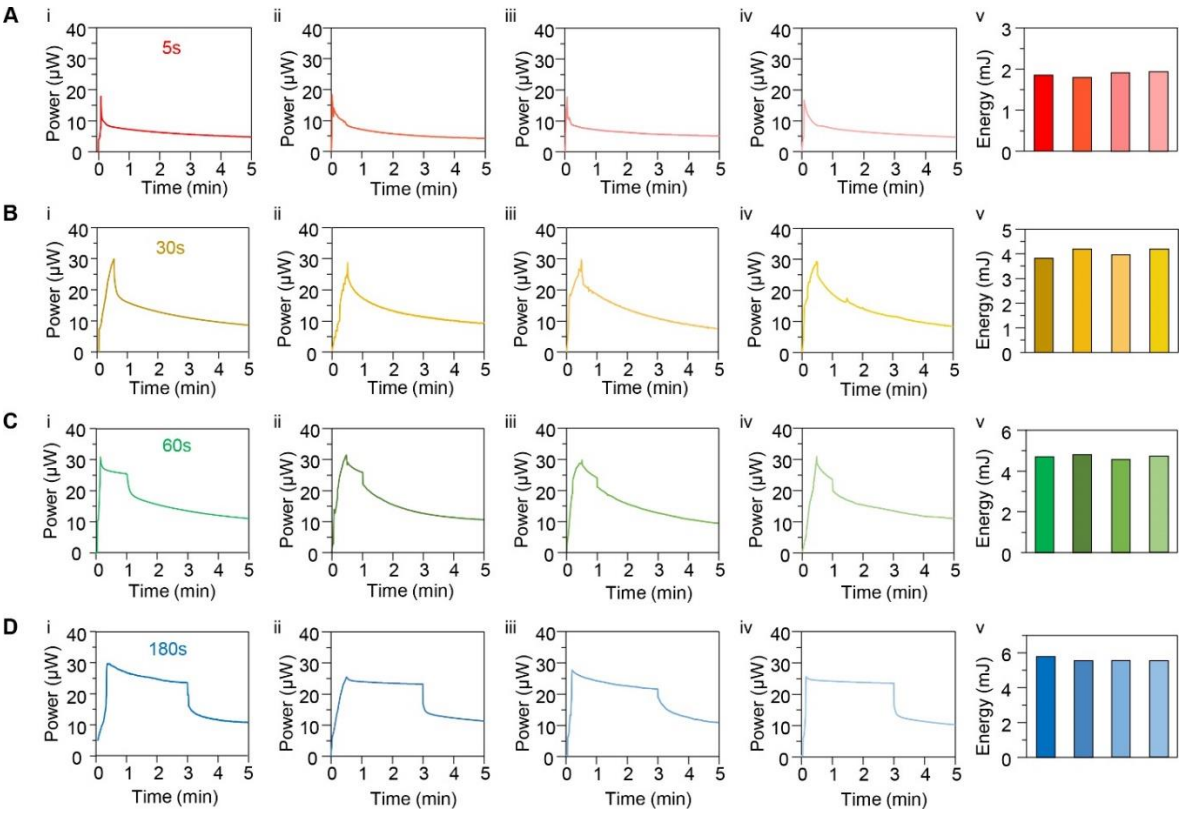

Figure 5.30. Power harvested from the BFC with different pressing times.
The (i-iv) power generation profile and (v) energy harvested within 5 min of 4 BFCs touched once with a bare finger using a pressing weight of 50 kPa for **A**, 5 s, **B**, 30 s, **C**, 60 s, **D**, 180 s.

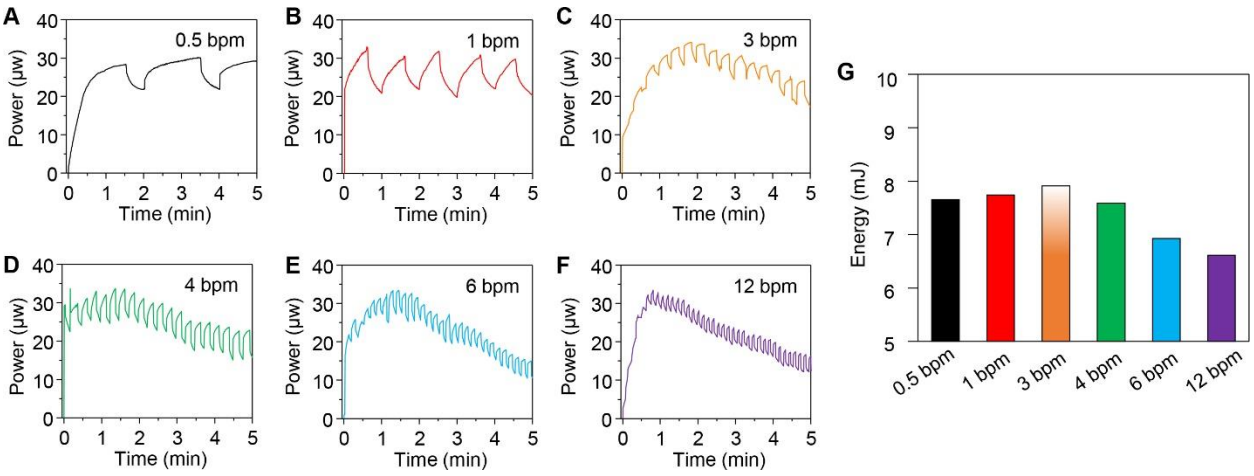

Figure 5.31. Power of the BFC pressed with different frequencies.
The BFC was pressed with different frequencies for 5 min while maintaining 60% of contact time, including **A**, 0.5 bpm (72 s pressing, 48 s release), **B**. 1 bpm (36 s pressing, 24 s release), **C**. 3 bpm (12 s pressing, 8 s release), **D**. 4 bpm (9 s pressing, 6 s release), **E**, 6 bpm (6 s pressing, 4 s release), and **F**,12 bpm (3 s pressing, 2 s release). **G**, The total amount of energy harvested in 5 min. Pressure applied, 50 kPa; discharge voltage, 0.4 V.

5.3.2 Integrated touch-based energy harvesters

After optimizing the operation of the fingertip BFC, we evaluated the potential of the efficient bioenergy harvesting approach towards practical autonomous and sustainable powering of wearable devices. To ensure the applicability of the self-powered device, the system is expected to store a sufficient amount of the harvested energy with the ability to boot the electronics as quickly as possible for the pulsed operation mode. To this end, the energy input from the harvesters, the energy storage for regulation, as well as the system energy consumption have to be characterized carefully along with budgeting of the energy flow for ensuring highly efficient system operation. The energy harvesting capability of the BFC was thus tested first via charging a capacitor that can be subsequently used for powering electronics in a pulsed manner. Due to the low potential input from the BFC, a low-power booster with energy regulation functions was

adopted to boost the BFC voltage for charging the capacitor up to 4 V. Furthermore, to fully exploit the energy input associated with the finger pressing action, a PZT-based PENG has been integrated with the BFC in a judicious layout using the same device footprint - to harvest the corresponding mechanical energy simultaneously. Such integration allows the synergistic harvesting of bioenergy associated with the same finger-pressing motion and requires careful considerations of the characteristics of the individual harvesters to maximize their power generation while minimizing their limitations. Due to the PENG's high alternating voltage nature, its input was regulated via a bridge rectifier before connecting to the capacitor. The system diagram of the integrated BFC-PENG harvester is shown in **Figure 5.32 A**. The PENG's energy harvesting relies entirely on the mechanical deformation of the PZT chip, located directly below the BFC energy harvester, and is activated upon a slight finger press. The power generated on the PZT increases upon raising the pressing force, frequency, and deformation (controlled by the thickness of the spacer) (**Figure 5.33**and **Figure 5.34**). Therefore, and as illustrated in **Figure 5.32 B,** the best performance of the integrated system is expected at a touching frequency exceeding that of the BFC system alone. After the successful integration of a single set of the mechanical and biochemical energy harvesters (**Figure 5.32 C-i)**, an identical set of PENG harvester was attached to the opposite side of the BFC, in a sandwich-like manner, to effectively harvest the mechanical energy through a pinching motion, hence harvesting the maximum amount of power without expanding the device footprint (**Figure 5.32 C-ii)**. Adopting the optimal pressing frequency of 6 BPM and a pressure of 50 kPa, the charging rate of BFC was tested against external capacitors ranging from 47 to 470 µF (**Figure 5.32 D**). The capacitors' charging time increases upon increasing the capacitance, with the prevailing contribution of BFC as the primary energy source. To gauge the charging behavior of the energy harvesters, a 100 µF capacitor with a set voltage window between 2 V and 4 V was

used to examine their corresponding charging times. Whereas the independently acting biochemical and mechanical energy harvesters were able to charge the selected 100 µF capacitors within 8 and 20 min, respectively, the integrated system completed this task within only 4 minutes (**Figure 5.32 E**). The contribution of individual energy harvesters shows that the amount of charge harvested by the capacitor in 2 min is the lowest for the PZT (~25 µC), moderate for BFC (~100 µC), and highest for the integrated harvesters (~125 µC). It should be noted that some synergistic behavior is expected to surpass the mere addition of the power from both harvesters, as shown in **Figure 5.32 E** at 4 min, where the total charge from the integrated harvesters (~220 µC) is higher than the combined BFC (~150 µC) and PZT (~40 µC). The increase in the total current input also enhances the conversion efficiency of the booster circuit, especially at higher voltages.

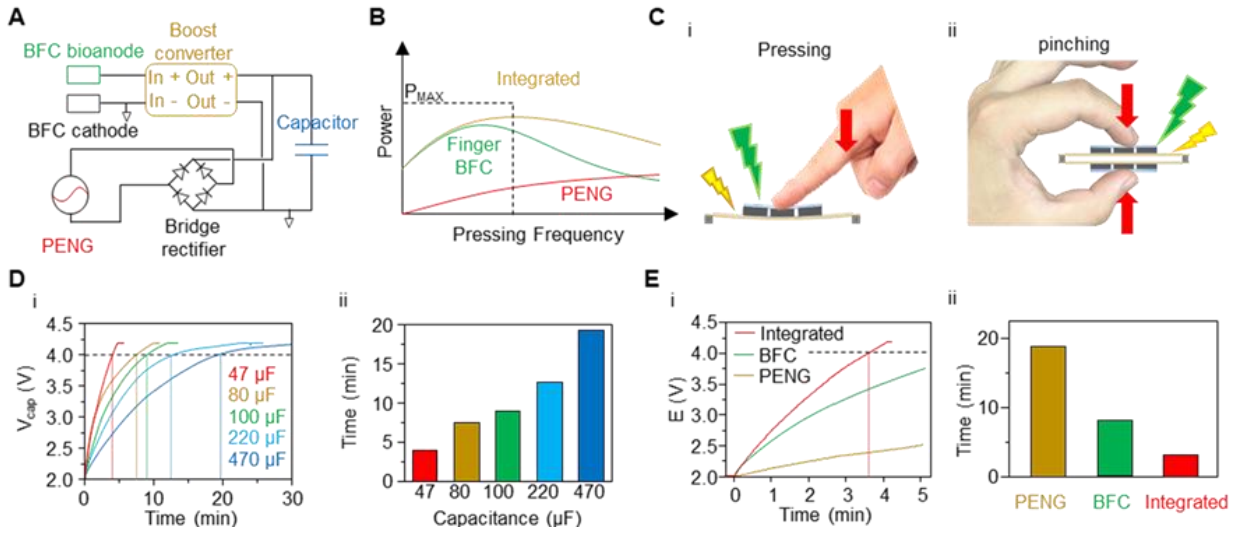

Figure 5.32. Performance of the touch-based BFC and the integrated harvesting system. **A**. System diagram of the integrated BFC-PZT touch energy harvesting system. **B**. Illustration of finding the optimal energy harvesting operation setup. **C**. The two modes of operation based on (i) pressing with 1 finger with 1 set of integrated harvesters and (ii) pinching with 2 fingers and 2 sets of integrated harvesters in a sandwich configuration. **D**. One BFC harvester pressed with 6 BPM frequency (i) charging capacitors with different capacitance and (ii) their corresponding charging time. **E**. (i) The charging of a 100 µF capacitor using only one PZT harvester, one BFC harvester, and one integrated harvester pressing at 6 PBM frequency, and (ii) their corresponding charging time.

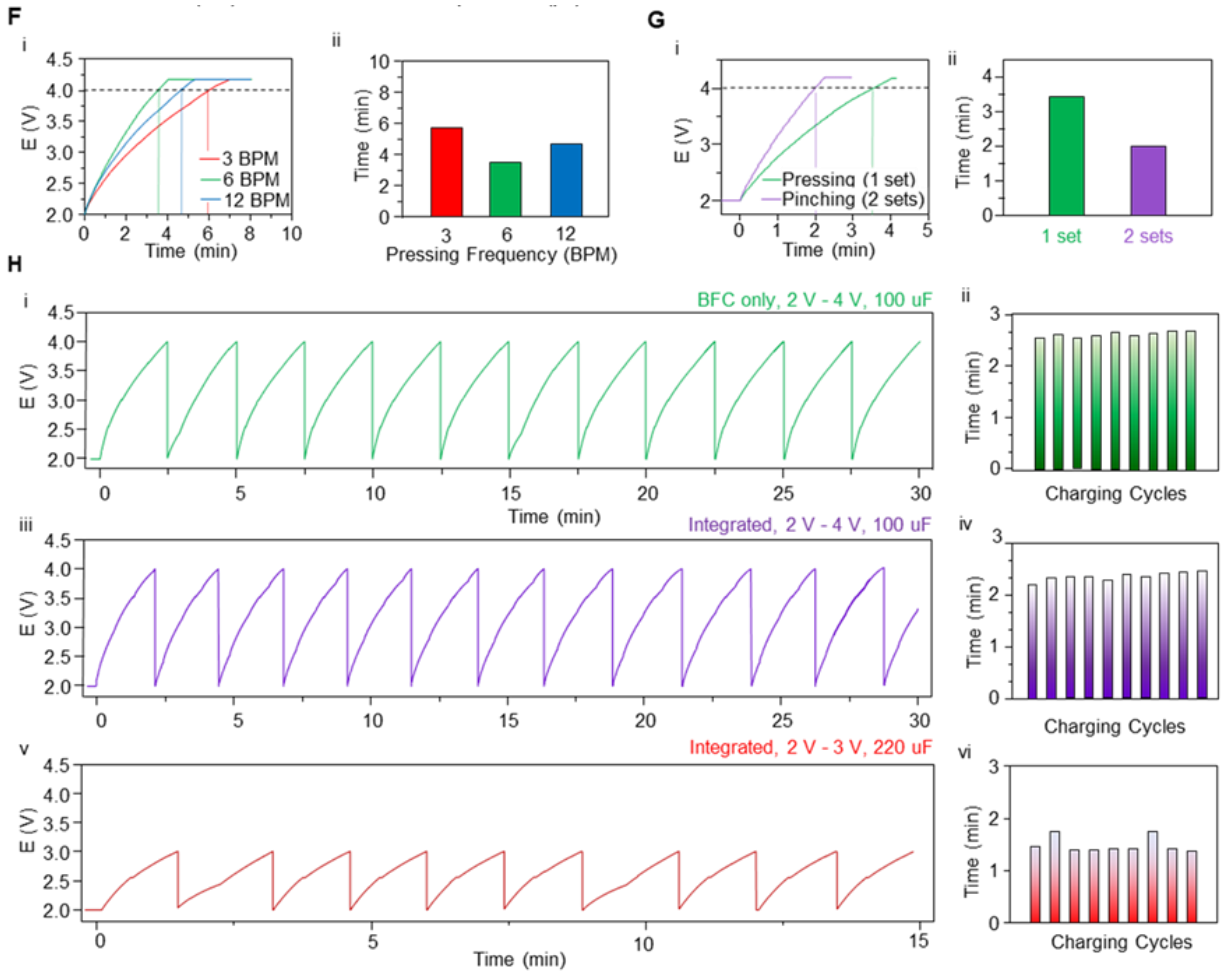

Figure 5.32. Performance of the touch-based BFC and the integrated harvesting system. (Continued)

F. (i) The charging of a 100 µF capacitor using one integrated harvester pressing at different frequencies, and (ii) their corresponding charging time. **G**. (i) The charging of a 100 µF capacitor using only one and two sets of integrated harvesters pressing at 6 PBM frequency, and (ii) their corresponding charging time. **H**. (i) The charging of a 100 µF capacitor from 2 V to 4 V (i) using only two BFC harvesters pressing at 6 PBM frequency, and (ii) their corresponding charging time, and (iii) using two integrated BFC-PZT harvesters pressing at 6 BPM frequency, and (iv) their corresponding charging time. (v) The charging of a 220 µF capacitor from 2 V to 3 V using two integrated BFC-PZT harvesters pressing at 6 BPM frequency and (vi) their corresponding charging time.

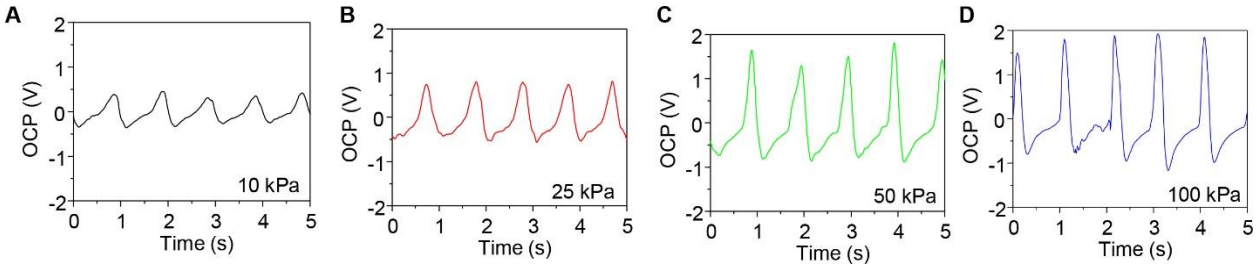

Figure 5.33. OCV of the PZT chips pressed with different pressures at the center.
The 1 cm × 2 cm PZT chip was pressed with **A**, 10 kPa, **B**, 25 kPa, **C**, 50 kPa, and **D**, 100 kPa on the center (~1 cm^2 area, corresponding to the BFC) with 0.5 mm high spacer on two sides on its back.

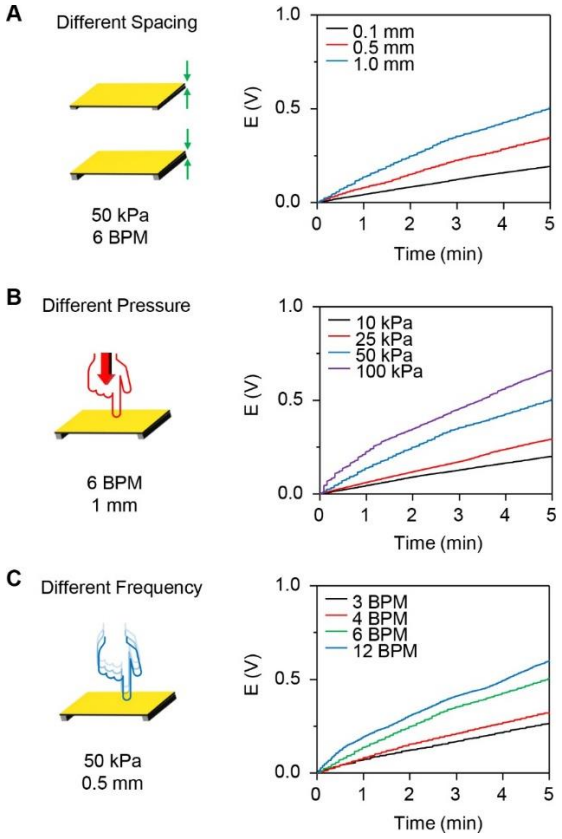

Figure 5.34. The energy harvesting using the PZT chip with different operating conditions.
The 1 cm × 2 cm PZT chip was pressed on the center with **A**, different height of spacer (0.1, 0.5, and 1 mm), **B**, pressure (10 kPa, 25 kPa, 50 kPa, and 100 kPa), and **C**, frequency (3 bpm, 4 bpm, 6 bpm, and 12 bpm). Pressing with 100 kPa and 1 mm high spacer showed the fastest charging speed compared to other conditions. However, applying 100 kPa can potentially damage the PVA hydrogel, whereas 1 mm spacer can lead to cracking on the PZT chip. Thus, 50 kPa pressure and spacer height of 0.5 mm was determined to be optimal for subsequent experiments.

The energy harvesting operation was also optimized in terms of the pressing frequency of the finger. As was discussed earlier, the 50 kPa pressure was found to be optimal in terms of convenience-to-power output ratio. Therefore, the influence of the touching frequency upon the bioenergy harvesting was evaluated using the 50 kPa pressure at pressing frequencies ranging from 1 to 24 BPM to determine the optimal pressing frequency that can charge the 100 μF capacitors in the shortest time. As shown in **Figure 5.32 F**, a charging rate of 6 BPM pressing patterns offers faster charging of the capacitor compared to the 3 and 12 BPM pressing frequencies and leads to the fastest charging speed. The trend observed in **Figure 5.32 F** is in agreement with the profiles shown in **Figure 5.32 B**, as the lower frequency (3 BPM) provided less mechanical energy input for the PZT, while the higher charging frequency reduces the biochemical energy harvesting efficiency (**Figure 5.28 E**), leading to an optimal charging rate at 6 BPM with the lowest charging time. With the optimized pressing frequency of 6 BPM, we compared the performance of a single BFC harvester to its sandwiched configuration (two back-to-back integrated devices), **Figure 5.32 G**. As expected, the double-sided harvesting device, employing two fingers' pressing motions for energy harvesting at 6 BPM, charges the 100 μF capacitors to 4 V within about 2 minutes, compared to the 4 minutes charging time observed with the single PZT-integrated BFC setup. Lastly, the continuous energy-harvesting ability of the double-sided BFC-PZT was examined at the previously optimized conditions (50 kPa at 6 BPM). As shown in **Figure 5.32 H-i** and **ii**, two sets of BFC harvesters can effectively and consistently charge the capacitor in ~ 2.8 min over the 30 min period. Similarly, the integrated BFC-PZT harvester pair also delivered consistent energy production, offering a faster charging time of ~ 2.3 min (**Figure 5.28 H-iii** and **iv**). The charging process was also tested on a subject with a lower sweat rate, which results in a slight increase in the charging time (**Figure 5.35**). Furthermore, in order to further reduce the charging time of the

system, a similar amount of charge can be harvested at a lower voltage employing capacitors with larger capacitance. As shown in **Figure 5.32 H-v** and **vi**, a 220 µF capacitor was charged in the voltage window between 2 V and 3 V, which takes only ~ 92 s, and is significantly faster compared to charging 100 µF capacitor to 4 V. Such change can be beneficial to the rapid powering of electronic devices, and the lower voltage can also limit the power consumption of MCUs. The PZT-integrated sandwiched BFC system was shown to be the most efficient, continuously and repeatedly charging the capacitor following by its polarization. The integrated system allows substantial energy harvesting using the pinching motion and natural sweat flow with negligible energy input. Considering the energy input of pressing the fingers every 10 s (~1 mW), such energy harvesting behavior is attractive compared to the typical tribo/piezoelectric harvesters and BFCs that require movements or exercise as energy input (>100 W).[28,29] These results exemplify the potential of the hybrid BFC-PZT harvesters integration for practical applications, demonstrating the most favorable EROI ever reported among all bioenergy harvesters and setting higher standards in the bioenergy collection efficiency of wearable harvesters.

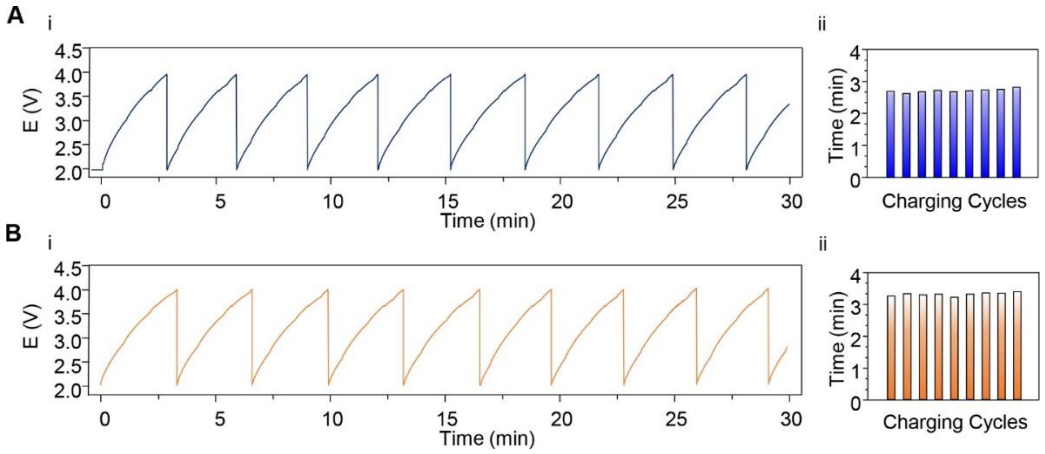

Figure 5.35. Charging the capacitor using the integrated device with subjects with different sweat rates.
The integrated harvester (with two BFC and two PZT chips) was powered by two subjects with different sweat rates (different from **Figure 5.32 H**), pressing the system to charge a 100 µF capacitor from 2 V – 4 V repeatedly. **A**, Subject 1, **B**, subject 2.

5.3.3 Self-powered sensing system

To demonstrate the practical utility of the finger-based integrated bioenergy harvester for powering electronics, a potentiometric sensing system with an ECD panel, operated in pulsed sessions, was developed (**Figure 5.36 A**). Such a system is composed of the energy regulation components that separately manage the low-voltage, continuous input from the BFCs via a booster circuit, and the high-voltage, alternating, and pulsed input from the PZT chips via a bridge rectifier (**Figure 5.36 B, Figure 5.37**). Both rectified energy inputs are collected in a capacitor. The overvoltage protection function of the booster was utilized, which was connected to an analog switch that controls the supply of energy to the MCU from the capacitor. A low-power MCU was chosen with a 10-bit analog-to-digital (ADC) resolution to read the voltage input from the sensor and control the "on" and "off" of 10 individual ECD pixels. The ECD, fabricated via layer-by-layer screen-printing (**Figure 5.36 C-i**), was chosen for its low energy consumption, as it required energy only while refreshing the displaying content. The pixels contain a 7-segment number display, along with two pixels for displaying the range ("×0.1" and "×10") of the sensing and one pixel displaying "mM" as the unit of the chemical sensing when the system boots for the first time (**Figure 5.36 C-ii**). The color change of the PEDOT:PSS relies on the redox reaction between two electrodes, with the reduced PEDOT:PSS showing the color of dark blue (on), and the oxidized PEDOT:PSS showing translucent blue color (off). By design, the 7-pixel segments on the top of the panel can display 1 digit of a number, and the 3 larger pixels on the bottom showing the ×0.1 and ×10 multipliers and the unit of mM. Combining the 10 pixels, 30 levels of concentration can be displayed using the printed ECD panel (**Figure 5.38**), as well as the letter "L" when the concentration is below the sensing range, or "H" when the concentration is above the sensing range.

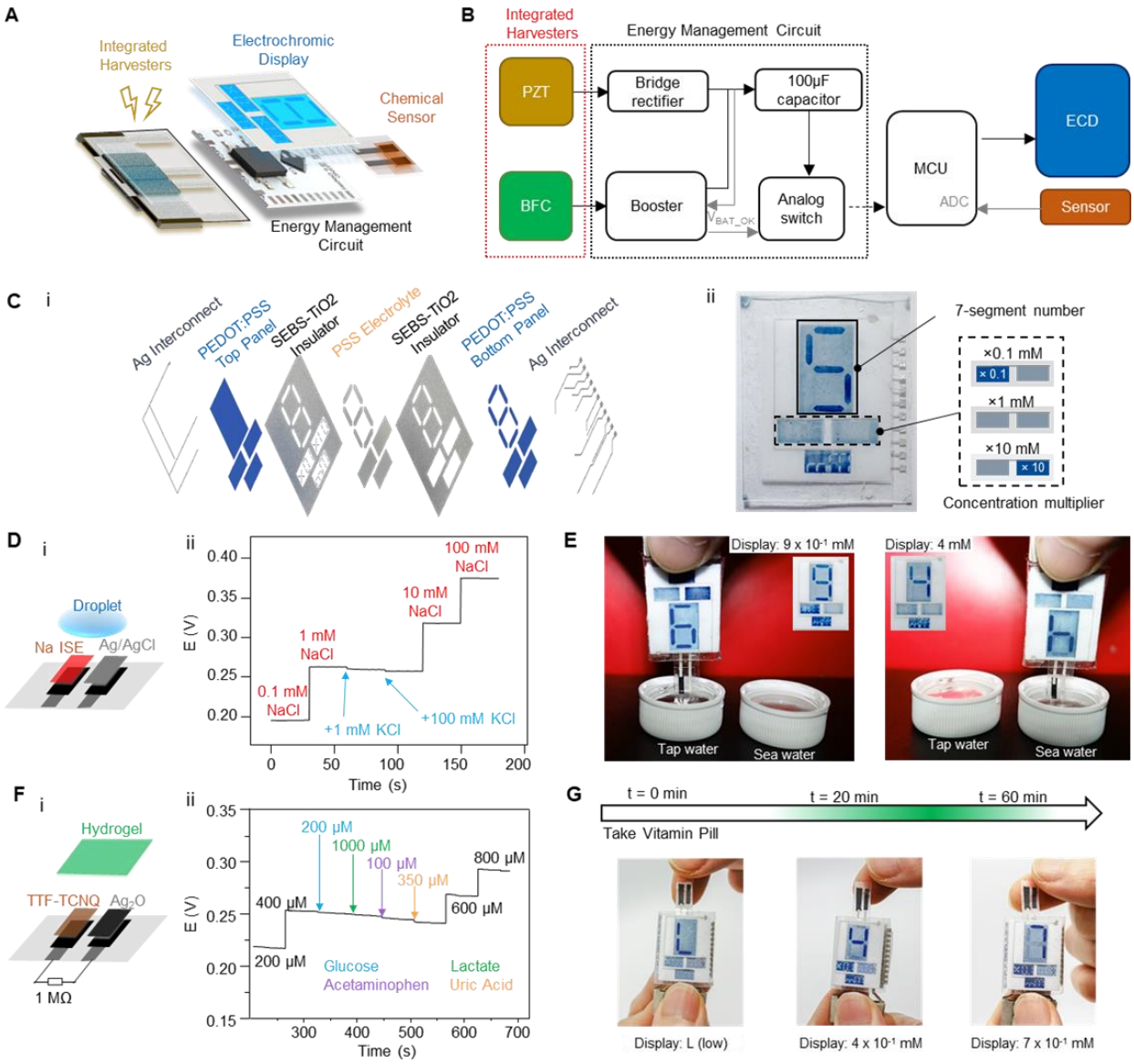

Figure 5.36. Operation of self-powered sensor-display system.
A. Exploded view of the device schematics which includes two pairs of BFC-PZT harvesters, 2-electrode sensor, ECD panel, and related MCU and power management circuit. **B**. System diagram of the self-powered system. **C**. The low-power ECD in (i) exploded view schematics and (ii) illustration of the readings on the display panel. **D**. (i) Illustration of the 2-electrode ion-selective sodium sensor, and (ii) the calibration and selectivity of the sodium sensor. **E**. Photos of the self-powered sensing system, detecting sodium concentration in tap water and 1:100 diluted seawater. **F**. (i) Illustration of the 2-electrode vitamin-C sensor, and (ii) the calibration and selectivity of the vitamin-C sensor. **G**. Time scale of the Vitamin C testing after taking a Vitamin pill (top) and corresponding photo images of the ECD reading at different times after taking the pill, tested using the self-powered sensing system.

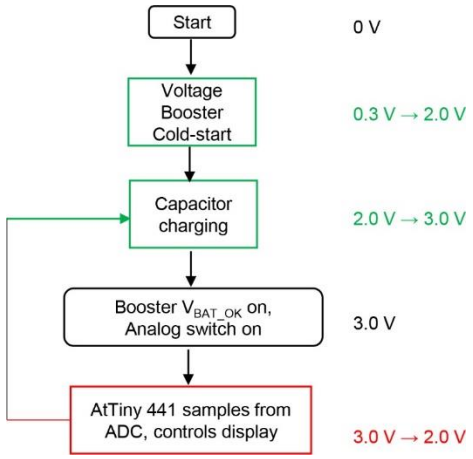

Figure 5.37. System flow chart of the integrated system and corresponding voltage values.

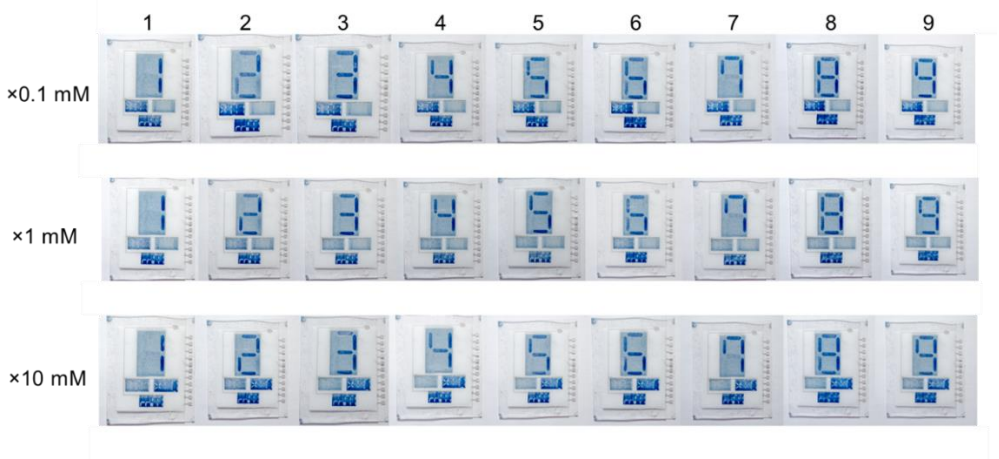

Figure 5.38. Photographic images of the printed ECD displaying different contents.

The system design obviates the integration of any wireless communication electronics, as such system would require external electronics (e.g., smartphone, smartwatch, computers) for data transmission and processing for obtaining the sensing results. To maximize the efficiency of the system while ensuring the ECD operation, the power and charge consumption for the MCU and the ECD were carefully characterized.

As the voltage and the amount of charge available from the capacitor are limited, the minimum voltage and the charge required for the color changing of the ECD were characterized in order to maximize the system efficiency. As the charge required of the ECD is mostly determined by the electrode area, the charge required and the turn-on behavior of the ECD should be characterized differently for the top 7 smaller pixels and the bottom 3 pixels. As shown in **Figure 5.39**, both pixels change color above 1.5 V, with the turn-on time below 100 ms. The smaller pixels consume 10 - 20 µC per pixel to change color, whereas the larger pixels reach 50 - 100 µC per pixel. In total, the minimum charge required to change the display content is 30 – 150 µC, depending on the number of pixels to turn "on" needed. Overall, the capacitance for energy storage was optimized at 220 µF, and the operation window of 3 V – 2 V (**Figure 5.40**, **Figure 5.41**, and **Figure 5.42**).

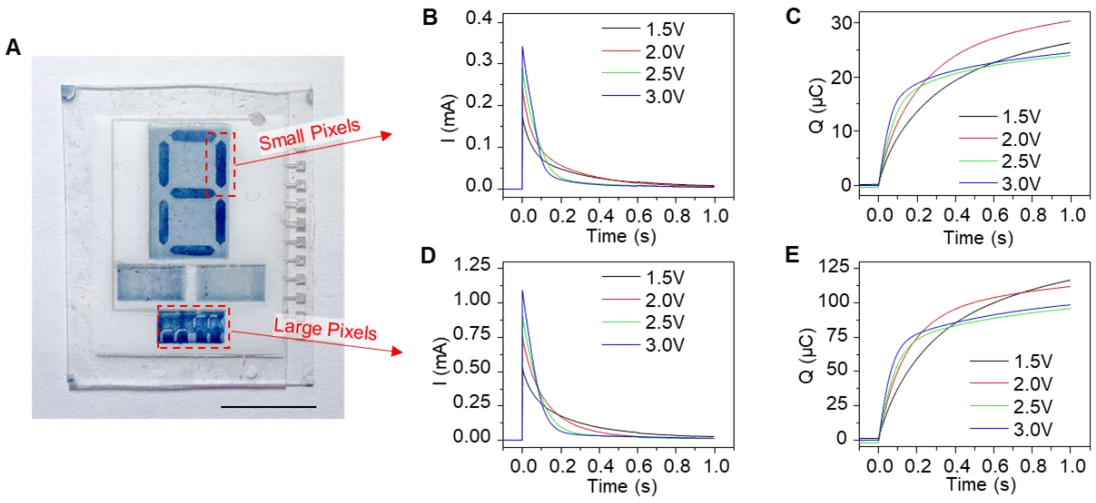

Figure 5.39. Current and charge consumption of the printed ECD.
A, Photographic image displaying two sizes of pixels on the panel, including the 7 smaller pixels on top and the 3 larger rectangular pixels on the bottom. **B**, The turn-on current and **C**, charge required for the smaller pixels at different voltages. **D**, The turn-on current and **E**, charge required for the smaller pixels at different voltages.

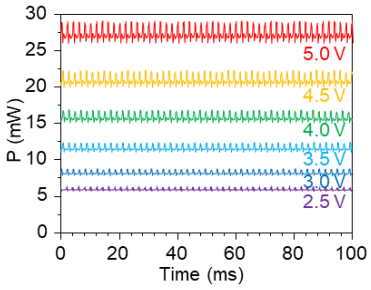

Figure 5.40. MCU power consumption at different operating voltages.

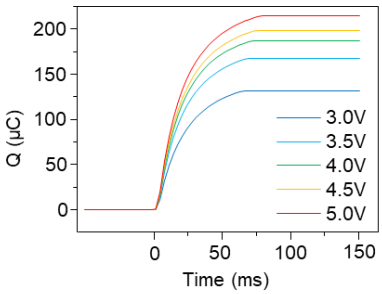

Figure 5.41. Capacitor charge flow to MCU.
A 220 µF capacitor was charged to different voltages and discharged to the MCU. As shown, there is no significant benefit from increasing the voltage of the capacitor to the runtime of the system.

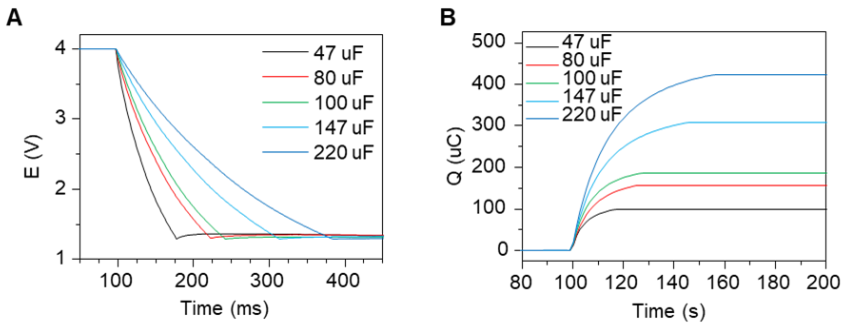

Figure 5.42. MCU output voltage and charge to ECD.
A. The voltage of different capacitors discharged from 4 V. **B**. The amount of charge available from the MCU to the display from capacitors charged to 4 V with different capacitances.

Two sets of integrated BFC-PZT harvesters, configurated back-to-back, were connected to the system to supply the harvested biochemical and mechanical energies from the pinching motions of the thumb and the index finger. Sensors can be connected to the system ADC channel for data acquisition, and the results are displayed via the ECD in the resolution of 1 significant figure (**Table 5.2** and **Table 5.3**).

Table 5.2. Na^+ sensor voltage to display content conversion.

Sensor Potential	Display content	Sensor Potential	Display content
<15 mV	L		
15-45 mV	1 ×0.1 mM	142-147 mV	6 mM
45-59 mV	2 ×0.1 mM	147-151 mV	7 mM
59-68 mV	3 ×0.1 mM	151-154 mV	8 mM
68-75 mV	4 ×0.1 mM	154-157 mV	9 mM
75-80 mV	5 ×0.1 mM	157-170 mV	1 ×10 mM
80-85 mV	6 ×0.1 mM	170-184 mV	2 ×10 mM
85-88 mV	7 ×0.1 mM	184-193 mV	3 ×10 mM
88-92 mV	8 ×0.1 mM	193-199 mV	4 ×10 mM
92-95 mV	9 ×0.1 mM	199-205 mV	5 ×10 mM
95-107 mV	1 mM	205-209 mV	6 ×10 mM
107-121 mV	2 mM	209-213 mV	7 ×10 mM
121-130 mV	3 mM	213-216 mV	8 ×10 mM
130-137 mV	4 mM	213-220 mV	9 ×10 mM
137-142 mV	5 mM	>220 mV	H

Table 5.3. Vitamin C sensor voltage to display content conversion.

Sensor Potential	Display content
<171 mV	L
171-201 mV	1 ×0.1 mM
201-224 mV	2 ×0.1 mM
224-241 mV	3 ×0.1 mM
241-255 mV	4 ×0.1 mM
255-266 mV	5 ×0.1 mM
266-274 mV	6 ×0.1 mM
274-280 mV	7 ×0.1 mM
280-285 mV	8 ×0.1 mM
285-289 mV	9 ×0.1 mM
>289 mV	H

Two types of sensors were employed for demonstrating the applicability of such a self-powered sensing system: a potentiometric sodium sensor and a vitamin-C sensor. The potentiometric sodium sensor relies on measuring the potential difference between the sodium-ion-selective membrane on the working electrode and the silver/silver chloride (Ag/AgCl) reference electrode when in contact with the sodium sample solution. (**Figure 5.36 D i**) The electrode-electrolyte interface results in a sodium concentration gradient (between the membrane and the solution) leading to a potential signal that depends logarithmically on the sodium concentration.[30] Such potentiometric sensing applies to a wide range of clinically or environmentally important electrolytes. **Figure 5.36 D** depicts the calibration of the fabricated sodium sensor, demonstrating a slope of 59.3 mV per decade of sodium concentration. It also indicates a good selectivity against potassium ions, which displays a negligible change in the sensor potential. As shown in **Figure 5.36 E**, the system can boot upon pressing the energy harvesters monitoring different sodium concentrations in tap water and 1:100 diluted seawater.

Vitamin C sensing commonly relies on amperometric measurements converted here into potentiometric ones via a controlled load. Such sensors usually referred to as "self-powered" sensors, are based on the autonomous oxidation reaction on the working electrode along with a complementary reduction reaction on the counter electrode, analogous to those of BFCs (e.g., enzymatic glucose, lactate, or alcohol sensors). In this case, the sensing principle is based on electrocatalytic oxidation of the vitamin, generating a proportional current flow, which is further converted into a potential difference signal (ΔE) under the applied load.[31,32] The vitamin C sensor relies on the selective, non-enzymatic oxidation of ascorbic acid (AA) on the anode catalyzed by the immobilized tetrathiafulvalene-tetracyanoquinodimethane (TTF-TCNQ) charge-transfer complex; silver oxide (Ag_2O) was used as the cathode material, which delivers a stable potential

throughout its reduction (**Figure 5.36 F i**). The sensing of vitamin C in stimulated sweat was described previously and was adapted here to detect the vitamin C levels in the natural fingertip sweat.[33,34] The load between the two electrodes was optimized at 10 MΩ. The calibration experiment in **Figure 5.36 F ii** and **Figure 5.43** demonstrates the sensitivity of the vitamin-C sensor, while the corresponding interference study illustrates the high selectivity of the sensor against common sweat constituents, including glucose, urea, lactate, and acetaminophen. For this, a hydrogel, similar to that used in the BFCs, was pre-soaked in artificial sweat and placed over the sensor to absorb the fingertip sweat upon touching. The on-body usage of the touch-based vitamin C sensing was optimized for sweat generation time (60 s) and sweat collection time (120 s) (**Figure 5.44**). As shown in **Figure 5.36 G**, a human subject was asked to take a vitamin pill and sense the vitamin C level continuously over 30 min. The ECD can quickly update the resulting vitamin C concentration (every 1-2 min), and the sensing system was able to capture the dynamics of the rise and fall of the vitamin C concentration within the natural fingertip sweat (**Figure 5.45**). Unlike other studies that use various energy harvester for self-powered sensing and require rapid movements and rigorous exercises, the present system can boot rapidly and continuously, and efficiently harvest energy from the slow pressing action of fingers and effortlessly supply power to complex electronic systems. Thus, the integrated harvesting system has shown its distinct advantage in practical application as an independent, self-powered electronics system toward personalized health and nutrition wellness, or environmental monitoring.

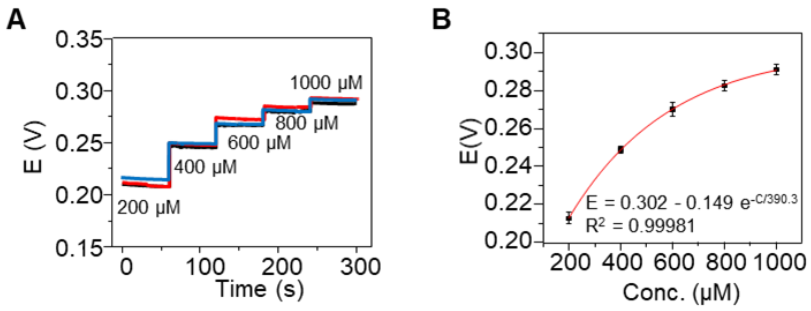

Figure 5.43. Vitamin C sensor calibration.
A, Potentiometric signal obtained in 0.1M PBS pH 7.4, upon spiking vitamin C concentrations from 200 to 1000 µM while discharging with a load of 10MΩ. **B**, Calibration curve and exponential fitting curve (n=3). RSD = 1.05%

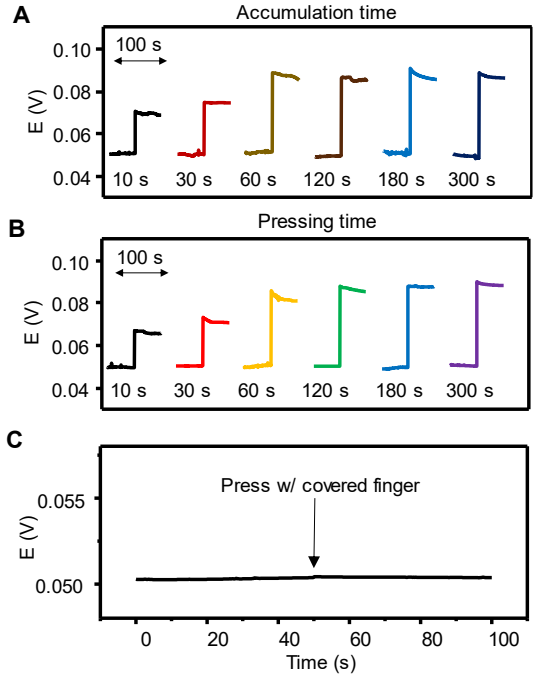

Figure 5.44. Optimization of the vitamin C sensor.
A, The voltage of the sensor before and after pressed by the finger with different sweat accumulation times (10, 30, 60, 120, 180, and 300 s) before touching the sensor. An optimal waiting time of 1 min was determined. **B**, The voltage of the sensor before and after pressed by the finger with different pressing times (10, 30, 60, 120, 180, and 300 s). An optimal pressing time of 2 min was determined. **C**, A control test using a covered finger. The sensor showed no response to the pressure applied by the finger.

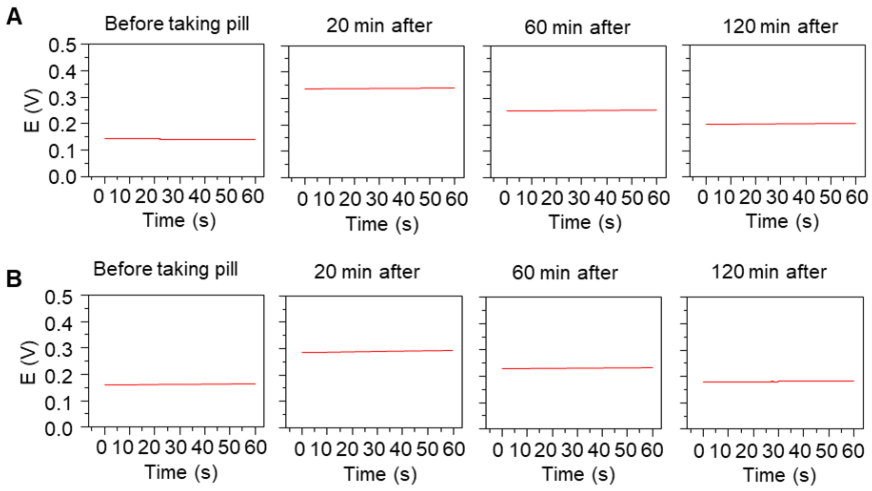

Figure 5.45. Vitamin C determination in sweat from fingertip for 2 subjects.
Potentiometric response was measured after 20, 60, and 120 min of intaking a 1000 mg vitamin C pill. A fresh hydrogel was used for each measurement. **A**. Subject 1, **B**, subject 2.

5.4 Conclusion

In this chapter, we have demonstrated a biofuel energy harvester with extremely high EROI, that effectively harvests energy from the natural fingertip sweating and the fingers' pressing motion, and its practical application in a self-powered and fully integrated sensing device. The demonstrated concept of utilizing continuous naturally pumped sweat and intuitive finger pinching motion for energy generation and operation of low-power electronics shifts the current paradigm of bioenergy harvesting devices from "work for power" into "live to power". This concept was demonstrated by energy harvesting while sleeping or low-intensity desk work, converting traces of kinetic and chemical energies, resulting from our daily activity, into electric form. Utilizing the effortless and continuous fingertip sweating as the energy source, the BFC harvester is further boosted by a piezoelectric PZT harvester that fully exploits the intuitive finger motion of pinching. With a small footprint of 2 cm^2, this system delivers similar energy collection performance while exhibiting a high energy harvesting efficiency compared to any previously reported bioenergy

harvesters which require vigorous motions or extreme sweat-inducing exercises. Pairing a low-power ECD with the touch-based harvester platform presented an energy-efficient electrochemical sensing system that can be applied to a wide variety of sensors for personalized health and nutrition monitoring applications, beyond the demonstrated sweat vitamin C and sodium sensors.

The integrated system has been designed around smart and highly efficient utilization of limited bioenergy to realize a fast-responding, extended, and autonomous operation in connection to complementary, synergistic harvesters, optimized energy storage units, low-power energy management integrated circuit, MCU, and displays. Future efforts will be directed towards further improvements of the power harvesting efficiency of the bioenergy harvesting device and its integration with other scenario-specific harvesters. The possibility of utilizing the passive sweat for a self-powered sensor can also be explored, where the sensor's power or open-circuit voltage can serve as the signals proportional to the sweat analyte concentration.[13,35] Attention will also be given to optimizing the porous, sweat-wicking current collectors and hydrogel for better durability and moisture retention under extended, repeated operation. Such highly efficient, user-friendly biocompatible energy harvesting technology, coupled with the system integration and corresponding judicious energy budgeting, offers considerable promise for establishing self-sustainable, reliable, and independent next-generation epidermal electronics systems for tracking healthcare and wellness.

Chapter 5, in full, is a reprint of the material as it appears in Joule, 2021, by Lu Yin, Jong-Min Moon, Juliane R Sempionatto, Muyang Lin, Mengzhu Cao, Alexander Trifonov, Fangyu Zhang, Zhiyuan Lou, Jae-Min Jeong, Sang-Jin Lee, Sheng Xu, and Joseph Wang. The dissertation author, Jong-Min Moon, and Juliane R Sempionatto were the primary investigators and co-authors of this paper.

5.5 References

1. Shi, Q. *et al.* Progress in wearable electronics/photonics—Moving toward the era of artificial intelligence and internet of things. *InfoMat* **2**, 1131–1162 (2020).

2. Bandodkar, A. J. *et al.* Sweat-activated biocompatible batteries for epidermal electronic and microfluidic systems. *Nature Electronics* **3**, 554–562 (2020).

3. Yu, Y. *et al.* Biofuel-powered soft electronic skin with multiplexed and wireless sensing for human-machine interfaces. *Science Robotics* **5**, eaaz7946 (2020).

4. Chen, J. *et al.* Micro-cable structured textile for simultaneously harvesting solar and mechanical energy. *Nature Energy* **1**, 16138 (2016).

5. Song, Y. *et al.* Wireless battery-free wearable sweat sensor powered by human motion. *Science Advances* **6**, eaay9842 (2020).

6. Grattieri, M. & Minteer, S. D. Self-Powered Biosensors. *ACS Sens.* **3**, 44–53 (2018).

7. Wu, W. & Haick, H. Materials and Wearable Devices for Autonomous Monitoring of Physiological Markers. *Advanced Materials* **30**, 1705024 (2018).

8. Zhao, J. *et al.* A Fully Integrated and Self-Powered Smartwatch for Continuous Sweat Glucose Monitoring. *ACS Sens.* **4**, 1925–1933 (2019).

9. Song, Y., Mukasa, D., Zhang, H. & Gao, W. Self-Powered Wearable Biosensors. *Acc. Mater. Res.* **2**, 184–197 (2021).

10. Yin, L. *et al.* A self-sustainable wearable multi-modular E-textile bioenergy microgrid system. *Nature Communications* **12**, 1542 (2021).

11. Wen, D.-L. *et al.* Wearable multi-sensing double-chain thermoelectric generator. *Microsystems & Nanoengineering* **6**, 1–13 (2020).

12. Bandodkar, A. J. *et al.* Soft, stretchable, high power density electronic skin-based biofuel cells for scavenging energy from human sweat. *Energy & Environmental Science* **10**, 1581–1589 (2017).

13. Jeerapan, I., Sempionatto, J. R. & Wang, J. On-Body Bioelectronics: Wearable Biofuel Cells for Bioenergy Harvesting and Self-Powered Biosensing. *Advanced Functional Materials* **30**, 1906243 (2020).

14. Siegel, J. A., Gilders, R. M., Staron, R. S. & Hagerman, F. C. Human Muscle Power Output During Upper-and Lower-Body Exercises. *The Journal of Strength & Conditioning Research* **16**, 173–178 (2002).

15. Taylor, N. A. & Machado-Moreira, C. A. Regional variations in transepidermal water loss, eccrine sweat gland density, sweat secretion rates and electrolyte composition in resting and exercising humans. *Extreme Physiology & Medicine* **2**, 4 (2013).

16. Lin, S. *et al.* Natural Perspiration Sampling and in Situ Electrochemical Analysis with Hydrogel Micropatches for User-Identifiable and Wireless Chemo/Biosensing. *ACS Sens.* **5**, 93–102 (2020).

17. Nagamine, K. *et al.* Noninvasive Sweat-Lactate Biosensor Emplsoying a Hydrogel-Based Touch Pad. *Scientific Reports* **9**, 10102 (2019).

18. Choi, J. *et al.* Soft, skin-mounted microfluidic systems for measuring secretory fluidic pressures generated at the surface of the skin by eccrine sweat glands. *Lab Chip* **17**, 2572–2580 (2017).

19. Peng, R. *et al.* A new oil/membrane approach for integrated sweat sampling and sensing: sample volumes reduced from μL's to nL's and reduction of analyte contamination from skin. *Lab Chip* **16**, 4415–4423 (2016).

20. Liu, Y. *et al.* Piezoelectric energy harvesting for self-powered wearable upper limb applications. *Nano Select* **2**, 1459–1479 (2021).

21. Nozariasbmarz, A. *et al.* Review of wearable thermoelectric energy harvesting: From body temperature to electronic systems. *Applied Energy* **258**, 114069 (2020).

22. Bastien, G. J., Willems, P. A., Schepens, B. & Heglund, N. C. Effect of load and speed on the energetic cost of human walking. *Eur J Appl Physiol* **94**, 76–83 (2005).

23. Wells, R. P. Mechanical energy costs of human movement: An approach to evaluating the transfer possibilities of two-joint muscles. *Journal of Biomechanics* **21**, 955–964 (1988).

24. Tang, W. *et al.* Touch-Based Stressless Cortisol Sensing. *Advanced Materials* **33**, 2008465 (2021).

25. Kumar, R. *et al.* All-Printed, Stretchable Zn-Ag2O Rechargeable Battery via Hyperelastic Binder for Self-Powering Wearable Electronics. *Advanced Energy Materials* **7**, 1602096 (2017).

26. Sempionatto, J. R. *et al.* An epidermal patch for the simultaneous monitoring of haemodynamic and metabolic biomarkers. *Nat. Biomed. Eng.* **5**, 737–748 (2021).

27. Lloyd, D. P. C. Secretion and Reabsorption in Sweat Glands. *PNAS* **45**, 405–409 (1959).

28. Yoshihuku, Y. & Herzog, W. Optimal design parameters of the bicycle-rider system for maximal muscle power output. *Journal of Biomechanics* **23**, 1069–1079 (1990).

29. Williams, K. R. & Cavanagh, P. R. A model for the calculation of mechanical power during distance running. *Journal of Biomechanics* **16**, 115–128 (1983).

30. Rich, M. *et al.* Circumventing Traditional Conditioning Protocols in Polymer Membrane-Based Ion-Selective Electrodes. *Analytical Chemistry* **88**, 8404–8408 (2016).

31. Bandodkar, A. J. *et al.* Battery-free, skin-interfaced microfluidic/electronic systems for simultaneous electrochemical, colorimetric, and volumetric analysis of sweat. *Science Advances* **5**, eaav3294 (2019).

32. Jin, X. *et al.* Modeling, design guidelines, and detection limits of self-powered enzymatic biofuel cell-based sensors. *Biosensors and Bioelectronics* **168**, 112493 (2020).

33. Sempionatto, J. R. *et al.* Epidermal Enzymatic Biosensors for Sweat Vitamin C: Toward Personalized Nutrition. *ACS Sens.* **5**, 1804–1813 (2020).

34. Falk, M., Andoralov, V., Silow, M., Toscano, M. D. & Shleev, S. Miniature Biofuel Cell as a Potential Power Source for Glucose-Sensing Contact Lenses. *Analytical Chemistry* **85**, 6342–6348 (2013).

35. Jeerapan, I., Sempionatto, J. R., Pavinatto, A., You, J.-M. & Wang, J. Stretchable biofuel cells as wearable textile-based self-powered sensors. *Journal of Materials Chemistry A* **4**, 18342–18353 (2016).

Chapter 6 Fully Integrated Epidermal Electronic Platform for Rapid Electrochemical Sensing

6.1 Introduction

Soft electronics have gathered considerable attention over the past decade as attractive alternatives to their rigid bulky counterparts, for applications in on-body sensing and human-machine interfacing.[1–4] In particular, many integrated epidermal sensing systems have been developed as "labs-on-the-skin", capable of recording a myriad of mechanical, electrical, physiological, and electrochemical signals, towards applications in healthcare, wellness and fitness.[5–8] In particular, epidermal sweat sensing represents an important route to non-invasive health monitoring, with electrochemical sensors used for capturing molecular information and detecting various electrolytes, metabolites, nutrients, and drugs for diverse applications such as precision medicine, personalized nutrition, or sports performance.[6-9] The current development of wearable sensors has evolved from the study of physical and chemical sensors alone towards the integration of sensors with energy management, signal acquisition, and data interfacing electronics.[9–14] Due to the lack of high-performance wearable batteries, most wearable electronics currently operate with commercial lithium polymer pouches or coin cells, which are rigid, unsafe, and bottleneck the product design. Avoiding such battery-related design limitations, conformal epidermal sensors were often designed with wired connections or short-range power delivery schemes, which in turn compromise the system autonomy and limit the user's mobility.[9,11,15–18] Furthermore, such integrated sensors rely on wireless data transmissions, which calls for the need for external devices (e.g., computers, mobile smartphones, customized receivers) for users to obtain the sensing results.[9,11,19–21] This lack of direct access to sensing results has led to the inconvenience and impracticality of many existing wearable sensors in their real-life applications.

The inclusion of visual data presentation would address these limitations, greatly simplify the workflow, improve the user experience, and offer exciting opportunities for smart skin-worn flexible electronic systems. Hence, there are major demands and barriers for integrating accurate on-body sensing and real-time display capabilities within a compact flexible wearable monitoring platform.[22]

To this end, integrated sensing systems with miniaturized display elements have been developed, offering an attractive route for visualizing the data in real-time for direct readout.[13,14,23–26] Among the various display technologies, colorimetric assays involve direct chemical reactions with the target analytes, such as glucose or chloride ion, report the results qualitatively via the naked eyes.[27] Electrochromic materials that change their color or opacity upon applying an electrical potential have also been integrated with sensing systems for data visualization.[28–31] However, such colorimetric display technologies involve long reaction times and lack spatial and colorimetric resolution associated with the naked eye readout, leading to inaccurate and unclear data presentation. Further analysis is usually required to convert such qualitative colorimetric information to precise numerical data, in connection to smartphones, spectral analyzers, or cameras.[24,26,32–34] While conventional display technologies have been converted recently to flexible wearable form factors, their high power consumption significantly limits their application in compact low-energy electronic systems.[35–37] Alternatively, non-emissive displays that consume low power (e.g., liquid crystal and electronic ink displays) and are controlled by microcontrollers can effectively present the processed data; yet, their lack of flexibility and stretchability limits their seamless integration with wearable devices.[23,38] Thus far, a wearable sensing system integrating power supply, *in situ* signal acquisition and processing, along with real-time accurate data visualization, into a compatible stretchable form factor, has yet to be developed. Achieving such

multifunctionality and self-sustainability will facilitate the creation of fully autonomous next-generation wearable electronics platforms.

Herein, we present an all-in-one powerful epidermal sensing platform with a dedicated electrochromic display (ECD) for rapid visualization of the analytical data along with high-performance battery. The all-printed wearable system is constructed with stretchable batteries featuring a safe Ag_2O-Zn chemistry for power supply, stretchable enzymatic and potentiometric electrochemical sensors for sensing various metabolites and electrolytes, along with ten fast responding and highly reversible poly(3,4-ethylene dioxythiophene) polystyrene sulfonate (PEDOT:PSS)-based electrochromic pixels for direct visual data presentation, all controlled by a single low-power microcontroller unit (MCU) chip, reliably attached to the stretchable substrate. Designed in a compact epidermal patch form factor, all components were fabricated with high-throughput screen-printing of customized stretchable composite inks on a heat-sealable thermoelastic styrene-ethyl butylene-styrene block copolymer (SEBS) substrate (**Figure 6.1 A** and **Figure 6.2**). The stretchable silver ink, utilizing chloride/lactate treatment, enables highly stable electrical connections under repeated stretching (**Figure 6.3**), and was printed as interconnections between all components within the system.[39] The system is solely powered by the integrated high-performance stretchable Ag_2O-Zn battery, allowing the device to be easily activated by a press of a switch, that firstly connects the batteries to the MCU, and samples the signal input from the electrochemical sensor via its analog-to-digital converter (ADC). The latter converts the analytical data into digital outputs which instantaneously control the ON and OFF states of 10 individual ECD pixels (**Figure 6.1 B**). As the sensor relies on potentiometric reading when in contact with the analyte and operates independently from the MCU, with the sensing and data visualization event take place instantaneously (<1 s) at the press of the switch and do not require any

stabilization time. The attractive performance of the fully integrated multifunctional system was showcased with four types of sensors, including potentiometric sodium ions and pH sensors and enzymatic amperometric glucose and lactate biosensors, under optimized loads, with the analyte concentrations, displayed instantly on the ECD for directly visual digital readout (**Figure 6.1 C**). Such an integrated epidermal patch exhibited excellent durability and mechanical robustness (**Figure 6.1 D-i** and **ii**), able to perform over 10,000 sensing sessions over 5 days while enduring thousands of stretching cycles. A rapid room-temperature "solvent welding" process was developed for bonding the rigid chip and the soft printed circuit (that have drastically different elastic modulus), hence securing the connection to the MCU without using any conductive adhesives to establish a reliable bonding on the interface during stretching (**Figure 6.1 D-iii** and **Figure 6.4**). Adapting the use of melanic anhydrite-grafted SEBS (SEBS-MA) can strengthen the bonding of the metal contact pads on the MCU to the substrate, allowing strain up to 300% strain without detachment (**Figure 6.5**). The wide applicability of the all-stretchable sensor patch platform was demonstrated using representative sweat sensors, including potentiometric sodium and pH sensors and enzymatic lactate and glucose sensors for monitoring electrolytes and metabolites, respectively. The all-printed multi-functional compact epidermal sensing platform thus integrates the ECD, batteries, and sensors, in a highly flexible, and stretchable form factor. The skin-interfaced platform is entirely autonomous and self-sustainable towards instantaneous sensing and direct visual data presentation and can operate independently from any external equipment. The presented sensing system, with a dedicated stretchable display and battery, is compatible with a myriad of wearable healthcare and wellness applications and paves the way towards a practical "lab-on-the-skin" for comprehensive epidermal monitoring.

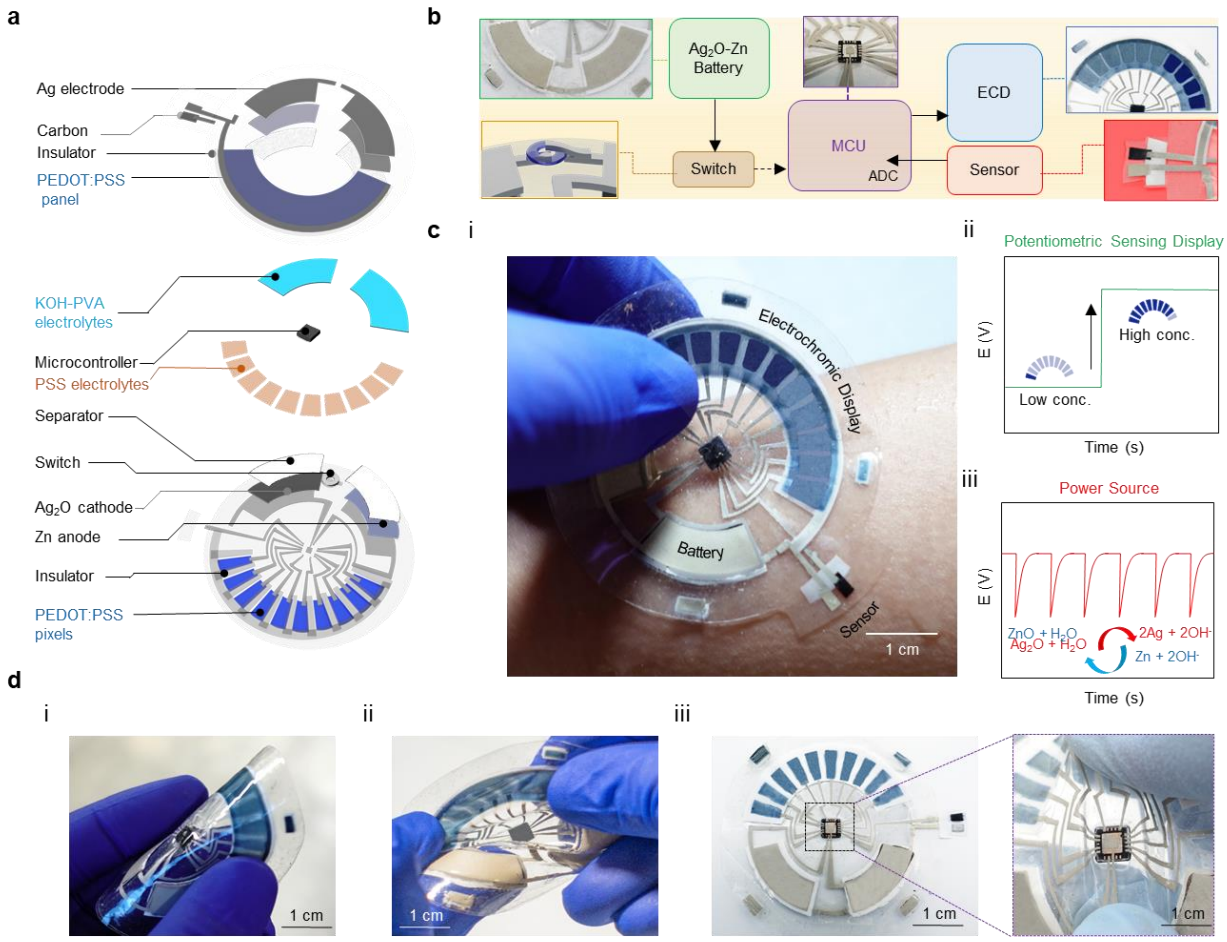

Figure 6.1. System overview of the all-printed skin interfaced ECD sensing patch.
A, Exploded view detailing the individual layers of the epidermal patch. **B**, System flow chart of the system and the zoom-in view of the individual modules. **C**, The operation of the patch: (i) Photographic image demonstrates the patch used for epidermal sweat sensing by revealing instantaneously the target concentration. (ii) Illustration of the change in the display that changes with the electrolyte concentration and readout of the potentiometric sensor, and (iii) the intermittent discharge mode of the Ag_2O-Zn battery that supplies power to the system. **D**, Photographic images demonstrating the mechanical performance and durability of the patch, including its (i) bending or (ii) stretching, and (iii) stretching of the connection between the interconnect and the MCU.

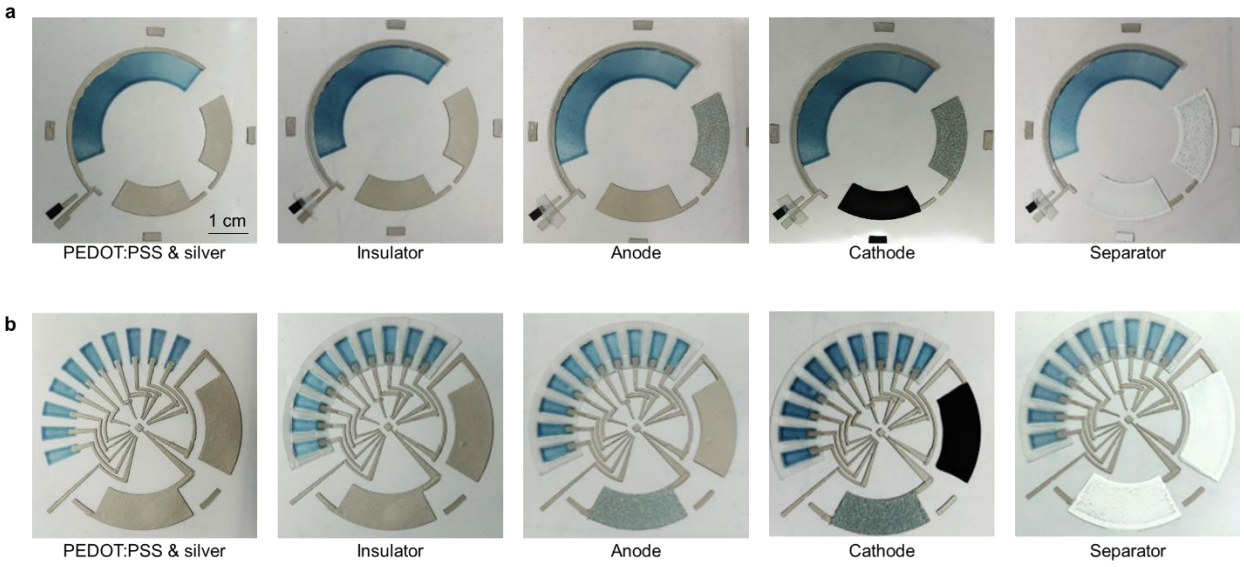

Figure 6.2. Photo images of the layer-by-layer printing of the ECD patch.
A, Printing of the top panel. **B**, Printing of the bottom panel.

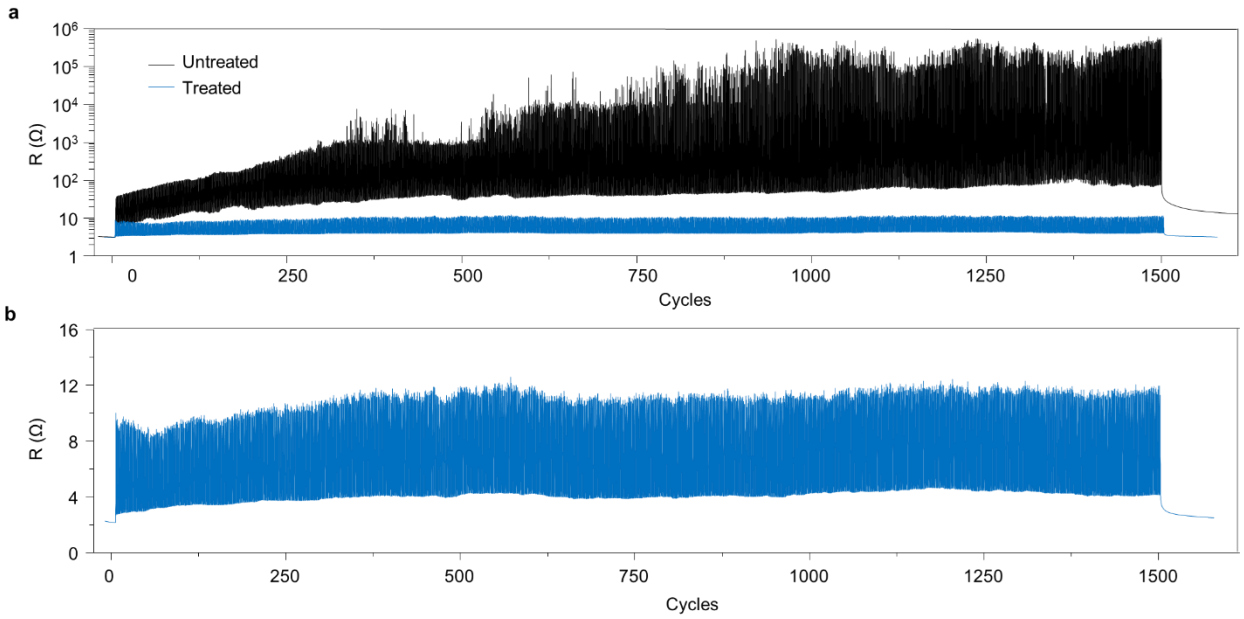

Figure 6.3. Effect of the chloride/lactate treatment
A, Resistance change of the printed stretchable silver ink before and after the chloride/lactate treatment during1500 cycles of 20% uniaxial stretching. **B**, Zoom-in of the 1500 cycles 20 % uniaxial stretching of the treated silver traces.

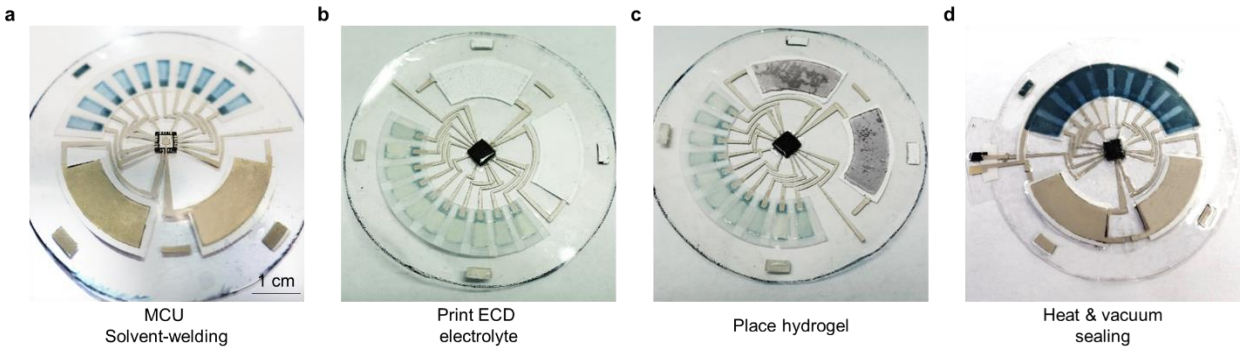

Figure 6.4. Photo images of the assembly of the ECD patch.
A, Solvent-welding the MCU to the SEBS polymer substrate with printed stretchable silver connections. **B**, Encapsulating the MCU with SEBS and printing the PSSNa electrolyte for the ECD pixels. **C**, Place the KOH-PVA hydrogel onto the battery electrodes. The silver ink is added to the terminals where the silver traces between the top and the bottom panel connect. **D**, The top and bottom panels were aligned and assembled, and the rim of the patch is heat and vacuum-sealed.

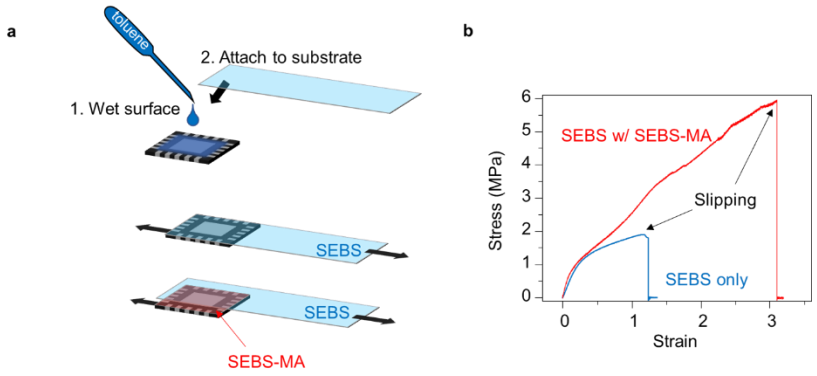

Figure 6.5. Solvent-welding process.
A, Illustrations of the "solvent-welding" process and the bonding strength test of the MCU chip to the SEBS substrate with and without a SEBS-MA inter-layer for enhanced bonding. **B**, The strain vs. stress curve of the SEBS during stretching of the SEBS substrate until the MCU detaches from the substrate. In both cases, the MCU was able to endure over 100% stretching without detaching from the surface.

6.2 Experimental Section

6.2.1 Chemicals

Graphite, toluene, acetone, ethanol, hydrochloric acid (HCl), 1,4-naphthoquinone (NQ), chitosan, glutaraldehyde, acetic acid, Nafion, lactic acid, D-(+)-glucose, glucose oxidase (GOx), Ag flake, Ag_2O powder, zinc (Zn), zinc oxide (ZnO), bismuth trioxide (Bi_2O_3), titanium dioxide (TiO_2), sodium ionophore X, sodium tetrakis[3,5-bis(trifluoromethyl)phenyl]borate (Na-TFPB), bis(2-ethylhexyl) sebacate (DOS), tetrahydrofuran (THF), polyvinyl butyral (PVB), poly(vinyl chloride) (PVC), sodium chloride (NaCl), polystyrene-block-poly(ethylene-ran-butylene)-block-polystyrene-graft-maleic anhydride (SEBS-MA), methanol, iron (III) chloride ($FeCl_3$), aniline, sodium phosphate anhydrous, citric acid, sodium polystyrene sulfonate (PSSNa), glycerol, D-sorbital, acrylamide, N,N'-methylenebisacrylamide, potassium peroxydisulfate, sodium dodecylbenzene sulfonate (DBSS) and bromocresol green were all purchased from Sigma Aldrich. The polyurethane (PU) (Tecoflex EG-80A) was obtained from Lubrizol. Styrene-ethylene-butylene-styrene (SEBS G1645) triblock copolymer was obtained from Kraton. MWCNT-COOH was purchased from Cheap Tubes inc. The screen printable PEDOT:PSS paste was purchased from Sun Chemical. The lactate oxidase (LOx) was purchased from Toyobo. The Capstone™ fluorosurfactant FS-65 was purchased from DuPont. The GBR6005 was obtained from Daikin.

6.2.2 Device Fabrication

A stretchable silver ink was used to fabricate the circuit that connects the various components of the device. The circuit pattern was designed with Autodesk AutoCAD (CA, USA) and made into a cut-through metal stencil by Metal Etch Services (San Marcos, CA, USA). The

stretchable silver ink was composed of silver flake, SEBS (40 wt% in toluene) and toluene in 4:2:1 weight ratio.

After the printing of the silver ink layers, a chloride/lactic acid treatment, adapted from a previous study[39] was employed to further functionalized the silver particles and enhance the stability and conductivity of the silver layer during stretching. The treatment involved preparing an aqueous solution of 100 mM sodium chloride and 50 mM lactic acid, which was repeatedly sprayed onto the printed pattern using a spray bottle and dry in the oven at 80 °C for 5 min for 3 times, followed by washing with deionized (DI) water and drying in the oven at the same temperature for 10 min. The treatment endowed the silver layer higher conductivity and stability, as shown in **Figure 6.3**. The subsequent PEDOT:PSS, Zn, Ag_2O, and insulator can be printed upon the treated silver layer.

The substrate for the ECD was composed of styrene ethylene butylene styrene (SEBS) dissolved in toluene (40 wt%) and was fabricated by doctor blade casting (1000 μm thick) the SEBS then followed by curing in the oven at 80 °C for 1 hour.

The ECD was fabricated using layer-by-layer screen-printing with customized four kinds of inks: the electrochromic poly(3,4-ethylenedioxythiophene) polystyrene sulfonate (PEDOT:PSS) ink, the silver ink for interconnection, the opaque insulator ink composed of SEBS and TiO_2, and the sodium polystyrene sulfonate-based electrolyte ink. The PEDOT:PSS ink was prepared using 1 g of PEDOT:PSS paste, 0.2 mL of toluene, 0.15 mL DBSS (75 mg ml^{-1} in DI water), and 0.0135 mL of Capstone™ fluorosurfactant FS-65. The use of the toluene enables better bonding between the PEDOT:PSS to the substrate, and the addition of the DBSS and Capstone surfactant was used to improve ink wettability to avoid contraction of the printed patterns due to surface tension of the

ink. Furthermore, the addition of the surfactant can further improve the PEDOT:PSS conductivity due to enhanced phase separation.[40] The opaque insulator ink was composed of TiO_2, SEBS (40 wt% in toluene) in 1: 10 weight ratio. The PSS electrolyte ink was formulated by mixing PSSNa, D-sorbitol, glycerol, TiO_2, and polyacrylamide (PAM) precursor solution in 4:1:1:0.8:2 weight ratio. The PAM solution was formulated by mixing acrylamide, DI water, potassium peroxydisulfate, and N,N'-methylenebisacrylamide in 2:10:0.05:0.02 ratio. Here, the TiO_2 was used to form a white, opaque electrolyte layer to enhance the color-change contrast, whereas the PAM solution was used to enhance the electrolyte viscosity to avoid the bleeding and short-circuiting of the printed PSS electrolyte ink among pixels (**Figure 6.6**). All inks are mixed in the planetary mixer at 1800 rpm for 10 min or until homogenous.

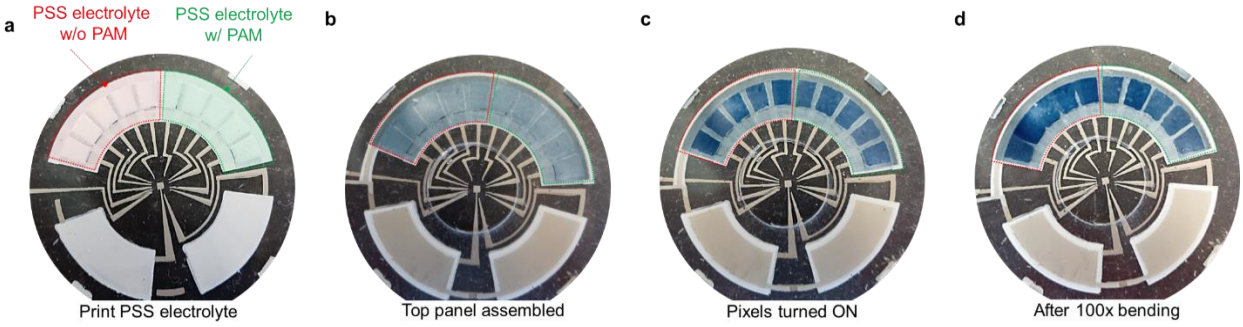

Figure 6.6. Comparison of PSS electrolyte with and without the addition of the PAM. **A**, The as-printed electrolyte layer on the bottom panel. **B**, The patch right after assembly. **C**, The patch with all pixels turned on right after assembly. **D**, The patch after 100 times 90° outward and inward bending and then all pixels turned on. The pixels with PSS electrolyte without PAM were connected and misshaped due to the patch deformation.

The ECD panel was composed of the color-changing top panel and the bottom panel to control the regional color change. The PEDOT:PSS ink was printed first onto the SEBS substrate and cured in the oven at 100 °C for 2 h. Then, the silver interconnection and the opaque insulator

layers were printed, with each layer cured at 80 °C for 5 min. Before assembly, the electrolyte was printed onto the bottom panel and briefly heated in the oven for 15 s at 80 °C to cross-link the PAM in the electrolyte.

The formulation of the battery inks and the electrolyte was adapted from previous studies.[17,41] The printing of the battery relied on four inks: Ag ink as current collector, Zn ink as anode, Ag_2O ink as cathode and separator ink. The Zn ink is prepared using Zn, ZnO, Bi_2O_3 and GBR binder (25 wt% in acetone) in 9:0.5:0.5:0.267 weight ratio. The Ag_2O ink was prepared using Ag_2O, super P carbon black and GBR binder (33 wt% in acetone) in 1.9:0.1:2.66 weight ratio. The separator ink was composed of TiO_2, TritonX-114, SEBS (40 wt% in toluene) and toluene in 3:0.1:1.5:1.5 weight ratio. All inks were mixed in the planetary mixer at 2500 rpm for 10 min or until homogenous. The PVA electrolyte gel was crosslinked initially by dissolving 0.9 g PVA into 9.1 ml DI water at 90 °C, followed by mixing with 14 g of 16.7 wt% NaOH solution and desiccating the mixture in a vacuum desiccator until removing 67% of the total weight. The formed hydrogel was then cut using a 3D-printed hole punch into the same shape as the electrodes, and soaked in 9 M NaOH solution for over 12 h before use. Here, NaOH was used instead of KOH to reduce self-discharge and extend cell shelf-life.

The stretchable battery was composed of two pairs of Zn-Ag_2O battery printed on the bottom and top panels, separately. The layer-by-layer printing steps of the battery were followed by using Ag ink, Zn anode or Ag_2O cathode ink and separator ink, with each layer cured at 80 °C for 5 min (**Figure 6.2**). Before assembly, a PVA electrolyte gel was placed between the anode and cathode, and a concentric circle switch was placed between the Ag interconnection of two panels. After aligning and combining two panels, the battery can work and power the MCU effectively by pressing the switch.

The sodium sensors and pH sensors were fabricated by using flexible silver and carbon inks. The formulation of the Ag ink is described above. The carbon ink was prepared using graphite, super-P carbon black, SEBS (40 wt% in toluene), and toluene in a 6:1:8.4:2.1 weight ratio. Both inks were mixed in a planetary mixer at 1800 rpm for 10 min or until homogenous.

The silver ink and the carbon ink were printed onto the top panel SEBS substrate layer-by-layer and were covered using SEBS resin to define the electrode area, exposing 2 mm^2 of carbon electrode as the working electrode and 1 mm^2 of the silver electrode as the reference electrode. A 0.1 M $FeCl_3$ solution was drop-cast onto the silver electrode to chlorinate the surface and form AgCl.

The sodium sensor was based on screen printed electrodes modified via drop-casting. A cocktail composed of PVB (78.1 mg ml^{-1}) and sodium chloride (50 mg ml^{-1}) dissolved in methanol was drop-cast onto the chlorinated reference surface (1.5 µl mm^{-2}). A PU resin (1 g in 20 g THF) was then drop-cast onto the dried cocktail layer (2 µl mm^{-2}) to prevent leaching. A cocktail for the sodium ion-selective electrode was formulated by dissolving 1 mg of sodium ionophore X, 0.77 mg Na-TFPB ion exchanger, 33 mg PVC, and 66 mg DOS in 660 mL nitrogen-purged THF. The resulting cocktail was subsequently drop-cast onto the carbon electrode (2 µl mm^{-2}).

Following the screen-printing fabrication protocol, the working and reference electrodes were created. The pH sensor was prepared by electropolymerization of aniline onto the working carbon layer. The carbon electrode was first electrochemically cleaned via 10 cyclic voltametric (CV) scans in 0.5 M HCl (40 µL) from 0.3 V to 1.1 V vs. Ag/AgCl at a scan rate of 0.1 V s^{-1}. Subsequently, polyaniline (PANi) electropolymerization was performed with a solution containing 0.1 M aniline in 1 M HCl by cyclic voltammetry (CV) from -0.2 V to 1.0 V (vs. Ag/AgCl) at 0.05

V s^{-1} to accumulative gain around 100 mC charge on the carbon electrode. Subsequently, the electrode was washed with DI water and was allowed to air-dry.

The glucose sensor and lactate sensor were fabricated by using flexible silver ink, carbon ink and Ag_2O ink as cathode. The Ag_2O ink is prepared by mixing Ag_2O, super P carbon black and GBR binder (21 wt% in acetone) in a 1.9:0.1:3.166 weight ratio. The Ag_2O is mixed in a planetary mixer at 2500 rpm for 10 min or until homogenous.

The silver ink and the carbon ink were printed onto SEBS substrate layer-by-layer followed by printing the Ag_2O ink onto one of the carbon electrodes to obtain the cathode of both sensors. Finally, the electrodes were covered using SEBS resin to define the electrode area, exposing 2 mm^2 of carbon electrode as the anode and 2 mm^2 of the Ag_2O electrode as the cathode.

The glucose sensor was fabricated by drop casting 0.2 M NQ solution dissolved in acetone: ethanol (9:1) mixture containing 2 mg mL^{-1} CNT-COOH onto carbon electrode (1.5 µL mm^{-2}). Then 40 mg mL^{-1} GOx solution dissolved in PBS containing 10 mg mL^{-1} BSA was drop casting after the first layer drying (1.5 µL mm^{-2}). Finally, 1.5 µl mm^{-2} chitosan layer (1 wt% in 0.1M acetic acid) and a 0.75 µL mm^{-2} glutaraldehyde layer (1% in water) were drop cast on the top for improved immobilization. A surface-mount resistor (75 kΩ, 150 kΩ, or 10 MΩ) was solvent-welded between the two electrodes as the discharging load.

The lactate sensor was fabricated similarly with glucose sensor, which drop cast 0.2 M NQ solution containing 2 mg/mL CNT-COOH (1.5 µL mm^{-2}), followed by 40 mg/mL LOx solution dissolved in PBS containing 10 mg/mL BSA (1.5 µL mm^{-2}), as well as 1.5 µl mm^{-2} chitosan (1 wt% in 0.1M acetic acid) and 0.75 µL mm^{-2} glutaraldehyde (0.5% in water) layer by layer after

each layer drying. Finally, 0.75 µL mm^{-2} PVC layer (3% in tetrahydrofuran) was drop cast on the top for enzyme immobilization.

6.2.3 Electrical circuit design

The control circuit was designed to digitalize the sensor output and control the ECD (**Figure 6.7**). A MCU (ATtiny 441, Microchip Technology, USA) with a 10-bit built-in analog-to-digital converter was used. The sensor voltage was firstly digitalized and then displayed by the 10-bit ECD. The sensor readout was mapped to the display bits per their corresponding sensor calibration curve, and the ECD would address individual pixels corresponding to the sensor voltage. The mapping of the ECD display and the sensor voltage input was summarized in **Table 6.1 - Table 6.6**.

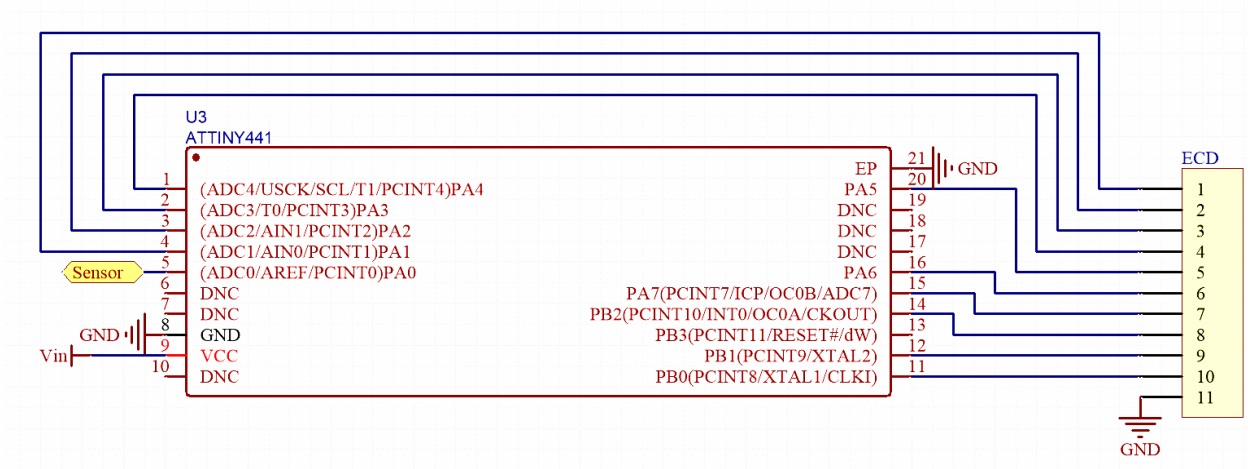

Figure 6.7. Schematics of the ECD control circuit.
The 10-bit ECD is controlled by ATtiny 441 to display the sensor output.

Table 6.1. Na sensor voltage-to-display conversion.

Sensor Potential (mV)	Conc. Range (mM)	Pixels on
0 - 34	< 0.1	1
34 - 59	0.1 - 0.25	2
59 - 140	0.25 - 5	3
140 - 96	5 - 1	4
96 - 121	1 - 2.5	5
121 - 140	2.5 - 5	6
140 - 159	5 - 10	7
159 - 184	10 - 25	8
184 - 202	25 - 50	9
202 - 221	50 - 100	10

Table 6.2. pH sensor voltage-to-display conversion.

Sensor Potential (mV)	Conc. Range (pH)	Pixels on
383 - 320	< 3	0
320 - 258	3 - 4	3
258 - 195	4 - 5	4
195 - 133	5 - 6	5
133 - 70	6 - 7	6
70 - 7	7 - 8	7
7 - 0	>8	10

Table 6.3. Lactate sensor with 75 kΩ load voltage-to-display conversion (0 to 15 mM)

Sensor Potential (mV)	Conc. Range (mM)	Pixels on
0 - 28	0 - 1.5	1
28 - 44	1.5 - 3	2
44 - 65	3 - 4.5	3
65 - 90	4.5 - 6	4
90 - 117	6 - 7.5	5
117 - 145	7.5 - 9	6
145 - 172	9 - 10.5	7
172 - 198	10.5 - 12	8
198 - 223	12 - 13.5	9
223 - 245	13.5 - 15	10

Table 6.4. Lactate sensor with 75 kΩ load voltage-to-display conversion (0 to 30 mM)

Sensor Potential (mV)	Conc. Range (mM)	Pixels on
0 - 44	0 - 3	1
44 - 90	3 - 6	2
90 - 145	6 - 9	3
145 - 198	9 - 12	4
198 - 245	12 - 15	5
245 - 286	15 - 18	6
286 - 320	18 - 21	7
320 - 349	21 - 24	8
349 - 372	24 - 27	9
372 - 392	27 - 30	10

Table 6.5. Glucose sensor with 75 kΩ load voltage-to-display conversion (0 – 10 mM)

Sensor Potential (mV)	Conc. Range (mM)	Pixels on
0 - 22	0 - 1	1
22 - 43	1 - 2	2
43 - 71	2 - 3	3
71 - 102	3 - 4	4
102 - 135	4 - 5	5
135 - 168	5 - 6	6
168 - 198	6 - 7	7
198 - 225	7 - 8	8
225 - 251	8 - 9	9
251 - 273	9 - 10	10

Table 6.6. Glucose sensor with 10 MΩ load voltage-to-display conversion (0 – 0.5 mM)

Sensor Potential (mV)	Conc. Range (mM)	Pixels on
0 - 25	0 - 0.05	1
25 - 44	0.05 - 0.1	2
44 - 61	0.1 - 0.15	3
61 - 76	0.15 - 0.2	4
76 - 89	0.2 - 0.25	5
89 - 102	0.25 - 0.3	6
102 - 113	0.3 - 0.35	7
113 - 123	0.35 - 0.4	8
123 - 133	0.4 - 0.45	9
133 - 142	0.45 - 0.5	10

6.2.4 Device Assembly

The microcontroller (MCU) chip was placed onto the bottom panel after the procedure of screen printing above by the "solvent welding" process to connect with Ag layer precisely. A 5 µl droplet of toluene and ethanol (3: 7 by volume) was used to temporarily soften the interconnecting silver traces followed by placing the MCU. The solvent was allowed to evaporate at room temperature for 5 min to facilitate physical crosslinking of the SEBS within the Ag ink and the substrate to the metal contact pads of the MCU chip. This rapid solvent welding process thus eliminates the use of any bonding layer or conductive paste. The connected MCU was sealed by 0.1 mL SEBS (40 wt% in toluene) and cured in the oven at 80 °C for 30 min after drying in room temperature. Subsequently, the electrolyte is printed onto the bottom panel and briefly cross-link the PAM in the electrolyte. Two PVA gels were placed onto the Zn anode and Ag_2O cathode of the bottom panel as electrolyte of the battery. The top panel was then aligned and covered onto the bottom panel. Lastly, the assembled device was heat-sealed on all four sides to finish the device assembly.

6.2.5 On-body Sensing with the patch

A stretchable adhesive (3M Adhesive Transfer Tape 468MP) was used to adhere the patch onto the skin surface. A simple fluidic patter was designed, allowing the adhesive layer to guide the sweat through the sensor and avoid sweat accumulation below the patch. The adhesive was initially cut using a computer-controlled cutter (Explore Air 2, Cricut Inc, UT, USA), and attached to the back panel of the patch. The patch can thereafter be attached to the subject's arm during on-body trials. During the trial, the subject was asked to ride a stationary bike until sweating before applying the patch. To perform one sensing session, the subject can simply press the switch

mechanism for ~ 1 s to refresh the display. To study the accuracy and temporal profile of sweat lactate, the sensing session was performed every 5 min, while the sweat on the other arm was collected and sensed using a commercial blood lactate meter (Lactate Plus, Nova Biomedical, MA, USA) as validation. To study the temporal profile of sweat glucose, the sensing session was performed every 10 min along with a blood glucose fingerstick reading taken. After 20 minutes of exercise, the subject was asked to drink a sugary drink and exercise for 30 minutes more.

6.3 Results and Discussion

6.3.1 All-stretchable PEDOT:PSS electrochromic displays

Integrating electrochromic displays into skin-interfaced electronic systems provides timely data visualization, such as the level of the target biomarker in the case of on-body sensing platforms. The new skin-interfaced integrated sensing platform features a dedicated and highly responsive low power ECD for such direct visualization of the analytical data. The ECD was chosen for its low power consumption compared to light-emitting display technologies, as it features low self-discharge and requires energy only while refreshing the displaying content. The electrochromic PEDOT:PSS electrode material was selected for its stretchability and compatibility with screen-printing processes. Fabricated via layer-by-layer screen-printing, the ECD was composed of a top PEDOT:PSS panel and 10 separately addressable pixels on the bottom panel, with a highly viscous PSS-based electrolyte to create ionic pathways between two panels while physically separating the opposing electrodes; stretchable and printed silver traces were used to connect the ECD to the MCU and were covered with an insulating elastomer layer to avoid short-circuiting and corrosion (**Figure 6.8 A**). The color of the PEDOT:PSS conducting polymer is dependent on its redox state, as described in half-reaction **Equation 6.1**:

$$(PEDOT)^{+}(PSS)^{-}\text{ (light blue)} + e^{-} \leftrightarrow \text{PEDOT (dark blue)} + PSS^{-} \quad \textbf{(Equation 6.1)}$$

The color change thus occurs on the front panel during the reductive PSS^{-} undoping process upon applying a potential above 1 V between the two electrodes, during which the reverse oxidative doping process takes place on the back panel PEDOT:PSS electrodes. Thus, to induce a color change, a positive potential can be applied to the bottom pixels, which results in the color-changing reduction of PEDOT:PSS within the corresponding region on the front panel covered by the block of PSS electrolyte (**Figure 6.8 B** and **Figure 6.9**). The printable PEDOT:PSS ink was optimized for stretchability and compatibility to the elastic SEBS substrate, and shows excellent mechanical behavior and electrochemical stability upon repeated 20% stretching deformation (**Figure 6.8 C** and **Figure 6.10**). Cyclic voltammetry (CV) of the electrochromic pixel was carried out with scan rates of 0.1, 0.5, 1 V s^{-1} over the 0 V to 1.5 V range (**Figure 6.8 D**). The ON/OFF switching ECD was characterized using potential stepping between 0 V and a set switching voltage while monitoring the current. As shown in **Figure 6.8 E**, **Figure 6.10**, and **Figure 6.11**, a switching voltage of 1.5 V was determined to be optimal as it results in the fastest turn-on response and turn-off response below 500 ms. In comparison, the 1 V switching voltage resulted in a slower turn-on and turn-off speed, whereas switching voltages of 2 V and 3 V, while giving in a fast turn-on rate, led to a slower turn-off speed due to excessive charge accumulation on the electrodes. Such high voltage can also lead to electrolyte breakdown as well as irreversible electrode overoxidation that limit the cycle life of the electrochromic cells, and should be avoided. The average power consumption of turning "ON" each pixel, upon applying the optimal 1.5 V for 1 s, was determined to be 0.08 mW (**Figure 6.12**). This behavior was examined again after 1500 cycles of repeated 20% uniaxial stretching along with two orthogonal directions. The results, displayed in **Figure 6.8 F**, and **Figure 6.13**, demonstrate a slightly reduced turn-on and turn-off current but a negligible

change in switching speed, indicating the excellent stretchability of the PEDOT:PSS electrodes. As characterized via electrochemical impedance spectroscopy (**Figure 6.8 G**), such reduction in the switching current can be attributed to a slight increase (< 200 Ω) in electrode serial resistance, whereas the charge transfer and diffusion impedance remained mostly constant. The electrochemical stability of the ECD was tested via repeated cycling of the PEDOT:PSS electrodes between on and off (**Figure 6.8 H i**) over 10000 cycles (**Figure 6.8 H ii**) via potential steps between 0 V and 1.5 V. The electrical current response of the pixel shows high reproducibility with only 17% decrease of the peak current after ca. 10000 ON/OFF cycles (**Figure 6.8 H iii** – **iv** and **Figure 6.14**), which can be caused by the increased cell impedance due to electrode overoxidation from repeated cycling (**Figure 6.15**). Such high mechanical and electrochemical stabilities ensure the continued and reliable operation of the ECD within the designed lifetime of the system.

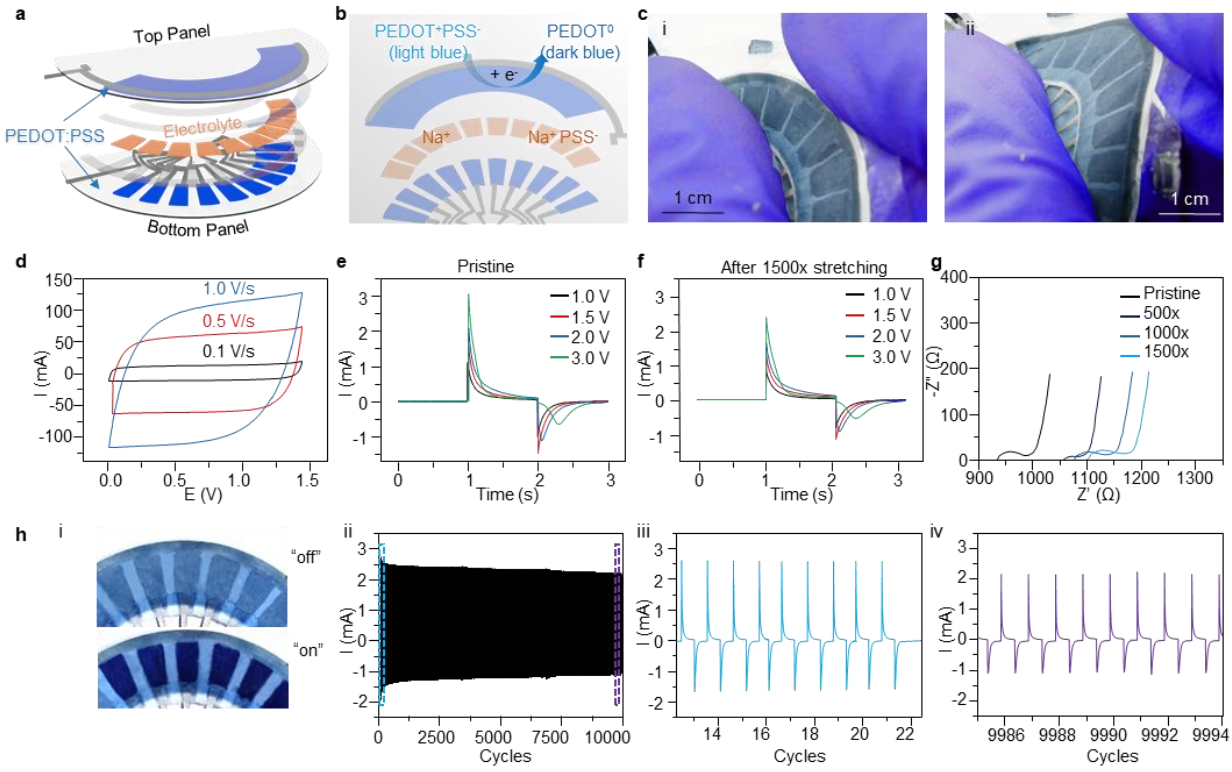

Figure 6.8. Characterization of the electrochromic display.
A, Exploded view of individual layers of the ECD display. **B**, Reaction mechanism of the ECD display. **C**, Photo images of ECD display before (i) and during (ii) stretching. **D**, CV of an ECD pixel at increasing scan rates of 0.1-1 V s^{-1}. **E**, The turn-on and turn-off current for pristine ECD pixel at different voltages. **F**, The turn-on and turn-off current for ECD pixel at different voltages after 1500 times of stretching. **G**, The EIS profile of a pixel before and after 500, 1000, and 1500 times of stretching. **H**, Photo images of the ECD display pixels in "OFF" and "ON" states (i). (ii) The stability of current profile of the ECD pixel with turn-on and turn-off for 10000 cycles, (iii-iv) zoom of current fluctuations for the 14-22 cycles (iii) and 9986-9994 cycles (iv).

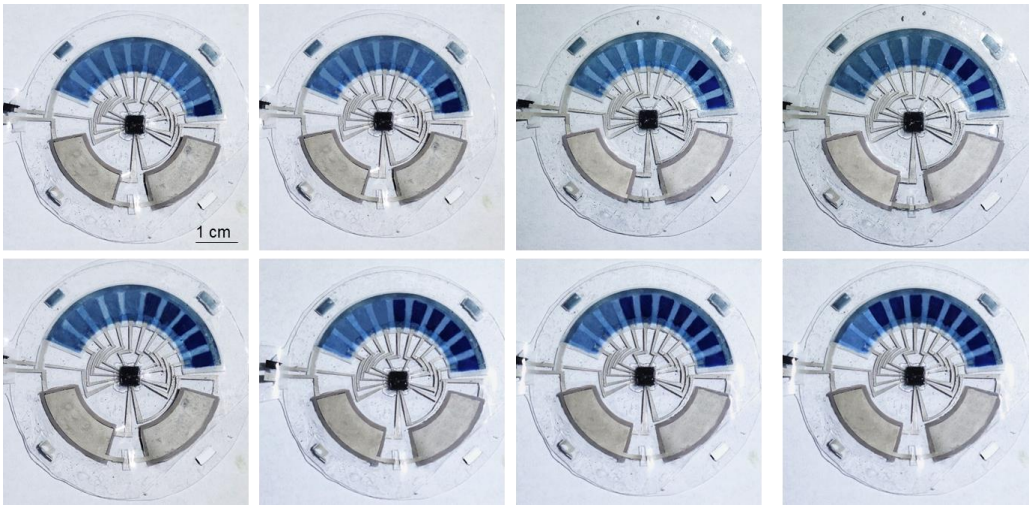

Figure 6.9. Photo images of the patch turning ON individual pixels sequentially.

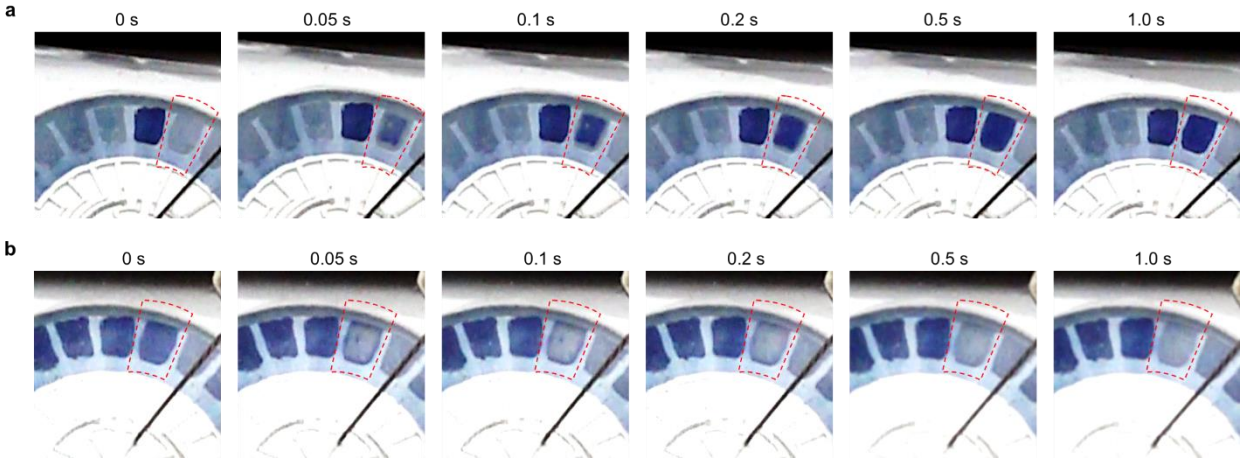

Figure 6.10. Frames from 960 frames per second (fps) high-speed recording of turning on and off the ECD pixels.
A, Frames corresponding to ca. 0, 50, 100, 200, 500, and 1000 ms after applying a 1.5 V potential. **B**, Frames corresponding to ca. 0, 50, 100, 200, 500, and 1000 ms after applying a 0 V potential. The pixel with the applied potential was labeled with red dashes.

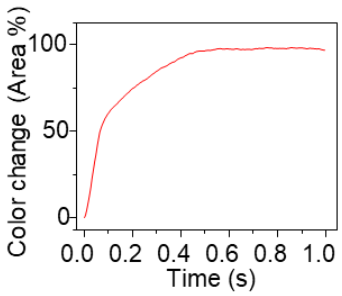

Figure 6.11. The area of color change using image brightness thresholds.

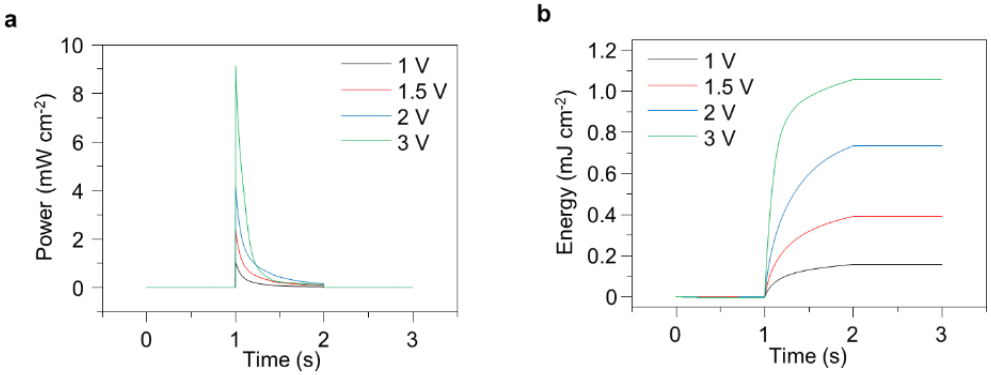

Figure 6.12. Power and energy consumption of turning each electrochromic pixel on and off. **A**, Power consumption of each pixel addressed with different voltages. **B**, Energy consumption of each pixel addressed with different voltages.

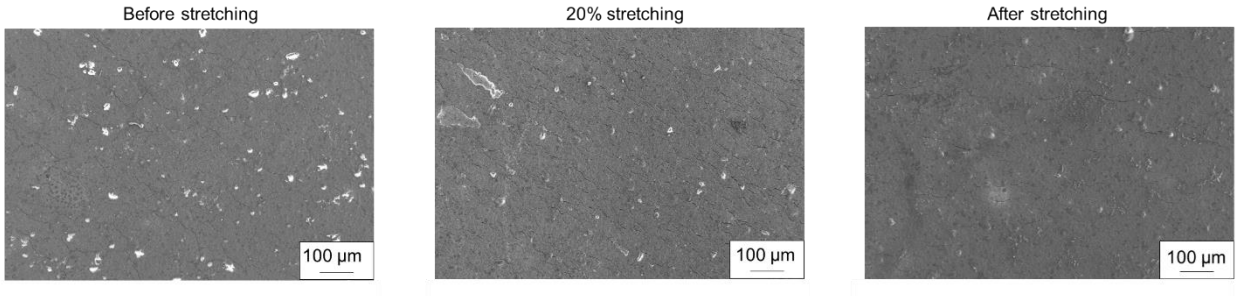

Figure 6.13. Scanning electron microscopic (SEM) images of the layers of the printed PEDOT:PSS electrodes before, during, and after 1500 cycles of 20% stretching.

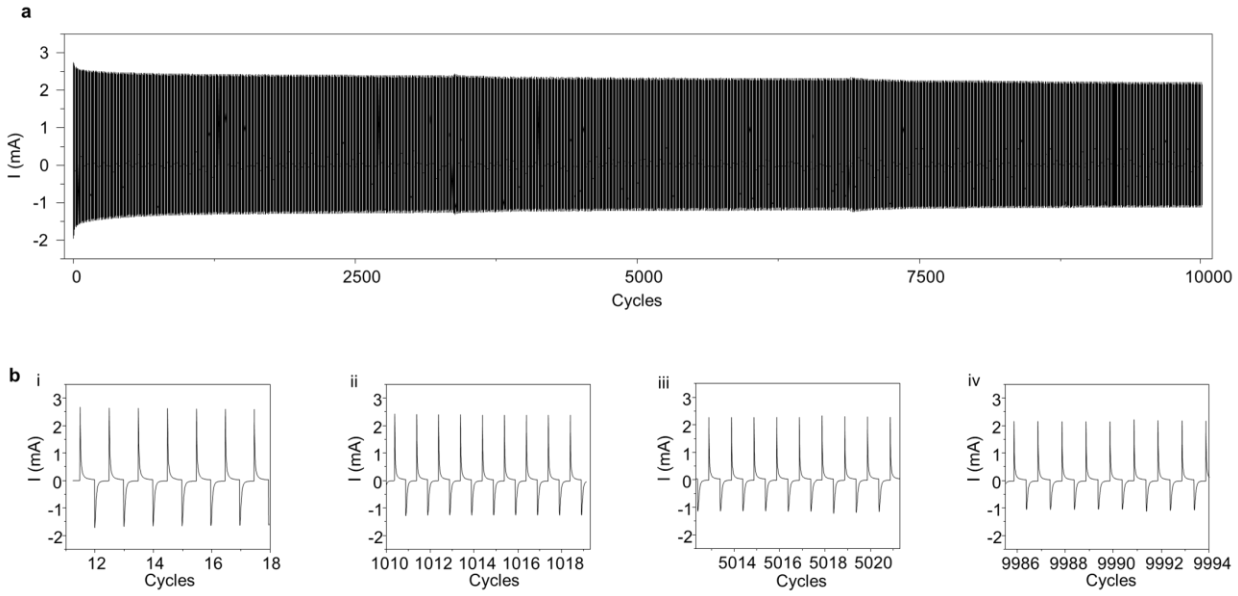

Figure 6.14. The stability of current profile of the ECD pixel with turn-on and turn-off for 10000 cycles.

A, The complete current profile over the 10000 cycles. **B**, zoom of current fluctuations for the 14-22 cycle (i), 1010-1018 cycles (ii), 5013-5020 cycles (iii), and 9986-9994 cycles (iv).

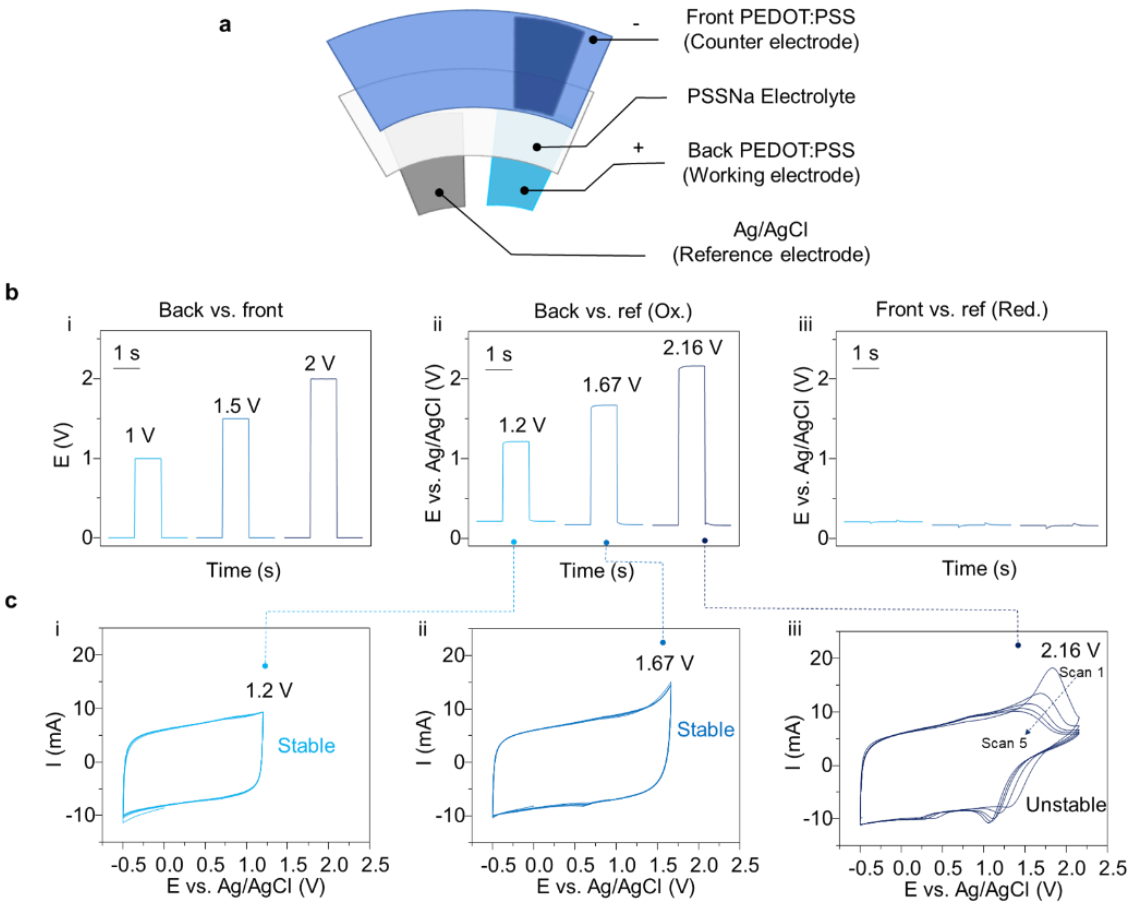

Figure 6.15. Redox potential analysis of the PEDOT:PSS electrodes.
A, Cell structure with PEDOT:PSS panels and Ag/AgCl reference electrode. **B**, The potential steps (1 V, 1.5 V, 2 V) applied to between the back and the front PEDOT:PSS electrode (i), the corresponding potential of the back PEDOT:PSS electrode vs. Ag/AgCl (ii), and the corresponding potential of the front PEDOT:PSS electrode vs. Ag/AgCl (iii). **C**, The CV of the PEDOT:PSS electrode cycled between -0.5 V to the potential of the back PEDOT:PSS electrode when applied with the potential steps vs. Ag/AgCl. Scan rate, 100 mV/s.

6.3.2 Battery performance

The all-printed fabrication of the flexible Ag_2O-Zn battery was designed based on the selection of the substrate and ink formulation that ensures mechanical stretchability, chemical resiliency, operational safety, light weight and comfort, as well as electrochemical stability of the

device. SEBS was selected as the binder for both electrodes, separator, as well as substrate, due to its chemical stability in the alkaline electrolyte used in the Ag_2O-Zn battery. Furthermore, as thermoelastomer SEBS also allows heat- and vacuum-sealing compatibility, which grants reliable packaging to protect and contain the electrolyte. Polyvinyl alcohol (PVA) hydrogel electrolyte infused with 9 M potassium hydroxide (KOH) was also formulated to physically contain the electrolyte and avoid leakage. A stacking configuration was designed to minimize the device footprint while reducing the ion diffusion distant between the battery electrodes for minimizing the internal resistance. The batteries, with the customized silver current collector, Zn anode, Ag_2O cathode, and TiO_2 separator inks, were printed layer-by-layer on the top and bottom panels and assembled via heat and vacuum sealing upon placing the electrolyte hydrogel (**Figure 6.16 A**). The redox reaction of the resulting Ag_2O-Zn battery relies on the dissolution of zinc ions (Zn^{2+}) and silver ions (Ag^{+}) in the alkaline electrolyte and their supersaturation-induced precipitation, which takes place rapidly while maintaining a stable voltage at 1.56 V (**Figure 6.16 B**):

Anode: $Zn + 2OH^- \leftrightarrow ZnO + H_2O + 2\,e^-$ E = -1.22 V versus SHE

(**Equation 6.2**)

Cathode: $Ag_2O + H_2O + 2\,e^- = 2Ag + 2OH^-$ E = +0.34 V versus SHE

(**Equation 6.3**)

The capacity of such printed stretchable battery can be adjusted by the loading of cathode material, as controlled by the number of layers of printing. As shown in **Figure 6.16 C**, batteries with different (1 – 4) layers of cathode printed were prepared and tested at the discharge rate of 1 mA cm^{-2}. Such thickness change results in a proportional increase in capacity with the number of

layers, reaching as high as 11.5 mAh cm^{-2} with 4 layers of cathode loading. The power consumption of the MCU was separately characterized at various operation potentials, and the current draw at the voltage of 1.55 V was determined to be at ca. 1 mA (**Figure 6.17**). The operation of the system was tested with 1 s of discharge at 1 mA discharge every 30 s, which simulates the repeated sensing and display sessions upon pressing the switch mechanism. As shown in **Figure 6.16 D**, the battery (with 2 layers of cathode) is able to deliver a stable voltage with a constant small ohmic drop throughout the continued usage of the device, indicating a constant cell impedance over its entire range of state of charge. Using this simulated discharge profile - where the sensor is used twice every minute - the system can provide energy for over 14000 sensing sessions, corresponding to a service time of over ca. 120 hours. The mechanical stability of the battery under repeated uniaxial stretching was evaluated at 1 mA discharge for 1500 cycles of 20% uniaxial stretching (**Figure 6.16 E** and **Figure 6.18**). As shown in **Figure 6.16 F**, the increase in ohmic drop due to the battery stretching was insignificant to the voltage delivered during the continuous 1 mA discharge, thus confirming its mechanical robustness as a reliable power source for the stretchable epidermal sensing platform. Moreover, the shelf-life of the battery was tested over 1000 hours, displaying a negligible change in voltage and internal resistance at < 40 Ω (**Figure 6.19**), reflecting the high chemical stability of the electrodes, electrolyte, and the packaging materials.

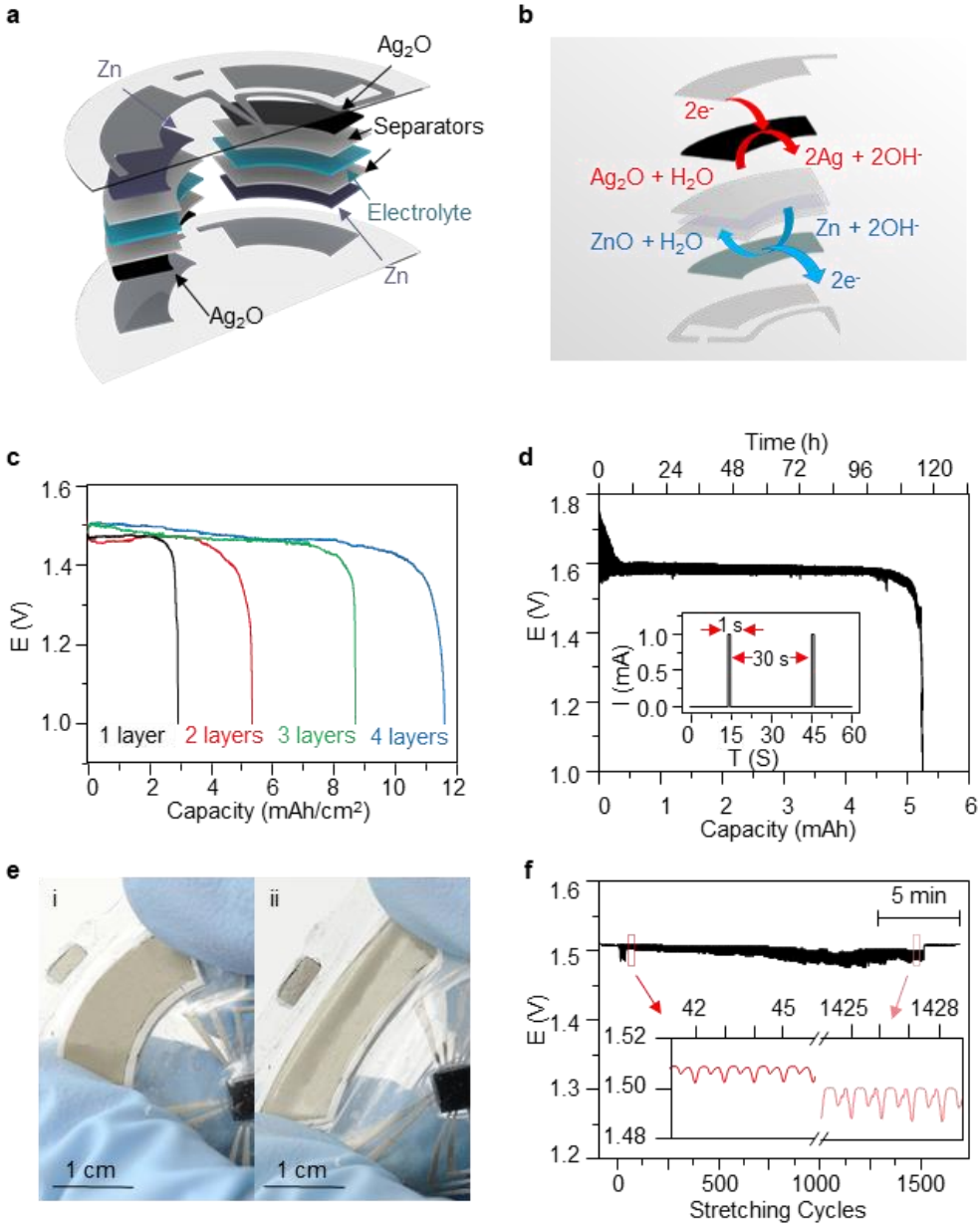

Figure 6.16. Characterization of the stretchable battery.
A, Exploded view of individual layers of the Zn/Ag_2O battery. **B**, Anode and cathode reaction mechanisms of Zn/Ag_2O battery. **C**, Constant 1 mA discharge of the printed battery with different cathode thicknesses. **D**, The stability of the potential profile of battery discharge at 1 mA cm^{-2} during 108 h with a 30 s resting time. **E**, Photo images of the battery before (i) and during (ii) stretching. **F**, Stability of potential profile of battery discharge at 1 mA cm^{-2} for 1500 stretching cycles and (inset) discharge-self-charging curves.

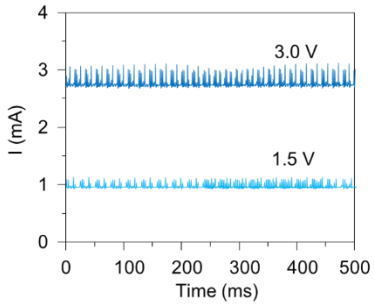

Figure 6.17. Current draw from the ATtiny441 microcontroller at the voltage of 3.0 V and 1.5 V.

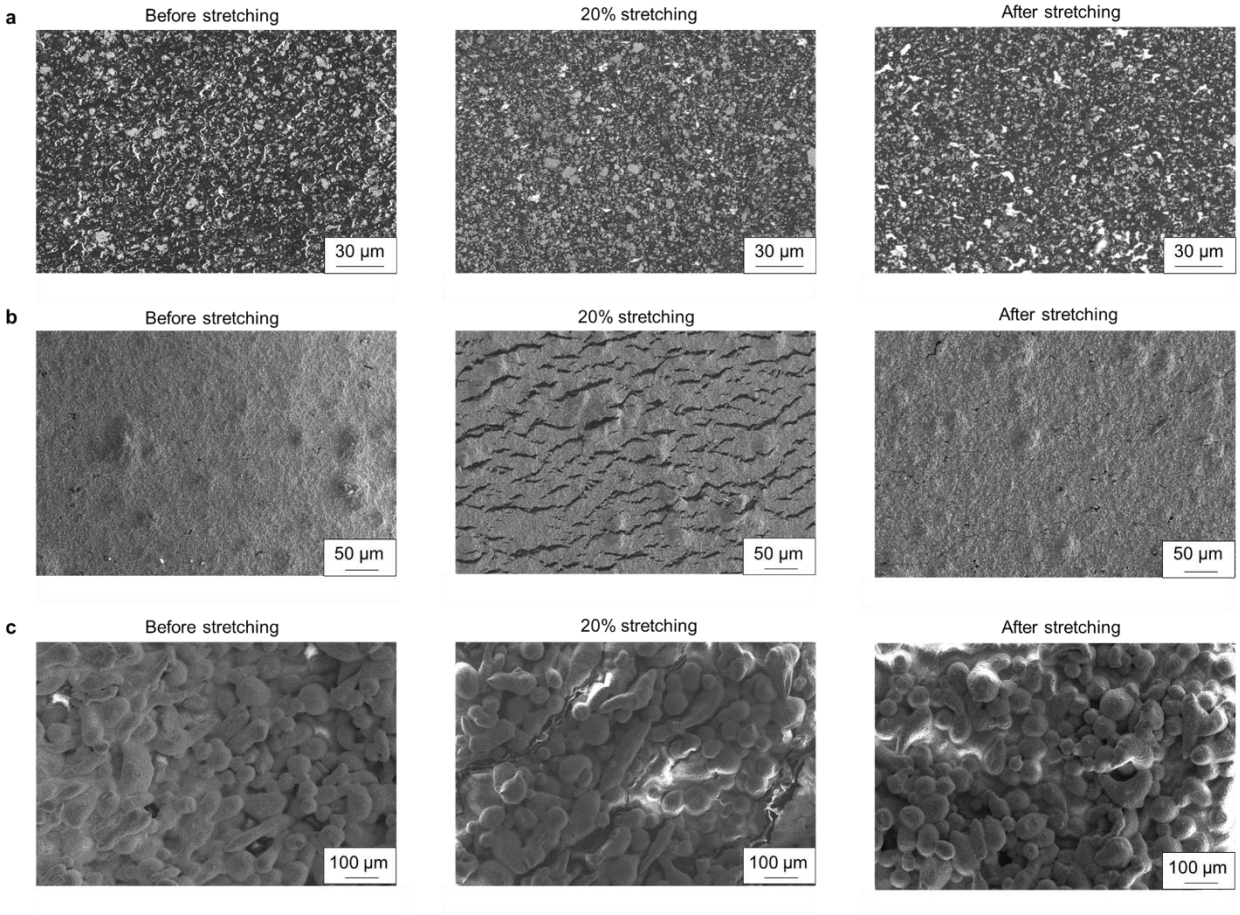

Figure 6.18. SEM images of the layers of the battery electrodes before, during, and after 1500 cycles of 20% stretching.
A, SEM images of the silver current collector layer. **B**, SEM images of the silver oxide cathode layer. **C**, SEM images of the zinc anode layer.

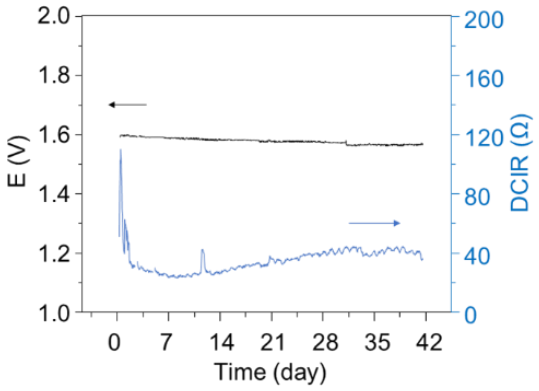

Figure 6.19. Battery shelf life of the battery.
The open circuit voltage and the direct-current internal resistance of the cell tested over 42 days continuously.

6.3.3 Stretchable display system with potentiometric sensors

Two types of potentiometric sensors, for monitoring pH and sodium, were employed for demonstrating the applicability of the all-in-one sensing device. Both sensors rely on measuring the potential difference between the modified working electrode and the silver/silver chloride (Ag/AgCl) reference electrode when in contact with the sample solution (**Figure 6.20 A**). Such potentiometric sensing applies to a wide range of clinically or environmentally important electrolytes. By printing the stretchable silver ink and carbon ink on the SEBS substrate, the two-electrode sensor shows satisfactory resiliency to 20% stretching (**Figure 6.20 B i-ii**). The electrode-electrolyte interface of sodium-ion-selective membrane-modified sodium sensor results in a sodium concentration gradient (between the membrane and the solution), leading to a potential signal that depends logarithmically on the sodium concentration (**Figure 6.20 C i**). **Figure 6.20 C ii** depicts the calibration of the fabricated sodium sensor, demonstrating a slope of 62.4 mV per decade of sodium concentration, with a high correlation coefficient (R^2 = 0.9996), over the 0.1 – 100 mM range. The high selectivity of the sodium sensor is demonstrated from the negligible

change in the sensor potential response in the presence of potassium and different pH (**Figure 6.21**). As shown in **Figure 6.20 C iii**, the potential response of the sensor in alternating 0.1 mM and 10 mM sodium solutions is highly reversible and exhibits minimal changes after 500, 1000, and 1500 stretching cycles, reflecting the excellent stretchability of the sodium sensor.

The pH sensor is fabricated by the electropolymerization of polyaniline (PANI) onto the working carbon electrode. The operation of the resulting pH sensor is based on the protonation and de-protonation of nitrogen atoms in the polymer chains of PANI (**Figure 6.20 D i**). The sensitivity of the fabricated pH sensor is evaluated by measuring the potential response at pH values in the range of 3 - 8 (**Figure 6.20 D i**). The sensors display a linear response of 62.62 mV/pH with a high correlation coefficient (R^2 = 0.9995) across the entire pH range (**Figure 6.20 D ii**). As illustrated in **Figure 6.20 D iii**, the modified pH sensor displays excellent stretchability, as evidenced by the highly stable potential signals measured at pH 4 and pH 7, with negligible changes after 500, 1000, and 1500 times of stretching. In addition, the pH sensor demonstrates good selectivity in the presence of Na^+ and K^+ (**Figure 6.21**). The operating voltage obtained from sodium and pH sensors is converted into logic outputs, programming the MCU and correlating the obtained voltage values to the display content (**Figure 6.20 E**). By integrating the pH sensor with the ECD, we thus fabricated an all-in-one epidermal patch for instant pH sensing and display (**Figure 6.20 F i-ii**).

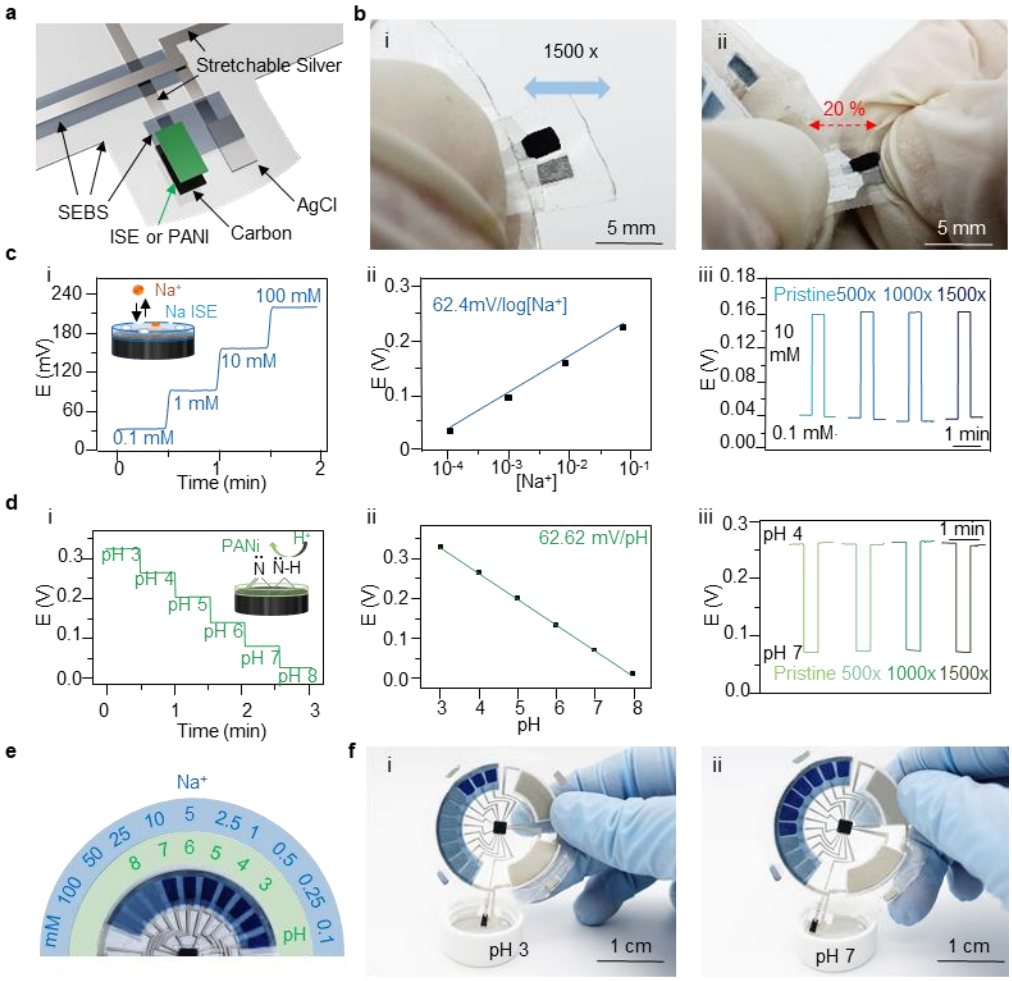

Figure 6.20. The device operation for potentiometric pH and Na^+ ion sensing.
A, Exploded view of individual layers of the potentiometric sensors. **B**, Photo images of the pH sensor (i) before and (ii) during 20% stretching. **C**, (i) Potentiometric signal obtained in 0.1M PBS pH 7.4 upon changing the Na^+ concentration and schematic illustration of the Na^+ sensor. (ii) The corresponding calibration plot of the Na^+ sensor. (iii) The open circuit potential response of the Na^+ sensor in 0.1 mM and 100 mM NaCl solutions after every 500 times of 20% stretching. **D**, (i) Potentiometric signal obtained in 0.1M PBS and schematic illustration of the pH sensor. (ii) The corresponding calibration plot of the pH sensor. (iii) The open circuit potential response of the pH sensor in solutions of pH 4 and pH 7 after every 500 times of 20% stretching. **E**, Illustration of the number of pixels for ECD patch related to the signals of the pH (green) and Na^+ (blue) sensors. **F**, Photos images of the ECD patch reading (i) pH 3 and (ii) pH 7 in 0.5 M PBS.

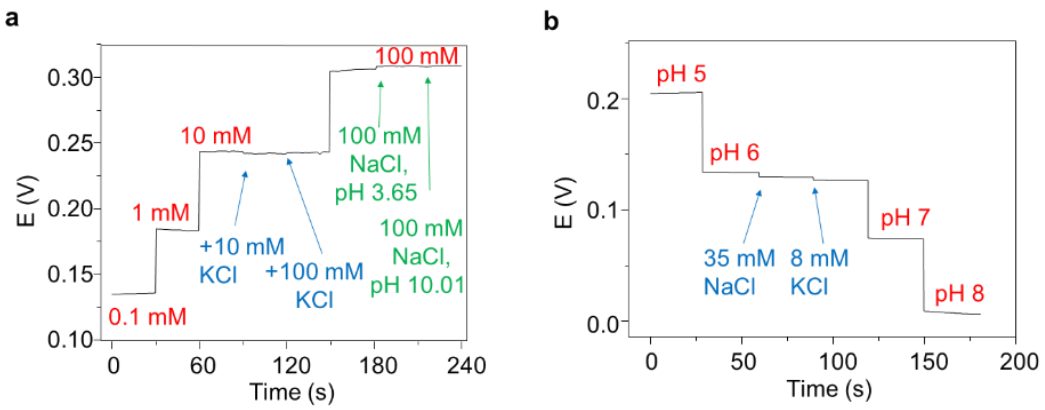

Figure 6.21. Potentiometric sensor selectivity.
A, Selectivity of the potentiometric sodium sensor against potassium ions interference and pH changes. **B**, Selectivity of the potentiometric pH sensor against sodium, potassium and chloride ions.

6.3.4 Stretchable display system with enzymatic sensors

Two enzymatic sensors for glucose and lactate were selected to demonstrate the applicability of the integrated ECD patch in a real-life scenario for epidermal sweat sensing of both metabolites. Both enzymatic sensors commonly rely on amperometric measurements, where the electrical current at a set potential can be correlated to the metabolite concentration using a sigmoidal fitting described with **Equation 6.4**:

$$E = E_0 - \frac{E_0 - a}{1 - \left(\frac{Conc.}{b}\right)^c} \qquad \textbf{(Equation 6.4)}$$

where E is the sensor voltage, E_0 is the open circuit potential of the sensor without load, *Conc.* is the analyte concentration, and a , b, and c are constants.[42] To enable rapid and low-power consumption sensing while obviating the need for potentiostats and amplifiers and removing them from the circuits, a self-powered sensing mechanism that converts the amperometric signal to a voltage signal was implemented under an optimized load. The sensor electrodes are composed of

a printed carbon working electrode along with a silver oxide (Ag_2O) counter electrode, where the carbon electrodes were thereafter functionalized with the corresponding enzymes for their target analytes (**Figure 6.22 A**). **Figure 6.22 B** displays the lengthwise stretching of the enzymatic sensor fabricated using the customized stretchable inks. As shown in **Figure 6.22 C**, the epidermal patch perfectly matches the skin curvature of the subject's forearm. After sweat is induced from the loaded exercise, the subject can mount the integrated system on the forearm for demonstrating its application in real conditions. Upon pressing the switch for 1s, the sensor was thus able to display the lactate concentration on the wearer's skin without needing any external devices, allowing the user to directly obtain the sensing results without the need of any stabilization time or delay.

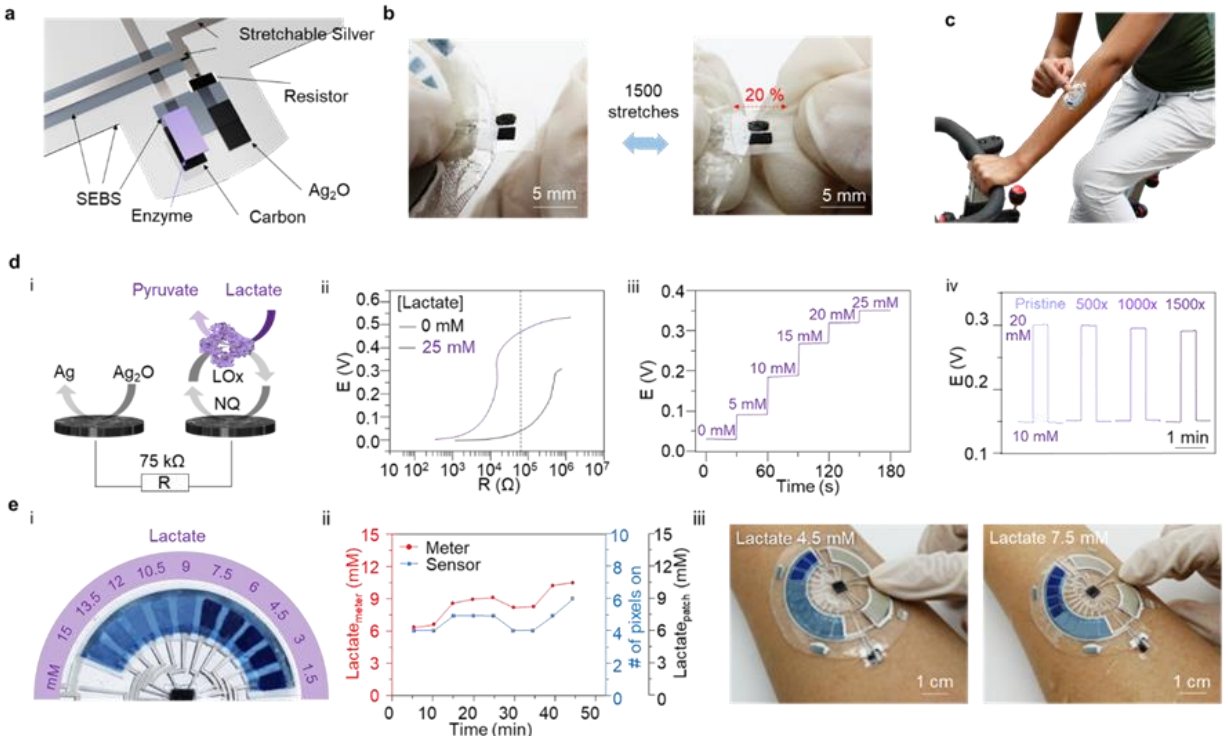

Figure 6.22. The device operation for glucose and lactate sensors.
A, Exploded view of individual layers of the enzymatic sensors. **B**, Photo images of the lactate sensor (i) before and (ii) during 20% stretching. **C**, Photo image of the on-body sensing by placing the ECD patch on the subject's forearm during stationary cycling. **D**, (i) Schematic illustration of the sensing mechanism of the lactate sensor. (ii) Linear sweep voltammetry curve for 0 mM and 25 mM lactate, scan rate 1 mV s^{-1}. (iii) Potentiometric signal obtained in 0.1M AS pH 7.4, upon increasing the lactate concentration from 5 - 30 mM under 75 kΩ load. (iv) The open circuit potential response in 2.5 mM and 15 mM lactate after every 500 times of 20% stretching. **E**, (i) Illustration of the number of pixels for ECD patch related to the signals of lactate sensors. (ii) Results of on-body sweat lactate sensing measured using a commercial meter and the patch. The patch was programmed to display in the range of 0 -15 mM. (iii) On-body lactate sensing by placing the ECD patch on the subject's forearm and displaying 4.5 mM and 7.5 mM results by constant-load exercising.

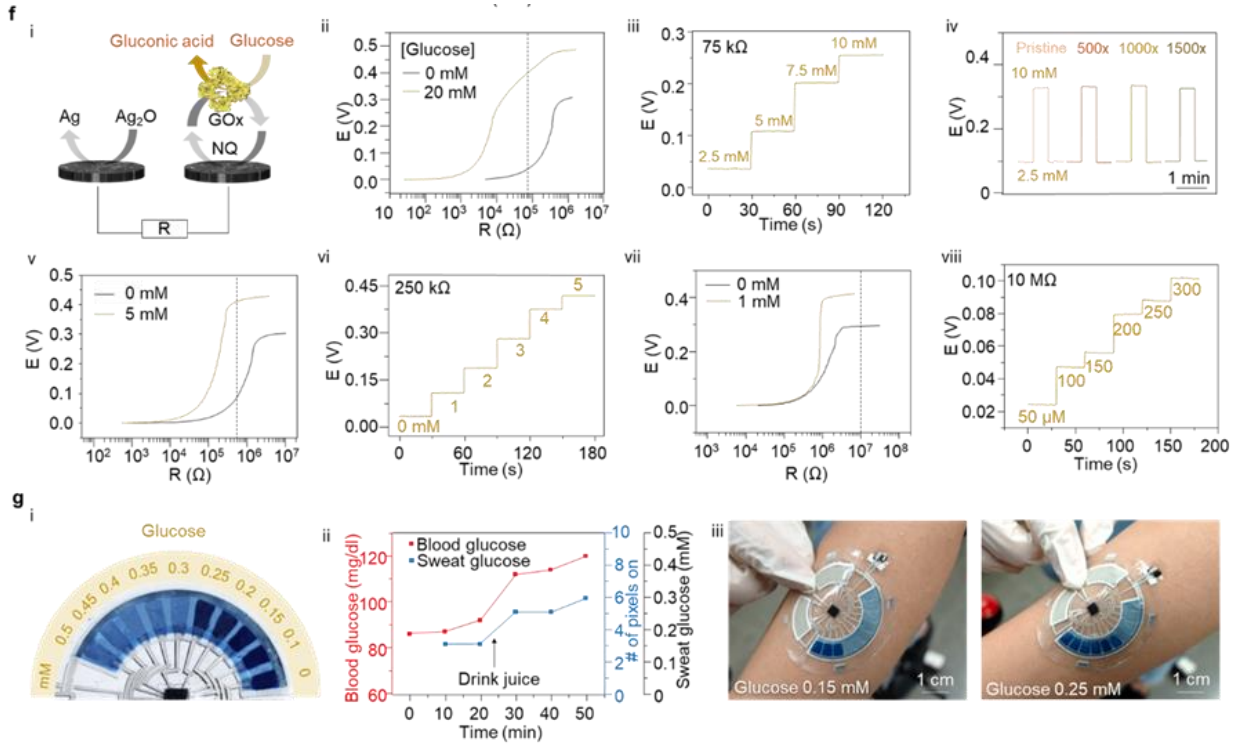

Figure 6.22. The device operation for glucose and lactate sensors. (Continued)
F, (i) Schematic illustration of the sensing mechanism of the glucose sensor. (ii) Linear sweep voltammetry curve for 0 mM and 20 mM glucose; scan rate 1 mV s^{-1}. (iii) Potentiometric signal obtained in AS at pH 7.4, upon increasing the glucose concentration from 2.5 to 10 mM under 75 kΩ load. (iv) The open circuit potential response in 2.5 mM and 10 mM glucose solutions after every 500 times of 20% stretching. (v) Linear sweep voltammetry curve for 0 mM and 5 mM glucose; scan rate 1 mV s^{-1}. (vi) Potentiometric signal obtained in AS at pH 7.4, upon increasing the glucose concentration from 0 to 5 mM under a 250 kΩ load. (vii) Linear sweep voltammetry curve for 0 mM and 1 mM glucose; scan rate 1 mV s^{-1}. (viii) Potentiometric signal obtained in AS at pH 7.4, upon increasing the glucose concentration from 0.05 to 0.3 mM under a 10 MΩ load. **G**, (i) Illustration of the number of pixels for ECD patch related to the signals of glucose sensors. (ii) Results of on-body sweat glucose sensing as measured using the patch and the corresponding blood glucose level. The patch was programmed to display in the 0 - 0.5 mM concentration range. (iii) On-body sweat glucose sensing by placing the ECD patch on the subject's forearm and displaying 0.15 mM and 0.25 mM results by constant-load exercising.

The lactate sensor operates based on the selective naphthoquinone (NQ)-mediated oxidation of lactate on the working electrode by the lactate oxidase (LOx) enzyme, immobilized on carbon nanotubes. The working electrode is coupled with the Ag_2O counter electrode that

undergoes a high reaction-rate reduction of Ag_2O to Ag, independent of the analyte concentration. Upon applying a load, a continuous current flow between the enzyme electrode and the Ag_2O electrode, which is dominated by the concentration-limited electrocatalytic reaction on the LOx electrode (**Figure 6.22 D i**). The optimization of the load ensures a maximized signal resolution over a desired concentration region. To this end, linear sweep voltammetry (LSV) was performed at a typical sweat lactate concentrations range, 0 mM and 25 mM,[43–45] and the potential was plotted against the load, as illustrated in **Figure 6.22 D ii**. As shown, a load of 75 kΩ was selected, where the potential difference between 0 mM and 25 mM lactate in artificial sweat (AS) was at the maximum. Subsequently, the in-vitro voltage response of the lactate sensor at different concentrations was measured under the 75 kΩ load and fitted with an sigmoidal model (**Figure 6.22 D iii** and **Figure 6.23 D**).[42] To further illustrate the importance of optimizing the load to the range and resolution of the lactate sensor, the sensor was also tested under different loads of 10 kΩ and 500 kΩ (**Figure 6.24**). This test showed a minimal potential change above the lactate concentration of 10 mM under the 500 kΩ, and poor voltage resolution across 0 – 30 mM lactate concentrations under the 10 kΩ load. **Figure 6.22 C iv** examines the stretchability of the lactate sensor, demonstrating highly stable and reversible voltage signal after 1500 cycles of lengthwise uniaxial 20% stretching. Additional characterization shows that the lactate sensor exhibits effective discrimination against common sweat constituents, including urea, ascorbate, acetaminophen, and glucose, as well as high electrochemical stability, operating continuously over 9 hours (**Figure 6.23**). Considering the potentially changing pH of human sweat, the fabricated lactate sensor was tested in different AS with variable pH of 5.5, 6.5, and 7.4 (**Figure 6.25**). No significant differences in potentiometric response were observed among the tested samples, demonstrating the reliability and practicality of the sensor. Based on the results obtained from the

lactate sensors, the MCU can be programmed to convert the voltage response of the sensors to the 10-pixel digital display within the desired range (**Figure 6.22 E i** and **Table 6.3**, and **Table 6.4**). The on-body application of the epidermal device was demonstrated by integrating the all-in-one lactate sensor system. A sweat-compatible adhesive layer with a simple fluidic design was attached to the back panel of the patch for directing the sweat flow through the sensor and establish temporal resolution (**Figure 6.26** and **Figure 6.27**). Validated using commercial lactate meters, the sensor thus shows the ability to track the temporal profile of sweat lactate level over a given period of time (**Figure 6.28**). The observed lactate level changed from the initial 6 mM at the beginning of the perspiration to 9 mM after 5 min, reflecting changes in the metabolic activity of the sweat gland. (**Figure 6.22 E ii-iii**).

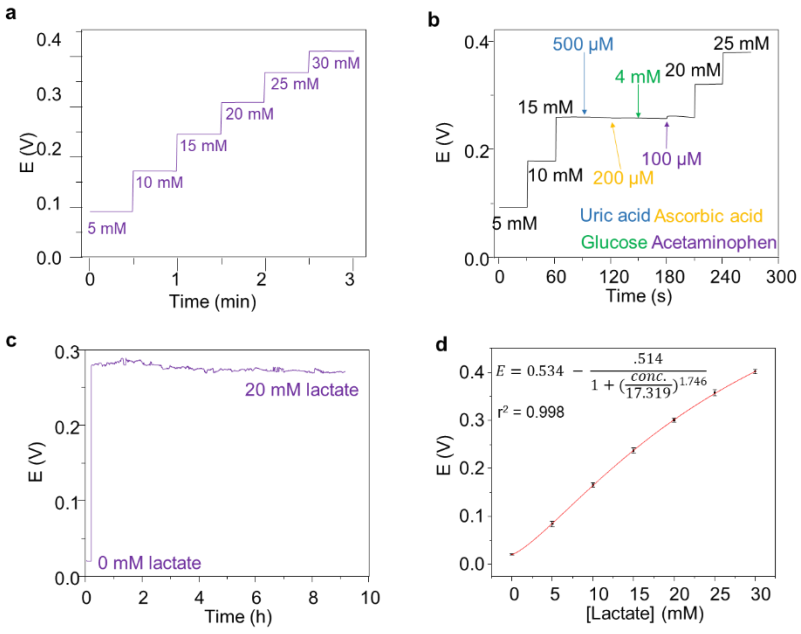

Figure 6.23. Additional in-vitro lactate sensor characterization.
A, Response of the lactate sensor under 75 kΩ with different lactate concentrations in 0.1M PBS. **B**, Selectivity of the lactate sensor under 75 kΩ load against common interfering chemicals in sweat, including uric acid, ascorbic acid, glucose, and acetaminophen. **C**, Stability of the lactate sensor over 9 hours under constant 75 kΩ load. **D**, Calibration and sigmoidal fitting of the lactate sensor response under constant 75 kΩ load. (n = 3)

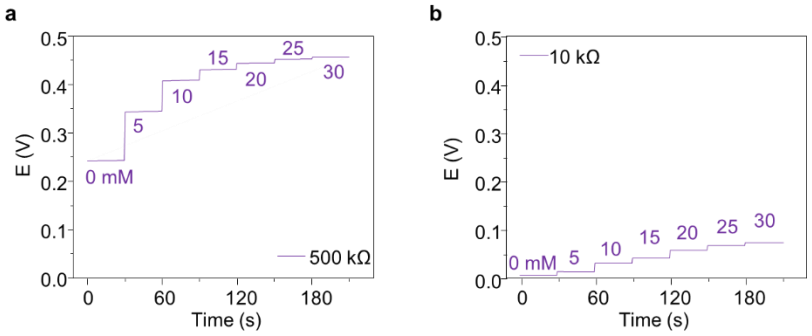

Figure 6.24. The response of the lactate sensor with an unoptimized load.
A, The response of the lactate sensor with a large load of 500 kΩ, which reduced the voltage response per concentration change of the sensor at higher potential. **B**, The response of the lactate sensor with a small load of 10 kΩ, which reduced the voltage response per concentration change of the sensor at lower potential.

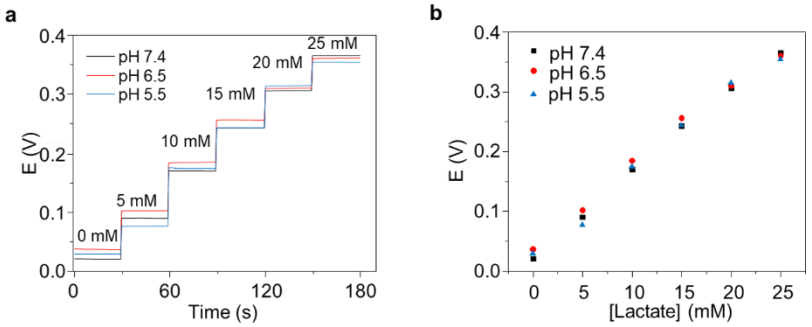

Figure 6.25. The response of the lactate sensor under 75 kΩ with different concentrations of lactate in artificial sweat environment with pH of 5.5, 6.5 and 7.4.
A, The voltage response of the sensor, and **B**, the calibration plot of the sensor.

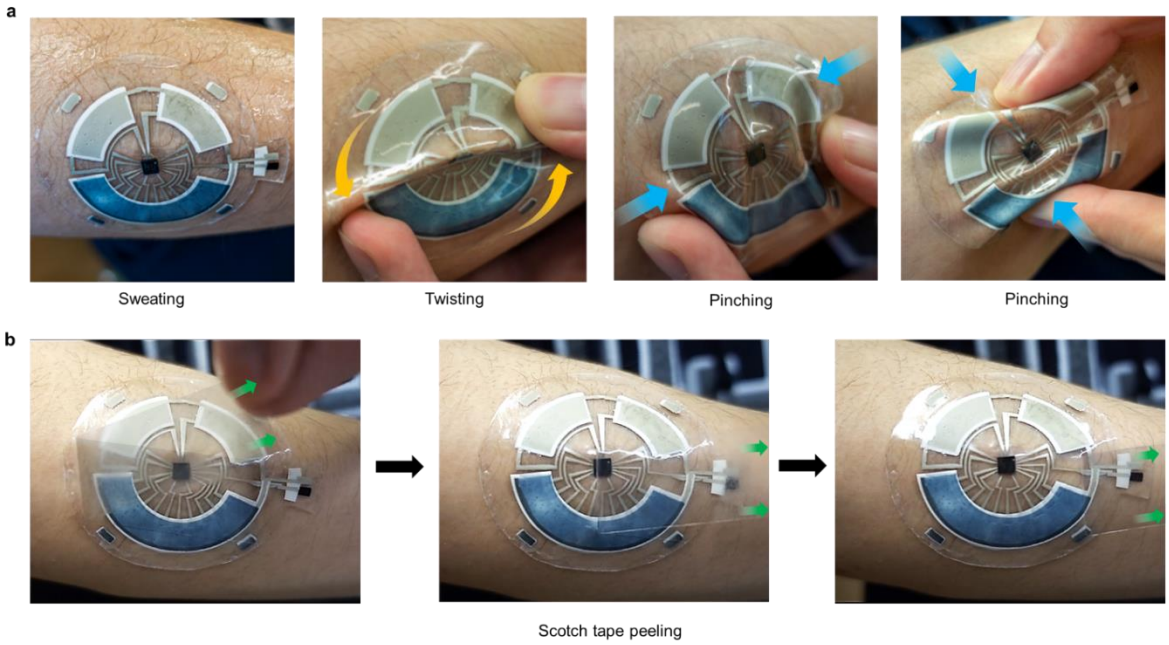

Figure 6.26. Stability of the patch on the skin.
A, The patch was applied to a sweaty skin surface, and was twisted and pinched, while maintaining good adhesion and conformity to the skin. **B**, A scotch tape testing of the patch's adhesion to the skin, where the tape was applied onto the skin and peeled off without affecting the patch.

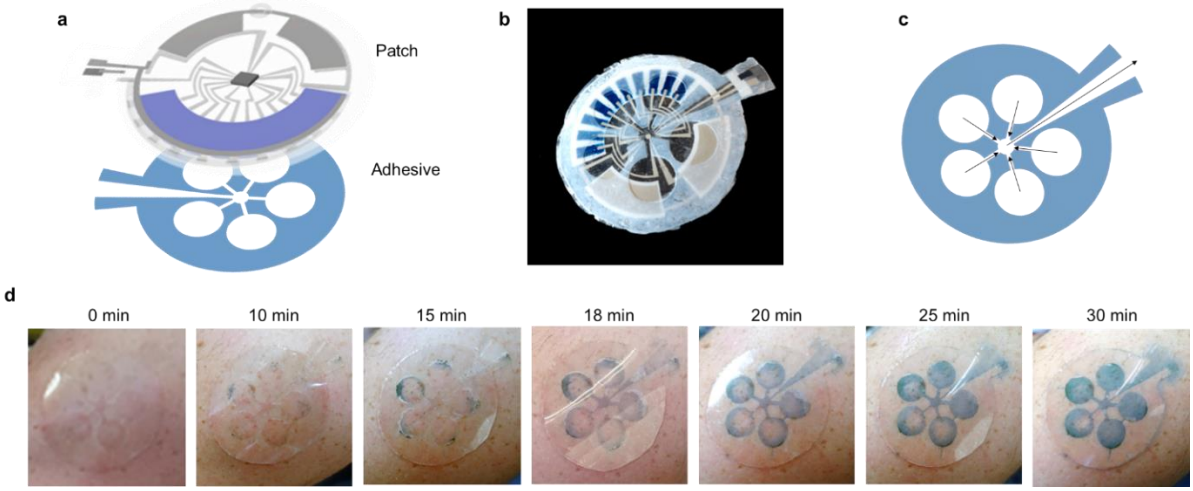

Figure 6.27. Adhesive layer with fluidic functions.
A, Schematics of the adhesive layer below the patch. **B**, Photo image of the patch with the adhesive on the back. The adhesive was dusted with TiO_2 powder for better contrast. **C**, The illustration of the direction of the sweat flow in the adhesive fluidics. **D**, Photo images of the dyed sweat flowing within the adhesive layer covered by a SEBS film (for better visualization) in a 30-min exercise session. A small amount of bromocresol green as sweat indicator was applied to the far edge of each circle, which turns blue-green when in contact with the sweat.

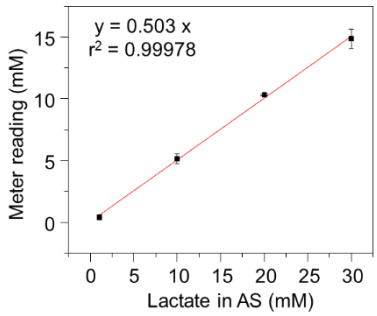

Figure 6.28. Lactate meter validation for the sweat lactate sensing.
A commercial fingerstick blood lactate meter was used for validating the sweat lactate. Artificial sweat with different lactate concentrations was prepared and measured with the blood lactate strips to establish a calibration curve (n = 3).

Using a similar 2-electrode construction, the NQ-mediated glucose oxidase (GOx) was used to obtain a highly selective glucose-sensing working electrode in connection to an Ag_2O counter electrode (**Figure 6.22 F i**). The load was optimized similarly via LSV at 75 kΩ and using 0 mM and 20 mM glucose solutions (**Figure 6.22 F ii**). The well-defined potential response of the resulting glucose sensor over the 0 –10 mM range is presented in **Figure 6.22 F iii**, while its high selectivity against common sweat constituents, including uric acid, ascorbic acid, acetaminophen and lactate, is displayed in **Figure 6.29**. The stretchability of the sensor was assessed via stretching the electrode while recording its potential response to 2.5 and 10 mM glucose solutions. As illustrated in **Figure 6.22 F iv**, the glucose response remained highly stable after 1500 cycles of lengthwise uniaxial 20 % stretching. Similar to the lactate sensor, the glucose sensor was tested in AS in variable pHs, demonstrating a stable voltage signal regardless of the environment, and confirming its practicality under real-life operating conditions (**Figure 6.30**). It is worth noting that such current-to-voltage signal conversion can be tailored for accommodating the lower glucose concentration in human sweat. This is accomplished by adjusting the load to a higher value which enhances the signal resolution in lower concentrations in exchange to a wider range. To this

end, an optimized load at 250 kΩ was applied for greatly enhancing the voltage difference for glucose concentrations over the 0 -5 mM range (**Figure 6.22 F v-vi**). Similarly, the load was optimized to 10 MΩ to enhance the difference below 1 mM glucose towards the monitoring of sweat glucose, which is typically below 0.5 mM (**Figure 6.22 F vii-viii**).[46] Similarly, the patch with glucose sensor can be placed on body to trace the glucose changes over a period of time. Based on the results obtained from the glucose sensors in the 0 – 0.5 mM range, the MCU was programmed to convert the voltage response of the sensors to the 10-pixel digital display (**Figure 6.22 G i** and **Table 6.6**). The glucose level increased significantly after the intake of sugary drinks during exercise, with the trend agrees with the changes in blood glucose level (**Figure 6.22 G ii-iii**).

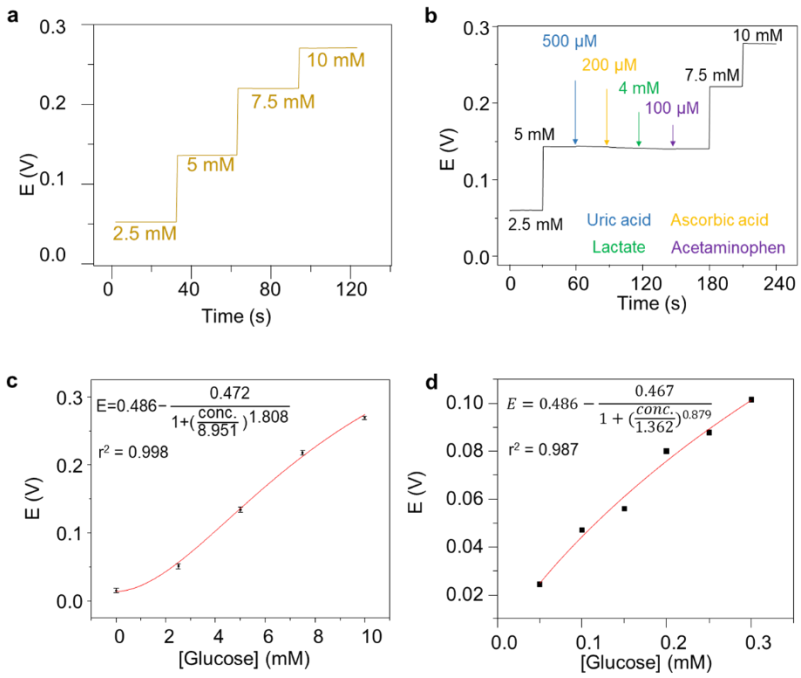

Figure 6.29. Additional in-vitro glucose sensor characterization.
A, Response of the lactate sensor under 75 kΩ with different lactate concentrations in 0.1M PBS. **B**, Selectivity of the glucose sensor under 75 kΩ load against common interfering chemicals in sweat, including uric acid, ascorbic acid, lactate, and acetaminophen. **C**, Calibration and sigmoidal fitting of the lactate sensor response under constant 75 kΩ load. (n = 3) **D**, Calibration and sigmoidal fitting of the lactate sensor response under constant 10 MΩ load.

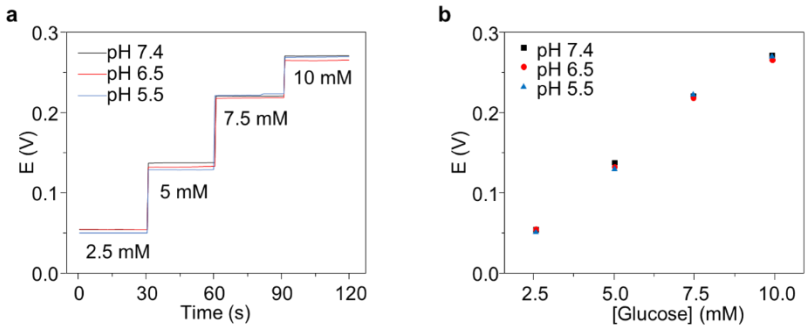

Figure 6.30. The response of the glucose sensor under 75 kΩ with different concentrations of lactate in artificial sweat environment with pH of 5.5, 6.5 and 7.4.
A, The voltage response of the sensor, and **B**, the calibration plot of the sensor.

6.4 Conclusion

In summary, we have presented an all-printed multi-functional autonomous epidermal monitoring system integrating the electrochemical sensors, ECD, and batteries, all in a highly compact, flexible and stretchable form factor. The new integrated sensing platform features a dedicated and highly responsive low power highly stretchable ECD for instantaneous visual data presentation, along with a high-performance safe printed Ag_2O-Zn battery that can power over 14,000 discrete sensing sessions while enduring thousands stretching cycles, for non-invasive wearable sweat-monitoring applications. Through the use of stress-enduring and chemically stable SEBS elastomer as the substrate and binder, highly stretchable devices have been fabricated via low-cost, high-throughput layer-by-layer stencil printing of formulated composite inks into a mechanically resilient epidermal platform. Utilizing PEDOT:PSS electrode material, the new digital ECD exhibited high electrochemical and mechanical stability with color reversibility for over 10,000 ON/OFF sensing cycles and 1,500 stretching cycles, endowing users with the remarkable ability to obtain accurate sensing data rapidly, directly, and independently, during normal daily activities, without needing external devices. A wide range of sensors, including

potentiometric pH and sodium electrolyte sensing devices and enzymatic glucose and lactate metabolic biosensors, were shown compatible with the integrated sensing platform, demonstrating the broad scope of the presented ECD-based data visualization. Our approach, combining high performance ECD and battery technologies, all in a highly compact and stretchable form factor that is compatible to commercially available MCUs, thus offers a practical solution to direct and real-time data visualization. Such development of mechanically resilient skin-worn multifunctional monitoring-display platform and attention to the battery bottleneck and related design limitations, are extremely useful for simultaneously sensing and directly visualizing the analytical information towards the creation of fully autonomous self-sustainable next-generation wearable monitoring platforms. Flexible microgrids are currently being designed for realizing such fully sustainable operation of autonomous wearable electronics.[13,47] We expect the coupling of stretchable ECDs and batteries to be increasingly explored towards improving user experience in wearable electronics platforms for personal wellness management, healthcare monitoring, professional sports, and beyond.

Chapter 6, in full, is a reprint of the materials as appears in the preprint on Research Square and has been submitted for publication for the material as it may appear in Nature Electronics, 2022, by Lu Yin, Mengzhu Cao, Kyeong Nam Kim, Muyang Lin, Jong-Min Moon, Juliane Sempionatto, Jialu Yu, Ruixiao Liu, Connor Wicker, Alexander Trifonov, Fangyu Zhang, Hongjie Hu, Jaekyung Go, Sheng Xu, Joseph Wang. The dissertation author, Mengzhu Cao, and Kyeong Nam Kim were the primary investigators and co-authors of this paper.

6.5 References

1. Wang, C., Wang, C., Huang, Z. & Xu, S. Materials and Structures toward Soft Electronics. *Advanced Materials* **30**, 1801368 (2018).

2. Ray, T. R. *et al.* Bio-Integrated Wearable Systems: A Comprehensive Review. *Chem. Rev.* **119**, 5461–5533 (2019).

3. Kang, J., Tok, J. B.-H. & Bao, Z. Self-healing soft electronics. *Nature Electronics* **2**, 144–150 (2019).

4. Shih, B. *et al.* Electronic skins and machine learning for intelligent soft robots. *Science Robotics* **5**, eaaz9239 (2020).

5. Liu, Y., Pharr, M. & Salvatore, G. A. Lab-on-Skin: A Review of Flexible and Stretchable Electronics for Wearable Health Monitoring. *ACS Nano* **11**, 9614–9635 (2017).

6. Kim, J., Campbell, A. S., de Ávila, B. E.-F. & Wang, J. Wearable biosensors for healthcare monitoring. *Nat. Biotechnol.* **37**, 389–406 (2019).

7. Yang, Y. & Gao, W. Wearable and flexible electronics for continuous molecular monitoring. *Chemical Society Reviews* **48**, 1465–1491 (2019).

8. Gao, W., Ota, H., Kiriya, D., Takei, K. & Javey, A. Flexible Electronics toward Wearable Sensing. *Acc. Chem. Res.* **52**, 523–533 (2019).

9. Gao, W. *et al.* Fully integrated wearable sensor arrays for multiplexed in situ perspiration analysis. *Nature* **529**, 509–514 (2016).

10. Emaminejad, S. *et al.* Autonomous sweat extraction and analysis applied to cystic fibrosis and glucose monitoring using a fully integrated wearable platform. *Proceedings of the National Academy of Sciences of the United States of America* **114**, 4625–4630 (2017).

11. Chung, H. U. *et al.* Binodal, wireless epidermal electronic systems with in-sensor analytics for neonatal intensive care. *Science* **363**, eaau0780 (2019).

12. Manjakkal, L., Yin, L., Nathan, A., Wang, J. & Dahiya, R. Energy Autonomous Sweat-Based Wearable Systems. *Advanced Materials* **33**, 2100899 (2021).

13. Yin, L. *et al.* A self-sustainable wearable multi-modular E-textile bioenergy microgrid system. *Nature Communications* **12**, 1542 (2021).

14. Yin, L. *et al.* A passive perspiration biofuel cell: High energy return on investment. *Joule* **5**, 1888–1904 (2021).

15. Kim, D.-H. *et al.* Epidermal Electronics. *Science* **333**, 838–843 (2011).

16. Kim, J. *et al.* Battery-free, stretchable optoelectronic systems for wireless optical characterization of the skin. *Science Advances* **2**, e1600418 (2016).

17. Yin, L. *et al.* High Performance Printed AgO-Zn Rechargeable Battery for Flexible Electronics. *Joule* **5**, 228–248 (2021).

18. Occupational Safety and Health Administration. Preventing Fire and/or Explosion Injury from Small and Wearable Lithium Battery Powered Devices. (2016).

19. Kim, J. *et al.* Noninvasive Alcohol Monitoring Using a Wearable Tattoo-Based Iontophoretic-Biosensing System. *ACS Sens.* **1**, 1011–1019 (2016).

20. Song, Y. *et al.* Wireless battery-free wearable sweat sensor powered by human motion. *Science Advances* **6**, eaay9842 (2020).

21. Kim, H.-J. *et al.* Review of Near-Field Wireless Power and Communication for Biomedical Applications. *IEEE Access* **5**, 21264–21285 (2017).

22. Kim, E. H. *et al.* Organic light emitting board for dynamic interactive display. *Nat Commun* **8**, 14964 (2017).

23. Zhao, J. *et al.* A Fully Integrated and Self-Powered Smartwatch for Continuous Sweat Glucose Monitoring. *ACS Sens.* **4**, 1925–1933 (2019).

24. Bandodkar, A. J. *et al.* Battery-free, skin-interfaced microfluidic/electronic systems for simultaneous electrochemical, colorimetric, and volumetric analysis of sweat. *Science Advances* **5**, eaav3294 (2019).

25. Koh, A. *et al.* A soft, wearable microfluidic device for the capture, storage, and colorimetric sensing of sweat. *Science translational medicine* **8**, 366ra165 (2016).

26. Choi, J. *et al.* Soft, Skin-Integrated Multifunctional Microfluidic Systems for Accurate Colorimetric Analysis of Sweat Biomarkers and Temperature. *ACS Sens.* **4**, 379–388 (2019).

27. Ghaffari, R. *et al.* Soft Wearable Systems for Colorimetric and Electrochemical Analysis of Biofluids. *Advanced Functional Materials* **30**, 1907269 (2020).

28. Aller-Pellitero, M. *et al.* Fully-printed and silicon free self-powered electrochromic biosensors: Towards naked eye quantification. *Sensors and Actuators B: Chemical* **306**, 127535 (2020).

29. Sun, X. *et al.* A naked-eye readout self-powered electrochemical biosensor toward indoor formaldehyde: On-site detection and exposure risk warning. *Biosensors and Bioelectronics* **177**, 112975 (2021).

30. Santiago-Malagón, S. *et al.* A self-powered skin-patch electrochromic biosensor. *Biosensors and Bioelectronics* **175**, 112879 (2021).

31. Farahmand Nejad, M. A. *et al.* Electrochromism: An emerging and promising approach in (bio)sensing technology. *Materials Today* **50**, 476–498 (2021).

32. Li, Z. & Suslick, K. S. Portable Optoelectronic Nose for Monitoring Meat Freshness. *ACS Sens.* **1**, 1330–1335 (2016).

33. Gao, L. *et al.* Epidermal photonic devices for quantitative imaging of temperature and thermal transport characteristics of the skin. *Nat Commun* **5**, 4938 (2014).

34. Araki, H. *et al.* Materials and Device Designs for an Epidermal UV Colorimetric Dosimeter with Near Field Communication Capabilities. *Advanced Functional Materials* **27**, 1604465 (2017).

35. Kim, J. *et al.* Ultrathin Quantum Dot Display Integrated with Wearable Electronics. *Advanced Materials* **29**, 1700217 (2017).

36. Shi, X. *et al.* Large-area display textiles integrated with functional systems. *Nature* **591**, 240–245 (2021).

37. Miyamoto, A. *et al.* Inflammation-free, gas-permeable, lightweight, stretchable on-skin electronics with nanomeshes. *Nature Nanotech* **12**, 907–913 (2017).

38. Pu, X. *et al.* Wearable Power-Textiles by Integrating Fabric Triboelectric Nanogenerators and Fiber-Shaped Dye-Sensitized Solar Cells. *Advanced Energy Materials* **6**, 1601048 (2016).

39. Lv, J. *et al.* Printable elastomeric electrodes with sweat-enhanced conductivity for wearables. *Science Advances* **7**, eabg8433.

40. Vosgueritchian, M., Lipomi, D. J. & Bao, Z. Highly Conductive and Transparent PEDOT:PSS Films with a Fluorosurfactant for Stretchable and Flexible Transparent Electrodes. *Advanced Functional Materials* **22**, 421–428 (2012).

41. Kumar, R. *et al.* All-Printed, Stretchable Zn-Ag2O Rechargeable Battery via Hyperelastic Binder for Self-Powering Wearable Electronics. *Advanced Energy Materials* **7**, 1602096 (2017).

42. Jin, X. *et al.* Modeling, design guidelines, and detection limits of self-powered enzymatic biofuel cell-based sensors. *Biosensors and Bioelectronics* **168**, 112493 (2020).

43. Derbyshire, P. J., Barr, H., Davis, F. & Higson, S. P. J. Lactate in human sweat: A critical review of research to the present day. *Journal of Physiological Sciences* **62**, (2012).

44. Buono, M. J., Lee, N. V. L. & Miller, P. W. The relationship between exercise intensity and the sweat lactate excretion rate. *J Physiol Sci* **60**, 103–107 (2010).

45. ÅStrand, I. Lactate Content in Sweat. *Acta Physiologica Scandinavica* **58**, 359–367 (1963).

46. Baker, L. B. & Wolfe, A. S. Physiological mechanisms determining eccrine sweat composition. *Eur J Appl Physiol* **120**, 719–752 (2020).

47. Yin, L., Kim, K. N., Trifonov, A., Podhajny, T. & Wang, J. Designing wearable microgrids: towards autonomous sustainable on-body energy management. *Energy Environ. Sci.* **15**, 82–101 (2021).

Chapter 7 Structural Innovations for Flexibility and Stretchability

7.1 Introduction

Over the past two decades, we have witnessed the rapid rise of the soft electronics, featuring attractive form factors and novel functionalities, as replacements for the traditional rigid and bulky electronic counterparts. The development of flexible and stretchable sensors, batteries, supercapacitors, solar cells, transistors, and circuits has gathered multidisciplinary efforts from the fields of electrochemistry, biochemistry, as well as material, mechanical, and electrical engineering, and has shaped the future of electronic devices.[1–7] Among many attractive features introduced to the emerging class of soft electronics, the stretchability - the ability for the fabricated device to be able to endure mechanical strain while maintaining normal functionality - is of particular interest as it imparts robust mechanical durability and conformity to nonplanar surfaces.[8]

Generally, two routes are employed to enable stretchability: material innovations, which rely on the synthesis of novel deformable or elastic materials that can withstand the intrinsic in-plane strain, and structural innovations which adapt specially designed shapes and structures that translate the global strain to local bending, twisting or buckling.[9] The former strategy often requires the re-engineering of a mixture of materials, where the individual ingredients responsible for the mechanical stretchability and the electrical or chemical performance (e.g. copolymers, hydrogels, particle-polymer composite, polymer-surfactant dispersion).[10–12] Adjusting the ingredient ratios often results in a trade-off between the superior mechanical performance and the inferior electrical/electrochemical performance compared to their non-stretchable counterparts. On the other hand, structural innovations are inclusive to a wider selection of materials, as traditional non-stretchable materials or components can simply adapt the specially designed structure to

achieve device-level stretchability. Non-stretchable materials, such as metals, oxides, semi-conductors, and composites, or rigid components, such as electrodes, sensors or integrated circuit chips, can thus be readily transformed into stretchable devices after adapting wrinkles, arches, serpentines interconnects in island-bridge structures, with little to no sacrifice in their performance.[3,7] Moreover, both material innovation and structural innovation can be engineered simultaneously into the same device for obtaining higher stretchability and robustness against mechanical deformation.[13]

Structurally stretchable devices can be fabricated with many processes, depending on the selection of materials and requirements of the device. Microfabrication techniques (e.g. photolithography, chemical/physical vapor deposition), subtractive manufacturing (e.g. computer numerical control (CNC) machining, laser ablation), and additive manufacturing (e.g. inject molding, thick-film printing, 3D printing), have all shown remarkable capabilities towards the fabrication of stretchable electronics.[14,15] Among them, microfabrication techniques have pioneered and advanced the development of soft electronics, and related fabrication techniques, mechanical behavior, and electrical performance have been studied extensively.[16] Yet, such processes are challenged by their high material and device cost, limited material compatibility, complex fabrication procedures, or low throughput, which hinder their ability to enter the market with sufficient scalability and competitive price. On the other hand, 2-dimensional (2D) planar ink-deposition processes, including inkjet printing, screen printing, stencil printing, spray printing, dip-coating, spin-coating, roll-to-roll printing and more, are extremely promising for the wide adaptation of soft electronics, due to their low cost, high throughput, well-established infrastructure, and wide material selection, making these processes ready for rapid scale-up and lab-to-market transition.[17] Many studies have reported the simple, low-maintenance printing of

structurally stretchable devices that rival or even surpass the performance of their photolithographically fabricated counterparts.[18] In addition, recent advances in soft robotics and actuators have demonstrated the application of shape-changing materials to build structures possessing various functionalities. Such shape-changing printed devices have expanded the need for functionalities of printed structures beyond stretchability. Instead of passively enduring mechanical strains, structures are thus capable to actively respond to stimuli by expanding, buckling, bending, or actuating for various applications. Planar printing methods are compatible with a wide range of materials, and can thus serve as attractive alternatives to expensive, complex, non-scalable fabrication methods for the fabrication of such novel, smart, and responsive structures.

In this chapter, we highlight various strategies for fabricating novel functional structures using planar printing processes. Early reviews on planar printed devices have focused primarily on their material and functionality aspects, with no focused discussion on functional structures and corresponding fabrication strategies.[17,19] Leveraging substrate engineering, shape design, selective bonding, strain localization and guided buckling strategies, can lead to the planar printing of a variety of devices with diverse wrinkling, textile-embedded, serpentines, and island-bridge structures, as well as to advanced 2D-transformed 3D and 4D devices (**Figure 7.1**). The fabrication of such stretchable structures can be applied to a wide range of applications, such as circuit interconnects, physical and electrochemical sensing, energy storage, energy harvesting, soft robotics, and more. We will closely examine the adaptation of various printing-specific strategies for fabricating novel functional structures which is unique compared to other fabrication methods. We will also discuss the combination of multiple fabrication strategies towards the 2D printing of 3D complex structures, which are compatible with a wide range of advanced materials. Such capabilities offer an attractive alternative to complex photolithographic and low-throughput 3D-

printing technologies. Furthermore, the theoretical limitations, practical challenges, and prospects of advancing the structural designs in printed devices beyond stretchability, and the possibility of transforming printed structures into nature-inspired responsive autonomous devices, will be discussed. Addressing such limitations, introducing advanced materials and fabrication strategies, and enhancing the fundamental understanding of printed structures will greatly expand the application of planar printing processes for fabricating a wide range of stretchable electronics and multi-functional smart devices.

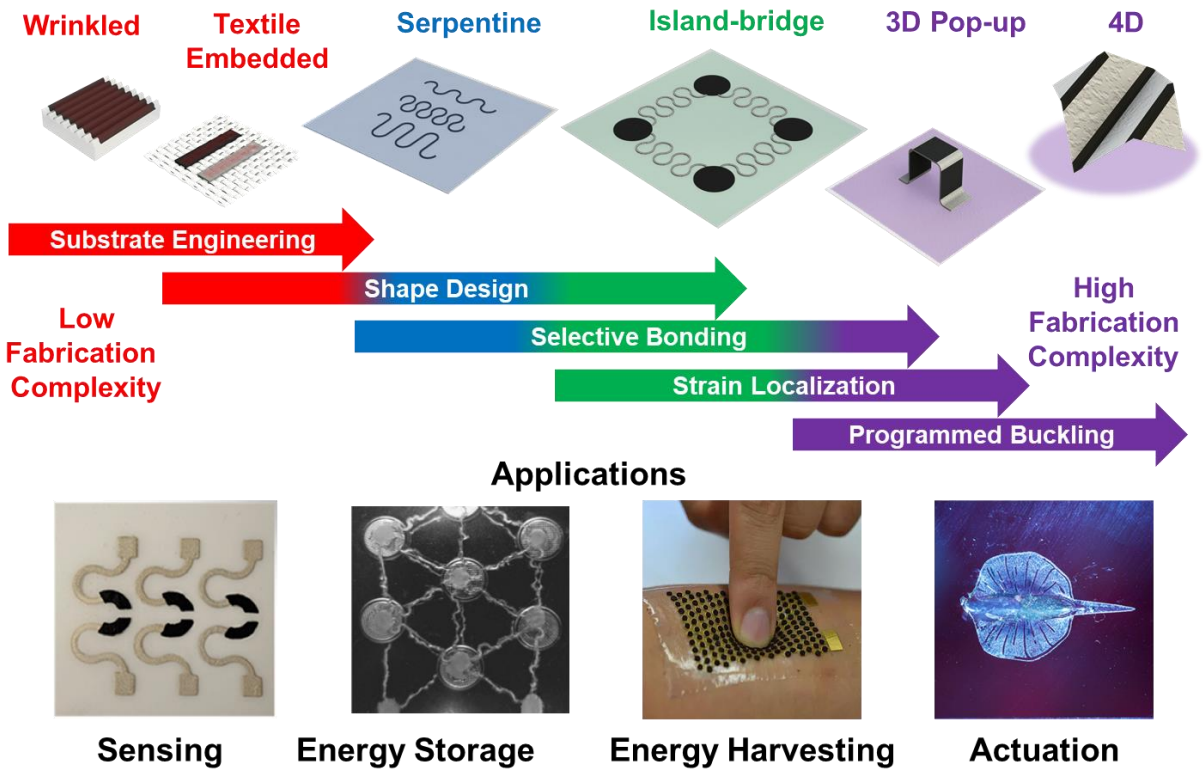

Figure 7.1. Strategies and applications of enabling structural stretchability.
The illustration of six types of printable innovative structures, the five corresponding fabrication strategies used to enable the planar printing of such structures, and possible applications of such innovative structures in the field of sensing, energy, and soft robotics. Bottom images are reproduced with permission.[28,95,96,126] Copyright 2015, American Chemical Society; 2018, Wiley ACH; 2017, The Royal Society of Chemistry; 2016, The American Association for the Advancement of Science.

7.2 Substrate Engineering

Substrate engineering is regarded as one of the simplest and most viable strategies for creating stretchable structures. By applying pretreatment onto the substrates or selecting substrates with special structures, a wide range of materials can be deposited and form structures or microstructures that allow the device to be flexible and stretchable. Substrates can be either heated, solvent-soaked, or simply strained uniaxially or biaxially to induce the formation of microstructures such as wrinkles, waves, or cracks in the deposited materials.[20–22] Alternatively, the use of porous, weaved substrates, such as textiles, offers a simple, one-step solution to create microstructures.[23–28] Materials can be synthesized into fibers or deposited onto yarns that weave into textiles or embedded onto woven textiles to form microstructures, with their stretchability depends primarily on the weaving patterns of the textile. The strategic cutting of substrates often referred to as the "kirigami" approach, can also introduce macroscopic stretchable structures.[29–31] The substrate engineering strategies are commonly used with microfabrication techniques and various thin-film deposition technologies, where common non-stretchable materials, such as metal foils or silicon ribbons, can be used to form a stretchable device upon the introduction of microstructures.

Planar printing technologies have also exploited the substrate engineering strategy to induce wrinkling microstructures within the deposited planar shapes to enable device stretchability. Among all, pre-stretching of elastomeric substrates to create wrinkle structures and embedding inks into porous, stretchable textile substrates are the most prominently adapted methods for their compatibility with the printing processes. Such strategies, not only endowing stretchability to non-stretchable ink composites, but can also enhance the performance of already-stretchable ink composites by alleviating the strain applied to the deposited inks via the microstructures. Details

of textile-engineering-based printing technologies, their practical and fundamental considerations, and challenges for fabricating wrinkled or textile-embedded devices are discussed below.

7.2.1 Wrinkling structures

Predating most of other strategies, mechanically-induced winkling structures symbolize the rise of stretchable electronics.[32] The formation of wrinkles can be attributed to the strain mismatch between the substrate and the deposited materials, which can be produced by depositing materials onto the substrate after heat, solvent, or strain-induced expansion and removing the expansion thereafter. The amplitude, frequency, and shape of the wrinkling waves can be adjusted based on the level of pre-applied tensile strain, the sizes, thicknesses, the mechanical properties of the substrate, and the deposited material, and the adhesion between the two.[33–35] Other reviews enumerated the devices adapting such structures to obtain stretchability, and are not discussed in length here.[36–40] However, specific to printing technologies, such phenomenon has been rarely studied systematically, mostly likely due to the complex mechanical property of the deposited inks, which are mixtures of different materials, and vary from study to study. Inks composed of carbon nanotubes (CNTs), conductive polymers, and binder-particle composites, that share drastically different mechanical properties, can adopt such wrinkling strategy to produce stretchable devices. As the deposition of ink usually involves the use of solvents and heat-based curing process after the deposition, heat and solvent-based substrate treatment are not considered compatible with the printing processes. As a result, substrate pre-strain is predominantly applied by mechanical stretching. As illustrated in **Figure 7.2 A**, usually two routes are used in the printing of winkle structures. The first approach involves the most traditional procedure, where the substrate is firstly pre-stretched, followed by the ink deposition and the release of the pre-strain to form wrinkles. The second approach is less common where a wrinkling structure is introduced first, followed by

the deposition of inks onto the wrinkled substrate. Similarly, the stretchability of the printed winkling structure varies with the level of pre-stretching and the mechanical property of the deposited material, which can be as high as to a few hundred percent.

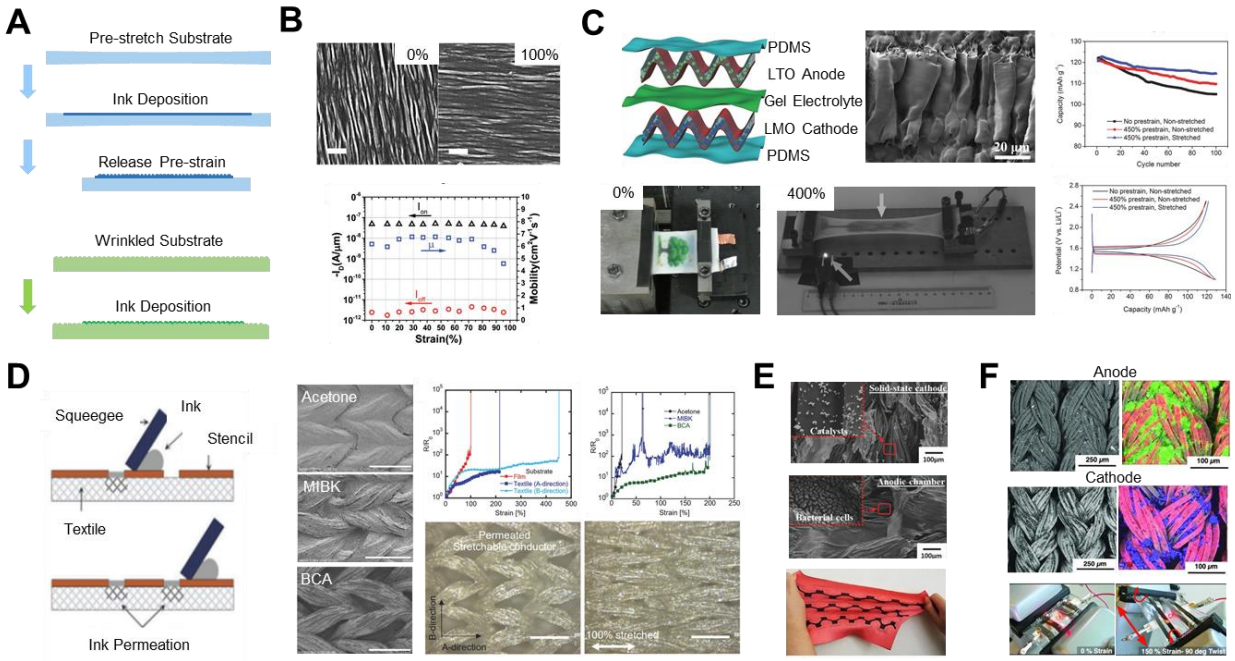

Figure 7.2. The printed device with substrate engineering.
A. Schematic illustration of creating wrinkling structures using planar printing techniques. **B**. Scanning electron microscopy (SEM) images of pristine and 100% stretched, doctor-blade cast CNT films, and the currents and mobility of the FET under up to 100% strain. Reproduced with permission.[57] Copyright 2015, AIP Publishing LLC. **C**. The structural schematics and SEM image of the stretchable battery with "arched electrodes" (top left): the images of the battery under 0% and 400% strain (bottom left); and the charge-discharge profile and the cycle life of the battery (right). Reproduced with permission.[58] Copyright 2015, Wiley-VCH. **D**. Schematic illustration of embedding ink into textiles via screen printing (left), SEM images of embedded inks with different solvent (middle); Comparing the resistance change between non-embedded inks and embedded inks, and the embedded inks with different solvents during stretching (top right); and the based Microscopic image of the ink-embedded conductive textile under 0% and 100% strain (bottom right). Reproduced with permission.[27] Copyright 2017, Wiley-VCH. **E**. The SEM and photographic images of the textile-embedded MFC. Reproduced with permission.[43] Copyright 2017, Wiley-VCH. **F**. SEM images and the corresponding energy-dispersive X-ray spectroscopy (EDX) of the anode and the cathode of the textile-embedded zinc-manganese alkaline battery (red: silver, blue: manganese, green: zinc), and the photo of two batteries connected in series illuminating a light-emitting diode (LED) under 0% strain and 150% strain with 90° twist. Reproduced with permission.[44] Copyright 2012, Wiley-VCH.

Using such strategies, a stretchable device containing complex mixtures of electrode materials that are incompatible with microfabrication thin-film deposition methods can be fabricated using planar printing techniques. As shown in **Figure 7.2 B**, CNT-based field-effect transistors (FETs) were fabricated by doctor-blade casting a CNT-polymer solution onto pre-stretched polydimethylsiloxane (PDMS) substrate and drop-casting ion gel.[41] The fabricated device shows a minimal change in electron mobility up to the strain of 90%. Weng et al. demonstrated the fabrication of highly stretchable lithium-ion batteries by printing CNT-lithium titanium oxide (LTO) anode and CNT-lithium manganese oxide (LMO) cathode slurry onto 450% pre-strained PDMS substrate (**Figure 7.2 C**).[42] Electrode with highly random winkles with the wavelength ~10 μm was fabricated that can buckle out-of-plane reversibly for thousands of times without breaking.[42] The battery was therefore able to sustain stretching up to 450% without significant change in charge-discharge cycles. Such strategies, however, can only be used for low material loading (< 6 mg/cm^2) as heavier loading resulting in thicker films delivered significantly less stable mechanical performance after repeated stretching. Lee et al. demonstrated the inkjet printing of silver films on the pre-strained PDMS substrate and annealing the printed traces simultaneously.[43] Compared to other printed metal films, the printed-then-annealed silver films are less prone to crack formation by compensating for the orthogonal strain caused by high Poisson's ratio of PDMS using thermal-expansion. This strategy enables the printed Ag electrodes to withstand 1000 repeated 10% stretching with negligible resistance change, demonstrating the potential of this low-cost printing method in fabricating highly conductive stretchable metal electrodes.

7.2.2 Textile Embedding

Textile serves as one of the most important yet underutilized platforms for integrated wearable soft electronics. It offers comfort, warmth, flexibility, body conformity, and sometimes outstanding stretchability, and is a crucial integral to our life.[44] Compared to other platforms for soft electronics integration, the textile is not an addition but already a necessary component of all human activities and has a great amount of area to be utilized. Correspondingly, the integration of devices onto the textile platform faces many challenges as its durability, flexibility, stretchability, and washability must match the textile itself, which can be demanding for many intricate, flexible, and stretchable electronics based on microfabrication. Various studies have led to exciting progress in a "bottom-up" approach where functional materials are fabricated into fibers, yarns, and fabrics that can be used for energy harvesting, energy storage, and sensing.[23–25] Device made using this approach can achieve stretchability by configuring and weaving the yarns into tortuous or coiled shapes that unfold and extend during stretching. However, the functionalization of the yarns and fibers is often low throughput, and the functionalized yarn can only hold a monolithic function, thus requiring complicated stitching or embroidering processes for integrating the components into a device. Alternatively, planar printing techniques, commonly used for applying patterns and logos onto graphic clothes, can be used to directly embed materials onto the textile, in low-cost, high-throughput processes that are compatible with a wide range of materials. The printing allows the deposition of various inks into their designated location and can thus be used easily to assemble individual components with their corresponding designed shapes into a textile-based device.

As shown in **Figure 7.2 D**, compared to ordinary printing processes, embedding printing on textiles requires inks that are high flow, slow drying, and excellent in wetting the textile. Inks deposited thus can permeate through the fabric and evenly coat the surface of the yarns of the

fabric before drying. During stretching, the structural integrity of the deposited material relies mostly on the fabric itself, transforming the elongation of inks to the flexing of individual yarns in the textile, and enhance the device stretchability, For example, **Figure 7.2 D** demonstrates an ink-embedded e-textile that could endure 450% elongation through screen printing of a stretchable Ag ink onto commercially available textiles.[26] Compared to the non-embedded inks, the permeated ink delivered significantly lower electrical resistance under the same strain. The key strategy used in this work for achieving the uniform ink permeation was the use of a high boiling point and low vapor pressure butyl carbitol acetate (BCA) as the solvent. The solvent delayed the drying of the ink, thus allowed it to uniformly coat the fibers instead of filling the vacancies and blocks further permeation. This process avoids the binding of the textile strands, allowing the wavy structure of the yarns to fully extend during stretching, hence leading to a higher ink conductivity at large strain.

Using such textile-embedding strategy, various inks can be formulated for printable, stretchable, and textile-based devices. Choi and coworkers demonstrated the fabrication of a textile-embedded microbial fuel cell by screen-printing ethylene glycol (EC)-modified conductive polymer PEDOT:PSS as the anode and PEDOT:PSS/Ag_2O as the cathode onto a commercial stretchable textile (**Figure 7.2 E**).[27] Although the non-stretchable PEDOT:PSS coating is cracked under stretching, the network remains conducting due to wrapping and embedding of the conductive materials by the fabric fibers. Relying on the embedding strategy, such microbial fuel cell printed using non-stretchable inks thus can deliver an overall device stretchability of 50%. Such strategy can also be used with functionalized textiles to achieve enhanced performance. For example, **Figure 7.2 F** displays the use of a conductive and stretchable textile woven with silver-coated nylon yarns.[28] A stretchable textile Zn-MnO_2 primary battery was then fabricated by directly coating functional particles, including Zn for the anode and MnO_2 cathode, on the

stretchable current collectors. In this work, the conductive textile served both as the mechanical supports and as current collectors, where its resistance even decreased during stretching due to the improved contact between fibers. The fabricated battery can, therefore, be stretched up to 100% without compromising its performance.

Overall, the textile-embedding strategy offers an alternative route compared to surface-based printing where the structural advantage of the substate is fully exploited. However, such process suffers also from limited resolution due to the non-directional permeation of ink and the wicking capillary effect of the fibers. The embedded printing techniques will be greatly benefit from future studies aimed at improving the resolution of the printing by utilizing strategies such as hydrophobicity treatment, special weaving patterns or special ink formulations which allow selective directional wetting of the substrate.

7.3 Tortuous 2D Designs

The use of 2D designs in stretchable devices symbolizes the utilization of geometry in the broad context of soft electronics. Patterns that represent the compression of 1D structure into a 2D plane such as zigzag (triangular wave), square waves, sine waves, serpentines (arcs), or spirals are adapted in devices to enable structural stretchability. The 2D designs are usually composed of repeating unit cell shapes with its geometric length longer than its physical sizes, allowing them to respond to strain by twisting, in-plane rotations, and out-of-plane buckling to release their geometric length to compensate for the increasing physical length. The concept of fractals or self-similar structures is later introduced into the mix, using the strategy of substituting basic unit cells with self-similar designs that resemble the full design, aiming to further enlarge the structural stretchability by compressing longer 1D structure into a give 2D area. The fabrication of these

tortuous 2D designs usually requires high resolution, and is typically done via photolithography, laser ablation, and transfer printing of thin films to constitute the stretchable structures. Based on their application, a selection of process-compatible materials, such as metals, semiconductors or insulators, can be used to fabricate antennas, interconnects, current collectors, energy harvesters or actuators.[45,46] The stretchability of devices utilizing such patterns depends upon several factors, including the mechanical property of the materials, the supporting substrate, and the bonding between the two, as well as the geometric properties such as the shape, width, thickness, radius, arm length (length of the linear segment within each unit), angle, and is summarized in numerous studies.[46–50] The majority of the method used for fabricating such structures involves transfer-printing of delicate fine features with low mechanical robustness. As a result, the complexity, throughput, and cost of fabricating 2D tortuous design via photolithography or laser ablation can shadow their widespread applications. Nonetheless, due to its conceptual simplicity, the strategy of using 2D geometric designs to enable device-level stretchability has been widely adapted by field of stretchable electronics.[51]

Inspired by this notion, the field of printed electronics quickly adapted tortuous 2D shapes into various printed devices to enable stretchability. Compared to photolithography or laser ablation, most of printing techniques have lower resolution, and hence are limited in fabricating miniaturized, highly complex 2D structures. However, printing technologies offer a significantly wider range selection of materials, as various polymers, hydrogels, or carbonaceous and metal composites can be synthesized into slurries or inks to be printed onto various substrates, thus enabling a wide range of applications that was previously extremely difficult or impossible to realize. In addition, direct printing obviates the need to transfer delicate structures, resulting in higher fabrication throughput, simplified operation, and lower costs. The deposition of soft,

conformal, and even stretchable inks onto elastic substrates using direct printing differs also from traditional microfabrication that uses stiff, non-stretchable thin films. If combined with intrinsically materials, the tortuous structure also enables the combination of structural stretchability and intrinsic material stretchability within one component to offer more robust mechanical and electrical performance towards much larger strains. Similar to traditional tortuous 2D structures, the mechanical behavior of the resulting structures depends upon the mechanical properties of the materials used and the geometric properties of the selected shape. Common for printing technologies, the deposited ink can form structures with elastic modulus several orders of magnitude smaller than the substrate, thus exhibiting a different mechanical behavior compared to the non-elastic thin films. Furthermore, due to the nature of direct printing approach, an innovative fabrication strategy is needed to allow lift-off of the structure from the substrate for free-standing out-of-plane buckling. In general, printed tortuous 2D structures can be classified into to 4 different types: bonded rigid 2D structures, bonded soft 2D structures, free-standing rigid 2D structures and free-standing 2D structures, which are discussed separately below.

7.3.1 Bonded, Rigid 2D Structures

The bonded, rigid 2D structures category involves the printing of materials that has elastic modulus that is significantly higher than their substrate while maintaining contact with the substrate during deformations. Common rigid materials deposited here include low-melting-point metals and alloys, oxides, as well as non-elastic polymers, which have Young's modulus ranging from 10^9 – 10^{12} Pa, significantly higher than elastic substrates that usually have modulus in the MPa domain.[48,52] The deposition of such material is mostly completed via transfer printing, rarely

involves with direct planar printing technologies, with a few exceptions using electrohydrodynamic printing, 3D printing and ink-jet printing (**Figure 7.3 A-C**). When the entire device undergoes stretching deformation, the printed rigid structures are able to resist the tensile stress from the substrate, exhibit little to no intrinsic expansion, and distribute the majority of the strain to the surrounding substrate.[53–57] Behaving similar to the lithographically etched or laser-cut counterparts, the tortuous 2D structure mostly rotates in-plane, and sometimes buckles out-of-plane by bending the substrate beneath it during stretching (**Figure 7.3 B**).[50,57] Such structures are usually limited in stretchability as their out-of-plane is restricted by the substrate, which in turn gives it better durability against sheer stress or entanglement. Due to the rigid, non-elastic behavior of the material, the structure has limited stretchability, and is prone to structural damages upon stretching beyond its design limit or having enough fatigue buildup that leads to irreversible device failure (**Figure 7.3 C**).[58]

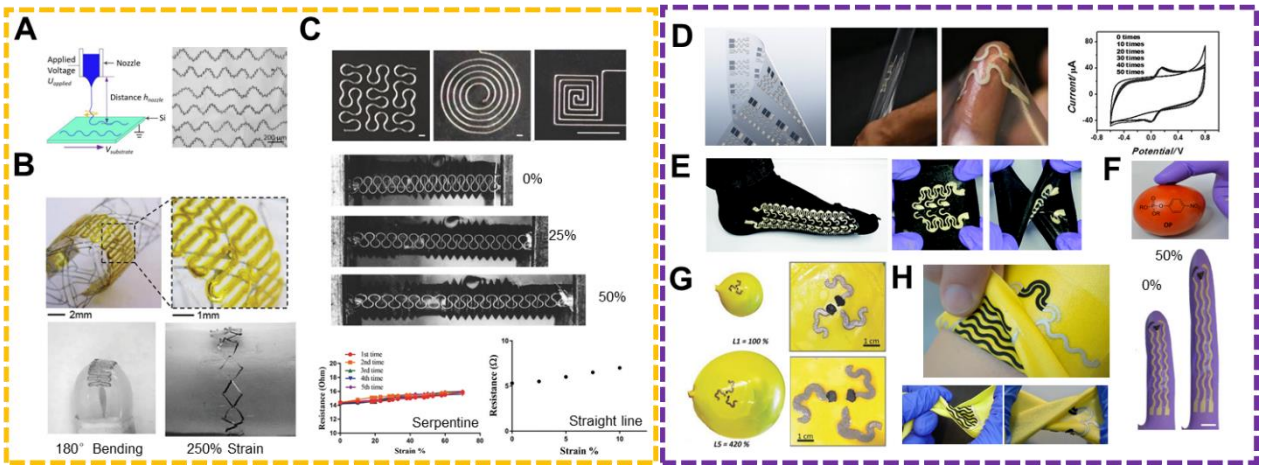

Figure 7.3. Printed tortuous designs.
Rigid, bonded structures: **A**. Illustration of electrohydrodynamic printing of polyvinylidene fluoride (PVDF) and the printed serpentine PVDF fibers on Ecoflex substrate. Reproduced with permission.[72] Copyright 2017, Elsevier. **B**. Optical images of the pristine printed silver-polyimide(PI) sensor and the sensor under 180° bending and 250% radial strain. Reproduced with permission.[76] Copyright 2019, Wiley-VCH. **C**. Optical images of electrohydrodynamic-method printed molten metal in different torturous shapes (top), in serpentine shape under 0%, 25%, and 50% stretch (middle), and the change in resistance of the printed structure in serpentine and in straight-line shape vs. strain. The straight-line molten metal breaks at the strain of 11%. Reproduced with permission.[73] Copyright 2017, Wiley-VCH. Soft, bonded structures: **D**. Illustration and optical images of screen-printed stretchable electrochemical sensors, and the change in cyclic voltammetry response of the sensor every 10 times within 50 times of 100% stretching. Reproduced with permission.[81] Copyright 2015, Wiley-VCH. **E**. Photographs of the textile-based stretchable biofuel cells (BFCs) screen-printed on socks. Reproduced with permission.[84] Copyright 2016, The Royal Society of Chemistry. **F**. Photographic illustrations of screen-printed glove-based sensors, and the sensor under 0% and 50% strain. Reproduced with permission.[82] Copyright 2017, American Chemical Society. **G**. Photographs of screen-printed balloon-based electrochemical sensors for vapor sensing under 0% and 420% strain. Reproduced with permission.[83] Copyright 2016, Wiley-VCH. Free-standing rigid structures: **H**. Photo images of the printed BFC-supercapacitor system worn on the skin and under flexing and twisting deformation. Reproduced with permission.[79] Copyright 2018, The Royal Society of Chemistry.

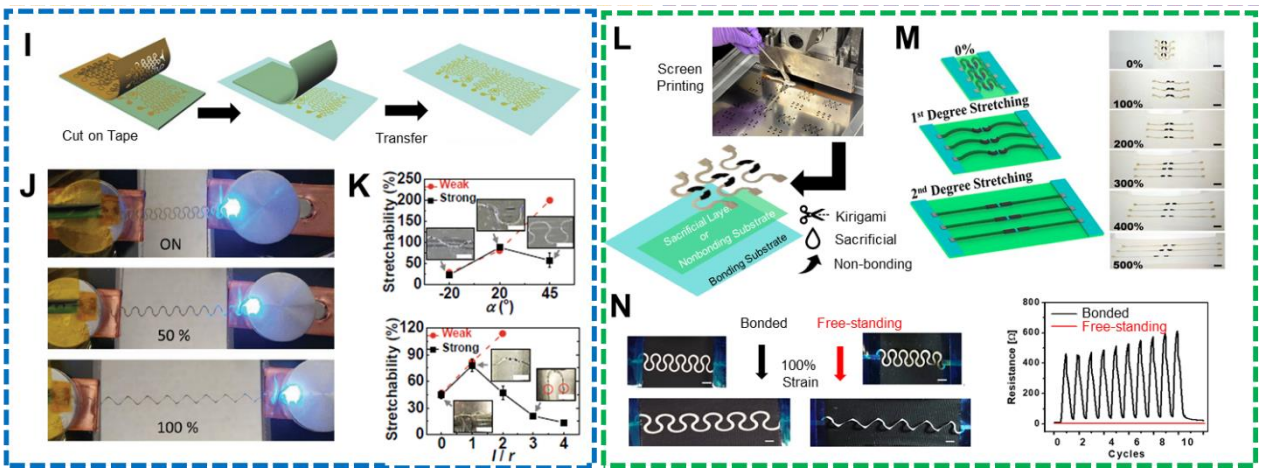

Figure 7.3. Printed tortuous designs. (Continued)
I. Illustration of the transfer printing process of non-bonded gold-on-PET serpentine ribbons on other substrates, such as medical tapes or tattoo papers. Reproduced with permission.[67] Copyright 2015, Wiley-VCH. **J**, Photographs of an aerosol-jet printed, free-standing, and dual-path silver-PI serpentine conductive wire used in illuminating LEDs while under 0%, 50%, and 100% strain. Reproduced with permission.[89] Copyright 2019, Wiley-VCH. **K**. Comparison of stretchability between well-bonded (strong) and weakly-bonded (weak)indium tin oxide (ITO) serpentine ribbons with different arc angle (top) and length-to-radius ratio (bottom). Reproduced with permission.[77] Copyright 2015, Elsevier. Free-standing soft structure. **L**. Illustration of the fabrication routes towards printing a free-standing tortuous structure. **M**. Illustration of the "two degrees of stretchability" of free-standing stretchable tortuous structures, and photos of the printed electrode array under from 0% to 500% stretch. Reproduced with permission.[28] Copyright 2016, American Chemistry Society. **N**. Photos and corresponding resistance change of bonded and free-standing serpentine under repeated 100% strain. Reproduced with permission.[91] Copyright 2017, Wiley-ACH.

7.3.2 Bonded, Soft 2D Structures

The bonded, soft 2D structures also involve direct printing of tortuous 2D shapes onto stretchable substrate without additional effort to lift-off said structure from the substrate. In this category of devices, the printed structures are composed of materials that have similar or smaller Young's modulus to the substrate, and are tightly bonded onto the substrate, and thus can be easily stretched, bent and twisted with the substrate. This approach can only be used in combination with intrinsically stretchable inks, as the printed soft composite bonded to the substrate experiences a

similar level of tensile strain when the substrate undergoes stretching deformations. Compared to the rigid materials, the soft counterparts can only direct a small part of the strain to the surrounding substrate, which depends on the Young's modulus and thickness of the printed structure and the substrate. As a rule of thumb, the thicker and stiffer the deposited materials, and the thinner and softer the substrate, the less intrinsic stretching deformation the structure will undergo.[59] As the printed structure bonds tightly with the substrate, its durability against sheer stress is generally better than their free-standing counterparts due to the protection from the substrate. In addition, the device exhibits good mechanical resiliency towards large deformation, as the intrinsically stretchable soft materials can effectively minimize the buildup of fatigue during repeated deformations. Several studies have reported the thick-film printing of various serpentine structures onto elastic substrates such as polymer films and textiles using a patterned stencil. **Figure 7.3 D-H** illustrate several examples of printed sensors and biofuel cells (BFCs) adapting serpentine structures for wearable sensing, energy storage and energy harvesting applications.[60–66] Using stretchable, electrochemically active particle-elastomer composite inks, the printed serpentine patterns expand with the substrate during stretching, and readily recovers to their original shape while maintaining its electrochemical behavior after repeated stretching cycles (**Figure 7.3 D**). While some studies reported similar electrochemical behavior during stretching, due to the expansion of the printed composite material, most of the 2D tortuous structure still experience a significant drop in conductivity, hence impeding the overall device stability during deformations.[67,68] Depending on the quality of the stretchable ink and of the substrate used, hysteresis effect has also been reported, where the conductivity of the printed inks changes temporally due to the viscoelastic behavior of the polymers and polymer composites.[69]

7.3.3 Free-standing, Rigid 2D Structures

Free-standing structures are structures that are partially or completely self-supporting and unbonded to the substrates. The strategy of selective bonding is introduced here, where the printed structure bonds to the substrate only at selective locations, allowing the remaining regions of the structure, which are free-standing from the substrate, to be deformed more unrestricted. During stretching, the free-standing domain of a tortuous 2D design usually resolves its strain via out-of-plane buckling in addition to the in-plane rotations, hence allowing the compressed geometric length to release with the growing physical length to its full extent, and achieving a higher device stretchability compared to the bonded counterparts using the 2D design. The printing fabrication of free-standing, rigid 2D structures has rarely been reported, with the majority of them relying on addition transfer-printing step to achieve selective bonding (**Figure 7.3 I**).[58,70] Printed-then-transferred tortuous 2D structures exhibit superior stretchability (**Figure 7.3 K**) while showing minor conductivity change during stretching (**Figure 7.3 J**).[58,71] The overall fabrication complexity of printed rigid, free-standing structure is comparable with that of its photolithographic or laser-ablation counterparts, therefore considered less advantageous compared to the direct planar printing methods.

7.3.4 Free-standing, Soft 2D Structures

Combining the soft, stretchable material, selective bonding strategy and the structurally advanced 2D designs, the free-standing soft 2D structures are considered most attractive among all types of printed tortuous 2D structures. Such structures combine the intrinsic material stretchability with the structural stretchability of the design, thus obtaining "two degrees of stretchability".[13,68] During stretching deformation, the free-standing tortuous structures initially

buckle out-of-plane to release its compressed geometric length. Due to the lack of intrinsic elongation at this stage, the conductivity of the buckling structure can remain mostly unchanged. After reaching the buckling limit of the shape, the structure can be further elongated without structural failure, leveraging the intrinsic stretchability of the material. The core of enabling free-standing in soft, printable inks is fabrication techniques offering selective bonding. Some of free-standing structure utilizes the "kirigami method" that involves printing the stretchable inks onto stretchable substrate followed by cutting out the tortuous patterns along with the substrate and transfer it to a secondary stretchable substrate, with selected location of the pattern adhered to the secondary substrate using tape or adhesive, as shown in **Figure 7.3 L**.[68,72] The cut-and-paste method, similar to transfer printing, allows the tortuous shape to buckle out-of-plane during stretching, but does not truly remove the printed ink from the primary substrate. The device is thus able to demonstrate outstanding mechanical behavior, enduring strain up to 500% (**Figure 7.3 M**) while maintaining good conductivity. However, the complexity and low throughput of the "kirigami" approach limits its scalability and practicality. Aiming to address this issue, the second generation of free-standing soft 2D structure turned to the development of a printable sacrificial layer that resembles the photoresist used in photolithographic etching process.[73] Similar to the process illustrated in **Figure 7.3 L**, during printing, a thin layer sacrificial ink is firstly printed onto the substrate which defines the non-bonding regions, followed by printing the main tortuous 2D structure. After curing, the sacrificial layer is dissolved from the substrate, leaving the regions above it free-standing from the substrate. Using this approach, the direct printing of free-standing tortuous structures can be achieved without the need for any transfer or cutting steps, hence greatly reducing the fabrication complexity of a free-standing structure. As shown in **Figure 7.3 N**, utilizing a water-soluble sacrificial ink, the fabricated free-standing serpentine exhibits

significantly smaller change in resistance compared to the bonded serpentine, proving the effectiveness of such strategy. A recent study also demonstrated the use of non-bonding inks that delaminates from the substrate upon stretching, further simplifying the fabrication procedure, allowing the low-cost, high-throughput printing of free-standing 2D structures and more complex structures, [13] as discussed in following sections.

7.4 "Island-Bridge" Structure

The "island-bridge" structure describes the separation of a non-stretchable, monolithic and bulky device into smaller, separated components that are connected by stretchable interconnects. Refereed also as "interconnect-island mesh" or the "rigid island" structure, the structure emphasize on accommodating the traditional bulky non-stretchable functional elements onto the non-stretchable island regions, while localizing the strain to the peripheral stretchable interconnects featuring structurally stretchable winkled, tortuous and buckling-enabled designs, hence achieve device-level stretchability.[1,3] The structure uses the strategy of strain localization, thus deconvolutes requirements for mechanical stability and device performance into different regions of a device. Numerous studies reported on stretchable sensors, energy storage devices and circuits incorporating non-stretchable transistors, electrodes or integrated circuit chips based on "island-bridge" structure.[74] In these applications, the interconnecting "bridges" contribute directly to the device stretchability, allowing the rigid, bonded functional "islands" to deliver unperturbed stable performance during deformations. However, such attractive performance comes with an expense – the fabrication of such highly complex structure usually requires highly precise, complex procedures that affect the fabrication cost and throughput.

On the other hand, fewer studies have been devoted to island-bridge structures in printable stretchable devices since these devices often rely on intrinsically stretchable inks. Yet, some printed functional electronics that requires high sensitivity, electrical stability and mechanical robustness, such as stretchable sensors and energy storage devices, cannot be satisfied solely by stretchable, conductive materials whose conductivity dominated by percolation theory and changes significantly with applied strain.[75] Furthermore, many developed non-stretchable inks have been optimized for high electrical or electrochemical performance; the re-engineering these inks for stretchable applications will require extravagant time and efforts while sacrificing the ink performance. The use of a stretchable structure as an "one-size-fits-all" solution that can accommodate a wide range or non-stretchable inks, while allowing the incorporation of thick electrodes or components, to deliver high stretchability along with high performance, can thus be considered extremely attractive for printed electronics. However, the successful adaptation of the "island-bridge" structure in printed electronics hinges on addressing several key aspects specific to printing technologies. The overall device stretchability is limited by the bridge stretchability, the bridge/island ratio, as well as the stability of the islands against tensile and shear stresses.[76,77] Therefore, the shape design of the bridges and the islands, the compatibility between inks, and the bonding between ink and the substrate must be taken into careful consideration. In addition, strain localization strategy requires the island region to undergo as little shape change as possible, thus requiring a combination of various inks to form strong, rigid islands to resist the deformation, with soft, resilient bridges to accommodate for the shape change. By addressing the above considerations via careful materials selection and process engineering, the "island-bridge" structure can be successfully implemented in printing technologies.

The occurrence of the "island bridge" structure started with initial proof-of-concept studies that did not address all challenges at once. Instead, the printed of "island-bridge" structure was initially fabricated conjointly with the use of photolithographic techniques.[18] As shown in **Figure 7.4 A**, the first generation of printed "island-bridge" structure relies on photolithographically fabricated metal thin-film current collectors followed by the thick-film deposition of functional materials onto the island regions. During stretching, the free-standing metal serpentines unbuckles from the Ecoflex substrate to accommodate for the shape change, whereas the rigid, isolated islands refrained from shape changes due to the high tensile strength of the metal film. Using such approach, various non-stretchable inks, such as commercial carbon ink, Prussian blue ink, Ag/AgCl ink or formulated CNT inks, were successfully printed onto the island regions, with negligible change in power output during uniaxial and biaxial stretching. As a platform for many electrochemical systems, the island-bridge structure merging printing and photolithography successfully demonstrated its application as stretchable dopamine, glucose and lactate sensors. Also used in the fabrication of stretchable BFC patches, the structure allowed the incorporation of thick pellet-type electrodes for high electrochemical performance to deliver at a record-high 1.2 mW/cm^2 power while maintaining good stretchability (**Figure 7.4 B**).[78]

Following development of numerous flexible and stretchable conductive inks and the successful implementation of the selective bonding strategy in printed structure, stencil printing was used for fabricating current collectors in "island-bridge" configuration.[79] Using five different types of ink and seven layers of accurately aligned stencil printing, hexagonal-arranged island-bridge current collectors for a highly stretchable and stable lithium-ion coin-cell battery pack were fabricated (**Figure 7.4 C**). To address the aforementioned challenges individually, multiple engineering strategies were implemented. The current collector features free-standing conductive

serpentine bridges enabled by printing a water-soluble sacrificial layer for high performance stability. The conductive current collector islands, where batteries bond to, were reinforced with rigid polymer backbone layer for minimized tensile strain, hence further ensuring the minimal resistance change during stretching. Several design considerations specific for batteries were also included: to avoid short-circuiting the batteries via the dangling free-standing serpentines, the conductive serpentine bridges are sandwiched by two soft polymer layers for insulation, in addition to a rigid polymer backbone to avoid entanglement during unbuckling. This study emphasizes the importance of the selective bonding and the strain localization strategies to the stability of the device by comparing the resistance across the printed island-bridge structures with and without free-standing serpentines and the strain-confining backbone layers. As illustrated on the bottom left of **Figure 7.4 C**, under 50% strain, the bonded serpentine connecting islands without backbone layers show the highest change in resistance, varying between several **Ω** to tens of k**Ω**. The free-standing serpentine greatly improved the performance, lowering the resistance change by ~ 2 order of magnitudes. However, upon implementing the strain confining backbone layers, the change in the structure resistance dropped by 2 more order of magnitude, with the resistance change confined within 1 **Ω**. Using this all-printed, free-standing island-bridge current collector with backbone layer reinforcement, a highly stable stretchable battery pack was fabricated, delivering power to loads with < 0.1 V voltage and < 0.03 mA current fluctuations when applied with 50% biaxial strain repeatedly.

The all-printed island-bridge structure has enabled various printable applications that accommodate various novel materials. For example, a stretchable biofuel cell epidermal patch was successfully developed using non-stretchable buckypaper as electrodes, as shown in **Figure 7.4 D**.[80] Similar to the pervious example, the buckypaper electrodes were mounted onto polystyrene

reinforced carbon-based islands and were connected by conducive silver bridges that were insulated, reinforced and free-standing from the substrate. Under repeated 20% strain, such biofuel cell delivered a stable current, with only < 1 $\mu A/cm^2$ fluctuation during the deformation. In another recent example, stretchable, eutectic gallium-indium liquid metal (LM) based conductive ink was used to further expand the device stretchability limit.[13] Here, the backbone-reinforced islands were printed directly using non-stretchable inks, thus allowing the entire device - including the interconnections and the functional islands - to be printed. Furthermore, due to the reduced adhesion of the LM ink to the substrate, the stretched serpentine bridges can delaminate from the substrate and become free-standing without the need for a sacrificial layer, hence significantly reducing the fabrication complexity of the island-bridge structure. Endowed by the shape morphing LM particles in the ink, the serpentine structure can be further elongated after reaching its buckling limit while maintaining conductive, thus showing superior stability under extremely large deformations. Leveraging both novel stretchable material and stretchable structures, the all-printed LM-based island-bridge device exhibited stable performance at repeated 100% biaxial strain both as a sensor and as a biofuel cell.

Overall, the adaptation of the island-bridge structure in printed electronics unifies stretchable structures and functional materials in a single printed platform. These structures allow ultra-stable device performance via the use of strain localization strategy, delegating the task of stretchability to the non-functional interconnections. Unlike metal-based island-bridge devices, printed island-bridge devices using soft, composite inks usually require the use of a rigid, strain-confining backbone layers to limit the deformation of the printed islands, as the modulus of the printed composites usually are a few orders of magnitude lower compared to the substrate. The other fabrication considerations used in printed winkles or free-standing serpentines, apply also in

the printed island-bridge devices, and should thus be taken into consideration when designing the device. The low-cost, scalable printing techniques allow the high-throughput fabrication of complex island-bridge devices, and various polymers and composite materials can be used without many considerations in their stretchability. However, such printed devices are limited by the resolution of the selected printing techniques, making it challenging to create devices requiring micron-level features. In addition, as common to island-bridge structures, such printed devices require larger footprints, as considerable amount of area is delegated to the interconnecting bridges, which usually has intricated, tortuous shape designs, and lowers the effective area utilization rate.

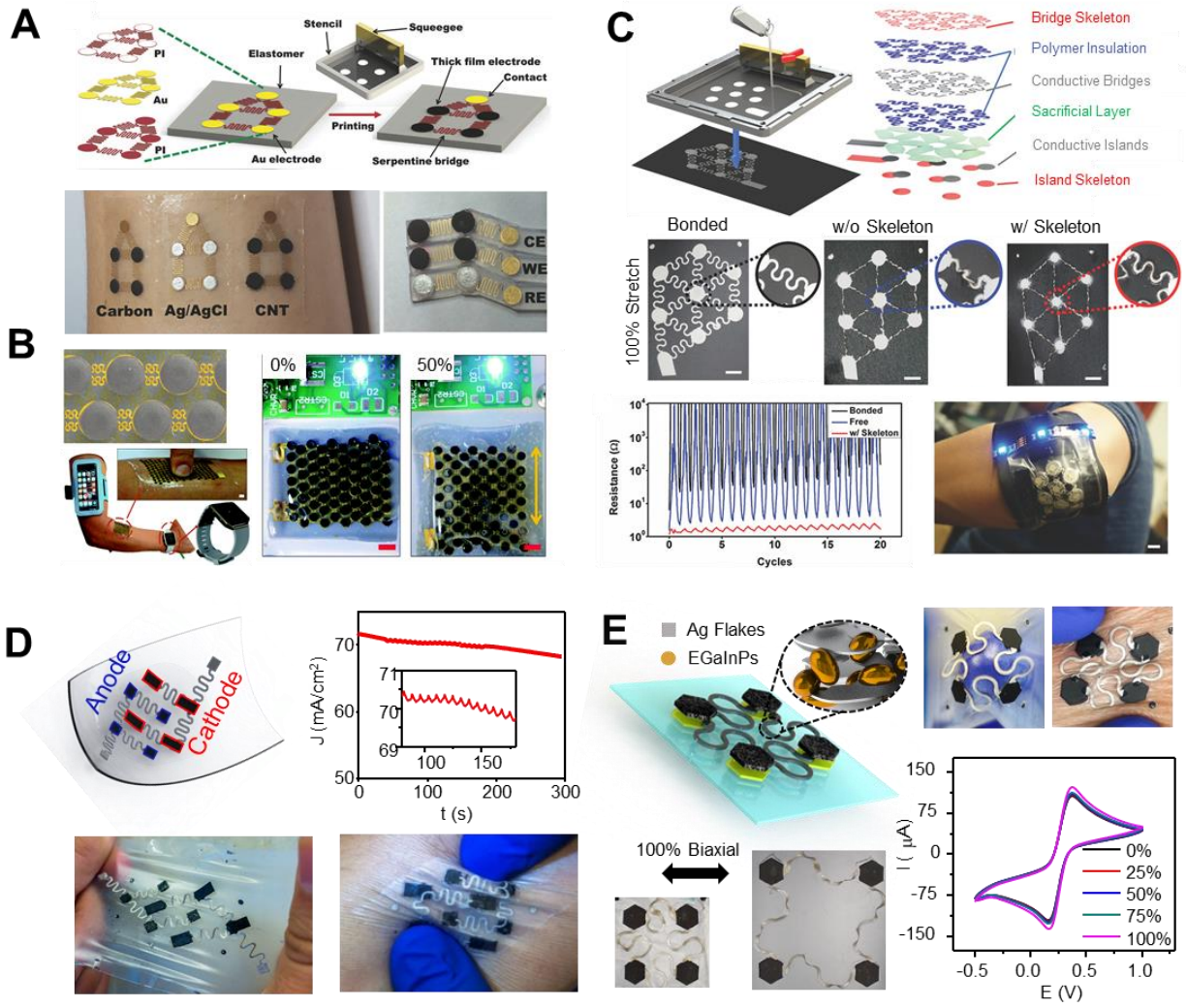

Figure 7.4. Printed island-bridge structures.
A. Illustration of screen-printing on the island region of photolithographically fabricated island-bridge structures (top), and photos of different inks printing onto the island-bridge structure. Reproduced with permission.[33] Copyright 2018, Wiley-VCH. **B**. Photos of the island-bridge structured BFC array and the BFC powering an LED while undergoing 50% strain. Reproduced with permission.[95] Copyright 2017, The Royal Society of Chemistry. **C**. Schematics of the layer-by-layer composition of the island-bridge current collectors (top), photo images of the bonded and partially free-standing island-bridge structure with and without the skeleton layer (middle), the corresponding resistance change during repeated stretching with 100% strain (bottom left), and the assembled battery group on body illuminating LEDs under deformation (bottom right). Reproduced with permission.[96] Copyright 2018, Wiley-VCH. **D**. Schematics and photos of the island-bridge structured buckypaper biofuel cell patch, and its current response under 33 kΩ load with repeated 20% stretch. Reproduced with permission.[6] Copyright 2018, Wiley-VCH. **E**. Schematics and photos of the island-bridge patch with liquid metal serpentine bridges, and the CV response of the patch with different amount of biaxial strain between 0% and 100%. Reproduced with permission.[26] Copyright 2018, Wiley-VCH.

7.5 Transforming beyond 2D

From the transformation from 1D linear interconnects to a tortuous design that occupies a 2D plane, and from the transformation from bonded 2D prints to free-standing structures buckling into the 3D space, printed complex structures offer distinct abilities to release the compressed designs in lower dimensions into the higher dimensions in exchange for stretchability. Such structural innovations in printed electronics have the potential to offer additional functionalities beyond stretchability. Through the introduction of multiple fabrication strategies in direct 2D printing technologies, additional control elements can be offered to prepare more complex structures that fully exploit the 3D space. Furthermore, often referred as "4D printing", the printing of transformative structures that react to external or internal stimulations has also been reported, which holds tremendous implication to establishing smart, responsive devices.[81] Several recent studies have reported on the use of 2D printing techniques to fabricate 3D and 4D structures through the combination of substrate processing, complex 2D designs, selective bonding and controlled buckling, which greatly expanded the functionality of innovative structures beyond stretchability. The strategies, considerations, and challenges of fabricating 3D and 4D structures using planar 2D printing are discussed below in connection to several representative examples.

7.5.1 Buckling from 2D to 3D

3D objects can be easily fabricated by the use of various additive 3D printing techniques or subtractive machining processes, but their production leveraging low-cost, high-throughput 2D printing techniques are often limited, as 2D printing usually relies on the use of flat substrate for deposition. The previous sections introduced several methods of enabling out-of-plane buckling to transforms 2D structure into 3D structures. The work by Xu et. al. introduced the concept of

fabricating 3D structures using buckling to transform mindfully designed 2D photolithographically patterned silicon ribbons and thin films.[82] A series of studies following this concept demonstrated the use of exact control of pre-stretching of elastomeric substrate and its selective bonding to the transferred silicon structures, based on 2D silicon thin films that can readily buckle into various complex 3D structures, such as coils, waves, helixes, tables, flowers and boxes.[82,83] While still relying on costly, complex fabrication techniques, this work leverages the combination of multiple strategies applicable in 2D printing processes.

Inspired by this work, the successful transformation of this concept from photolithographic fabrication to screen printing was firstly presented by Yin et al.[73] Not only combining the aforementioned substrate engineering, selective bonding and strain localization strategies, Yin's study also introduced the concept of programmed buckling to thick-film printing technologies. For this purpose, the sacrificial layer and multiple layers of soft polymer composite inks were printed onto a pre-stretched substrate. Upon dissolving the sacrificial layer and releasing the strain from the substrate, the printed composites were able to buckle into 3D structures. The shape of the 3D structures was "programmed" into the 2D stencil printed designs by the accurate control of the deposition thickness and the appropriate selection of ink composites. Screen printing, as a thick-film technology, uses viscous polymer and composite inks to deposit films with thickness up to several hundreds of microns.[17,73] As illustrated in **Figure 7.5 A**, by depositing multiple layers of inks, the printed 2D structure was segmented into thicker and thinner regions, where the thinner regions were more prone to deformation when applying a buckling stress, as predicted by finite element analysis (FEA). The thicker regions, referred as the "guiding layer", acting similar to the skeleton layer that localizes the strain, define the area where buckling is to be avoided, and direct the strain to the thinner regions, where the majority of the buckling took place. Coupling these

free-standing segmented 2D prints with different levels of pre-stretching on the substrate, allowed the fabrication of various 3D structures, including coils, triangular waves, square waves, tables, and pyramids, via programmed buckling. The selection of material is also crucial when using such strategy, as the localized buckling results in high local tensile stress, which may lead to structural failure if the stress surpasses the ultimate strength of the composite. In this work, a flexible and stretchable elastomer composite ink was used, which allowed the reversible transformation between the 2D and 3D structure without build-up of fatigue, as well as some allowances to stretching deformations without immediate structural failure. Using printing, various functional material, can be deposited onto the guiding layer, which can serve its distinct functionality upon transforming into the programmed 3D structure.

The programmable buckling strategy allows a wide range of structures that can reversibly morph between the 2D and 3D spaces. Cafferty et al. adapted such strategy in the direct printing of elastomeric objects.[84] Adjusting several parameters, including the magnitude and direction of the pre-stretching, the patterns and thickness of the deposited layers, the location of inter-layer bonding, and the mechanical properties of the deposited elastomers, led to a myriad of 3D structures, such as helixes, boxes, tables, and grippers (**Figure 7.5 B**). Furthermore, this work has demonstrated the possibility of pneumatically actuating a gripper structure by introducing pneumatic chambers in the structure via selective bonding between the layers. Overall, the combination of multiple fabrication strategies with programmed buckling allows the printing of diverse complex 3D structures via mechanically buckled 2D planar shapes. When paired with highly scalable printing techniques, which are compatible with a wide range of materials, such strategies pose as a competitive alternative to complex photolithographic methods and 3D printing technologies.

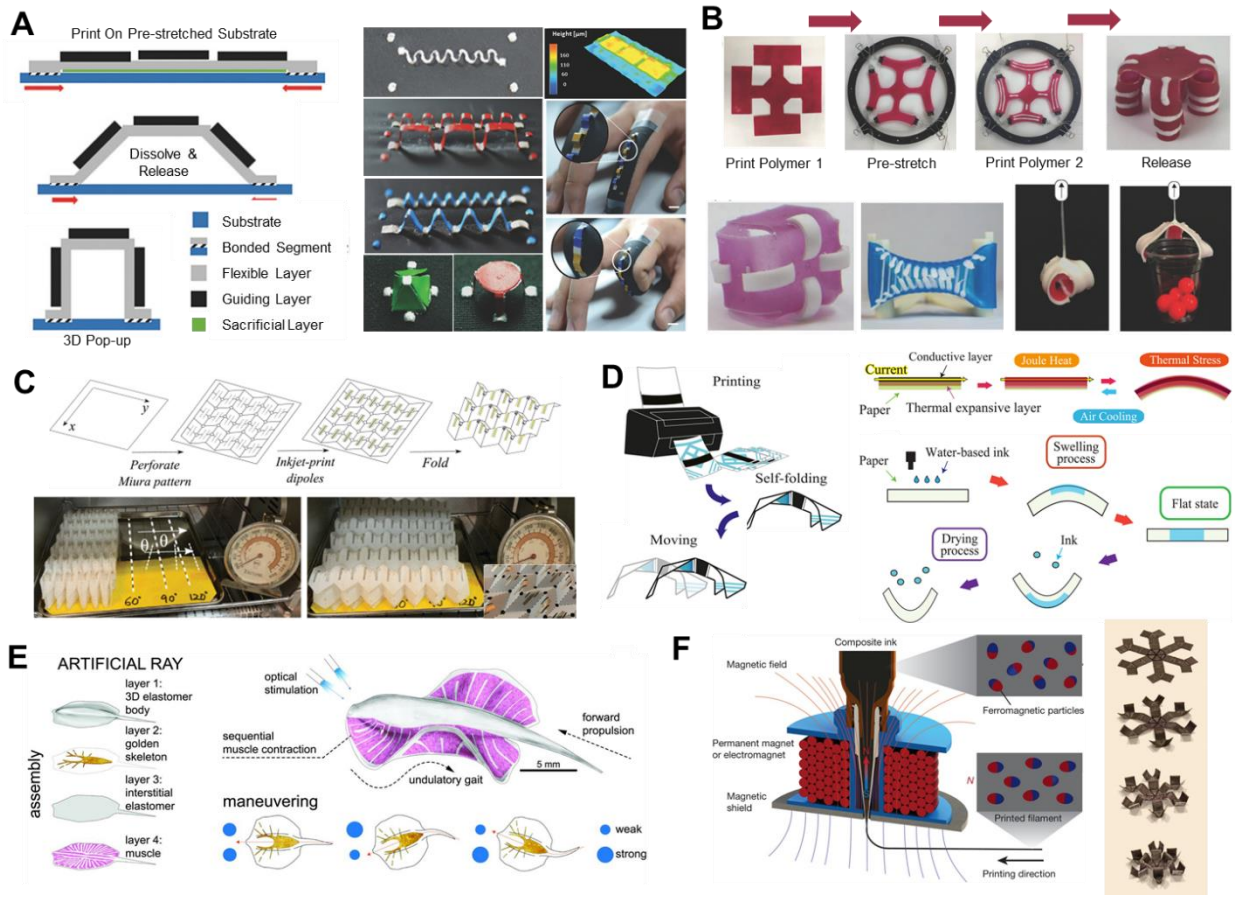

Figure 7.5. Transforming from 2D to 3D and 4D structures.
A. Illustration of the buckling-induced, thickness-guided, 2D-to-3D transformation of printed devices (left), photos of various screen-printed 2D-to-3D structures, and thickness profile of a segment of the printed structure (top right). Reproduced with permission.[91] Copyright 2018, Wiley-VCH. **B**. Photo illustrations of the fabrication of strain-induced 2D-to-3D structures (top) and photo images of fabricated 3D structures and pneumatic actuators. Reproduced with permission.[104] Copyright 2018, Wiley-VCH. **C**. Illustration of the polyester-based, inkjet-printed frequency selective surface using Miura-patterned origami (top) and the shape change of the device induced by heat (bottom). Reproduced with permission.[117] Copyright 2019, IEEE. **D**. Illustrations of inkjet printing of a self-folding and moving paper-based robot, the joule-heating expansion moving mechanism, and the water swelling/drying shape change mechanism. Reproduced with permission.[119] Copyright 2018, IEEE. **E**. Schematics of the layer-by-layer structure and the maneuvering mechanism of the artificial ray soft robot. Reproduced with permission.[126] Copyright 2016, The American Association for the Advancement of Science. **F**. Illustration of the magnetic field aligning ink deposition method of fabricating the magnetic robot (left) and the photo of the shape-morphing of the printed robot. Reproduced with permission.[127] Copyright 2018, Springer Nature and MIT.

7.5.2 From 2D to 4D: smart and responsive structures

The name 4D structures, also known as shape-morphing systems, suggests the ability of the structure to respond to external or internal stimuli using various novel materials to change its shape, and hence to add an extra dimension of time into the design. Different stimuli can be used for such time-depended actuation of structures, including temperature, moisture, pH, light, strain, electric current, and magnetic field, which can cause shape changing in various types of materials, such as hydrogels, polymers, oxides or metals that are shape-memory, photo-reactive, thermo-reactive or hydro-reactive.[85–89] Such devices are commonly fabricated in both 3D printing and planar 2D printing methods, depending on the compatibility of deposited material with different deposition techniques.[89] Several studies have described the planar printing of stimuli-responsive devices using advanced responsive materials for achieving new functionalities such as camouflage, self-healing, controlled dissolution, and shape changing.[90–94] Such printable materials have enabled the planar printing of various types of 4D structures that actuate based on time-dependent deformation. Such deformation can be controlled passively or actively based on the judicious selection of specialized substrates and inks and can be used for imparting additional functionalities beyond enabling flexibility and stretchability. A few examples of the fabrication of such 4D structures based on planar printing techniques are introduced here.

The ancient art of origami relies on the simple technique of folding to transform 2D paper into intricate 3D structures. 4D printing realized the concept of "active origami" by printing responsive materials onto flat substates that can "self-fold" into its pre-programmed structure upon applying the corresponding stimuli. **Figure 7.5 C** displays an example of inkjet-printed active origami based on thermal stimulation.[95] Using substrate engineering, this work demonstrates the actuation of polyester film that folded in Miura structure which expands upon the application of

heat. Conductive traces can be printed onto the film prior to folding to obtain a tunable frequency-selective surface, as the distance between traces - that determines the response frequency - increases and decreases with the temperature change. In another example, water-based ink and low-conductivity carbon ink were used together for the actuation of a paper-based origami robot, where the water-based ink induces local swelling on one side of the paper to achieve self-folding, and the low-conductivity carbon ink undergoes Joule heating to induce thermal stress to the paper substrate to achieve reversible actuation (**Figure 7.5 D)**.[96,97] Such approach leverages simple, scalable fabrication techniques with easily obtainable materials to fabricate simple, rudimentary 4D structures that can undergo reversible shape changing upon applying external stimuli. Relying on the folding of substrate for shape transformations, such printed origami structures must be fabricated with carefully selected substrates and inks that are compatible with the low radius folding deformations. The smoothness of the substrate, the flexibility of the ink and the bonding between the materials must be carefully optimized to avoid cracking, delamination, and disconnection without sacrificing the flexibility and foldability of the device.[98]

The shape changing, relying on varying the chemical or physical environment, enables the global shape change of the entire device. However, achieving additional functionalities will require complex, sequential and localized shape transformations. Such transformations usually rely on stimuli that are more directional, tunable and localizable, such as light, electric signals, or magnetic fields. Complex 2D patterns can be printed, where responsive materials are deposited at designated locations with optimized thicknesses and shapes, to transform these 2D patterns selectively into 3D shape structures upon applying stimuli. **Figure 7.5 E** illustrates a bio-inspired robotic ray fish, where photo-reactive fibronectin is microcontact printed onto elastomeric substrate in serpentine shapes.[99] The activation delay and maneuver of the ray fish were controlled by the serpentine

pattern density and optical stimuli location and frequency, allowing the fish to swim in the controlled direction as the fibronectin "muscles" contract and relax under pulsed optical stimulation on both sides of its body to generate undulatory movements. In another example, Kim et al. demonstrated the printing of ferromagnetic 2D planar structures that can be rapidly transformed into 3D structures under applied magnetic fields.[100] Using direct ink writing with specialized nozzles, a polymer-magnetic particle composite can be printed while being reoriented locally to obtain the desired pre-programmed shape (**Figure 7.5 F**). Upon applying the external magnetic field, 2D structure printed in the Miura-ori, hollow cross, quadrupedal, and hexapedal shapes, can instantly buckle into their corresponding 3D structures according to the magnetic orientation of the printed composite. Such approach can establish a wide range of free-standing untethered 3D structures without the need for substrate pre-stretching, and can reversibly transform the 3D structure back to a 2D planar one upon exerting an external stimulus, making it attractive to the field of soft robotics and printed electronics. Upon selecting a proper soft and flexible stimuli-responsive material, various 2D printing techniques can be implemented to fabricate such 4D smart and responsive structures that react, based on the shape design, strain localization and programmed buckling, to achieve a wide range of important functionalities beyond stretchability.

7.6 Conclusions and Outlook

In this chapter, we have discussed recent advances in the fabrication of innovative structures for printed electronics via various planar printing methods. Compared to microfabrication techniques, subtractive fabrication techniques, and 3D printing techniques, planar printing methods - such as screen printing, inkjet printing, electrohydrodynamic printing, extrusion printing - hold the advantages of low operating cost, high production throughput, and a wide choice of materials. Customized for meeting the specific requirements of individual deposition methods,

inks composed of a wide variety of materials (e.g., polymers, metals, oxides, carbonaceous materials, hydrogels, novel 1D and 2D materials) can thus be formulated and printed onto various substrates to fabricate a wide range of devices for diverse applications including sensing, energy harvesting, energy storage, and soft robotics. Utilizing the combination of material innovations and structural innovations, printed electronics thus possess attractive features, such as flexibility, stretchability, stable performance, and responsiveness to the environment. The strategies used in enabling such novel printed structures have been summarized throughout our text.

We have discussed several printing strategies - substrate engineering, tortuous 2D pattern designs, selective bonding, strain localization, and controlled buckling – that were used to fabricate intricate 2D, 3D, and 4D structures using solely planar printing techniques. Simply by pre-stretching the elastomeric substrate, printed inks can form winkling and wavy structures upon releasing the substrate; while the slow-drying inks allow printed particle-composite to firmly embed into stretchable textiles Such substrate-based strategies endow stretchability to non-stretchable materials or enhance the stretchability of already-stretchable materials. 2D tortuous pattern designs compressing 1D lines into 2D planes to form serpentine structures, which can divert in-plane expansion to bending or out-of-plane buckling upon applied tensile strains. Such strategy can be further paired with the selective bonding strategy, achieved by the kirigami approach or the use of printable sacrificial inks, further allowing the free-standing tortuous structure to buckle out-of-plane for enhanced stretchability while maintaining stable electrical conductivity. When pairing with soft, stretchable printed structures, such free-standing 2D tortuous structures exhibit “two degrees of stretchability” where the buckling and intrinsic elongation take place sequentially during extreme stretching deformation, pushing the limit of stretchability in printed electronics. The serpentine design has thus been the one most adapted structure in printed

stretchable electronics for its efficacy and reliability. Taking such advantage, the “island-bridge” structure combines stretchable structures and non-stretchable functional island materials, establishing a decentralized network where rigid, bonded functional island materials are connected by free-standing stretchable serpentine as bridges. Rigid islands that do not deform easily under tensile stress, can thus accommodate a wide range of materials without the need for re-engineering the materials. Hence, the combination of rigid and soft domains can effectively localize the strain within the stretchable domains and deliver stable performance during stretching deformations using selectively bonded tortuous interconnections. Lastly, as the most sophisticated strategy, programmed buckling enables the transformation of 2D planar designs into various 3D and even 4D structures by accurately control the location, time, and degree of buckling. Used in parallel with advanced 2D shape designs, strain localization, and selective bonding strategies, programmed buckling requires an in-depth understanding of the property of the selected materials and adroit maneuvering of the deposition techniques. As a result, a myriad of functional structures that can morph reversibility from 2D to 3D structures and respond to external stimuli, such as strain, light, heat, current, or magnetic field, can be fabricated using planar printing techniques. These novel structures, printed with advanced fabrication strategies with an increasing amount of structural intricacy and fabrication complexity, have greatly expanded the horizon of traditional printed electronics and enabled new possibilities in the fabrication of functional, responsive, and smart structures.

Despite of such impressive rate of development, the fabrication of novel structures via planar printing methods is still facing many limitations. Currently, the majority of printing techniques are still limited in resolution compared to the microfabrication techniques and are thus not suitable yet for highly miniaturized devices. The printing processes usually involve the

synthesis of inks or slurries that require binders, fillers, and solvents, hence sacrificing their electrical or chemical performance compared to the bulk materials in exchange for processability. The free-standing, buckling-enabled structures are mechanically robust against tensile strain but can be fragile against torsion and shear stress, thus requiring stronger materials for reinforcement to increase their practicality while maintain flexibility and stretchability. Many recent studies have reported novel engineering solutions for addressing the issues of resolution, composite performance, and structural integrity. The conductivity of printed traces can be enhanced by subsequent heat, chemical or photonic sintering to enable close contact among conductive particles.[101] Special materials have been developed using shrinking polymer to obtain sub-micron resolution, and the assembly of various mesostructures with superior mechanical performance has also been proposed in various fabrication processes that can be translated and adapted for planar printing techniques.[102,103] Unlike the microfabrication-based structures, most of the current printed structures are still lacking complementary mechanical studies that systematically summarize their behaviors. Due to the use of unconventional soft composite materials, mechanical studies based on rigid, non-viscoelastic materials cannot be generalized in these situations, and comprehensive studies focusing on the new materials are needed for gaining the insights necessary for guiding the development and improvement of printable structures. Overall, addressing the limitations and enriching the fundamental understanding of the printed materials will greatly expand the possibilities of using planar printing processes for the fabrication of various 3D and 4D structures with high resolution, resiliency, and performance. The enriched mechanical studies will provide understanding of the limitations and possibilities of planar printing as a practical alternative to other complex, low-throughput fabrication techniques.

Looking forward, the structural innovations in printed electronics are steadily advancing toward the development of more intricate and complex structures with additional functionalities. The preparation of such novel structures will rely on the introduction of more advanced fabrication techniques and their integration to previous strategies. Beyond the stretchability endowed by the wavy/wrinkling, textile-embedded or tortuous structures, future printed devices may focus more on the incorporation new properties, such as device stability, conformity, environmental responsiveness, and accurate actuations. Such functionalities will require the use of advanced materials that bend, twist, buckle or expand accurately on command to transform from 2D designs to 3D and 4D structures. The advanced 3D and 4D structures, fabricated using such controlled structural deformations, will allow diverse applications, such as color modulation, frequency regulation, actuation in diverse fields such as sensing, display, energy harvesting, energy storage, soft robotics and more.[90,92,104–106] The introduction of bio-inspired structures can also bring different innovations to the development of printable structures. Macroscopic and microscopic shape-changing structures, found on natural objects for camouflage, reinforcement, rapid actuation or energy-efficient movement, can be readily programmed into printable materials to obtain smart, responsive, untethered, and autonomous 3D and 4D structures.[107,108] Novel fabrication techniques, such as in-mold printing, non-planar stamp printing or hydro dipping, also allow the high-throughput deposition of inks onto non-developable surfaces using planar printing, and their integration with such advanced materials to obtain smart 4D structure is yet to be explored.[109–111] By combining novel structures and advanced fabrication strategies, we envision the development of various devices that are truly resilient, responsive and smart, such as sensors that can morph in respond to the change in the subject, solar cells that can actively trace the direction of sunlight, or robots that can autonomously move, interact and transform, all fabricated using scalable, low-cost

and high-throughput planar printing techniques. By addressing the current limitations and developing novel fabrication strategies, research on structural innovations in printed electronics is expected to have a significant impact towards the preparation of nature-inspired, resilient, autonomous, and multi-stimuli responsive smart flexible devices.

Chapter 7, in full, is a reprint of the material as it appears in Advanced Materials Technologies, 2020, by Lu Yin, Jian lv and Joseph Wang. The dissertation author and Jian Lv were the co-authors of this paper.

7.7 References

1. Xie, K. & Wei, B. Materials and Structures for Stretchable Energy Storage and Conversion Devices. *Advanced Materials* **26**, 3592–3617 (2014).

2. Amjadi, M., Kyung, K.-U., Park, I. & Sitti, M. Stretchable, Skin-Mountable, and Wearable Strain Sensors and Their Potential Applications: A Review. *Advanced Functional Materials* **26**, 1678–1698 (2016).

3. Matsuhisa, N., Chen, X., Bao, Z. & Someya, T. Materials and structural designs of stretchable conductors. *Chem. Soc. Rev.* **48**, 2946–2966 (2019).

4. Song, W.-J. *et al.* Recent Progress in Stretchable Batteries for Wearable Electronics. *Batteries & Supercaps* **2**, 181–199 (2019).

5. Liu, Y., Pharr, M. & Salvatore, G. A. Lab-on-Skin: A Review of Flexible and Stretchable Electronics for Wearable Health Monitoring. *ACS Nano* **11**, 9614–9635 (2017).

6. Chen, D., Lou, Z., Jiang, K. & Shen, G. Device Configurations and Future Prospects of Flexible/Stretchable Lithium-Ion Batteries. *Advanced Functional Materials* **28**, 1805596 (2018).

7. Yan, C. & Lee, P. S. Stretchable Energy Storage and Conversion Devices. *Small* **10**, 3443–3460 (2014).

8. Wang, C., Wang, C., Huang, Z. & Xu, S. Materials and Structures toward Soft Electronics. *Advanced Materials* **30**, 1801368 (2018).

9. Wang, B., Bao, S., Vinnikova, S., Ghanta, P. & Wang, S. Buckling analysis in stretchable electronics. *npj Flexible Electronics* **1**, 1–9 (2017).

10. Benight, S. J., Wang, C., Tok, J. B. H. & Bao, Z. Stretchable and self-healing polymers and devices for electronic skin. *Progress in Polymer Science* **38**, 1961–1977 (2013).

11. Ahn, J.-H. & Je, J. H. Stretchable electronics: materials, architectures and integrations. *J. Phys. D: Appl. Phys.* **45**, 103001 (2012).

12. Dang, W., Vinciguerra, V., Lorenzelli, L. & Dahiya, R. Printable stretchable interconnects. *Flex. Print. Electron.* **2**, 013003 (2017).

13. Silva, C. A. *et al.* Liquid Metal Based Island-Bridge Architectures for All Printed Stretchable Electrochemical Devices. *Advanced Functional Materials* **30**, 2002041 (2020).

14. Yao, S. *et al.* Nanomaterial-Enabled Flexible and Stretchable Sensing Systems: Processing, Integration, and Applications. *Advanced Materials* **32**, 1902343 (2020).

15. Fernandes, D. F., Majidi, C. & Tavakoli, M. Digitally printed stretchable electronics: a review. *J. Mater. Chem. C* **7**, 14035–14068 (2019).

16. Kim, D.-H., Xiao, J., Song, J., Huang, Y. & Rogers, J. A. Stretchable, Curvilinear Electronics Based on Inorganic Materials. *Advanced Materials* **22**, 2108–2124 (2010).

17. Kim, J., Kumar, R., Bandodkar, A. J. & Wang, J. Advanced Materials for Printed Wearable Electrochemical Devices: A Review. *Advanced Electronic Materials* **3**, 1600260 (2017).

18. Mohan, A. M. V. *et al.* Merging of Thin- and Thick-Film Fabrication Technologies: Toward Soft Stretchable "Island–Bridge" Devices. *Advanced Materials Technologies* **2**, 1600284 (2017).

19. Huang, Q. & Zhu, Y. Printing Conductive Nanomaterials for Flexible and Stretchable Electronics: A Review of Materials, Processes, and Applications. *Advanced Materials Technologies* **4**, 1800546 (2019).

20. Tang, Y. *et al.* Programmable Kiri-Kirigami Metamaterials. *Advanced Materials* **29**, 1604262 (2017).

21. Tanaka, T. *et al.* Mechanical instability of gels at the phase transition. *Nature* **325**, 796–798 (1987).

22. Khang, D.-Y., Jiang, H., Huang, Y. & Rogers, J. A. A Stretchable Form of Single-Crystal Silicon for High-Performance Electronics on Rubber Substrates. *Science* **311**, 208–212 (2006).

23. Wang, L. *et al.* Weaving Sensing Fibers into Electrochemical Fabric for Real-Time Health Monitoring. *Advanced Functional Materials* **28**, 1804456 (2018).

24. Jost, K. *et al.* Knitted and screen printed carbon-fiber supercapacitors for applications in wearable electronics. *Energy & Environmental Science* **6**, 2698 (2013).

25. Dong, K., Peng, X. & Wang, Z. L. Fiber/Fabric-Based Piezoelectric and Triboelectric Nanogenerators for Flexible/Stretchable and Wearable Electronics and Artificial Intelligence. *Advanced Materials* **32**, 1902549 (2020).

26. Jin, H. *et al.* Enhancing the Performance of Stretchable Conductors for E-Textiles by Controlled Ink Permeation. *Advanced Materials* **29**, 1605848 (2017).

27. Pang, S., Gao, Y. & Choi, S. Flexible and Stretchable Biobatteries: Monolithic Integration of Membrane-Free Microbial Fuel Cells in a Single Textile Layer. *Advanced Energy Materials* **8**, 1702261 (2018).

28. Gaikwad, A. M. *et al.* Highly Stretchable Alkaline Batteries Based on an Embedded Conductive Fabric. *Advanced Materials* **24**, 5071–5076 (2012).

29. Shyu, T. C. *et al.* A kirigami approach to engineering elasticity in nanocomposites through patterned defects. *Nature Materials* **14**, 785–789 (2015).

30. Song, Z. *et al.* Kirigami-based stretchable lithium-ion batteries. *Scientific Reports* **5**, 10988 (2015).

31. Lamoureux, A., Lee, K., Shlian, M., Forrest, S. R. & Shtein, M. Dynamic kirigami structures for integrated solar tracking. *Nature Communications* **6**, 8092 (2015).

32. Bowden, N., Brittain, S., Evans, A. G., Hutchinson, J. W. & Whitesides, G. M. Spontaneous formation of ordered structures in thin films of metals supported on an elastomeric polymer. *Nature* **393**, 146–149 (1998).

33. Jiang, H. *et al.* Finite deformation mechanics in buckled thin films on compliant supports. *PNAS* **104**, 15607–15612 (2007).

34. Song, J. *et al.* Buckling of a stiff thin film on a compliant substrate in large deformation. *International Journal of Solids and Structures* **45**, 3107–3121 (2008).

35. Khang, D.-Y., Rogers, J. A. & Lee, H. H. Mechanical Buckling: Mechanics, Metrology, and Stretchable Electronics. *Advanced Functional Materials* **19**, 1526–1536 (2009).

36. Lee, Y., Shin, M., Thiyagarajan, K. & Jeong, U. Approaches to Stretchable Polymer Active Channels for Deformable Transistors. *Macromolecules* **49**, 433–444 (2016).

37. Tang, J. *et al.* Highly Stretchable Electrodes on Wrinkled Polydimethylsiloxane Substrates. *Scientific Reports* **5**, 16527 (2015).

38. Yin, D. *et al.* Mechanically robust stretchable organic optoelectronic devices built using a simple and universal stencil-pattern transferring technology. *Light: Science & Applications* **7**, 35 (2018).

39. Bae, H. J. *et al.* Self-organization of maze-like structures via guided wrinkling. *Science Advances* **3**, e1700071 (2017).

40. Kim, D.-H. *et al.* Stretchable and Foldable Silicon Integrated Circuits. *Science* **320**, 507–511 (2008).

41. Wu, M.-Y. *et al.* Highly stretchable carbon nanotube transistors enabled by buckled ion gel gate dielectrics. *Appl. Phys. Lett.* **107**, 053301 (2015).

42. Weng, W. *et al.* A Gum-Like Lithium-Ion Battery Based on a Novel Arched Structure. *Advanced Materials* **27**, 1363–1369 (2015).

43. Lee, J., Chung, S., Song, H., Kim, S. & Hong, Y. Lateral-crack-free, buckled, inkjet-printed silver electrodes on highly pre-stretched elastomeric substrates. *J. Phys. D: Appl. Phys.* **46**, 105305 (2013).

44. Xiong, J. & Lee, P. S. Progress on wearable triboelectric nanogenerators in shapes of fiber, yarn, and textile. *Science and Technology of Advanced Materials* **20**, 837–857 (2019).

45. Lu, N. & Kim, D.-H. Flexible and Stretchable Electronics Paving the Way for Soft Robotics. *Soft Robotics* **1**, 53–62 (2013).

46. Zhang, Y., Huang, Y. & Rogers, J. A. Mechanics of stretchable batteries and supercapacitors. *Current Opinion in Solid State and Materials Science* **19**, 190–199 (2015).

47. Zhang, Y. *et al.* Experimental and Theoretical Studies of Serpentine Microstructures Bonded To Prestrained Elastomers for Stretchable Electronics. *Advanced Functional Materials* **24**, 2028–2037 (2014).

48. Lu, N. & Yang, S. Mechanics for stretchable sensors. *Current Opinion in Solid State and Materials Science* **19**, 149–159 (2015).

49. Zhang, Y. *et al.* Mechanics of ultra-stretchable self-similar serpentine interconnects. *Acta Materialia* **61**, 7816–7827 (2013).

50. Su, Y. *et al.* In-Plane Deformation Mechanics for Highly Stretchable Electronics. *Advanced Materials* **29**, 1604989 (2017).

51. Rogers, J. A., Someya, T. & Huang, Y. Materials and Mechanics for Stretchable Electronics. *Science* **327**, 1603–1607 (2010).

52. Jang, K.-I. *et al.* Soft network composite materials with deterministic and bio-inspired designs. *Nature Communications* **6**, 6566 (2015).

53. Huang, Y. *et al.* Hyper-stretchable self-powered sensors based on electrohydrodynamically printed, self-similar piezoelectric nano/microfibers. *Nano Energy* **40**, 432–439 (2017).

54. Han, Y. & Dong, J. Electrohydrodynamic (EHD) Printing of Molten Metal Ink for Flexible and Stretchable Conductor with Self-Healing Capability. *Advanced Materials Technologies* **3**, 1700268 (2018).

55. Bower, I. A., Taylor, C. L. & Sitaraman, S. K. Study of inkjet-printed serpentine structure on flexible substrates deformed over sculptured surfaces. *Flex. Print. Electron.* **5**, 015010 (2020).

56. Ambrosi, A. & Pumera, M. 3D-printing technologies for electrochemical applications. *Chem. Soc. Rev.* **45**, 2740–2755 (2016).

57. Herbert, R., Mishra, S., Lim, H.-R., Yoo, H. & Yeo, W.-H. Fully Printed, Wireless, Stretchable Implantable Biosystem toward Batteryless, Real-Time Monitoring of Cerebral Aneurysm Hemodynamics. *Advanced Science* **6**, 1901034 (2019).

58. Yang, S., Ng, E. & Lu, N. Indium Tin Oxide (ITO) serpentine ribbons on soft substrates stretched beyond 100%. *Extreme Mechanics Letters* **2**, 37–45 (2015).

59. Joo, H., Jung, D., Sunwoo, S.-H., Koo, J. H. & Kim, D.-H. Material Design and Fabrication Strategies for Stretchable Metallic Nanocomposites. *Small* **16**, 1906270 (2020).

60. Lv, J. *et al.* Sweat-based wearable energy harvesting-storage hybrid textile devices. *Energy Environ. Sci.* **11**, 3431–3442 (2018).

61. Abellán-Llobregat, A. *et al.* A stretchable and screen-printed electrochemical sensor for glucose determination in human perspiration. *Biosensors and Bioelectronics* **91**, 885–891 (2017).

62. Bandodkar, A. J., Nuñez-Flores, R., Jia, W. & Wang, J. All-Printed Stretchable Electrochemical Devices. *Advanced Materials* **27**, 3060–3065 (2015).

63. Mishra, R. K. *et al.* Wearable Flexible and Stretchable Glove Biosensor for On-Site Detection of Organophosphorus Chemical Threats. *ACS Sens.* **2**, 553–561 (2017).

64. Cánovas, R., Parrilla, M., Mercier, P., Andrade, F. J. & Wang, J. Balloon-Embedded Sensors Withstanding Extreme Multiaxial Stretching and Global Bending Mechanical Stress: Towards Environmental and Security Monitoring. *Advanced Materials Technologies* **1**, 1600061 (2016).

65. Jeerapan, I., Sempionatto, J. R., Pavinatto, A., You, J.-M. & Wang, J. Stretchable biofuel cells as wearable textile-based self-powered sensors. *J. Mater. Chem. A* **4**, 18342–18353 (2016).

66. Parrilla, M., Cánovas, R., Jeerapan, I., Andrade, F. J. & Wang, J. A Textile-Based Stretchable Multi-Ion Potentiometric Sensor. *Advanced Healthcare Materials* **5**, 996–1001 (2016).

67. Lopez, L. *et al.* Electrochemistry on Stretchable Nanocomposite Electrodes: Dependence on Strain. *ACS Nano* **12**, 9223–9232 (2018).

68. Bandodkar, A. J., Jeerapan, I., You, J.-M., Nuñez-Flores, R. & Wang, J. Highly Stretchable Fully-Printed CNT-Based Electrochemical Sensors and Biofuel Cells: Combining Intrinsic and Design-Induced Stretchability. *Nano Lett.* **16**, 721–727 (2016).

69. Jin, L. *et al.* Microstructural origin of resistance–strain hysteresis in carbon nanotube thin film conductors. *PNAS* **115**, 1986–1991 (2018).

70. Yang, S. *et al.* "Cut-and-Paste" Manufacture of Multiparametric Epidermal Sensor Systems. *Advanced Materials* **27**, 6423–6430 (2015).

71. Jing, Q. *et al.* Freestanding Functional Structures by Aerosol-Jet Printing for Stretchable Electronics and Sensing Applications. *Advanced Materials Technologies* **4**, 1900048 (2019).

72. Li, X. *et al.* Large-area, kirigami topology structure-induced highly stretchable and flexible interconnects: Directly printing preparation and mechanic mechanism. *Sci. China Mater.* **62**, 1412–1422 (2019).

73. Yin, L. *et al.* From All-Printed 2D Patterns to Free-Standing 3D Structures: Controlled Buckling and Selective Bonding. *Advanced Materials Technologies* **3**, 1800013 (2018).

74. Xue, Z., Song, H., Rogers, J. A., Zhang, Y. & Huang, Y. Mechanically-Guided Structural Designs in Stretchable Inorganic Electronics. *Advanced Materials* **32**, 1902254 (2020).

75. Kumar, R. *et al.* All-Printed, Stretchable Zn-Ag2O Rechargeable Battery via Hyperelastic Binder for Self-Powering Wearable Electronics. *Advanced Energy Materials* **7**, 1602096 (2017).

76. Zhang, Y. *et al.* Buckling in serpentine microstructures and applications in elastomer-supported ultra-stretchable electronics with high areal coverage. *Soft Matter* **9**, 8062–8070 (2013).

77. Zhang, Y. *et al.* A hierarchical computational model for stretchable interconnects with fractal-inspired designs. *Journal of the Mechanics and Physics of Solids* **72**, 115–130 (2014).

78. Bandodkar, A. J. *et al.* Soft, stretchable, high power density electronic skin-based biofuel cells for scavenging energy from human sweat. *Energy Environ. Sci.* **10**, 1581–1589 (2017).

79. Yin, L. *et al.* Highly Stable Battery Pack via Insulated, Reinforced, Buckling-Enabled Interconnect Array. *Small* **14**, 1800938 (2018).

80. Chen, X. *et al.* Stretchable and Flexible Buckypaper-Based Lactate Biofuel Cell for Wearable Electronics. *Advanced Functional Materials* **29**, 1905785 (2019).

81. Kuang, X. *et al.* Advances in 4D Printing: Materials and Applications. *Advanced Functional Materials* **29**, 1805290 (2019).

82. Xu, S. *et al.* Assembly of micro/nanomaterials into complex, three-dimensional architectures by compressive buckling. *Science* **347**, 154–159 (2015).

83. Zhang, Y. *et al.* A mechanically driven form of Kirigami as a route to 3D mesostructures in micro/nanomembranes. *Proc Natl Acad Sci USA* **112**, 11757–11764 (2015).

84. Cafferty, B. J. *et al.* Fabricating 3D Structures by Combining 2D Printing and Relaxation of Strain. *Advanced Materials Technologies* **4**, 1800299 (2019).

85. Gracias, D. H. Stimuli responsive self-folding using thin polymer films. *Current Opinion in Chemical Engineering* **2**, 112–119 (2013).

86. Ahmed, S. *et al.* Multi-Field Responsive Origami Structures: Preliminary Modeling and Experiments. in *Proceedings of the ASME 2013 International Design Engineering Technical Conferences and Computers and Information in Engineering Conference* vol. 6B (American Society of Mechanical Engineers Digital Collection, 2014).

87. Gu, H., Boehler, Q., Ahmed, D. & Nelson, B. J. Magnetic quadrupole assemblies with arbitrary shapes and magnetizations. *Science Robotics* **4**, eaax8977 (2019).

88. Cui, J. *et al.* Nanomagnetic encoding of shape-morphing micromachines. *Nature* **575**, 164–168 (2019).

89. Lambert, C.-H. *et al.* All-optical control of ferromagnetic thin films and nanostructures. *Science* **345**, 1337–1340 (2014).

90. Karshalev, E. *et al.* Multistimuli-Responsive Camouflage Swimmers. *Chem. Mater.* **30**, 1593–1601 (2018).

91. Bandodkar, A. J. *et al.* All-printed magnetically self-healing electrochemical devices. *Science Advances* **2**, e1601465 (2016).

92. Karshalev, E. *et al.* Small-Scale Propellers Deliver Miniature Versions of Themselves. *Small* **16**, 2000453 (2020).

93. Yin, L. *et al.* Dissolvable Metals for Transient Electronics. *Advanced Functional Materials* **24**, 645–658 (2014).

94. Grau, G., Frazier, E. J. & Subramanian, V. Printed unmanned aerial vehicles using paper-based electroactive polymer actuators and organic ion gel transistors. *Microsystems & Nanoengineering* **2**, 1–8 (2016).

95. Nauroze, S. A. & Tentzeris, M. M. A Thermally Actuated Fully Inkjet-Printed Origami-Inspired Multilayer Frequency Selective Surface With Continuous-Range Tunability Using Polyester-Based Substrates. *IEEE Transactions on Microwave Theory and Techniques* **67**, 4944–4954 (2019).

96. Shigemune, H., Maeda, S., Hara, Y. & Hashimoto, S. Design of paper mechatronics: Towards a fully printed robot. in *2014 IEEE/RSJ International Conference on Intelligent Robots and Systems* 536–541 (2014). doi:10.1109/IROS.2014.6942611.

97. Shigemune, H., Maeda, S., Hara, Y., Hosoya, N. & Hashimoto, S. Origami Robot: A Self-Folding Paper Robot With an Electrothermal Actuator Created by Printing. *IEEE/ASME Transactions on Mechatronics* **21**, 2746–2754 (2016).

98. Nogi, M., Komoda, N., Otsuka, K. & Suganuma, K. Foldable nanopaper antennas for origami electronics. *Nanoscale* **5**, 4395–4399 (2013).

99. Park, S.-J. *et al.* Phototactic guidance of a tissue-engineered soft-robotic ray. *Science* **353**, 158–162 (2016).

100. Kim, Y., Yuk, H., Zhao, R., Chester, S. A. & Zhao, X. Printing ferromagnetic domains for untethered fast-transforming soft materials. *Nature* **558**, 274–279 (2018).

101. Kamyshny, A. & Magdassi, S. Conductive nanomaterials for 2D and 3D printed flexible electronics. *Chem. Soc. Rev.* **48**, 1712–1740 (2019).

102. Zhang, Y. *et al.* Printing, folding and assembly methods for forming 3D mesostructures in advanced materials. *Nature Reviews Materials* **2**, 1–17 (2017).

103. Gong, J. *et al.* Complexation-induced resolution enhancement of 3D-printed hydrogel constructs. *Nature Communications* **11**, 1267 (2020).

104. Shih, B. *et al.* Electronic skins and machine learning for intelligent soft robots. *Science Robotics* **5**, eaaz9239 (2020).

105. Mackanic, D. G., Chang, T.-H., Huang, Z., Cui, Y. & Bao, Z. Stretchable electrochemical energy storage devices. *Chem. Soc. Rev.* **49**, 4466–4495 (2020).

106. Patel, B. B. *et al.* Tunable structural color of bottlebrush block copolymers through direct-write 3D printing from solution. *Science Advances* **6**, eaaz7202 (2020).

107. Erb, R. M., Sander, J. S., Grisch, R. & Studart, A. R. Self-shaping composites with programmable bioinspired microstructures. *Nature Communications* **4**, 1712 (2013).

108. R. Studart, A. & M. Erb, R. Bioinspired materials that self-shape through programmed microstructures. *Soft Matter* **10**, 1284–1294 (2014).

109. Sim, K. *et al.* Three-dimensional curvy electronics created using conformal additive stamp printing. *Nature Electronics* **2**, 471–479 (2019).

110. Kao, H. In-Mold Decorating: A Review of Process and Technology. *Plastics Engineering* **74**, 40–43 (2018).

111. Le Borgne, B., De Sagazan, O., Crand, S., Jacques, E. & Harnois, M. Conformal Electronics Wrapped Around Daily Life Objects Using an Original Method: Water Transfer Printing. *ACS Appl. Mater. Interfaces* **9**, 29424–29429 (2017).

Chapter 8 Conclusion and Future Directions

8.1 Theoretical Limits and Limitations

Alongside the boom in consumer wearable electronics, researchers have pursued during the past 15 years next-generation wearable electronics featuring thin, soft, conformal, flexible, and stretchable form factors for applications in advanced human-machine interaction and comprehensive sensing. These efforts have conceived a wide class of wearable sensors, displays, integrated circuits, batteries, supercapacitors, and energy harvesters, that assemble into an ecosystem of future wearable devices.[1,2] Similar to other types of electronics, wearable electronics require a constant power source for uninterrupted operation. As the demand for wearable electronics grows, so does the demand for wearable power sources. Excitingly, the concept of self-powered wearable systems has recently gained increasing popularity, entailing the integration of energy harvesters and energy storage devices to wearable electronics towards the energy-autonomous extended on-body operation.[1] While the research for wearable energy harvesting and storage devices and the integration thereof are soaring, to this day, most of them have not been able to meet the energy demands of the majority of existing wearable applications. As examples, wireless earbuds or smartwatches use 300-1500 mWh batteries, while most of flexible batteries feature less than 5 mWh/cm^2 energy; low-power microcontrollers for wearable sensors typically require 1-100 mW power input, while wearable bioenergy harvesters can only harvest <1 mW/cm^2 power.[1] Such major gaps between energy demand and supply become the bottleneck of the ecosystem. To date, few wearable electronics possessing ubiquitous conformity and flexibility and compatible with diverse lifestyles, exist on the market. While the performance of wearable energy devices has certainly not reached its full potential, yet many practical factors hinder the development of the next-generation commercially viable wearable electronics. This chapter

summarizes the theoretical limits and the practical limitations of wearable energy devices towards addressing these major issues (**Figure 8.1**).

Many electrochemical energy storage devices, predominantly batteries, and supercapacitors have been developed into soft wearable form factors.[3] While some compromises between mechanical flexibility and electrical performance must be made, wearable energy storage devices with high power and energy density have been reported, including Li-ion batteries (538 Wh/L), Zn batteries (300 Wh/L), supercapacitors (88.1 Wh/L), which are close to those of their commercial, non-wearable rigid counterparts.[4–6] In addition, battery and supercapacitor technologies still have plenty of room for improvement towards approaching the theoretical limit of the specific energies for Li-air metal battery and Zn-air battery of ca. 5 Wh/g and 1 Wh/g, respectively, which may be also obtainable one day for wearable batteries.[7] On the other hand, a myriad of energy harvesting devices - based on photovoltaic, electromagnetic, piezoelectric, triboelectric, thermoelectric, and electrobiocatalytic energy conversion mechanisms - has also been developed.[8] The integration of multiple harvesting mechanisms into a "wearable microgrid" can potentially maximize the energy harvestable using wearable devices, with the theoretical limit of harvesting a few hundred watts from bodily movements as well as from the sunlight and heat.[1] This allows the maximum of hundreds of watt-hours of energy harvestable from wearables, which can sustain the continuous and autonomous operation of the majority of consumer electronics on the market. Assuming reaching only 50% of the theoretical energy density of batteries and only 1 % of the theoretical efficiency for energy harvesters, their performance would still be practical and attractive for commercialization. However, the reality is that many practical limitations still exist, and we are still very far away from reaching these fundamental limits of the wearable energy system.

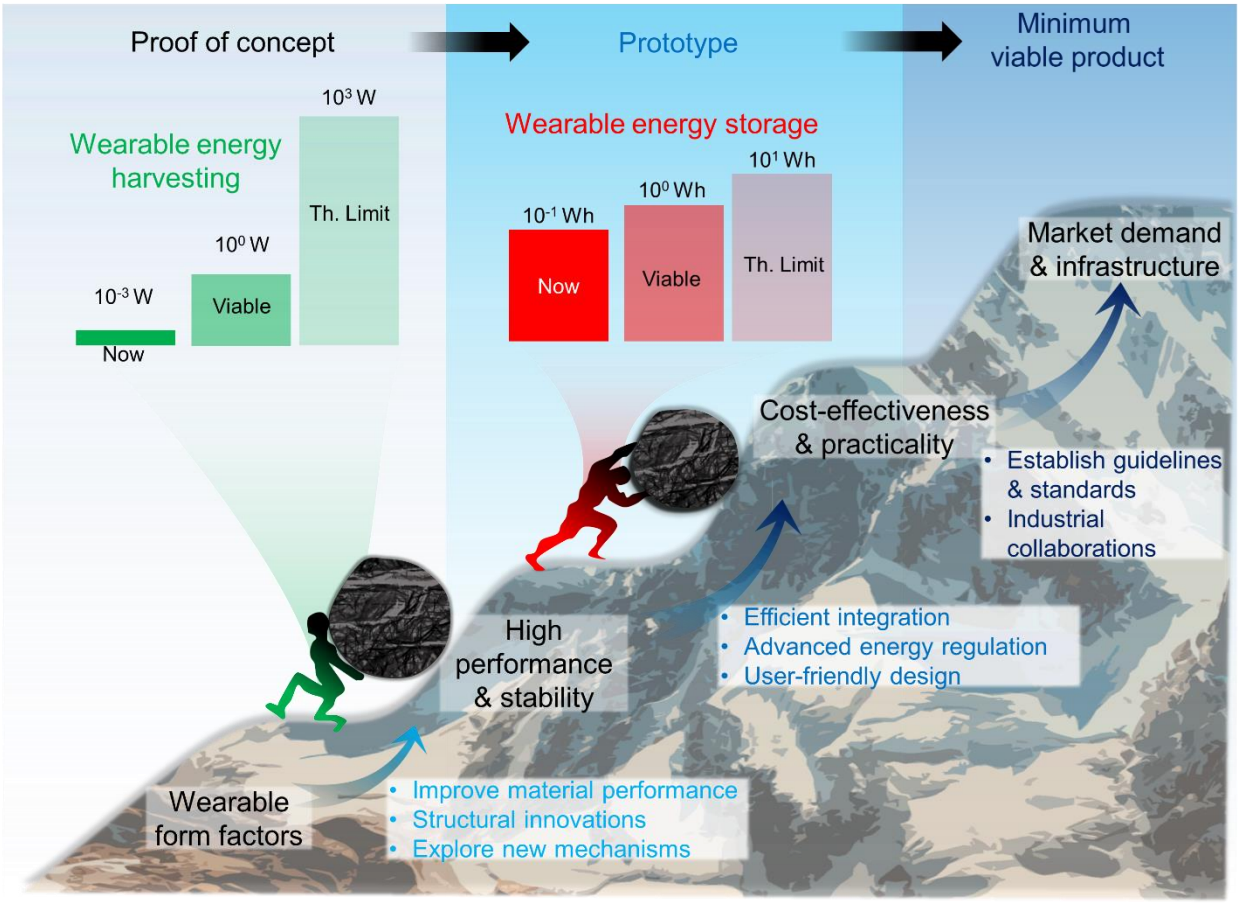

Figure 8.1. Theoretical limits of performance, practical limitations, and potential solutions for the next-generation wearable energy harvesting and storage devices from the proof of concept to commercialization.

8.2 Future Directions of Wearable Energy Systems

To our belief, the most immediate limitation of soft wearable electronics is the lack of a high-performance flexible battery. While many companies have developed small, safe, thin and flexible batteries, they are characterized by low energy (below 100 mWh) and low power (below 10 mW), due to trade-offs between compactness and flexibility of structures (e.g., kirigami/origami), or between the electrochemical and mechanical performance of materials. These small flexible batteries thus are unable to power existing integrated circuits

(microcontrollers, microprocessors, system-on-chip, etc.) with basic computing, storage, and wireless transmission capabilities that typically require 20 – 100 mW power and active runtime of at least several hours.[1] Although flexible batteries with performance comparable to that of existing Li-ion or Li coin cells have been reported recently,[3,9] their commercialization may still face many practical limitations. As of now, most wearable original electronics manufacturers (OEM) elect to use bulky and non-flexible Li-ion or lithium-polymer pouch cells due to their stable performance, abundant supply, and well-established "infrastructures", including their form factors, connection conventions, and energy management solutions. On the other hand, soft battery technologies usually do not deliver sufficient performance and lack the established infrastructure. As the result, current OEMs have little incentive to adopt new flexible energy storage technologies, and new technologies facing very low immediate market demand and require heavy research and development (R&D) cost in developing the auxiliary ecosystem while forming a technological gridlock.

On the other hand, after over a decade of development, wearable energy harvesters, are still limited significantly in their performance and practicality. Despite frequent media coverage of various attractive wearable prototypes, few wearable products with integrated energy harvesters are commercially available for practical consumer use. While countless wearable energy harvesters with great mechanical flexibility, stretchability, and conformity have been reported, their areal powers are below 5 mW per cm^2 and total harvestable energy is only < 10 mWh per day, making them not practical even for most of the low-power wearable applications. The conversion of these thermal, biomechanical and biochemical energies into electrical energy is characterized by extremely low efficiency, due to limitations in both the bulk material performance, device architecture, and their respective energy regulation. Using these energy sources in most

wearable systems is characterized by intermittent supply and demands constant high-frequency movement, high temperature gradient, or heavy sweating, therefore deemed low "energy return-on-investment", non-user-friendly, and impractical.[10] Wearable energy harvesters that work continuously and lead to high levels of electrical energy generation are required. Beyond these, many harvesting devices have limitations in cost, scalability, biocompatibility, washability, and long-term durability, hence restricting their practical viability in commercial wearable systems.

Enabling the next-generation wearable electronics hinges heavily on addressing the challenges involved in approaching the theoretical limits of wearable energy systems. Encouragingly, the current trend in developing product-like integrated wearable systems has promoted interdisciplinary collective efforts in material and structural engineering, electrochemistry, power regulation, energy harvesting and storage, circuit design and programming, product design, and manufacturing. Furthermore, recent development in ultra-low-power electronics, long-range wireless power delivery, and dual-function devices (e.g., photo-rechargeable batteries, self-charging biosupercapacitors, self-powered sensors) can revolutionize the current design concepts of integrated wearable systems. We believe that such multi-disciplinary efforts will identify and address the missing links in the wearable ecosystem. In addition, extensive efforts should be directed towards improving device performance, efficiency, and durability, as well as exploring new energy harvesting and storage mechanisms towards significantly higher energy outputs. Universal testing, design guidelines, standards, and reporting protocols on flexibility, stretchability, and washability (similar to those of certifying solar cells), should be established for fair assessment and proper comparison of the performance of wearable energy harvesting and storage devices. Upper-level efforts channeling industrial R&D with academic research output can facilitate breaking the technological gridlock, ensuring a market-

demand-guided development of wearable energy devices, and aiding OEMs' transition from legacy energy solutions to the next generation of efficient and practical wearable energy systems. With these efforts, we trust the next-generation wearable soft electronics will morph from the hype of today to the practical reality of tomorrow.

Chapter 8, in full, is a reprint of the material as it appears in National Science Review, 2022, by Lu Yin and Joseph Wang. The dissertation author was the primary author of this paper.

8.3 References

1. Yin, L., Kim, K. N., Trifonov, A., Podhajny, T. & Wang, J. Designing wearable microgrids: towards autonomous sustainable on-body energy management. *Energy Environ. Sci.* (2021) doi:10.1039/D1EE03113A.

2. Heng, W., Solomon, S. & Gao, W. Flexible Electronics and Devices as Human-Machine Interfaces for Medical Robotics. *Advanced Materials* 2107902 doi:10.1002/adma.202107902.

3. G. Mackanic, D., Chang, T.-H., Huang, Z., Cui, Y. & Bao, Z. Stretchable electrochemical energy storage devices. *Chemical Society Reviews* **49**, 4466–4495 (2020).

4. Yang, Q. *et al.* Categorizing wearable batteries: Unidirectional and omnidirectional deformable batteries. *Matter* **4**, 3146–3160 (2021).

5. MacKenzie, J. D. & Ho, C. Perspectives on Energy Storage for Flexible Electronic Systems. *Proceedings of the IEEE* **103**, 535–553 (2015).

6. Li, Z. *et al.* Tuning the interlayer spacing of graphene laminate films for efficient pore utilization towards compact capacitive energy storage. *Nat Energy* **5**, 160–168 (2020).

7. Lee, J.-S. *et al.* Metal-Air Batteries with High Energy Density: Li-Air versus Zn-Air. *Advanced Energy Materials* **1**, 34–50 (2011).

8. Gao, M. *et al.* Power generation for wearable systems. *Energy Environ. Sci.* **14**, 2114 (2021).

9. Yin, L. *et al.* High Performance Printed AgO-Zn Rechargeable Battery for Flexible Electronics. *Joule* **5**, 228–248 (2021).

10. Yin, L. *et al.* A passive perspiration biofuel cell: High energy return on investment. *Joule* **5**, 1888–1904 (2021).